DESIGN, SYNTHESIS AND BIOLOGICAL SCREENING OF SOME GLUTAMINE BASED ZINC-DEPENDENT METALLOENZYMES ESPECIALLY HDAC8 AND DUAL MMP2 AND MMP9 INHIBITORS FOR THE MANAGEMENT OF HEMATOLOGICAL CANCER

Thesis Submitted by

SANJIB DAS

Doctor of Philosophy (Pharmacy)

DEPARTMENT OF PHARMACEUTICAL TECHNOLOGY

FACULTY COUNCIL OF ENGINEERING & TECHNOLOGY

JADAVPUR UNIVERSITY

KOLKATA, INDIA

2024

JADAVPUR UNIVERSITY
KOLKATA – 700032, INDIA

Registration No. 1021913004 **Index No. 278/19/Ph**

1. Title of the Thesis:

Design, synthesis and biological screening of some glutamine based zinc-dependent metalloenzymes especially HDAC8 and dual MMP2 and MMP9 inhibitors for the management of hematological cancer

2. Name, Designation & Institution of the Supervisor/s:

A) Prof. Tarun Jha, Professor, Department of Pharmaceutical Technology, Jadavpur University, Kolkata 700032, India.

B) Dr. Shovanlal Gayen, Assistant Professor, Department of Pharmaceutical Technology, Jadavpur University, Kolkata 700032, India.

3. List of Publications:

Published research papers

[1] Amin SA, Khatun S, Gayen S, **Das S**, Jha T. Are inhibitors of histone deacetylase 8 (HDAC8) effective in hematological cancers especially acute myeloid leukemia (AML) and acute lymphoblastic leukemia (ALL)? European Journal of Medicinal Chemistry. 2023;258:115594. doi: 10.1016/j.ejmech.2023.115594.

[2] **Das S**, Amin SA, Jha T. Inhibitors of gelatinases (MMP-2 and MMP-9) for the management of hematological malignancies, European Journal of Medicinal Chemistry. 2021;223:113623. doi:10.1016/j.ejmech.2021.113623.

[3] Datta S, Halder AK, Adhikari N, Amin SA, **Das S**, Jha T. Synthesis, anticancer activity, SAR and binding mode of interaction studies of substituted pentanoic acids: part II. Future Medicinal Chemistry. 2022;14:17-34. doi:10.4155/fmc-2021-0049.

[4] **Das S**, Amin SA, Datta S, Adhikari N, Jha T. Synthesis, biological activity, structure activity relationship study and liposomal formulation development of some arylsulfonyl pyroglutamic acid derivatives, Journal of Molecular Structure. 2022;1248:131512. doi:10.1016/j.molstruc.2021.131512.

[5] **Das S**, Amin SA, Jha T. Insight into the structural requirement of aryl sulphonamide based gelatinases (MMP-2 and MMP-9) inhibitors - Part I: 2D-QSAR, 3D-QSAR topomer CoMFA and Naïve Bayes studies - First report of 3D-QSAR Topomer CoMFA analysis for MMP-9 inhibitors and jointly inhibitors of gelatinases together, SAR and QSAR in Environmental Research. 2021;32:655-687. doi:10.1080/1062936X.2021.1955414.

[6] **Das S**, Amin SA, Gayen S, Jha T. Insight into the structural requirements of gelatinases (MMP-2 and MMP-9) inhibitors by multiple validated molecular modelling approaches: Part II. SAR and QSAR in Environmental Research. Res. 2022;33:167-192. doi:10.1080/1062936X.2022.2041722.

[7] **Das S**, Gayen S, Jha T. In-house glutamine based compound loaded poly-(D-L-lactide-coglycolide) nanoparticles as a possible candidate for the management of chronic myeloid leukemia. Materials Today Proceedings. 2023. doi:10.1016/j.matpr.2023.10.158.

[8] Amin SA, Trivedi P, Adhikari N, Routholla G, Vijayasarathi D, **Das S**, Ghosh B, Jha T. Quantitative activity–activity relationship (QAAR) driven design to develop hydroxamate derivatives of pentanoic acids as selective HDAC8 inhibitors: synthesis, biological evaluation and binding mode of interaction studies. New Journal of Chemistry. 2021;45:17149-17162. doi:10.1039/D1NJ02636D.

[9] Dutta S, Halder AK, Adhikari N, Amin SA, **Das S**, Saha A, Jha T. Synthesis, anticancer activity, structure-activity relationship and binding mode of interaction studies of substituted pentanoic acids. Future Medicinal Chemistry. 2019;11(14):1679-1702. doi:10.4155/fmc-2018-0361.

[10] Moinul M, Amin SA, Khatun S, **Das S**, Jha T, Gayen S. A detail survey and analysis of selectivity criteria for indole-based histone deacetylase 8 (HDAC8) inhibitors. Journal of Molecular Structure. 2023;1271:133967. doi:10.1016/j.molstruc.2022.133967.

[11] Amin SA, Kumar J, Khatun S, **Das S**, Qureshi IA, Jha T, Gayen S. Binary quantitative activity-activity relationship (QAAR) studies to explore selective HDAC8 inhibitors: In light of mathematical models, DFT-based calculation and molecular dynamic simulation studies, Journal of Molecular Structure. 2022;1260:132833. doi:10.1016/j.molstruc.2022.132833.

Book Chapters

[1] **Das S**, Amin SA, Gayen S, Jha T. Chapter 1: 2D-QSAR studies: Regression and classification-based QSAR studies. In Jha, T. (Ed.). (2023). Modeling Inhibitors of Matrix Metalloproteinases (1st ed.). CRC Press. doi: 10.1201/9781003303282-2

[2] Amin SA, Gayen S, **Das S**, Jha T. Chapter 3: Other modeling approaches: Pharmacophore mapping, molecular docking and molecular dynamic simulation studies. . In Jha, T. (Ed.). (2023). Modeling Inhibitors of Matrix Metalloproteinases (1st ed.). CRC Press. doi: 10.1201/9781003303282-4.

[3] Amin SA, **Das S**, Gayen S, Jha T. Chapter 5: Gelatinases and their inhibitors. In Jha, T. (Ed.). (2023). Modeling Inhibitors of Matrix Metalloproteinases (1st ed.). CRC Press. doi: 10.1201/9781003303282-7.

4. List of Patents: NIL

5. List of Presentations in National / International / Conferences / Workshops:

[1] Oral Presentation in International Conference on “Chemical Engineering Innovations & Sustainability (ICEIS2023)” held during 26th-27th February 2023 at the Department of Chemical Engineering, Jadavpur University.

[2] Poster presentation (online mode) in the "International Bioresource Conclave & Ethnopharmacology Congress" at City Convention Centre, Imphal, Manipur between 24 and 26 February 2023.

STATEMENT OF ORIGINALITY

I, ***SANJIB DAS*** registered on ***May 22, 2019***, do hereby declare that this thesis entitled "***Design, synthesis and biological screening of some glutamine based zinc-dependent metalloenzymes especially HDAC8 and dual MMP2 and MMP9 inhibitors for the management of hematological cancer***" contains literature survey and original research work done by the undersigned candidate as part of Doctoral studies.

All information in this thesis has been obtained and presented by existing academic rules and ethical conduct. I declare that, as required by these rules and conduct, I have fully cited and referred all materials and results that are not original to this work.

I also declare that I have checked this thesis as per the "Policy on Anti Plagiarism, Jadavpur University, 2019", and the level of similarity as checked by iThenticate software is 2% (checked on 30-4-2024).

Sanjib Das 06.05.24

(SANJIB DAS)

Certified by Supervisor(s):

Tarun Jha
6.5.2024

Prof. Tarun Jha
Department of Pharmaceutical Technology
Jadavpur University
Kolkata- 700032

TARUN JHA, Ph.D
Ex Professor
Dept. of Pharm. Tech.
Jadavpur University
Kolkata-700 032

Shovanlal Gayen 6.5.24

Dr. Shovanlal Gayen
Department of Pharmaceutical Technology
Jadavpur University
Kolkata- 700032

DR. SHOVANLAL GAYEN
Assistant Professor
Dept. of Pharmaceutical Technology
Jadavpur University
Kolkata - 700 032 INDIA

CERTIFICATE FROM THE SUPERVISORS

This is to certify that the thesis entitled "***Design, synthesis and biological screening of some glutamine based zinc-dependent metalloenzymes especially HDAC8 and dual MMP2 and MMP9 inhibitors for the management of hematological cancer***" submitted by **SANJIB DAS (Registration No. 1021913004; Index NO.: 278/19/Ph)**, who got his name registered on **22.05.2019** for the award of **Ph.D. (Pharmacy)** degree of Jadavpur University is absolutely based upon his own work under the joint supervision on **Prof. Tarun Jha** and **Dr. Shovanlal Gayen** and that neither his thesis nor any part of the thesis has been submitted for any degree/diploma or any other academic award anywhere before.

Tarun Jha 6.5.2024

Prof. Tarun Jha
Department of Pharmaceutical Technology
Jadavpur University
Kolkata- 700032

TARUN JHA, Ph.D
Ex- Professor
Dept. of Pharm. Tech.
Jadavpur University
Kolkata-700 032

Shovanlal Gayen 6.5.24

Dr. Shovanlal Gayen
Department of Pharmaceutical Technology
Jadavpur University
Kolkata- 700032

DR. SHOVANLAL GAYEN
Assistant Professor
Dept. of Pharmaceutical Technology
Jadavpur University
Kolkata - 700 032, INDIA

ACKNOWLEDGEMENT

This thesis is the result of a protracted, difficult journey during which many individuals helped and supported me. Everything I've accomplished is a direct result of their ongoing support and encouragement. It is a pleasure to have this opportunity to thank them.

To begin with, I would like to convey my profound appreciation, sincere thanks, and gratitude to my mentors, **Prof. Tarun Jha** of the Jadavpur University Department of Pharmaceutical Technology and **Dr. Shovanlal Gayen** of the same department, for their excellent guidance throughout my research project, from choosing a title to determining the findings. They have given me so much inspiration, patience, motivation, and insightful advice. I am very grateful. I acknowledge that my thesis would not have been feasible without their creative and original ideas, clear explanations, and helpful critiques.

I won't forget to express my gratitude to the rest of the team: **Dr. Balaram Ghosh**, BITS-Pilani, Hyderabad campus, **Dr. Nilanjan Adhikari**, of the Jadavpur University Department of Pharmaceutical Technology, **Dr. Sanchita Datta,** IACS, Kolkata, **Dr. Sk Abdul Amin**, JIS University, Kolkata, all the faculty members of Department of Pharmaceutical Technology, Jadavpur University, for sharing insightful suggestions and encouragement.

I owe my deep respect to **Prof. Amalesh Samanta**, Head, Department of Pharmaceutical Technology, Jadavpur University, and former Heads of the Department Prof. **Sanmoy Karmakar, Prof. Kunal Roy, Prof. Pulok K. Mukherjee,** and **Prof. Biswajit Mukherjee** for their continuous help and encouragement. I am thankful to all of my respected **Teachers,** especially to **Ex. Prof. Biswanath Sa, Ex. Prof. Tanmoy Bera, Prof. Tapan Kumar Maity, Prof. Pallab Kanti Halder, Dr. Saikat Dewanjee, Dr. Prabir Kumar Ojha, Dr. Manas Bhowmick, Dr. Md. Emdad Hossain,** and **non-teaching staffs** for their support and help.

I am grateful to the authorities of **Jadavpur University, Kolkata** for providing all the necessary facilities to pursue my research work. I also owe my gratitude to **Prof. Achintya Saha,** Department of Chemical Technology, University of Calcutta, for motivating me and always being instrumental in any guidance whenever required.

I would like to convey my sincere thanks to the **All India Council of Technical Education (AICTE), New Delhi (2018-2022)** for providing National Doctoral Fellowships (NDF). I will always remember my fellow lab mates too for the memorable time we spent together, and the sleepless nights that gave us the courage to complete tasks before deadlines. I am extremely grateful to **Mr. Sandip Kumar Baidya** and Mr. **Suvankar Banerjee** of the Department of Pharmaceutical Technology, Jadavpur University for their endless efforts and continuous help. I also express my sincere thanks to all my laboratory seniors and juniors, especially to **Dr. Avinaba Mukherjee, Mr. Saptorshi Sanyal, Mis. Subha Mondal, and Mr. Rajat Sarkar** of the Department of Pharmaceutical Technology, Jadavpur University for their valuable cooperation and necessary help.

I would like to acknowledge all my friends and no words can suffice my feelings of gratitude to my Ph.D. colleagues, especially from the Department of Chemistry, Department of Physics, Bioequivalence Study Centre, and Department of Chemical Engineering of Jadavpur University.

I would like to acknowledge all the scientists, Faculty members, scholars, and staff members especially from the Department of Pharmaceutical Technology, Department of Chemistry, Department of Physics, Bioequivalence Study Center, and Department of Chemical Engineering of Jadavpur University; IICB main campus, Jadavpur, Kolkata; IICB TRUE campus, Saltlake, Kolkata; IACS, Kolkata; Department of Chemistry and Department of Chemical Technology, Rajabazer Science College, Kolkata ICMR-NISED, Kolkata and Chittaranjan Cancer Institute, Kolkata.

Finally, I want to express my gratitude to my **family**, especially to my **wife** and **daughter**, who have sacrificed extensively to make me available in the laboratory for years, especially in the period of the Covid-19 pandemic.

Date: 06/05/24

Place: Jadavpur, Kolkata

Sanjib Das

(SANJIB DAS)

Dedicated to

Prof. (Dr.) Tarun Jha

(Dr. Jha was one of the very few pioneer professors of pharmaceutical and medicinal chemistry in India who developed in-sillico drug design, synthesis, and cell culture facilities in his laboratory at the Department of Pharmaceutical Technology, Jadavpur University, in the mid-2000s).

PREFACE

Glutamine is a potential nutrient for rapidly growing cancer cells and inhibition of glutamine catabolism induces apoptosis Zinc-dependent metalloenzyme contains a metal ion cofactor for their enzymatic activity. At least 1000 human proteins (out of ~20,000) contain zinc-binding protein domains. Zinc-dependent metalloenzymes especially histone deacetylase 8 (HDAC8) and dual matrix metalloproteinase 2 (MMP2) and matrix metalloproteinase 2 (MMP9) have strong correlations with important hallmarks of cancer like cancer cell progression, invasion, migration, apoptosis, and angiogenesis. So structural fragments that fit into different catalytic sub-sites of the above-mentioned enzyme may be considered for the development of glutamine-based anti-cancer agents.

The terms "hematological malignancy" refers to cancerous conditions originating from cells in the blood or bone marrow. These malignancies involve abnormal cell growth in the hematopoietic system. Overexpression of zinc-dependent metalloenzymes like HDAC8, MMP2, and MMP9 has been strongly associated with several hematological malignancies in particular ALL, AML, and CML. Thus, the structural fragment that fits into different catalytic sub-site of the above-mentioned enzymes may be considered for the development of zinc-dependent metalloenzyme inhibitors for the management of hematological malignancies.

Quantitative structure-activity relationship (QSAR) analysis is a chemometric technique in drug discovery that establishes mathematical correlations between structural modifications of chemical compounds and changes in their biological activities. QSAR-based *in-sillico* studies play a crucial role in reducing the number of compounds requiring synthesis and biological evaluation, facilitating hit discovery, hit-to-lead conversion, and lead optimization.

By three-dimensional drug designing approach like molecular modeling, synthesis of designed molecules, and *in vitro* biological screening as well as other biological work and also considering glutamine-like structural fragments into the lead comprises a fruitful strategy for the management of hematological cancer.

This PhD thesis consists of seven Chapters (**Chapter 1-7**). **Chapter 1** (Introduction) of provides an outline of different hematological cancer and their drug availability and challenges of targeted small molecule drugs for hematological cancer along with a brief discussion on metalloenzymes

especially HDAC8, MMP2 and MMP9, and their relation with hematological cancer. In addition, a brief description of QSAR-based and other *in-sillico* drug design and discovery is also incorporated. **Chapter 2** is the literature review which discusses the HDAC8, MMP2, and MMP9 inhibitors which are in the clinic as well as reached in the different phases of clinical trials along with the HDAC8, MMP2 and MMP9 inhibitors reported against hematological cancer. **Chapter 2** also provides the relationship between glutamine and cancer along with the discussion on reported glutamine-based HDAC8, MMP2, and MMP9 inhibitors in hematological cancer. **Chapter 3** discussed on the rationale and objectives of my PhD work which comprises of Biological screening of isoglutamine derivatives [Part-I], Synthesis and biological screening of (*L*)-pyroglutamic acid derivatives [Part-II], QSAR-based molecular modeling studies [Part-III] and synthesis, and Synthesis, biological studies and binding interaction studies of (*D*)-glutamine derivatives (Part-IV). **Chapter 4** provides materials and methods used in the design, synthesis, and biological screening of this entire work. **Chapter 5** comprises the results and discussions of every *in-sillio* and experimental study performed. **Chapter 6** deals with **the** conclusion of this work whereas **Chapter 7** discusses the future objectives. The details are provided in the respective chapters.

Table of Content

Chapters

Table of Content

Table of Content

Table of Content

Table of Content

Table of Content

Table of Content

Abbreviations

2D-QSAR: Two-Dimensional Quantitative Structure-Activity Relationship

3D: Three-Dimensional

3D-QSAR: Three-Dimensional Quantitative Structure-Activity Relationship

ABL1: Abelson Murine Leukemia viral oncogene homolog 1

AD: Applicability Domain

ADCC: Antibody-Dependent Cellular Cytotoxicity

ADME: Absorption, Distribution, Metabolism, and Excretion

ALL: Acute Lymphoblastic Leukemia

AML: Acute Myeloid Leukemia

ANN: Artificial Neural Networks

AP: Accelerated Phase

AUC: Area Under the Curve

AUROC: Area Under the Receiver Operating Characteristic Curve

BC: Blast Crisis

BCR: Breakpoint Cluster Region

BM-MNCs: Bone Marrow Mononuclear Cells

BP: Blast Phase

Cas9: CRISPR-associated protein 9

Catalytic: CAT

CBF: Core-Binding Factor

CD: Cluster of Differentiation

CFDA: Chinese Food and Drug Administration

CRISPR: Clustered Regularly Interspaced Palindromic Repeats

CLL: Chronic Lymphocytic Leukemia

CML: Chronic Myeloid Leukemia

CoMFA - Comparative Molecular Field Analysis

CoMSIA - Comparative Molecular Similarity Indices Analysis

Abbreviations

CP: Chronic Phase

CSCs: Cancer Stem Cells

CTCL: Cutaneous T Cell Lymphomas

CXCL: Chemokine Ligand

CXCR: Chemokine Receptor

DAPI: 4',6-Diamidino-2-phenylindole

DMEM: Dulbecco's Modified Eagle Medium

DS: Discovery Studio

EBV: Epstein-Barr Virus

ECFP_6: Extended Connectivity Fingerprint of diameter 6

ECM: Extracellular Matrix

EMA: European Medicines Agency

EMT: Epithelial-Mesenchymal Transition

EATCs: Ehrlich Ascites Tumour Cells

EU: European Union

FAK: Focal Adhesion Kinase

FGFR: Fibroblast Growth Factor Receptor

FBS: Fetal Bovine Serum

FDA: Food and Drug Administration

GA: Genetic Algorithm

GLS: Glutaminase

GPI: glycosyl phosphatidylinositol

GS: Glutamine Synthetase

GSH: Glutathione

PEX: hemopexin

HATs: Histone Acetylases

HDAC8: Histone Deacetylase 8

HDACs: Histone Deacetylases

Abbreviations

HDACIs: histone deacetylase inhibitors

HL: Hodgkin Lymphoma

HPV: Human Papilloma Virus

HRMS: High-Resolution Mass Spectrometry

HSCs: Hematopoietic Stem Cells

HTS: High Throughput Screening

IC_{50}: Half-maximal Inhibitory Concentration

IGF: Insulin-like Growth Factor

IL-1β: Interleukin-1β

JNK: c-Jun N-terminal Kinase

KGA: Kidney Type Glutaminase

KRAS: Kirsten Rat Sarcoma virus

kNN: k-Nearest Neighbors

LBDD: Ligand-Based Drug Design

LDA: Linear Discriminant Analysis

LG/F NHL: Low-Grade, or Follicular Non-Hodgkin's Lymphoma

LOO: Leave-One-Out

LR: Linear Regression

LSCs: Leukemic Stem Cell

MAPK: Mitogen-Activated Protein Kinase

MCC: Matthew's Correlation Coefficient

MD: Molecular Dynamics

MDM2: Mouse Double Minute 2

MIC: Minimum Inhibitory Concentration

MLR - Multiple Linear Regressions

MM: Multiple Myeloma

MM/GBSA - Molecular Mechanics Generalised Born and Surface Area

MMP9: Matrix Metalloproteinase 2

Abbreviations

MMP2: Matrix Metalloproteinase 9

MMPIs: Matrix Metalloproteinase Inhibitors

MMPs: Matrix Metalloproteinases

MPN: Myeloproliferative Neoplasms

MSS - Musculoskeletal Syndromes

mTOR: mammalian Target Of Rapamycin

MTT: 3-(4,5-Dimethylthiazol-2-yl)-2,5-Diphenyltetrazolium Bromide

MYH11: Smooth Muscle Myosin Heavy Chain 11

NADPH: Nicotinamide Adenine Dinucleotide Phosphate

NF-κB: Nuclear Factor κB

nHBA: Number of Hydrogen Bond Acceptors

nHBD: Number of Hydrogen Bond Donors

NHL: Non-Hodgkin Lymphoma

NK: Natural Killer

NLP-HL: Lymphocyte-Predominant Hodgkin lymphoma

NMR: Nuclear Magnetic Resonance

nR: Number of Rings

OECD: Organization for Economic Co-operation and Development

PaDEL: PubChem Assay Data Extended Connectivity Fingerprint Descriptors

PCA: Principal Component Analysis

PDB: Protein Data Bank

PDF: Probability Density Function

PROTAC: Proteolysis Targeting Chimaera

PI: Propidium Iodide

PK: Pharmacokinetic

PI3K: Phosphoinositide 3-Kinase

PLS: Partial Least-Square

PPI: Protein-Protein Interaction

Abbreviations

PTCL: peripheral T-cell lymphoma

QSAR: Quantitative Structure-Activity Relationship

RAN: Ras-Related Nuclear Protein

RCC1: Regulator Of Chromosome Condensation 1

RCSB: Research Collaboratory for Structural Bioinformatics

ROC: Receiver Operating Characteristic

ROCED: Receiver Operating Characteristics Curve Euclidean Distance

ROCFIT: Receiver Operating characteristics curve Euclidean distance Corrected with the Fitness function

ROS: Reactive Oxygen Species

RUNX: Runt-related transcription factor

SAR: Structure-Activity Relationship

SBDD: Structure-Based Drug Design

SE: Standard Error

SMI: Small Molecule Inhibitor

SLR: Simple Linear Regression

S-MLR: Stepwise Multiple Linear Regression

SMILES: Simplified Molecular Input Line Entry System

SMMHC: Smooth Muscle Myosin Heavy Chain

SPSS: Statistical Package for the Social Sciences

SVM: Support Vector Machines

TCA: Tricarboxylic Acid Cycle

TIMPs: Tissue Inhibitors of Metalloproteinases

TKIs: Tyrosine Kinase Inhibitors

TLC: Thin Layer Chromatography

TME: Tumor Microenvironment

TNF: Tumor Necrosis Factor

TNF-α: Tumor Necrosis Factor α

Abbreviations

topomer CoMFA: topomer Comparative Molecular Field Analysis

USFDA: United States Food and Drug Administration

VEGF: Vascular Endothelial Growth Factor

WHO: World Health Organization

XPO5: Exportin-5

ZBG: Zinc Binding Group

CHAPTER 1

INTRODUCTION

Chapter 1: Introduction

1.1. Cancer

Cancer is a complex group of diseases characterized by the uncontrolled growth and spread of abnormal cells in the body. Normal cells in the body divide and grow in an orderly and controlled way, but cancer cells divide and grow uncontrollably, forming tumors or hematological malignancies invading nearby tissues and organs. These abnormal cells can also travel to other parts of the body through the blood and lymph systems, forming secondary tumors in a process known as metastasis. Cancer can affect almost any part of the body and can be classified into many different types based on the affected cells or tissues (www.cancer.org/treatment/). Many factors that can contribute to the development of cancer, including genetic mutations, exposure to carcinogens such as tobacco smoke, radiation, and certain chemicals, as well as lifestyle and environmental factors such as diet, physical activity, and pollution. While some cancers may be preventable through lifestyle changes and screening, others may be more difficult to prevent or detect early, making treatment more challenging (www.cancer.gov/about-cancer/). According to the World Health Organization (WHO), cancer is the second leading cause of death globally, accounting for approximately 1 in 6 deaths (www.who.int/news-room/fact-sheets/). One-third of cancer-related fatalities, account for the use of tobacco, having a high body mass index, drinking alcohol, eating few fruits and vegetables, and not exercising (www.who.int/news-room/fact-sheets/). In low- and lower-middle-income nations, cancer-causing infections including the human papillomavirus (HPV) and hepatitis are thought to be the cause of 30% of cancer cases (www.who.int/news-room/fact-sheets/). In 2023, an estimated 1,958,310 new cancer cases will be diagnosed in the United States, and 609,820 people will die from the disease (Siegel et al., 2023). In India, 14,61,427 incidents of cancer are anticipated in 2022, according to research (crude rate:100.4 per 100,000) (Sathishkumar et al., 2022). One in nine individuals has a lifetime risk of developing cancer in India. The most common cancers in men and women were lung and breast cancers, respectively. Among the childhood (0-14 yr) cancers, the most prevalent diagnosis was lymphoid leukaemia (boys: 29.2%; girls: 24.2%) (Sathishkumar et al., 2022). According to this estimates, there will be 12.8% more cancer cases in 2025 in India than there were in 2020 (Sathishkumar et al., 2022). The anticipated numbers of new cases and fatalities for each prevalent cancer type in 2023 are shown in **Table 1.1** (Siegel et al., 2023).

Table 1.1. The estimated numbers of new cases and deaths for each prevalent cancer type in 2023

Cancer type	Estimated new cases	Estimated deaths
Breast (Female – Male)	297,790 – 2,800	43,170 – 530
Prostate	288,300	34,700
Lung (Including Bronchus)	238,340	127,070
Colon and Rectal (Combined)	153,020	52,550
Melanoma	97,610	7,990
Bladder	82,290	16,710
Kidney (Renal Cell and Renal Pelvis)	81,800	14,890
Non-Hodgkin Lymphoma	80,550	20,180
Endometrial	66,200	13,030
Pancreatic	64,050	50,550
Leukemia (All Types)	59,610	23,710
Thyroid	43,720	2,120
Liver and Intrahepatic Bile Duct	41,210	29,380

1.2. Solid tumor malignancies and hematological malignancy

Solid tumors may be defined as abnormal tissue mass that usually does not contain cysts or liquid areas. Solid tumor malignancies refer to cancers that originate in tissues that form solid masses, such as the breast, lung, prostate, colon, and liver. They are typically detected by imaging techniques such as X-rays, CT scans, and MRI as well as biopsies. They are treated with surgery, radiation therapy, chemotherapy, and targeted therapy (www.cancer.gov/publications/dictionaries/). The terms "hematological malignancy" also known as a hematopoietic malignancy or blood cancer refer to cancerous conditions originating from cells in the blood or bone marrow. These malignancies involve abnormal cell growth in the hematopoietic system, which includes the production of blood cells. Hematological malignancies encompass a wide range of cancers, including leukemia, lymphoma and multiple myeloma. Leukemia is characterized by the abnormal production of white blood cells, lymphoma affects the lymphatic system, and multiple myeloma involves the plasma cells in the bone marrow (www.bloodcancer.org.uk/understanding-blood-cancer/).

1.3. Leukemia

A malignancy of the early blood-forming cells is called leukemia. Although leukemia often starts in white blood cells, other blood cell types can also develop leukemia. Leukemia comes in a variety of forms, which are categorized mainly by how quickly or slowly it grows, as well as whether it originates in lymphoid or myeloid cells. Although the precise etiology of leukemia is uncertain, it is believed to be a result of both hereditary and environmental factors. Radiation exposure, the use of particular medicines and chemicals, and genetic diseases are some risk factors for leukemia. Leukemia symptoms may include fatigue, weakness, fever, chills, night sweats, swollen lymph nodes, unexplained weight loss, and easy bruising or bleeding. These symptoms might vary depending on the kind and stage of the disease. Leukemia is often diagnosed through a process that combines physical examination, blood testing, and bone marrow biopsy. Radiation therapy, chemotherapy, targeted therapy, and bone marrow transplant are among the possible treatments of leukemia. Acute lymphoblastic leukemia (ALL), acute myeloid leukemia (AML), chronic lymphocytic leukemia (CLL) and chronic myeloid leukemia are the four main subtypes of leukemia (CML) (www.cancer.org/cancer/leukemia).

1.3.1. Acute lymphoblastic leukemia (ALL)

Acute lymphoblastic leukemia (ALL) is defined by the unchecked proliferation of immature lymphocytes that may have their origins in the bone marrow's lymphoid lineage and have faulty differentiation at an earlier stage of hematopoiesis (Stanulla et al., 2009). It is not well understood about the origin of ALL. The existence of leukemia stem cell in case of ALL is not clear. Lymphoid progenitor cell may be cell of origin of ALL. ALL is frequently identified in children, hence it is also known as children's leukemia (Masetti et al., 2011). Along with symptoms like exhaustion, dyspnea, bone marrow failure, and weight loss, ALL is recognized by the presence of 20% lymphoblasts within the bone marrow and blood. When extramedullary regions are involved, disorders including hepatomegaly, splenomegaly, and lymphadenopathy may additionally be detected (Zhang et al., 2015).

1.3.2. Chronic lymphoblastic leukemia (CLL)

The most prevalent form of leukemia in Western nations is chronic lymphocytic leukemia (CLL). The average age at diagnosis for older male cancer patients with CLL is 72 years (Hallek,

2019). According to research, CLL could have its roots in multipotent self-renewing hematopoietic stem cells (HSCs), which are normally identified by clonal proliferation and an increase of mature CD5 positive B cells in the bone marrow, blood, lymph nodes, and spleen (Kikushige et al., 2011). More than 95% of the time, CLL is linked to an overabundance of tiny, dormant, mature, and long-lived B lymphocytes. Blood counts and the detection of the circulating clonal B-cell population by the CD5+ antigen as well as other common B-cell markers including CD19, CD23, CD21, CD24, CD40, CD20, and CD22 are used to confirm the diagnosis (Hallek, 2019 and Keating, 2002).

1.3.3. Acute myeloid leukemia (AML)

Either an HSC or a myeloid progenitor cell can give rise to acute myeloid leukemia (AML). Myeloid precursor cells that have improperly differentiated and unchecked clonal proliferation are the hallmarks of AML. The presence of 20% or more myeloblasts in the peripheral blood or bone marrow meets the criteria for an AML diagnosis, according to the 2016 WHO update on myeloid diseases. AML typically develops as a result of inherited genetic pathways, specific gene translocations, genetic mutations, and other genetic abnormalities. Adults frequently have AML, and as people get older, the prevalence of the disease rises. Every year 9 to 17 individuals out of every 100,000 adults older than 65 are diagnosed with AML (Davis et al., 2018).

1.3.4. Chronic myeloid leukemia (CML)

Chronic myeloid leukemia (CML) is a clonal myeloproliferative illness that is caused by a reciprocal translocation of the Philadelphia chromosome and is characterized by the expression of the BCR-ABL fusion oncogene. Tyrosine kinase, which is produced by the BCR-ABL fusion oncogene, promotes unchecked myeloid cell proliferation and differentiation in the bone marrow, which advances CML. With a median age of 67 years at diagnosis. CML accounts for 15% of adult leukemias (Updyke et al., 2017). The stages of CML are blast crisis (BC), accelerated phase (AP), and chronic phase (CP). The presence of the Philadelphia (Ph) chromosome or BCR-ABL1 (resulting from a translocation between the Abelson murine leukemia viral oncogene homolog 1 (ABL1) gene on chromosome 9 and the breakpoint cluster region (BCR) gene on chromosome 22) along with other characteristics, such as leukocytosis [total white cell count (TWC) of 12-1000x10^9/L], various stages of neutrophil maturation (peaks

in myelocytes and segmented neutrophils) in peripheral blood films (PBF), and hypercellularity and granulocytic proliferation with maturation similar to PBF in bone marrow aspirations (BMA) (Kuan et al., 2018A and Vardiman et al., 2017). Absolute basophilia and eosinophilia are frequent in CML, and less than 10% of blasts are found in peripheral blood (PB) or BMA. When the total white cell count (TWC) is greater than $50x10^9$/L, splenomegaly and symptoms are typically present. At the time of diagnosis, 20 to 50 percent of CML patients had no symptoms when leukocytosis was observed incidentally, often during a health check-up (Kuan et al., 2018A and Kuan et al., 2018B).

1.4. Lymphoma

Lymphomas are a type of cancer that begins in cells of the lymphatic system, which is part of the body's immune system. They can be broadly classified into two main types: Hodgkin lymphoma (HL) and non-Hodgkin lymphoma (NHL) (www.cancer.gov/types/lymphoma).

1.4.1. Hodgkin lymphoma (HL)

HL, formerly known as Hodgkin's disease, is an uncommon monoclonal lymphoid tumor with a high possibility of cure. Hodgkin lymphoma and nodular lymphocyte-predominant Hodgkin lymphoma (NLP-HL) are two different subtypes of this disease entity that have been distinguished by the biological and clinical research. The pathology and clinical manifestations of these two disease types differ. Approximately 95% of all HL are classified as classical Hodgkin lymphomas, which are further separated into four subgroups: nodular sclerosis (NSHL), lymphocyte-rich (LRHL), mixed cellularity (MCHL), and lymphocyte-depleted (LDHL). They frequently start in the cervical lymph nodes. The disease affects young adults more frequently. There are sporadic large mononuclear Hodgkin and multinucleated cells (Reed-Sternberg) mixed in with a background of non-neoplastic inflammatory cells, and T lymphocytes are frequently seen surrounding the distinctive neoplastic cells. With an almost 80% cure rate, Hodgkin lymphoma has a very good overall prognosis (www.ncbi.nlm.nih.gov/books/NBK499969/). It is unclear what causes Hodgkin lymphoma specifically. But Epstein - Barr virus (EBV) infection, autoimmune conditions, and immunosuppression are associated with the higher risk of HL. HL has also been linked to hereditary risk. EBV has been reported to be more prevalent in both the

mixed cellularity and lymphocyte-deficient subtypes of Hodgkin lymphoma (Piris et al., 2020 and www.ncbi.nlm.nih.gov/books/NBK499969/).

1.4.2. Non-Hodgkin lymphoma (NHL)

Non-Hodgkin lymphomas are a class of neoplasms that develop in lymphoid tissues, primarily the lymph nodes. NHL is a cancer that develops from B cell precursors, mature B cells, T cell progenitors and mature T cells (www.ncbi.nlm.nih.gov/books/NBK559328/). Follicular lymphoma, Burkitt lymphoma, diffuse large B cell lymphoma, mantle cell lymphoma, marginal zone lymphoma, and primary CNS lymphoma are the most prevalent adult B cell neoplasms. Adult T cell lymphoma and mycosis fungoides are the most prevalent mature T cell lymphomas (Armitage et al., 1998). Several variables, like infections, environmental factors, immunodeficiency conditions and chronic inflammation, may be linked to NHL. Various infectious agents like Epstein-Barr virus (EBV), human T-cell leukemia virus type 1 (HTLV-1), hepatitis C virus (HCV), human herpesvirus 8 and helicobacter pylori infection have been implicated in various NHL subtypes (www.ncbi.nlm.nih.gov/books/NBK559328/). Non-Hodgkin lymphoma is also linked to medications including phenytoin, digoxin, and tumor necrosis factor (TNF) antagonist. The development of NHL is also linked to exposure to organic chemicals, pesticides, phenoxy-herbicides, wood preservatives, dust, hair colour, solvents, chemotherapy and radiation (Zhang et al., 2008 and Eriksson et al., 2008).

1.5. Multiple myeloma (MM)

The clonal plasma cell proliferative condition known as multiple myeloma (MM) is characterized by an aberrant rise in monoclonal immunoglobulins. If left unchecked, the excessive generation of these plasma cells can eventually result in particular end-organ damage. This is most frequently observed when at least one of the following clinical symptoms is present: hypercalcemia, renal failure, anemia, or bone pain associated with lytic lesions (www.ncbi.nlm.nih.gov/books/NBK534764/ and Kiss et al., 2021). In the United States, just 1.8% of all newly diagnosed cases of cancer are multiple myeloma, making it a very uncommon disease. With a median diagnosis age of roughly 70 years old and a slightly higher prevalence of males than females (1.4:1), it primarily affects the elderly population. Black and African American people appear to have up to a two-fold higher incidence than White populations

(www.ncbi.nlm.nih.gov/books/NBK534764/). Multiple myeloma's actual cause is unknown. The promoter genes, particularly those on chromosome 14, are frequently altered and translocated in multiple myeloma, though, and they probably contribute to the onset of the illness. Additionally, other oncogenes like NRAS, KRAS, and BRAF may involved in the growth of plasma cells. Obesity, alcohol usage, and environmental triggers such as insecticides, organic solvents, agent orange and radiation exposure are additional risk factors for illness (Pasca et al., 2019).

1.6. Drugs available against hematological malignancy

The medications used to treat hematological malignancies historically fall into the following categories based on their mode of action: antimetabolites, anti-tubulin compounds, deoxyribonucleic acid (DNA)-interactive substances, and molecular targeting substances such monoclonal antibodies and certain small molecules. The primary subcategories of DNA interaction agents, the oldest family of anticancer medications, include alkylating agents, cross-linking agents, intercalating agents, topoisomerase inhibitors, and DNA-cleaving agents (Nussbaumer et al., 2011). Chlormethine (mechlorethamine), commonly known as the nitrogen mustard, was the first alkylating agent to receive FDA approval. In 1946, Goodman and colleagues revealed the pharmacological action of mechlorethamine on leukemia, lymphosarcoma, and Hodgkin's lymphoma (Goodman et al., 1946). Aminopterin, the 4-amino derivative of folic acid, was used to treat acute leukemia in children, as reported by Farber in 1948 (Farber et al., 1948). Methotrexate (amethopterin) took the role of aminopterin in the treatment of patients in 1953 because it has the higher therapy-versus-toxicity ratio (Wright et al., 1951). After that, the first structural analogs of purine and pyrimidine, mercaptopurine and fluorouracil, respectively, were found. Mercaptopurine was synthesized in 1952 (Elion et al., 1952) and gained its first FDA permission in 1953, whereas fluorouracil was synthesized in 1957 (Dushinsky et al., 1957) and received its first approval in 1962. These medications were frequently used to treat hematological cancer and solid tumors (Sochacka-Ćwikła et al., 2021). Natural plant alkaloids with anti-tubulin action were the following therapeutics for the treatment of hematological malignancies. Vinblastine and vincristine, the first two vinca alkaloids, were isolated by Noble and Beer from *Catharanthus roseus* (L.) G. Don. Following thorough clinical testing of both substances, in 1963, the FDA approved vincristine as a treatment for several malignancies (Sochacka-Ćwikła et al., 2021). Cytotoxic medicines such as bleomycin and

doxorubicin were among other natural compounds. In 1962, Umezawa et al. discovered bleomycin in *Streptomyces verticillus*. This antibiotic, which can be used to treat malignant lymphoma, was the first DNA-cleaving drug to be registered in 1973 (Watson et al., 2018 and Takeuchi et al., 1995). Doxorubicin was discovered in 1967 in Italy from *Streptomyces peucetius* var. *caesius*, and the FDA first approved it in 1974 (Bonadonna et al., 1969 and Doxorubicin Hydrochloride NDA #050467—Drugs@FDA). The medication demonstrated anticancer action through multiple mechanisms, including DNA intercalation and topoisomerase II activity inhibition. Numerous hematological cancers were commonly treated with doxorubicin (Thorn et al., 2011). Cisplatin, the platinum coordination compound, was first discovered by Rosenberg and colleagues in 1965, caused inhibition of cell division (Rosenberg et al., 1965) although Peyrone synthesized cisplatin for the first time in 1845 (Sochacka-Ćwikła et al., 2021). Then, cisplatin was entered into clinical trials against a number of malignancies, and through cross-linking DNA, it demonstrated powerful anticancer action. Since the medication's FDA approval in 1978, individuals with leukemia or lymphomas have utilized it as their first line of defense. It continues to be one of the most effective anticancer drugs used in the clinic today (Ghosh S., 2019). Development of targeted therapy using monoclonal antibodies or small selective molecules was a turning point in the treatment of blood cancer. Inhibiting molecular targets, which are particular molecules involved in the development, progression, and spread of cancer, is the main component of targeted therapy (Sochacka-Ćwikła et al., 2021). Rituximab, a genetically designed chimeric anti-cluster of differentiation 20 (CD20) antibody, was the first monoclonal antibody for the treatment of hematological cancers. Rituximab got FDA approval in 1997 for the treatment of B-cell, low-grade, or follicular non-Hodgkin's lymphoma (LG/F NHL) that has relapsed or is resistant to treatment (Grillo-López et al., 2000). Imatinib was the first small molecule inhibitor (SMI) identified as being selective against various protein tyrosine kinases. Imatinib was synthesized in 1996 by Buchdunger. The drug was approved by the FDA in 2001 for patients with CML (Cohen et al., 2002).

After the approval of rituximab and imatinib targeted medications have significantly replaced broad-spectrum cytotoxic agents in the treatment of cancer. Targeted medications have a higher potency and lower toxicity than conventional chemotherapeutic drugs because they can directly target cancer cells while sparing healthy cells (Bedard et al., 2020). The number of FDA-approved targeted medications for the treatment of cancer has significantly increased over the

past 20 years. Targeted medications can be loosely divided into two groups: small molecules and macromolecules (such as monoclonal antibodies, polypeptides, antibody-drug conjugates, and nucleic acids) (Wilkes et al., 2018 and Lee et al., 2018). Small-molecule targeted therapies have advantages over macromolecule medications in various areas, such as pharmacokinetic (PK) characteristics, prices, patient compliance, and drug storage and transportation. Despite recent competition from monoclonal antibody-based macromolecule medications, small-molecule targeted therapeutics continue to advance significantly (Zhong et al., 2021).

1.7. Challenges of targeted small molecule drugs for hematological malignancies

The development of small-molecule targeted anti-cancer therapies has accelerated due to the advancement of contemporary molecular biology and the application of some cutting-edge technologies, including computer-aided drug design, structural biology, and combinatorial chemistry. Despite the enormous advancements made, small-molecule focused anti-cancer medications still confront several difficulties (Zhong et al., 2021). Hematological malignancies are effectively treated with more than 40 small molecule medications that have been given clinical approval in the post-imatinib era. Still, to decrease the treatments' failure rates at the clinical level, some constraints must be considered while developing more active drugs. Certain small molecular inhibitors attach to several molecular targets, such as intracellular proteins and cell surface receptors, which raises the possibility of adverse effects.

Tyrosine kinase inhibitors (TKIs) have established themselves as the most powerful pathway-directed anti-cancer medicines since they were developed in the early 2000s. TKIs have proven to be extremely helpful in the treatment of numerous hematological malignancies in addition to solid tumors. As a result of their extensive use, TKI-related side effects have been documented more frequently. The heart is involved in some of the most serious consequences despite the fact that TKIs are known to affect many other body organs, including the lungs, liver, gastrointestinal tract, kidneys, thyroid, blood, and skin. The most often reported cardiovascular side effects include everything from sudden death to heart failure, atrial fibrillation, hypertension, and impaired cardiac function (Shyam et al., 2023).

Drug resistance is yet another significant issue. After being used in clinical settings for a period of time, almost all targeted anti-cancer medications encounter resistance. Numerous processes,

such as gene mutation, amplification, cancer stem cells (CSCs), efflux transporters, apoptotic dysregulation, autophagy, and others as well, have been related to drug resistance (Zhong et al., 2021). The primary factor causing anticancer drug-resistance is gene mutation. When it comes to drug-resistant gene alterations, there are two opposing perspectives. One is that certain drugs can cause gene alterations. The second is that there have already been drug-resistant mutations. Cancer cells with drug-sensitive mutations predominate in the early stages of treatment and control the growth of cancer cells with drug-resistant mutations. Sensitive mutant cells are eliminated and the resistant mutant cells spread and exhibit resistance (Zhong et al., 2021). TKIs are now widely used for several types of hematological malignancies. TKI resistance is a significant obstacle in the treatment of hematological malignancies and significantly lowers patient compliance, survival, and quality of life. The aberrant activation of PTK-related signaling pathways linked to gene mutations is the primary cause of TKI resistance. The tumor microenvironment (TME) has a significant role in tumor development and TKI resistance in addition to mutations. TME is essential for the development of tumors, contributes to epithelial-mesenchymal transition (EMT) and metabolic reprogramming, and is crucial for TKI resistance (Yang et al., 2022). A single therapy approach cannot overcome drug resistance in all patients due to the variety of TKI resistance pathways in various tumor types (Yang et al., 2022).

Therefore, the emergence of drug-resistant variants of hematological malignancies remains a significant and formidable problem that necessitates new generation anticancer drugs to effectively treat hematological malignancies in the clinic.

1.8. Zinc-dependent metalloenzymes as important targets for hematological malignancies

An estimated one-third of all proteins in the human body need a metal cofactor to function. A vast range of crucial biological processes, such as protein degradation and nucleic acid modification, depend on metalloenzymes. Due to their importance in these processes and the development of many diseases, metalloenzymes are therefore potential targets for therapeutic intervention. The importance of metalloenzymes as a class of targets and the growing understanding of the role they play in disease have increased interest in finding new ways to create inhibitors and ultimately effective medications. Zinc-dependent metalloenzyme contains a metal ion cofactor for their enzymetic activity (Chen et al., 2019). At least 300 human proteins (out of ~20,000) contain zinc-binding protein domains (Ponomarenko et al., 2016 and Cheng et

al., 2021). Overexpression of zinc-dependent metalloenzymes like histone deacetylases (HDACs), especially HDAC8 and matrix metalloproteinases (MMPs), especially MMP2 & MMP9 has strongly associated with several hematological malignancies in particular ALL, AML, and CML (Amin et al., 2023 and Das et al., 2021A). Thus, structural fragment which fits into different catalytic sub-site of the above mentioned enzymes may be consider for development of zinc-dependent metalloenzymes inhibitors for the management of hematological malignancies.

1.9. Histone deacetylases (HDACs)

Histone deacetylases (HDACs) are a family of enzymes that are crucial for the post-translational epigenetic alteration of histone proteins. In other words, HDACs and histone acetylases (HATs) are enzymes that control chromatin structure and function by deacetylating and acetylating the lysine residues on the core nucleosome histones (Cheshmazar et al., 2022). Histone proteins wrap long eukaryotic DNA, creating compact chromosomes. The transcriptional machinery's access is limited by the compact nucleosome structure, which is primarily caused by the ionic contact between the strongly positively charged histones and the negatively charged DNA backbone. When the HAT neutralizes the positive charge of the lysine residues on the histone surface, the tight nucleosomes can become loose (**Figure 1.1**). This causes RNA polymerase II to be more accessible, which leads to gene activation. However, the restoration of a compact chromatin structure brought about by the action of the enzyme HDAC prevents RNA polymerase from accessing the lysine side chain of the histone surface, reducing gene repression (**Figure 1.1**) (Park et al., 2020 and Adhikari et al., 2021). For the accurate and timely expression of numerous genes related to signal transduction, cell development, and cell death, optimal control of the activities of HATs and HDACs is essential. The inhibition of the intrinsic enzyme activity of either HAT or HDAC might potentially result in an imbalance between their respective activities. The timely expression of a target gene is impeded when HAT activity is suppressed. On the other hand, suppressing HDAC activity maintains the target gene's ongoing expression. In this context, the control of HDAC activities participate in various biological signalling processes because of

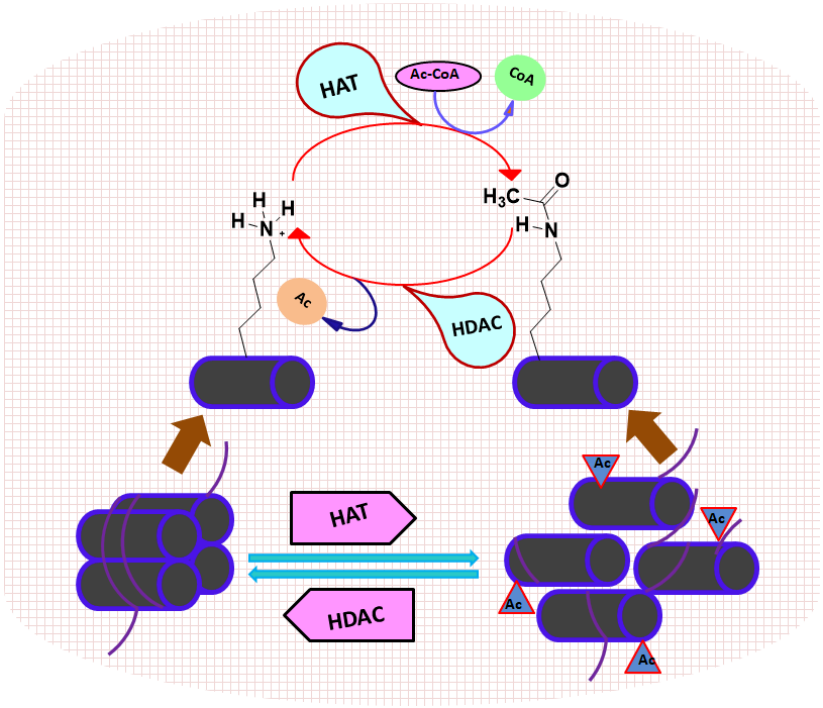

Figure 1.1. Lysine deacetylation of histone proteins catalyzed by HDAC.

their role in histone deacetylation and epigenetic modifications (Park et al., 2020). HDACs regulate a number of pathophysiological and disease events, including malignancies, neurodegenerative disorders, inflammatory illnesses, metabolic disorders, autoimmune diseases, etc., in addition to maintaining a variety of normal physiological events (Adhikari et al., 2021).

1.9.1. Classification of HDACs

18 mammalian HDACs have been reported so far, and they are divided into four classes: class I, class II, class III, and class IV. Class I HDACs comprises of HDAC1, HDAC2, HDAC3, and HDAC8. These are associated with the reduced potassium dependence 3 (*Rpd3*) gene found in yeast. HDAC1, HDAC2, and HDAC8 are expressed in the nucleus whereas HDAC3 shuttles between the nucleus and cytoplasm. There is a unique deacetylase domain seen in class I HDACs. The HDACs belonging to class II are again grouped in two classes, class IIA (HDAC4, HDAC5, HDAC7, and HDAC9) and class IIB (HDAC6, and HDAC10). The Class II HDACs show structural similarities with the yeast gene *Hda1* and are found in both the nucleus and cytoplasm. Class IIA HDACs have an N-terminal domain that has a separate myocyte enhancer factor (MEF) binding region in addition to the deacetylase domain (**Figure 1.2**).

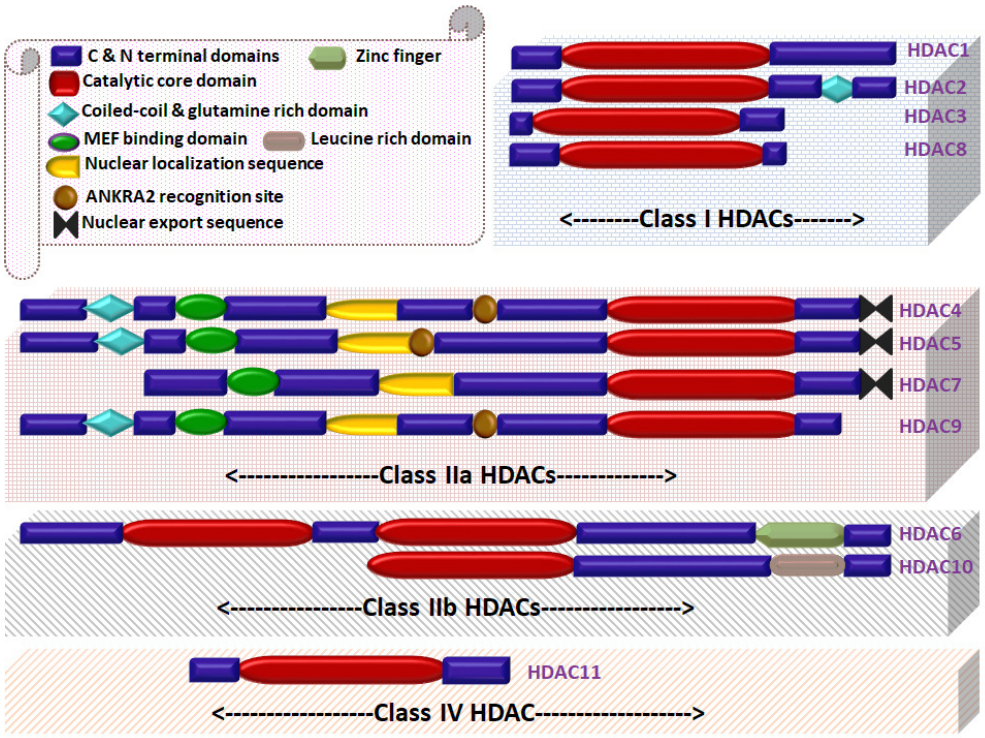

Figure 1.2. Different classes of HDACs.

HDACs in class IIB have a distinctive C-terminal domain. While HDAC10 has a leucine-rich domain, HDAC6 has a zinc-finger ubiquitin binding domain (ZnF-UBP) (**Figure 1.2**). The distinct N-terminal domain of HDAC6 helps to deacetylate α-tubulin. The class IV HDAC enzyme HDAC11 is present in both the cytoplasm and nucleus. It's interesting that sirtuins (SIRT1–SIRT7) are classified as class III HDACs. Their functions, however, are not connected to class I and class II HDACs. The catalytic function of Class I, class II, and class IV HDACs are totally dependent on Zn^{2+} ions, whereas sirtuins (SIRT1 through SIRT7) are dependent on a cofactor named nicotinamide adenine dinucleotide (NAD). Due to the presence of a conserved tyrosine residue that participates in the catalytic process, each HDAC exhibits a high degree of structural homology at the active site. Mammal class IIA HDACs lack the tyrosine residue instead of the histidine residue, which lowers their catalytic activity (Park et al., 2020 and Adhikari et al., 2021).

1.9.2. HDACs and cancer

HDAC inhibitors are being found to modulate a wide range of diverse biological activities and cellular functions, as well as various genetic manipulations related to the prevention of tumor

growth, apoptosis, cell cycle arrest, cell migration, and motility, autophagy, antiangiogenic effects, DNA repair, and mediation of nuclear and inflammatory signalling processes (Hassell et al., 2019 and Liang et al., 2023). Numerous studies have demonstrated that HDAC overexpression is closely related to the development of tumors, and 13 out of 15 tumor types (breast cancer, colon cancer, gastric cancer, kidney cancer, liver cancer, lung cancer, ovarian cancer, lymphoma, pancreatic cancer, prostate cancer, medulloblastoma, neuroblastoma, and chronic lymphocytic leukemia) overexpress HDACs (Liang et al., 2023). In the development of tumors, HDACs play a variety of roles (**Figure 1.3**). Transcriptional silencing of tumor suppressor genes occurs when HDACs are overexpressed, which aids in the development of tumors. In the development of tumors, overexpressed HDACs: (1) trigger angiogenesis through hypoxia-inducible factor-1 (HIF-1); (2) interfere with cell cycle progression and promote tumor cell proliferation; (3) enhance cell infiltration and increase metastasis as well as invasion of tumor cells; and (4) decrease the sensitivity of tumor cells to apoptosis signals or drugs, leading to apoptosis escape or drug resistance (Liang et al., 2023). Therefore, HDACs have gained a great deal of research interest as promising anticancer targets.

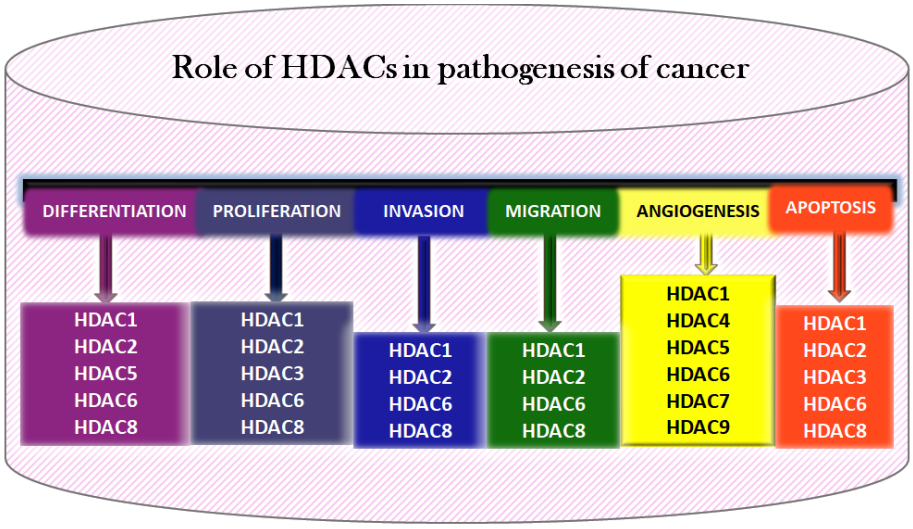

Figure 1.3. Involvement of different HDACs in the development of cancer pathogenesis.

1.9.3. Involvement of HDAC8 in cancers

HDAC8, one of the crucial HDACs, aberrantly deacetylates histone and non-histone proteins. A number of histone and non-histone proteins, such as the structural maintenance of chromosome 3

(SMC3) cohesin protein, retinoic acid induced 1 (RAI1), p53, etc., are aberrantly deacetylated by HDAC8 enzyme. This controls a variety of operations, including the maintenance and transformation of leukemic stem cells (LSCs) (Chakrabarti et al., 2015). Experimental evidence supports the hypothesis that HDAC8 can deacetylate peptides produced from H3 and H4 in vitro. Notably, some HDAC8 inhibitors caused histone hyper-acetylation, despite the lack of conclusive evidence that histones are deacetylated by HDAC8 in vivo (Chakrabarti et al., 2015; Schölz et al., 2015 and Amin et al., 2023). Recent research and other evidence point to the involvement of HDAC8 in the aetiology of cancer (**Figure 1.3**) (Rajaraman et al., 2023; Guo et al., 2023; Wang et al., 2023; Zhou et al., 2023 and Kim et al., 2023). In addition, it has been demonstrated that the proliferation of human lung, colon, and cervical cancer cell lines is inhibited by the knockdown of HDAC8 by RNA interference and/or targeted HDAC8 inhibition using si-HDAC8 and/or selective HDAC8 inhibitor (HDAC8I). This emphasizes the significance of selective HDAC8 inhibition (Bassett et al., 2014). Acute therapy-related toxicities linked to pan-HDACIs are also thought to be alleviated by HDAC8 selective inhibitors (Ho et al., 2020). Watters et al. (Watters et al., 2021) investigated the impact of HDAC8 on MCL cell lines. Mantle cell lymphoma (MCL) cells underwent apoptosis as a result of HDAC8 suppression or hereditary HDAC8 impairment. Contrarily, A HDAC8I had no impact on the survival, expression of the receptors, or antibody-dependent cellular cytotoxicity (ADCC) of primary human natural killer (NK) cells. HDAC8 inhibition was found to cause an increase in NK cells, which are responsible for producing the effector cytokine interferon-gamma (IFN-γ). Together, the results of this investigation indicate that selective HDAC8Is may concurrently sustain the functional activity of NK cells while lowering the growth of MCL tumors. Federico et al. (Federico et al., 2022) used diphenylazetidin-2-one scaffold to design a new class of dual-acting HDAC6/8 inhibitors by examining a combination of bulky cap groups and certain thin linkers. The most effective substances were evaluated as antiproliferative agents in leukemia U937 cell lines. The specific HDAC8 inhibition triggers calcium/caspase-dependent apoptosis in blood cancer cells and HDAC8 deregulation has repeatedly been linked to the beginning of leukemia. Suppression of HDAC8 enzyme in particular is a promising approach for the treatment of numerous tumors (Federico et al., 2022). Additionally, Chotitumnavee et al. (Chotitumnavee et al., 2022) created the first proteolysis targeting chimaera (PROTAC) for the targeted degradation of HDAC8. The PROTAC degraded HDAC8 in cellular studies without altering the levels of

other HDACs and more potently inhibited Jurkat T-cell leukemia cell proliferation than the typical HDAC8 inhibitor (Chotitumnavee et al., 2022). The PROTAC method was also employed by Zhao et al. (Zhao et al., 2023). PROTAC CT-4 significantly displayed substantial anti-migration activity in MDA-MB-231 cells but only marginally stronger antiproliferative activity. Using the flow cytometry method and a test for caspase 3/7 activity, it was also reported that CT-4 was effective in inducing apoptotic cell death in Jurkat cells. According to these most recent studies the discovery of HDAC8 degradation inducers has great potential for the treatment of leukemia (Zhao et al., 2023). Additionally, T-cell-derived tumors and lymphomas may also be prevented by a selective HDAC8I. It triggers cytochrome C (cyt C) release from mitochondria and calcium (Ca^{2+}) efflux from the endoplasmic reticulum (ER) as a result of phospholipase C-1 (PLC-1) activation. As a result, HDAC8 may be useful as a therapeutic target for T-cell lymphoma and other hematological malignancies (Banerjee et al., 2021). In another study, Katayama et al. (Katayama et al., 2018) reported that HDAC8 deacetylated the differentiation of neurons in P19 pluripotent embryonic carcinoma (EC) cells by controlling the development of embryoid body (EB) formation and reduced EBs were also detected in CRISPR-Cas9-mediated HDAC8 knockout (KO) cells. Later in 2020, the same team reported that neuronal nuclei (NeuN) expression was lower in the HDAC8 KO clones than in the wild-type cells, indicating the significance of HDAC8 for neurodevelopment in P19 EC cells without embryoid body formation (Morii et al., 2020).

1.9.4. HDAC8 in hematological cancer

Despite the fact that research into the role of HDAC8 in hematological cancers is still in its early phases, important results have been revealed in recent years that have led to HDAC8 being considered a possible target for hematological malignancies (Amin et al., 2023). There are reports in the literature that HDAC8 is overexpressed in different sub-types of hematological cancers like AML, ALL, CLL, and others (Zhang et al., 2021; Spreafico et al., 2020; Richter et al., 2016; Qi et al., 2015 and Wilson et al., 2009). Hematopoietic stem cells (HSCs) transition and maintenance are mediated by the HDAC8 gene. Because of their exceptional ability to differentiate into several cell types, HSCs can produce all types of blood cells (Passegué et al., 2005 and Hua et al., 2017). The p53, a transcriptional regulator, is one of the essential HDAC8

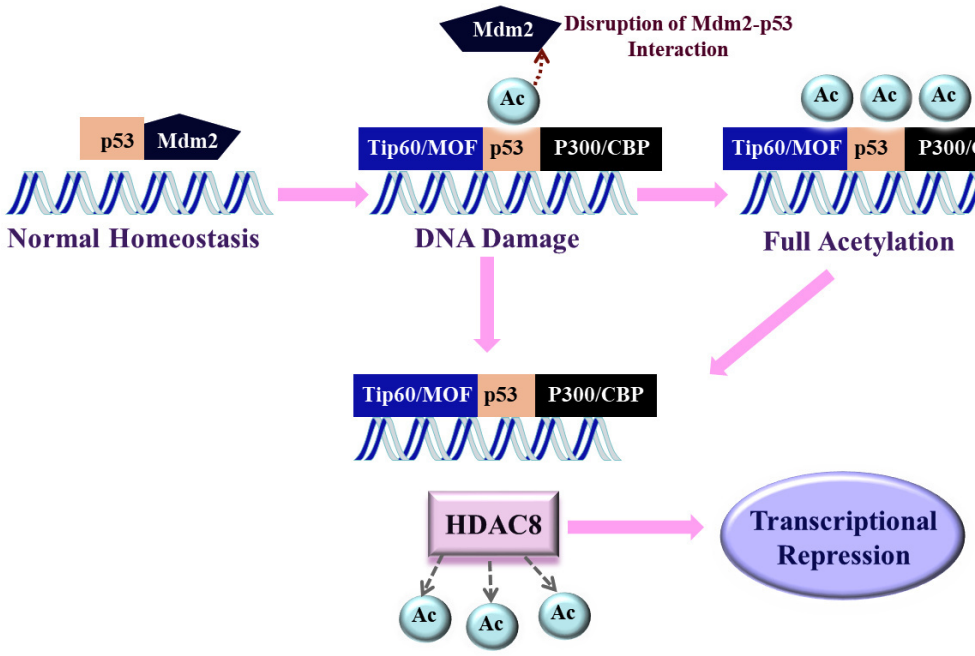

Figure 1.4. Repression of the p53 transcription by HDAC8

non-histone substrates (Lotem et al., 1993; Dumble et al., 2007 and Wang et al., 2011). The p53 gene is recognized to play a major role in regulating cellular processes and is essential for HSC differentiation, apoptosis, proliferation, and ageing. The p53 has also been shown to regulate HSC quiescence and self-renewal in steady-state hematopoiesis (Liu et al., 2009A and Liu et al., 2009B). Under normal physiological circumstances the tumor suppressor p53 levels in cells are low because of the interaction with primary negative regulator murine double minute 2 (mdm2). However, several mechanisms enable the quick accumulation and activation of p53 upon DNA damage or other cellular stresses to stop the unchecked growth of cells with harmful genetic alterations. When p53 is acetylated, the Mdm2-p53 connection is disrupted, which causes the recruitment of numerous HATs [for instance, p300/CREB binding protein (CBP)] involved in DNA repair and cell cycle regulation (**Figure 1.4**) (Gu et al., 1997; Sakaguchi et al., 1998; Brooks et al., 2011; Sykes et al., 2006; Tang et al., 2006; Luo et al., 2000; Rodriguez et al., 2000; Brooks et al., 2003; Vousden et al., 2007; and Tang et al., 2008). However, mammalian HDACs, such as HDAC8, suppress the acetylation of p53 (Kruse et al., 2009). It was shown that upon interaction with p53, HDAC8 deacetylates p53, which modifies the p53 activity and prevents transcription (**Figure 1.4**) (Hua et al., 2017). HDAC8 deacetylation is an essential component of signalling cascades ranging from cellular senescence to metabolism as well as aging (Bordone et

al., 2005). Increased apoptosis and hypersensitivity to hematological stress are encouraged in HSCs with HDAC8 deficiency via hyper activation of p53. The inactivation of p53 completely restored the hypersensitivity and apoptosis caused by the HDAC8 deletion. Additionally, it was shown by the same team that repetitive 5-fluorouracil treatment greatly hindered hematological recovery and increased mortality in HDAC8-deficient mice (Hua et al., 2017). Collectively, these findings demonstrate that HDAC8 modulates p53 activity to enhance HSC maintenance and cell survival during cellular or genotoxic stress (Hua et al., 2017). The sections that follow provide a thorough explanation of how HDAC8 functions in AML and ALL cells.

1.9.4.1. HDAC8 is a potential target for AML

AML is the most common type of acute leukemia in adults. Genetic alterations in myeloid progenitors and hematopoietic stem cells (HSCs) cause this sort of heterogeneous hematological disease. The inversion of chromosome 16 [inv(16)] is one of the most common chromosomal translocations found in AML patients. The core-binding factor (CBF) complex, which consists of the DNA-binding RUNX protein and the non-DNA-binding CBF protein, is an essential transcriptional regulator of hematopoiesis and a frequent target of leukemia-related mutation (**Figure 1.5**) (Qi et al., 2015). Core-binding factor gene β (CBFβ) and MYH11 (encodes smooth muscle myosin heavy chain, SMMHC) genes have been fused by inv(16). The resultant fusion protein, CBFβ-SMMHC, has both the RUNX1 binding interface of CBF and the coiled-coil rod domain of SMMHC (Qi et al., 2015). Here, RUNX1 is an important transcription factor that is necessary for the production of HSCs during hematopoiesis (**Figure 1.5**) (Okuda et al., 2001 and Imperato et al., 2015). The protein CBFβ-SMMHC (CM) is encoded by the expression of CBFβ-MYH11. For the formation of AML, the CBFβ-SMMHC protein promotes specific aberrant myeloid progenitors. According to studies, the CBFβ-SMMHC fusion protein binds with HDAC8 as one of its binding partners (Zhang et al., 2021; Spreafico et al., 2020; Richter et al., 2016; and Qi et al., 2015). HDAC8 controls the enhanced deacetylation of post-translational p53 with inv(16) fusion protein. Pharmacological inhibition of HDAC8 is efficient in precisely targeting CBFβ-SMMHC-expressing leukemia cells and inhibits p53 (**Figure 1.5**).

The transcription factor p53, which also binds to CBF-SMMHC, is deacetylated as a result of the interaction between CBFβ-SMMHC and HDAC8 (Qi et al., 2015). This interaction reduces p53 activity in inv (16)+ AML LSCs, which promotes LSC maintenance and transformation (**Figure**

1.5). Importantly, HDAC8 inhibition encourages apoptosis in inv(16)+ AML CD34+ cells while protecting healthy hematopoietic progenitor cells. Furthermore, *in vivo*, HDAC8I therapy greatly decreases AML propagation and eliminates LSCs' capacity to start leukemia (Qi et al., 2015). On the other hand, it is found that a microRNA connection is also significant for cytogenetics and prognosis in AML. The abnormal expression of miR-126 (miR-126) results in CD34 + 38- leukemic stem/progenitor cells in acute myeloid leukemia. According to Zhang and colleagues (Zhang et al., 2021), the CBFβ-MYH11 fusion gene up-regulates miR-126 expression. This is caused by abnormal miR-126 transcription. They also showed that the HDAC8/RAN-XPO5-RCC1 axis is involved in miR-126 biogenesis (Zhang et al., 2021). **Figure 1.5** demonstrates that RAN-RCC1 activation is promoted by HDAC8-mediated deacetylation of RAN. As a result, this encourages RAN-XPO5-mediated transcription, which in turn controls the overexpression of miR-126/EGFL7 in leukemic cells. Therefore, it is obvious that HDAC8 is a viable target for AML.

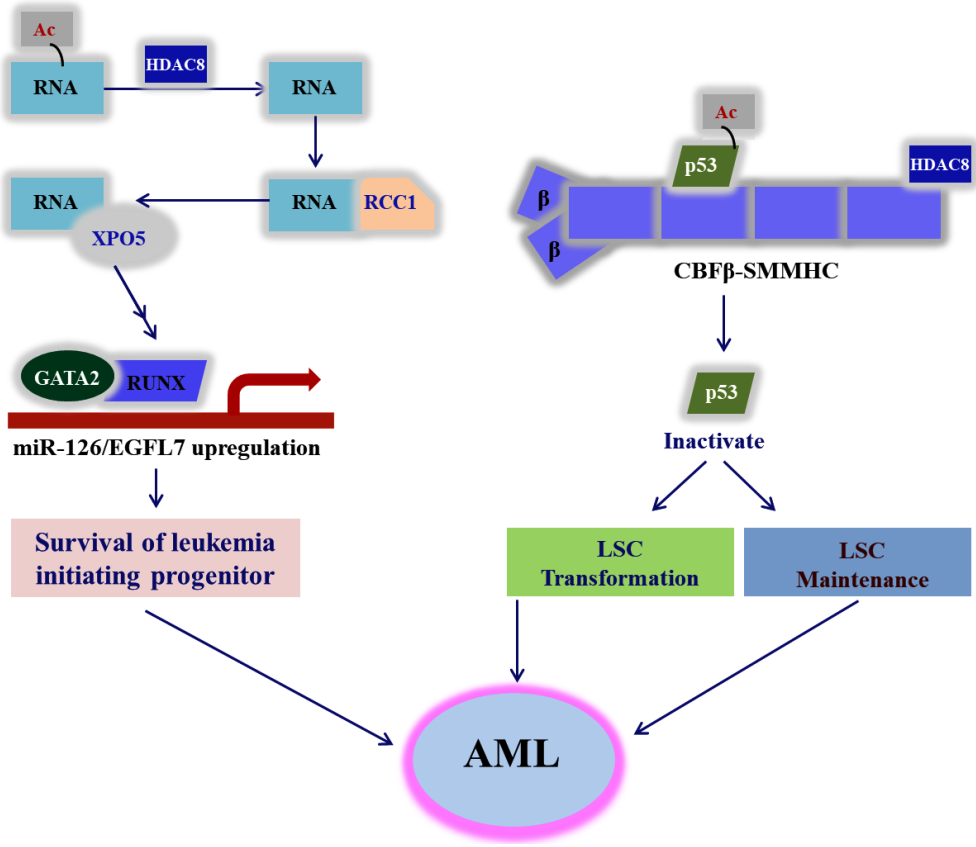

Figure 1.5. HDAC8 mediated molecular mechanisms that regulate AML.

1.9.4.2. HDAC8 is a potential target for ALL

Recent findings on the molecular pathogenesis of leukemia have demonstrated that genetic changes contribute to the emergence and maintenance of ALL (Mehrpouri et al., 2020; Agarwal et al., 2021; Mehrpouri et al., 2022; Markouli et al., 2022; and Amin et al., 2023). The clonal

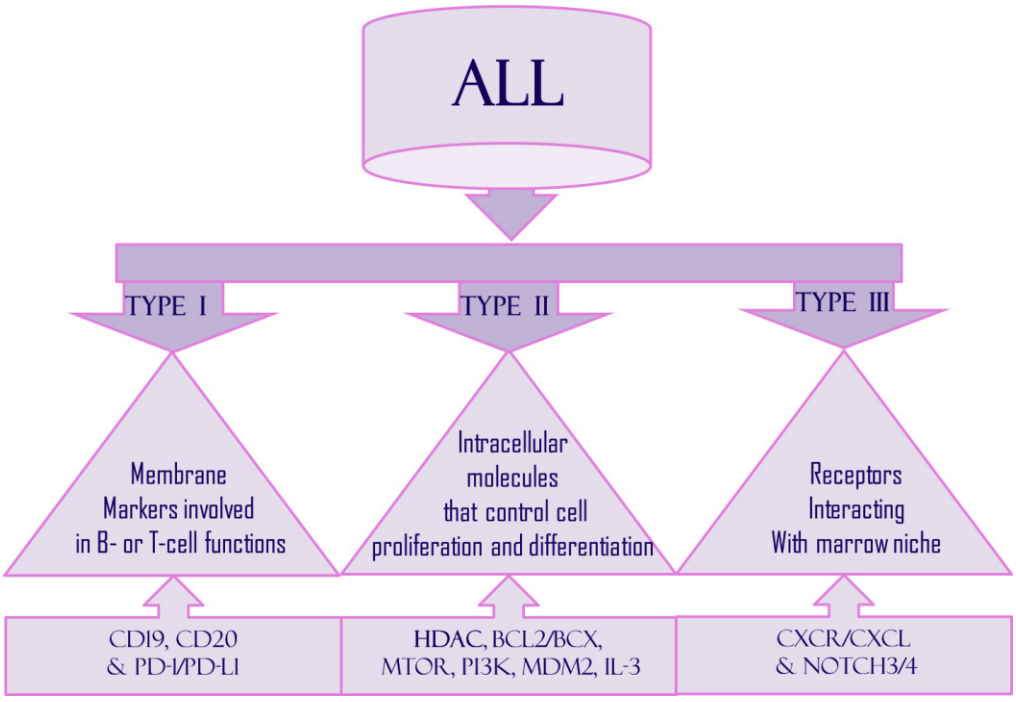

Figure 1.6. Possible therapeutic targets of ALL.

proliferation of variably differentiated lymphoid precursors is a hallmark of ALL. In general, ALL has been regarded as a genetic disorder that affects kids most frequently between the ages of 2 and 5 years old. HDAC8 is a promising therapeutic target for the treatment of ALL. There is evidence that ALL and other hematological neoplasms have high levels of HDAC8 expression (Balasubramanian et al., 2008; Xiao et al., 2010; Advani et al., 2010; Bassan et al., 2018; Zhao et al., 2021; and Amin et al., 2023). Potential ALL therapeutic targets may be classified into three types (**Figure 1.6**). Type I targets are membrane markers involved in B- or T-cell functions [e.g., CD19, CD20, programmed cell death protein 1 (PD-1)/PD-Ligand (PD-L1)]; type II targets are primarily intracellular molecules (e.g., HDAC, BCL2/BCX, mTOR, PI3K, MDM2, IL-3) that control cell proliferation and differentiation pathways (Bassan et al., 2018) and type III target category includes receptors like CXCR/CXCL and NOTCH3/4 interacting with the supporting

marrow niche (Wilson et al., 2009). The selective HDAC8 inhibitor PCI-34051 triggers caspase-dependent apoptosis in T-cell ALL or CTCL but not in solid tumor cell lines or other hematopoietic cell lines (**Figure 1.7**) (Balasubramanian et al., 2008).

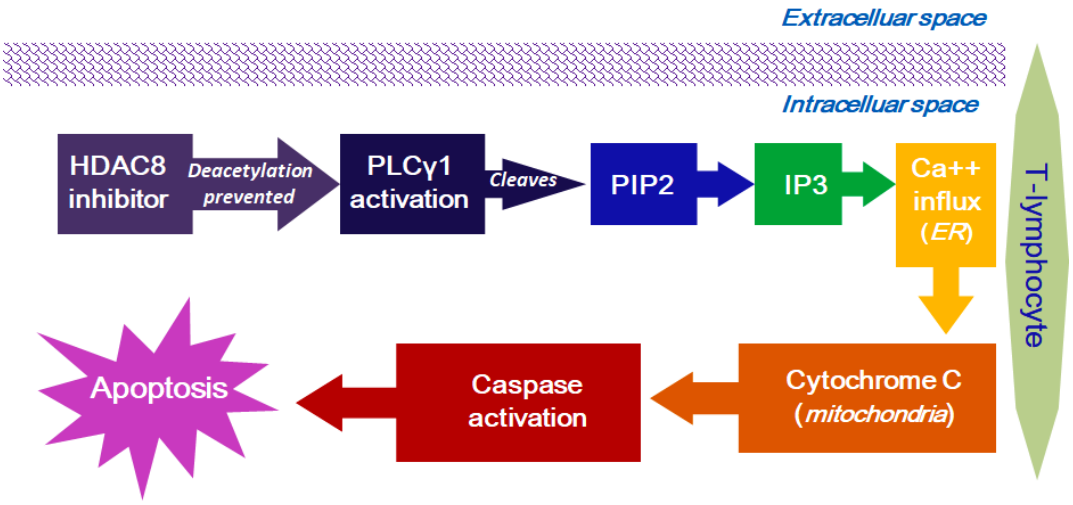

Figure 1.7. Relationship of HDAC8 inhibition with apoptosis in T-cell ALL.

Therefore, these increasing results suggested that HDAC8 plays a crucial role in the development of leukemia and is a good target for anti-ALL therapy.

1.10. Matrix metalloproteinases (MMP)

In the late 1980s, Harris and colleagues (Okada et al., 1987) first coined the term matrix metalloproteinase. Latre, in front of more than 250 delegates at an international MMP conference held in Destin, Florida in 1989, the name "matrix metalloproteinase" and its numerical designation were formally announced (Brinckerhoff et al., 2002). 28 MMP subtypes have been identified in vertebrates so far. Out of 28, humans have 23 paralogs of MMPs, and at least 14 of these MMPs are expressed in vascular endothelium. The MMP family can be divided into at least six subfamilies based on substrate specificities and sequence homology. The six subfamilies are collagenases, gelatinases, stromelysins, matrilysins, membrane-type MMPs, and other MMPs. The collagenases subfamily consists of MMP1, MMP8, MMP13, and MMP18. MMP2 and MMP9 are collectively called gelatinases. stromelysin subfamily grouped with MMP3, MMP10, and MMP11. MMP7 and MMP26 are collectively known as matrilysins. The membrane-type

MMPs are MMP14, MMP15, MMP16, MMP17, MMP24 and MMP25. The rest of the members belong to other MMPs subfamily (MMP12, MMP19, MMP20, MMP21, MMP22, MMP23, MMP27, and MMP28) (Laronha et al., 2020). Before the 1950s, humans were not aware of any enzyme that could break down collagen polypeptides. The only enzyme family that truly acts as a collagenase is the MMP family. However, during the process of bone resorption, the cysteine protease cathepsin K is also able to destroy type I collagen (Lu et al., 2018 and Laronha et al., 2020).

1.10.1. Structural features of MMPs

MMPs are zinc-containing endopeptidases that are dependent on calcium. Tissue inhibitors of metalloproteinases, or TIMPs, are responsible for their endogenous regulation. MMPs typically contain a pro-peptide sequence, a catalytic metalloproteinase domain (CAT), a hinge region, also known as a linker peptide and a hemopexin (PEX) domain. Two Zn^{2+} ions are found in MMPs, one of which is structural and the other of which is found in the CAT domain. The MMP family has some subgroups that show unusual structural diversity. For instance, MMP2 and MMP9 have three fibronectin type II repeats in their CAT domains. On the other hand, MMP7, MMP23, and MMP26 lack the hemopexin domain and hinge region. A recognition sequence that resembles furin can be found in the C-terminus of MMP11, MMP21, and MMP28. Transmembrane and cytosolic domains are frequently seen in membrane-type MMPs (MT-MMPs), however, glycosyl phosphatidylinositol (GPI) anchors are present in MMP17 and MMP25. Despite the variations stated above, the catalytic region of all MMP sub-types contains a conserved zinc-binding motif with the sequence HEXXHXXGXXH. All of these MMP zymogens, with the exception of MMP23 and MMP28, have a cysteine switch with the sequence PRCGXPD that chelates the Zn^{2+} ion by a cysteine sulfhydryl (-SH) group to maintain pro-MMPs' latency. The enzymatic latency is kept in place in the case of Pro-MMP23 by an N-terminal signal anchor in the pro-domain and a cysteine-rich region with an ALCLLPA sequence at the C-terminus, which is followed by a terminal immunoglobulin (Ig)-like region. The sequence PRCGVTD is found in the cysteine switch motif of Pro-MMP28. **Figure 1.8** displays simplified domain architectures of the MMP family members and how they differ between various MMP sub-types (Laronha et al., 2020).

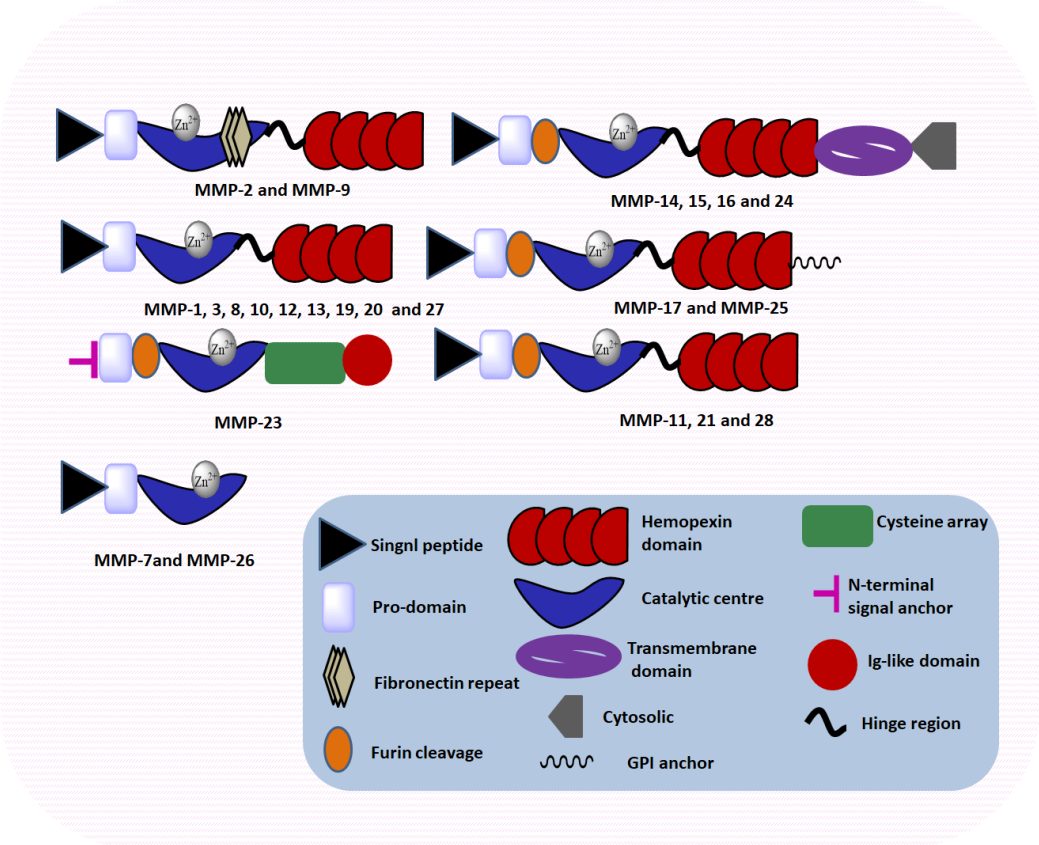

Figure 1.8. Domain structures of MMP family members.

1.10.2. Structure and function of Gelatinases (MMP2 and MMP9)

Gelatinases are the terminology for MMP2 and MMP9 together. Individually, MMP2 and MMP9 are referred to as gelatinase-A and gelatinase-B, respectively. Despite having a unique collagen-binding domain made up of three fibronectin type II tandem repeats at the N-terminus of the catalytic domain, gelatinases are similar in structure to other proteinases in the MMP family. Additionally, MMP9 possesses a distinct type V collagen-like domain unlike MMP2 (**Figure 1.9**) (Hsiao et al., 2019). These three fibronectin type II tandem repeats are important for gelatin binding (Cui et al., 2017). Typically, fibroblasts, vascular smooth muscle cells, and leukocytes release MMP2 and MMP9. More specifically, MMP2 is predominantly secreted by endothelial cells, leukocytes, platelets, monocytes, chondrocytes, osteoblasts, dermal fibroblasts, and keratinocytes, whereas, MMP9 is released by epithelial cells, fibroblasts, polymorphonuclear leucocytes, granulocytes, neutrophils, macrophages, T-cells, osteoblasts, dendritic cells and keratinocytes (Laronha et al., 2020). Gelatinases are secreted in latent forms, and after being

released, these endopeptidases are preferably guided into the spaces between cells and tissues to digest the proteins in the extracellular matrix and control the expression of cell surface proteins in various physiological and pathological circumstances (Cui et al., 2017).

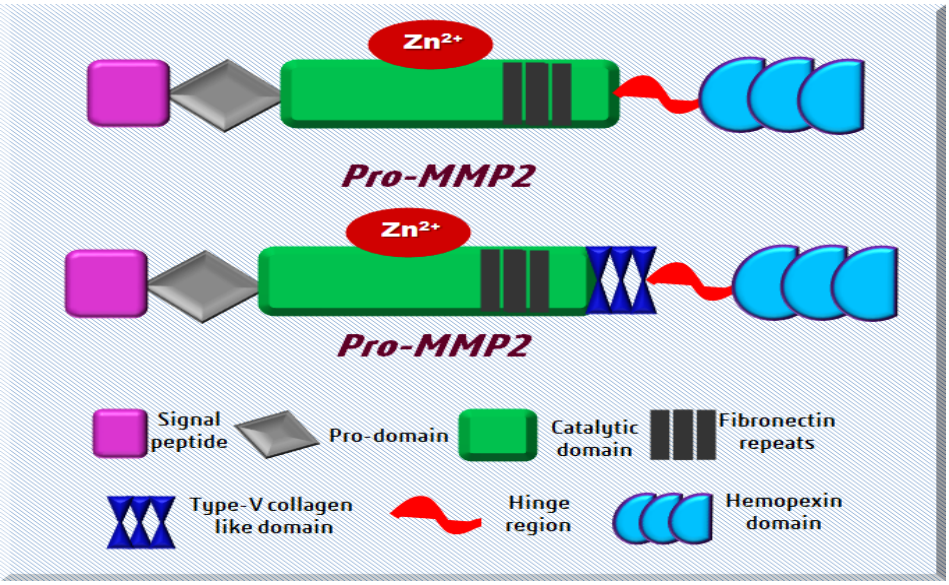

Figure 1.9. Structure of MMP2 and MMP9.

Gelatinases primarily break down type-IV collagen and gelatin, while they can also break down other forms of collagen, including types V, VIII, X, XI, and type-XIV collagens (Laronha et al., 2020). Compared to MMPs from collagenase subfamilies, MMP2 has substantially lower collagenase activity. MMP2 breaks down collagen in two steps. In the first step, MMP2 divides triple helix collagens at specific collagen cleavage sequences located at the 3/4 from N-terminal. In the second step, with the aid of a fibronectin-like domain, denatured collagens or gelatins are digested (Cui et al., 2017 and Laronha et al., 2020). MMP9 also digests both type IV collagen and gelatin. Even in the state of enzymatic latency, gelatinases bind with the α-2 chain of type-IV collagen so as to ensure substrate availability. Pro-MMP9 has a stronger affinity for the type-IV collagen's α-2 chain than pro-MMP2 (Olson et al., 1998). Gelatinases also break down a wide variety of non-collagenous ECM proteins, such as fibronectin, elastin, aggrecan, proteoglycan core proteins, versican, laminin, and nidogen (Olson et al., 1998). The activation of numerous other non-matrix proteins, including fibroblast growth factor receptor 1 (FGFR1), insulin-like growth factor-binding protein-3 and -5 (IGF-BP-3 and -5), interleukin-1β (IL-1β), tumor necrosis

factor-α (TNF-α), and transforming growth factor-β (TGF-β), is also a result of the activity of MMP2 and MMP9 (Cui et al., 2017).

1.10.3. Gelatinases (MMP2 and MMP9) and cancer

The primary function of MMPs is to digest the components of the extracellular matrix like collagen, elastin, fibronectin, laminin, and proteoglycans. When physiological processes like morphogenesis, bone remodelling, wound healing, and angiogenesis take place, the extracellular matrix (ECM) is remodelled. In contrast, aberrant remodelling of the ECM can promote cancer cell invasion and proliferation as well as tissue fibrosis (Chang et al., 2023). MMP2, MMP9 and other members of MMP family have long been linked to tumor invasion, metastasis, and angiogenesis (Johansson et al., 2000; Giannelli et al., 2002; Björklund et al., 2005; Fink et al., 2012; Yu et al., 2017; Winer et al., 2018; Gonzalez-Avila et al., 2019; Quintero-Fabián et al., 2019; Fields, 2019A; and Mondal et al., 2020A). A sufficient number of evidence is available which supports that gelatinolytic activity involved in the pathogenesis of different types of cancer like melanoma, lung cancer, colorectal cancer esophageal squamous cell cancer, gastric carcinoma, breast cancer, hepatic cancer, thyroid cancer, prostate cancer, ovarian cancer, and head and neck cancer (Das et al., 2021A).

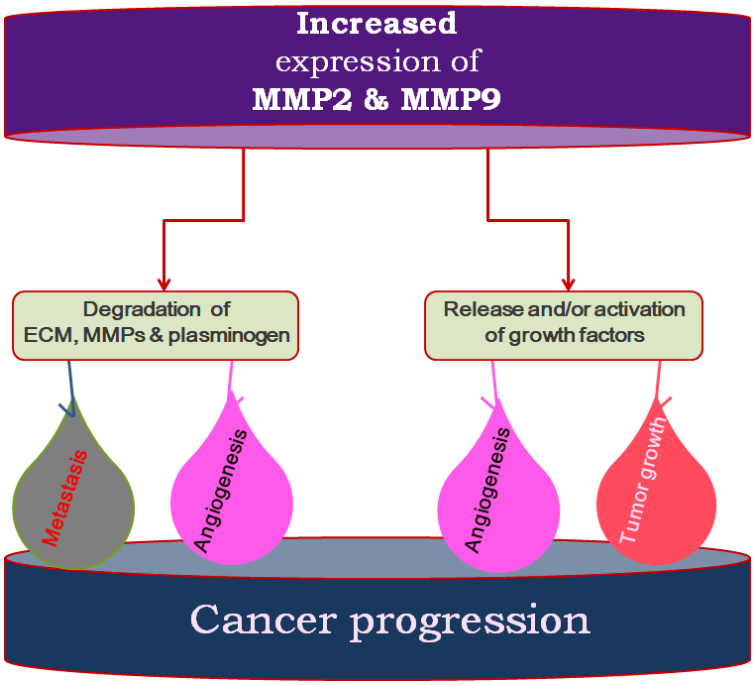

Figure 1.10. Role of MMP2 and MMP9 in the development of cancer.

Numerous cell types are known to express MMP2 and MMP9 during the development of cancer. Stromal, endothelial, and inflammatory cells can also express gelatinases in addition to tumor cells (Klein et al., 2004). The key factor contributing to MMP2 and MMP9's involvement in the development of cancer is their capacity for degrading ECM protein. This leads to a wide range of products that can influence the development of cancer. The three primary stages of cancer development—tumor angiogenesis, tumor growth, and metastasis—can be broadly separated to show how gelatinases are involved in the disease process. However, these stages are intertwined (Klein et al., 2004).

All of these processes have been linked to MMP2 and MMP9. In **Figure 1.10** a schematic representation of MMP2 and MMP9's function in the development of cancer is depicted. The relationship between gelatinases and angiogenesis, and tumor growth, as well as metastasis will be covered in the following paragraphs.

1.10.3.1. MMP2 and MMP9 in angiogenesis and tumor growth

Tumor angiogenesis is a crucial step in the development of cancer. Since tumors cannot grow larger than a few mm^3 when new vessel development is inhibited, it is recognized that angiogenesis is a prerequisite for tumor growth (Klein et al., 2004 and Lugano et al., 2020). In the process of angiogenesis, new blood vessels develop from pre-existing ones. The breakdown of basement membrane and ECM component by MMP2 and MMP9 is one of the initial stages of tumor angiogenesis. Due to the lack of cell-matrix and cell-cell interactions, degradation of the ECM can lead to the migration of tumor cells as well as endothelial cells. For instance, laminin-5 (Ln-5) degradation by MMP2 exposes an Ln-5 cryptic site that promotes endothelial cell migration. The migration and proliferation of endothelial cells, ultimately leads to the development of new blood vessels. Endothelial cells move away from the old blood vessel to form new ones as a consequence of the basement membrane being ruptured, and they also release ECM-bound factors (Klein et al., 2004 and Mondal et al., 2020A). Along with degrading ECM, gelatinases can also release growth factors from ECM and/or inactive complexes. MMP2 and MMP9 cleave growth factor receptors, and activate growth factors that are excreted as pre-pro-enzymes, such as transforming growth factor (TGF)-α, TGF-β, macrophage-colony stimulating factor (M-CSF), insulin-like growth factor (IGF), and fibroblast growth factor receptor (FGFR)-1. The release or activation of growth factors directly or indirectly induces

tumor angiogenesis and might also lead to tumor growth independent of angiogenesis (Klein et al., 2004). Systemically, MMPs can act as the negative regulator of angiogenesis by releasing fragments such as endostatin and angiostatin, which are the negative regulators of angiogenesis. These fragments are known to circulate throughout the body and can be up-regulated during the cancerous process. MMP2, MMP7, MMP9, and MMP12 are responsible for the digestion of plasminogen to angiostatin. The resultant angiostatin can boost apoptosis in tumor cells (Klein et al., 2004 and Mondal et al., 2020A). In general, MMPs play significant roles in controlling tumor angiogenesis and subsequent tumor growth, mostly through their ECM degradative activity and/or activation of pre-pro-growth factors. In addition to this, MMPs play a role in tumor growth other than tumor angiogenesis.

1.10.3.2. MMP2 and MMP9 in metastasis

The primary cause of death in cancer patients is metastasis. Gelatin and type IV, V, XI, and XVI collagens, which are necessary for metastasis, are degraded by MMP2 and MMP9. Gelatinases encourage metastasis by dismantling the ECM's physical defenses. Multiple steps are involved in metastasis (Song et al., 2021 and Niu et al ., 2022). The following phenomena can be used to roughly classify metastatic processes: dissociation of metastatic tumor cells from the bulk tumor, migration to blood and/or lymph vessels, penetration of the vascular lumen, escape from immune cells, adhesion to vascular endothelium at distant sites, extravasation from vessels into new host tissue, and tumor cell survival, and growth in the new host environment (Mondal et al., 2020A). Increased metastasis and tumor stage have been associated with a number of studies, such as malignant versus benign breast tumors and advanced ovarian tumors versus benign tumors (Schmalfeldt et al., 2001; Hanemaaijer et al., 2000; and Sheen-Chen 2001). MMP-9 expression was found to be higher in various invasive cell lines when compared to non-invasive counterparts (Lin et al., 2000 and Stack et al., 1998). Additionally, studies using recombinant TIMPs, synthetic MMP inhibitors, or MMP overexpression have shown evidence for the involvement of MMP2 and MMP9 in the metastatic process (Khokha et al., 1994; DeClerck et al., 1992; Imren et al., 1996; DeClerck et al., 1991; and Koivunen et al., 1999). For example, overexpression of MMP2 or MMP9 enhanced the incidence of metastasis in immunocompromised mice (Bernhard et al., 1990; Bernhard et al., 1994; and Kawamata et al., 1995). The majority of the above-mentioned research was conducted using endpoint studies, in

which mice were implanted with tumors, and the number of metastases was counted. These findings show that gelatinases contribute to metastases, however, do not specify which stages of the metastatic process they affect. However, MMP2 and MMP9 may be engaged throughout the entire process of metastasis, according to methods other than endpoint studies (Klein et al., 2004).

1.10.4. MMP2 and MMP9 in hematological cancer

The activities of MMP2 and MMP9 are mainly controlled at the transcriptional level, activation from latent form, and inhibition via endogenous inhibitors like tissue inhibitors of MMP (TIMPs) (Cui et al., 2017). MMP2 is activated by MMP14 and a low concentration of TIMP2. MMP9 is activated by cathepsin G, trypsin, chymase, kallikrein, elastase, neutrophil elastase, and MMPs (MMP1, MMP2, MMP3, MMP7, MMP10, MMP13, and MMP26). Activation of the latent MMP-9 by other MMPs or enzymes is prevented by the TIMP-1's interaction with the hemopexin domain of pro-MMP9 (Farina et al., 2014 and Raeeszadeh-Sarmazdeh et al., 2020). It is already widely recognized that gelatinases and solid tumor malignancies are related. However, it's important to understand the specific function that gelatinases play in hematological malignancy. The association between gelatinases and solid tumor malignancies is already well known, however, the relationship between gelatinases and hematological malignancies has not received as much attention (Das et al., 2021A). In the ChEMBL database, over 5000 chemical compounds have been reported. Those compounds at least inhibit MMP-2 or MMP-9, one of the two gelatinases (www.ebi.ac.uk/chembl/). A small portion of the gelatinase inhibitors described, have been tested against leukemia or other hematological cancers (Das et al., 2021A). Over the past two decades, evidence has accumulated that suggests that a significant association exists between elevated levels of expression of MMP2 and MMP9 with disease progression of hematological cancers (Das et al., 2021A). Evidence that MMP2 and MMP9 play a key role in the development, invasion, and metastasis of hematologic neoplasia has been piling up in recent years.

1.10.4.1. MMP2 and MMP9 in ALL

The expression of MMP2 and MMP9 in ALL was first published in an *in vitro* study in 1999 (Ivanoff et al., 1999). High MMP-2 expression was linked to infantile T-ALL, according to

another study (Scrideli et al., 2010). The expression of MMP2 and MMP9 in the clinical development of ALL has been examined by Kuittinen et al. (Kuittinen et al., 2001) with 20 adult and 55 paediatric ALL patients. Paediatric and adult ALL displayed significant variations in the expression of MMP2 and MMP9. In adult ALL, 65% of patients had positive staining for MMP2 and 25% for MMP9 in blast cells. Only 12.7% of the paediatric ALL cases, in comparison, displayed a positive response to either of the gelatinases (Kuittinen et al., 2001). MMP2 expression has been linked to extramedullary disease patterns in adult ALL, including involvement of the spleen, liver, nodes, bones, testicles, and/or central nervous system. Moreover, those with MMP9-positive blasts showed the tendency for worse survival. MMP2 and MMP9 expression and survival did not appear to be correlated in paediatric ALL (Kuittinen et al., 2001). According to Schneider et al. (Schneider et al., 2010), MMP-9 production by paediatric B-ALL cells has independent predictive value for survival among ALL patients, whereas paediatric T-ALL cells have poor prognostic value but release more MMP9 than B-ALL cells. In an *in vivo* animal experiment, it was reported that the release of TNF-α by B-ALL cells causes the bone marrow microenvironment's mesenchymal stem cells (MSC) to express MMP9 and, as a result, activates the NF-kβ pathway (Verma et al., 2020). Growth factors can control both MMP2 and MMP9. Vascular endothelial growth factor-A (VEGF-A) and platelet-derived growth factor-BB (PDGF-BB) both increase the production of gelatinase-A (MMP2) in gastric cancer cell lines and rat aorta vascular smooth muscle cells, respectively (Cui et al., 2017). VEGF-A and epidermal growth factor (EGF) also increase the production of gelatinase-B (MMP9) (Cui et al., 2017; and Hollborn et al., 2007). VEGF-A is an angiogenic factor and angiogenesis is associated with childhood ALL (Perez-Atayde et al., 1997). Hematological malignant cells release VEGF-A, and individuals with recurrent childhood ALL exhibit considerably greater levels of VEGF-A expression compared to those with newly diagnosed childhood ALL (Bellamy et al., 1999 and Koomagi et al., 2001). Childhood ALL was found to secrete gelatinases when autocrine VEGF was present. The VEGF autocrine loop and gelatinase activities were associated with clinical and prognostic factors in paediatric ALL patients (Poyer et al., 2009). An elevated plasma MMP9 and VEGF level were seen in cases of adult acute T-cell leukemia also. Additionally, it was found that elevated plasma levels of VEGF and MMP9 were significantly correlated with the infiltration of adult acute T-cell leukemia cells (Hayashibara et al., 2002). Lin et al. reported (Lin et al., 2017) genetic variants of MMP2 and MMP9 contribute

to the risk of childhood T-ALL. According to the study, MMP2 -1306C/T and MMP9 -1562C/T polymorphisms may be linked to a higher risk of developing T-ALL. The MMP9 -1562C>T polymorphism might have an impact on the prognosis of T-ALL patients (Lin et al., 2017).

1.10.4.2. MMP2 and MMP9 in AML

There are substantial number of evidences in the literature which display the relationship of AML with MMP2 and MMP9. There was a report (Ries et al., 1999) that in the case of patients with AML, leukemia blast cells produce MMP2, whereas bone marrow mononuclear cells express MMP9. Another study reported (Sawicki et al., 1998) that MMP2 expression contributes to the increased vascular density seen in the bone marrow of AML patients. The primary acute myelogenous leukemia cells secrete both pro-MMP2 and pro-MMP9. On the cell surface of AML cells, only the activated form of MMP2 was found (Sawicki et al., 1998) whereas, in the case of non-leukemic cells the active form of MMP2 was not detected. They suggested that the active form of MMP2 is essential for the in vitro invasion of leukemic cells (Sawicki et al., 1998). Janowska-Wieczorek et al. (Janowska-Wieczorek et al., 1999) also suggested that MMP2 and MMP9 may be responsible for the invasive phenotype of AML. Lin et al. (Lin et al., 2002) first proposed, MMP9 levels found in the bone marrow microenvironment, a potential surrogate measure for tracking the disease status of AML. Aref et al. showed that AML patients who had greater levels of MMP2 had a worse prognosis and shorter survival times than those who had lower levels (Aref et al., 2007). Additionally, in another study it was reported that AML blasts with elevated MMP2 and MMP9 expression may be related to the invasive nature of AML (Travaglino et al., 2008). Increased MMP2 expression in AML patients was linked to leukemogenesis, chemosensitivity, and AML blast cell invasion (Reikvam et al., 2010). Wang et al. (Wang et al., 2010A) reported the correlations of gelatinase-A, MT1-MMP, and TIMP-2 with the invasive nature of AML using the SHI-1 cell line. This study found that SHI-1 cells displayed high levels of active MMP2, MT1-MMP, and TIMP2, which led to more extramedullary infiltration in AML. The suppression of MMP2, MT1-MMP, and TIMP2 significantly reduced SHI-1 cell invasion (Wang et al., 2010A). Furthermore, when pro-MMP2 was activated, the constitutive strong expression of TIMP-2, MMP2, and MT1-MMP did not have a suppressive effect on the invasion of SHI-1 cells but rather had an activating effect (Wang et al., 2010A). Chaudhary et al. (Chaudhary et al., 2016) reported that MMP9 mRNA expression

increased 2.5-fold in AML patients (60-70% blasts) in comparison with healthy control whereas, patients having more blast crises expressed more MMP9 and its mRNA. MMP2 mRNA expression of C/T and T/T genotypes showed 2 fold increase in AML whereas the increase of MMP9 mRNA expression of C/T and T/T genotypes was 2.5-fold. Only MMP9 (-1562 C/T) showed significant polymorphic association in AML ($p<0.02$) and 3 fold ($p<0.04$) increased risk with tobacco and cigarette smokers in AML (Chaudhary et al., 2016). Pietrzak et el. (Pietrzak et el., 2021) performed a cytogenetic experiment on patients with AML and compared it with healthy control where genetic expressions of *MMP2, MMP9, and MMP16* were analyzed. The study reported that the genetic expression of *MMP2 and MMP16* is reduced while the expression of *MMP9* gene is unchanged in patients with AML in comparison with healthy control. The outcomes in patients with AML are in contrast to those seen in patients with different forms of solid tumors, where increased expression of *MMP2* and *MMP9* is frequently seen. The expression of these genes may be regulated differently, and there may be changes in gene transcription or posttranscriptional pathways in AML (Pietrzak et el., 2021). Therefore, the biological role of MMP-2 and MMP-9 in AML is yet to be well understood.

1.10.4.3. MMP2 and MMP9 in CML

Similar to AML, the biological roles of MMP-2 and MMP-9 in CML have not been well investigated, despite data suggesting that gelatinases could be a useful target for the treatment of CML. *In vitro* cell-based study using CML cells (K562) from bone marrow also revealed the production of MMP9 transcripts and a modest degree of MMP9 activity (Janowska-Wieczorek et al., 1999). The bone marrow mononuclear cells (BM-MNCs) of CML patients were also found to have MMP9 activity (Ries et al., 1999). In another investigation, peripheral blood MNC from 6 CML patients was found to express MMP2 in 3 samples while MMP9 was present in all 6 samples. The expressions of both MMP2 and MMP9 were also found in transfected murine FL5.12 cells with the bcr-abl constructs. The study also noted that the expression of MMP-9 in primary CML cells was up-regulated by the angiogenesis-promoting factor VEGF (Janowska-Wieczorek et al., 2002). Zhu et al. (Zhu et al., 2015) reported that TGF-1-mediated CML-specific BCR/ABL+ oncogene increased the expression of MMP9 (**Figure 1.11**). The study (Zhu et al., 2015) demonstrated that MMP9 could facilitate HSC transition from quiescence to the proliferative niche in CML. TGF-β1 induced PI3K/Akt/NF-κB/MMP9 signalling pathway which

is required for HSC recruitment in the CML niche. Quiescent c-kit+ HSCs remain in close proximity to stromal cells in a niche under steady-state conditions (Zhu et al., 2015). Membrane-bound cytokines like type III receptor tyrosine kinase ligand (mKitL) and intercellular adhesion

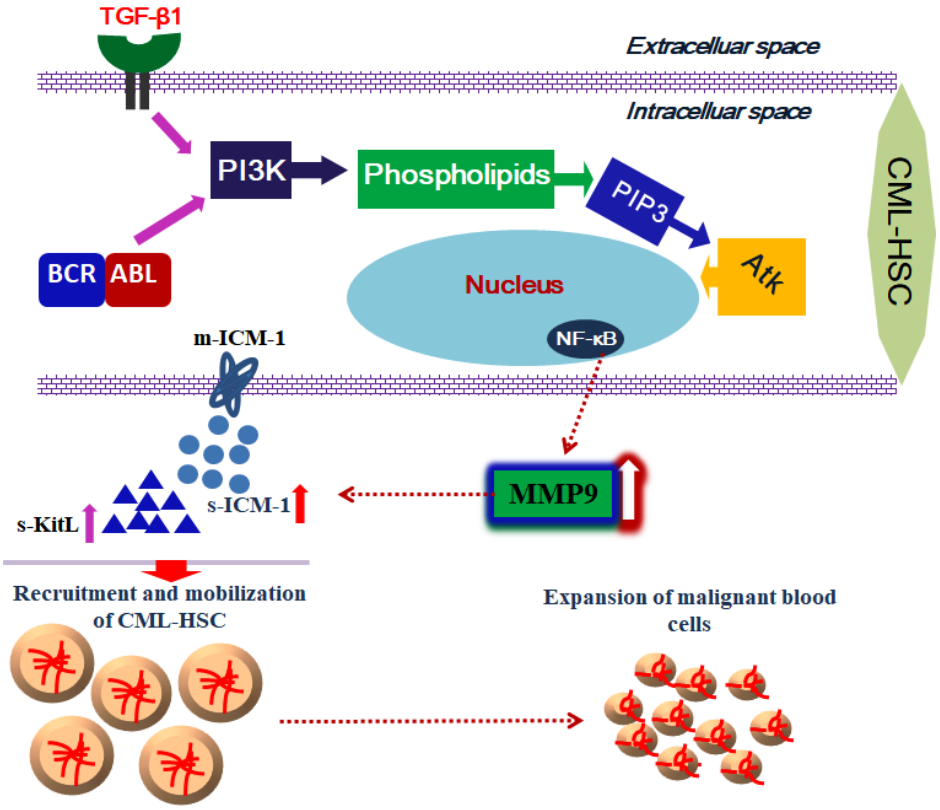

Figure 1.11. CML-specific oncogenes triggered the PI3K/Akt/NF-κB/MMP9 signalling pathway; enhance tumor stem cell mobilization and recruitment to the peripheral circulation.

molecule 1 (mICAM-1) help stem cells attach to the stroma as well as transmit survival signals (**Figure 1.11**). TGF-β1 produced by CML-specific oncogenes triggered the PI3K/Akt/NF-κB/MMP9 signalling pathway, releasing s-KitL (soluble KitL) and s-ICAM-1 ((soluble ICAM-1)) and enhancing tumor stem cell mobilization and recruitment to the peripheral circulation (**Figure 1.11**) (Zhu et al., 2015).

1.11. Application of QSAR in early stages of drug discovery

Drug discovery is a complex, lengthy, and costly process involving multiple stages, starting from identifying and validating targets, progressing through hit-to-lead generation, lead optimization, preclinical studies, and several phases of clinical trials. Bringing a new drug from initial research

to the market typically takes 10-15 years and requires an investment of approximately $2.5 billion (Tautermann, 2020; Hu et al., 2011; Gurung et al., 2021). To mitigate the time and cost involved in drug discovery, high-throughput screening and combinatorial technologies emerged in the 1990s, enabling faster synthesis and screening of large compound libraries (Baig et al., 2018). Presently, the drug discovery pipeline heavily relies on data-driven approaches, particularly leveraging bioactivity data from high throughput screening (HTS) campaigns (Nantasenamat and Prachayasittikul, 2015). However, acquiring new hit molecules through HTS campaigns is expensive, despite the vast amount of chemical and biological data stored in various databases. For instance, Chemical Abstract Services holds records of over 74 million molecules, with approximately 1,060 classified as new drug-like molecules (Achary, 2020).

Quantitative structure-activity relationship (QSAR) analysis is a chemometric technique in drug discovery that establishes mathematical correlations between structural modifications of chemical compounds and changes in their biological activities (Sharma and Bhatia, 2021). QSAR methods significantly contribute to enhancing the potency, efficacy, and selectivity of lead compounds intended for clinical studies (Sharma and Bhatia, 2021). QSAR analysis proves to be a cost-effective and potent in-silico drug discovery method due to its high throughput and good hit rate obtained from virtual screening studies (Neves et al., 2018). These models play a crucial role in reducing the number of compounds requiring synthesis and biological evaluation, facilitating hit discovery, hit-to-lead conversion, and lead optimization (Neves et al., 2018).

In recent years, QSAR approaches have become dominant in guiding lead optimization processes, garnering acceptance not only in academia and industry but also from regulatory bodies such as the FDA, Health Canada, and the European Union (EU) authorities (Kar et al., 2020). Regulatory agencies, including Health Canada and the Danish EPA, employ QSAR models for assessing and prioritizing substances, particularly under environmental protection regulations (Kar et al., 2020).

QSAR modeling revolves around constructing predictive models correlating the biological activity of chemicals with descriptors representative of molecular structure (Amin et al., 2016A). These models aim to quantitatively understand the relationship between molecular structures and changes in biological activities (Roy et al., 2009; Cherkasov et al., 2014). Statistical methods are employed to study correlations between biological activity and compound properties, leading to

the development of QSAR equations (Amin et al., 2016A). Various regression and classification-based approaches are utilized, and diagnostic statistics are employed to assess the reliability and predictability of QSAR equations. Ultimately, QSAR models enable the prediction of biological activities for novel candidate molecules (Cherkasov et al., 2014).

1.11.1. Various types of QSAR studies

The methodologies of QSAR can be classified in three main ways: based on the dimension of descriptors, based on chemometric methods, and based on the number of targets (**Figure 1.12**). Molecular descriptors in QSAR analysis encode chemical information that characterizes the behavior of compounds. These descriptors are computed numerically using appropriate algorithms and serve as independent variables for developing QSAR models (Roy et al., 2014).

In contrast, the dimension of an object refers to the minimum number of coordinates required to define a point within it. Dimension is an intrinsic property unaffected by the space in which the object exists (Crilly et al., 1999). In QSAR analysis, incorporating higher-dimensional descriptors provides a deeper level of structural information. Dimensionality acts as a constraint shaping the nature of the analysis, with increasing dimensionality in descriptors associated with greater complexity in modeling techniques. The dimension of a descriptor corresponds to the dimension of the compound it represents, specifically capturing that molecular feature.

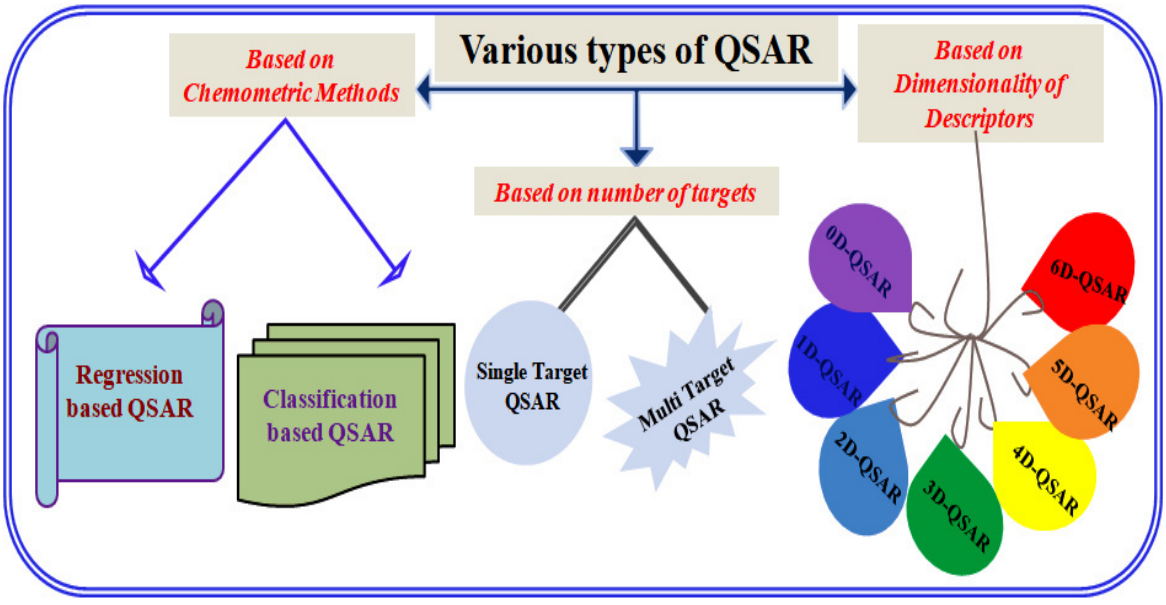

Figure 1.12. Various types of QSAR studies.

Hence, the dimensionality of QSAR analysis corresponds to the dimension of the computed descriptors utilized in constructing the QSAR model (Roy and Das, 2014). Based on the dimensionality of descriptors, QSAR methodologies are categorized into various dimensions, including 0D-QSAR, 1D-QSAR, 2D-QSAR, 3D-QSAR, 4D-QSAR, 5D-QSAR, and 6D-QSAR. Zero-dimensional (0D)-QSAR models rely on descriptors derived from molecular information such as molecular weight, atom count, atom types, and summed atomic properties. In contrast, 1D-QSAR models correlate activity or property with global molecular properties like pKa, solubility, logP, and functional groups (Todeschini and Consonni, 2009). Similarly, 2D-QSAR models correlate activity with structural patterns, employing descriptors derived from the topological representation of molecules. These descriptors encode information about molecular shape, size, branching, presence of multiple bonds, and heteroatom count, thus playing a crucial role in modeling various biological endpoints and physicochemical properties (Roy and Das, 2014). Commonly used topological indices include connectivity indices, Wiener index, Kier shape, Zagreb indices, and Balaban J index, with Wiener index being particularly prevalent (Danishuddin, 2016). Computation of topological indices is rapid and efficient as it only requires hydrogen-suppressed 2D-structural information of molecules (Danishuddin, 2016). Additionally, physicochemical descriptors such as hydrophobic, electronic, and steric features are vital in 2D-QSAR analysis and can be experimentally determined or computed from compound structures without energy minimization or conformational analysis (Roy and Das, 2014). On the other hand, 3D-QSAR involves the spatial orientation of molecules in three-dimensional space and correlates activity or property with non-covalent interaction fields (steric and electrostatic) surrounding the molecules (Tosco and Balle, 2011; Cramer, 2011; Cramer, 2012). 4D-QSAR extends this approach by incorporating an ensemble of ligand configurations, while 5D-QSAR and 6D-QSAR further integrate induced-fit and solvation models, respectively (Scior et al., 2012). QSAR methods can also be classified based on the type of chemometric methods employed, with linear methods such as linear regression (LR), multiple LR (MLR), principal component analysis (PCA), partial least squares (PLS), and genetic function approximation (GFA) being traditional options. However, newer techniques like support vector machine (SVM), artificial neural networks (ANN), k-nearest neighbors (kNN), and Bayesian neural nets have emerged as nonlinear and algorithmic alternatives (Nantasenamat et al., 2008;

Nantasenamat et al., 2013; Worachartcheewan et al., 2009; Ajmani et al., 2006; Klon et al., 2006).

Moreover, QSAR can be classified based on the number of dependent variables, such as single-target QSAR or multi-target QSAR, with recent studies emphasizing the benefits of multi-target drug design for complex diseases like Alzheimer's, cancer, diabetes, malaria, and tuberculosis (Ling et al., 2020; Benek et al., 2020; Makhoba et al., 2020).

1.11.2. 2D-QSAR model development

In accordance with the guidelines set forth by the Organization for Economic Co-operation and Development (OECD), the construction of a QSAR model necessitates adherence to specific criteria. These criteria encompass the clear definition of an endpoint, the utilization of an algorithm that ensures the model's transparency, the establishment of a defined domain of applicability, rigorous validation measures encompassing both internal performance (evaluated through measures like goodness-of-fit and robustness) and predictability (assessed through external validation), as well as the potential for providing mechanistic explanations (OECD, 2004). The process of developing a 2D-QSAR model generally involves several standardized steps. These steps encompass the careful selection and preparation of the dataset, the segmentation of the dataset into distinct training and test sets, the computation of molecular descriptors, the identification of pertinent features, the creation of the 2D-QSAR model itself, the validation of the model using appropriate metrics, and an analysis of the model's applicability domain (Peter et al., 2019).

1.11.2.1. Dataset selection and pre-processing of data

The initial step in QSAR analysis involves the meticulous preparation of a dataset, ensuring its integrity by eliminating errors, noise, and redundancy (Peter et al., 2019; Roy et al., 2015A). Biological activity or response data should be sourced from reliable and authentic references, with particular attention paid to excluding response values associated with high standard error values (Roy et al., 2015A). Furthermore, the dataset should ideally exhibit a normal distribution pattern concerning the values of the biological endpoint (Roy et al., 2015A). In cases where data are aggregated from various research laboratories, thorough scrutiny is essential to ensure consistency in experimental protocols across different groups (Roy et al., 2015A). Specifically,

all compounds and their associated response values considered for QSAR model development must originate from identical experimental protocols (Roy et al., 2015A).

The size of the dataset plays a critical role in QSAR model development to mitigate the risk of overfitting. According to Tropsha, for continuous response variables, a minimum of 40 compounds is recommended, with 20 in the training set and 10 each in the test and external evaluation sets (Tropsha et al., 2010). Similarly, for category or classification response variables, a minimum of 20 compounds is advised, with 10 in the training set and 5 each in the test and external evaluation sets (Tropsha et al., 2010). Ideally, the dataset should comprise 150-300 molecules in total for optimal QSAR model development, with approximately equal representation of compounds in each category or class in the case of classification-based QSAR (Tropsha et al., 2010).

For effective interpolation, the range of biological response/activity should span approximately 3.0 orders of magnitude on a logarithmic scale (Scior et al., 2009; Gedeck et al., 2006; Hamzeh-Mivehroud et al., 2015). When sourcing data from online databases, manual verification of compounds and their associated biological endpoint values is crucial to minimize errors (Roy et al., 2015A). In instances where the number of descriptors is excessive, a descriptor thinning process should be applied. This involves discarding descriptors with constant values across all observations, those exhibiting very low variance, and those showing excessive mutual inter-correlation (Roy et al., 2015A). Additionally, descriptors demonstrating minimal correlation with the biological endpoint values should be omitted to streamline the descriptor matrix (Roy et al., 2015A).

1.11.2.2. Dataset division (training set and test set)

The dataset is typically partitioned into two distinct subsets: the training set and the test set (Peter et al., 2019). The training set is utilized for the development of the QSAR model, while the test set serves to assess the model's predictability and accuracy (Peter et al., 2019). Employing an appropriate dataset-splitting technique is crucial to enhance the quality and predictability of the model. Various methods are employed for QSAR dataset division, including random selection, k-means clustering, Kennard-Stone selection, statistical molecular design, Kohonen's self-organizing map selection, sphere exclusion, and extrapolation-oriented test set selection (Peter et

al., 2019; De et al., 2022). Further detailed discussions on dataset division methods can be found in the existing literature (Golbraikh et al., 2002A; Roy et al., 2015B).

1.11.2.3. Calculation of molecular descriptors

According to Tropsha (Tropsha et al., 2003A), the cornerstone of successful QSAR model development lies in descriptors, descriptors, and descriptors (Dastmalchi et al., 2018A). Descriptors serve as numerical representations of molecular structures in QSAR modeling, enabling the conversion of molecular structures into quantifiable data (De et al., 2022; Dastmalchi et al., 2018A). These descriptors are essential as they act as predictors (X) of the dependent variable (Y) in a QSAR study (De et al., 2022). Molecular descriptors can be categorized into two main types. Firstly, structure-based descriptors, which can be theoretically computed from molecular representations, and secondly, non-structure-based descriptors such as Log P, pKa, dipole moment, molar refractivity, and polarizability (Dastmalchi et al., 2018A). Furthermore, molecular descriptors can also be classified based on their dimensionality (D) into zero-dimensional (0D), one-dimensional (1D), two-dimensional (2D), three-dimensional (3D), and so forth (Dastmalchi et al., 2018A; Engel et al., 2012; Roy and Mitra, 2012). Zero-dimensional (0D) descriptors are independent of molecular connectivity, conformation, and structure, encompassing constitutional descriptors, counts of atoms, and bond types (Dastmalchi et al., 2018A). One-dimensional (1D) descriptors represent counts of molecular groups as fragments and fingerprints, as well as physicochemical properties, with examples including Sybyl line notation (SLN) and simplified molecular input line entry system (SMILES) (Dastmalchi et al., 2018A). Two-dimensional (2D) descriptors are derived from molecular graph theory and encapsulate topological properties of molecules such as molecular connectivity indices, shape, size, and branching, independent of molecular conformation. Examples include Kier–Hall connectivity indices, Weiner index, and Randic connectivity index (Dastmalchi et al., 2018A). In contrast, three-dimensional (3D) descriptors correspond to the 3D representation of compounds, reflecting geometrical properties. Examples include WHIM (Weighted Holistic Invariant Molecular), GETAWAY (Geometry, Topology, and Atom-Weights AssemblY), and 3D-MoRSE (Molecular Representation of Structures based on Electronic diffraction) descriptors, potential energy descriptors, surface area, shape and volume descriptors, and quantum chemical-based parameters (Dastmalchi et al., 2018A). Furthermore, 4D descriptors are associated with

reference grids and molecular dynamic simulations (Peter et al., 2019). Various software tools are available for calculating molecular descriptors, as outlined in **Table 1.3** (Danishuddin et al., 2016). The comprehensive discussion of molecular descriptors can be found in existing literature (Doweyko et al., 2004; Dastmalchi et al., 2018A; Mauri et al., 2016).

Table 1.3. List of softwares and web servers available for the calculation of molecular descriptors.

Software	Type of descriptors	No. of descriptors	Web address	Paid/Free
PaDEL descriptor	1D, 2D, 3D descriptors, molecular fingerprints	1,875	www.padel.nus.edu.sg	Free
CDK	Topological, electronic, geometrical, constitutional	-	http://cdk.github.io	Free
E-DRAGON	Molecular descriptors		www.vcclab.org/lab/edragon/	Free
ALOGPS2.1	log P, log S	-	http://www.vcclab.org/lab/alogps/	Free
ACD/labs	log P, log S, log D, pKa	-	www.acdlabs.com	Free
ChemDes	Molecular descriptors	3,679	www.scbdd.com/chemdes	Free (Web)
PreADMET	Constitutional, physicochemical, geometrical, topological	>2,000	https://preadmet.webservice.bmdrc.org/preadmet-pc-version-2-0/	Paid
PowerMV	Constitutional, atom pairs, BCUT, fingerprints	1,000	www.niss.org/PowerMV	Free
ADAPT	Topological, physicochemical geometrical, electronic	260	www.research.chem.psu.edu	Free
MOLD2	1D, 2D	779	www.fda.gov	Free
JOELib	Counting, topological, geometrical properties, etc.	40	www.ra.cs.uni-tuebingen.de	Free
MODEL	Molecular descriptors	3,778	http://jing.cz3.nus.edu.sg/cgi-bin/model/model.cgi	Free (Web)
DRAGON	2D-autocorrelations, constitutional, topological, geometrical, GETAWAY, WHIM, RDF, functional groups, etc.	4,885	www.talete.mi.it	Paid
ADMET predictor	Constitutional, topological, functional group counts, E-state, acid-base ionization, molecular patterns, empirical estimates of quantum, 3D descriptors	297	www.simulations-plus.com	Paid
ADRIANA. Code	Constitutional, topological, functional group counts, E-state, Meylan flags, Moriguchi, 3D descriptors, etc.	1,244	www.molecularnetworks.com	Paid
CODESSA	Constitutional, geometrical, topological, semi-empirical, charge-related, thermodynamical	1,500	www.codessa-pro.com	Paid
MOE	Topological, structural keys, physical properties, etc.	300	www.chemcomp.com	Paid
MOLCONN-Z	Topological	40	www.edusoft-lc.com/molconn	Paid
MOLGEN-QSPR	Constitutional, geometrical, topological, etc.	707	www.molgen.molgenqspr.html	Paid
Sarchitect	Constitutional, 2D, 3D	1,084	www.strandls.com/sarchitect/index.html	Paid

1.11.2.4. Feature selection technique

The process of selecting an appropriate subset of descriptors from a vast pool of initial descriptors for a single compound is known as feature selection, a pivotal step in QSAR model development (Goodarzi et al., 2012). The primary objective of feature selection is to pinpoint significant predictor variables that establish correlations with the response variable (Goodarzi et al., 2012). This process serves to reduce model complexity, minimizing the risks associated with over-training and over-fitting (Goodarzi et al., 2012). The judicious selection of a subset of molecular descriptors directly impacts the predictive quality, stability, reliability, and robustness of developed QSAR models (Shahlaei et al., 2013; Khan et al., 2018).

In QSAR model development techniques, Khan and Roy (Khan et al., 2018) broadly categorized feature selection methods into three major groups:

a) **Classical Feature Selection Methods**: This group encompasses traditional techniques such as forward selection, backward elimination, stepwise regression, variable selection, modeling method based on prediction (VSMP), and Leaps-and-Bounds regression method.

b) **Feature Selection Applying Artificial Intelligence Algorithms**: Techniques in this group leverage artificial intelligence algorithms, including genetic algorithm (GA) method, ANN method, particle swarm optimization (PSO) method, ant colony optimization (ACO) method, simulated annealing (SA) method, and automatic relevance determination (ARD) method.

c) **Miscellaneous Methods**: This category includes approaches like replacement method (RM), k-nearest neighbors (k-NN) method, and successive projections algorithm (SPA), among others.

Feature selection techniques can also be classified as filter, wrapper, and hybrid methods based on their reliance on a learning algorithm (Shahlaei et al., 2013).

- **Filter methods** are unsupervised techniques that select features without using a learning algorithm. These methods include GSS coefficient, Shannon entropy, odds ratio, correlation-based feature selection, chi-square analysis, Kolmogorov-Smirnov statistics, Fisher score, distance-based method, and principle component analysis (Peter et al., 2019).
- **Wrapper methods** utilize both descriptors and a learning algorithm, with feature selection dependent on both dependent and independent variables. Examples include Bayesian

regularized neural network, recursive feature elimination, genetic algorithm, k-nearest neighbor, backward elimination, forward selection, variable selection, modeling based on prediction, factor analysis, and combinatorial protocol (Peter et al., 2019).

- **Hybrid feature selection methods** combine elements of both filter and wrapper methods.

Extensive discussions on feature selection techniques can be found in the existing literature (Shahlaei, 2013; Khan et al., 2018).

1.11.3. 2D-QSAR model building

In 2D-QSAR model-building approaches, the aim is to establish a mathematical relationship between descriptors and the biological endpoint or response values. Here, a set of descriptors, predictor variables, or independent variables are considered as a function of biological endpoint values or response variables, which are the dependent variables (Tropsha, 2010).

Statistical techniques employed for 2D-QSAR modeling are generally divided into two main classes: linear QSAR models and non-linear QSAR models (Golbraikh et al., 2002B).

1.11.3.1. Linear 2D-QSAR Models

Linear methods are extensively used in 2D-QSAR model building due to their simplicity, interpretability, and reproducibility. Linear 2D-QSAR models are straightforward and easily interpretable, making them highly favored. A variety of regression- and classification-based methods are employed to develop linear-based 2D-QSAR models (Roy et al., 2015C). Regression-based statistical approaches are applied when the biological response data of chemical compounds are entirely numerical or quantitative. Conversely, classification-based statistical techniques are generally employed when dealing with qualitative or semi-quantitative biological responses to chemical compounds (Roy et al., 2015C). In both cases, whether using regression-based or classification-based statistical methods, the descriptor values are quantitative (Roy et al., 2015C). In regression-based statistical techniques, the emphasis is on quantitatively predicting biological endpoints. In contrast, classification-based statistical techniques enable the classification or categorization of chemical compounds into various classes or groups based on their biological endpoints, such as active and inactive compounds (Roy et al., 2015C).

1.11.3.1.1. Regression-based 2D-QSAR model

Multiple linear regression (MLR) and partial least squares (PLS) represent regression-based linear statistical methods frequently employed in the development of QSAR models (Shahlaei et al., 2013).

1.11.3.1.1.1. Multiple linear regression (MLR) analysis

MLR analysis stands out as the most commonly utilized statistical approach in 2D-QSAR studies due to its simplicity, transparency, reproducibility, and ease of interpretation. MLR analysis extends from simple linear regression (SLR) by involving multiple independent variables. SLR, which forms the foundation of this analysis, is defined by the following mathematical ***Eq. (1.1***):

$$Y = mX + c \qquad (1.1)$$

Eq. (1.1) represents a two-dimensional linear equation, where Y denotes the dependent or response variable, X represents the independent variable or input value, m symbolizes the slope, and c denotes the constant term. Conversely, the mathematical model for MLR is expressed as ***Eq. (1.2)***:

$$Y = a_0 + a_1X_1 + a_2X_2 + a_3X_3 + a_4X_4 + \ldots\ldots\ldots\ldots + a_nX_n \qquad \textit{Eq. (1.2)}$$

Eq. (1.2) is a multi-dimensional linear equation where Y is dependent variable or biological endpoint value; a_0 is the slope of the line; X_1, X_2, X_3, …… X_n is independent variables or molecular descriptors with their respective coefficients a_1, a_2, a_3, a_4, …..a_n (Roy et al., 2015B; Roy et al., 2015C and Dastmalchi et al., 2018B).

1.11.3.1.1.2. Partial least squares (PLS) method

In the partial least squares method, the dependent variables or descriptors (X) and the independent variables or biological response values (Y) are typically transformed into new variables known as latent variables (LVs). These LVs (t1, …., tn) are linear combinations of the descriptors (X1, ……,Xm) (Dastmalchi et al., 2018B). Before employing the PLS technique, the response or dependent variables (Y) are commonly transformed into a logarithmic scale, and the independent variables (X) should be suitably scaled (Roy et al., 2015C). If the number of LVs equals the number of original variables, the PLS model effectively becomes an MLR model (Roy

et al., 2015C). The mathematical equations for the PLS method is presented below in ***Eq. (1.3-1.6):***

$$Y = a_1t_1 + a_2t_2 + ….. + a_nt_n \quad \textbf{(1.3)}$$

$$t_1 = b_{11}X_1 + b_{12}X_2 + …. + b_{1m}X_m \quad \textbf{(1.4)}$$

$$t_2 = b_{21}X_1 + b_{22}X_2 + …. + b_{2m}X_m \quad \textbf{(1.5)}$$

….

….

$$t_n = b_{n1}X_1 + b_{n2}X_2 + …. + b_{nm}X_m \quad \textbf{(1.6)}$$

In the PLS method, t1, …., tn represent latent variables that are orthogonal to each other and derived from independent variables (X1, ……, Xm) (Dastmalchi et al., 2018B). These latent variables encapsulate the variations of both descriptors (X) and biological activities (Y) (Dastmalchi et al., 2018B). PLS is particularly well-suited for datasets featuring a large number of X-variables that are highly collinear, noisy, and correlated. When the number of molecular descriptors approaches or exceeds the number of response variables, there's a risk of overfitting. In such scenarios, PLS analysis is preferred over MLR (Roy et al., 2015B).

1.11.3.1.1.3. Principal component analysis (PCA) technique

The principal component analysis (PCA) technique serves as a powerful tool for multivariate data analysis and data reduction. It aims to decrease the dimensionality of large datasets by transforming a comprehensive set of variables into a more condensed form without significant loss of information. Before initiating PCA, standardization of the initial dataset is essential to address potential issues arising from variations in variable ranges. This standardization ensures that variables with larger ranges do not dominate those with smaller ranges. Subsequently, the covariance matrix of variables is computed to discern correlations among them. Highly correlated variables may contain redundant information, which can be identified through the covariance matrix.

Next, eigenvectors and eigenvalues are derived from the covariance matrix to ascertain the principal components (PCs) of the data. These principal components are newly constructed

variables, formed as linear combinations of the initial variables, with the objective of being uncorrelated. The majority of information from the initial variables is consolidated into the first principal component. In a dataset with 'n' variables or dimensions, the number of PCs will also be 'n'. The eigenvector with the highest eigenvalue is designated as the first principal component, followed by the eigenvector with the second highest eigenvalue as the second principal component, and so forth. The significance of principal components is ordered according to the eigenvalues, with the first component containing the maximum possible information, followed by the second, and so on. After discarding less significant PCs, a matrix of vectors containing the remaining ones, referred to as feature vectors, is computed. Finally, using the feature vector derived from the eigenvectors of the covariance matrix, data from the original axes are transformed or reoriented to those represented by the principal components. This process elucidates how PCA operates as a data reduction tool (Jolliffe, 2002; Johnson and Wichern, 2007).

PCA finds extensive application in 2D-QSAR studies for analyzing complex datasets and identifying outliers (Yoo and Shahlaei, 2018). However, despite its widespread use, PCA also possesses limitations. It is not suitable for datasets with nonlinear relationships between descriptors, and it cannot handle missing values or mixed descriptors. Additionally, interpreting PCs and their correspondence to descriptors may be subjective and challenging (Yoo and Shahlaei, 2018).

1.11.3.1.1.4. Statistical metrics for regression-based 2D-QSAR models

Various statistical metrics are employed to assess the quality of regression-based 2D-QSAR models, including the correlation coefficient (R), squared correlation coefficient (R^2), adjusted R^2 (R^2_a), variance ratio (F) at specified degrees of freedom (df), and standard error of the estimate (SEE) (Amin et al., 2016A). However, it's important to note that these metrics are not validation parameters for the constructed 2D-QSAR models. To validate the predictive capability of a regression-based 2D-QSAR model on a new set of data, several internal and external validation parameters are utilized (Golbraikh et al., 2003). Internal validation parameters typically include leave-one-out (LOO) cross-validated R^2 (Q^2), the sum of squared deviations between the actual and predicted activities of the test set compounds (PRESS), and the sum of squared deviations error of prediction (SDEP) values. Conversely, R^2_{pred} is commonly

considered as the model's external validation parameter (Amin et al., 2016A; Todeschini et al., 2016).

1.11.3.1.1.4.1. Model quality parameters of regression-based 2D-QSAR study

In assessing model quality, the correlation coefficient (R) indicates how closely the observed data aligns with the fitted regression line. Meanwhile, the squared correlation coefficient (R2) is computed according to ***Eq. (1.7)***.

$$R^2 = 1 - \frac{\sum(y_{obs} - y_{calc})^2}{\sum(y_{obs} - y_{mean})^2} \qquad \textbf{(1.7)}$$

In ***Eq. (1.7)***, the squared correlation coefficient involves actual (y_{obs}) and predicted (y_{calc}) activity values of molecules within the training set, alongside the mean (y_{mean}) of the biological response values of those training set compounds. It's worth noting that the number of descriptors isn't factored into this equation, potentially diminishing its statistical reliability (Roy et al., 2015B). To address this limitation, adjusted R^2 (R^2_a) is calculated using ***Eq. (1.8)***, where n represents the number of scores and p denotes the number of descriptors.

$$R_a^2 = \frac{(n-1)\times R^2 - p}{n-p-1} \qquad \textbf{(1.8)}$$

The standard error of estimate (SEE) for the residuals is calculated using ***Eq. (1.9)***.

$$SEE = \sqrt{\frac{\sum(y_{obs} - y_{calc})^2}{n-p-1}} \qquad \textbf{(1.9)}$$

Where y_{obs} and y_{calc} represent the actual and predicted activity of the training set, respectively, n is the total number of data points, and p is the total number of molecular descriptors. A lower value of SEE indicates better model quality.

1.11.3.1.1.4.2. Model validation parameters of regression-based 2D-QSAR study

The predictive ability of any regression-based 2D-QSAR models can be judged by leave-one-out (LOO) cross-validation Q^2 and standard deviation of error of predictions (SDEP). Each molecule was deleted from the training set at each time and the activity of the deleted molecule was predicted simultaneously by the model constructed from the remaining compounds of the training set. The leave-one-out (LOO) Q^2 value was calculated as per equation **1.10**.

The predictive ability of any regression-based 2D-QSAR model can be assessed using leave-one-out (LOO) cross-validation Q^2 and the standard deviation of error of predictions (SDEP). For each molecule, it is removed from the training set, and its activity is predicted using a model constructed from the remaining compounds in the training set. The leave-one-out (LOO) Q^2 value is calculated according to ***Eq. (1.10)***.

$$Q^2 = 1 - \frac{\Sigma(y_{obs} - y_i)^2}{\Sigma(y_{obs} - y_{mean})^2} \qquad \textbf{(1.10)}$$

Where y_{obs} and y_i are the respective actual and predicted biological activity of the i^{th} compound belonging to the training set, and y_{mean} denotes the mean biological activity of the training set molecules. Additionally, PRESS and SDEP values were determined to assess the internal predictability of the model.

The external predictability of the developed 2D-QSAR models was also evaluated through external validation using the test set compounds. The R^2_{pred} is the external validation parameter, which is calculated according to ***Eq. (1.11)***.

$$R^2_{pred} = 1 - \frac{\Sigma(y_{obs} - y_i)^2}{\Sigma(y_{obs} - y_{mean})^2} \qquad \textbf{(1.11)}$$

Where y_{obs} and y_i are the respective actual and predicted biological activity of the i^{th} molecule of the training dataset, and y_{mean} is the mean biological activity of the test dataset.

The R^2_{pred} value alone is not sufficient to confirm the external predictability of a model. Its value is primarily influenced by the sum of squared differences between observed biological activities of the test set compounds and the mean observed activities of the training set compounds. Therefore, it may not accurately reflect the predictability of the model (Roy and Mitra, 2012). To address this limitation, the r^2_m metrics ($r^2_{m(LOO)}$, $r^2_{m(test)}$ and $r^2_{m(overall)}$) are utilized to estimate the closeness between the values of the predicted and observed biological activities of the training set, the test set, and the total dataset, respectively. The r^2_m value should exceed 0.50 and is calculated as per ***Eq. (1.12)*** (Roy et al., 2015B).

$$r^2_{m(test)} = r^2 \times \left(1 - \sqrt{r^2 - r_0^2}\right) \qquad \textbf{(1.12)}$$

Where r^2 and r^2_0 are the squared correlation coefficients between the actual and predicted biological responses of the test set molecules.

1.11.3.1.1.4.3. Y-Randomization test

The Y-randomization test is a widely used technique to ensure the robustness and validation of a 2D-QSAR model (Rücker et al., 2007). In this test, the dependent or response variable (Y), is randomly and repeatedly shuffled, and new QSAR models are generated using the independent-variable matrix. The expectation of the Y-randomization test is that the resulting QSPR models should generally have low R^2 and low LOO Q^2 values. It is likely that sometimes, high Q^2 values may be obtained due to a chance correlation or structural redundancy of the training set. If all QSPR models generated in the Y-randomization test have relatively high R^2 and LOO Q^2 values, an acceptable QSPR model cannot be built by the current modeling method for the given data set of compounds (Tropsha et al., 2003B).

1.11.3.1.2. Classification-based 2D-QSAR model

The widely employed techniques in classification-dependent QSAR investigations encompass linear discriminant analysis (LDA), Bayesian classification modeling, and the recursive partitioning method.

1.11.3.1.2.1. Linear discriminant analysis (LDA)-QSAR model

Linear discriminant analysis (LDA) serves as a pattern-recognition method utilized for constructing classification-based models and is particularly valuable for dimensionality reduction (Ren et al., 2016). Similar to MLR analysis, the LDA technique undertakes a comparable role by predicting an output when the response variable is categorical, while the molecular descriptors are continuous variables (Roy et al., 2015A).

1.11.3.1.2.1.1. Validation parameters for LDA

The statistical validation parameters utilized for LDA encompass metrics such as accuracy, sensitivity, specificity, precision, Matthews's correlation coefficient (MCC), and the F1 measure (Pérez-Garrido et al., 2011; Gálvez-Llompart et al., 2011; Roy and Mitra, 2011; and Roy et al., 2015B). Additionally, the quality of the training set is evaluated through the Wilks parameter (λ), while the relative significance of selected descriptors employed in the LDA-QSAR model is

assessed based on the Fisher-Snedecor parameter (F) (Pérez-Garrido et al., 2011; Gálvez-Llompart et al., 2011; Roy and Mitra, 2011; and Roy et al., 2015B). These statistical validation parameters, including sensitivity, specificity, precision, accuracy, F1 measure, and Matthews's correlation coefficient (MCC), are calculated to ensure the robustness and reliability of the LDA model as per ***Eq. (1.13-1.18)***.

$$Sensetivity = \frac{TP}{(TP+FN)} \quad \textbf{(1.13)}$$

$$Specificity = \frac{TN}{(TN+FP)} \quad \textbf{(1.14)}$$

$$Precision = \frac{TP}{(TP+FP)} \quad \textbf{(1.15)}$$

$$Accuracy = \frac{(TP+TN)}{(TP+FP+TN+FN)} \quad \textbf{(1.16)}$$

$$F1 = \frac{2TP}{(2TP+FP+FN)} \quad \textbf{(1.17)}$$

$$MCC = \frac{(TP*TN)-(FP*FN)}{\sqrt{(TP+FP)(TP+FN)(TN+FP)(TN+FN)}} \quad \textbf{(1.18)}$$

Where TP is the true positive or the number of known 'active' compounds that appeared as 'active' in the model. The FN is the false negative which is known as 'active' compound that appeared 'inactive'. The TN denotes the true negative which is the total number of known 'inactive' molecules predicted as 'inactive'. The FP is false positive which is the number of known 'inactive' predicted as 'active'.

Additional validation parameters for the LDA model include the receiver operating characteristics curve Euclidean distance (ROCED) and the receiver operating characteristics curve Euclidean distance corrected with the fitness function (ROCFIT). ROCED and ROCFIT are calculated using the following formulas (Rücker et al., 2007 and Pérez-Garrido et al., 2011) in ***Eq. (1.19-1.21)***:

$$d_i = \sqrt{(1 - Sensitivity)^2 + (1 - Specificity)^2} \quad \textbf{(1.19)}$$

$$ROCED = (|d_1 - d_2| + 1)(d_1 + d_2)(d_2 + 1) \quad \textbf{(1.20)}$$

$$ROCFIT = \frac{ROCED}{FIT(\lambda)} \quad \textbf{(1.21)}$$

Where d_i = Euclidean distance between the perfect and a real classifier, $i = 1$ denotes the training set, $i = 2$ denotes the test set, and FIT(λ) = Wilk's parameter.

The performance of the LDA-QSAR model is assessed by determining the area under the receiver operating characteristic curve (AUROC) (Fawcett, 2006).

1.11.3.1.2.2. Bayesian classification model

The Bayesian classification study relies on the principles of Bayes' theorem (Zhang et al., 2016 and Liu et al., 2014A) which is given below in ***Eq. (1.22)***.

$$P(M/N) = \frac{P(N/M)P(M)}{P(N)} \qquad \textbf{(1.22)}$$

In Bayesian classification modeling, M represents the model and N represents the observed data. The posterior probability is denoted as P(M/N), while the likelihood is represented by P(N/M). P(M) stands for the prior belief, and P(N) represents the evidence data.

Bayesian classification modeling studies aim to classify or discriminate important sub-structural features in molecules. Various structural and physiochemical descriptors, such as lipophilicity, number of rotatable bonds, molecular weight, total number of rings and aromatic rings, number of hydrogen bond donors and acceptors, molecular polar surface area, and molecular extended connectivity fingerprints of maximum diameter 6 (ECFP_6), are typically considered for developing Bayesian models (Das et al., 2021B; Adhikari et al., 2018A; Adhikari et al., 2018B; Jha et al., 2018 and Das et al., 2022A).

1.11.3.1.2.2.1. Validation parameters for Bayesian classification model

The validation parameters for the Bayesian model typically include leave-one-out (LOO) cross-validation and 5-fold cross-validation (Das et al., 2021B; Adhikari et al., 2018A; Adhikari et al., 2018B; Jha et al., 2018 and Das et al., 2022A). Similar to the LDA method, the internal and external predictability performances of the Bayesian classification model are also assessed by evaluating metrics such as the area under the receiver operating characteristic curve (AUROC), accuracy, specificity, sensitivity, precision, F1 measure, Matthews's correlation coefficient (MCC), etc., for both the training and test set compounds (Zhang et al., 2016; Liu et al., 2014A; Klon et al., 2006; Das et al., 2021B and Adhikari et al., 2018A).

1.11.3.1.2.3. Recursive Partitioning Method

The recursive partitioning (RP) method is another classification-based QSAR approach that constructs one or more decision trees to elucidate the relationship between a dependent or biological response variable (Y) and a set of independent variables or molecular descriptors (X). The RP method categorizes data by employing a set of hierarchical rules to partition a dataset into progressively smaller subsets. The outcome of the RP method is a decision tree generated through a recursive partitioning process. This process involves splitting the study samples based on whether a particular selected predictor is above a chosen cutoff value or not. At each splitting step, all molecular descriptors are sequentially examined to identify the optimal criterion for subdividing compounds. Once the best criterion is determined, a similar process is repeated for each obtained class of molecules (Amin et al., 2021A and Chen et al., 2011).

1.11.3.2. Non-linear QSAR models

To explore potential non-linear relationships between descriptors and biological endpoints or response values, several machine learning methods are utilized. Among these, SVM and ANN are commonly employed techniques for developing non-linear QSAR models (Nantasenamat et al., 2008; Nantasenamat et al., 2013; Das et al., 2022A; Amin et al., 2016B; Amin et al., 2017A).

Optimization of SVM parameters such as the exponent value (ε), complexity parameter (C), kernel type, and corresponding parameters (γ), along with ANN parameters including the number of hidden nodes, learning momentum, learning rate, and training time, is carried out using Autoweka software (Nantasenamat et al., 2015). Subsequently, regression-dependent nonlinear models are generated with optimized parameters using Weka software (Hall et al., 2009).

1.11.3.2.1. Support vector machine (SVM) technique

Support vector machine (SVM) (Hall et al., 2009) employs a non-linear mapping of input descriptors into a higher dimensional feature space through a kernel function (Vapnik et al., 1998; Yao et al., 2004; Evgeniou et al., 2001). This method focuses on estimating model parameters using a convex optimization approach (Vapnik et al., 1998; Yao et al., 2004; Evgeniou et al., 2001), making it suitable for both classification and regression problems (Nantasenamat et al., 2013). Various kernel functions, including linear, polynomial, sigmoid kernels, and radial basis function (RBF) kernel, are integrated into the SVM method

(Nantasenamat et al., 2013). In SVM-based nonlinear QSAR studies, the descriptor matrix is transformed into a high-dimensional feature space from the input feature space using kernel functions [K(x, y)]. Mathematically, the kernel function [K(x, y)] allows the SVM to efficiently handle complex relationships between descriptors and biological endpoints is described by ***Eq. (1.23)***.

$$K(x, y) = \{Ø(x) * Ø(y)\} \qquad (1.23)$$

Where K is a kernel function and Ø is a mapping from input space X € x, y to the feature space F.

1.11.3.2.2. Artificial neural network (ANN) method

Artificial neural network (ANN) (Livingstone et al., 1993; Tetko et al., 1995; Livingstone et al., 1997) is widely used for building QSAR models (Amin et al., 2017A). ANN operates on a framework akin to the human brain, where nodes in the network resemble biological neurons, and layers (input, hidden, and output layers) correspond to synaptic weights in neurons. In the ANN-based QSAR approach, molecular information encoded in descriptors is input into the input layer, transmitted through the hidden layer nodes, and finally processed in the output layer (Livingstone et al., 1993).

Commonly used ANN architectures in QSAR include Bayesian regularized neural networks, backpropagation neural networks, probabilistic neural networks, and Kohonen self-organizing maps. ANNs are highly adaptable and effective for modeling nonlinear systems with high variability in datasets. They often outperform traditional linear models like MLR or PLS (Peter et al., 2019). However, ANNs have limitations, such as lacking explicit knowledge representation in the form of rules and having a higher computational burden. Additionally, ANN model development is empirical and prone to overfitting (Shi et al., 2010).

1.11.3.2.3. Validation Parameters for Non-Linear QSAR Study

The Pearson's correlation coefficient for the training set (r_{train}), cross-validated correlation coefficient (r_{cv}), the test set correlation coefficient (r_{test}), and the corresponding root mean squared error (RMSE) are essential statistical parameters used to assess the validation and robustness of SVM and ANN models (Amin et al., 2021A).

1.11.4. Interpretation and applicability domain analysis

The descriptors utilized in constructing QSAR models should possess interpretability, enabling a mechanistic understanding of their impact on predicted activity. Conducting AD analysis proves instrumental in comprehending the extent to which QSAR models can effectively predict the behavior of new compounds (Peter et al., 2019; Roy et al., 2015B). AD is conceptually defined as the theoretical region within the chemical space spanned by the molecular descriptors employed in the QSAR model alongside response variables (Gramatica, 2007). The predictive relevance of QSAR model outputs hinges on whether the compound being predicted falls within the model's AD (Roy et al., 2015B). Various methods are employed to identify or estimate this theoretical region in chemical space, including distance-based methods, geometrical methods, probability density distribution, ranges in descriptor space, and response variable ranges (Jaworska et al., 2005). Approaches such as distance-based methods, geometrical methods, probability density distribution, and ranges in descriptor space rely on the model descriptor space for interpolation space characterization. Conversely, the methodology for determining the range of response variables is solely based on the response space of the training set molecules. In the ranges approach, a compound is deemed outside the domain of applicability if at least one descriptor falls outside the defined range. Likewise, in the distance-based method, if the distance between the compound and the center of the training dataset exceeds a specified threshold, the compound is considered beyond the domain of applicability (Roy et al., 2015B).

1.12. Topomer CoMFA technique

The topomer comparative molecular field analysis (topomer CoMFA) technique is a method for investigating 3D-QSAR that is fragment-based and alignment-independent (Tong et al., 2020; Tong et al., 2021; Chhatbar et al., 2019; Niu et al., 2018). This approach involves dissecting three-dimensional molecular structures into smaller fragments, aligning each fragment based on their meeting points to establish an absolute orientation for each piece. Subsequently, three-dimensional steric and electrostatic fields are estimated to generate descriptors, while the carbon sp3 probe is utilized to assess the interaction energy between solids and electrons. In the construction of topomer CoMFA models using PLS regression analysis, these descriptors serve as independent variables, with pKi values acting as dependent variables. The quality of the models is evaluated based on key parameters such as the coefficient of determination (R^2) and

the leave-one-out (LOO) cross-validated R^2 (Q^2). A Q^2 value exceeding 0.5 and an R^2 value greater than 0.6 indicate excellent predictive performance of the model (Tong et al., 2021 and Chhatbar et al., 2019).

1.13. Molecular docking study

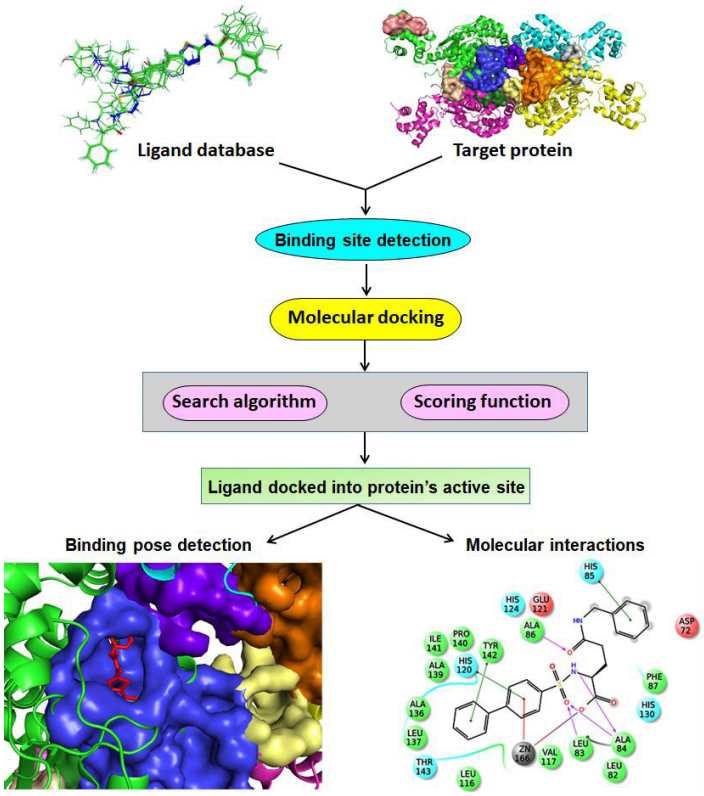

Figure 1.12. Overall workflow of molecular docking.

The interaction between drugs and target proteins can be likened to a handshake, where both entities attempt to adjust to accommodate each other to some extent. Molecular docking studies represent one of the most potent methods for comprehending protein-ligand interactions (Kalyaanamoorthy and Chen, 2011). Presently, molecular docking has become a routine tool employed at various stages of drug design processes (Tripathi and Bankaitis, 2017). In protein-ligand docking, typically, a candidate ligand, a target of interest, and a procedure for estimating binding interaction poses are required. The general workflow of molecular docking is illustrated in **Figure 1.12**. In molecular docking studies, the candidate ligand can encompass a variety of molecules, including small molecules, DNA, peptides, and occasionally even proteins themselves. The RCSB Protein Data Bank (PDB) serves as the primary repository of protein

target structures, offering access to biomolecular structures for molecular docking investigations (Burley et al., 2018). Presently, the RCSB Protein Data Bank (https://www.rcsb.org/) hosts over 62,000 PDB entries of protein-ligand complexes, with approximately 60,000 solved via X-ray crystallography and around 1,700 via nuclear magnetic resonance (NMR) methods. A plethora of commercial and open-source molecular docking algorithms are available, capable of accurately predicting protein-ligand poses and computing binding energies. Table 1.4 presents a compilation of protein-ligand docking tools.

Table 1.4. List of protein-ligand docking software/tools.

Software/tools	Source	Method	Types
3D-Dock Suite	http://www.sbg.bio.ic.ac.uk/docking/index.html	Fourier correlation algorithm, self-consistent mean field optimization procedure, single distance constraint empirically derived pair potential	PLI[a]
ArgusLab	http://www.arguslab.com	Genetic algorithm and ArgusDock	PLI[a]
AutoDock	http://autodock.scripps.edu/	Lamarckian genetic algorithm	PLI[a]
BiGGER	http://www.cqfb.fct.unl.pt/	Soft-docking	PLI[a]
ClusPro	https://cluspro.org/	10 most populated low energy clusters, irmsd > 9 Å	ADW[b]
Dock Vision	http://dockvision.com/	Hybrid evolutionary algorithm	PLI[a]
DOT	http://www.sdsc.edu/CCMS/DOT/	Fast Fourier transforms	PLI[a]
FlexX	http://www.biosolveit.de/FlexX/	Sequential importance sampling (SIS)-algorithm	PLI[a]
FRED	http://www.eyesopen.com/fred	Directed docking with SMiles ARbitrary target specification (SMARTS) patterns	PLI[a]
Gold	http://www.ccdc.cam.ac.uk/	Genetic algorithm	PLI[a]
GRAMM-X	http://vakser.compbio.ku.edu/resources/gramm/grammx/	Up to 300 lowest energy conformations	ADW[b]
HADDOCK	https://wenmr.science.uu.nl/haddock2.4/	Fully flexible for interacting residues of peptide and protein	ADW[b]
HADDOCK	http://www.nmr.chem.uu.nl/haddock/	Uses ambiguous interaction restraints of NMR	PLI[a]
HDOCK	http://hdock.phys.hust.edu.cn/	Top 100 lowest energy clusters, lmrsd > 5 Å	ADW[b]
Hex	http://www.loria.fr/ritchied/hex/	Similar to conventional fast Fourier transform (FFT)	PLI[a]
InterPred	http://bioinfo.ifm.liu.se/inter/interpred/	No conformational search (template-based)	ADW[b]
LZerD	https://lzerd.kiharalab.org/	Up to 50,000 generated geometries	ADW[b]
MDockPP	https://zougrouptoolkit.missouri.edu/MDockPP/	Up to 3000 generated geometries; clustering cutoff adjustable	ADW[b]
PatchDock	http://bioinfo3d.cs.tau.ac.il/PatchDock/	Up to 100 top ranking candidates; clustering cutoff adjustable	ADW[b]
pyDockWEB	http://life.bsc.es/servlet/pydock	Top 100 lowest energy conformations	ADW[b]
rDock	http://www.ysbl.york.ac.uk/rDock	Weighted sum of intermolecular, ligand intramolecular, site intramolecular and external restraint terms	PLI[a]
RosettaDock	http://rosettadock.graylab.jhu.edu	1000 decoys can be downloaded	ADW[b] servers
Surflex-Dock	http://www.tripos.com/	Hammerhead docking system	PLI[a]
ZDOCK	https://zdock.umassmed.edu/	Top 10 lowest energy conformations; possibility to retrieve top 500	ADW[b]

[a]PLI, protein-ligand interactions; [b]ADW, automatic docking web servers.

Over the past five decades, protein-ligand docking has demonstrated a remarkable track record of practical applications, ranging from the identification of novel enzyme inhibitors, receptor antagonists and agonists, to ion channel blockers. This has culminated in the approval of new drugs discovered through structure-based drug design methodologies. With the ongoing advancements in computational power, the field of molecular modeling is rapidly evolving, with developments aimed at achieving a finer balance between accuracy and computational efficiency. These endeavors are expected to pave the way for even more captivating applications in the future.

1.13.1. Stages of molecular docking study

Molecular docking primarily consists of two key stages: (1) sampling and (2) scoring function, as illustrated in **Figure 1.13** (Salmaso and Moro, 2018). The sampling process efficiently explores the conformational space defined by the free energy landscape, while the scoring function assigns a score to each predicted pose generated during the sampling process (Huang and Zou, 2010; Abagyan and Totrov, 2001; Kitchen et al., 2004). Essentially, the scoring function facilitates the identification of the native bound conformation by associating it with the global minimum of the energy hypersurface.

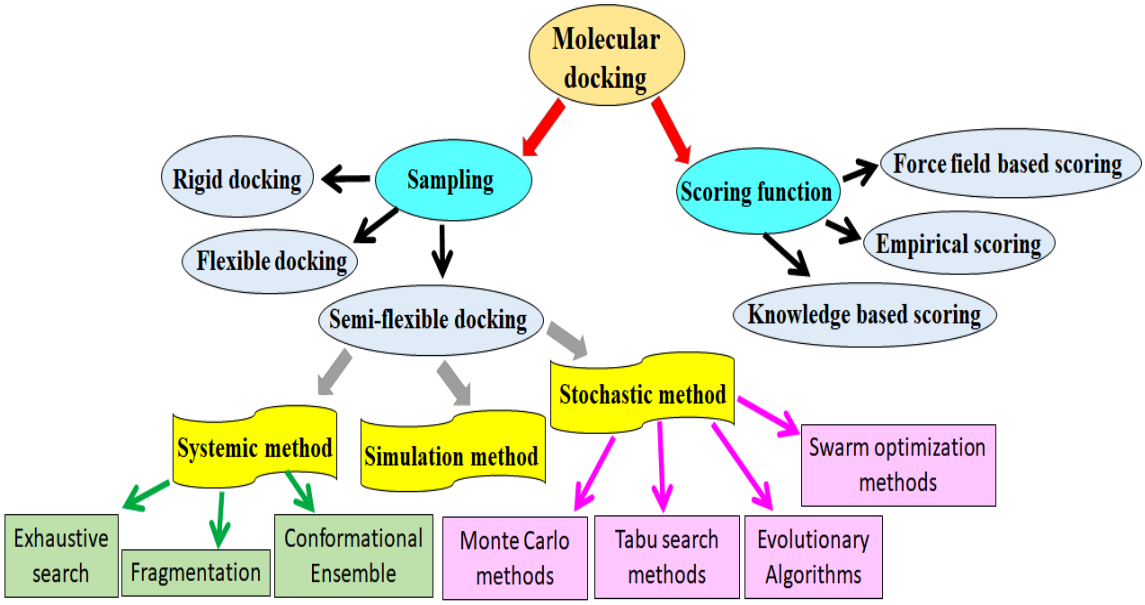

Figure 1.13. Schematic representation of the stages of molecular docking - (1) sampling and (2) scoring function.

1.13.1.1. Sampling

Kuntz et al. (Kuntz et al., 1982) introduced the first molecular docking algorithm in the 1980s. This pioneering method utilized a series of spheres to approximate the surface clefts of the receptor, along with another set of spheres to estimate the volume of the ligand. The primary objective was to identify the optimal steric overlap between the binding site and receptor spheres, without considering conformational mobility. As per Nussinov and colleagues' classification of docking methods based on the flexibility of the molecules involved, this approach falls under the category of fully-rigid docking procedures (**Figure 1.13**) (Halperin et al., 2002). Notably, any docking software necessitates protein-ligand sampling algorithms to generate suitable ligand poses. These algorithms, crucial for achieving accurate ligand posture and active site placement, can be categorized into three types: systematic search algorithms, shape-matching algorithms, and stochastic algorithms.

1.13.1.1.1. Rigid docking study

In rigid docking studies, both the ligand and the protein are treated as rigid entities, with only the three translational and three rotational degrees of freedom being considered during sampling (Salmaso et al., 2018). This approach corresponds to the "lock-key" binding model and is commonly employed in protein-protein docking, particularly when the number of conformational degrees of freedom is prohibitively large to sample. Typically, these approaches estimate the binding site and ligand using "hot" points, and assess the superposition of matching points (Taylor et al., 2002).

1.13.1.1.2. Semi-flexible docking study

In semi-flexible docking studies, the ligand is the only molecule allowed to be flexible, while the protein remains rigid. Along with the six translational and rotational degrees of freedom, the structural flexibility of the ligand is sampled. These approaches operate under the assumption that a protein's stable conformation corresponds to one that can effectively recognize the ligands being docked (Salmaso et al., 2018). However, it's important to note that this assumption may not always hold true.

1.13.1.1.2.1. Systematic search techniques

Table 1.5. Three types of systemic search techniques

Search type	Characteristic	Incorporated by software/tool
Exhaustive search	Search in the strict sense since all the rotatable bonds of the ligands are examined in a systematic way	**Glide** (Friesner et al., 2004 and Halgren et al., 2004)
Fragmentation		**FlexX** (Rarey et al., 1996) **Hammerhead** (Welch et al., 1996)
Conformational Ensemble	an ensemble of previously generated conformers of the ligand is docked to the target	**FLOG** (Miller et al., 1994) **EUDOC** (Pang et al., 2001) **MS-DOCK** (Sauton et al., 2008)

Systematic search involves exploring a predefined set of discretized values associated with each degree of freedom, systematically traversing all coordinate values in a combinatorial manner (Brooijmans and Kuntz, 2003). These techniques can be categorized into three types (**Table 1.5**).

1.13.1.1.2.2. Stochastic methods

Table 1.6. The most famous stochastic algorithms

Algorithms	Characteristic	Incorporated by software/tool
Monte Carlo (MC) methods	Metropolis Monte Carlo algorithm, which introduces an acceptance criterion in the evolution of the docking search	**AutoDock** (Gohlke et al., 2000; Morris et al., 1996) **ICM** (Abagyan et al., 1994) **QXP** (McMartin and Bohacek, 1997) **MCDOCK** (Liu and Wang, 1999) **AutoDock Vina** (Trott Olson, 2010) **ROSETTALIGAND** (Meiler and Baker, 2006)
Tabu search methods		**PRO_LEADS** (Baxter et al., 1998) **PSI-DOCK** (Pei et al., 2006)
Evolutionary Algorithms (EA)	Based on the idea of biological evolution, with the most famous Genetic Algorithms (GAs). The concept of the gene, chromosome, mutation, and crossover is borrowed from biology.	**GOLD** (Jones et al., 1995 and Jones et al., 1997) **AutoDock 3 & 4** (which implement a different version of GA, the Lamarckian GA) (Morris et al., 1998) **PSI-DOCK** (Pei et al., 2006) **rDock** (Ruiz-Carmona et al., 2014)
Swarm optimization (SO) methods	These methods take inspiration from swarm behavior.	**PLANTS** (Korb et al., 2006) **SODOCK** (Chen et al., 2007) **pso@autodock** (Namasivayam Günther, 2007)

In stochastic methods, the values of the system's degrees of freedom are altered randomly instead of following a systematic pattern. The advantage of stochastic algorithms lies in their speed, as they have the potential to rapidly identify the best solution. However, stochastic approaches are limited in that they do not guarantee a comprehensive exploration of the conformational space, which could result in the true solution being overlooked. Increasing the number of iterations may partially address the issue of convergence deficiency (Huang and Zou, 2010). **Table 1.6** provides an overview of the prominent stochastic algorithms.

1.13.1.1.3. Flexible docking study

Flexible docking studies are founded on the premise that proteins are not passive rigid entities during binding, and that both the ligand and the protein exhibit flexibility. Over time, various techniques have emerged for flexible docking, some rooted in the induced fit binding model and others in conformational selection (Salmaso et al., 2018). Flexible docking introduces numerous degrees of freedom, resulting in a potential energy surface that depends on many coordinates. Consequently, the computational demands of docking calculations increase, necessitating fine-tuning of sampling and scoring to strike a suitable balance between accuracy and speed (Salmaso et al., 2018). Indeed, the speed of docking calculations often determines the success of virtual screening campaigns involving millions of molecules. Therefore, advancements have been made in developing novel algorithms capable of thoroughly exploring phase space without compromising speed.

1.13.1.2. Scoring functions

Within the pool of poses generated by the sampling engine, scoring functions act as pose selectors, distinguishing potential valid binding modes and binders from non-binders. Another approach involves combining multiple scoring functions to achieve what is referred to as consensus scoring (Charifson et al., 1999). Additionally, novel scoring functions, such as interaction fingerprints and those utilizing quantum mechanical scores, have been developed using machine learning technology (Yuriev et al., 2015).

Table 1.7. Three types of scoring functions

Scoring functions	Characteristics	Incorporated by software/tool
Force-field based	Force-field is a molecular mechanics concept that approximates the potential energy of a system composed of bonded (intramolecular) and nonbonded (intermolecular) components. Nonbonded components are generally taken into account in molecular docking, with presumably the addition of ligand-bonded terms, particularly torsional components. It also includes the solvation terms (Brooijmans and Kuntz, 2003).	**GoldScore** (Verdonk et al., 2003) **AutoDock** (Morris et al., 1998) (improved as a semiempirical version in **AutoDock4** (Huey et al., 2007) **GBVI/WSA** (Corbeil et al., 2012)
Empirical	These functions are the sum of various empirical energy terms such as van der Waals, hydrogen bond, electrostatic, entropy, desolvation, hydrophobicity, etc., which are weighted by coefficients optimized to reproduce binding affinity data of a training set by least squares fitting (Huang and Zou, 2010).	**LUDI** (Böhm, 1994); **GlideScore** (Friesner et al., 2004 and Halgren et al., 2004) **ChemScore** (Eldridge et al., 1997) **PLANTSCHEMPLP** (Korb et al., 2006)
Knowledge-based	These approaches assume that statistically more explored ligand-protein contacts are associated with favourable interactions.	**DrugScore** (Velec et al., 2005) **GOLD/ASP** (Mooij and Verdonk, 2005)

1.14. Molecular Dynamics (MD) Simulations

Molecular dynamics (MD) simulations have become a cornerstone of many drug discovery programs from hit identification to lead optimization and far beyond (Sussman and Silman, 2020). MD simulations have quite a substantial effect not just on drug development, but also on molecular biology. It analyses the time-resolved motion of proteins and other biomolecules by preserving the movements of macromolecules in full atomic detail while maintaining a good temporal resolution. The visualization of MD trajectories offers a rapid and instinctive comprehension of dynamics and function (**Figure 1.14**) (Hollingsworth and Dror, 2018). It can generate a plethora of information regarding protein and ligand interactions as well as dynamic structural information on biomacromolecules (Adcock and McCammon, 2006). This knowledge is crucial for establishing the target's structure-function relationship and the fundamentals of protein-ligand interactions, as well as for directing the drug development and design approach

(**Figure 1.14**). As a result, MD simulations have been extensively and reliably used in all stages of current drug discovery research (Liu et al., 2018). Based on a general model of the physics driving interatomic interactions, it also predicts how each atom in a protein or other molecular system would move over time (Karplus et al., 2002). These simulations are capable of capturing a wide range of key biomolecular processes, such as conformational change, ligand binding, and protein folding. At femtosecond temporal resolution, it can reveal the positions of all atoms (Hildebrand et al., 2019). Moreover, such simulations may also anticipate how biomolecules will respond to perturbations such as mutation, phosphorylation, protonation, or the addition or removal of a ligand at the atomic level (Hollingsworth and Dror, 2018).

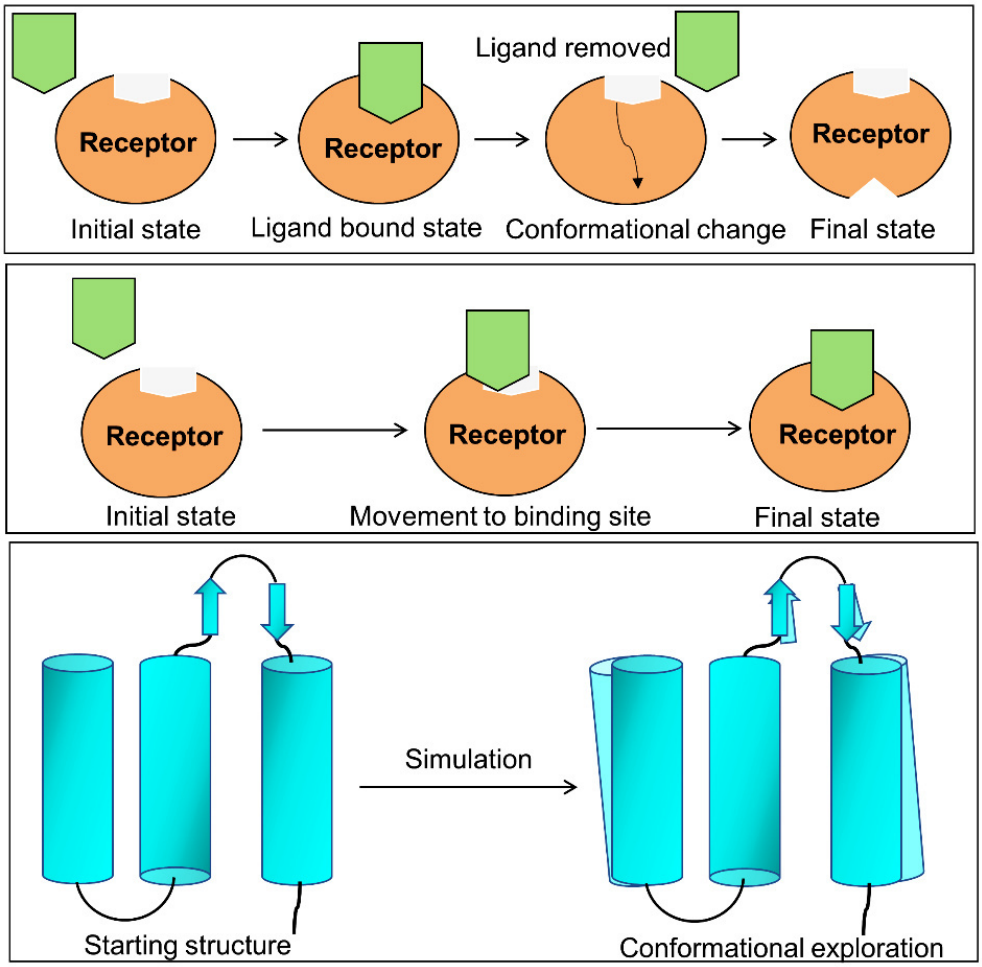

Figure 1.14. Applications of Molecular Dynamics Simulations. This illustration highlights some of the most common applications of MD simulations.

Table 1.8. Commonly used Software/Tools for MD.

Software/Tools	Source	Features
Amber	https://ambermd.org/	A biomolecular simulation program developed in the 1970s
Desmond	https://www.schrodinger.com/products/desmond	high-speed molecular dynamics simulations of biological systems
Gromacs	https://www.gromacs.org/	molecular dynamics package mainly designed for simulations of proteins, lipids, and nucleic acids.
Molecular operating environment (MOE)	https://www.chemcomp.com/Products.htm	A popular molecular dynamics tool
NAMD	https://www.ks.uiuc.edu/Research/namd/	molecular dynamics code designed for high-performance simulation of large biomolecular systems
Yasara dynamics	http://www.yasara.org/	molecular-graphics, -modeling, and -simulation program for Windows, Linux, MacOS, and Android developed since 1993

CHAPTER 2

LITERATURE REVIEW

In **chapter 1**, I have discussed about the involvement of HDAC8 and (MMP2 and MMP9) in hematological malignancy sup-types like ALL, AML and CML. This chapter covers the inhibitors of HDAC8, MMP2 and MMP9 which are in clinic (if any) or clinical trial (if any) intendent for ALL, AML and CML. This chapter also covers the promising inhibitors of HDAC8, MMP2 and MMP9 reported in the literature for the management of ALL, AML and CML.

2.1. HDAC inhibitors (HDACIs)

To date, several histone deacetylase inhibitors (HDACIs) have been synthesized, and most of them share a common pharmacophore model (Pulya et al., 2021). As shown in **Figure 2.1**, the zinc-binding group (ZBG), also known as a chelating group, the cap group (surface recognition unit), and the linker that joins the ZBG and cap area are the main pharmacophore properties of Zn^{+2}-dependent HDACIs (Amin et al., 2017B; Amin et al., 2018; Banerjee et al., 2019 and Pulya et al., 2021). Changes to any of these three regions- the cap group, linker, or ZBG have significantly altered the HDACIs' potency, stability, and most importantly the selectivity.

2.1.1. HDAC inhibitors (HDACIs) in the clinic

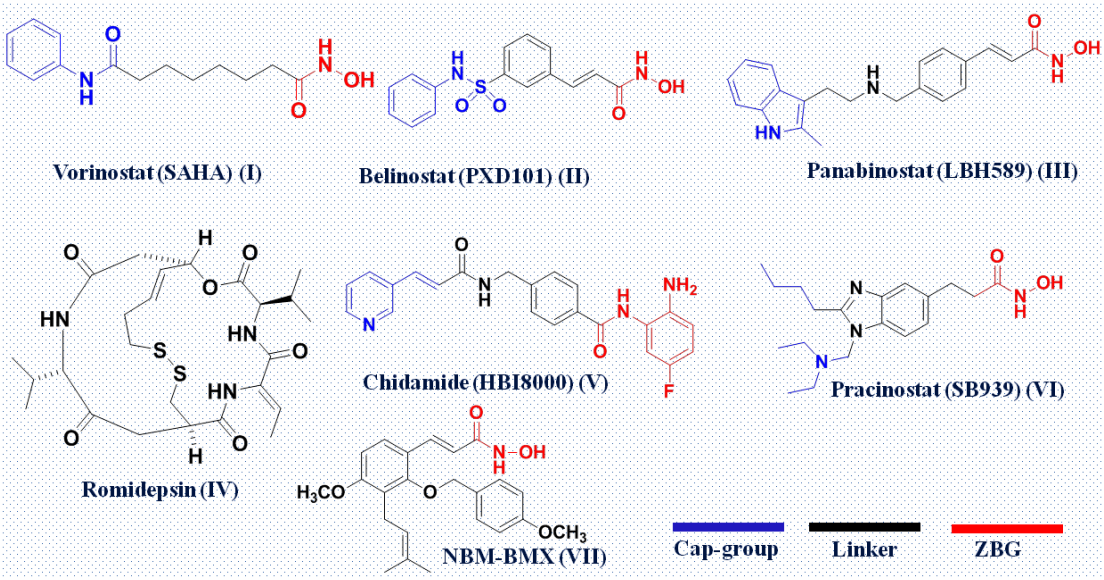

Figure 2.1. Structure of approved HDAC inhibitors

Presently, the United States Food and Drug Administration (USFDA) has approved four HDACIs: vorinostat [SAHA (I)], belinostat [PXD101 (II)], panabinostat [LBH589 (III)], and

romidepsin (IV). The Chinese Food and Drug Administration (CFDA) has approved one HDACI: chidamide (V), or HBI8000. The European Medicines Agency (EMA) has designated pracinostat [SB939 (VI)] as an orphan drug. (**Figure 2.1**) (Amin et al., 2023).

Table 2.1. Approved HDACIs along with their indications and adverse events.

Name	Agency	Year	Indication	Adverse events	Route	References
Vorinostat (I)	USFDA	2006	CTCL	Gastrointestinal, hematologic and constitutional disturbances	Oral	(Mann et al., 2007 & Bondarev et al., 2021)
Belinostat (II)	USFDA	2014	PTCL	Anemia & thrombocytopenia	Injectable	(Lee et al., 2015 and Bondarev et al., 2021)
Panabinostat (III)	USFDA & EMA	2015	MM	Nausea, diarrhea, leucopenia, lymphopenia, neutropenia & thrombocytopenia	Oral	(Bondarev et al., 2021)
Romidepsin (IV)	USFDA	2009; 2011	CTCL (2009) & PTCL (2011)	leucopenia, neutropenia & thrombocytopenia	Injectable	(Bondarev et al., 2021)
Chidamide (V)	CFDA	2014; 2019	PTCL (2014) & advanced postmenopausal breast cancer (2019)	Anemia, thrombocytopenia, fatigue, anorexia, increase in blood alkaline phosphate, dysgeusia, thrombosis & hyperglycemia	Oral	(Bondarev et al., 2021)

CTCL (cutaneous T-cell lymphoma); PTCL (peripheral T-cell lymphoma); MM (multiple myeloma).

The first clinically effective HDACI was Vorinostat (Zolinza®), also called SAHA (I). The FDA approved this oral pan-HDACI in 2006 for the treatment of cutaneous T-cell lymphoma (CTCL) (Mann et al., 2007). The FDA approved Belinostat [Beleodaq® (II)], an injectable pan-HDACI, in 2014 to treat peripheral T-cell lymphoma (PTCL) (Lee et al., 2015). Another pan-HDACI recommended for multiple myeloma (MM) is panobinostat [Farydak® (III)], which was approved by the USFDA and EMA in 2015 (Tzogani et al., 2018). In 2009 and 2011, the USFDA approved romidepsin [Istodax® (IV)], an injectable cyclic depsipeptide, for CTCL and PTCL, respectively (Barbarotta et al., 2015). Modifications in cardiac electrical conduction have also been linked to romidepsin (IV). A member of the non-hydroxamic benzamide class, chidamide [Epidaza® (V)], is also referred to as tucidinostat (Lu et al., 2016). The National Medical Products Administration of China approved its usage in combination with exemestane, a steroidal aromatase inhibitor, for the treatment of PTCL in 2014 and advanced postmenopausal breast cancer (2019). Several haematological malignancies and solid neoplasms have been found to respond effectively to chidamide (V) treatment, both in combination and alone (Lu et al., 2016). Five drugs have been clinically established for the treatment of different diseases, all of

which have verified HDAC-mediated mechanisms of action (**Table 2.1**). Remarkably, the majority of these approved HDACIs are pan-HDACIs (Amin et al., 2017B). Owing to their lack of selectivity for a specific HDAC isozyme, these exhibit certain undesirable biological events. (**Table 2.1**) (Bondarev et al., 2021 and Lee et al., 2021). **Table 2.2** highlighted the HDAC isozyme inhibitory activities of the approved agents.

Table 2.2. IC_{50} values (nM) for the approved agents against different HDAC isozymes.

Name	HDAC1	HDAC2	HDAC3	HDAC4	HDAC6	HDAC8	HDAC10	References
Vorinostat (I)	60	42	36	20	29	173	60	79
Belinostat (II)	26	22	19	15	10	22	59	79
Panabinostat (III)	3	2	2	1	1	22	31	79
Romidepsin (IV)	1	1	1	647	226	>1,000	1	79
Chidamide (V)	100	200	100	>10,000	>10,000	700	100	79

2.1.2. Clinical trial survey of HDACIs

There are 859 HDACI clinical studies aimed at various diseases that have been carried out so far (www.clinicaltrials.gov/search?term=Histone%20Deacetylase%20Inhibitor&cond=cancer). In most HDACI clinical studies (767 trials), cancer was the disease target (www.clinicaltrials.gov/search?term=Histone%20Deacetylase%20Inhibitor&cond=cancer).

Among 767 HDACI clinical trials targeting cancer, 185 trials were conducted in patients with hematologic malignancies. A total of 36 clinical trials of hematologic malignancies were stopped because of issues such as unacceptable toxicity, slow accrual, and low medication efficacy. 6 HDACI clinical trial studies in patients with hematologic malignancies have been withdrawn, some of which involved the withdrawal of licensed HDACIs from various combination therapies for a variety of medical diseases (www.clinicaltrials.gov/search?term=Histone%20Deacetylase%20Inhibitor&cond=Hematologic%20Malignancies; and Amin et al., 2023). For example, panobinostat (III) was removed from treatment for patients with relapsed or refractory ALL or AML due to lack of efficacy (Schlenk et al., 2018). For T-cell lymphoma, romidepsin (IV) in combination with 5-azacitidine, doxorubicin, and duvelisib was removed due to safety concerns with PI3 kinase inhibitors (www.clinicaltrials.gov/study/NCT04639843?term=NCT04639843&rank=1). NBM-BMX (VII) is the first selective HDAC8 inhibitor in the world, undergone clinical trials in humans

developed by NatureWise Bioteach & Medical Corporations (www.naturewise.com.tw/). NBM-BMX (VII) (**Figure 2.1.1**) exhibited a minimal level of toxicity and was able to pass the blood-brain barrier, according to preclinical testing. It has also been observed that downregulating the β-Catenin/c-Myc/SOX2 pathway can overcome temozolomide resistance in glioblastoma multiforme (Tsai et al., 2021). NBM-BMX (VII) has undergone two successful Phase I open-label dose escalation trials (NCT03726294, NCT03808870) to evaluate its pharmacokinetics, safety, effectiveness, and tolerability in patients with advanced solid tumors. In summary, there is a lot of promise for the development of NBM-BMX (VII) moving forward (Amin et al., 2023). NBM-BMX (VII) received USFDA approval on January 4th, 2023 to proceed phases Ib/II clinical trial in newly diagnosed glioblastoma multiforme (www.naturewise.com.tw/2023/05/22/nbm-bmx-received-usfda-approval-to-proceed-phase-ib-ii-clinical-trial-in-newly-diagnosed-glioblastoma-multiforme-gbm/). As a whole, most of the unsuccessful clinical trials have focused on the application of HDACI in combination therapy for cancer. The phase I clinical trial was completed by NBM-BMX (VII), the first and only isozyme-specific HDAC8 inhibitor. NBM-BMX (VII) has a lot of potential for future advancement. Furthermore, there is a dearth of clinical research on HDAC8 inhibitors in hematological malignancies, specifically AML and ALL. Therefore, there is still much to learn about developing HDAC8-specific inhibitors for hematological malignancies.

2.1.3. HDAC8 inhibitors against hematological cancer

It is crucial to look for specific HDAC8 inhibitors because of their unique involvement in hematological malignancy and other diseases (Halder et al., 2015A and Dutta et al., 2019). Potential HDAC8 inhibitors (**LR1-LR31**) (Balasubramanian et al., 2008; Suzuki et al., 2014; Huber et al., 2011; Kim et al., 1999; Chen et al., 2011; Zhang et al., 2019; Shouksmith et al., 2019; Wang et al., 2014A and Duan et al., 2015) that are cytotoxic to AML and ALL cell lines are included in **Table 2.3**. The structures of compounds **LR1-LR3** are displayed in **Figures 2.2** and **Figures 2.3**. **PCI-34051 (LR1)**, a selective HDAC8 inhibitor, may prevent lymphomas and tumors originating from T cells. **PCI-34051 (LR1)** has been shown to trigger apoptosis in Jurkat and HuT 78 T-cell lymphoma cell lines at low micromolar doses. At low micromolar doses does **PCI-34051 (LR1)** cause apoptosis in T-cell lymphomas (Jurkat and HuT78T cell lines). Remarkably, even at dosages as high as 20 μM of **PCI-34051 (LR1)**, no effect is observed on

solid tumor cell lines or myeloid-derived or B-cell lymphomas. Using PLCγ1-driven calcium mobilization, **PCI-34051 (LR1)** induced apoptosis (Balasubramanian et al., 2008).

Table 2.3. List of potential HDAC8 inhibitors with cytotoxic properties (IC_{50} in μM) against AML and ALL cell lines.

Cpd. ID	HDAC8	Jurkat	KG-1	Molt-3	Molt-4	MV4-11	THP-1	Molm-13	Reference
LR1	**0.01**	**2.4***	--	--	**3.3***	--	**15.4***	--	Balasubramanian et al., 2008
LR2	**0.19**	**0.11***	--	--	**0.12***	--	**0.075***	--	Balasubramanian et al., 2008
LR3	**0.07**	**2.2***	--	--	--	--	--	--	Suzuki et al., 2014
LR4	**0.00026**	**10**	--	--	--	--	--	--	Huber et al., 2011
LR5	**0.00037**	**5.9**	--	--	--	--	--	--	Huber et al., 2011 & Kim et al., 1999
LR6	**0.011**	--	--	--	--	**0.00019**	--	--	Chen et al., 2016
LR7	**0.012**	--	--	--	--	--	**0.91**	--	Zhang et al., 2019
LR8	**0.0145**	**6.1**	--	--	--	--	--	--	Huber et al., 2011
LR9	**0.018**	--	--	--	--	--	**5.4**	--	Zhang et al., 2019
LR10	**0.022**	--	--	--	--	**0.00069**	--	--	Chen et al., 2016
LR11	**0.024**	--	--	--	--	**0.00015**	--	--	Chen et al., 2016
LR12	**0.028**	--	--	--	--	**3.33**	--	**5.11**	Shouksmith et al., 2019
LR13	**0.0379**	--	--	--	--	**3.41**	--	**5.46**	Shouksmith et al., 2019
LR14	**0.053**	**24***	--	--	--	--	--	--	Suzuki et al., 2014
LR15	**0.0854**	--	--	--	--	**4.24**	--	**10.6**	Shouksmith et al., 2019
LR16	**0.0906**	--	--	--	--	**5.8**	--	**8.05**	Shouksmith et al., 2019
LR17	**0.09292**	--	--	--	--	**0.0048**	--	--	Chen et al., 2016
LR18	**0.12**	--	--	**1.6***	--	--	--	--	Montero et al., 2009
LR19	**0.12**	**2.1***	--	--	--	--	--	**NA**	Suzuki et al., 2014
LR20	**0.133**	--	--	--	--	**1.62**	--	**2.98**	Shouksmith et al., 2019
LR21	**0.15**	--	**5.37**	--	--	--	--	--	Wang et al., 2014A
LR22	**0.15**	**2.0***	--	--	--	--	--	--	Suzuki et al., 2014
LR23	**0.191**	--	--	--	--	**0.00043**	--	--	Chen et al., 2016
LR24	**0.2**	--	**3.8**		--	--	--	--	Wang et al., 2014A
LR25	**0.217**	--	--	--	--	**0.00765**	--	--	Chen et al., 2016
LR26	**0.224**	--	--	--	--	**3.24**	--	**14.1**	Shouksmith et al., 2019
LR27	**0.245**	--	--	--	--	**0.576**	--	**6**	Shouksmith et al., 2019
LR28	**0.32**	--	**2.88**	--	--	--	--	--	Chen et al., 2016
LR29	**0.343**	--	**1.75**	--	--	--	--	--	Duan et al., 2015
LR30	**0.573**	--	--	--	--	**14.6**	--	**24.8**	Shouksmith et al., 2019
LR31	**0.635**	--	--	--	--	**3.12**	--	**10.3**	Shouksmith et al., 2019

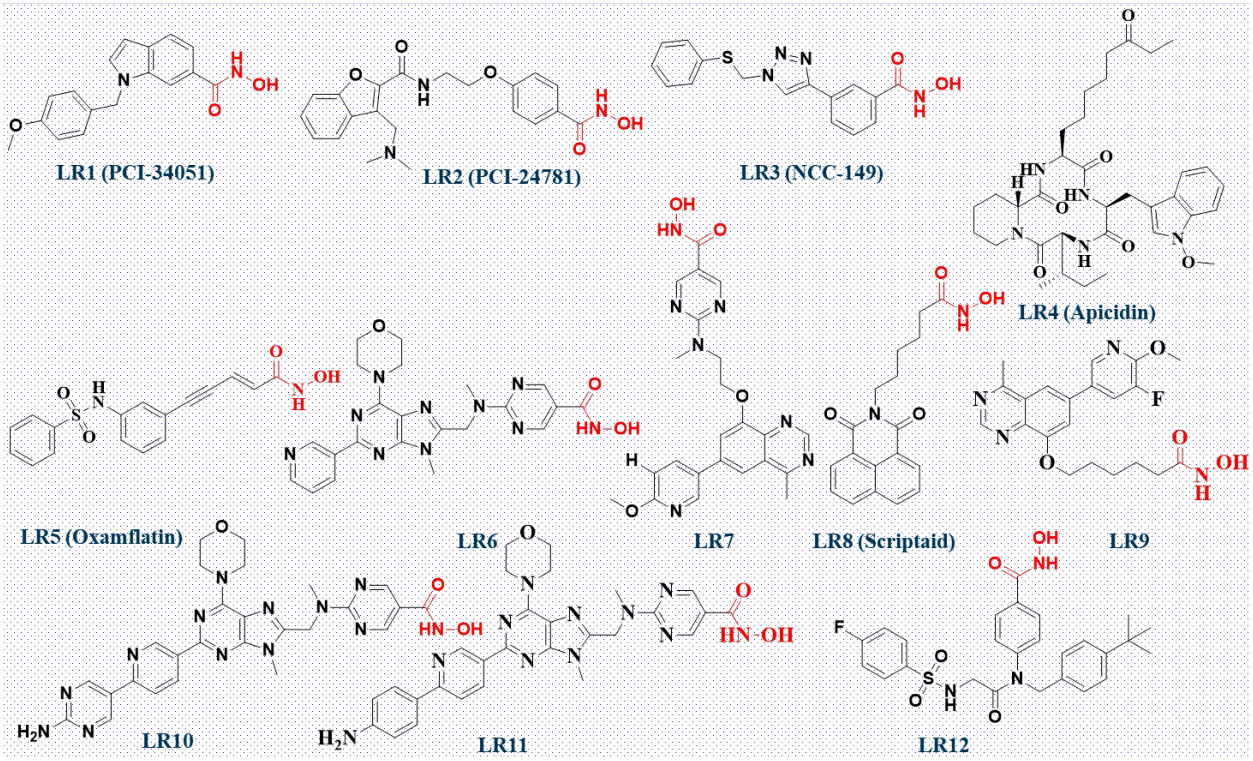

Figure 2.2. Structures of compounds **LR1 - LR12**.

Another selective HDAC8 inhibitor **LR3** (**Figure 2.2**) exhibits distinct growth-inhibitory effects on T-cell lymphoma (GI50: Jurkat = 2.8 μM; HH = 21 μM; MT4 = 22 μM; HuT 78 = 32 μM) and neuroblastoma cell lines, all without interfering with the growth of peripheral blood mononuclear cells (PBMCs) from healthy donors. Furthermore, LR3 (**Figure 2.2**) downregulates the expression of the cyclin A2 and B1 genes and prevents cellular proliferation through the buildup of the G2/M phase. In comparison to untreated P19 cells, LR3-treated P19 cells had a smaller embryoid body (EB) and lower levels of the neuronal marker NeuN expression (Katayama et al., 2018).

In comparison to **LR3** (**Table 2.2**), **LR14** (**Figure 2.3**), a reversed triazole analog of **LR3** (**Figure 2.2**), has somewhat greater efficacy and selectivity towards HDAC8. **LR14** (**Figure 2.3**) is almost 1886-fold more HDAC8 selective than HDAC1, HDAC2, HDAC3, and HDAC4 isozymes, according to Suzuki et al. (Suzuki et al., 2014). Furthermore, **LR14** (**Figure 2.3**) has an approximately 41-fold higher HDAC8 selectivity than the HDAC6 enzyme. Here HDAC8 selectivity was superbly modulated by little geometric variations in the triazole rings. These inhibitory actions in enzyme assays, however, are inconsistent with the data on cell cytotoxicity.

Comparatively, **LR14** (**Figure 2.3**) is less effective than **LR3** (**Figure 2.2**) at inhibiting T-cell lymphoma cell proliferation (GI_{50}: Jurkat = 24 μM; HH = 40 μM; MT4 = 43 μM; HuT 78 = 50 μM) (Suzuki et al., 2014).

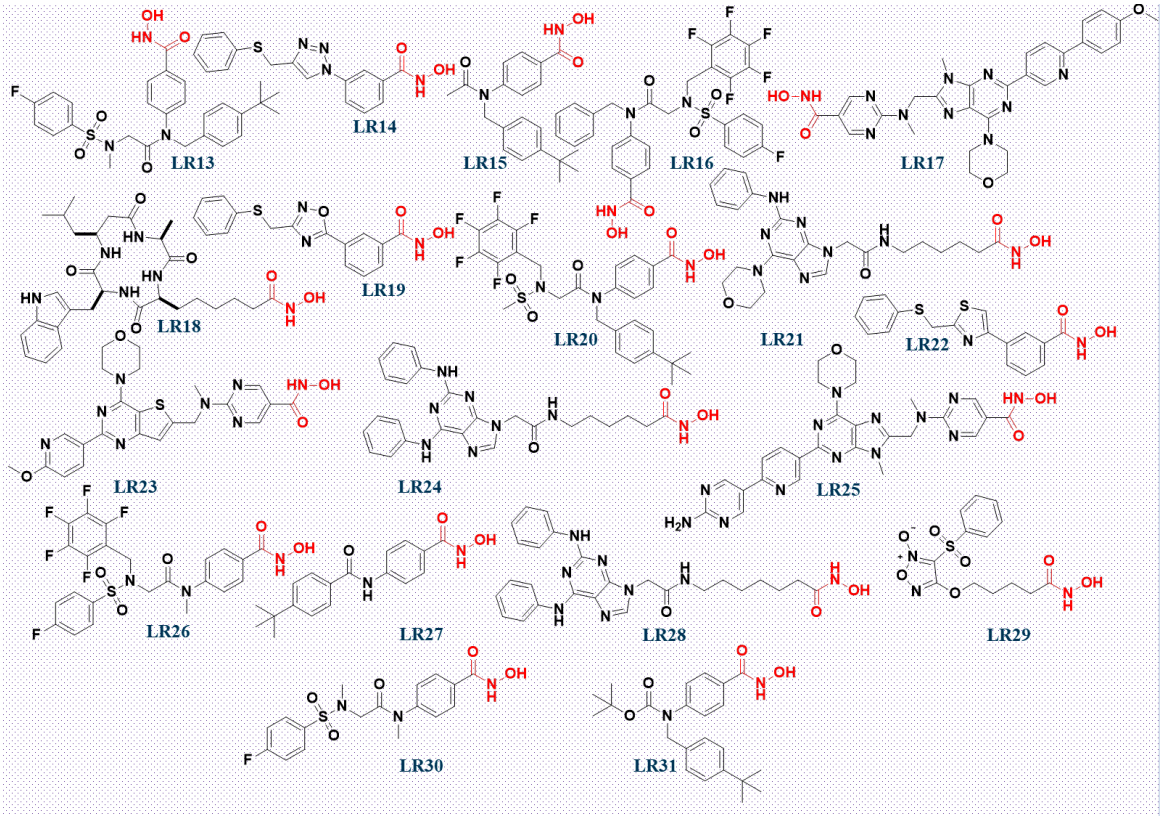

Figure 2.3. Structures of compounds LR13 - LR31.

2.2. MMP inhibitors (MMPIs) and their clinic trials

Over the past three decades, many of MMPI have been synthesised in laboratories; yet, the USFDA has only approved Periostat®, or doxycycline hydrate, for the treatment of periodontal disease (Li et al., 2020). Based on encouraging pre-clinical data, primarily from solid tumour malignancies, and understanding of X-ray crystallographic studies of MMP catalytic domain-inhibitor complexes, a number of synthetic anti-cancer matrix metalloproteinase inhibitors (MMPIs) had advanced to clinical trials. However, over 50 MMPIs consistently failed to meet the requirements of clinical trial endpoints (Winer et al., 2018 and Razai et al., 2020).

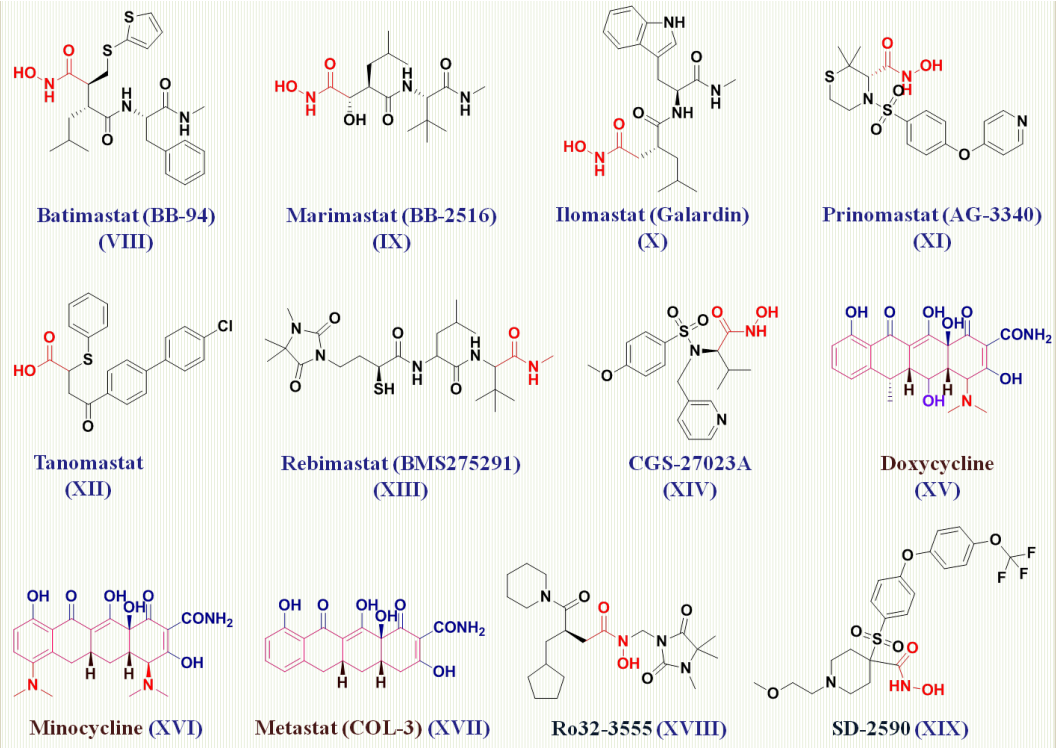

Figure 2.4. Chemical structures of MMPI which entered clinical trials.

2.2.1. Collagen based pseudopeptides

Collagen serves as MMP's primary substrate. Early MMPIs were made by taking advantage of the way the substrate peptide is structured around scissile bonds which can bind zinc (such as hydroxamate or carboxylate) to chelate with catalytic zinc ions and bind to the MMP active site in a reversible, competitive, and stereospecific manner. Most MMPIs studied in clinical trials are hydroxamic acid-based inhibitors; the substrate-based first-generation anticancer clinical trial candidates include batimastat (VIII), marimastat (IX), and ilomastat (X) (**Figure 2.4**) (Betz et al., 1997).

Batimastat (VIII) (**Figure 2.4**), also known as BB-94, is a pan MMP inhibitor having IC_{50} values (MMP1=0.75, MMP2=0.50, MMP3=0.73, MMP9=0.67, and MMP-14=2.90) in the nanomolar range. It was the first MMPI to undergo a phase I clinical trial (Fray et al., 2001). With the help of a substrate-based pseudopeptide, this synthetic small molecule hydroxamic acid mostly binds with primed subsites of enzymes to build a trigonal bipyramidal sphere around the catalytic zinc ion (Grams et al., 1995). Batimastat has been used in several clinical trials (Davies et al., 1993;

Chirivi et al., 1994; Beattie et al., 1998; Taraboletti et al., 1995; Watson et al., 1995; Sledge et al., 2002; Low et al., 1996; Wojtowicz-Praga et al., 1996; Parsons et al., 1997; and Macaulay et al., 1999) against solid tumor malignancies; these trials, which were primarily early ones (phase I or phase I/II), were not intended to be true drug efficacy studies but rather to track drug tolerance, pharmacokinetic profile, and dose limitations. An early analysis of the drug's effectiveness was also discussed, revealing that batimastat (VIII) may delay the growth of tumors rather than having any appreciable anti-tumor effects. When drug plasma concentrations rose above IC_{50} values, none of the phase I trials revealed any cytotoxic or cytostatic effects, and there was no evidence of a direct correlation between MMPs and the suppression of metastatic tumor cells. Phase III trials were started, but they were quickly terminated because of the drug's slow accumulation, patients' noncompliance with intraperitoneal or intrapleural administration, significant side effects such as peritoneal irritation, and, in the end, the availability of marimastat (IX), an oral bioavailable analogue of BB-94 (Rothenberg et al., 1999).

The structural analogue of batimastat (VIII), known as marimastat (IX) or BB-2516 (**Figure 2.4**), is a pan MMPI having IC_{50} values of 5, 6, 230, 16, and 3 nM against MMP1, MMP2, MMP3, MMP7, and MMP9 respectively. The majority of the preclinical results of BB-94 in different tumour models served as the foundation for the clinical trials of BB-2516 because the inhibitory profile is extremely comparable to batimastat (VIII) (Hoekstra et al., 2001). Compared to batimastat (VIII), marimastat (IX) has a higher patient compliance rate since it can be given orally to humans and has a plasma half-life of about 15 hours (Millar et al., 1998). The MMPI that has been studied the most in clinical trials is marimastat. Metastatic solid tumours, including those of the ovary, lung, pancreas, colorectal, prostate, breast, gastric, and brain, cancer were the subject of numerous phase I, II, and III trials (Millar et al., 1998; Malfetano et al., 1997; Poole et al., 1996; Primrose et al., 1996; Zaknoen et al., 1997; Boasberg et al., 1997; Adams et al., 1998; Wojtowicz-Praga et al., 1998; Gradishar et al., 1998; Nemunaitis et al., 1998; Goffin et al., 2005; Rosemurgy et al., 1999; Tierney et al., 1999; Larson et al., 2002; Quirt et al., 2002; Miller et al., 2002; Shepherd et al., 2002; Rosenbaum et al., 2005; Bramhall et al., 2002A; King et al., 2003; Sparano et al., 2004; and Levin et al., 2006). Like batimastat (VIII), marimastat (IX) was also discontinued in phase III clinical trials because of a lack of ability to show uniformity in disease prolongation in comparison with standard anticancer drugs or placebo (Gore et al., 1996). Due to a lack of selectivity among different subtypes of MMPs, musculoskeletal syndrome (MSS)

related untoward effects like joint stiffness, joint inflammation, and pain were experienced by patients upon administration of marimastat which is also a major issue with marimastat as well as other early non-selective inhibitors of MMP (Shepherd et al., 2002; Bramhall et al., 2002A; Sparano et al., 2004; and Bramhall et al., 2002B).

Another broad-spectrum MMPI based on hydroxamic acid is called galardin or ilomastat (X) (**Figure 2.4**), and its IC50 values fall into the nanomolar range (MMP1=1.5, MMP2=1.1, MMP3=1.9, MMP9=0.5, and MMP14=13.4) (Moroy et al., 2007). It (X) is one of the first powerful MMPIs and was developed as well using the structure of collagen. Phase I human trials involved a dose escalation study conducted on healthy volunteers, and phase II/III studies were started on patients with infected frank corneal ulcers; however, no further progress was recorded (Galardy et al., 1994). Ilomastat's (X) low bioavailability and the availability of more effective chemicals may be the reason why clinical trials involving cancer patients were not started.

2.2.2. Non-peptidomimetics MMPI

Three-dimensional active site structures of various MMP members have been accessible since 1994. Prinomastat (XI), tanomastat (XII), rebimastat (BMS275291) (XIII), and CGS27023A (VIX) (**Figure 2.4**) are examples of non-peptidomimetic MMPIs, a family of MMPIs created by utilizing the knowledge obtained from the active site of enzyme-inhibitor complexes. Clinical trials for these were initiated after peptidomimetic MMPIs. After a phase I marimastat results revealed toxicity related to MSS (Wojtowicz-Praga et al., 1998), it was hypothesized that MSS was caused by broad-spectrum MMPIs inhibiting MMP1 (Freskos et al., 1999; Becker et al., 2001; and Reiter et al., 2004). Additionally, it was proposed that gelatinase-specific inhibition might effectively reduce tumor growth, invasion, angiogenesis, and metastasis (Rothenberg et al., 1999). Here, in addition to improved enzyme inhibition, the creation of selective inhibitors was given top priority when making decisions about moving further into clinical stages to eradicate MSS of marimastat.

Prinomastat (XI) (**Figure 2.4**), also known as AG-3340, is a new class of relatively selective and potent multimodal phase inhibitors (MMPIs) based on arylsulphonyl synthesis. Agouron Pharmaceuticals, Inc., a subsidiary of Pfizer Company, La Jolla, California, USA, developed it utilizing information obtained from the X-ray crystallographic structure of several available

MMP active sites with bound inhibitors (Brown, 2000). The primary goal of prinomastat's design was to achieve selectivity over MMP1 to combat the musculoskeletal syndrome (MSS) caused by early, non-selective MMPIs. Prinomastat (XI) has an inhibitory profile for MMP2, MMP3, MMP9, MMP13, and MMP14 in the picomolar range (K_i values 30 to 330 pM), sparing MMP-1 with K_i values 8,300 pM. This is due to the arylsulfonyl group connected to a substituted thiomorpholine heterocycle and the hydoxamic acid group at thiomorpholine ring (Hande et al., 1998). In contrast to the shallow S_1' pocket of MMP1, the large hydrophobic arylsulfonyl moiety of prinomastat (XI) interacts favorably with the deep S_1' pockets of MMP2, MMP3, MMP9, and MMP13, whereas the hydroxamate function is in charge of the bidentate chelation with the catalytic zinc ion (Pirard 2007; and Gomis-Rüth 2009). Time-dependent and dose-dependent toxicities of MSS were identified in the phase I clinical trial of prinomastat, which was surprising because AG-3340 (XI) spared MMP1 inhibition (Hande et al., 1998). AG-3340 (XI) was once again suggested to be the cause of MSS-related toxicities, even though it has selectivity for MMP2 (166 fold) and MMP9 (32 fold) over MMP1, but its IC_{50} or K_i value falls in the lower nanomolar range (Brown, 2000). Various combinations of AG-3340 (XI) with conventional medications were studied in phase III trials to treat patients with advanced cancer. These combinations included mitoxantrone and prednisone for patients with hormone-refractory prostate cancer, prinomastat (XI), gemcitabine, and cisplatin, or AG-3340 (XI), paclitaxel, and carboplatin for patients with non-small cell lung cancer. All those phase III trials showed severe musculoskeletal toxicities, and no improvement in patient survival or inhibition of disease progression was documented (Ahmann et al., 2001 and Bissett et al., 2005).

It was expected that weaker zinc binders would be the next step towards the creation of selective anticancer MMPIs since earlier cancer clinical trials yielded negative results about the toxicities of hydroxamate-based MMPIs associated with MSS (Hodgson, 1995; Tamura et al., 1998; Tochowicz et al., 2007; and Agrawal et al., 2008). Tanomastat (XII) (**Figure 2.4**), an analog of butanoic acid, was created by Bayer and has an enzyme inhibition profile with Ki values >5,000, 11, 134, 301, and 1,470 nM for MMP1, MMP2, MMP3, MMP9, and MMP13 respectively (Gatto et al., 1999). For catalytic zinc chelation, tanomastat has a carboxylate function that is about 50 times less potent and a weaker zinc chelator than the hydroxamate function (Gooley et al., 1994; Monovich et al., 2009). To achieve selectivity in the structural development of MMPIs, protruding into the S_1' pocket for extra constructive interaction is a legitimate technique (Fabre et

al., 2014). Tanomastat (XII) also has a 4-chloro-biphenly moiety, which allows it to fit into the deep S1′ pockets of MMP2, MMP3, MMP9, and MMP13 as opposed to the shallow S_1' pocket of MMP1. This means that tanomastat (XII) is more selective than prinomastat against MMP2 (>554 fold), and that in the case of tanomastat, the K_i value of MMP1 is also very high (>5 μM). As anticipated, tanomastat was well tolerated and orally bioavailable in phase I clinical trials; no drug-related arthralgias were reported, however, dose-dependent toxicities included nausea, mild to moderate thrombocytopenia, reversible increases in bilirubin, and liver enzymes were reported (Erlichman et al., 2001; Rowinsky et al., 2000; and Heath et al., 2001). Disappointing outcomes, however, were noted in phase III trials, where there was no appreciable improvement in overall patient survival and no major impact on disease suppression (Moore et al., 2003 and Hirte et al., 2006).

Rebimastat (XIII), also known as BMS275291 (**Figure 2.4**), is a different broad-spectrum multi-mechanism protein inhibitor (MMPI) with IC_{50} values of 9, 39, 157, 23, 27, and 40 nM for MMP1, MMP2, MMP3, MMP7, MMP9, and MMP14, respectively. It was first developed by Chiroscience R&D (now known as Celltech Group plc) and then by Bristol-Myers Squibb. Rebimastat (XIII) is designed to prevent MMP-mediated shedding events by inhibiting closely related members of the MMP family such as ADAM sheddases (ADAM-10 and TACE or ADAM-17) (Lombard et al., 1998; Poulaki 2002 ; Naglich et al., 2001; Maskos et al., 1998). Rebimastat (XIII) has a marcaptoacyl function for catalytic zinc chelation. BMS-275291 (XIII) was well tolerated in phase I/II trials (up to 1,200 mg q.d.); nevertheless, MSS-associated toxicities, such as myralgia and arthralgia, were noted as a major disappointment, despite the fact that reported side events linked to MSS were not dose-dependent. On the other hand, nausea, headache, skin-rash, fatigue, and altered taste were also recorded as other side effects (Rizvi et al., 2004; Brinker et al., 2008; Miller et al., 2004; Lara et al., 2006; and Douillard et al., 2004). Increased toxicities were also noted in the phase III trial including NSCLC patients receiving combined therapy with carboplatin or paclitaxel, and a noteworthy improvement in patient survival was not documented (Leighl et al., 2005). The first possible sulfonamide-based, non-peptidic, broad-spectrum MMPI was CGS-27023A (MMI-270) in which hydroxamic acid functions for zinc chelation. CGS-27023A (XIV) (**Figure 2.4**) possesses K_i values for MMP1, MMP2, MMP3, and MMP9 were 33, 20, 43, and 8 nM respectively. Ciba Geigy originally

developed CGS-27023A (XIV) in 1995 (MacPherson et al., 1997) to treat osteoarthritis. MMI-270 (XIV) is bioavailable when taken orally and is beneficial in preventing cartilage deterioration caused by stromelysin in animal models. Despite being a non-selective MMPI of the second generation, it provided a template for the subsequent creation of MMPIs containing hydroxamic acid that are based on sulfonamide (O'Byrne et al., 1995; Levitt et al., 2001; and Adhikari et al., 2017). Early in the 2000s, CGS-27023A (XIV) was enrolled in a phase I clinical trial for colorectal and solid tumors; however, it (XIV) was quickly discontinued due to significant MSS toxicities and restricted efficacy, which had already been reported with batimastat (VIII) and marimastat (IX) (Eatock et al., 2005).

2.2.3. Tetracycline based MMPIs

This tetracycline category of MMPIs includes doxycycline (XV), minocycline (XVI) and metastat or COL-3 (XVII) (**Figure 2.4**). They are chemically modified tetracyclines (CMT), which suppress gene transcription, scavenge reactive oxygen shock, or metal ion binding, such as zinc, to inhibit both catalytic activity and MMP synthesis (Golub et al., 1991; Golub et al., 1998; Hanemaaijer et al., 1998; Ryan et al., 2001; and Gu et al., 2005). On the other hand, CMT do not exhibit antibiotic activity and only cause limited toxicities. Doxycycline (XV) is a CMT used to treat periodontitis. It is the only MMPI approved by the USFDA and inhibits MMP7 and MMP8 (Kivelä-Rajamäki et al., 2003; and Ozmeric and Gokmenoglu 2015). A CMT, metastat (COL-3) (XVII) is a significant contender for cancer treatment. COL-3 (XVII) demonstrated a disease-stabilizing effect in phase I/II trials with refractory metastatic cancer, however, it (XVII) was unable to increase overall patient survival (Syed et al., 2004 and Chu et al., 2007). On the other hand, metastat (XVII) produced both an objective response to patient survival and a disease stabilising impact in the instance of AIDS-related Kaposi's sarcoma (Cianfrocca et al., 2002 and Dezube et al., 2006). Phototoxicity, increased liver enzyme levels, anorexia, anaemia, headache, mucositis, thrombocytopenia, leucopenia, diarrhoea, nausea, and vomiting are among the dose-related toxicities of COL-3 (Ozmeric and Gokmenoglu, 2015). The most effective MMPI among CMTs, minocycline (XVI) is a semisynthetic tetracycline that either directly inhibits MMP or interferes with MMP gene expression (Paemen et al., 1996). In preclinical settings, minocycline has demonstrated encouraging results in terms of its antitumor and anti-metastatic properties in melanoma, lung, breast, and prostate malignancies (Lokeshwar, 2011).

2.2.4. Learning experiences from failure of MMPIs in clinical trials

The MMPIs discussed above, which were enrolled in various phases of clinical trials intended for people with advanced solid cancer, did not correspond with preclinical advantages observed in several animal cancer models and did not match expected benefits. The insufficient efficacy and toxicity of MMPIs were the main causes of their failure in clinical studies. Over the past 25 years, efforts have been made to create selective MMPIs to address toxicities, particularly adverse events connected to MSS. It was later thought that inhibition of MMP1, ADAM10 & ADAM17 was associated with MSS. Some relatively selective molecules were also developed sparing MMP1 [prinomastat (XI) and tanomastat (XII)] or ADAM10 and ADAM17 [rebimastat (XIII)]. The first generation MMPIs (batimastat, marimastat, and ilomastat) failed primarily due to experience of MSS related toxicities. Clinical trials with prinomastat (XI), tanomastat (XII), and rebimastat (XIII) were unsuccessful as well because of their low efficacy, inability to increase patient survival, and propensity for myalgia and arthralgia. Regarding the clinical trials with broad-spectrum MMPIs, the development of MSS was thought to be caused by MMP1 suppression. The MMP1 inhibition approach did not hold up well against MSS. The relationship between MMP1 and MSS was also incongruous because Ro32-3555 (XVIII) (**Figure 2.4**) is a selective hydroxamate-based MMPI for MMP1, MMP8, and MMP13 (Ki values 3.0, 4.4, and 3.4 nM) over MMP2, MMP3, and MMP9 (Ki values 154, 527, and 59 nM) that did not show any MSS-related toxicities in clinical trials conducted with healthy male volunteers and subsequently with patients with rheumatoid arthritis (Wood et al., 1998 and Hemmings et al., 2001). A further illustration is SD-2590 (XIX) (**Figure 2.4**), an alpha-sulfone-alpha-piperidine hydroxamic acid containing orally active MMPI with IC_{50} values >10,000 <0.1, 28.7, 7,000, 1.7, 0.18, and <0.1 nM for MMP1, MMP2, MMP3, MMP7, MMP8, MMP9, and MMP13 that was created for cancer patients in the early stages. SD-2590 (XIX) exhibits >1,000,000 fold selectivity for MMP2 and MMP13 over MMP1, and >50,000 fold selectivity for MMP9 over MMP1. Although SD-2590 (XIX) inhibited tumor growth in an animal model, adverse effects related to MSS also occurred (Becker et al., 2010). Two ADAM (a disintegrin and metalloproteinase) family members, ADAM10 and ADAM17, were hypothesized to have been inhibited as a result of MSS-related toxicities in patients treated with early non-selective MMPIs such batimastat (VIII) and marimastat (IX) (Winer et al., 2018; Fingleton, 2008; and Barlaam et al., 1999). There are multiple explanations for the MSS that are seen during MMPI administration. A further theory

pertaining to MSS is the suppression of MMP14. Compared to other null mice in the animal model, MMP14 deficient mice developed severe MSS (Holmbeck et al., 1999 and Zhou et al., 2000). Therefore, premature inferences have been made about MMP and MSS by sparing one or two MMP subtypes. In contrast, selective MMPI, such as anti-MMP9 antibody GS-5745, has not been shown to cause MSS-related toxicities in phase 1b clinical trials of rheumatoid arthritis (Gossage et al., 2018).

Finally, it is now evident from improved knowledge of MMP biology and the pharmacokinetic characteristics that the early-phase MMPI has been miscarried into different phases of clinical trials because of premature inferences drawn from faulty pre-clinical models (Winer et al., 2018 and Fields, 2019B). The catalytic domain can be targeted to block specific MMP members separately. Currently, selective MMP2, MMP9, MMP13, and MMP14 inhibitors have also been reported. On the other hand, there is no correlation between any of these MMPIs (MMP2, MMP9, MMP13, and MMP14) and musculoskeletal syndrome (Winer et al., 2018; Fields, 2019B; Piperigkou et al., 2018 and Yang et al., 2016A). Therefore, it is possible to speculate that targeted inhibition of gelatinases (MMP2 and MMP9) is a very promising approach for the development of more effective and safe anti-cancer medications in the future.

2.2.5. Gelatinase inhibitors in hematological cancer

As a clear literature search has shown, MMP2 and MMP9 covered the greatest number of articles in the first thirty years of the MMP study. When antibodies for immunoblotting techniques were unavailable, zymography was the only technique of choice for measuring MMP levels and activity (Das et al., 2021A). Compared to zymography utilizing casein or other substrates, gelatin zymography was far more technically accessible. Additionally, MMP2 and MMP9 were the most uncomplicated MMPs to quantify (Das et al., 2021A). Because of this, there is a log-fold increase in research articles assessing MMP2 and MMP9 in comparison to other MMPs. Many databases, like ChEMBL, Drug Bank, BindingDB, etc., contain thousands of matrix metalloproteinase inhibitors (MMPIs) placed in them. Sadly, the majority of synthetic small molecules MMPIs that have been identified are pan inhibitors, and most of these drugs have not been tested in animal models or cell-based research following in vitro enzyme assay. Following the failure of pan MMPIs in clinical trials, the development of selective MMPIs that target distinct MMP domains has received particular attention. The development of selective gelatinase

inhibitors is the primary strategy for the management of hematological malignancies, according to the talks in the preceding sections regarding the failures of clinical trial MMPIs and the relationship between gelatinases and numerous hematological malignancies. Only a small number of synthetic gelatinase inhibitors have been studied so far for hematological malignancies (Das et al., 2021A). Important gelatinases inhibitors which are effective against hematological cancer are discussed in the next sub-section.

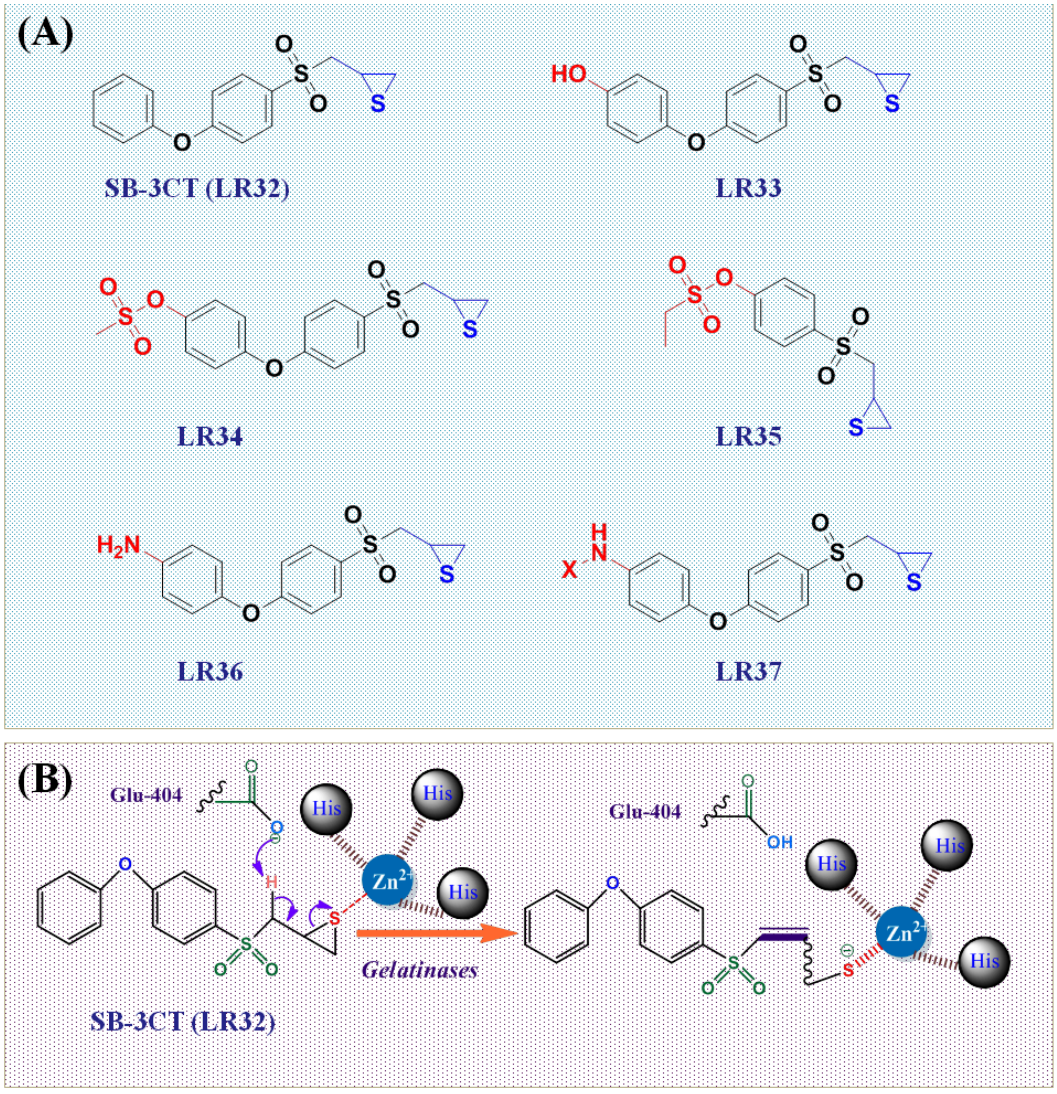

Figure 2.5. (A) Chemical structures of some sulfonyl methylthiirane based gelatinase inhibitors. (B) Mechanism of Gelatinases inhibition by catalytic action of Glu-404 residue of gelatinase active site.

2.2.5.1. Mechanism-based gelatinase inhibitors

The first selective mechanism-based gelatinase inhibitor combining methyl thiirane and the 4-phenoxy phenylsulfonyl moiety is **SB-3CT (LR32**) (**Figure 2.5A)** In 2000, **SB-3CT** (**LR32**) was reported to have K_i values for MMP2 of 14 ± 1 nM and MMP9 of 600 ± 200 nM (Ikejiri et al., 2005). The gelatinases inhibitor **SB-3CT** (**LR32**) has a sluggish binding rate and causes an irreversible conformational shift in the inhibitor-enzyme complex (**Figure 2.5B**). The gelatinase active site's Glu-404 residue catalyzed the deprotonation of **SB-3CT** (**LR32**), converting it to the equivalent thiolate. The equivalent thiolate is produced when **SB-3CT** (**LR32**) is deprotonated, which is catalyzed by the gelatinases. The thiolate and the zinc ion of the gelatinases active site work together closely. **SB-3CT** (**LR32**) exhibits a competitive binding with gelatinases and a prolonged residence time; however, the reversal of this reaction proceeds at a relatively slow pace (Meisel and Chang 2017 and Krüger et al., 2005). In an aggressive mouse model of T-cell lymphoma, **SB-3CT** (**LR32**) decreased liver metastases and enhanced survival (Lee at al., 2007). **SB-3CT** (**LR32**) is poorly water soluble and easily metabolized by hydroxylation at the terminal phenyl ring and the α-position to the sulfone. The p-hydroxy metabolite compound **LR33** (**Figure 2.5**) of **SB-3CT** (**LR32**) showed a more powerful gelatinase inhibitor profile compared with parent **SB-3CT** (**LR32**) (Lee at al., 2009). Better water-soluble analogues and pro-drugs based on the structure of **SB-3CT** (**Figure 2.5**; compounds **LR34-LR36** and **LR37**) have also been developed, although they have not yet been tested against hematological malignancies (Testero et al., 2010; Gooyit et al., 2011 and Song et al., 2013).

2.2.5.2. Gelatinase inhibitors targeting signaling pathways

It's crucial to understand how different endogenous signaling molecules and exogenous synthetic inhibitors interact to control the production of gelatinase. Another approach to prevent hematological malignancies may also involve the use of inhibitors (**Figure 2.6**; compound LR**38–LR43**) that target the signaling pathways responsible for gelatinase expressions (Liu et al., 2010). Lew et al. (2010) (Liu et al., 2010) found that MMP2 and MMP9 expression is downregulated in U937 cells treated with caffeine (**LR38**) due to Ca2+/ROS-mediated inhibition of the ERK/c-Fos pathway and activation of the p38 MAPK/c-Jun pathway. Galic acid (**LR39**) administration reduced MMP2 and MMP9 expression through pathways regulated by JNK1-c-Jun/ATF-2 and Akt/ERK-c-Jun/c-Fos, respectively (Chen and Chang 2012).

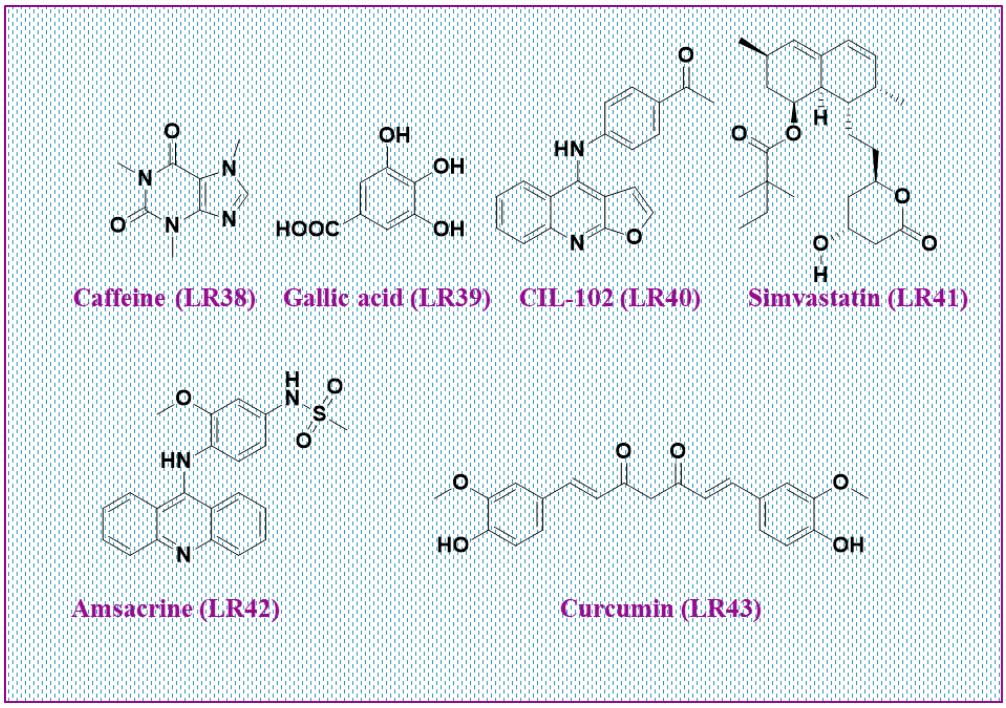

Figure 2.6. Chemical structures of gelatinase inhibitors targeting signaling pathways.

Gelatinase expression was down-regulated in K562 cells as a result of CIL-102 (**LR40**) treatment, which also suppressed genetic transcription and mRNA stability (Liu et al., 2012). Leukaemia cells that are exposed to simvastatin (**LR41**) exhibit p65 instability, which results in the down-regulation of MMP9 (Chen and Chang 2014). It was shown that amsacrine (**LR42**)-induced ERK inactivation and p38 MAPK/JNK activation enhanced MMP2/MMP9 mRNA degradation, and suppressed MMP2/MMP9 promoter luciferase activity respectively. In U937 cells treated with amsacrine, p38 MAPK/JNK activation resulted in the up-regulation of protein phosphatase 2A catalytic subunit a (PP2Aca). Additionally, on Jurkat, HL-60, K562, KU812, and MEG-01 cell lines, amsacrine promoted down-regulation of MMP2 and MMP9 by up-regulation of PP2Aca (Liu et al., 2014B). Treatment with curcumin (LR**43**) inhibits NF-kB and ERK signaling while activating p38 and JNK to cause apoptosis in the human monocytic leukemia SHI-1 cell line. Additionally, curcumin reduced MMP2 and MMP9's protein expression and mRNA transcription (Zhu et al., 2016 and Zhu et al., 2020).

2.3. Glutamine

Glutamine is the most abundant free amino acid in the human body. It transports almost one third of circulating amino acids and nitrogen. It is not recognized as an essential amino acid, but may become conditionally essential in certain situations including intensive athletic training or certain gastrointestinal disorders. Its side-chain is an amide formed by replacing the side-chain hydroxyl of glutamic acid with an amine functional group, making it the amide of glutamic acid. In human blood, glutamine is the most abundant free amino acid, with a concentration of about 500–900 μM/L (Brosnan 2003). Glutamine is one of the few amino acids that can directly cross the blood–brain barrier (Zaragozá 2020). In the body, it is found circulating in the blood as well as stored in the skeletal muscles. It becomes conditionally essential (requiring intake from food or supplements) in states of illness or injury (Lacey and Wilmore 1990 and Curi et al., 2016). It is the precursor for biosynthesis of several biomolecules including purine and pyrimidine bases as well as other amino acids (Trejo-Solis et al., 2023). In the cells, glutamine is an important precursor that provides nicotinamide adenine dinucleotide phosphate (NADPH) and glutathione (GSH) for redox homeostasis (Trejo-Solis et al., 2023). Glutamine also activates the mTOR signaling pathway to coordinate cell growth and proliferation (Nicklin et al., 2009). It is the principle metabolic fuel for rapidly dividing cells including enterocytes, colonocytes, fibroblasts, lymphocytes, macrophages and neutrophils (Miller 1999). Numerous enzymes play roles in glutamine metabolism; the two primary intracellular enzymes are phosphate-dependent glutaminase (GLS, EC 3.5.1.2) and glutamine synthetase (GS, EC 6.3.1.2). GS initiates the reaction that produces glutamine from ammonium ion (NH_4^+) and glutamate through ATP consumption. GLS is in charge of glutamine hydrolysis, which turns glutamine back into glutamate and NH_4^+ (Cruzat et al., 2018). Within the cell, GLS (in its active form) is mostly present in the mitochondria, while GS is mostly found in the cytoplasm. These sites align with the roles of the enzymes: GLS catalyses the conversion of glutamine to glutamate, a crucial step in the tricarboxylic acid cycle (TCA, also called the Krebs cycle), which is initiated at 2-oxoglutarate as a source of energy or metabolic intermediates, while GS produces glutamine for the synthesis of cytoplasmic proteins and nucleotides (Curi et al., 2016).

2.3.1. Glutamine and cancer

Cancer cells that are proliferating have a high glutamine requirement. Glutamine can be taken up by cancer cells from the extracellular environment or by increasing their production (Halama and Suhre 2022). Patients with various cancer types have reduced plasma levels of glutamine, which has been linked to the higher uptake of glutamine by cancer cells (Miyagi et al., 2011). In fact, 18F-(2S,4R)-4-fluoroglutamine PET imaging is being used to investigate the enhanced uptake of glutamine by tumors for diagnostic purposes (Pollard et al., 2022). The oncogenes MYC and KRAS upregulate the primary glutamine transporter ASCT2 (alanine, serine, cysteine transporter 2), that is linked to the increased glutamine absorption of the cancer cells due to its high expression (Bhutia and Ganapathy 2016 and Cormerais et al., 2018). Once within the cell, glutamine catabolism supplies the TCA cycle, facilitates lipogenesis, biosynthesizes nucleotides and non-essential amino acids (NEAAs), and aids in the maintenance of elevated glutathione levels (Halama and Suhre 2022). Glutaminase-1 (GLS1), an enzyme that catalyzes the conversion of glutamine to glutamate, is upregulated in response to the oncogene MYC (Wise et al., 2008). A poor prognosis is linked to GLS1 overexpression, which is elevated in a variety of cancer types (Lee et al., 2016; Xiang et al., 2019; Myint et al., 2021 and Kim et al., 2013). Many cancer cells also exhibit increased glutamate conversion to α-ketoglutarate (αKG), most likely as a result of upregulating the enzymes glutamate dehydrogenase-1 (GLUD1), aspartate aminotransferase-1 (GOT1), aspartate aminotransferase-2 (GOT2), and alanine aminotransferase-2 (GPT2) through the expression of MYC, KRAS, and PI3KCA (Yoo et al., 2020; Hao et al., 2016; and Bernfeld and Foster 2019). Under the influence of oncogenic MYC, KRAS, and PIK3CA, glutamine may develop into a crucial AA for cancer cells (Yoo et al., 2020). Potential anticancer therapies have been investigated, including limiting glutamine (Gln) levels and focusing on Gln uptake and utilization. The in vivo anticancer efficacy of glutamine-deficient diets has not been thoroughly studied. In 2017, it was discovered that dietary restriction of glutamine induced anticancer activity in vivo and in vitro in a medulloblastoma xenograft model that expressed p73 (Niklison-Chirou et al., 2017).

The role of glutamine metabolism in the course of human leukemia remains unclear, even though significant investigations have long since demonstrated the role of glutamine in the regulation of leukemia metabolism. Raivio and Andersson (Raivio and Andersson 1982) reported that the two

glutamine-requiring pathways of purine metabolism, guanine nucleotide synthesis and purine synthesis de novo, proceed at reduced rates in T ALL cells in the absence of glutamine, but are dependent on exogenous glutamine in B and null lymphoblasts. Nguyen et al. (Nguyen et al., 2021) reported that due to the downregulation of glutamine synthetase, notch1 overexpression in T-ALL caused a shift in the metabolism of glutamine. In Notch1-driven T-ALL, glutamine addiction was caused by the downregulation of glutamine synthetase in both *in vitro* and *in vivo* settings. They additionally suggested a rise in Notch1-mediated glutaminolysis. A critical regulator of cell growth, mTORC1 pathway, was activated as a result of increased glutaminolysis. Glutaminolysis, however, was not involved in Notch1-induced glutamine addiction. Overall, restricting glutamine availability and targeting mTORC1 together synergistically induced apoptosis and stopped the evolution of Notch1-driven leukemia (Nguyen et al., 2021). Sbirkov et al. (Sbirkov et al., 2023) suggested that in the case of relapsed childhood, acute lymphoblastic leukemia (cALL) blocking glutamine availability impairs mitochondrial function and induces apoptosis in both glucocorticoid-sensitive and glucocorticoid-resistant cALL cells.

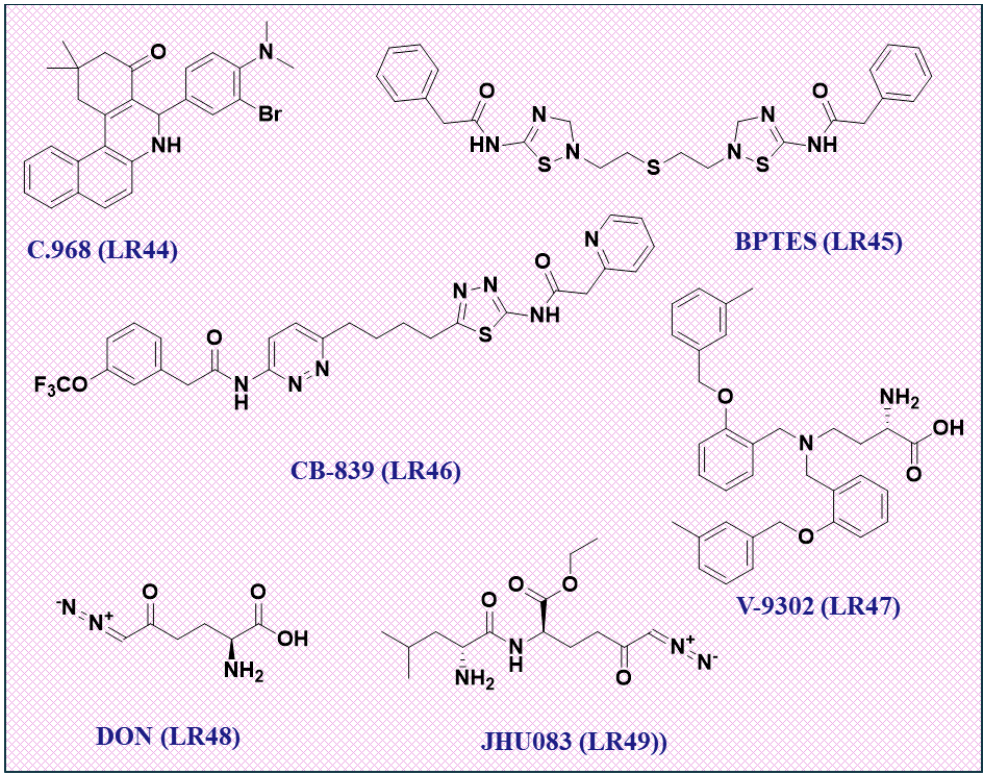

Figure 2.7. Chemical structures of anti-cancer drugs targeting glutamine metabolism.

2.3.2. Anti-cancer agents targeting glutamine metabolism

The majority of anticancer agents (**Figure 2.7**; compounds LR**44–LR49**) that target glutamine metabolism of cancer cells have concentrated on pharmacologically inhibiting the uptake and utilization of glutamine (Halama and Suhre 2022). Among these include the inhibition of GLS1 using inhibitors such as **C.968** (**LR44**) (Wang et al., 2010B), **BPTES** (**LR45**) (Robinson et al., 2007), and **CB-839** (**LR46**) (Gross et al., 2014). Orally bioavailable **CB-839** (**LR46**) has been evaluated in clinical trials. Eight of the phase I-II clinical trials have been completed, out of the minimum of 21 that are underway or completed (Clinical Trials Using CB839 in Cancer). **CB-839** (**LR46**) was used in combination with other anticancer medications in the majority of the finished clinical trials (Halama and Suhre 2022). Thus far, its impact on the advancement of cancer has been negligible (Halama and Suhre 2022). In mouse cancer models, anticancer efficacy was elicited by **V-9302** (**LR47**), an inhibitor of the ASCT2, inhibiting glutamine absorption (Schulte et al., 2018). A prodrug of the glutamine antagonist **DON** (**LR48**) (Leone et al., 2019), **JHU083** (**LR49**) is selectively activated in the tumor microenvironment, where it impairs the metabolism of cancer cells and enhances T-cell responses against cancer. The metabolism of glutamine may potentially be impacted by the side effects of certain anticancer medications. In a mouse leukaemia model resistant to asparagine depletion, for instance, the asparagine-depleting enzyme L-asparaginase, which is employed against leukemia and depends on an external supply of asparagine, can also deplete glutamine. This effect may account for its anticancer effectiveness (Chan et al., 2019 and Offman et al., 2011).

While the compounds **LR44–LR49** in **Figure 2.7** have demonstrated potential anticancer effects, glutamine limitation may be harmful because this amino acid is required for non-malignant proliferating cells (Reinfeld et al., 2021 and Pallett et al., 2021). In rats, a glutamine-restricted diet caused atrophy of the small intestinal mucosa and loss of muscular mass (Horvath et al., 1996). In randomized clinical studies with cancer patients, oral glutamine supplementation has been demonstrated to improve mucosal damage (mucositis, stomatitis, pharyngitis, esophagitis, and enteritis) caused by chemotherapy and radiation therapy (Chattopadhyay et al., 2014; Tsujimoto et al., 2015; and Anderson and Lalla 2020). Supplementing with glutamine may increase the protective effects of leucine on cancer cachexia (Beaudry and Law 2022), as glutamine is essential for the cellular uptake of leucine (Hodson et al., 2017). According to a

recent study, glutamine supplementation increased the susceptibility of tumors to a serine/threonine-protein kinase B-Raf (BRAF; RAF = rapidly accelerated fibrosarcoma) inhibitor through epigenetic reprogramming and produced in vivo anticancer efficacy in a transgenic melanoma model (Ishak et al., 2020). The researchers noticed that while the concentrations of glutamine and αKG in tumors increased when fed a diet high in glutamine (20%), the other biosynthetic intermediates required for cell proliferation did not increase. The hypo-methylation of H3K4me3 caused by the rise in αKG concentration suppressed the epigenetically activated carcinogenic pathways in melanoma (Ishak et al., 2020). Another studies found that giving glutamine supplements to several artificial meals increased the anticancer activity in mice with metastatic tumors; the majority of those active diets had 5-6% glutamine in them (Calderón-Montaño et al., 2022; Jiménez-Alonso et al., 2022 and Guillén-Mancina et al., 2023). Thus, even though glutamine is essential for the metabolism of cancer cells, this amino acid can be supplemented or restricted to have anticancer effects.

2.3.3. Isoglutamine based HDAC8 inhibitor in hematological cancer

Isoglutamine, or α-glutamine, is a gamma-amino acid produced by replacing the carboxyl group in position 1 of glutamic acid with an amide group. In comparison, glutamine, the 5-amide of glutamic acid, is a proteinogenic amino acid (Debnath et al., 2002). Since isoglutamine is an isostere of glutamine, it may competively inhibit glutamine at the enzyme active site and produce the biological activity. The Department of Pharmaceutical Technology, at Jadavpur University is actively searching for targeted HDAC8 inhibitors to treat hematological malignancies, specifically ALL and AML (**Table 2.4**) (Halder et al., 2015A; Dutta et al., 2019 and Amin et al., 2021B). The design of HDAC8Is was initiated by researchers at Jadavpur University's Natural Science Laboratory using N2-phenylacetyl-L-isoglutamine, a metabolite of antineoplastons (Halder et al., 2015A). To create molecules that might meet the pharmacophoric requirements for HDAC8Is, they have used methods including ligand-based pharmacophore mapping and molecular docking. The selective hits were tailored to produce a targeted library of 35 potential dual-acting MMP2 and HDAC8 inhibitors. The derivative that shows the most promise, compound **LR55** (**Table 2.4**), has an IC_{50} of 2.89 μM against HDAC8 while it did not affect nuclear HDACs at a dose of 100 μM (Halder et al., 2015). Compound **LR55** mildly inhibits MMP8 and MMP12 (IC50 MMP8 = 205.89 μM and MMP12 = 138.32 μM), Furthermore, non-

selective inhibitory activity is demonstrated on MMP2, MMP9 and MMP14 (IC_{50} values for MMP2 = 6.4 μM, MMP9 = 4.83 μM, and MMP14 = 56.33μM). Next, compound **LR55**'s anti-proliferative, anti-invasive, and anti-migratory properties were investigated using A549 cell lines that represent non-small cell lung cancer. At a 50 μM dosage, the MTT assay findings demonstrated good anti-invasive properties but no appreciable cytotoxicity (Halder et al., 2015A). The assay for wound healing revealed a significant anti-migratory effect. These findings

Table 2.4. Structures, HDAC8 [IC_{50} values (μM)] inhibitory activity and cytotoxicity [IC_{50} values (μM)] against different cancer cell lines of the isoglutamine derivatives

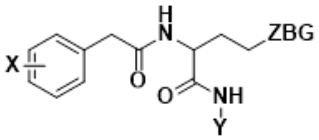

Cpd. ID	X	Y	ZBG	Nuclear extract of HDAC1 &2	HDAC 3	HDAC 8	Jurkat E6.1	U937	Molt-4	MDA-MB-231	PBMC
LR50	H	Bnz	-COOH	>100	-	6.05	66.59	63.74	61.77	>200	>400
LR51	4-OMe	Bnz	-COOH	>100	-	5.09	44.21	25.32	26.89	>200	>400
LR52	2-Cl	Bnz	-COOH	>100	-	6.29	42.93	32.95	33.97	>200	>400
LR53	4-Br	Bnz	-COOH	>100	-	3.03	37.85	11.16	9.32	>200	>400
LR54	4-Br	*n*-Hex	-COOH	>100	-	4.21	43.98	19.56	21.33	>200	>400
LR55	4-Br	4-NO_2Bnz	-COOH	>100	-	2.89	10.59	2.77	4.58	>200	>400
LR56	4-Cl	*n*-Hex	-COOH	>100	-	5.02	23.62	12.57	11.91	>200	>400
LR57	2,4-diCl	*n*-Hex	-COOH	>100	-	8.60	32.94	11.37	21.93	>200	>400
LR58	2,4-diCl	Bnz	-COOH	>100	-	6.07	39.44	23.86	25.32	>200	>400
LR59	4-Br	*n*-Hex	-CONHOH	67.16	11.96	5.53	28.66	-	-	-	-
LR60	4-Cl	*n*-But	-CONHOH	48.12	7.73	6.32	34.42	-	-	-	-
LR61	4-Cl	*n*-Pent	-CONHOH	41.46	12.67	5.71	18.57	-	-	-	-
LR62	2,4-diCl	*n*-But	-CONHOH	60.11	13.63	5.53	30.08	-	-	-	-
LR63	2,4-diCl	*n*-Pent	-CONHOH	59.42	20.33	4.33	17.24	-	-	-	-
LR64	H	*n*-Pent	-CONHOH	45.52	10.10	5.31	>50	-	-	-	-
LR65	H	*n*-Hex	-CONHOH	51.69	11.08	5.69	>50	-	-	-	-

made it possible to identify novel dual MMP2/HDAC8Is. Furthermore, it was reported that compound **LR55** was the most effective against each of these leukemia cell lines (IC_{50} in Jurkat-E6.1 = 2.77 μM, IC_{50} in MOLT-4 = 4.58 μM, and IC_{50} in U937 = 10.59 μM) (**Table 2.4**) (Dutta et al., 2019). According to the Jurkat-E6.1 cell line annexin V/PI apoptosis assay, compound

LR55 effectively and dose-dependently induced apoptosis. Compound **LR55** effectively inhibited the expression of the enzymes HDAC8 and MMP2 (Dutta et al., 2019). Studies using flow cytometry showed that **LR55** reduced MMP2 expression by 70% and HDAC8 expression by 68%. Furthermore, it produced a potent fluorescent signal to cause nicks in Jurkat-E6.1 cells, suggesting that apoptosis may be induced. Compound **LR55**'s cell cycle analysis also demonstrated cellular arrest in the sub-G_0 phase. The mitochondrial membrane potential experiment suggested that compound **LR55** caused the leukemia cells Jurkat-E6.1 to undergo apoptosis (Dutta et al., 2019).

Later, the same research group reported the synthesis of selective HDAC8 inhibitors, based on isoglutamine-based hydroxamate derivatives (Amin et al., 2021B). An enzyme assay was used to screen these derivatives. Despite this, it was shown that the majority of these substances were more effective HDAC8 inhibitors when compared to other HDAC class I enzymes. Compound **LR64** showed the inhibition of HDAC8 enzyme and the highest cytotoxicity againt acute myeloid leukemia cell line U937. Compound **LR64** showed good selectivity for HDAC8 over HDAC3 (**Table 2.4**). The efficacious compounds were further evaluated for their potential to be cytotoxic against human cancer cell lines. It's interesting to note that the majority of these substances were cytotoxic to the ALL cell line Jurkat E6.1 (**Table 2.4**). G1 cell cycle arrest was impressively displayed by compound **LR64** against Jurkat E6.1 cell line (Amin et al., 2021B).

2.3.4. Glutamine based gelatinases (MMP2 and MMP9) inhibitor in hematological cancer

Glutamines contain carboxylate function for catalytic zinc chelation while aryl function fits nicely into the S_1' sub-site of the MMP catalytic domain for the best suppression of enzyme catalysis (Adhikari et al., 2016). Adhikari and co-warkers (Adhikari et al., 2016) reported some potent and selective biphenlysulfonyl-(*L*)-glutamine based MMP2 inhibitors (**LR66-LR71**) over other isoforms of MMP (**Table 2.5**). In human non-small-cell lung carcinoma (A549), glutamine-based gelatinase inhibitors (**LR67, 69** and **LR70**) coupled with arylsulfonyl function as a P_1' fragment demonstrated anti-migration and anti-invasive characteristics without showing any cytotoxicity (Adhikari et al., 2016).

Table 2.5. Structures, MMP [IC_{50} values (nM)] inhibitory activity of the aryl sulfonyl glutamine derivatives.

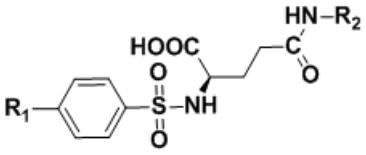

IC_{50} (nM)									
Cpd. ID	**R_1**	**R_2**	**ZBG**	**MMP2**	**MMP9**	**MMP1**	**MMP8**	**MMP12**	**MMP14**
LR66	C_6H_5	*n*-C_4H_9	-COOH	44.65	714.90	>10,000			
LR67	C_6H_5	C_5H_{11}	-COOH	41.00	5715.00	>10,000	59.00	52.30	1000.00
LR68	C_6H_5	*c*-C_6H_{11}	-COOH	30.00	636.75	>10,000	64.80	73.20	2407.00
LR69	C_6H_5	CH_2-C_6H_5	-COOH	24	492.6	>10,000	21.3	53.2	427
LR70	C_6H_5	3,4-diCF_3-CH2-C_6H_5	-COOH	51	6740	>10,000	228	462	6311
LR71	C_6H_5	2-Cl-CH2-C_6H_5		31	880	>10,000	39	63	1614

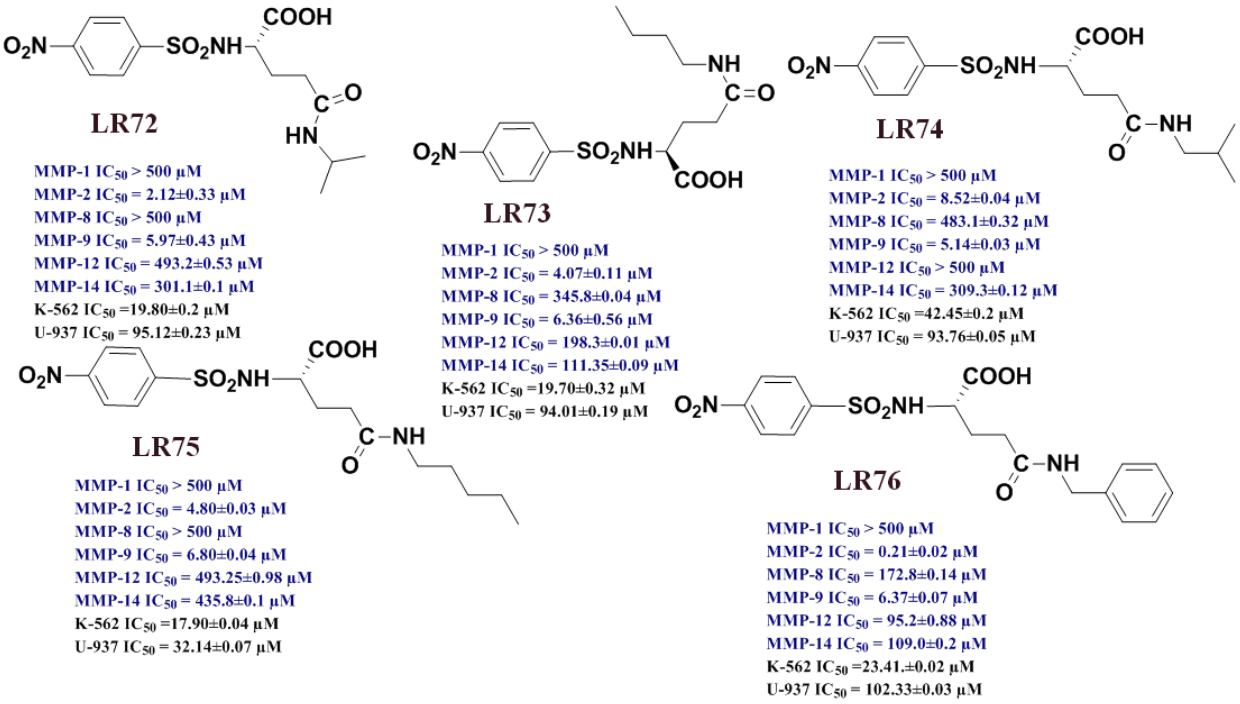

Figure 2.8. Structures, MMPI activity [IC_{50} values (µM)] and cytotoxicity [IC_{50} values (µM)] against different leukemia cell lines of the glutamine derivatives.

Mukherjee et al. (Mukherjee et al., 2017) reported several arylsulfonyl-based L-glutamines with gelatinase inhibitory profiles in the lower micromolar range and also reported their cytotoxicity against hematological malignancy (**Figure 2.8**; **LR72–LR76**). That study was the first to show that CML cells underwent apoptosis when their gelatinase activity was downregulated in vitro. The glutamine-based gelatinase inhibitors (**LR72–LR76**) were found to selectively induce anti-proliferative action towards leukemia cells (K-562 and U-937) over solid tumor cells (A549 and MDA-MB-231) in an in vitro cell culture investigation involving diverse solid and leukemia cell lines. Significant cytotoxicity was seen in the case of CML cells (K-562) when compared to U-937 cells among hematological malignant cells. The most effective cytotoxic drug against the K-562 cell line was found to be compound **LR75**, which also demonstrated anti-invasive effects on the K-562 cells. Compound **LR75** exhibited selectivity towards MMP1, MMP3, MMP12, and MMP14, but was non-selective towards two gelatinases. Following Annexin-V/PI staining, an apoptotic experiment using flow cytometry demonstrated that compound **LR75**-induced CML cell death happened upon activation of the apoptotic pathway. The study found that across leukemia subtypes, the gelatinase A (MMP2) and gelatinase-B (MMP9) enzyme inhibition profiles also showed significant treatment strategies. For example, less selective MMP2 inhibitors (**Figure 2.8**; compound **LR76**) over MMP9 resulted in cytotoxicities against both CML cells (K-562) and acute myeloid leukemia cells (U-937), whereas potent and highly selective MMP2 inhibitors (**Figure 2.8**; compound **LR75**) over MMP9 resulted in selective cytotoxicity against K-562 in comparison with U-937. Moreover, it was found that molecule (compound **LR74**), which exhibited lesser MMP2 activity than MMP9, did not significantly cause cytotoxicity against either CML or acute myeloid leukemia cells (Mukherjee et al., 2017).

CHAPTER 3

RATIONALE AND OBJECTIVES

Chapter 3: Rationale and Objectives

3.1. Rationale

Synthetic pharmaceutical compounds known as "small molecule drugs" are made to resemble, improve, or decrease the actions of natural substances or products in the body. Their structures are quite basic and can be tailored to achieve particular treatment objectives. They hardly ever require specific storage conditions because they are usually stable. Because of their often predictable behavior in vivo, or within the body, simple dose regimens, often oral are developed that are simple for patients to follow (Southey and Brunavs 2023).

Glutamate is a potential food source for cancer cells since it donates its amide nitrogen atom to them. It is a reductively potent anaplerotic chemical essential to cancerous cell growth (Halama and Suhre 2022 and Chen et al. 2015). Numerous cancer forms are characterized by increased glutamine metabolism (Pacifico et al., 2023). Glutamate plays a major role in the survival and proliferation of proliferating cancer cells (Jin et al., 2023). A key factor in cancer's pathophysiology and treatment resistance is altered metabolism. One of the biological processes controlling the growth of tumors and their reactivity to treatment in several malignancies is related to robust glutamine metabolism (Feng et al., 2021). In a recent study it was reported (Feng et al., 2021) that inhibiting glutamine absorption resulted in cell-cycle arrest, autophagy, and apoptosis, as well as a reduction in melanoma cells' two- and three-dimensional growth and mTOR signaling. After entering into the cell, glutamine is catabolized to glutamate by a phosphate dependent enzyme glutaminase [glutaminase 1 (GLS1) and glutaminase 2 (GLS2)] and also a metabolic byproduct NH^{4+} is generated which stimulates autophagy. The enzyme GLS1 is induced by the oncogene c-Myc which enhances glutamine catabolism to support cell survival and proliferation (De Vitto et al. 2016). Using Jurkat T cells Chang and co-workers (Chang et al. 2002) reported that the activity of glutaminase enzyme is high in various types of tumours and it is an established feature regarding glutamine metabolism of cancer cells. Glutamine triggers Bcl-2 protein which is anti-apoptotic and inhibits CD95 which is pro-apoptotic, lead to the protection from apoptosis of malignant cells (Chang et al. 2002). It was reported in several studies that phosphate dependent kidney type glutaminase (KGA) is highly expressed with optimum activity in rapidly growing cells of rat and human hepatomas, Ehrlich ascites tumour cells (EATCs), human breast cancer cells and in human leukaemia cells.

Inhibition of KGA in EATCs induces apoptosis and makes these cells resistant to the toxicity of methotrexate and hydrogen peroxide (Lu et al. 2010, Szeliga et al. 2009).

By considering the above discussion regarding the relationship between cancer and glutamine, it may be hypothesized that compounds having structural similarities with glutamine may be consider for designing and development of anticancer agents. Based on this hypothesis and providing a scientific rationale, three structural variants of glutamic acid (**Figure 3.1**) are considered for the development of small molecule anticancer agents. These structural variants of glutamic acid are isoglutamine, pyroglutamic acid and glutamine (**Figure 3.1**).

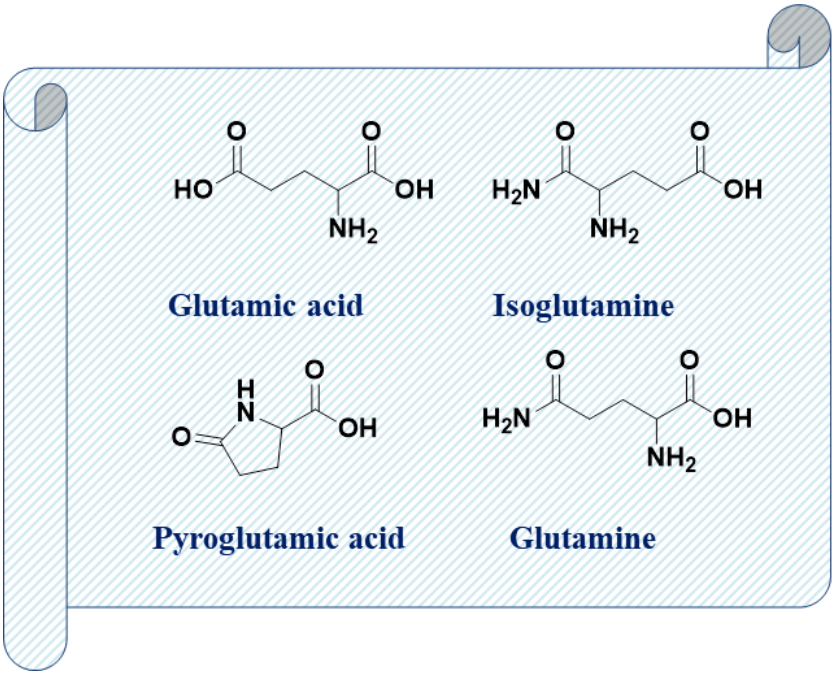

Figure 3.1. Important structural variants of glutamine.

After iron, zinc is the second most common transition metal ion in organisms. Zinc is a vital part of life. Approximately 9–10% of eukaryotic proteins are dependent on this metal to carry out their biological processes (Cuajungco et al., 2021). More than half of the zinc-bound proteins are enzymes, and the majority of them have a catalytic function for the metal, according to a bioinformatics study (Andreini and Bertini 2012). Zinc is used structurally in around 20% of them, and it is a substrate or regulator of enzyme activity in a smaller number. The fact that so many proteins require zinc demonstrates the essential role that metal plays in a wide range of biological functions (Cuajungco et al., 2021). Zinc-dependent metalloenzymes like HDAC8 (Li

and Seto 2016; Hontecillas-Prieto et al., 2020; Liang et al., 2023; Kim et al., 2022; Spreafico et al., 2020 and Amin et al., 2023) MMP2 and MMP9 (John and Tuszynski et al., 2019; Siddhartha and Garg 2021; Mustafa et al., 2022; Almutairi et al., 2023; Baidya et al., 2021; Das et al., 2021 and Kalali 2023) have strong link with cancer cell progression, invasion, migration, apoptosis and angiogenesis in the case of several solid tumor malignancies as well as hematological cancers.

Changes in the transcription of essential genes governing crucial cancer pathways, including cell proliferation, cell cycle regulation, and apoptosis, are brought about by the abnormal expression of HDACs. As a result, HDACs are thought to be interesting therapeutic targets, and the creation of HDAC inhibitors (HDACI), which block the start or spread of tumors, is a topic that holds promise for the development of novel anticancer medications (Mayer et al., 2022). There are 6 HDACI approved for clinical use for cutaneous T-cell lymphoma, peripheral T-cell lymphoma and multiple myeloma by different regulatory agencies (USFDA approved vorinostat, belinostat, panabinostat, and romidepsin; CFDA approved chidamide and EMA approved pracinostat) (Amin et al., 2023). All these clinical compounds are non-selective HDAC inhibitors which are associated with several toxicities. More selective HDACIs are promising in terms of better efficacy and less toxicity (Cengiz Seval and Beksac 2019). HDAC8, one of the crucial HDACs, affects the epigenetic gene regulating processes in solid and hematological cancer progressions especially AML, and ALL (Amin et al., 2023). HDAC8 disrupts a variety of activities, including the transformation and maintenance of leukemic stem cells (LSCs), by abnormally deacetylating histone and nonhistone proteins, such as p53, cohesin protein, retinoic acid-induced 1 (RAI1), and structural maintenance of chromosome 3 (SMC3) (Amin et al., 2023). PCI-34051, a specific HDAC8 inhibitor, demonstrated encouraging outcomes against AML and T-cell lymphoma (Balasubramanian et al., 2008).

The prevalence of haematological cancers, such as lymphoma, melanoma, and leukaemia, has been rising daily. Chemotherapy is the mainstay of traditional haematological cancer treatment protocols. Conventional chemotherapy has weak pharmacokinetic and biocompatibility characteristics, as well as poor drug selectivity (Amin et al., 2023). Therefore, HDAC8 specific inhibitors having structural similarity with glutamine analog has motivated the design of new compounds for hematological cancer to overcome challenges, such as the selectivity,

unpredictable pharmacokinetic profile as well as strategies focused on avoiding unwanted side effects.

On the other hand, gelatinases (MMP2 and MMP9) and other MMPs have long been linked to angiogenesis, metastasis, and solid tumour invasion; however, little information is known about the function of gelatinases in hematological cancers (Das et al., 2021A). Recent research has demonstrated a correlation between hematological cancers and gelatinases' functioning or activations. Methods for creating more targeted gelatinase inhibitors against hematologic malignant cells were documented during *in vitro* cell-based research (Das et al., 2021A). Many substrate-based non-selective to non-substrate-based relatively selective synthetic anti-cancer matrix metalloproteinase inhibitors (MMPIs) have been advanced due to encouraging pre-clinical evidence and knowledge of X-ray crystallographic studies of MMP catalytic domain-inhibitor complexes. These are primarily in the case of solid cancers. However, more than 50 MMPI consistently failed to pass the tests of clinical trial endpoints (Winer et al., 2018; Razai et al., 2020 and Das et al., 2021A). The reasons why anticancer MMPIs failed in clinical trials included poor pharmacokinetic profile, metabolic instability of broad spectrum MMPI, lack of selectivity and/or off-target interactions, and dose-limiting toxicity such as musculoskeletal syndrome (MSS) (Fields 2019B). Evidence supports the claim that specific inhibitions of MMP2 and MMP9 are unrelated to MSS (Fields 2019B). To the best of my knowledge, there hasn't been any reported clinical trial using synthetic small molecule MMP inhibitors against hematological malignancy. As a result, the structural resemblance of the gelatinases (MMP2 and MMP9) selective inhibitor to the glutamine analog has spurred the development of novel molecules for hematological cancer to mitigate undesirable side effects and produce more potent anticancer efficacy.

3.2. Objectives

The main objective of this present work is to design, synthesis and biological screening of glutamine based HDAC8 and gelatinase (MMP2 and MMP9) inhibitors for the management of hematological cancers. In this regard I have considered three structural variants of glutamic acid which are isoglutamine, pyroglutamic acid and glutamine (**Figure 3.1**). Therefore, the present work consists of four primary parts which are the biological screening of isoglutamine derivatives **[Part-I],** synthesis and biological screening of (*L*)-pyroglutamic acid derivatives

[**Part-II**], QSAR-based molecular modeling studies **[Part-III]** and synthesis, biological studies and binding interaction studies of (*D*)-glutamine derivatives **[Part-IV].**

3.2.1. Biological screening of isoglutamine derivatives [Part-I]

The migration, invasion, and metastases of cancer are associated with HDACs and MMPs (Mittal et al., 2014; Fabre et al., 2013 and Park et al., 2011). Furthermore, through upregulating the RECK protein; HDAC inhibitors prevent MMP2 activation and lung cancer cell invasion (Liu et al., 2003). In breast cancer cell lines, downregulation of MMP2 and MMP9 was seen as a result of HDAC inhibition, which also suppressed migration and invasion (Jeon et al., 2010). Using pharmacophore mapping techniques, my senior Dr. Amit Kumar Halder from the Natural Science Laboratory, Department of Pharmaceutical Technology, Jadavpur University, developed (Halder 2015B) a series of compounds with unique dual HDAC8/MMP2 inhibitors in his PhD work. The ligand-based and structure-based pharmacophore studies suggested that the structural requirements for HDAC8 and MMP2 inhibitors were a hydrogen bond acceptor, a hydrophobic aromatic group, and a zinc-binding group. Learning from the pharmacophore mapping techniques Dr. Halder synthesized a series of compounds. Some potent dual MMP2/HDAC8 inhibitors showed considerable anti-migratory and anti-invasive properties (Halder 2015B).

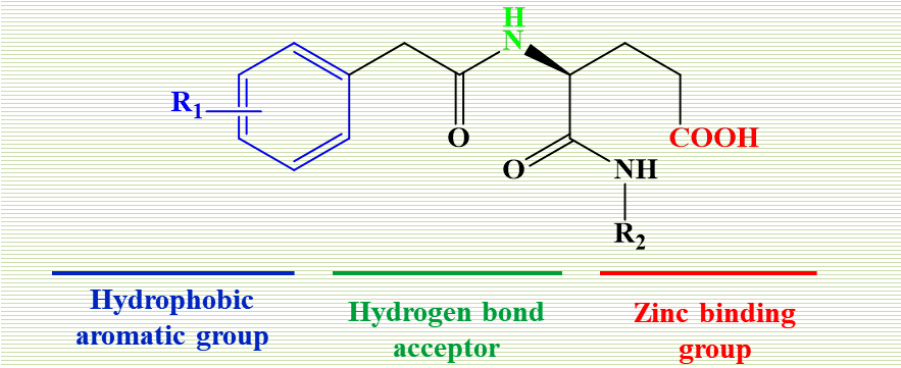

Figure 3.1. Scaffold for dual HDAC-8/MMP-2 inhibitors reported by Dr. Halder.

Later, a set of the 35 isoglutamine derivatives reported by Dr. Halder was screened against hematological cancer by another senior Dr. Sk. Abdul Amin from the Natural Science Laboratory, Department of Pharmaceutical Technology, in his PhD work (Amin 2022). Among those 35 isoglutamine derivatives lead molecules showed promising apoptosis mediated cytotoxic activity against acute lymphoblastic leukemia (ALL) cell line (Amin 2022).

Table 3.1. Structure and HDAC8 inhibitory profile of 29 (**I1-I29**) *in-house* isoglutamine derivatives.

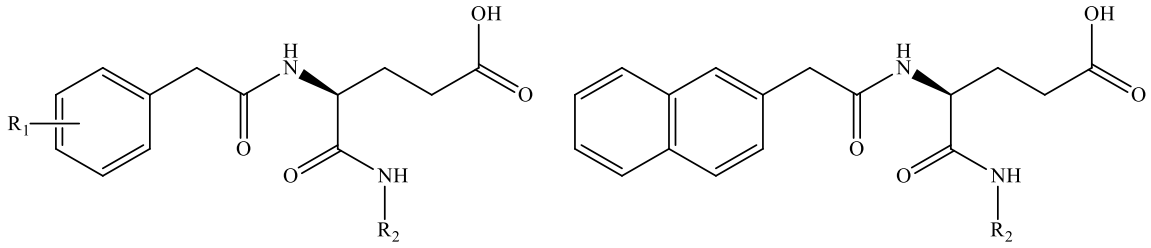

Cpd[a]	R_1	R_2	HDAC8*	Nuclear HDACs*	MMP2*	MMP9*
I1	2-F	*n*-C_6H_{13}	-	-	-	-
I2	2-Br	*n*-C_6H_{13}	-	-	-	-
I3	4-Cl	*t*-C_4H_9	-	-	-	-
I4	4-Cl	*c*-C_6H_{11}	-	-	-	-
I5	4-NO_2	*n*-C_4H_9	-	-	-	-
I6	4-NO_2	Bnz	-	-	-	-
I7	2,4-diCl	*n*-C_4H_9	-	-	-	-
I8	2,4-diCl	*n*-C_5H_{11}	-	-	-	-
I9	-	*n*-C_3H_7	-	-	-	-
I10	-	*n*-C_4H_9	-	-	-	-
I11	-	*i*-C_4H_9	-	-	-	-
I12	-	*n*-C_5H_{11}	-	-	-	-
I13	-	*c*-C_6H_{11}	-	-	-	-
I14	2-F	*n*-C_4H_9	-	-	140.60	-
I15	2-F	*n*-C_5H_{11}	-	-	80.40	-
I16	2-F	Phenyl	-	-	151.36	-
I17	2-Br	*i*-C_3H_7	-	-	177.83	-
I18	2-Br	*i*-C_4H_9	-	-	84.30	-
I19	2-Br	*n*-C_5H_{11}	-	-	110.60	-
I20	2-Br	C_6H_5	-	-	182.18	-
I21	4-NO_2	*t*-C_4H_9			101.60	
I22	4-NO_2	*n*-C_5H_{11}			67.90	
I23	4-Br	2-ClBnz	6.29	>100	7.70	86.01
I24	4-Br	4-ClBnz	4.09	>100	23.30	64.82
I25	4-Br	3,4-diClBnz	4.45	>100	49.70	>250
I26	4-Br	4-OCH_3Bnz	5.09	>100	38.30	5.64
I27	4-Br	4-FBnz	4.27	>100	42.40	70.42
I28	-	*i*-C_3H_7	-	-	91.42	-
I29	-	Bnz	6.05	>100	43.40	74.57

$(IC_{50}, \mu M)$

Here, the **part-I** of my PhD work comprises the biological screening of another set of 29 isogutasmine derivatives (**Table 3.1**) against hematological cancer. These compounds (**Table 3.1; compound I1-I29**) were previously reported by my senior Dr. Amit Kumar Halder. Here I have done the biological screening of those compounds (**Table 3.1; compound I1-I29**) against hematological cancer.

3.2.2. Biological screening of (*L*)-pyroglutamic acid derivatives [Part-II]

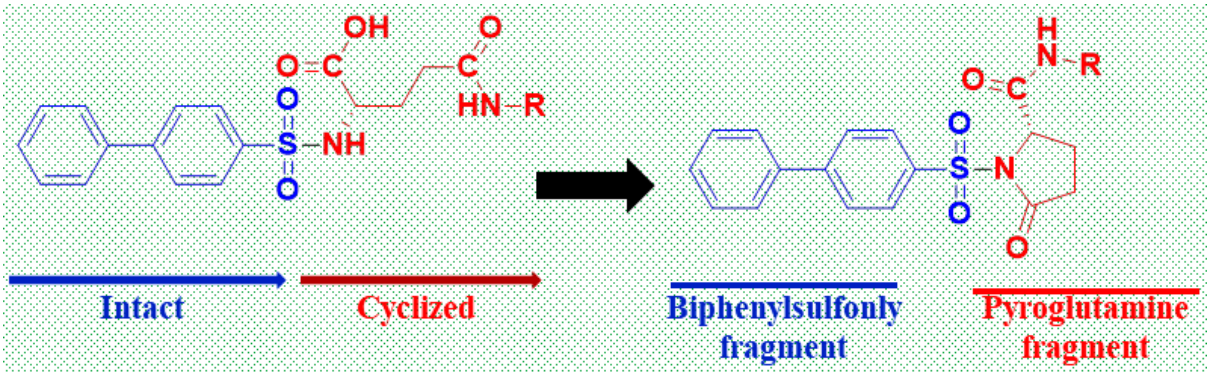

Figure 3.2. Structural modification of arylsulphonyl-*L*(+)glutamine to arylsulphonyl-*L*(+)pyroglutamine.

Researchers from Natural Science Laboratory, Department of Pharmaceutical Technology, Jadavpur University, reported some arylsulfonyl-*L*(+)glutamine-based gelatinases (MMP2 and MMP9) inhibitors which demonstrated acceptable anti-invasive and anti-migratory effects against human non-small cell lung cancer (NSCLC) cell line A549 (Adhikari et al., 2016). Arylsulfonyl-*L*(+)glutamine was also found to have good anti-proliferative action towards leukemia cell lines (K-562 and U-937) as opposed to solid tumor cell lines (A549 and MDA-MB-231) (Mukherjee et al., 2017). Taking guidance from these studies (Adhikari et al., 2016 and Mukherjee et al., 2017), I changed the glutamine fragment to pyroglutamine (**Figure 3.2**), a cyclic variant while keeping the aryl group as the biphenyl function to test if these compounds could cause cytotoxicity in the leukemia cell line Jurkat E6.1, the K562 and U937 cell lines and the solid tumor cell line MDA-MB-231 as well as their gelatinases (MMP2 and MMP9) activity.

Table 3.2. The general structure and reported (Das 2018) cytotoxicity values (IC_{50} in μM) of *in house* pyroglutamic acid derivatives

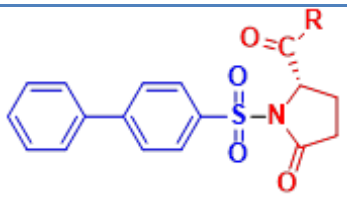

Cpd#.	R	Chemical Formula	K562	Jurkat E6.1
P4	OH	$C_{17}H_{15}NO_5S$	62.85±1.3	82.52±1.5
P6	NH-H	$C_{17}H_{16}N_2O_4S$	64.30±3.1	66.85±1.1
P7	NH-OH	$C_{17}H_{16}N_2O_5S$	46.16±1.7	49.10±1.9
P8	NH-CH_3	$C_{18}H_{18}N_2O_4S$	51.28±1.1	61.71±2.6
P9	NH-C_2H_5	$C_{19}H_{20}N_2O_4S$	60.02±0.9	57.73±2.7
P10	NH-*n*-C_3H_7	$C_{20}H_{22}N_2O_4S$	39.65±2.1	44.32±0.9
P11	NH-*i*-C_3H_7	$C_{20}H_{22}N_2O_4S$	68.36±2.4	98.06±0.7
P12	NH-*n*-C_4H_9	$C_{21}H_{24}N_2O_4S$	76.36±3.7	120.34±4.1
P13	NH-*i*-C_4H_9	$C_{21}H_{24}N_2O_4S$	119.1±2.6	116.93±3.8
P14	NH-*t*-C_4H_9	$C_{21}H_{24}N_2O_4S$	123.36±1.8	123.90±4.8
P15	NH-*n*-C_5H_{11}	$C_{22}H_{26}N_2O_4S$	98.32±2.5	126.29±3.9
P16	NH-*c*-C_6H_{11}	$C_{23}H_{26}N_2O_4S$	87.39±1.6	118.70±4.7
P17	NH-CH_2-C_6H_5	$C_{24}H_{22}N_2O_4S$	101.06±2.8	121.44±3.6
P18	NH-4F-CH_2-C_6H_5	$C_{24}H_{21}FN_2O_4S$	120.24±3.3	117.57±2.6

In my M. Pharm (Das 2018), I had synthesized 14 Biphenylsulphonyl-*L*(+)-pyroglutamic acid derivatives (**Table 3.2;** compound **P4, P6-P18**) and also the initial cytotoxicity studies (MTT assays), were performed against K562 and Jurkat E6.1 cell lines. I had continued my M. Pharm work in PhD also for further progress. Here, the **part-II** of my PhD work comprises the MTT assay of these compounds (**Table 3.2;** compound **P4, P6-P18**) against cancer cell line U937, MDA-MB-231, and normal healthy peripheral blood mononuclear cells line (PBMC) as well as detailed biological studies (flow cytometric apoptosis studies against K562 and Jurkat E6.1 cell lines and mitochondrial membrane potential studies against K562 and Jurkat E6.1 cell lines). The **part-II** of my PhD work also comprises the gelatinase activity of the lead molecules and structure-activity relationship (SAR) study.

3.2.3. QSAR-based molecular modeling studies [Part-III]

This part consists of the rational design of both gelatinases (MMP2 and MMP9) inhibitors. The rational design was performed by *in-sillico* 2D-QSAR-based techniques like regression-based 2D-QSAR including step-wise multiple linear regression (S-MLR), SVM (support vector machine) and ANN (artificial neural network), as well as classification-based QSAR study to refine structural features for attaining better gelatinases (MMP2 and MMP9) inhibitory activity.

3.2.4. Synthesis, biological studies and binding interaction studies of (*D*)-glutamine derivatives [Part-IV]

Learning from the structural information obtained in *in-sillico* QSAR studies as well as incorporating the structural fragment of glutamine/glutamate some molecules had been synthesized, purified, and characterized by HRMS, 1H-NMR, and 13C-NMR.

Following the synthesis *in-vitro* cell culture-based biological studies were also performed against several cancer cell lines. Finally, the lead compounds obtained in biological studies were subjected to *in-sillico* binding interaction studies with MMPs by molecular docking and molecular dynamics simulation to understand the binding mechanism of these matrix metalloproteinase inhibitors with the enzymes (MMPs).

CHAPTER 4

MATERIALS AND METHODS

Chapter 4: Materials and Methods

The current work focuses on three distinct domains: (**4.1**) computer-aided drug design (CADD); (**4.2**) synthetic organic chemistry; and (**4.3**) biological studies. This chapter delves into the materials and methodologies employed within each of these fields, discussed individually.

4.1. Computer-aided drug design (CADD)

The utilization of computers in drug discovery is encapsulated by the term computer-aided drug design (CADD). CADD encompasses a spectrum of algorithms and computational tools designed to streamline the drug development process, resulting in significant time and cost savings (Baig et al., 2018). The quantitative structure-activity relationship (QSAR) study is a ligand-based chemometric technique in drug discovery, offering a quantitative mathematical correlation between structural modifications of chemical compounds and corresponding changes in biological activities (Sharma S, Bhatia 2021). These QSAR methods play pivotal roles in the drug discovery pipeline, enhancing the potency, efficacy, and selectivity of lead compounds earmarked for clinical studies (Sharma S, Bhatia 2021). QSAR analysis stands out as a cost-effective and potent in-silico drug discovery method, owing to its high and rapid throughput. It achieves a favorable hit rate through ligand-based virtual screening studies of extensive compound databases (Kar et al., 2020).

The QSAR analysis encompasses classification-dependent QSAR, including Bayesian classification (Chen et al., 2011; Amin et al., 2019; Jain et al., 2020) and recursive partitioning studies (Chen et al., 2011; Moinul et al., 2022). Additionally, regression-dependent QSAR involves specific techniques such as stepwise multiple linear regression (S-MLR) (Ambure and Roy, 2014; Adhikari et al., 2016) and support vector machine (SVM) (Amin et al., 2016B; Nantasenamat et al., 2008).

Bayesian classification (Chen et al., 2011; Amin et al., 2019; Jain et al., 2020) and recursive partitioning studies (Chen et al., 2011; Moinul et al., 2022) were employed to unveil key structural fingerprints influencing specific pharmacological activities. These classification models effectively distinguished favorable versus unfavorable molecular fragments for the investigated inhibitory activity, as indicated by the fingerprint descriptor, enhancing the design of more potent inhibitors.

Moreover, molecular docking studies (Ferreira et al., 2015; Pinzi and Rastelli, 2019; Torres et al., 2019; Saikia and Bordoloi, 2019) and molecular dynamics simulation studies were conducted to identify critical enzyme-ligand interactions at the enzyme's active site crucial for enzyme inhibitory activity.

4.1.1. Datasets

Here, different molecular modelling techniques were applied into two studies by taking two datasets separately which may be designated as **dataset 1**and **dataset 2**.

4.1.1.1 Dataset 1

The researchers from the Universita` degli Studi, Italy, compiled a library of diverse aryl sulfonamide-based gelatinase inhibitors (Scozzafava and Supuran 2000A; Scozzafava and Supuran 2000B; and Scozzafava and Supuran 2002), which served as the initial dataset for my first study (**dataset 1**), as depicted in **Table A1** of **Appendex** section**.** The library molecules include gelatinase binding affinity values (K_i), which were expressed as their corresponding negative logarithmic values, denoted as pKi values (Roy et al., 2015C). Compound structures were drawn using ChemDraw software (ChemDraw Ultra 5.0) and saved in ".mol" format. Subsequently, these structures were converted into their 3D forms and subjected to an energy minimization process using ChemDraw Ultra 5.0 software (ChemDraw Ultra 5.0). The optimized compounds were then used to calculate the PaDEL descriptors (Yap 2011), with constant and near-constant descriptors being eliminated (Shahlaei 2013).

4.1.1.2 Dataset 2

Another set of 110 gelatinase inhibitors (MMP-2 and MMP-9) was compiled from the work of Rossello and colleagues (Santos et al., 2006; Biasone et al., 2007; Nuti et al., 2007; Marques et al., 2008; Rubino et al., 2009; Nuti et al., 2009A; Nuti et al., 2009B; Nuti et al., 2010; Nuti et al., 2011; Nuti et al., 2015; and Nuti et al., 2018), showcasing structural diversity and varying potencies, as summarized in **Table B1** of **Appendex** section**.** Initially, these compounds were drawn using ChemDraw Ultra 5.0 software (ChemDraw Ultra 5.0) and saved in ChemDraw's native file format (.cdx). Subsequently, these '.cdx' files were converted into '.mol' files using the ChemDraw 3D Pro package. All mol files were then imported into the Discovery Studio 3.0 platform (Discovery Studio 3.0), where the "Prepare Ligands for QSAR" protocol was executed

to identify any structural duplicates within the dataset. The entire set of molecules was then saved as a single structure document file (*.sdf). This '.sdf' file served as the basis for calculating the descriptors of all 110 molecules. Then the compounds were used to calculate the PaDEL descriptors (Yap 2011), with constant and near-constant descriptors being eliminated (Shahlaei 2013).

4.1.2. 2D-QSAR study

In these studies (**Part-IIIA** and **Part-IIIB** in **Chapter 5**), a 2D-QSAR analysis utilizing multiple linear regression (MLR) was employed to establish correlations between molecular descriptors and biological activity separately for MMP2 and MMP9 inhibitors (Vapnic 2000). The quality of the constructed stepwise multiple linear regression (S-MLR) models were evaluated using both internal and external validation metrics. Statistical parameters including the square of the correlation coefficient (r^2), adjusted r^2 (r^2_a), standard error of estimate (SEE), and predicted residual sum of square (PRESS) were computed. Additionally, internal cross-validation using leave-one-out (LOO) cross-validated r^2 (Q^2) was performed. Furthermore, r_m^2 matrices were calculated (QSAR tools, DTC laboratory 2015; and Golbraikh and Tropsha 2002B).

4.1.2.1. 2D-QSAR study for Dataset 1

Y-randomization tests were conducted to assess the robustness of the S-MLR models. In this procedure, the pK_i values were randomly shuffled, and new models were constructed separately. The resulting r^2 and Q^2 values for these new models were expected to be lower than those obtained for the initial main model. External validation using test set compounds was also performed to assess the predictability of these MLR models individually, by calculating externally cross-validated r^2 values (r^2_{Pred}) (Golbraikh and Tropsha 2002B). Furthermore, the most effective MLR models from the two datasets (MMP2 inhibitors and MMP9 inhibitors) were chosen for non-linear QSAR analysis. Support vector machine (SVM) and artificial neural network (ANN) models were constructed using the methods described previously (Nantasenamat et al., 2013). Prior to model construction, SVM and ANN parameters were optimized. Subsequently, an RBF kernel-based SVM model was developed using the "SMOreg" module of the Weka tool (Smith and Frank et al., 2016) with optimized SVM parameters. Similarly, an ANN model was created using the "MultilayerPerceptron" module in the Weka tool (Smith and

Frank et al., 2016), with optimized ANN parameters including hidden nodes, learning rate, learning momentum, and training time.

4.1.2.2. 2D-QSAR study for Dataset 2

Here the genetic algorithm (GA) technique was employed to select relevant descriptors, which were then utilized in the "best subset selection" method. Subsequently, multiple linear regression (MLR) models were generated using a combination of 8 descriptors. Among these models, only those with an r^2 greater than or equal to 0.70 were retained, while others were eliminated. Finally, the best 2D-QSAR models for each group were determined based on conventional squared correlation coefficient (r^2), leave-one-out (LOO) cross-validation correlation coefficient (Q^2), and standard error of estimation (SEE) (QSAR tools, DTC laboratory 2015). These constructed models were also utilized to predict the activities of the corresponding test set compounds (QSAR tools, DTC laboratory 2015; and Golbraikh and Tropsha 2002B). The best MLR models from each MMP2 and MMP9 group were chosen for non-linear QSAR study (Vapnic 2000; Nantasenamat et al., 2013; and Kovács et al., 2021). Support vector machine (SVM) and artificial neural network (ANN) are widely recognized learning methods for constructing classification and regression-based QSAR/QSPR models. The SVM approach involves estimating model parameters using convex optimization (Vapnic 2000), while the ANN method employs a backpropagation of error algorithm that simulates neuronal functions in the biological brain (Nantasenamat et al., 2013). In this study, non-linear QSAR models such as SVM and ANN were constructed using the similar methodologies outlined in **2D-QSAR study for Dataset 1**.

4.1.3. Bayesian classification study

Prior to conduct the classification-based analyses, the dataset compounds (**Dataset 1** and **Dataset 2**) were categorized into *actives* and *inactives* separately for MMP2 and MMP9 in case of both of the studies (**Dataset 1** and **Dataset 2**) (Wang et al., 2014B and Chen et al., 2011). The Bayes theorem (Zhang et al., 2016 and Liu et al., 2014A), which is provided here, is the foundation of the Bayesian classification study [Eq. (1)].

$$P(M/N) = \frac{P(N/M)P(M)}{P(N)} \qquad \text{Eq. (1)}$$

Where, P (N/M) indicates likelihood; P (M/N) represents posterior probability; N is the observed data and M denotes the model. P (M) and P (N) represent the prior belief and evidence data, respectively.

In this study, molecular properties (MPs) such as molecular weight (MW), lipophilicity (ALogP), number of rings (nR), number of aromatic rings (nAR), number of rotatable bonds (nRB), number of hydrogen bond donors (nHBD), number of hydrogen bond acceptors (nHBA), and molecular polar surface area (MPSA), in addition to the functional class fingerprint-extended connectivity fingerprints with a diameter of 6 (ECFP_6) (Rogers et al. 2005; and Rogers and Hahn 2010), were utilized to develop Naïve Bayes classifier models using DS software (Discovery Studio 3.0). The final models underwent external cross-validation on test set populations. Sensitivity (Se), specificity (Sp), precision (Pr), and overall accuracy (Acc) were calculated for statistical evaluation of these Naïve Bayes models according to equations (2) through (5), where TP represents the true positive count of 'active' compounds correctly classified as 'active' by the model, FN is the false negative count of 'active' compounds misclassified as 'inactive', TN is the true negative count of 'inactive' molecules correctly predicted as 'inactive', and FP is the false positive count of 'inactive' molecules incorrectly predicted as 'active'.

$$Se = \frac{TP}{(TP + FN)} \qquad \text{Eq. (2)}$$

$$Sp = \frac{TN}{(TN + FP)} \qquad \text{Eq. (3)}$$

$$Pr = \frac{TP}{(TP + FP)} \qquad \text{Eq. (4)}$$

$$Acc = \frac{(TP + TN)}{(TP + FP + TN + FN)} \qquad \text{Eq. (5)}$$

Receiver operating characteristic (ROC) plots were employed to assess the performance of the developed classification models (Fawcett 2006).

4.1.4. Recursive Partitioning study

With the **dataset 2** Recursive partitioning (RP) study was performed. RP is a statistical technique used in classification. It generates one or more decision trees by partitioning the population members into smaller subsets (nodes) based on whether a specific predictor selected meets a chosen cut-off value or not (Chen et al., 2011). In non-linear QSAR studies focusing on classification, RP analysis processes inhibitor data (descriptors) alongside biological threshold criteria. This allows RP analysis to directly predict inhibitors and non-inhibitors through the creation of decision trees (Chen et al., 2011).

4.1.5. Topomer CoMFA for Dataset 1

In case of Study with **dataset 1** Topomer Comparative Molecular Field Analysis (Topomer CoMFA) study was performed. Topomer CoMFA is a rapid fragment-based method for three-dimensional quantitative structure-activity relationship (3D-QSAR) studies that does not rely on alignment (Chhatbar et al., 2019; Tong et al., 2020; Tong et al., 2021; and Niu et al., 2018). The SYBYL-X 2.0 molecular modeling package was utilized to conduct Topomer CoMFA investigations (SYBYL-X 2.0.). In this approach, 3D molecular structures are fragmented, and each fragment is aligned based on overlapping regions to establish an absolute orientation. Descriptors are then generated by calculating the three-dimensional steric and electrostatic fields, with a carbon sp3 probe used to determine interaction energies between atoms and electrons. These descriptors serve as independent variables, while pKi values act as dependent variables in partial least squares (PLS) regression analysis to develop Topomer CoMFA models. The square of the correlation coefficient (R^2) and leave-one-out (LOO) cross-validated R^2 (Q^2) are key parameters used to assess model quality. A model is deemed to possess excellent predictive capability when the Q^2 value exceeds 0.5 and the R^2 value surpasses 0.6 (Chhatbar et al., 2019; Tong et al., 2020; Tong et al., 2021; and Niu et al., 2018).

4.1.6. Molecular docking study

In this study, the *GLIDE* module from the Schrodinger Suite (Schrodinger Suite 2019) was used to perform the molecular docking study of the synthesized compounds at the active site of MMP2 (PDB ID: 1HOV), MMP9 (PDB ID: 1HOV), MMP8 (PDB ID: 1HOV), and MMP12 (PDB ID: 1HOV) using our previously reported protocols (Baidya et al., 2023). Initially, in the

molecular docking study, the NMR/X-Ray crystallographic data of the aforementioned MMP isoforms were collected from the RCSB Protein Data Bank (PDB) (RCSB Protein Data Bank 2022). The *Protein Preparation Wizard* of the Schrodinger Maestro v12.3 Software (Schrodinger Suite 2019) was used for the pre-processing of the protein including the removal of crystal-bound water molecules, the addition of polar hydrogen atoms, and protein preparation at *pH* 7.0 (±2.0). Additionally, the *OPLS_2005* forcefield was used to minimize the protein structures. Next, the centroid of the co-crystallized ligands bound at the active site of the crystallographic data of each MMP isoform was considered for the receptor grid generation in the *Receptor Grid Generation Wizard* of Schrodinger Maestro Software (Schrodinger Suite 2019) while considering the catalytic Zn^{2+} ions of each of isoforms as metal constrains. The *Epik* module was used to prepare the synthesized molecules for the molecular docking study. The preprocessing was performed for a *pH* 7.0 (±2.0) by applying *OPLS_2005* forcefield without generating any tautomer in the *Ligprep wizard* of Schrodinger Maestro Suite (Schrodinger Suite 2019) before the molecular docking study. Finally, the *extra precision* (*XP*) with the *Flexible Ligand Sampling* method and *OPLS_2005* forcefield were used for the molecular docking study.

4.1.7. Molecular dynamics (MD) simulation study

The *Desmond* Module of the Schrodinger Suite was used for the 100 ns MD simulation study of the compounds at the active site of MMP2 (PDB ID: 1HOV) (RCSB Protein Data Bank 2022). Initially, a similar protein preparation protocol performed for the molecular docking study was used to prepare the MMP2-inhibitor complexes. The *TIP3P* water model with a 10 Å buffer distance for the *Cubic* box shape was used for the system development by applying the *OPLS_2005* forcefield. The systems were neutralized by incorporating Na^+ ions while preserving an isotonic condition by introducing Na^+ and Cl^- ions at a concentration of 0.15 (M). Prior to conducting the MD simulation studies, the default *NVT* protocol is used for the system relaxation. Finally, the *OPLS_2005* forcefield was used to simulate each of the complexes for 100ns time at a temperature of 310.15K (37 °C) and 1 bar pressure (Baidya et al., 2023).

4.2. Synthetic organic chemistry

Analytical-grade solvents and reagents were employed in the synthesis of intermediates and final compounds. The progression of reactions was monitored via analytical thin layer

chromatography (TLC) utilizing silica gel G plates (TLC silica gel GF254, Merck, Germany). The visualization of spots occurred under ultraviolet light (254 nm), supplemented by the utilization of an iodine chamber for spot development. Melting points were determined using a VEGO digital melting point apparatus equipped with capillary tubes. The synthesized compounds underwent characterization through high-resolution mass spectrometry (HRMS), proton nuclear magnetic resonance (^{1}H NMR), and carbon-13 nuclear magnetic resonance (^{13}C NMR) spectroscopy. HRMS spectra were captured utilizing the Xevo G2-XS QTof mass spectrometry system (Waters Corporation, MA, USA) in positive electrospray ionization (ESI) mode, operated via Waters Informatics software. ^{1}H NMR and ^{13}C NMR spectra were acquired using a JEOL JNM ECZ400S NMR 400MHz spectrometer, a Bruker 300MHz FT-NMR spectrometer, and a Bruker 400 MHz FT-NMR spectrometer employing deuterated dimethyl sulfoxide (DMSO-d_6) as the solvent. Tetramethyl silane served as the internal standard in NMR studies, with chemical shift values reported in parts per million (ppm). Spin multiplicities were denoted by symbols: s (singlet), d (doublet), dd (doublet of doublet), ddd (doublet of doublet of doublet), t (triplet), dt (doublet of triplet), and m (multiplet). A PerkinElmer LX-1 FTIR spectrophotometer (4000−400 cm-1) was used to obtain Fourier transform infrared (FT-IR) spectra utilizing a modern diamond attenuated total reflectance (ATR) accessory method of compounds **3a-3h and 3a′-3h′**. The Λ_{max} values of representative compounds were determined by a dual-beam UV-vis spectrophotometer (Shimadzu UV-1800, Kyoto, Japan) in the wavelength range of 200-500 nm with a resolution of 1 nm. The HPLC system consisted of a quaternary pump (Model: Agilent 1260 series) with an autosampler, UV-visible detector, and thermostat column compartment (TCC). EZ Chrome Elite software was used for data collection and analysis. The column was a Phenomenex Luna octadecylsilane, 250 mm x 4.6 mm, particle size 5 µm. The mobile phase (MP) containing buffer (7.2 mM monobasic sodium phosphate solution of pH 2.5) and acetonitrile (ACN) as a ratio of 50:50 (v/v) in an isocratic mode of elution with a flow rate (fr) of 1 mL/min. The mobile phase was degassed and filtered before use. The HPLC column oven temperature was set at 35°C. All the samples were injected with a load of 20 µL.

4.2.1. Synthesis of *(D)*-glutamine derivatives

The general synthetic route for the preparation of *D*-(-)glutamine derivatives is outlined in **scheme 4.1**.

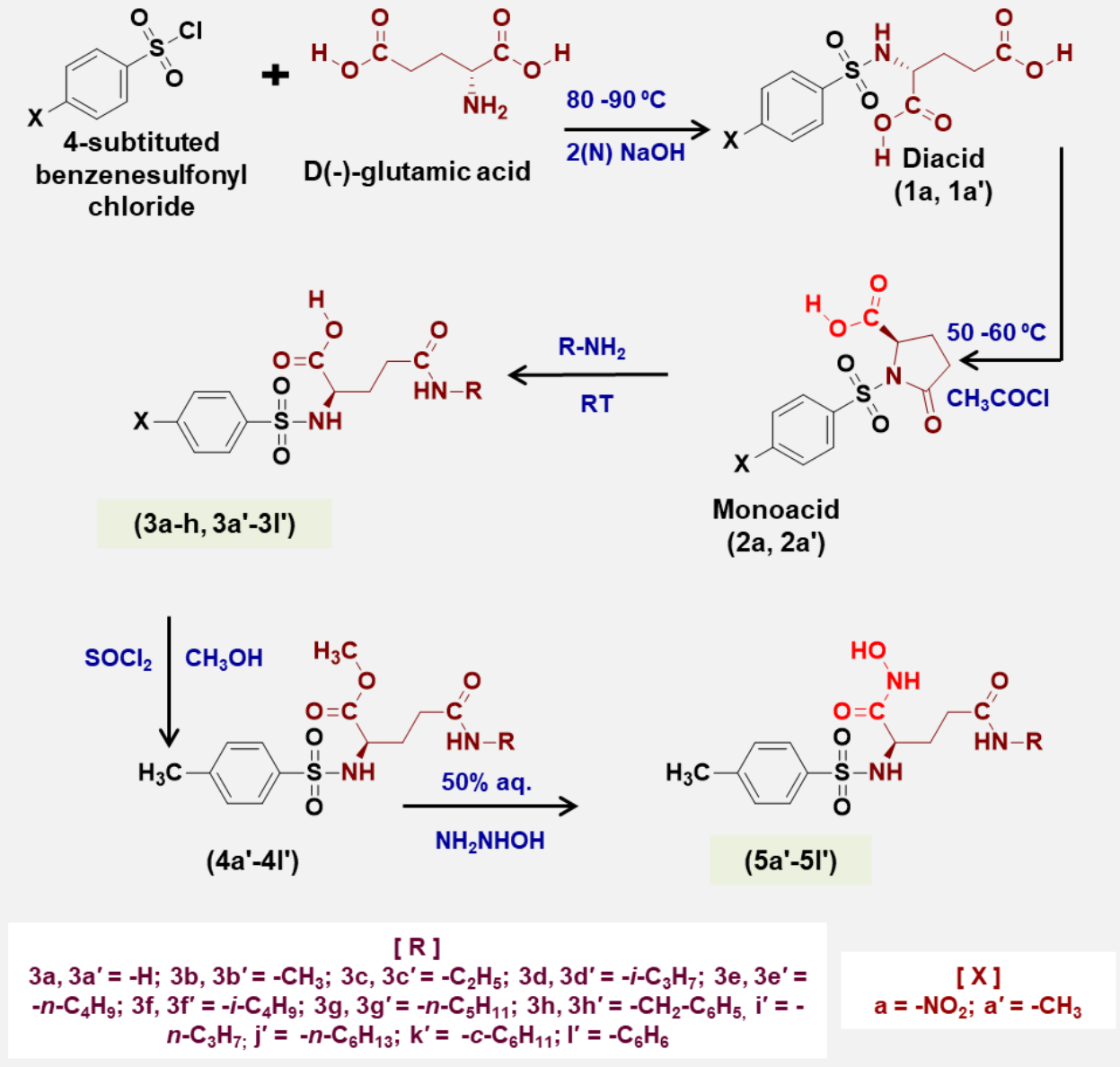

Scheme 4.1. Synthetic route of the *D*-(-)glutamine derivatives (**3a-3h; 3a′-3l′** and **5a′-5l′**).

4.2.1.1. Preparation of (*R*)-2-(4-nitrophenylsulfonamido)pentanedioic acid (1a)

The first intermediate (**Scheme 4.1**) of the 4-nitrobenzenesulfonyl-*D*-(-)glutamine series, was conducted following a previously reported general procedure (Adhikari et al., 2016). In brief, 1.5 g of *D*-(-)glutamic acid (0.01 moles) were placed in a 250 mL conical flask, and 2 N NaOH solution was added until the reaction mixture achieved an alkaline state (pH 8-9). The system was placed on a temperature-controlled magnetic stirrer and stirred at 1,200–1,400 rpm. The temperature was gradually increased and maintained between 80°C to 90°C until the reaction

was complete. 2 g of 4-nitrobenzenesulfonyl chloride (0.009 moles) were weighed and kept moisture-free before gradually added to the solution. Once the 4-nitrobenzenesulfonyl chloride had completely dissolved into the reaction mixture, additional portions were incrementally added. Throughout the procedure, small quantities of 2N NaOH solution were periodically added to maintain the pH (8-9) of the reaction mixture. A total of 2 g of 4-nitrobenzenesulfonyl chloride were utilized during the reaction, which lasted 6-8 hr. Subsequently, the reaction mixture was filtered, allowed to cool, and then acidified with conc. HCl, resulting in the precipitation of intermediate (**1a**). This precipitate was then subjected to thrice extraction using 50 mL portions of ethyl acetate (EA). After combining the EA extracts, anhydrous sodium sulfate was added. Then the mixture was left overnight to remove adherent water. The crude solid product (**1a**) was obtained by filtering sodium sulfate and subsequently distilling the filtrate to remove the EA solvent. The crude product was washed thrice with 20 mL of toluene and dried under vacuum. The resulting compound **1a** was utilized in the subsequent step without further purification.

4.2.1.2. Preparation of (*R*)-1-((4-nitrophenyl)sulfonyl)-5-oxopyrrolidine-2-carboxylic acid (2a)

With minor adjustments, the standard procedure for synthesizing (*R*)-1-((4-nitrophenyl)sulfonyl)-5-oxopyrrolidine-2-carboxylic acid (**2a**) was conducted based on the protocol outlined in the literature (Adhikari et al., 2016). In essence, 1.18 mL of acetyl chloride (0.015 mol) was added dropwise to 1 g of compound **1a** (0.003 mol) in a round-bottom flask (RBF) under anhydrous conditions. The mixture was then refluxed at 50–60°C for 4-6 hrs. The completion of the reaction was confirmed by TLC. Subsequently, the reaction mixture was poured into crushed ice. Then it was kept to refrigerate until the crude precipitate of product **2a** formed. The crude product was extracted with 30 mL of chloroform using a separating funnel, and this extraction process was repeated three times. The chloroform extracts were combined, and anhydrous magnesium sulfate was added to dry the organic phase. The resulting organic extract was then stored in an airtight container for 24 hrs. Upon filtration, the drying agent (magnesium sulfate) was removed. After the chloroform was evaporated by distillation, a light yellow solid product (**2a**) was obtained. This product was recrystallized from 70% (v/v) ethanol in water to yield the final purified compound.

4.2.1.3. Preparation of (*R*)-5-amino-2-(4-nitrophenylsulfonamido)-5-oxopentanoic acid (3a)

To produce the target compound (**3a**), compound **2a** underwent amination with aqueous ammonia using a previously described standard procedure (Mukherjee et al., 2017). Initially, 20 milliliters of distilled water were employed to create slurry of 1 gram (0.003 mol) of compound **2a** in a conical flask. Subsequently, an excess of 25% ammonia solution (1 milliliter, 0.015 mol) was introduced to this suspension. The reaction mixture was then sealed with a stopper and left in a dark location for 12 hours. Monitoring of the reaction progress and formation of compound 3a was carried out via TLC. Unreacted excess amines were removed by heating the reaction mixture in a water bath, followed by cooling to room temperature. To isolate the desired compound (**3a**), 6N HCl was added dropwise into the reaction vessel in an ice bath. Then the crude compound **3a** was filtered and washed three times with 10 milliliters of cold water. Subsequently, the crude compound **3a** was subjected to recrystallization by an isopropyl alcohol-water mixture (70% IPA and 30% water) to obtain the desired product.

Compounds **3b-3h** were prepared following the synthetic procedure of compound **3a**. The crude compounds (**3b-3h**) were recrystallized individually by an ethanol-water mixture (70% ethanol and 30% water).

4.2.1.4. Preparation of (*R*)-2-(4-methylphenylsulfonamido) pentanedioic acid (1a′)

The first intermediate (**1a′**) of the 4-methylbenzenesulfonyl-*D*(-)glutamine series was synthesized following the previously described general procedure (Adhikari et al., 2016). In summary, 0.88 grams (0.006 moles) of *D*(-)glutamic acid was placed in a 250 mL conical flask, and 2 N NaOH solution was added until the solution reached alkalinity (pH 8-9). The mixture was then placed on a temperature-controlled magnetic stirrer and stirred at 1,200–1,400 rpm. The temperature was gradually raised and maintained between 80°C to 90°C until the reaction was complete. Subsequently, 1 g (0.005 mol) of toluenesulfonyl chloride, accurately weighed and kept moisture-free, was gradually added in small portions to the solution. After the complete dissolution of the initially added 4-methylbenzenesulfonyl chloride into the reaction mixture, additional portions of toluenesulfonyl chloride were added incrementally. Throughout the process, small amounts of 2N NaOH solution were periodically added to maintain the pH (8-9) of the reaction mixture. Approximately 1 gram of toluenesulfonyl chloride was consumed during

the reaction over six to eight hr. Following this, the reaction mixture was filtered, allowed to cool, and acidified with concentrated HCl, leading to the precipitation of the intermediate (**1a′**), which was then extracted three times using 50 mL of ethyl acetate (EA). The combined ethyl acetate extract was washed three times with 10 milliliters of brine solution. Anhydrous sodium sulfate was added to the mixture, and it was left overnight to remove any residual water. Ultimately, the crude solid product (**1a′**) was obtained by filtering out the sodium sulfate, followed by distillation of the filtrate to remove the solvent EA. A sticky semisolid crude product was obtained, which was stored in a desiccator. After 2-3 days, a white crystalline solid of compound **1a′** was obtained and utilized in the subsequent steps without further purification.

4.2.1.5. Preparation of (*R*)-5-oxo-1-tosylpyrrolidine-2-carboxylic acid (2a′)

With some modifications, the general method of preparation of (*R*)-5-oxo-1-tosylpyrrolidine-2-carboxylic acid (**2a′**) was carried out by following the literature (Adhikari et al., 2016). In short, 1.30 mL (0.015 mol) of acetyl chloride was added dropwise to 1 g of compound **1a′** (0.003 mol) in an RBF under anhydrous condition. The mixture was refluxed at 50–60 °C for 4-6 hr. The end of the reaction was verified by TLC. Then, the content was transferred into crushed ice and refrigerated until the crude product (**2a′**) precipitated. This was extracted with three portions of 30 mL of chloroform each using a separating funnel. The chloroform extracts were pooled and anhydrous magnesium sulfate was added. The extract was stored in an airtight container for 24 hr. The drying agent (magnesium sulfate) was eliminated by filtration. Chloroform was removed by distillation, and a white solid product (**2a′**) was obtained which had been recrystallized from 70% (v/v) ethanol.

4.2.1.6. Preparation of (*R*)-5-amino-2-(4-methylphenylsulfonamido)-5-oxopentanoic acid (3a′)

To get the desired product (**3a′**), compound **2a′** was treated with aqueous ammonia using the protocol reported earlier (Mukherjee et al., 2017). 10 mL of distilled water was utilized to prepare 1 g (0.003 mol) of compound **2a′** slurry in a flask. To the suspension, an excess ammonia solution (1 mL, 0.015 mol) was added. After closing the conical flask and having the reaction mixture with a stopper, it was kept in a dark place for 12 hr. The formation of compound **3a′** and the completion of the reaction were monitored by TLC. The excess amines were

eliminated by heating the reaction mixture in a steam bath. Then the mixture was cooled to room temp. To obtain the desired compound (**3a′**), 6N HCl was added dropwise to the reaction mixture placed in an ice bath for precipitate formation. Then the precipitate was filtered and washed three times with 10 mL of cold water. The crude compound **3a′** was recrystallized was recrystallized by isopropyl alcohol-water mixture (70% IPA and 30% water) to obtain the desired product.

Compounds **3b'-3l'** were prepared following the synthetic procedure of compound **3a'**. The crude compounds (**3b'-3l'**) were recrystallized individually by ethanol-water mixture (70% ethanol and 30% water)

4.2.1.7. (*R*)-methyl 5-amino-2-(4-methylphenylsulfonamido)-5-oxopentanoate (4a')

In the next step, 1 g (0.003 mol) of compound **3a'** was taken in an iodine flask and dissolved in dry methanol. Then the flask was kept in an ice bath and 1.18 mL of acetyl chloride (0.015 mol) was added drop by drop into the solution in moisture condition. The reaction mixture was continuously stirred using a magnetic stirrer. The reaction progress was monitored by TLC. After two to three hours, when the reaction was completed the excess methanol and unreacted thionyl chloride were removed by heating the reaction mixture in the water bath. The resulting ester was then dissolved in ethyl acetate. The ethyl acetate solution was extracted with 1(N) sodium bicarbonate solution by using a separating funnel. The ethyl acetate portion was kept overnight by adding sodium sulfate. The next day, the ethyl acetate solution was filtered and distilled out the ethyl acetate and the dry ester derivative (**Scheme 4.1**; **4a'**) of (*R*)-5-amino-2-(4-methylphenylsulfonamido)-5-oxopentanoic acid (**3a'**) was obtained. Finally crude intermediate compound (**4a')** was recrystallized with 70% ethanol.

Compounds **4b'-4k'** (**Scheme 4.1**) were prepared following the synthetic procedure of compound **4a'**.

4.2.1.8. (*R*)-N^1-hydroxy-2-(4-methylphenylsulfonamido)pentanediamide (5a')

0.5 g (0.0015 mol) of compound **4a'** was taken in in an RB flask and dissolved in dry methanol. Then in a 1:18 molar ratio, 50% aqueous hydroxyl amine was added into the solution mixture. 10% sodium hydroxide solution was added periodically to keep the solution alkaline. Then the reaction mixture was kept stirring for 24-30 hr by using a magnetic starrier. The progress of the reaction was monitored by TLC. After the end of the reaction, 2(N) hydrochloric acid was added

and stored in a cool, dry location. Then the final desired hydroxamate derivatives (**5a'**) of (*R*)-methyl 5-amino-2-(4-methylphenylsulfonamido)-5-oxopentanoate (**4a'**) (**Scheme 4.1**) was filtered and washed with diethyl ether and lastly purified by hot isopropyl alcohol-water mixture (70% IPA and 30% water) to obtain the desired product as a precipitate.

Compounds **5b'-5k'** (**Scheme 4.1**) were prepared following the synthetic procedure of compound **5a'**. Lastly the crude compounds were individually purified by hot ethanol-water mixture (70% ethanol and 30% water) to obtain the desired products as precipitates.

4.2.1.9. X-ray crystallography

An X-ray quality crystal of compound **3h′** was selected for data collection. X-ray crystallographic data of the compound **3h′** were collected at 273K using a Bruker D8 QUEST area detector diffractometer equipped with graphite monochromated MoKα radiation (λ = 0.71073 Å). The molecular structure was solved by direct method and refined by full-matrix least squares on F2 using the SHELXL-2018/3 package (Usón and Sheldrick, 2018). An empirical absorption correction method (SADABS) (Bruker 2002) was applied. Non-hydrogen atoms were refined with anisotropic thermal parameters. All hydrogen atoms were placed in their geometrically idealized positions and ride on their parent atoms located in the Fourier map. Successful convergence was indicated by the maximum shift / error of 0.001 for the last cycle of the least-squares refinement. Due to the high thermal parameter, we were unable to assign any desirable disorder model for guest molecule. SQUEEZE subroutine of the Olex2 (Dolomanov et al., 2009) software suite was applied to remove the scattering from the highly disordered guest molecules.

4.3. Biological screening

4.3.1. Cell lines and cell culture

Chemicals such as antibiotics (penicillin, streptomycin), phosphate buffer saline (PBS, pH 7.4), fetal bovine serum (FBS) and cell culture media- RPMI-1640, Dulbecco's Modified Eagle medium (DMEM), Eagle's Minimum Essential Medium (EMEM) medium, and Dimethylsulfoxide (DMSO) were procured from HiMedia Laboratories Pvt. Ltd., Mumbai, India. The tissue culture-grade plastic wares used in this study were obtained from Eppendorf India Private Limited.

Human cancer cell lines U937 (acute myeloid leukemia), Jurkat-E6.1 (T-acute lymphocytic leukemia, T-ALL), MOLT-4 (T-ALL), K562 (chronic myeloid leukemia), A549 (non-small cell lung cancer), MDA-MB-231 (breast cancer), U-87MG (glioblastoma), HT1080 (fibrosarcoma), and normal human embryonic kidney cells (HEK-293) were collected from the National Centre for Cell Science (NCCS), Pune, India. Peripheral blood mononuclear cell (PBMC) was purchased from Sigma-Aldrich (USA). U937, Jurkat-E6.1, K562, MOLT-4 and PBMC the cell lines were non-adherent or suspension cell lines and, therefore, cultured in RPMI-1640 media with 10% FBS and 1% penicillin-streptomycin antibiotic solution. A549, U-87MG, HT1080, and HEK-293 cell lines were adherent cells. A549 and MDA-MB-231 cell lines were cultured in DMEM medium with 10% FBS and 1% streptomycin-penicillin antibiotic solution. U-87MG, HT1080, and HEK-293 cell lines were cultured in EMEM medium with 10% FBS and 1% streptomycin-penicillin antibiotic solution. 0.025% Trypsin in saline was used for harvesting these adherent cells. These cells were kept at 37°C with 5% CO_2 in a humidified incubator.

4.3.2. Cell viability assay

Cell viability was carried out using PrestoBlue® and MTT reagent. Briefly, U937, Jurkat-E6.1, K562, MOLT-4, A549, U-87MG, HT1080, PBMC, MDA-MB-231, and HEK-293 cells were added in 96 well plates having 1 x 10^4 cells/well. Before treatment, these cells were given a 24-hour period to settle. The treatment compounds were solubilized in tissue culture grade DMSO and added into the cell culture medium while preparing the drug solution separately. The cells were treated with compounds with a concentration range of 0.048 µM - 500 µM for 72 hr. The control values for the untreated cells were assumed to be 100%, and the viability statistics for the treated cells were expressed as a percentage of the control. Using Graph Pad Prism 8.0.1., the obtained results were represented in the dose-response curve for the IC_{50} determination.

4.3.3. Cell cycle analysis

In short, cells (~5 x10^4 cells/mL) were seeded in 12 well plates and exposed to selected compounds for 72 hr at their respective IC_{50} dose. After treatment, cells were centrifuged, washed two times with cold phosphate buffer saline (PBS, pH 7.4), and fixed with 70% cooled ethanol overnight at -20°C. After two PBS washes, the cells were treated with 100 µg/mL of RNAse A for one hour at room temperature. Following that, cells were treated with 50 µg/mL PI

for 15 minutes in the dark. The cells were then examined using a BD Aria III flow cytometer (Mukherjee et al., 2017). Using the proper gate to select a single cell population, 10,000 events were examined for every sample; the same gate was applied to all of these samples.

4.3.4. Apoptotic assay by flow cytometry after annexin V/PI staining

A TACs/Annexin V kit purchased from BioLegend US was used for the apoptosis assay. In a nutshell, cells (~5 x 10^4 cells/mL) were treated with selected compounds for 72 hr at respective IC_{50} doses. Following cell harvesting, PBS (pH 7.4) wash was given to cells. Following a 15-minute dark incubation period at room temperature in 100 µL Annexin V incubation reagent freshly prepared including 10X binding buffer (10 µL), FITC (1 µL), PI (10 µL) making up to 100 µL using double distilled water. The cell suspension was subjected to an analysis utilizing a BD Aria III, with a minimum of 10,000 cells per sample (Mukherjee et al., 2017).

4.3.5. DNA deformation assay by DAPI staining

The nuclear morphology of cells, both before and after treatment, was assessed by individually staining the nucleus with DAPI (Mukherjee et al., 2017). A total of 5x10^4 cells were plated in 6-well plates and allowed to incubate overnight at 37°C in a CO_2 incubator. Subsequently, treatments with selected compounds were administered separately at specific concentrations for durations of 12 hr and 30 hr, respectively. The cells were then harvested and rinsed twice with PBS. Following this, the cells were fixed in 100% chilled ethanol. After fixation, the cells were rehydrated with PBS and permeabilized with NP-40 (0.1%). Subsequently, the cells were stained with DAPI (3µg/mL) for 15 min in the dark at room temperature. Finally, the cells were washed with PBS and examined under a Leica Fluorescence microscope (Germany).

4.3.6. Acridine orange/ethidium bromide (AO/EB) staining

The differential acridine orange/ethidium bromide (AO/EB) staining was utilized to evaluate apoptosis and cell viability (Arunachalam et al., 2022). AO as acridine orange hemi(zinc chloride) salt was procured from Sisco Research Laboratories Pvt. Ltd., Mumbai, India, and EB was purchased from HIMedia Laboratories Pvt. Ltd., Mumbai, India. The cells (1 x 10^4 cells/mL) were placed in a 6-well plate and before treatment; these cells were given a 24 hr time to settle in a humified incubator at 37 °C with 5% CO_2. Then, the treatment was given by the selected compounds at their respective IC_{50} dose for 24 hours, 48 hours, and 72 hours. The

control group was treated with solvent only (0.1% tissue culture grade DMSO). The treated and untreated live cells were stained with 1 µL of AO/EB dye mix (100 µL/mL AO and 100 µL/mL EB, both prepared in PBS). After 5 min later, the cells were visualized via a fluorescence microscope (Magnus) using 480nm and 535 nm filters (Magnification-40x; Scale bar 50µm) (Das et al., 2022B).

4.3.7. Reactive oxygen species (ROS) assay

Intracellular changes in ROS were assessed using the H_2DCFDA probe (Datta et al., 2012; Halder et al., 2015A). A total of $5x10^4$ cells were seeded into 6-well plates and incubated overnight in a CO_2 incubator at 37°C. Subsequently, treatment with selected compounds at specific concentrations was administered separately for 48 hours. After the incubation period, cells were harvested and suspended in phosphate-buffered saline (PBS), and H_2DCFDA at a concentration of 2 µM was added separately. Incubation was conducted at room temperature in the dark for 30 min. The cells were then harvested, washed with PBS, and analyzed for generated DCF fluorescence using an excitation wavelength of 510 nm and an emission wavelength of 525 nm in an LS50B spectrophotometer from Perkin-Elmer, USA. The measurements were expressed in arbitrary units.

4.3.8. Mitochondrial membrane potential detection assay

The mitochondrial membrane potential was assessed using the BD™ Mitoscreen mitochondrial membrane potential detection JC-1 kit (Cat. No. 551302) purchased from BD Bioscience, San Diego, CA, USA. Leukemia cells were treated with selected compounds separately at a specific concentration for 48 hr. Cells treated with 0.1% DMSO served as the control. Following treatment, cells were stained with JC-1 according to the manufacturer's instructions. The sorting of cells based on their polarized/depolarized mitochondrial membrane potential was performed using the FACS technique (BD LSR Fortessa, Becton Dickinson, USA), with 10,000 cells analyzed for each sample.

4.3.9. Angiogenesis assay

The *in vitro* morphogenesis experiment was conducted with selected molecules present at IC_{50} concentrations. For the experiment, ACHN cells after three to four passages were used. In brief, 200 µL/well of Cultrex was carefully pipetted into a 12-microwell plate at 4°C after being pre-

chilled at -20°C. The cells underwent trypsinization and were subsequently suspended in 100 µL of complete medium, either with or without inhibitors with IC_{50} values. Thereafter, cells were carefully layered on top of the polymerized basement membrane matrix after it had been polymerized for an hour at 37°C. The cell arrangement was examined under a microscope following a 72 hr incubation period on Cultrex. Tubulogenic efficiency was directly measured by counting the number of tubes, meshes, branches, and nodes using the Angiogenesis tool and ImageJ software. For every test inhibitor, two wells were seeded for statistical analysis.

4.3.10. MMP2 and HDAC8 expression analysis

The cells (1 x 10^4 cells/mL) were plated in the presence of Monensin sodium (1µM) (Sisco Research Laboratories Pvt. Ltd., Mumbai, India), and after 24 hr, incubated with selected compounds (except the untreated control). The quantity of intracellular proteins is increased by monensin sodium, which improves the ability to distinguish between positive cells and background signals brought on by autofluorescence (Oviedo-Orta et al., 2008). After 48 hr of treatment, cells were collected and washed twice in a cold wash buffer and fixed with 0.5 mL fixation solution for 20 min. The wash buffer consisted of 1% bovine serum albumin (BSA) (Sisco Research Laboratories Pvt. Ltd., Mumbai, India) in PBS (pH 7.4). The fixation solution consisted of 0.4% paraformaldehyde solution in PBS (pH 7.4). Cells were then washed twice in wash buffer-saponin solution (0.1% saponin in wash buffer) followed by exposure to blocking solution (5% BSA in PBS) for 1 hr. Paraformaldehyde and saponin were brought from HiMedia Laboratories Pvt. Ltd., Mumbai, India. Cells were then washed twice followed by incubated overnight with anti-MMP2 primary antibody (1:250 dilutions) and anti-HDAC8 primary antibody (1:250 dilutions) separately. Then after washing cells were treated with the FITC conjugated secondary antibody (1:250 dilutions) for 1hr. Anti-MMP2 antibody, anti-HDAC8 antibody, and anti-mouse FITC conjugated secondary antibody used were procured from Santa Cruz Biotechnology Inc. (CA, USA). Then, the cells were washed once and subjected to flow cytometry (BD-FACS) for MMP2 and HDAC8 expression individually. To keep the cells permeable for antibody penetration, all antibody incubations and washes were carried out in a wash buffer-saponin solution (Dutta et al., 2019 and Oviedo-Orta et al., 2008).

4.3.11. Matrix metalloproteinase (MMP) inhibition assay

Using MMP inhibitor profiling kits (Enzo Life Science International, Inc., Pennsylvania, USA) inhibition assays for MMPs (MMP2 and MMP9) were performed by the manufacturer's instructions. In a microplate photometer (Thermo Scientific Multiscan FC, USA), the absorbance value at 410 nm of the chromogenic substrates was used to determine their concentration. Enzyme reactions were carried out at 37°C for 1 hour in a final volume of 100 mL of solutions. The increase in absorbance at 410 nm was measured using a microplate photometer (Thermo Scientific Multiscan FC, USA) at 1-minute intervals for 30 minutes after the addition of the substrate. As a prototype control inhibitor, N-isobutyl-N-(4-methoxyphenylsulfonyl) glycylhydroxamic acid (NNGH) was used. Semi-logarithmic dose-response graphs were used to identify the doses of substances that provide 50% enzyme inhibition (IC_{50}).

CHAPTER 5

RESULTS AND DISCUSSIONS

Chapter 5: Results and Discussions

The results and discussions chapter is divided into three parts (**Part-I** to **Part-IV**). **Part-I** deals with biological studies (in-vitro cell culture method) of some reported in-house HDAC8 inhibitors (L-isoglutamine derivatives) against hematological cancers. **Part-II** deals with biological studies (*in-vitro* cell culture method) of some *L-(+)* pyroglutamic acid-based gelatinases (MMP2 and MMP9) inhibitors against hematological cancers. **Part-III** deals with the QSAR-based *in-sillico* technique to refine a glutamine-like scaffold for effective and potent inhibitors of both of the gelatinases (MMP2 and MMP9). **Part-IV** deals with the synthesis of these designed glutamine-based gelatinases (MMP2 and MMP9) inhibitors, and biological studies (*in-vitro* cell culture method) against hematological cancers as well as binding interaction studies of leads with MMPs.

5.1. Biological screening of isoglutamine derivatives [Part-I]

The **part-I** comprises the biological screening of 29 isogutasmine derivatives (**Table 5.1; compound I1-I29**) against hematological cancer. These compounds (**compound I1-I29**) were previously reported by my senior Dr. Amit Kumar Halder. Here I have done the biological screening of those compounds (**compound I1-I29**) against hematological cancer.

5.1.1. Cytotoxicity assay

The cytotoxicity of a compound denotes its capacity to induce cell death, either through necrosis or apoptosis. In this study, we assessed the cytotoxicity of 29 previously reported (Halder 2015B) isoglutamine derivatives (**I1-I29**) on various human cancer cell lines (such as breast cancer MDAMB-231, leukemia JurkatE6.1, U937, MOLT-4, and non-small cell lung cancer A549), as well as normal peripheral blood mononuclear cells (PBMC) from healthy individuals. Each compound was tested at five different concentrations. Notably, none of these compounds (**I1-I29**) exhibited activity against adherent cancer cell lines (MDAMB-231 and A549), but they displayed cytotoxic effects on leukemia cell lines, with the most pronounced effect observed in Jurkat E6.1 cells. Compound **I27** demonstrated the most potent cytotoxic activity against Jurkat E6.1 cells among the tested compounds (**Table 5.1**). Analysis of **Table 5.1** reveals that while these compounds exerted cytotoxic effects on leukemia cell lines, they exhibited no toxicity towards PBMC.

Table 5.1. Cytotoxicity of compounds (**I1-I29**) against a variety of cancer cell lines

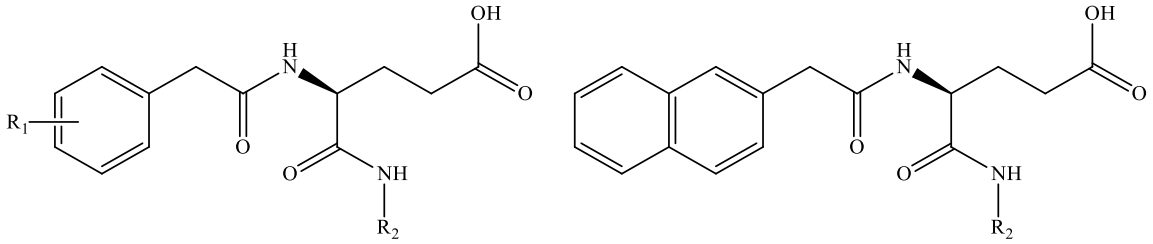

Cpd[a]	R_1	R_2	IC_{50} (µM)					
			Jurkat E6.1	U937	MOLT-4	A549	MDAMB-231	PBMC
I1	2-F	*n*-C_6H_{13}	31.27±3.2	58.79±3.1	26.34±1.5	≥ 100	≥ 100	≥ 400
I2	2-Br	*n*-C_6H_{13}	20.16±1.9	33.19±3.6	21.33±2.7	≥ 100	≥ 100	≥ 400
I3	4-Cl	*t*-C_4H_9	19.82±2.6	37.62±1.3	20.09±2.6	≥ 100	≥ 100	≥ 400
I4	4-Cl	*c*-C_6H_{11}	23.15±2.5	47.52±2.5	25.17±1.2	≥ 100	≥ 100	≥ 400
I5	4-NO_2	*n*-C_4H_9	18.31±0.7	45.92±1.6	17.54±3.2	≥100	≥100	≥ 400
I6	4-NO_2	Bnz	**13.94±3.0**	44.59±2.9	13.38±2.6	≥ 100	≥ 100	≥ 400
I7	2,4-diCl	*n*-C_4H_9	27.61±2.2	55.78±3.4	22.44±2.6	≥ 100	≥ 100	≥ 400
I8	2,4-diCl	*n*-C_5H_{11}	16.35±1.4	31.11±3.8	12.73±1.9	≥ 100	≥ 100	≥ 400
I9	-	*n*-C_3H_7	18.31±1.3	45.92±2.4	17.54±2.3	≥ 100	≥ 100	≥ 400
I10	-	*n*-C_4H_9	25.63±1.1	39.49±2.7	23.56±3.2	≥ 100	≥ 100	≥ 400
I11	-	*i*-C_4H_9	47.81±2.1	99.31±1.8	56.37±1.1	≥ 100	≥ 100	≥ 400
I12	-	*n*-C_5H_{11}	19.59±2.5	41.13±4.7	23.42±3.1	≥ 100	≥ 100	≥ 400
I13	-	*c*-C_6H_{11}	21.57±0.5	76.89±1.6	19.32±2.8	≥ 100	≥ 100	≥ 400
I14	2-F	*n*-C_4H_9	23.59±2.3	69.81±0.7	37.33±0.7	≥100	≥100	≥ 400
I15	2-F	*n*-C_5H_{11}	21.77±1.4	36.11±0.4	23.89±0.8	≥100	≥100	≥ 400
I16	2-F	Phenyl	21.34±3.4	49.82±0.9	33.94±2.9	≥100	≥100	≥ 400
I17	2-Br	*i*-C_3H_7	61.72±3.0	93.34±3.3	53.84±0.9	≥100	≥100	≥ 400
I18	2-Br	*i*-C_4H_9	25.61±2.9	63.92±4.1	23.85±1.6	≥100	≥100	≥ 400
I19	2-Br	*n*-C_5H_{11}	43.87±2.0	51.79±3.6	45.95±1.3	≥100	≥100	≥ 400
I20	2-Br	C_6H_5	53.14±3.2	89.12±2.6	51.73±1.3	≥100	≥100	≥ 400
I21	4-NO_2	*t*-C_4H_9	63.81±0.8	79..56±3.7	59.39±1.4	≥ 100	≥ 100	≥ 400
I22	4-NO_2	*n*-C_5H_{11}	23.82±1.7	36.79±1.8	19.56±4.1	≥100	≥100	≥ 400
I23	4-Br	2-ClBnz	39.43±1.4	46.24±2.3	49.53±2.1	≥100	≥100	≥ 400
I24	4-Br	4-ClBnz	18.56±4.2	37.56±2.5	16.44±0.9	≥100	≥100	≥ 400
I25	4-Br	3,4-diClBnz	13.32±0.5	44.93±2.7	11.39±2.6	≥100	≥100	≥ 400
I26	4-Br	4-OCH_3Bnz	21.37±3.6	35.33±3.1	22.59±3.7	≥100	≥100	≥ 400
I27	4-Br	4-FBnz	**1.62±1.1**	43.89±2.9	6.57±2.3	≥100	≥100	≥ 400
I28	-	*i*-C_3H_7	31.15±2.1	47.33±2.9	42.56±1.5	≥ 100	≥ 100	≥ 400
I29	-	Bnz	14.56±4.2	29.57±3.3	36.63±3.7	≥ 100	≥ 100	≥ 400

[a] Compound numbers

5.1.2. Apoptosis assay

The most active compound, **I27**, along with another compound, **I6**, which exhibited superior activity, underwent apoptosis assays against Jurkat E6.1 cells. Annexin V protein exhibits a high affinity for phosphatidylserine (PS) in a Ca^{2+}-dependent manner. This Annexin V staining method detects various stages of apoptosis, as PS becomes exposed on the surface of apoptotic cells (Fadok et al., 1998; Nagata et al., 2016). During early apoptosis, PS translocate from the

inner to the outer membrane leaflet of the cell. Cells showing increased Annexin V/FITC fluorescence without a concurrent increase in PI fluorescence are considered to be in early apoptosis, while an increase in both Annexin V and PI fluorescence signifies late apoptosis. In this experiment, Jurkat E6.1 cells were treated with **I6** at a concentration of 15 µM and with **I27** at a concentration of 2 µM for 48 hours. The Annexin V/PI assay revealed no significant increase in the percentage of cells in early apoptosis after 48 hours of treatment with either of these compounds (**I6** and **I27**) compared to untreated cancer cells (**Figure 5.1**). Although negligible apoptosis was observed in the Annexin V/PI assay, it aids in determining the appropriate doses for other biological screening assays involving the treatment of these compounds.

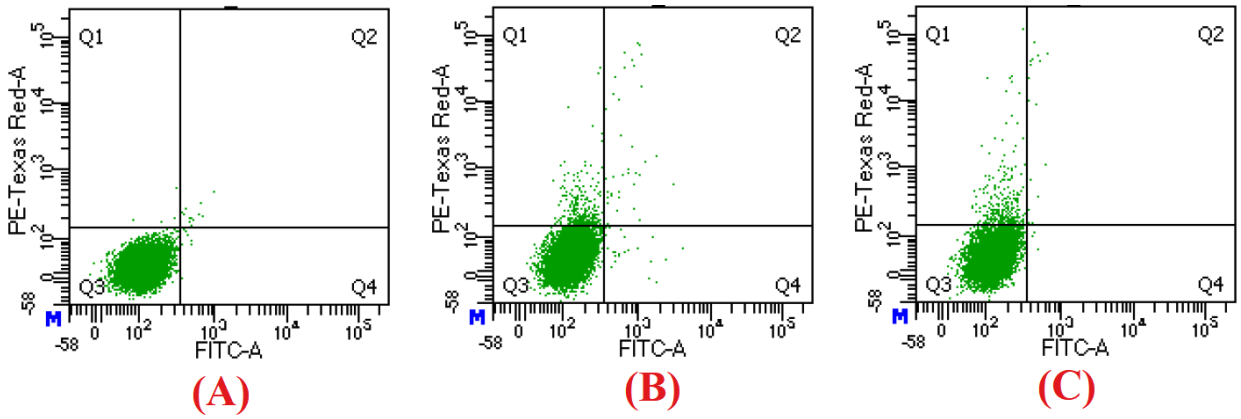

Figure 5.1. The Annexin V-FITC/PI assay, coupled with flow cytometric analysis, was performed on Jurkat E6.1 cells under various conditions: (**A**) untreated, (**B**) treated with compound **I6** at a concentration of 15 µM, and (**C**) treated with compound **I27** at a concentration of 2 µM. The results revealed no significant increase in the percentage of apoptotic cells following treatment compared to the control group.

5.1.3. DNA deformation assay by DAPI staining

The DAPI staining method, utilized to examine alterations in nuclear morphology post-treatment, contrasts nuclear changes between treated and untreated conditions (Mukherjee et al., 2017). DAPI, a fluorescence stain, specifically binds to AT-rich regions of DNA. In this investigation, Jurkat E6.1 cells were subjected to staining at two distinct time intervals subsequent to treatment with compounds **I6** (15 µM) and **I27** (2 µM). Cells treated for 30 hours exhibited more pronounced DNA deformation compared to those treated for 12 hours. Such

DNA deformation serves as an indicator of cell shrinkage and nuclear fragmentation (**Figure 5.2**).

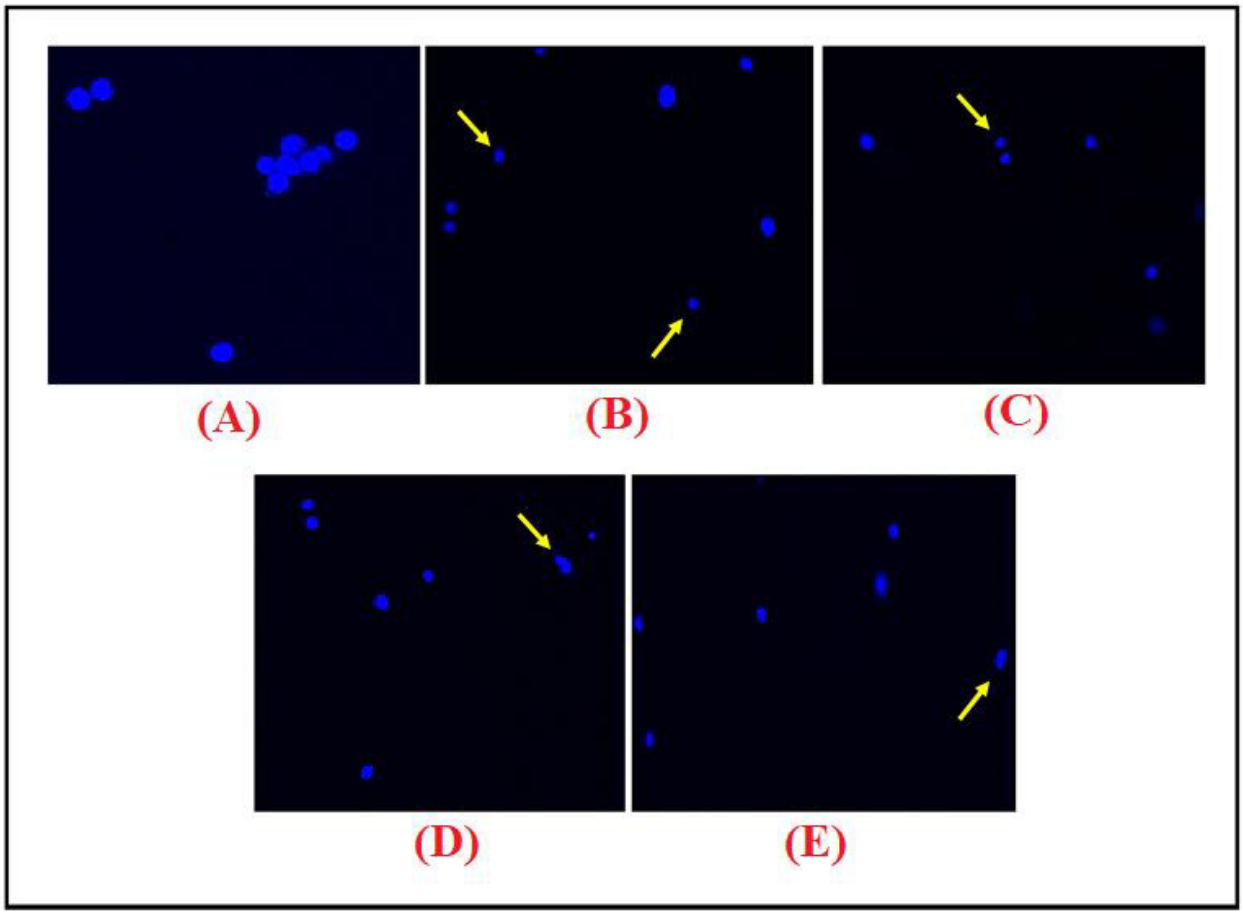

Figure 5.2. Nuclear staining of Jurkat E6.1 cells, both untreated and treated with DAPI. (**A**) Untreated Jurkat E6.1 cells. (**B**) Jurkat E6.1 cells were treated with **I6** (15 µM) for 12 hours. (**C**) Jurkat E6.1 cells were treated with **I6** (15 µM) for 30 hours. (**D**) Jurkat E6.1 cells were treated with **I27** (2 µM) for 12 hours. (**E**) Jurkat E6.1 cells were treated with **I27** (2 µM) for 30 hours. Microscopic examination reveals cell shrinkage and nuclear fragmentation in the treated cells. Arrows indicate nuclear deformation in the treated groups.

5.1.4. Reactive oxygen species (ROS) assay

Reactive oxygen species (ROS) play crucial roles in cell signaling and homeostasis, regularly produced within biological systems. Cancer cells exhibit heightened ROS levels compared to normal cells, altering mitochondrial metabolism and cellular signaling pathways (Yang et al., 2016B). Moreover, ROS overexpression is reported to induce cell death via apoptosis (Gupta et

al., 2014). Consequently, increasing oxidative stress through ROS generation selectively targets cancer cells while sparing normal cells (Aghaei et al., 2012). ROS assays conducted with compounds **I6** and **I27**, at concentrations of 15 µM and 2 µM, respectively, on the Jurkat E6.1 cell line, revealed significant increases in ROS production following treatment with both compounds (**Figure 5.3**).

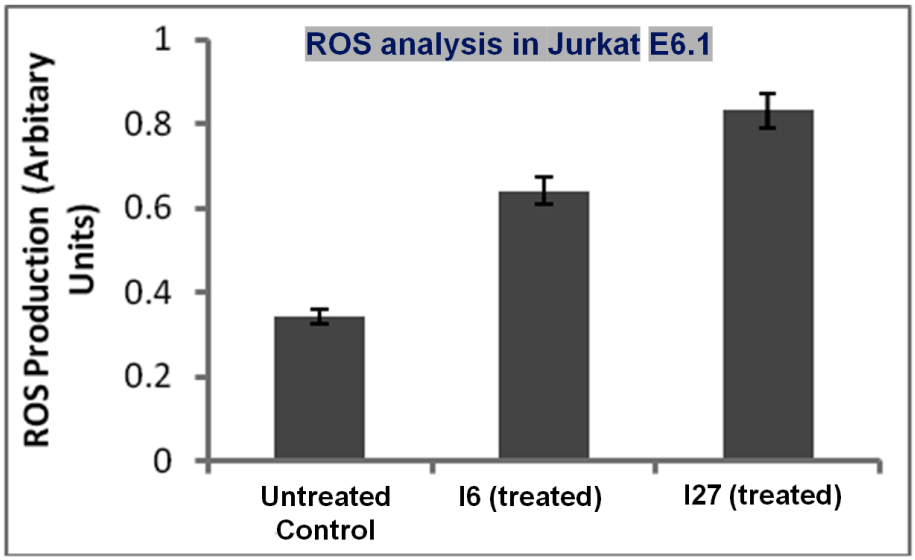

Figure 5.3. The ROS assay utilizing H_2DCFDA was conducted on Jurkat E6.1 cells, with treatments administered using **I6** (15 µM) and **I27** (2 µM). Following treatment, a notable increase in ROS production, ranging from 50% (for **I6**) to 75% (for **I27**), was observed compared to untreated Jurkat E6.1 cells. The data presented represent the mean ± SD of triplicate results per group and are indicative of three independent experiments. Statistical analysis was performed using paired two-tailed Student's t-test, where statistical significance was defined as a p-value of less than 0.05.

5.1.5. MMP2 and HDAC8 expression assay

The changes in expression levels of two enzymes, MMP2 and HDAC8, were assessed via flow cytometry. Treatment with compound **I6** (at concentrations of 10 µM and 20 µM) resulted in a decrease in MMP2 expression by 30-45%, whereas compound **I27** (at concentrations of 2 µM and 5 µM) led to a decrease in MMP2 expression by 40-65%, in a dose-dependent manner, compared to untreated Jurkat E6.1 cells. Similarly, treatment with compound **I6** (at concentrations of 10 µM and 20 µM) resulted in a decrease in HDAC8 expression by 35-52%,

while compound **I27** (at concentrations of 2 µM and 5 µM) led to a decrease in HDAC8 expression by 47-70%, in a dose-dependent manner, compared to untreated Jurkat E6.1 cells. This study demonstrated a significant decrease in the expression levels of both MMP2 and HDAC8 enzymes in a dose-dependent manner (**Figure 5.4**).

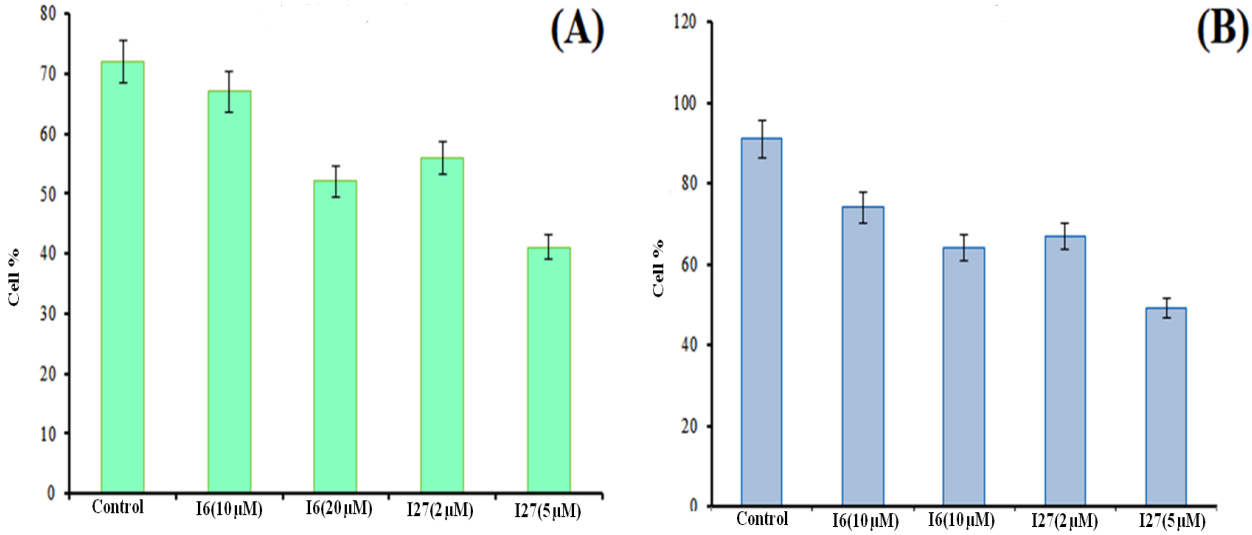

Figure 5.4. (**A**) Examination of MMP2 expression in Jurkat E6.1 cells treated with compounds **I6** (10 µM, 20 µM) and **I27** (2 µM, 5 µM), in comparison to the untreated control, indicates a notable decrease in MMP2 expression post-treatment. (**B**) Examination of HDAC8 expression in Jurkat E6.1 cells treated with compounds **I6** (10 µM, 20 µM) and **I27** (2 µM, 5 µM), relative to the untreated control, illustrates a significant reduction in HDAC8 expression following treatment.

5.1.6. Structure-activity relationship (SAR) study

The compounds (**I1-I29**) underwent cytotoxicity evaluation against various cancer cell lines, including leukemia (Jurkat E6.1, U937, and MOLT-4), breast cancer (MDAMB-231), non-small cell lung cancer (NSCLC) (A549), and normal peripheral blood mononuclear cells (PBMC).

Interestingly, while these compounds demonstrated moderate cytotoxicity against leukemia cell lines (measured in µM), they were ineffective against solid tumor cell lines such as MDAMB-231 and A549. Notably, most of these compounds showed comparable cytotoxicity against Jurkat E6.1 and MOLT-4 acute lymphoblastic leukemia (ALL) cell lines compared to U937 acute myeloid leukemia (AML) cells.

Regarding the structure-activity relationship (SAR), it was observed that the 4-bromo (**R1**) derivative with a 4-fluorobenzyl group at the **R2** position (compound **I27**) exhibited the highest cytotoxicity against Jurkat E6.1 and MOLT-4 cell lines. Compound **I27** outperformed the corresponding 2-chlorobenzyl analogue (compound **I23**), while the 4-methoxybenzyl analogue (compound **I26**) showed similar efficacy compared to the 4-chlorobenzyl analogue (compound **I24**). However, the 3,4-dichlorobenzyl analogue (compound **I25**) demonstrated superior efficacy in Jurkat E6.1 and MOLT-4 cell lines compared to the 4-chlorobenzyl (compound **I24**) and 4-methoxybenzyl (compound **I26**) analogues.

Regarding the 4-nitro and 2-bromo (**R1**) derivatives, linear alkyl groups at the **R2** position exhibited better cytotoxicity than branched alkyl groups. For example, the n-butyl (compound **I5**), n-pentyl (compound **I22**), and n-hexyl (compound **I2**) derivatives were more effective than the i-propyl (compound **I17**) or t-butyl (compound **I21**) analogues. Additionally, benzyl substitution at the R2 position (compound I6) showed better efficacy than corresponding alkyl or branched alkyl compounds (**I5**, **I21**, and **I22**).

Among the 2-bromo derivatives (**R1**), the phenyl group at the **R2** position (compound **I20**) exhibited lower efficacy than corresponding alkyl or branched alkyl substitutions (compound **I2**, **I17-I19**). Nevertheless, the 2-fluoro (**R1**) derivatives (**I1**, **I14-I16**) were more effective than the corresponding 2-bromo (**R1**) derivatives (**I2**, **I17-I20**). Furthermore, 4-chloro derivatives (**I3-I4**) and 2,4-dichloro (**R1**) derivatives (**I7-I8**) demonstrated effective cytotoxicity.

Concerning the naphthalene derivatives, alkyl (**I9-I10**, **I12**), cycloalkyl (**I13**), and aryl (**I29**) derivatives were more effective than branched alkyl derivatives (**I11**, **I28**).

5.1.7. Molecular docking interactions

Using Maestro Software from Schrodinger Inc., USA, compounds **I6** and **I27** were docked into the active sites of MMP2 (PDB: 1HOV) and HDAC8 (PDB: 1VKG). In terms of their binding to the MMP2 active site, both compounds **I6** and **I27** were observed to interact with the catalytic Zn^{2+} ion through their carboxylic acid groups, forming salt-bridge interactions (**Figure 5.5**). Notably, the benzyl moieties attached to the amino groups of both compounds were found to individually engage in π-cation interactions with the catalytic Zn^{2+} ion. Another crucial amino acid residue involved in the interaction was His85, where both compounds **I6** and **I27** formed π-

π interactions separately. Furthermore, the amino groups associated with the 4-bromophenylacetyl group (compound **I27**) and 4-nitrophenylacetyl group (compound **I6**) were identified as hydrogen bond donors, interacting individually with Ala84. The α-carbonyl group linked with the benzylamide function formed hydrogen bonds with amino acid residues Ala84 and Leu83. Moreover, the benzyl group (for compound **I6**) or 4-fluorobenzyl group (for compound **I27**) were observed to orient towards the hydrophobic S_1' pocket, which is surrounded by amino acid residues Leu83, Leu82, Gly81, Ala139, Pro140, Ile141, and Tyr142 (**Figure 5.5**).

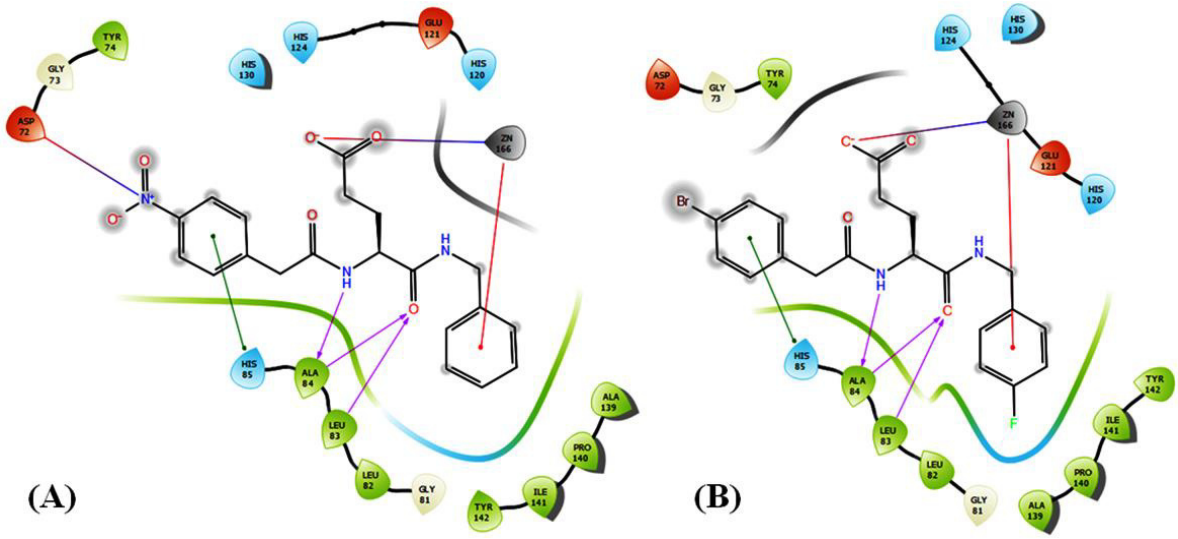

Figure 5.5. Molecular docking interactions of the compounds **I6** (**A**) and **I27** (**B**) with MMP2 enzyme (PDB: 1HOV)

Concerning the binding interactions of compounds **I6** and **I27** with the HDAC8 active site, distinct mechanisms were observed. In compound I27, the carboxylic acid group exhibited a π-cation interaction with the catalytic Zn^{2+} ion, while in compound **I6**, this group formed a hydrogen bonding interaction with a water molecule (**Figure 5.6**). In compound **I6**, the catalytic Zn^{2+} ion interacted with the nitro group through a salt-bridge interaction. Conversely, compound **I27**'s Tyr306 accepted a hydrogen bond from the amido group, while simultaneously donating a hydrogen bond to the hydroxyl function of the carboxylic acid group. Furthermore, Tyr306 residues in both **A** and **B** chains interacted with the nitro and phenyl groups through hydrogen bonding and π-π interactions, respectively. Additionally, in compound **I6**, the nitro group also formed a salt-bridge interaction with Asp267 (**Figure 5.6**).

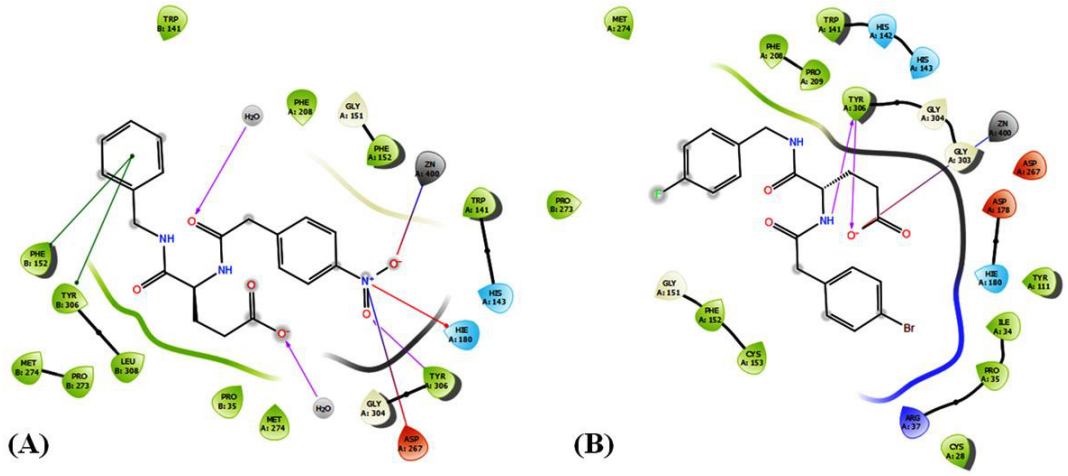

Figure 5.6. Molecular docking interactions of the compounds **I6** (A) and **I27** (B) with HDAC8 enzyme (PDB: 1VKG)

Regarding the molecular docking interaction with MMP9 (PDB: 2OW1), both compounds **I6** and **I27** were observed to interact independently with the catalytic Zn^{2+} ion using their carboxylic acid residues (**Figure 5.7**). The amido groups present in both molecules (**I6** and **I27**) acted as hydrogen bond donors individually with Pro421. Additionally, compound **I27** formed a π-π interaction with the 4-bromophenyl group, whereas one carbonyl group of compound **I6** served as a hydrogen bond acceptor with Leu188 (**Figure 5.7**).

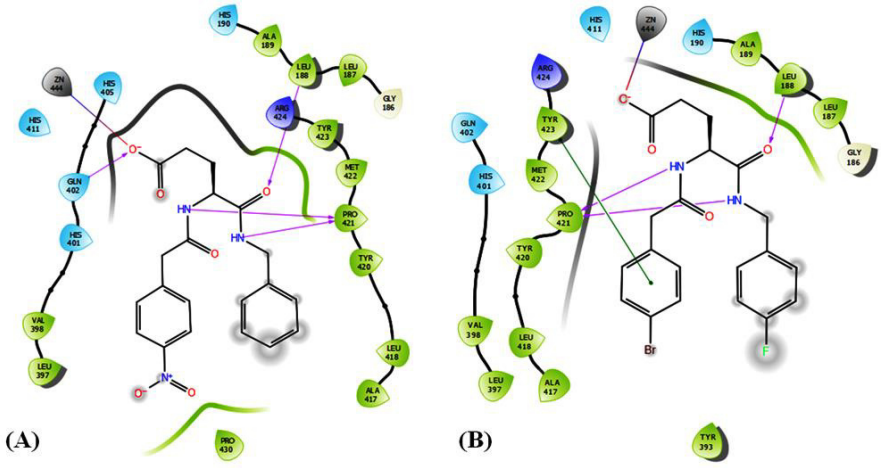

Figure 5.7. Molecular docking interactions of the compound **I6** (**A**) and compound **I27** (**B**) with MMP9 enzyme (PDB: 2OW1).

5.1.8. Summary of Part-I

In the Part-I study, twenty nine compounds (**I1-I29**) which were reported earlier, were screened against different human cancer cell lines at different concentrations. The better activities of these compounds were observed on human leukemia cell lines specifically on Jurkat E6.1 cell line. From the cytotoxicity study, the most active compound (**I27**) as well as another better active compound (**I6**) on the target cell line (Jurkat E6.1) was selected for further biological studies. Hence, all biological studies were carried out with these two compounds (**I6** and **I27**) against Jurkat E6.1 cell line. Both of these molecules (**I6** and **I27**) showed insignificant apoptosis. Further, a DNA deformation assay was performed to know whether the DNA of the nucleus of the treated cells showed any abnormality or not. This assay showed DNA deformation clearly and that is an indication of cell shrinkage and nuclear fragmentation. ROS plays an important role in cancer. The induction in ROS production is conventional in cancer treatment (Sánchez Alcázar et al., 2015). In this study (**Part-I**), it was seen that these better active molecules **I6** and **I27** have the potential to increase ROS in the treated Jurkat E6.1 cell line. Finally, to investigate the MMP2 and HDAC8 inhibitory activity of compounds **I6** and **I27** in Jurkat E6.1 cells MMP2 and HDAC8 expression assays were performed. It was confirmed from these assays that these two compounds **I6** and **I27** have dual inhibitory properties of MMP2 and HDAC8 enzymes. These findings were further supported by the results of molecular docking of these compounds **I6** and **I27** in the drug-binding pockets of MMP2 and HDAC8 enzymes. Moreover, molecular docking analysis also suggested that these two compounds (**I6** and **I27**) **were** not only MMP2 and HDAC8 metalloenzymes but also MMP9 enzymes. In summary, this study (**Part-I**) demonstrates that compounds **I6** and **I27** have good cytotoxic activities in the leukemia Jurkat E6.1 cell line. The mechanism of cytotoxicity is through inducing ROS generation and DNA deformation. This study also suggests that these phenyl/naphthylacetyl-based isoglutamine derivatives exhibit MMP2 and HDAC8 dual inhibitory properties.

5.2. Biological screening of (*L*)-pyroglutamic acid derivatives [Part-II]

In **Part-II**, the glutamine fragment has been modified to its cyclic variant, i.e., pyroglutamine whereas the biphenyl function was retained as the aryl group to see whether these compounds can produce cytotoxicities in hematological cancer cell lines like Jurkat E6.1, K562, and U937 as well as solid tumor cell line MDA-MB-231. The synthesis and the initial cytotoxicity studies

(MTT assays), were performed against K562 and Jurkat E6.1 cell lines were reported in my M. Pharm. dissertation (Das 2018). Here, the **part-II** of my PhD work comprises the MTT assay of these compounds (**Table 5.2;** compound **P4, P6-P18**) against cancer cell line U937, MDA-MB-231, and normal healthy peripheral blood mononuclear cells line (PBMC) as well as detailed biological studies (flow cytometric apoptosis studies against K562 and Jurkat E6.1 cell lines and mitochondrial membrane potential studies against K562 and Jurkat E6.1 cell lines). The **part-II** of my PhD work also comprises the gelatinase activity of the lead molecules and structure-activity relationship (SAR) study.

5.2.1. Cytotoxicity assay

The cytotoxic activity of cytarabine was demonstrated using it as the positive control; the precise IC_{50} values were not determined. Cytarabine, the positive control, demonstrated cytotoxic action (< 0.2 μM) against all hematological cancer cell lines (K-562, U937, and Jurkat E6.1), as well as PBMC (< 5 μM) and MDA-MB-231 (< 3 μM). Table 5.3 displays these synthesized compounds' IC_{50} values (μM), which are **P4** and **P6–P18**.

All compounds listed in **Table 5.2** exhibit cytotoxicity within the range of 200 μM in leukemia cell lines, while none of them demonstrate notable cytotoxicity against the MDA-MB-231 cell line (with IC_{50} values >250 μM). This observation aligns with our previous findings, where we reported that aryl sulfonamide-based glutamine derivatives selectively displayed anti-proliferative activity against leukemia cells (K562 and U937) compared to solid tumor cell lines (A549 and MDA-MB-231) (Mukherjee et al., 2017). Notably, the synthesized compounds are cyclic variants of aryl sulfonamide-based glutamine derivatives. Consequently, these synthesized compounds may warrant consideration for lead discovery in leukemia rather than for solid breast tumor malignancies.

Furthermore, it's worth noting that in contrast to leukemia cell lines, the synthesized compounds exhibit significantly lower cytotoxicity towards normal PBMCs (with IC_{50} values > 500 μM). Among the leukemia cell lines tested, the synthesized compounds generally perform better against Jurkat E6.1 and K562 cell lines. Specifically, Compound **P7** and Compound **P10** displayed notable cytotoxicity with IC_{50} values of 44.32±0.9 μM and 49.10±1.9 μM, as well as 39.65±2.1 μM and 46.16±1.7 μM against Jurkat E6.1, K562, and U937 cell lines, respectively.

Based on their high cytotoxicity profile, Compound **P7** and Compound **P10** were selected for apoptosis studies to investigate the nature of cell death, employing Jurkat E6.1 and K562 cell lines as representative models of lymphoid and myeloid leukemia, respectively.

Table 5.2. Cytotoxicity (IC_{50}) profile of pyroglutamic acid derivatives

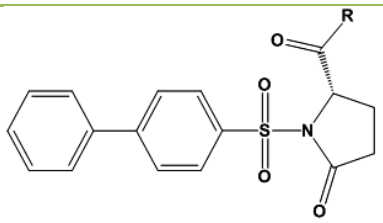

			IC_{50} (μM)				
Sl. No.	**Cpd**[#]	**R**	**K562**[*]	**Jurkat E6.1**[*]	**U937**	**MDA-MB-231**	**PBMC**
1	**P4**	OH	62.85±1.3	82.52±1.5	131.13±3.6	>250	>500
2	**P6**	NH-H	64.30±3.1	66.85±1.1	104.66±4.4	>250	>500
3	**P7**	NH-OH	46.16±1.7	49.10±1.9	60.57±2.8	>250	>500
4	**P8**	NH-CH_3	51.28±1.1	61.71±2.6	90.07±3.4	>250	>500
5	**P9**	NH-C_2H_5	60.02±0.9	57.73±2.7	96.34±2.9	>250	>500
6	**P10**	NH-*n*-C_3H_7	39.65±2.1	44.32±0.9	52.83±3.2	>250	>500
7	**P11**	NH-*i*-C_3H_7	68.36±2.4	98.06±0.7	121.75±2.7	>250	>500
8	**P12**	NH-*n*-C_4H_9	76.36±3.7	120.34±4.1	140.31±4.1	>300	>500
9	**P13**	NH-*i*-C_4H_9	119.1±2.6	116.93±3.8	129.46±1.7	>250	>500
10	**P14**	NH-*t*-C_4H_9	123.36±1.8	123.90±4.8	180.25±0.8	>250	>500
11	**P15**	NH-*n*-C_5H_{11}	98.32±2.5	126.29±3.9	179.55±3.3	>250	>500
12	**P16**	NH-*c*-C_6H_{11}	87.39±1.6	118.70±4.7	112.86±2.3	>250	>500
13	**P17**	NH-$CH_2C_6H_5$	101.06±2.8	121.44±3.6	167.57±3.7	>250	>500
14	**P18**	NH-4F$CH_2C_6H_5$	120.24±3.3	117.57±2.6	111.98±3.9	>250	>500

[#] compound ID; [*] presented here comparison

5.2.2. Flow cytometric study for Apoptosis by annexin V-FITC/PI

The highly active compounds (**P10** and **P7**) underwent further investigation through flow cytometric in-vitro apoptosis studies to elucidate the pathway of cell death (general mechanism of action). This involved dual staining of Jurkat-E6.1 and K562 cell lines separately with FITC-conjugated annexin V and propidium iodide (PI). The resulting dot plot graph, after fluorescence-activated cell sorting (FACS) analysis, revealed distinct populations: annexinV- & PI- (Q3) representing healthy cells, annexinV+ & PI- (Q4) indicating early apoptotic cells, annexinV+ & PI+ (Q2) representing late apoptotic cells, and annexinV- & PI+ (Q1) representing necrotic cells.

Table 5.3. Time-dependent apoptotic profile of compound P10 and compound P7 against Jurkat E6.1 cell line

Experiment		**Figure ID**	**%Viable (Q3)**	**%Apoptotic (Q2+Q4)**	**%Early apoptotic (Q4)**	**%Late apoptotic (Q2)**	**%Necrotic (Q1)**
Unstained		**UN**	96.5	3.4	1.7	1.7	0.1
Control		**CTRL**	93.1	6.7	1.6	5.1	0.2
Treatment							
Cpd# ID	**Time (hrs)**						
P10	**6**	**N1**	80.7	16.9	2.2	14.7	2.4
	12	**N2**	71.8	27.1	8.4	18.7	1.1
	24	**N3**	67.2	30.2	3.3	26.9	2.6
	36	**N4**	3.9	95.4	0.9	94.5	0.7
	48	**N5**	5.2	84	2.5	81.5	10.8
P7	**6**	**H1**	87.3	11.8	2.5	9.3	0.9
	12	**H2**	83.3	16.2	03	13.2	0.5
	24	**H3**	72.1	26.1	6.8	19.3	1.8
	36	**H4**	5.0	92.3	1.1	91.2	2.7
	48	**H5**	4.1	84.7	1.3	83.4	11.2

Compound

The study was conducted in a time-dependent manner (6, 12, 24, 36, and 48 hr) following treatment with compound **P10** and compound **P7** at their respective IC_{50} doses. A significant increase in apoptosis was observed in both drug-treated cells (Jurkat E6.1 and K562) compared to untreated controls ($p< 0.05$). After treatment with compound **P10**, the percentages of apoptotic events (early and late) at 6, 12, 24, 36, and 48 hr against Jurkat E6.1 cells were 16.9%, 27.1%, 30.2%, 95.4%, and 84%, respectively. Similarly, for compound **P7**, the percentages of apoptotic events (early and late) at 6, 12, 24, 36, and 48 hr against Jurkat E6.1 cells were 11.8%, 16.2%, 26.1%, 92.3%, and 84.7%, respectively. In contrast, untreated control (treatment with solvent only) Jurkat E6.1 cells showed 6.7% apoptotic events at 48 hr (**Table 5.3** and **Figure 5.8**)

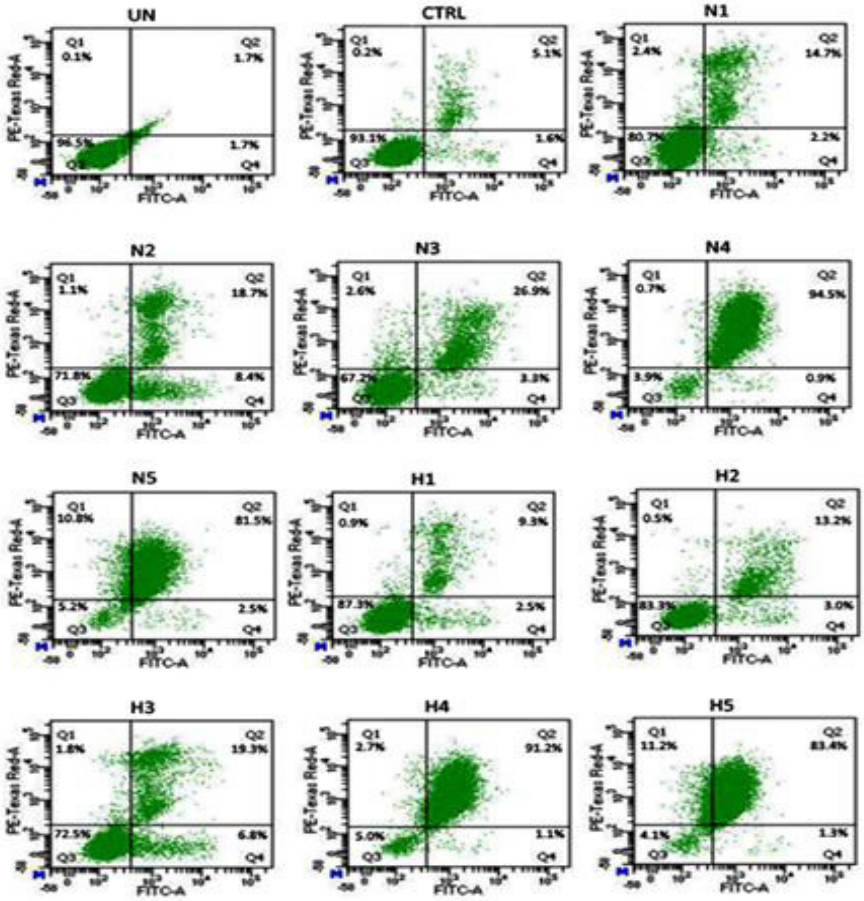

Figure 5.8. The dot plot from the time-dependent flow cytometric study for apoptosis in the Jurkat E6.1 cell line is depicted as: N1, N2, N3, N4, and N5 represent treatment with compound **P10** (40 µM) at 6, 12, 24, 36, and 48 hours, respectively. H1, H2, H3, H4, and H5 represent treatment with compound **P7** (40 µM) at 6, 12, 24, 36, and 48 hr, respectively.

Similarly, results of compound P**10** and compound P**7** against K562 cell line are shown in **Table 5.4** and **Figure 5.9**.

Table 5.4. Time-dependent apoptotic profile of compound **P10** and compound **P7** against K562 cell line

Experiment		**Figure ID**	**%Viable (Q3)**	**%Apoptotic (Q2+Q4)**	**%Early apoptotic (Q4)**	**%Late apoptotic (Q2)**	**%Necrotic (Q1)**
Unstained		**UN**	98.7	0.4	0.1	0.3	0.9
Control		**CTRL**	95.6	0.7	0.0	0.7	3.7
Treatment							
Cpd[#] ID	**Time (hrs)**						
P10	**6**	**N1**	90.0	6.4	0.6	5.8	3.6
	12	**N2**	87.0	8.2	0.7	7.5	4.8
	24	**N3**	73.6	18.2	0.7	17.5	8.2
	36	**N4**	47.9	50.6	16.5	34.1	1.5
	48	**N5**	25.8	37.8	1.4	36.4	36.4
P7	**6**	**H1**	90.1	9.3	3.5	5.8	0.6
	12	**H2**	89.1	7.3	1.0	6.3	3.6
	24	**H3**	88.2	8.2	0.9	7.3	3.6
	36	**H4**	55.7	38.5	9.8	28.7	5.8
	48	**H5**	31.2	31.8	1.5	30.3	37.0

Compound

For the K562 cell line, following drug treatment with compound **P10**, the percentages of apoptotic events (both early and late) at 6, 12, 24, 36, and 48 hours were 6.4%, 8.2%, 18.2%, 50.6%, and 37.8%, respectively. Similarly, with compound **P7** treatment, the percentages of apoptotic events (early and late) at 6, 12, 24, 36, and 48 hr against K562 cells were 9.3%, 7.3%, 8.2%, 38.5%, and 31.8%, respectively. In contrast, untreated control K562 cells (treated with solvent only) showed 6.7% apoptotic events at 48 hr (**Table 5.4** and **Figure 5.9**).

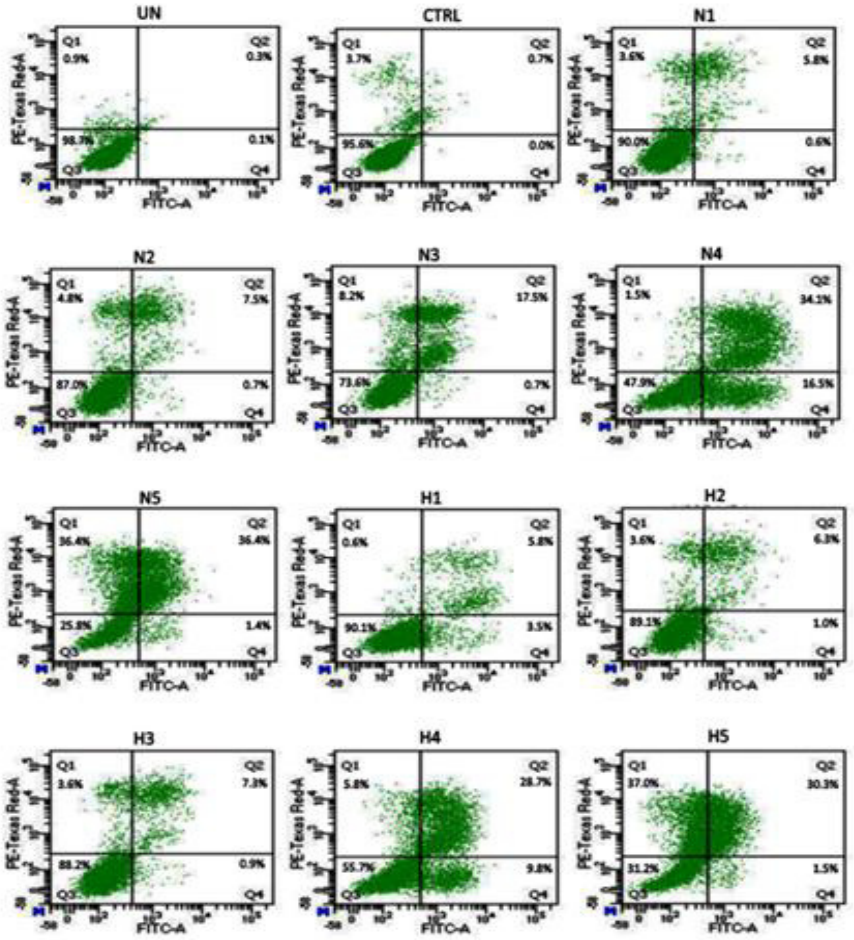

Figure 5.9. The dot plot from the time-dependent flow cytometric study for apoptosis in the K562 cell line is represented as: N1, N2, N3, N4, and N5 represent treatment with compound **P10** (40 µM) at 6, 12, 24, 36, and 48 hr, respectively. H1, H2, H3, H4, and H5 represent treatment with compound **P7** (40 µM) at 6, 12, 24, 36, and 48 hr, respectively.

After 36 hours of treatment with compound **P10** and compound **P7**, Jurkat E6.1 cells exhibited an 88.7% and 85.6% increase in apoptotic events, respectively, compared to untreated controls. Similarly, for the K562 cell line, a 49.9% and 36.8% increment in apoptotic events was observed with compound **P10** and compound **P7** treatment, respectively, in comparison with the untreated control. Up to 36 hours of treatment with compound **P10** and compound **P7**, the percentage of necrotic cell population in Jurkat E6.1 cells ranged from 0.7% to 2.6% and 0.5% to 2.7%, respectively. For the K562 cell line, the percentage of necrotic cell population up to 36 hr of drug treatment with compound **P10** and compound **P7** varied from 1.5% to 8.2% and 0.6% to 5.8%,

respectively. However, the percentages of necrotic cell populations increased to 10.1% and 8.5% for Jurkat E6.1, as well as 31.9% and 34.2% for K562 cells, after 48 hr of drug treatment with compound **P10** and compound **P7**, respectively. These results suggest that a significant number of apoptotic events (both early and late) were induced by both of the most active compounds (**P10** and **P7**), where $p < 0.05$ was considered significant. While compound **P10** and compound **P7** induced more or less similar apoptotic events in the Jurkat E6.1 cell line, compound **P10** exhibited a better apoptotic profile than compound **P7** in the K562 cell line.

From **Figures 5.8** and **5.9**, it is evident that with the gradual increment of drug treatment time, there was a linear increase in apoptotic events observed in both Jurkat E6.1 and K562 cell lines. Although the observed apoptosis was mostly late in nature, there were no notable percentages of necrotic events observed up to 36 hours of drug treatment; however, necrotic events markedly increased at 48 hr. Thus, the results of this experiment may indicate apoptosis-mediated cell cytotoxicity.

5.2.3. Mitochondrial membrane potential detection study

Two hypotheses exist regarding the mitochondrial role in apoptosis. The first proposes the activation of pro-caspase-9 through the release of cytochrome c and other essential proteins, while the second considers whether mitochondria act as facilitators after caspase activation (Leist et al., 2001). This assay focuses on the state of mitochondrial membrane potential ($\Delta\Psi$), where early depolarization of $\Delta\Psi$ is observed during apoptosis in numerous studies. However, it's worth noting that mitochondrial membrane depolarization doesn't always occur during apoptosis and can also happen during necrosis (Lemasters et al., 1998).

In this study, 5,5’,6,6’-tetrachloro-1,1’,3,3’-tetraethylbenzimidazolcarbocyanine iodide (JC-1), a membrane-permeable lipophilic cationic fluorochrome, is utilized to assess the state of $\Delta\Psi$ and discern the specific mechanism of action. When live cells are stained with JC-1, polarized mitochondria rapidly uptake JC-1 monomers, resulting in the formation of JC-1 aggregates that exhibit high red fluorescence in flow cytometry. However, in apoptotic conditions, JC-1 does not accumulate in mitochondria with depolarized $\Delta\Psi$ and remains in the cytoplasm as monomers, leading to a decrease in red fluorescence in flow cytometry (Reers et al., 1995; and Cossarizza et al., 1993).

In this experiment, it was observed that after 24 hr of treatment with compound **P10** (40 µM) and compound **P7** (40 µM), the percentage of cell populations with depolarized ΔΨ increased by 39.2% and 45.0%, respectively, in Jurkat E6.1 cells, and by 35.1% and 21.9%, respectively, in K562 cell lines, compared to the untreated control, as shown in **Figure 5.10**.

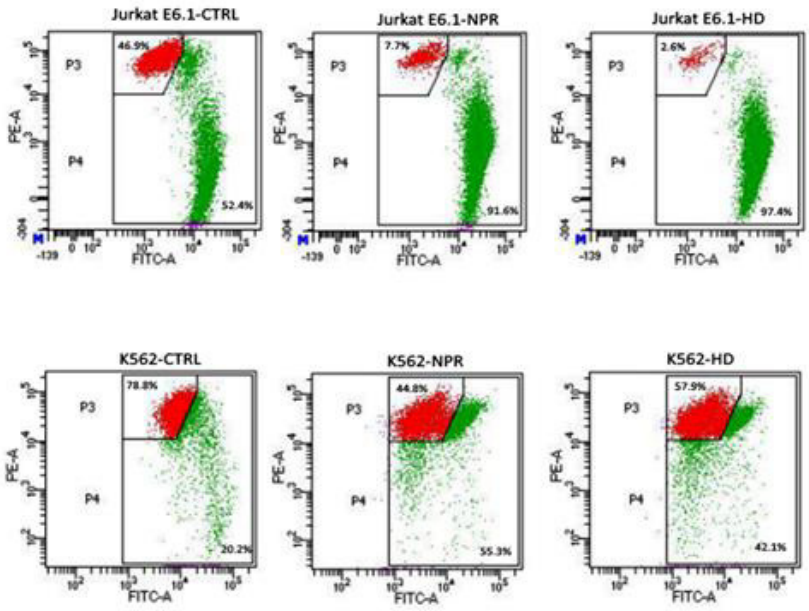

Figure 5.10. Dot plot graph of of Mitochondrial membrane potential detection study after 24 hr treatment with compound P**10** (40 µM) and compound **P7** (40 µM) in Jurkat E6.1 and K562 cell lines.

5.2.4. Matrix metalloproteinase (MMP) inhibition assay

The best antileukemic compounds (**P7** and **P10**) were further subjected to gelatinase (MMP2 and MMP9) inhibitory efficacy as well as another medium size S_1' pocket containing matrix metalloproteinase (MMP12) to judge both the potency and selectivity (**Table 5.5**).

Table 5.5. MMP2 and MMP9 inhibitory activity (IC_{50}) of compound **P10** and **P7**

Compound	MMP2 (µM)	MMP9 (µM)	MMP12 (µM)
P7	5.07	10.06	9.61
P10	3.73	4.14	1.47

Importantly, both of these compounds (**P7** and **P10**) showed gelatinases (MMP2 and MMP9) inhibitory profile in the micromolar range and did not show considerable selectivity over other medium-size S_1' pocket matrix metalloproteinase enzymes like MMP12. Among gelatinases (MMP2 and MMP9) all the better cytotoxic compounds (**P7** and **P10**) against leukemia cell lines showed better MMP2 enzyme inhibitory activity in comparison with MMP9.

5.2.5. Structure-activity relationship (SAR) study

From the data presented in **Table 5.2**, it's evident that all the synthesized compounds (**P4** and **P6-P18**) demonstrate moderate cytotoxicity in leukemia cell lines (K562, Jurkat E6.1, and U937), but remain inactive in the breast cancer cell line (MDA-MB-231). Notably, these compounds exhibit relatively higher activity in the K562 and Jurkat E6.1 cell lines compared to the U937 cell line.

In the case of the chronic myelogenous leukemia cell line (K562), compound **P10** emerges as the most potent cytotoxic compound. Interestingly, compounds containing short-chain aliphatic groups (**P8**, **P9**, and **P10**) in the carboxamide functions exhibit greater cytotoxicity compared to those with long-chain aliphatic groups (**P12** and **P15**). Additionally, compounds with linear aliphatic chains (**P10** and **P12**) show higher cytotoxicity compared to those with branched aliphatic chains (**P11**, **P13**, and **P14**) in the carboxamide function. This observation may be attributed to the potential inhibition of matrix metalloproteinase (MMP) activities by compounds **P8**, **P9**, and **P10**, as documented in prior research indicating that down-regulation of MMP2 and MMP9 activities correlates with apoptosis-mediated cytotoxicity in leukemia cells (Das et al., 2021A).

Structurally, MMP inhibitors typically require an aryl moiety fitting into the S_1' pocket of the MMP catalytic domain, a zinc-binding group, and an alkyl substituent accommodating the S_2' pocket (Adhikari et al., 2017; Rush et al., 2004). While all synthesized compounds (**P4** and **P6-P18**) possess the biphenyl fragment for the S1' pocket and a common carbonyl group (C=O) of the lactam ring as the zinc-binding group, the fragment intended for the S_2' pocket varies. Compounds with smaller P_2' residues (such as **P8**, **P9**, and **P10**) may better fit into the S_2' pocket, leading to enhanced MMP inhibition and higher activity. Notably, the n-propyl group appears to be particularly accommodated in this regard, thereby exhibiting the highest activity.

The presence of a hydroxamic acid function at the 2 position of the 5-oxopyrrolidine ring (**P7**) appears to be advantageous for cytotoxicity towards the chronic myelogenous leukemia cell line (K562) compared to the carboxylic acid function (**P4**), which may account for its superior activity. Previous reports from our research have indicated that the catalytic domain-based MMP2 and MMP9 selectively exhibit anti-proliferative activity against leukemia cell lines (K562 and U937) over solid tumor cell lines (A549 and MDA-MB-231) (Mukherjee et al., 2017; Das et al., 2021A). Compound **P7**, containing the hydroxamic acid function, may demonstrate stronger inhibition of gelatinases (MMP2 and MMP9) compared to compound **P4** with the carboxylic acid function, as the hydroxamic acid function serves as a stronger zinc-binding group than the carboxylic acid function (Das et al., 2021B). Furthermore, regarding cytotoxic activity against the K562 cell line, the presence of a cyclic aliphatic group (**P16**) is relatively more active than that of a long linear aliphatic chain (**P15**) in the carboxamide function, whereas the presence of a benzyl (**P17**) or substituted benzyl (**P18**) group exhibits poor cytotoxicity.

Against the leukemic T-cell lymphoblast (Jurkat E6.1) cell line, the presence of short-chain aliphatic chains (up to 3 carbons) (**Table 5.2**) in the carboxamide functions (compounds **P8**, **P9**, and **P10**) demonstrates greater cytotoxicity compared to bulkier groups (number of carbons > 3) as carboxamide functions (compounds **P12**, **P15**, **P16**, **P17**, and **P18**). Similarly to the K562 cell line, the presence of a linear aliphatic chain (compounds **P10** and **P12**) in carboxamide functions is favorable compared to a branched aliphatic group (compounds **P11**, **P13**, and **P14**). The observed better cytotoxicity of compound **P7** with the hydroxamic acid function at the 2 position of the 5-oxopyrrolidine ring compared to compound **P4** with the carboxylic acid function may be attributed to stronger inhibition of gelatinases, as reported in previous studies (Das et al., 2021A; Das et al., 2021B).

Similarly, regarding the cytotoxic activity towards the Jurkat E6.1 cell line, the presence of the cyclic aliphatic group (**P16**) demonstrates relatively higher activity than the long linear aliphatic group (**P15**) in the carboxamide function, while the presence of the benzyl (**P17**) or substituted benzyl (**P18**) group leads to less active compounds. Compound **P10** also emerges as the most cytotoxic molecule in the Jurkat E6.1 cell line.

Despite demonstrating cytotoxicity against leukemia cells (K562, Jurkat E6.1, and U937), the reported molecules (compounds **P4** and **P6**-**P18**) surprisingly did not exhibit cytotoxicity (**Table**

5.2) with IC_{50} values of 250 µM against the breast cancer cell line (MDA-MB-231). This outcome indicates that the reported compounds (**P4** and **P6-P18**) are selectively cytotoxic against leukemia cell lines (K562, Jurkat E6.1, and U937) compared to the solid tumor cell line (MDA-MB-231). Similar observations were noted in our previous studies with glutamines (Mukherjee et al., 2017) and isoglutamines (Dutta et al., 2019) derivatives.

In general, it can be inferred that the substituted glutamic acid derivatives and their cyclic variants (pyroglutamic acid derivatives) exhibit selective cytotoxicity against leukemia cell lines over solid tumor cell lines. To assess whether the synthesized molecules (compounds **P4** and **P6-P18**) exhibit any toxic effects on normal human healthy cells, human peripheral blood mononuclear cells (PBMCs) were utilized. None of the synthesized molecules (compounds **P4** and **P6-P18**) demonstrated cytotoxicity (**Table 5.2**) below IC_{50} values of 500 µM against PBMCs. The K562 cell selectivity index (IC_{50} PBMC/IC_{50} K562) for compound **P7** and compound **P10** were 10.84±0.34 and 12.63±0.67 respectively, and the Jurkat E6.1 cell selectivity index (IC_{50} PBMC/IC_{50} Jurkat E6.1) for compound **P7** and compound **P10** were 10.19±0.39 and 11.28±0.23 respectively. Based on the selectivity index values of leukemia cells (IC_{50} PBMC/IC_{50} leukemia Cell line), it can be hypothesized that the reported molecules (compounds **P4** and **P6-P18**) are selectively toxic towards leukemia cells compared to normal human peripheral blood mononuclear cells (PBMCs).

5.2.6. Summary of Part-II

In this part of the investigation (**Part-II**), a majority of the synthesized compounds, particularly the carboxamides combined with low molecular weight primary amines (up to 4 carbons), exhibited cytotoxic effects against leukemia cell lines. The most potent compounds, **P10** and **P7**, demonstrated moderate cytotoxicity with IC_{50} values of 44.32±0.9 µM and 49.10±1.9 µM, 39.65±2.1 µM and 46.16±1.7 µM, and 52.83±3.2 µM and 60.57±2.8 µM against Jurkat E6.1, K562, and U937 cell lines, respectively. These effects could be attributed to potential inhibition of matrix metalloproteinase (MMP) activities, as evidenced by previous studies indicating that down-regulation of matrix metalloproteinase 2 (MMP2) and matrix metalloproteinase 9 (MMP9) activities leads to apoptosis-mediated cytotoxicity in leukemia cells (Das et al., 2021A). The presence of a small alkyl substituent attached to the nitrogen atom of the carboxamide function may enable effective accommodation into the small hydrophobic S_2' pocket of gelatinases

compared to bulkier substituents, thereby enhancing the inhibitory effect on gelatinases (Adhikari et al., 2017; Rush et al., 2004). The *n*-propyl function at the R position of compound **P10** appears to be optimally suited for the S_2' pocket of MMP2 and MMP9. Conversely, Compound **P7**, featuring the hydroxamic acid function, acts as a robust zinc binder and likely contributes to stronger inhibition of gelatinases (MMP2 and MMP9) (Das et al., 2021B). Importantly, all synthesized compounds exhibited no activity against the breast cancer MDA-MB-131 cell line and normal human PBMCs. To explore the pathway of cellular death, a time-dependent flow cytometric in-vitro apoptosis investigation was carried out using the most potent compounds, **P10** and **P7**, on Jurkat E6.1 and K562 cell lines. Following a 36-hr treatment with compound **P10** and compound **P7** at their respective IC_{50} doses, Jurkat E6.1 cells showed an increase of 88.7% and 85.6% in apoptotic events, while the K562 cell line exhibited a 49.9% and 36.8% rise in apoptotic events compared to the untreated control, respectively, indicating apoptosis-driven cell demise. Furthermore, mitochondrial membrane potential detection studies provided additional evidence supporting apoptosis-mediated cell death in both the Jurkat E6.1 and K562 cell lines.

Taking into account all these findings, compounds **P10** and **P7** emerge as promising lead candidates for the development of targeted anti-leukemic agents with minimal adverse effects on normal cells. These compounds warrant further investigation for potential structural refinement aimed at enhancing their target specificity.

5.3. QSAR-based molecular modeling studies [Part-III]

Part-**III** deals with the QSAR-based *in-sillico* techniques to refine glutamine-like scaffold for effective and potent inhibitors of both of the gelatinases (MMP2 and MMP9). **Part-III** is being subdivided into two sub-parts; **Part-IIIA** and **Part-IIIB.** Several QSAR-based *in-sillico* techniques were performed in two studies (**Part-IIIA** and **Part-IIIB**) with two different datasets of gelatinases (MMP2 and MMP9) separately. Ultimately, structural information gained from these two studies (**Part-IIIA** and **Part-IIIB**) were compared for designing the glutamine-based compounds to be synthesized in the next step (**Part-IV**).

5.3.1. QSAR-based molecular modeling studies with dataset 1 (Part-IIIA)

Here, a library of various aryl sulfonamide-based gelatinases inhibitors (**dataset 1**) from the researchers at Universita degli Studi, Italy, was gathered (Scozzafava and Supuran 2000A; Scozzafava and Supuran 2000B; and Scozzafava and Supuran 2002). This library is displayed in **Table A1** in the **Appendix** section. The binding affinity values (K_i) of gelatinases are present in the library molecules. The gelatinase binding affinity (K_i) numerical data were presented as their corresponding negative logarithmic values, or *pKi* values (Roy et al., 2015C).

To achieve effective inhibition of matrix metalloproteinase 2 (MMP2) and matrix metalloproteinase 9 (MMP9), extensive focus has been placed on understanding the structure of its catalytic domain. Since the 1990s, numerous inhibitors targeting MMP2 and MMP9 with activities ranging from picomolar (pM) to micromolar (μM) levels have been documented (Laronha and Caldeira et al., 2020; Das et al., 2021A). Among the six sub-sites (S_1-S_3 and S_1'-S_3') within MMP catalytic domains, the hydrophobic S_1' binding pocket holds particular importance for ligand selectivity. Notably, the depth of this pocket varies considerably among different members of the MMP family. In MMP2 inhibitors, the P_1' moiety inserts into the moderately deep S_1' binding pocket architecture of the MMP2 enzyme. To guide future endeavors in designing selective and potent MMP2 inhibitors, we have initiated preliminary work on developing a 2D-QSAR model using aryl sulfonamides as starting points (Verma et al., 2010; Cherkasov et al., 2014; and Pourbasheer et al., 2011). This part (**Part-IIIA**) will be followed by subsequent efforts, incorporating additional datasets (**dataset 2** in **Part-IIIB**) to further enhance the robustness of the design process.

5.3.1.1. Training/test division and Principal component analysis (PCA)

The *Generate Training and Test Data protocol* of the DS program was used to separate the dataset molecules into training and test sets prior to the construction of the 2D-QSAR model (Discovery Studio 3.0). The dataset was divided several times using the random division option of the DS software's Generate Training and Test Data protocols. From each split, comparable statistical parameters were derived. For this study, the best one was taken into account. Furthermore, principal component analysis (PCA), as shown in **Figure 5.11**, was carried out to

determine whether or not the training set was representative of the entire data set. PC1, PC2, and PC3 were found to have explained variance percentages of 69.8, 15.3, and 12.5 correspondingly.

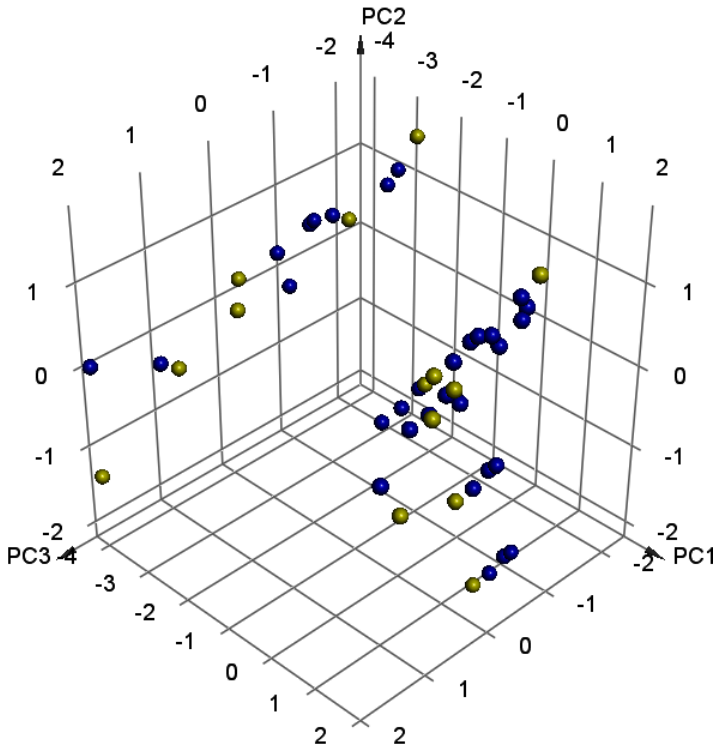

Figure 5.11. Principal component analysis (PCA) of the MMP2 and MMP9 inhibitors (blue: training set; yellow: test set).

5.3.1.2. Stepwise-multiple linear regressions (S-MLR) analysis

The predictive accuracy of a 2D-QSAR model is impacted by both the modeling approach and the selection of descriptors. Descriptors contain information about molecular structures, allowing them to correlate with observed biological activity. However, employing a large pool of descriptors can lead to overfitting. In this investigation, a genetic algorithm (GA)-based approach was utilized to identify relevant descriptors for the 2D-QSAR study. Through multiple runs of GA with varying initial populations, thirty (30) descriptors were ultimately selected. These descriptors were then used to develop linear models using stepwise-multiple linear regression (S-MLR) analysis. The resulting optimal 2D-QSAR models for MMP2 and MMP9 are presented below:

pKi (*MMP2*) = 4.032 (± 0.089) + 3.158 (± 0.090) *nsssN* + 0.051 (± 0.004) *SHBint6* + 0.036 (± 0.006) *SHBint7* + 0.429 (± 0.115) *PubchemFP629* **Eq. 1a**

N_{Train} = 48; *R* = 0.989; R^2= 0.978; R_A^2= 0.976; *SEE* = 0.278; *PRESS* = 3.313; *F* (4, 43) = 486.468; *p* < 0.00; Q^2= 0.972; Average $r_{m(LOO)}^2$= 0.961; $\Delta r_{m(LOO)}^2$ = 0.017;

N_{Test} = 15; R_{Test} = 0.893; $R^2{}_{Test}$ = 0.798; $R^2{}_{Pred}$ = 0.810; Average $r_{m(Test)}^2$= 0.702; $\Delta r_{m(Test)}^2$ = 0.122

and

pKi (*MMP9*) = -7.641 (± 2.108) + 2.997 (± 0.092) *nsssN* + 0.069 (± 0.007) *SHBint10* + 0.080 (± 0.014) *AATS2i* **Eq. 2a**

N_{Train} = 48; *R*= 0.987; R^2= 0.974; R_A^2= 0.972; *SEE* = 0.295; *PRESS* = 3.829; *F* (3, 44) = 540.473; *p* < 0.00; Q^2= 0.969; Average $r_{m(LOO)}^2$= 0.957; $\Delta r_{m(LOO)}^2$ = 0.019;

N_{Test} = 15; R_{Test} = 0.894; $R^2{}_{Test}$ = 0.799; $R^2{}_{Pred}$ = 0.830; Average $r_{m(Test)}^2$= 0.740; $\Delta r_{m(Test)}^2$ = 0.084.

The external predictive performance of these developed models was assessed using the corresponding test sets. Descriptors referred to as (Todeschini et al., 2009) in ***Eq. 1a*** and ***Eq. 2a*** are presented in **Table 5.6**.

Table 5.6. Descriptors in ***Eq. 1a*** and ***Eq. 2a***

Descriptor	Type	Defination
nsssN	Electrotopological state atom type descriptor	Count of atom-type E-State: >N-
SHBint6	Atom type electrotopological state	Sum of E-State descriptors of strength for potential hydrogen bonds of path length 6
SHBint7	Atom type electrotopological state	Sum of E-State descriptors of strength for potential Hydrogen Bonds of path length 7
PubchemFP629	Pubchem fingerprint	S-C:C:C-N
SHBint10	Atom type electrotopological state	Sum of E-State descriptors of strength for potential Hydrogen Bonds of path length 10
AATS2i	Autocorrelation descriptor	Average Broto-Moreau autocorrelation - lag 2 / weighted by first ionization potential

The statistical parameters derived from the S-MLR models indicate a strong correlation coefficient (***Eq. 1a***: R^2 = 0.978; ***Eq. 2a***: R^2 = 0.974) and low standard error of estimation (***Eq. 1a***: *SEE* = 0.278; ***Eq. 2a***: *SEE* = 0.295). The high values of leave-one-out (LOO) cross-validation (Q^2 = 0.972) and average squared correlation coefficient for the LOO method (Avg. $r^2_{m(LOO)}$ = 0.961 for Eq.) for ***Eq. 1a*** suggest that the regression model exhibits excellent internal predictive capability. A similar trend is observed for ***Eq. 2a*** as well (Q2 = 0.969; Avg. $r^2_{m(LOO)}$ = 0.957). Correlation matrices for ***Eq. 1a*** and ***Eq. 2a*** are provided in **Table A2** of the **Appendix** section.

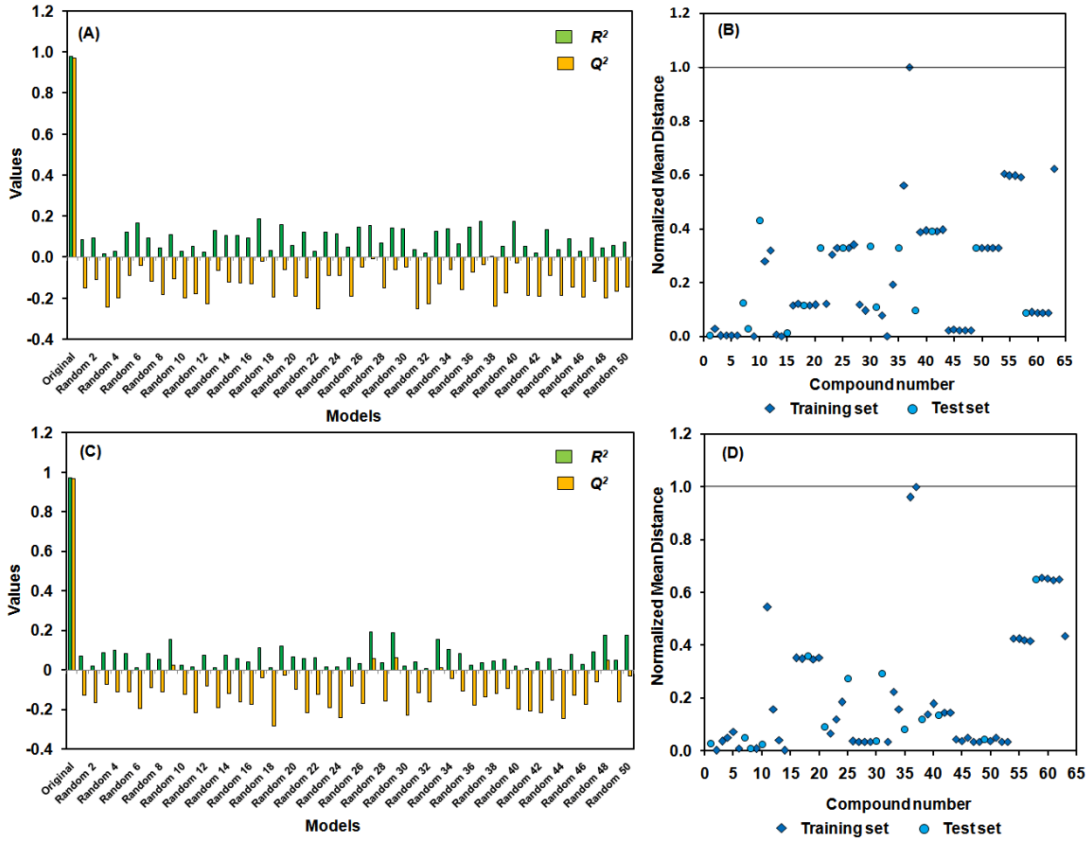

Figure 5.12. (**A**) The R^2 and Q^2 values following multiple Y-randomization tests for MMP2 inhibitors. (**B**) Visualization of the applicability domain of Eq. (6) using the Euclidean distance approach. (**C**) Assessment of R^2 and Q^2 values post various Y-randomization tests for MMP9 inhibitors. (**D**) Depiction of the applicability domain of ***Eq. 2a*** using the Euclidean distance approach.

The Y-randomization test was conducted to assess the reliability of the S-MLR model. The resulting random models (generated through the random shuffling of Y-variables) exhibited R^2

and Q^2 values lower than those of the original models, namely ***Eq. 1a*** and ***Eq. 2a*** (as depicted in **Figures 5.12A** and **5.12C**, respectively). Detailed values are presented in **Table A3** and **Table A4** of the **Appendix** section for MMP2 and MMP9, respectively.

The variation inflation factor (VIF), which serves as a measure of multicollinearity within a set of multiple regression variables, along with the t-value and p-level for each descriptor of ***Eq. 1a*** and ***Eq. 2a***, were computed and are presented in **Table A5** of the **Appendix** section. Correlation coefficient values below 0.50 indicate that the selected descriptors for ***Eq. 1a*** and ***Eq. 2a*** are independent. Additionally, all variables have VIF values below 5, suggesting that the selected descriptors are not highly correlated, and thus, the developed models are deemed acceptable (Pourbasheer et al., 2011; and Pourbasheer et al., 2017). Furthermore, the constructed S-MLR models were utilized to predict the data within the test set.

The results from external validations (***Eq. 1a***: R^2_{Test} = 0.798; R^2_{Pred} = 0.810; Average $r^2_{m(Test)}$= 0.702; ***Eq. 2a***: R^2_{Test} = 0.799; R^2_{Pred} = 0.830; Average $r^2_{m(Test)}$= 0.740) provide encouraging evidence of the highly satisfactory predictive ability of the constructed models, namely ***Eq. 1a*** and ***Eq. 2a***. Importantly, the applicability domains of ***Eq. 1a*** and ***Eq. 2a*** were assessed using Euclidean-based normalized mean distance calculation (as illustrated in **Figure 5.12B-5.12D**). Additionally, both ***Eq. 1a*** and ***Eq. 2a*** meet the Golbraikh and Tropsha model acceptability criteria (Golbraikh and Tropsha 2002B) (refer to **Table 5.7**).

Table 5.7. Golbraikh and Tropsha acceptable model criteria of ***Eq. 1a*** and ***Eq. 2a***

Parameter	Threshold value	*Eq. 6*	*Eq. 7*
Q^2	$Q^2 > 0.5$	0.972	0.969
r^2	$r^2 > 0.6$	0.798	0.799
$\lvert r^2_0 - r^2_{0'} \rvert$	$\lvert r^2_0 - r^2_{0'} \rvert < 0.3$	0.013	0.007
k	$0.85 < k < 1.15$	1.042	1.028
k'	$0.85 < k' < 1.15$	0.946	0.959
$(r^2 - r^2_0) / r^2$	$(r^2 - r^2_0) / r^2 < 0.1$	0.022	0.009
$(r^2 - r^{2'}_0) / r^2$	$(r^2 - r^{2'}_0) / r^2 < 0.1$	0.007	0.017

Where (i) Q^2 is the cross-validated correlation coefficient
(ii) The parameter r^2 is the squared correlation coefficient between the observed *vs* predicted response values of the test set compounds,
(iii) while r^2_0 and $r^2_{0'}$ represent the corresponding values for regression through origin (observed vs. predicted and predicted vs. observed, respectively),
(iv) the slope of the regression lines through the origin are assigned by k and k'.

Figure 5.13A illustrates the observed versus predicted biological activity plots for the constructed MLR model for MMP2, while **Figure 5.13B** depicts the same for MMP9. The observed activity of training and test set compounds (Y_{obs}), along with the calculated/predicted activity of compounds (Y_{pred}), absolute residual, residual squared (residual^2) values from both of these MLR models, and LOO predicted values are presented in the **Appendix** section (**Tables A6-A9**). From **Figure 5.13**, it is evident that compound **A38**, with an observed activity (Obs) of 7.046, was notably predicted as a lower active compound (Pred: 4.452) by ***Eq. 1a*** (**Table A7** in the **Appendix** section). Upon removing compound **A38** from the dataset, the R^2_{Test} value increased to 0.951, representing a significant improvement over the previous value of 0.797. This trend was similarly observed in ***Eq. 2a***, as detailed in **Table A9** in the **Appendix** section. The descriptors introduced by this S-MLR model offer insights into chemical features that contribute to MMP2 and MMP9 binding affinities.

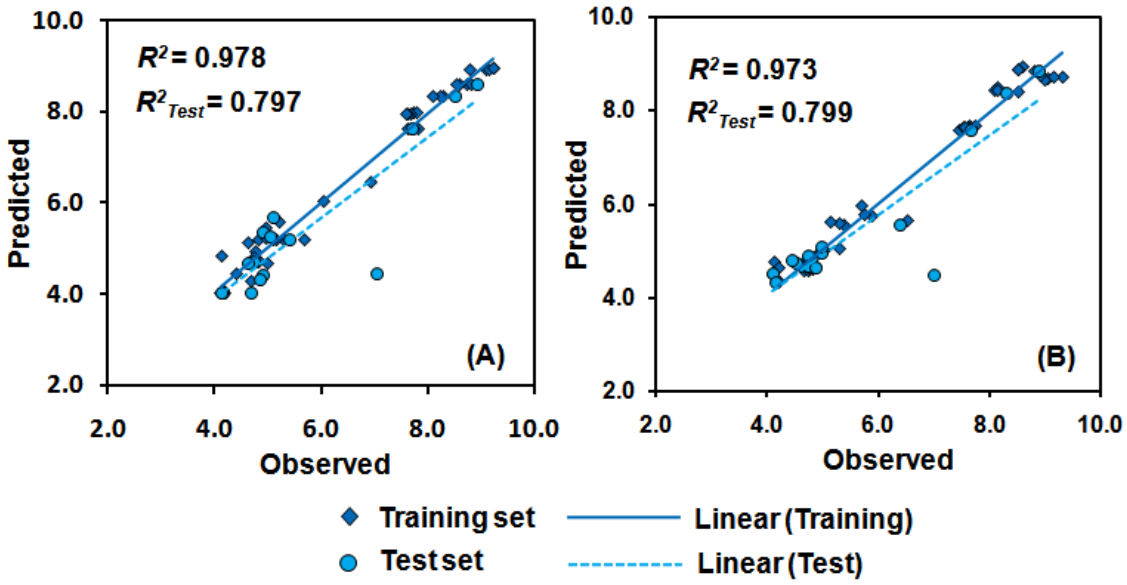

Figure 5.13. The observed *vs* predicted activity of the training and test sets from (**A**) ***Eq. 1a*** and ***Eq. 2a*** for MMP2 and MMP9 respectively.

Moreover, the optimal ***Eq. 1a*** and ***Eq. 2a*** were employed to develop nonlinear QSAR models. A comparative analysis of the predictive capabilities of multiple linear regression (MLR), artificial neural network (ANN), and support vector machine (SVM) models is provided in **Table 5.8**.

Table 5.8. Summary of the predictive performances of MLR, ANN and SVM models

		MLR			ANN			SVM		
		Train	**CV**	**Test**	**Train**	**CV**	**Test**	**Train**	**CV**	**Test**
MMP2	***r***	0.989	0.987	0.893	0.993	0.991	0.908	0.989	0.986	0.891
	MAE	0.207	0.229	0.445	0.157	0.205	0.358	0.201	0.238	0.432
MMP9	***r***	0.987	0.984	0.984	0.986	0.982	0.899	0.985	0.983	0.891
	MAE	0.217	0.241	0.362	0.239	0.261	0.380	0.211	0.248	0.399

r, correlation coefficient; *MAE*, Mean absolute error; *CV*, 10-fold cross validation.

The predictive performance of the artificial neural network (ANN) models appears to be quite satisfactory (For MMP2: r_{Train} = 0.993, MAE_{Train} = 0.157, r_{CV} = 0.991, MAE_{CV} = 0.205; For MMP9: r_{Train} = 0.986, MAE_{Train} = 0.239, r_{CV} = 0.982, MAE_{CV} = 0.261). The RBF kernel-based support vector machine (SVM) models demonstrate notable performance, as evidenced by the results presented in **Table 5.9** (For MMP2: r_{Train} = 0.989, MAE_{Train} = 0.201, r_{CV} = 0.986, MAE_{CV} = 0.238; For MMP9: r_{Train} = 0.985, MAE_{Train} = 0.211, r_{CV} = 0.983, MAE_{CV} = 0.248).

5.3.1.3. 3D-QSAR Topomer CoMFA study

The classical 2D-QSAR method has notable limitations, including (a) challenges in visualizing results due to the absence of proper three-dimensional graphical outputs and (b) insufficient information regarding drug-receptor interactions. Consequently, the introduction of three-dimensional QSAR (3D-QSAR) aimed to address these shortcomings (Verma et al., 2010). Comparative Molecular Field Analysis (CoMFA), a pioneering 3D-QSAR method, was developed by Cramer et al. in 1988 (Cramer et al., 1988). In the CoMFA approach, the bioactive 3D conformations of molecules in the training set are aligned using manual or automated techniques. Subsequently, these aligned molecules are positioned within a lattice grid, and the steric and electrostatic fields of overlapping molecules are computed in three dimensions by placing different probe groups at all intersections of the lattice. A 3D-QSAR model is then constructed using the partial least squares (PLS) technique (Verma et al., 2010). The field values (steric and electrostatic fields) of aligned molecules are regarded as predictor variables (X values) and correlated with biological activities (Y values) (Verma et al., 2010).

A modified version of CoMFA, known as Comparative Molecular Similarity Indices Analysis (CoMSIA), was introduced as an extension of the 3D-QSAR methodology, incorporating ligand

hydrogen bonding and hydrophobic effects alongside steric and electrostatic field variations (Cherkasov et al., 2014). Schrödinger software offers PHASE for the development of 3D-QSAR models (Dixon et al., 2006). Various types and methodologies of 3D-QSAR models have been extensively discussed by Verma and colleagues (Verma et al., 2010). Among these models,

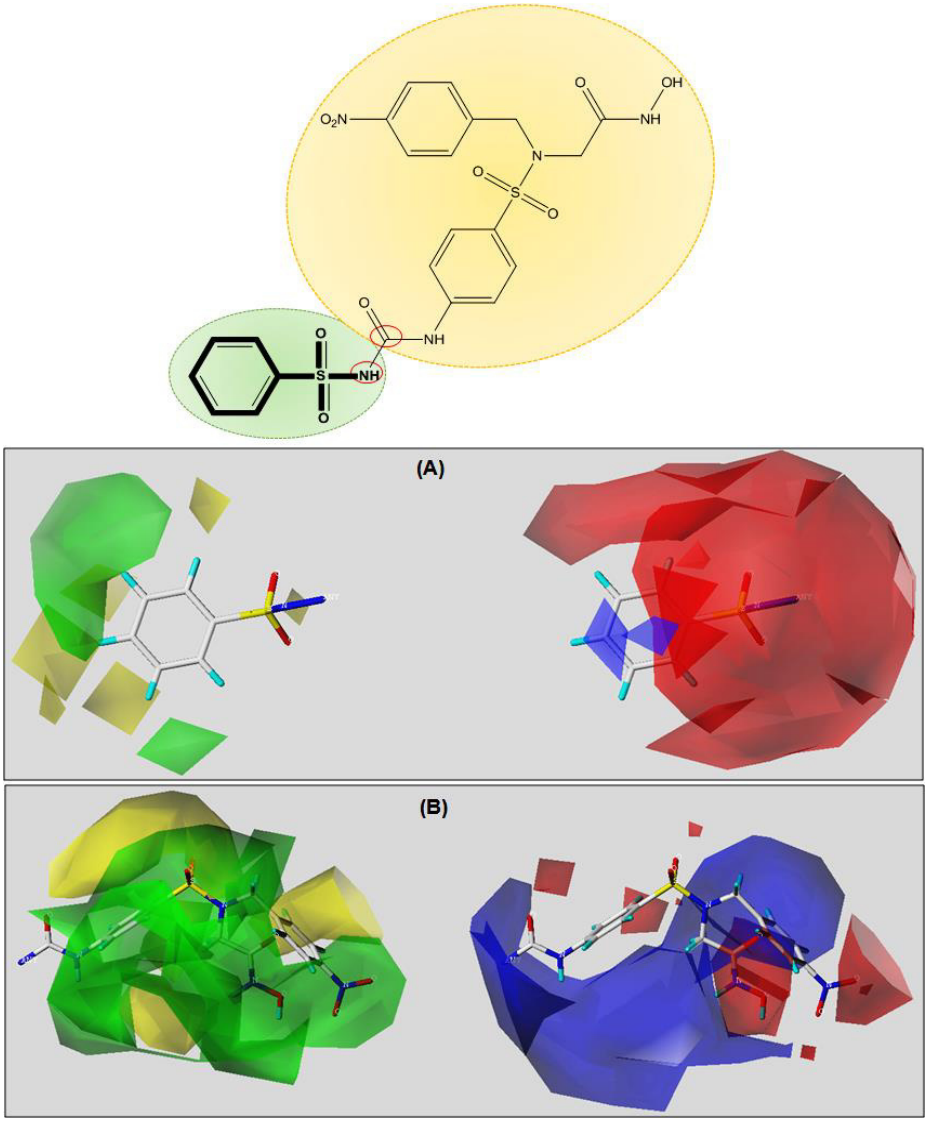

Figure 5.14. Topomer CoMFA model-1 (for MMP2 dataset) contour map in transparent mesh for the best active compound A**54** (A for R1 and B for R2) (green, steric favorable; yellow, steric unfavorable; blue, electropositive favorable; red, electropositive unfavorable).

CoMFA remains the most cited and widely used method (Ragno 2019). However, despite its widespread adoption, CoMFA has limitations. Aligning ligand conformations of each molecule

with absolute orientation in CoMFA is a tedious and time-consuming process (Cramer 2003). To address this limitation, topomer CoMFA was introduced in 2003. It is an alignment-free 3D-QSAR method developed by integrating topomer technology with the CoMFA approach for rapid lead optimization (Cramer 2003). Reports indicate that the topomer protocol consistently demonstrates promising predictive performance in discovery projects (Tong et al., 2020; Tong et al., 2021; Chhatbar et al., 2019; Niu et al., 2018).

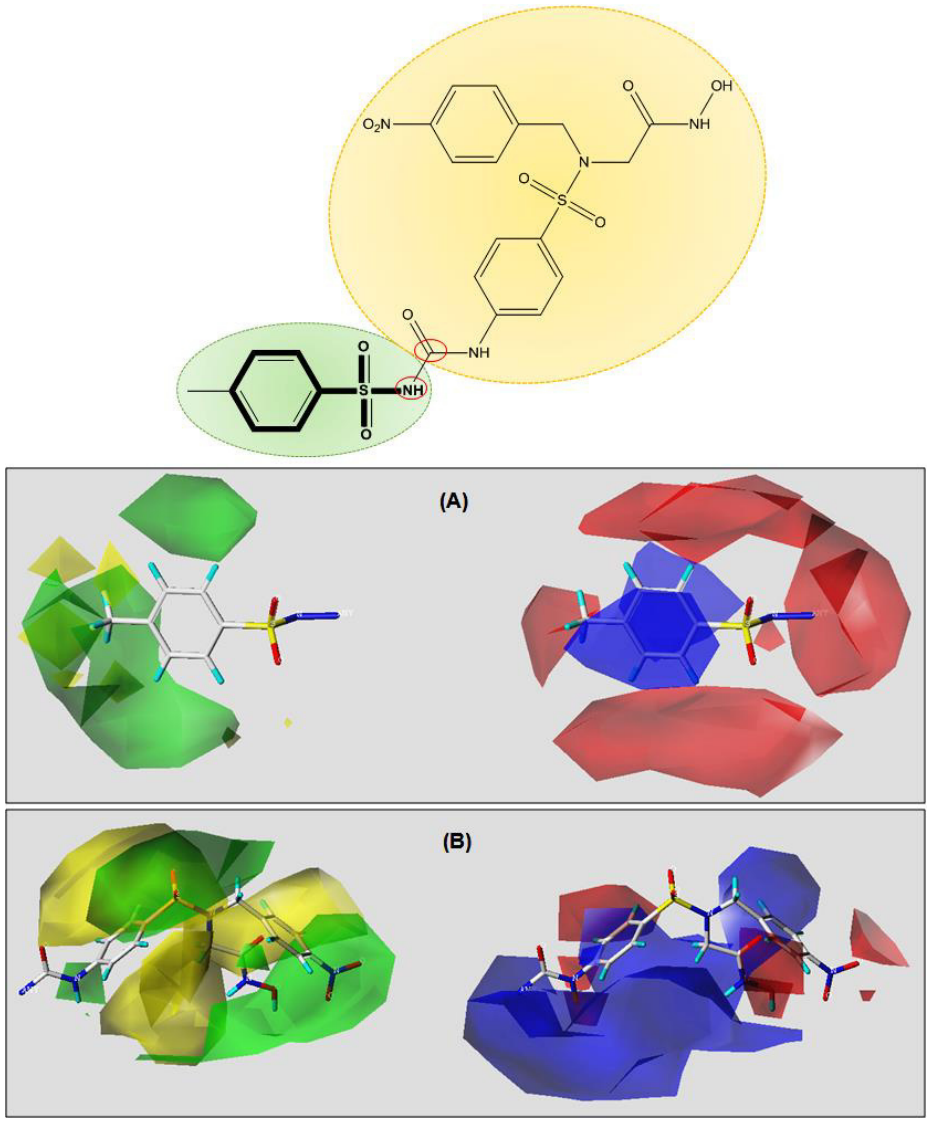

Figure 5.15. Topomer CoMFA model-2 (for MMP9 dataset) contour map in transparent mesh for the best active compound **A56** (A for R1 and B for R2) (green, steric favorable; yellow, steric unfavorable; blue, electropositive favorable; red, electropositive unfavorable).

In this study, the topomer CoMFA model was developed on the training set compounds by dividing them into R1 (arylsulphonamide moiety) and R2 fragments (the remaining features) (as depicted in **Figure 5.14** and **Figure 5.15**). For the topomer CoMFA analysis of the MMP2 dataset, compound **A54** was selected as the reference molecule, while compound **A56** was chosen as the reference molecule for the MMP9 dataset. Topomer CoMFA models for gelatinases (MMP2 and MMP9) were constructed using partial least squares (PLS) regression analysis. The statistical significance of these topomer CoMFA models was evaluated based on the leave-one-out cross-validation correlation coefficient (Q^2), the square of the correlation coefficient (R^2), and the correlation coefficient of the test set (R^2_{Test}). The cross-validated Q^2 and R^2 values for topomer CoMFA model-1 (MMP2 dataset) were determined to be 0.958 and 0.983, respectively. For topomer CoMFA model-2 (MMP9 dataset), the Q^2 value and non-cross-validated R^2 value were found to be 0.931 and 0.963, respectively. Overall, the R^2, Q^2, and R^2_{Test} values exceeding 0.6, 0.5, and 0.5, respectively, confirm the excellent predictive ability (Adhikari et al., 2018B) of these topomer CoMFA models-1 and -2. The observed activity of the training and test set compounds (Y_{obs}) and the calculated/predicted activity of compounds (Y_{pred}) from the topomer CoMFA models are provided in the **Appendix** section (**Tables A10-A11**).

Figure 5.14 and **Figure 5.15** present the steric and electrostatic contour maps derived from topomer CoMFA model-1 for MMP2 and topomer CoMFA model-2 for MMP9, respectively. In these figures, the green contours represent regions where the presence of bulkier groups would enhance biological activity, while the yellow contours indicate regions where such bulkier groups would diminish biological activities. In the topomer CoMFA electrostatic contour maps (**Figure 5.14** and **Figure 5.15**), red contours depict regions where electron-rich groups contribute to an increase in biological activity, while blue contours indicate areas where the presence of positive charge (or decreased negative charge) groups would enhance biological activity. The topomer CoMFA steric contour map reveals green contours near the benzene sulphonyl moiety, suggesting that steric features in this area may augment both MMP2 and MMP9 inhibitory activities. This observation aligns with the findings for compounds with bulky substitutions, which exhibit promising MMP2 and MMP9 inhibitory properties. These insights are corroborated by the topomer CoMFA contour plots in **Figures 5.14** and **5.15**, which indicate green regions at the R2 fragment where bulky substitutions would be advantageous for improving both MMP2 and MMP9 inhibitory activities.

5.3.1.4. Bayesian classification study

Table 5.9. Statistical parameters of the best Bayesian models for MMP2 (model-1) and MMP9 (model-2)

Model	Set	ROC	TP	FN	FP	TN	Sensitivity	Specificity	Concordance
1	**Training#**	0.990	22	02	00	24	0.917	1.000	0.958
	Test	0.977	03	01	00	11	0.750	1.000	0.933
2	**Training#**	0.962	22	01	00	25	0.957	1.000	0.979
	Test	0.880	03	02	00	10	0.600	1.000	0.867

Where, TP=True positive; FN=False negative; FP=False positive; TN=True negative; #a 5-fold cross validation is performed for the training set to calculate the statistics.

A Naïve Bayes classifier model-1 was developed for MMP2 inhibitors using a training set consisting of 48 molecules divided into two subsets: active (24 compounds) and inactive (24 compounds). The classification matrix yielded significant results for the training set, with 91.7% of correct predictions for the actives (i.e., 22 out of 24 compounds) correctly classified in the active set (**Table 5.9**), while all inactives were accurately classified in the inactive group (100%). Additionally, the external (test) set predictivity of model-1 was evaluated. This test set comprised 15 compounds that were not part of the training set. A Naïve Bayes classifier model-2 was constructed for MMP9 inhibitors using a training set consisting of 48 molecules divided into two subsets: active (23 compounds) and inactive (25 compounds). Of these 48 compounds, 22 out of 23 MMP9 inhibitors were correctly classified (resulting in 95.7% sensitivity), while all 25 inactive compounds were accurately classified (100% specificity). To further assess the performance of the constructed classification models, ROC plots were utilized, as depicted in **Figure 5.16**.

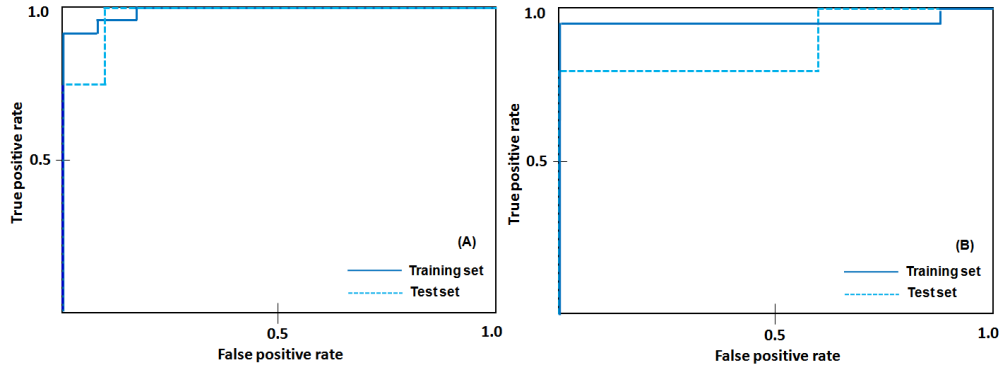

Figure 5.16. ROC plots obtained from the Bayesian model training (fivefold CV) and test sets for (A) MMP2 inhibitors and (B) MMP9 inhibitors.

Fingerprints were employed to capture molecular features relevant to molecular activity, as illustrated in Figures **5.17A** and **5.17B**.

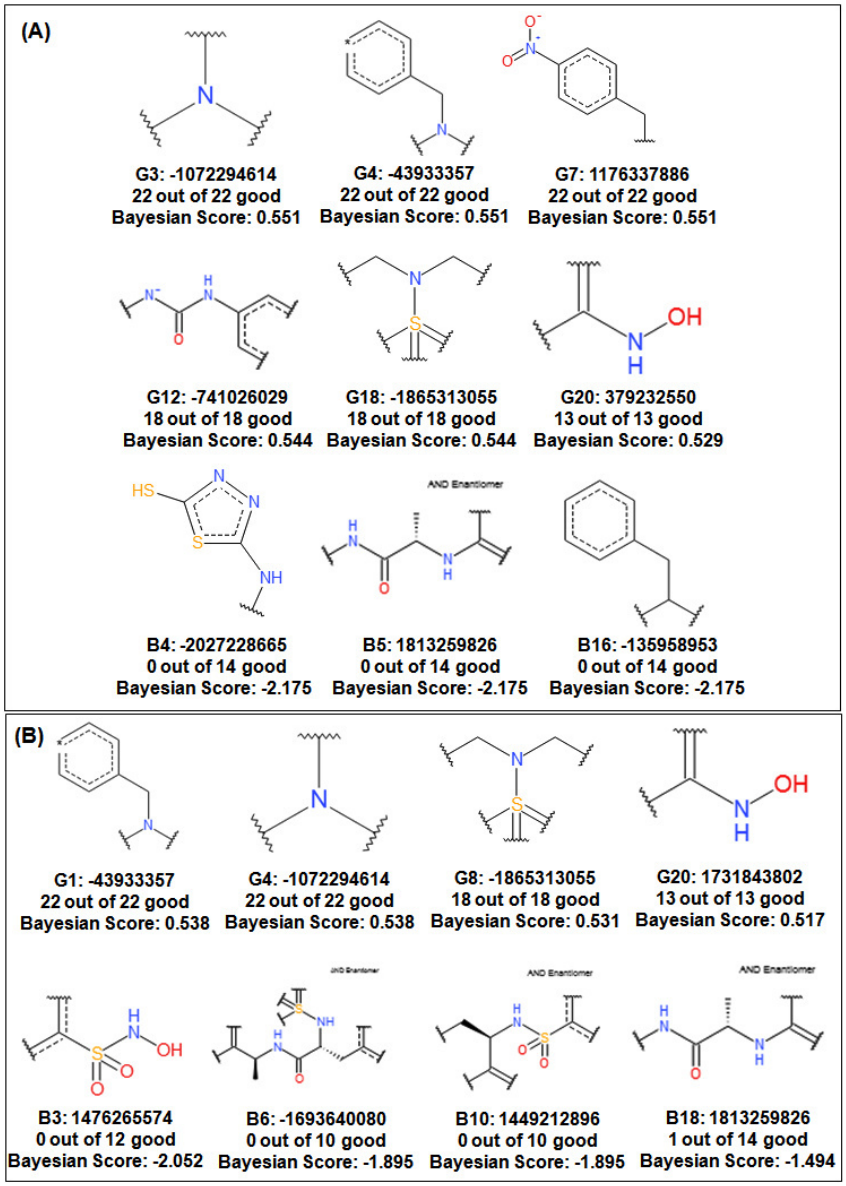

Figure 5.17**.** Molecular fragments (**G**: good, **B**: bad) crucial for (**A**) MMP2 and (**B**) MMP9 inhibition were generated using the *ECFP_6* fingerprint descriptor. Each panel displays the naming convention for each fragment, the number of molecules it is present in that are actives, and the Bayesian score for the fragment. Dashed lines indicate conjugated double bonds, while an asterisk represents a site that can be replaced by different atoms.

5.3.1.5. Mechanistic interpretation of 2D-QSAR and 3D-QSAR models along with identified fingerprint features of Bayesian model

MMP2 and MMP9 exhibit an intermediate binding pocket enveloped by a flexible Ω-loop (Laronha and Caldeira et al. in 2020). The presence of a bulky hydrophobic P_1' fragment interacts with the S_1' pockets of gelatinases, providing selectivity over the shallow (MMP1, MMP7, MMP11, and MMP20) and deep (MMP3, MMP10, and MMP13) pockets among MMP family members (Gimeno et al. in 2020). Additionally, the P_1' group is effectively directed towards the S_1' pocket by the sulfonamide function linked with the aryl group (P_1') (Gimeno et al. in 2020). The dataset (compounds **A1-A62**) can be categorized into three classes: i) Phe-Ala peptidomimetic derivatives (compounds **A1-A20**), ii) substituted aryl N-hydroxy sulfonamides (compounds **A21-A38**), and iii) N-4-nitrobenzylglycine derivatives (compounds **A39-A62**).

5.3.1.5.1. Phe-Ala peptidomimetic derivatives

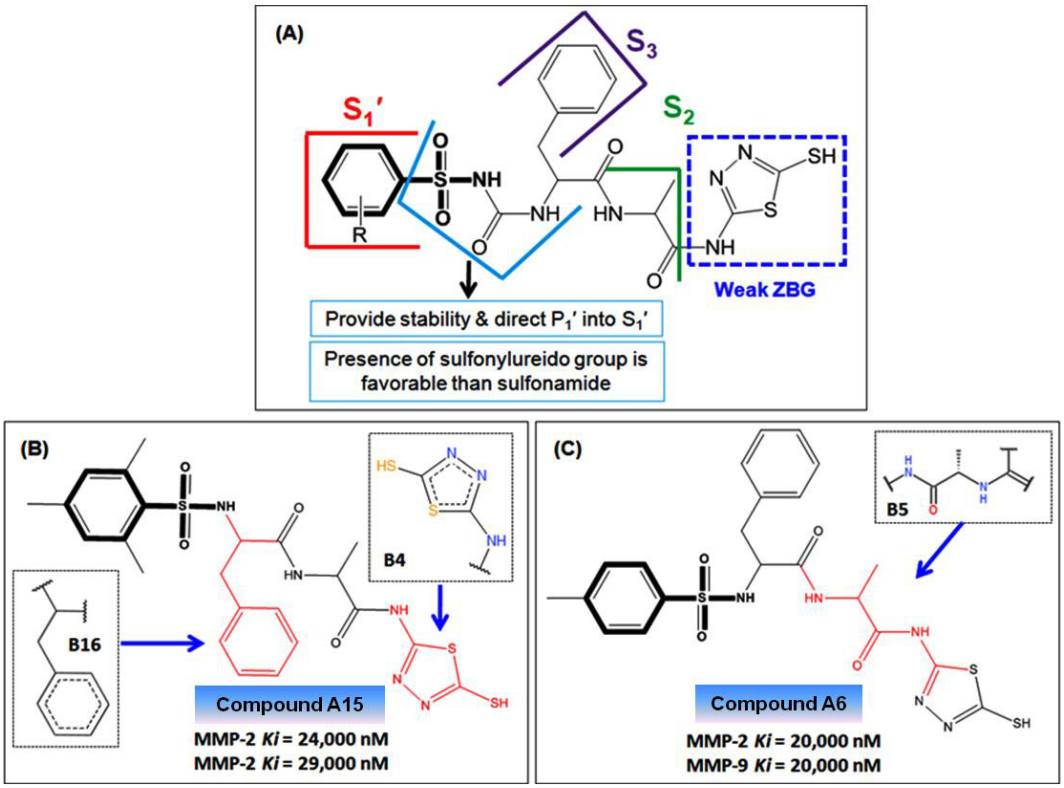

Figure 5.18. (**A**) Comparative SARs of Phe-Ala peptidomimetic derivatives; (**B**) Structures of compound **A15** having bad B4 and B16 fingerprints; (**C**) Structures of compound **A6** having bad B5 fingerprint.

Compounds **A1-A20** are classified as Phe-Ala peptidomimetic derivatives. Within this category, the substituted aryl function (P_1') is likely to fit into the S_1' sub-site. The stability of these compounds is ensured by either the sulfonamide group (compounds **A1-A15**) or the sulfonylurea group (compounds **A16-A20**), both of which form hydrogen bonds with adjacent amino acid residues. Additionally, a 5-mercapto-1,3,4-thiadiazole group serves as the zinc-binding group for the catalytic domains of MMP2 and MMP9 (**Figure 5.18A**).

The presence of the zinc-binding group (ZBG) (5-mercapto-1,3,4-thiadiazole) results in a >3.8 fold increase in MMP2 enzyme affinity compared to a non-ZBG inhibitor (compound **A21**). However, the outcomes are not entirely promising. This discrepancy can be elucidated by the fingerprint feature B4, which suggests the negative influence of 5-mercapto-1,3,4-thiadiazole on poor MMP2 enzyme affinity (**Figure 5.18B**).

Furthermore, substitutions of the phenyl ring primarily exhibit a similar pattern across sulfonamides (compounds **A1-A15**) and N-hydroxy sulfonamides (compounds **A21-A38**), except compounds **A11** and **A12**. In the case of compound **A11**, perfluoro-substitution unexpectedly resulted in lower activity (MMP2 $\boldsymbol{K_i}$ = 6,000 nM) compared to compound **A36** (MMP2 $\boldsymbol{K_i}$ = 900 nM). Similarly, in the case of compound **A12**, trifluoromethyl-substitution of the phenyl ring led to decreased activity (MMP2 $\boldsymbol{K_i}$ = 11,000 nM) compared to compound **A37** (MMP2 $\boldsymbol{K_i}$ = 120 nM). Molecules containing the sulfonylurea function (compounds **A16-A20**) exhibited increased inhibitor activity (compounds **A16-A19**) by more than 3-fold compared to sulfonamides (compounds **A1-A5**).

The analysis findings are consistent with those obtained from the topomer CoMFA models. Additionally, the inclusion of the benzyl group (highlighted by Bayesian bad fingerprint B16, as depicted in **Figure 5.18B**) in Phe-Ala peptidomimetic derivatives (compounds **A1-A20**) may be oriented towards the well-defined deeper left-hand side S_3 pocket of MMPs, while the methyl amide carbonyl function is directed towards the relatively hydrophilic S_2 pocket of MMPs, particularly MMP1 (**Figure 5.18C**).

A similar trend in structure-activity relationship to that observed for MMP2 is also evident in MMP9 inhibitors (compounds **A1-A20**), which are Phe-Ala peptidomimetic derivatives. Within this group, the substituted aryl function (P_1') fits well into the S_1' sub-site. The sulfonamide

group (compounds **A1-A15**) or the sulfonylurea group (compounds **A16-A20**) provides stability through hydrogen bonding with adjacent amino acid residues of the enzyme, while the 5-mercapto-1,3,4-thiadiazole group serves as the zinc-binding group (ZBG). The presence of the ZBG (5-mercapto-1,3,4-thiadiazole) also enhances MMP9 enzyme affinity (as seen in compound **A1**) compared to a non-ZBG inhibitor (compound A21). In the case of compound **A11**, 2,3,4,5,6-pentafluoro-substitution resulted in lower activity (MMP9 K_i = 2,000 nM) compared to compound **A36** (MMP9 K_i = 1,300 nM). Similarly, in the case of compound **A12**, trifluoromethyl-substitution in the phenyl ring led to decreased activity (MMP9 K_i = 5,000 M) compared to compound **A37** (MMP9 K_i = 1,700 nM). Notably, compounds **A11** and **A12** exhibit better MMP9 affinity than MMP2. Compounds containing the sulfonylurea function (compound **A16**) show increased inhibitory activity compared to sulfonamides (compound **A1**). Substitutions in the para-position with halogens (compounds **A17-A18**) are particularly advantageous for MMP9 compared to MMP2.

5.3.1.5.2. Substituted aryl *N*-hydroxy sulfonamides (R-Ph-SO_2-NHOH)

The compounds from **A21** to **A38** share a common structure, R-Ph-SO_2-NHOH, which consists of the P_1' fragment (R-Ph-group) likely fitting into the S_1' pocket. Additionally, the SO_2-NH-group provides stability and directs the hydrophobic aryl group (P_1') towards the S_1' pocket of MMP2. However, due to the absence of the zinc-binding group (ZBG), substituted aryl N-hydroxy sulfonamides (compounds **A21-A35**) generally exhibit lower MMP2 inhibitory activity, with the exception of compounds **A36-A38** (**Figure 5.19A**).

The 2D-QSAR descriptor SHBint6 sheds light on the diminished activities of compounds **A21-A35**. These molecules demonstrate reduced capability to form hydrogen bond interactions with the catalytic amino acid residues of MMP2, as evidenced by comparatively lower SHBint6 values, except for compound **A36**. Furthermore, unsubstituted aryl N-hydroxy sulfonamides show poor inhibition of gelatinase, which can be further elucidated by the MMP9 bad fingerprints B3 (**Figure 5.19B**).

Among the substituted aryl N-hydroxy sulfonamides (R-Ph-SO_2-NHOH), compound **A38** stands out as the most potent, displaying MMP2 inhibitory activity in the nanomolar range (MMP2 K_i = 90 nM), thanks to the presence of a carboxylate function in the ortho-position of the phenyl ring.

Moreover, the ortho-carboxylate function near the -SO_2-NHOH group might facilitate interaction with the catalytic Zinc ion, leading to a more than 700-fold increase in binding affinity compared to the unsubstituted (compound **A21**) and over 400-fold increase compared to the ortho-NO_2 substituent (compound **A29**). Para-substitutions by halogens (compounds **A22-A25**) and a methyl group (compound **A26**) are unfavorable, while para-substitution by acetamido (compound **A31**), amino (compound **A32**), methoxy (compound **A34**), and nitro (compound **A27**) groups are favorable.

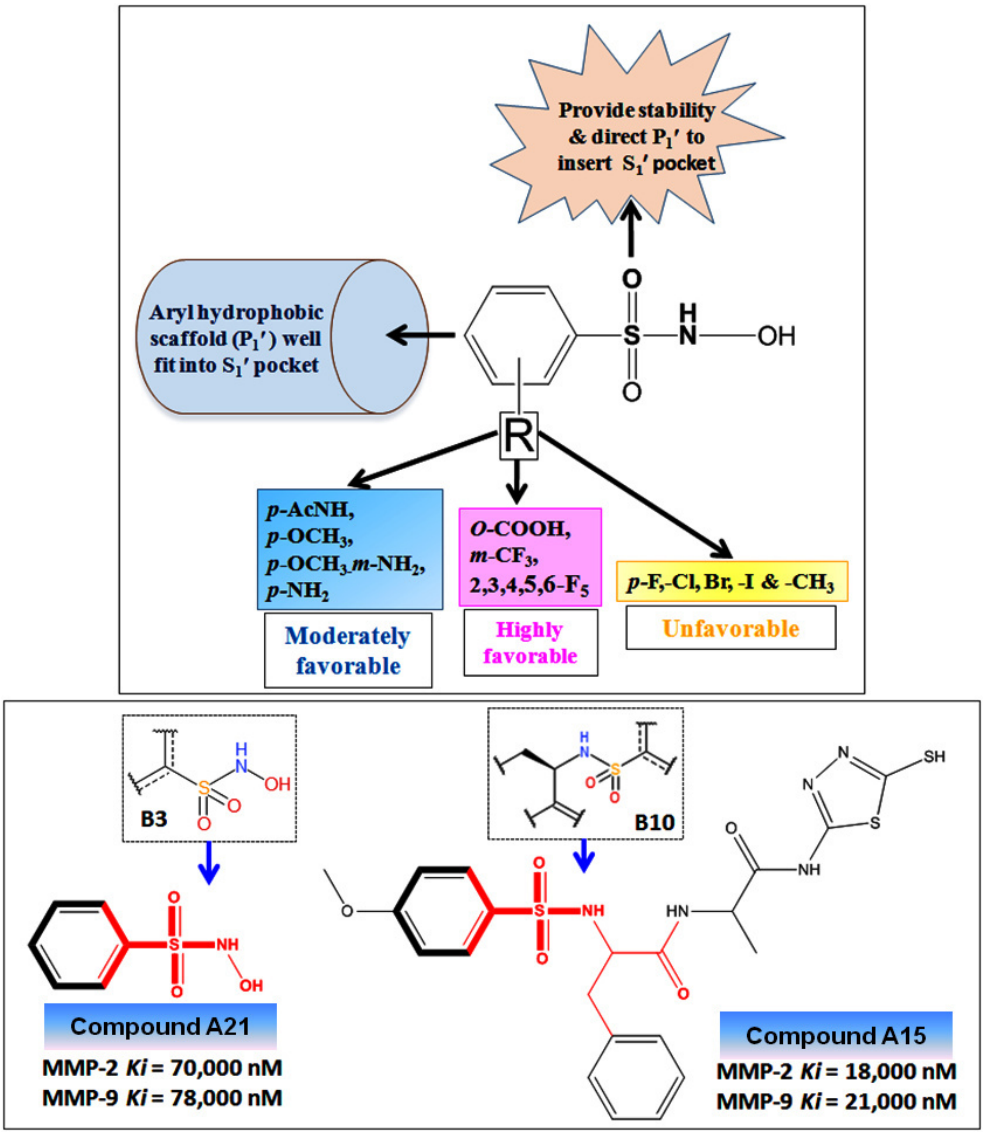

Figure 5.19. (**A**) Comparative SARs of substituted aryl *N*-hydroxy sulfonamides; (**B**) Structure of compounds **A21** and **A14** having MMP9 bad fingerprints bad B3 and B10 respectively.

Substituting the nitro group at the meta-position of the phenyl ring (compound **A28**) proves beneficial. However, introducing a trifluoromethyl-group at the meta-position (compound **A37**) significantly raises the K_i value (120 nM) of MMP2. Generally, para-substitution with halogens (compounds **A22-A25**) doesn't notably enhance MMP2 K_i values. Nonetheless, incorporating a 2,3,4,5,6-pentafluoro-substitution in the aromatic ring of R-Ph-SO_2-NHOH derivatives (compound **A36**) substantially boosts the MMP2 v value (900 nM). Similarly, for MMP9, employing a 2,3,4,5,6-pentafluoro-substitution (compound **A36**) notably heightens enzyme inhibition (v = 1,300 nM) compared to para-substitution with halogens (compounds **A22-A25**). These findings align with the indications of the topomer CoMFA model-2, as depicted by the green contours.

5.3.1.5.3. *N*-4-nitrobenzylglycine derivatives

Compounds **A39** to **A62** are derivatives of N-4-nitrobenzylglycine. Within this group, the structural features shared include substituted (R) aryl sulfonylureido (compounds **A39-A43**), as well as an elongated aryl sulfonyl fragment where two aryl sulfonyl groups are connected with m- (compounds **A49-A53, A58-A62**) and p- (compounds **A44-A48, A54-A57**) protected ureido function, aimed at anchoring P_1'. Additionally, they incorporate a carboxylate/hydroxamate group designed for moderate/strong zinc-binding group functionality, along with a common N-4-nitrobenzyl moiety serving as P_2' (**Figure 5.20A**).

The results from molecular modeling unequivocally highlight the significance of the N-4-nitrobenzyl moiety for both MMP2 and MMP9 inhibitions (**Figure 5.20B**). Concerning Phe-Ala peptidomimetic derivatives (compounds **A1-A20**), Scozzafava et al. suggested that while the benzyl moiety adjacent to the peptide nitrogen atom serves as P_2 anchoring, the 4-nitrobenzyl moiety substituting the amino hydrogen of glycine is already optimized as P_2'. Among the three groups studied, N-substituted aryl sulfonylurea or N-substituted aryl sulfonamido-N-4-nitrobenzylglycinyl carboxylates (compounds **A44-A53**) and hydroxamates (compounds **A39-A43, A54-A62**) demonstrate significantly better activity, with carboxylates (compounds **A44-A53**) exhibiting double-digit nanomolar K_i values. Remarkably, hydroxamates (compounds **A39-A43, A54-A62**) display single-digit nanomolar K_i values. This observation aligns with the Bayesian good fingerprint G20, which suggests the positive influence of the hydroxamate moiety on both gelatinases.

Moreover, Bayesian good fingerprint G3 (**Figure 5.17A**) underscores the importance of the tertiary nitrogen atom for MMP2 inhibitors (**Figure 5.20C**). This finding also correlates well with the SAR study of MMP9 inhibitors (G4 fingerprint as indicated in **Figure 5.17B**). Compounds **A39 to A62**, containing a tertiary nitrogen atom in their structure, exhibit significant MMP2 and MMP9 binding affinities.

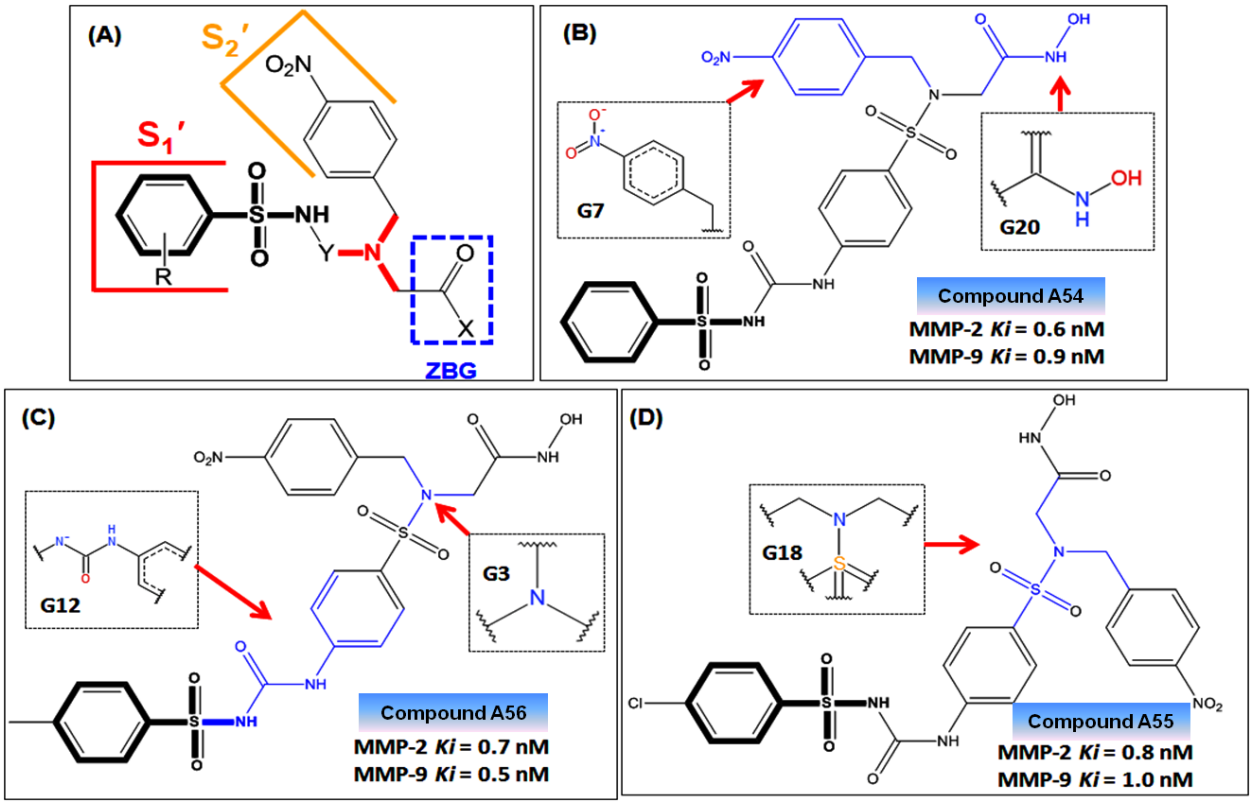

Figure 5.20. (**A**) Comparative SARs of *N*-4-nitrobenzlyglycine derivatives; (**B**) Structures of compound **A54** having G7 and G20 fingerprints; (**C**) Structures of compound **A56** having G3 and G12 fingerprints; (**D**) Structures of compound **A55** having G18 fingerprint.

The tertiary nitrogen atom establishes a three-point attachment with (a) the aryl sulfonyl or aryl sulfonylurea S_1' anchoring function, (b) the N-4-nitrobenzyl S_2' anchoring function, and (c) the zinc-binding group (ZBG). This observation finds support in compound A55, which exhibits a favorable G18 fingerprint (**Figure 5.20D**).

Concerning aryl substitutions in the phenyl ring, *para*-fluoro or *para*-chloro substitutions (compounds **A40-A41, A45-A46, A50-A51, A59-A60**) prove more advantageous than *ortho*- or

meta-methyl substitutions (compounds **A42-A43, A47-A48, A52-A53, A61-A62**). Additionally, an elongated aryl sulfonyl fragment containing a hydroxamate function, where two aryl sulfonyl groups are linked with *meta*- and *para*-protected ureido groups (compounds **A54-A62**), exhibits greater activity than aryl sulfonylurea hydroxamates (compounds **A39-A43**). These findings align with the topomer CoMFA contour plots in **Figures 5.14** and **5.15**, which reveal green regions at the R2 fragment, indicating that bulky substitution would be beneficial for improving both MMP2 and MMP9 inhibitory activities.

Fingerprint G12 (for MMP2 and MMP9 inhibitors) clearly indicates that *meta*- and *para*-protected ureido functions (compounds **A44-A63**) are favorable for activity, a feature also observed in most active gelatinase inhibitors (**Figure 5.20C**). Among the elongated aryl sulfonyl fragments where two aryl sulfonyl groups are linked with *meta*- and *para*-protected ureido functions, *para*-protected ureido compounds (**A44-A48, A54-A57**) demonstrate higher activity as gelatinase inhibitors compared to their *meta*-protected analogs (**A49-A53, A58-A62**).

5.3.1.6. Summary of Part-IIIA

In this study, we utilize regression-based 2D-QSARs (S-MLR, SVM, and ANN), topomer CoMFA, and Bayesian classification models to enhance the structural features aimed at improving gelatinase inhibitory activities (in case of MMP2 inhibitors ***Eq. 1a***: R^2= 0.978; Q^2= 0.972; R^2_{Test} = 0.798; R^2_{Pred} = 0.810; and for MMP9 inhibitors ***Eq. 2a***: R^2= 0.974; Q^2= 0.969; R^2_{Test} = 0.799; R^2_{Pred} = 0.830). The descriptors nsssN, SHBint6, SHBint7, and PubchemFP629 exhibit direct correlations with MMP2 binding affinities. Likewise, nsssN, SHBint10, and AATS2i are directly related to MMP9 binding affinities. Significantly, the robust correlations observed between experimental and predicted biological values for both training and test set compounds confirm the reliability of the developed topomer CoMFA models. Similarly, existing Naïve Bayes predictive models show promising results in terms of sensitivity, specificity, positive predictive value, and negative predictive value. Additionally, significant molecular characteristics linked to the binding affinities of MMP2 and MMP9, as well as certain active and inactive fragments, have been discovered. Taking into account all of these QSAR models, it can be inferred that:

(1) The aryl hydrophobic structure aligns effectively within the S_1' pocket, as illustrated in **Figure 5.21**. This deduction originates from investigations utilizing both 2D-QSAR and Naïve Bayes approaches.

(2) Having two aryl sulfonyl groups connected with a ureido function is more advantageous than having a single aryl sulfonyl group at P_1' (**Figure 5.21**). This observation is corroborated by topomer CoMFA models.

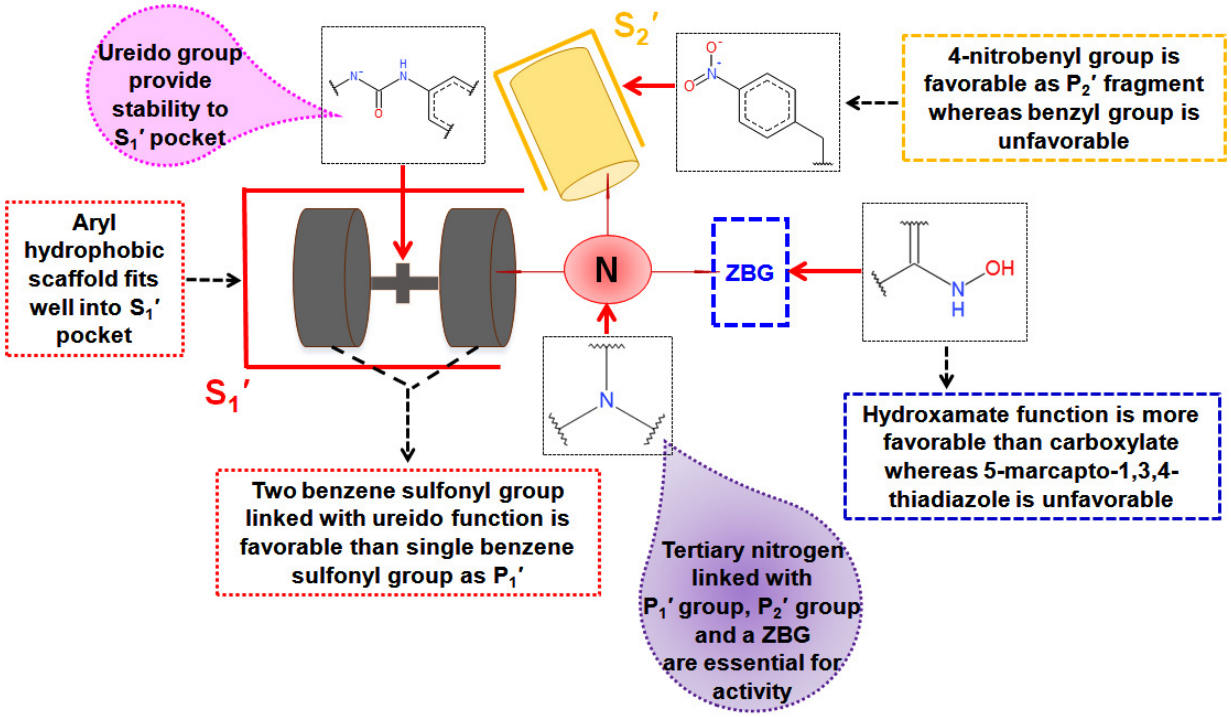

Figure 5.21. The structural prerequisites for more desirable inhibitors targeting both MMP2 and MMP9.

(3) The presence of the ureido group contributes to the stability of the S_1' pocket, which is a crucial aspect in modulating gelatinases' binding affinity (**Figure 5.21**). This aspect is elucidated through 2D-QSAR and 3D-QSAR models.

(4) A tertiary nitrogen atom linked with the P_1' group, P_2' group, and a ZBG plays a pivotal role in gelatinases' binding affinities. This linkage's significance is underscored by evidence from 2D-QSAR, 3D-QSAR, and Naïve Bayes studies.

(5) The 4-nitrobenzyl group is advantageous as a P_2' fragment, while the benzyl group is unfavorable, as indicated by topomer CoMFA analysis.

(6) The beneficial effect of the hydroxamate moiety on both of these gelatinases is evident from these modeling studies (**Figure 5.21**).

Therefore, these initial findings could serve as valuable insights for the future development of more refined strategies for lead optimization of gelatinases inhibitors based on aryl sulfonamides. Conversely, it can be asserted that the predictive models constructed here, along with additional research efforts, will be utilized for evaluating gelatinases inhibitors effectively.

5.3.2. QSAR-based molecular modeling studies with dataset 2 (Part-IIIB)

In Part-IIIA, the critical structural prerequisites for designing inhibitors based on aryl sulfonamides targeting both MMP2 and MMP9 enzymes were outlined, with aryl sulfonyl groups being identified as common structural components occupying the S_1' sub-sites of gelatinases. In this Part-IIIB study, an analysis was conducted on a dataset comprising 110 inhibitors of gelatinases reported by Rossello and his research team between 2006 and 2018 (Santos et al., 2006; Biasone et al., 2007; Nuti et al., 2007; Marques et al., 2008; Rubino et al., 2009; Nuti et al., 2009A; Nuti et al., 2009B; Nuti et al., 2010; Nuti et al., 2011; Nuti et al., 2015; and Nuti et al., 2018). In this part (Part-IIIB) various aryl functionalities and ZBGs with diversity were selected to conduct rigorous linear and non-linear regression-based 2D-QSAR analyses, along with classification-based 2D-QSAR studies. The aim of this study to identify crucial structural prerequisites for developing improved inhibitors for both MMP2 and MMP9. The dataset utilized in this part (**Part-IIIB**) of the QSAR-based molecular modeling study is larger and was reported later (2006-2018) compared to the dataset used in our previous part **(Part-IIIA**) of the QSAR-based molecular modeling study.

5.3.2.1. Linear 2D-QSAR study

Initially, the genetic algorithm (GA) technique was employed to select pertinent descriptors. Following several runs of GA with various initial population sets, 19 important descriptors were chosen for MMP2 inhibitors. These 19 descriptors were then utilized in the "best subset selection" method. Numerous models were created using the multiple linear regression (MLR) technique with a combination of 8 descriptors ($^{19}C_8$). Among these models, only a few were

retained after excluding those with an R^2 value below 0.70 (**Figure 5.22A**). Ultimately, the optimal 2D-QSAR model for MMP2 is as follows:

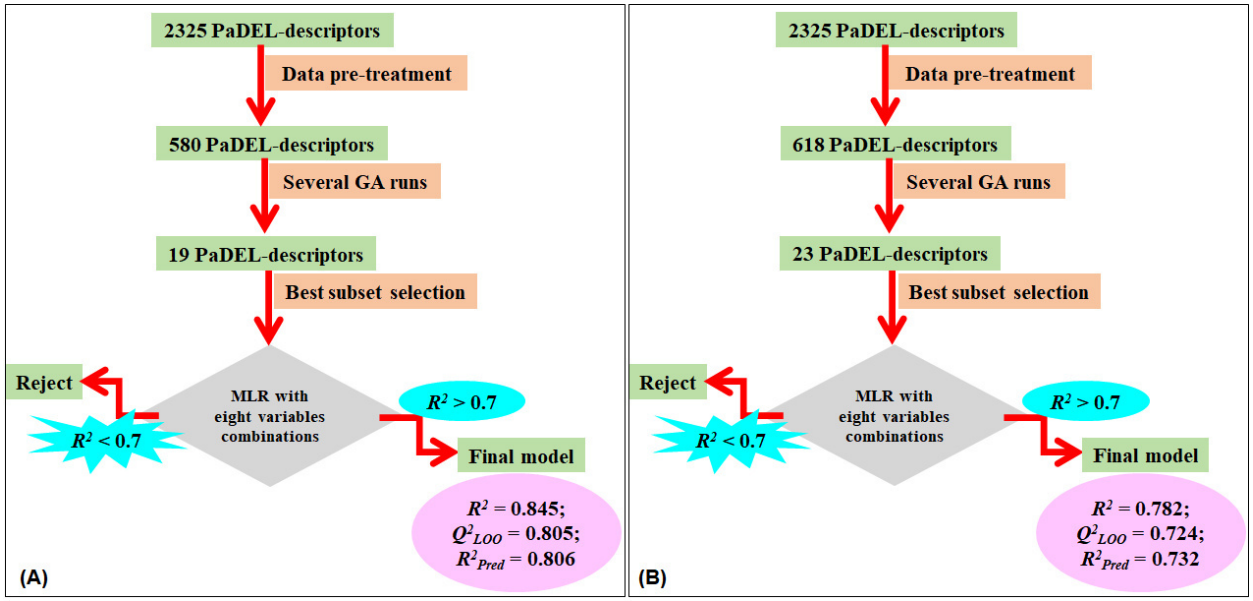

Figure 5.22. Schematic representations of the steps involved in the development of 2D-QSAR study for (A) MMP2 inhibitors and (B) MMP9 inhibitors.

MMP2 $_{p}IC_{50}$ = -11.093 (± 1.58013) + 0.348 (± 0.042) *minsOH* + 1.784 (± 0.220) *PubchemFP643* + 0.262 (± 0.034) *R_TpiPCTPC* + 2.474 (± 0.334) *PubchemFP33* + 1.068 (± 0.211) *PubchemFP338* + 0.205 (± 0.065) *nHBAcc_Lipinski* + 4.490 (± 0.836) *GATS8i* + 2.883 (± 0.842) *GATS3m* ***Eq. 1b***

Likewise, for MMP9 inhibitors, multiple runs of the genetic algorithm (GA) resulted in the identification of 23 significant descriptors. These descriptors were then subjected to the "best subset selection" method. Similarly, several models were developed using the multiple linear regression (MLR) approach with a combination of 8 descriptors ($^{23}C_8$). After filtering out models with an R^2 value below 0.70 (**Figure 5.22B**), only a select few models were retained. Ultimately, the optimal 2D-QSAR model for MMP9 is as follows:

MMP9 $_{p}IC_{50}$ = 11.151 (± 4.070) + 0.001 (± 0.001) *ATS5s* - 45.346 (± 22.225) *VE2_Dze* + 3.286 (± 0.363) *PubchemFP33* + 0.282 (± 0.049) *minsOH* + 1.907 (±0.265) *PubchemFP643* + 0.001 (± 0.000) *ATSC7m* - 2.463 (± 0.837) *SpMax1_Bhs* + 1.593 (±0.395) *PubchemFP21* ***Eq. 2b***

Various descriptors (**Table 5.10**) namely *minsOH, PubchemFP643, R_TpiPCTPC*, *PubchemFP33, PubchemFP338*, *nHBAcc_Lipinski*, *GATS8i* and *GATS3m* were found to be important for ***Eq. 1b***. On the other hand, *ATS5s*, *VE2_Dze*, *PubchemFP33*, *minsOH*, *PubchemFP643, ATSC7m*, *SpMax1_Bhs*, *PubchemFP21* were used to develop the ***Eq. 2b***.

Eq. 1b accounts for 82.9% of the variances in MMP2 inhibitory activity and predicts 80.5% of these variances. ***Eq. 2b***, on the other hand, explains 76.1% of the variances in MMP9 inhibitory activity and predicts 72.4% of these variances. Various internal and external validation parameters of the model are provided in **Table 5.11**.

Table 5.10. Contributions of descriptors of ***Eq. 1b*** and ***Eq. 2b***

Descriptor	Defination	Influence
minsOH[a,b]	Minimum atom-type E-State: -OH	Positive
PubchemFP643[a]	[#1]-C-C-N-[#1]	Positive
R_TpiPCTPC[a]	Ratio of total conventional bond order (up to order 10) with total path count (up to order 10)	Positive
PubchemFP33[a]	Hierarchic Element Counts, 1 S	Positive
PubchemFP338[a]	C(~C)(~C)(~H)(~N)	Positive
nHBAcc_Lipinski[a]	Number of hydrogen bond acceptors (using Lipinski's definition: any nitrogen; any oxygen)	Positive
GATS8i[a]	Geary autocorrelation - lag 8 / weighted by first ionization potential	Positive
GATS3m[a]	Geary autocorrelation - lag 3 / weighted by mass	Positive
ATS5s[b]	Broto-Moreau autocorrelation - lag 5 / weighted by I-state	Positive
VE2_Dze[b]	Average coefficient sum of the last eigenvector from Barysz matrix / weighted by Sanderson electronegativities	Negative
PubchemFP33[b]	Hierarchic Element Counts, 1 S	Positive
PubchemFP643[b]	[#1]-C-C-N-[#1]	Positive
ATSC7m[b]	Centered Broto-Moreau autocorrelation - lag 7 / weighted by mass	Positive
SpMax1_Bhs[b]	Largest absolute eigenvalue of Burden modified matrix - n 1 / weighted by relative I-state	Negative
PubchemFP21[b]	Hierarchic Element Counts, 8 O	Positive

[a]used for MMP2; [b]used for MMP9

Table 5.11. Summary of the predictive performance of MLR (***Eq. 1b*** and ***Eq. 2b*****)** for MMP2 and MMP9 respectively.

Parameter	***Eq. 1b***	***Eq. 2b***
n_{Train} **and** n_{Test}	n_{Train} = 88; n_{Test} = 22	n_{Train} = 88; n_{Test} = 22
r	0.919	0.884
R^2	0.845	0.782
R^2_A	0.829	0.761
Q^2	0.805	0.724
Average $r^2_{m(LOO)}$	0.729	0.627
R^2_{Test}	0.852	0.720
R^2_{Pred}	0.806	0.732
Q^2_{F1}	0.806	0.732
Q^2_{F2}	0.767	0.700
Average $r^2_{m(Test)}$	0.789	0.616

The correlation matrices of descriptors for ***Eq. 1b*** and ***Eq. 2b*** are provided in Table B2 and B3, respectively, in the Appendix section. The correlation coefficient values of each pair of descriptors, as observed in these tables, are below 0.55, indicating independence among the selected descriptors (Pourbasheer et al., 2019). Additionally, the p-statistics and VIF values for ***Eq. 1b*** and ***Eq. 2b*** are presented in Table B4 in the Appendix section. With VIF values below 3, it is evident that the developed models exhibit significant statistical significance (Pourbasheer et al., 2019). Furthermore, the MLR models generated (***Eq. 1b*** and ***Eq. 2b***) have satisfactorily met the criteria based on MAE for both the training and test sets. Collectively, these models are deemed acceptable for subsequent screening and predictive applications in the future.

5.3.2.1. Interpretation of the descriptors

The positive coefficients associated with the descriptors *minsOH*, a *R_TpiPCTPC*, *nHBAcc_Lipinski* and *PubchemFP33* suggest that higher values of these descriptors may contribute to MMP2 inhibition. The *minsOH* descriptor represents the Minimum atom-type E-State for -OH groups. Compounds containing N-acylmethanesulfonamide (compounds **B43** and **B46**), N-acyl(trifluoromethane)sulfonamido (compounds **B47** and **B48**), and methylsulfonylethanone (compound **B49**) groups exhibit a *minsOH* value of 0. Therefore, a lower value of minimum atom-type E-State for -OH groups is crucial for MMP2 inhibitory activities. Conversely, compounds with ZBGs such as N-acylmethanesulfonamide (compounds **B43** and **B46**), N-acyl(trifluoromethane)sulfonamide (compounds **B47** and **B48**), and methylsulfonylethanone (compound **B49**) demonstrate inferior MMP2 inhibitory activities.

The decreasing trend observed in the *R_TpiPCTPC* descriptor, which represents the ratio of total conventional bond order (up to order 10) to total path count (up to order 10), indicates that lower values of this ratio may be detrimental to achieving higher MMP2 inhibition. Compounds **B55, B76, B74, B80, B75, B71 and B100**, which display *R_TpiPCTPC* values below 3, demonstrate poor MMP2 inhibitory activities. This suggests that a higher ratio of total conventional bond order to total path count contributes to elevated *R_TpiPCTPC* values, thereby indicating a greater potential for MMP2 inhibition.

The presence of hierarchic element S, as indicated by the *PubchemFP33* descriptor, influences the MMP2 inhibitory activities of compounds. Those compounds with a *PubchemFP33* value of 0, such as **B74, B71, B98, B99, B79, B77, B78, B76, B80, B75** and **B100**, demonstrate poor MMP2 inhibitory properties. Thus, the presence of hierarchic element S is deemed important for MMP2 inhibition. Moreover, compounds **B2, B3, B8, B52, B54, B56, B57** and **B107-B110**, which exhibit *nHBAcc_Lipinski* values exceeding 10, are considered excellent MMP2 inhibitors with pIC_{50} values ranging from 7.597 to 9.886. This suggests that the number of hydrogen bond acceptors plays a significant role in MMP2 inhibitory activity. Furthermore, the descriptors *GATS8i* (Geary autocorrelation - lag 8 weighted by first ionization potential) and *GATS3m* (Geary autocorrelation - lag 3 weighted by mass) positively contribute to MMP2 inhibitory activities. Notably, compounds **B75** and **B76**, which have the lowest values of the *GATS3m* descriptor (0.911), exhibit poor MMP2 inhibitory activities. In the case of MMP9 inhibitors, the positive coefficients associated with descriptors *ATS5s*, *VE2_Dze*, *PubchemFP33*, *minsOH*, *PubchemFP643*, *ATSC7m*, and *PubchemFP21* suggest that higher values of these parameters may enhance MMP9 inhibition. *ATS5s*, defined as the Broto-Moreau autocorrelation - lag 5 weighted by I-state, is positively correlated with MMP9 inhibition. Notably, compounds **B104-B106** and **B110**, which contain an isopropyl moiety in their structure, exhibit higher values of *ATS5s* and demonstrate promising MMP9 inhibitory activity. Structure-based contour studies confirm that the isopropyl moiety, located adjacent to the hydroxamate, penetrates deep into the S1 pocket and may shield the adjacent amide bond. On the other hand, *VE2_Dze*, representing the average coefficient sum of the last eigenvector from the Barysz matrix weighted by Sanderson electronegativities, and *SpMax1_Bhs*, denoting the largest absolute eigenvalue of the Burden modified matrix - n 1 weighted by relative I-state, are negatively correlated with MMP9 inhibitory activities. This implies that lower values of *VE2_Dze* and *SpMax1_Bhs* may lead to increased MMP9 inhibitory activities. For instance, compound **B49** exhibits the lowest *VE2_Dze*

value (0.00006) and displays poor MMP9 inhibitory activity. Similarly, thioaryl-based compounds **B37-B39** and **B44**, which possess comparatively low *SpMax1_Bhs* values, exhibit inferior MMP9 inhibitory activities. Furthermore, the positive contribution of *PubchemFP21* suggests the importance of eight oxygen atoms for promising MMP9 inhibitory activity. Only compounds **B54, B107, B109** and **B110**, which contain eight oxygen atoms in their structures, are deemed excellent MMP9 inhibitors. Hence, the number of oxygen atoms is crucial for MMP9 receptor binding.

5.3.2.2. Non-linear QSAR study

Two types of non-linear QSAR models were created using artificial neural network (ANN) and support vector machine (SVM) methods, utilizing the same dataset of MLR ***Eq. 1b*** and ***Eq. 2b***.

Table 5.12. Performance of the best selected liner and non-liner models for MMP2 dataset (MLR-1, ANN-1 and SVM-1) and MMP9 dataset (MLR-2, ANN-2 and SVM-2).

		***Eq. 1b* (MLR)#**			***Eq. 2b* (MLR)#**	
Parameter	**Train Set**	**Cross-validation**	**Test Set**	**Train Set**	**Cross-validation**	**Test Set**
r	0.919	0.895	0.923	0.884	0.847	0.849
RMS	0.495	0.561	0.619	0.541	0.616	0.719
		ANN-1			**ANN-2**	
Parameter	**Train Set**	**Cross-validation**	**Test Set**	**Train Set**	**Cross-validation**	**Test Set**
r	0.953	0.788	0.732	0.897	0.800	0.790
RMS	0.582	0.783	1.023	0.583	0.788	0.824
		SVM-1			**SVM-2**	
Parameter	**Train Set**	**Cross-validation**	**Test Set**	**Train Set**	**Cross-validation**	**Test Set**
r	0.917	0.889	0.924	0.872	0.851	0.859
RMS	0.483	0.582	0.586	0.523	0.593	0.743

r: Correlation coefficient; *RMS*: root mean square error; #for comparison

For the ANN models, initial parameter optimization involved an empirical trial-and-error search (Pourbasheer et al., 2014 and Pourbasheer et al., 2019). The ANN models were developed with the following parameters: the number of hidden nodes set to 2, learning rate at 0.3, learning momentum at 0.2, and training time of 500 iterations. Similarly, the SVM models were optimized with the following parameters: complexity parameter C set to 1.0, exponent E set to 1.0, epsilon parameter at 0.001, and tolerance T at 0.001. The results obtained from the ANN method yielded promising predictive models (as shown in **Table 5.12**) for predicting the MMP2 (ANN-1) and MMP9 (ANN-2) inhibitory activities, evident from the correlation coefficients of r_{tr} = 0.953 (ANN-1); r_{tr} = 0.897 (ANN-2) and r_{cv} = 0.788 (ANN-1); r_{cv} = 0.800 (ANN-2).

Meanwhile, SVM was identified as the optimal learning approach for predicting the inhibitory activities of gelatinases (MMP2 and MMP9), while ANN and MLR models exhibited similar levels of performance. Various statistical parameters of the models (SVM-1 for MMP2 dataset and SVM-2 for MMP9 dataset) were summarized for both the test and training sets, as presented in **Table 5.12**.

The descriptor values associated with these models (MLR-1, ANN-1, SVM-1 for MMP2 inhibitors, and MLR-2, ANN-2, SVM-2 for MMP9 inhibitors) can be readily computed from the 2D structures of the compounds of interest (e.g., database molecules or novel molecules) using easily accessible software like PaDEL-descriptors (Yap 2011). These calculated values can then be used as inputs to predict the potential MMP2 and MMP9 activities in terms of IC_{50} values. Consequently, these QSAR models serve as valuable screening tools for exploring various databases to identify potential MMP2 and MMP9 inhibitors.

5.3.2.3. Recursive partitioning (RP) study

Using Discovery Studio 3.0 software, RP models were created employing molecular properties and a feature-class fingerprint of diameter 6 (*FCFP_6*) for MMP2 and MMP9 inhibitors. **Table 5.13** displays the statistical parameters of different RP models for gelatinase A (MMP2). Notably, the tree-1 model with 4 leaves exhibited the most promising performance, as evidenced by the five-fold cross-validated ROC values for both the training and test set compounds (**Table 5.13**).

Table 5.13. The results of the RP model as obtained from the training and test sets of gelatinase A (MMP2) and gelatinase B (MMP9) inhibitors.

Model	Tree	Tree information	Confusion Matrix for Train set	ROC_{Train}	ROC_{CV}	Confusion Matrix for Test set	ROC_{Test}
01	**01**	**Tree 1: 4 leaves**	**Actual\Pred. 0 1** **0 33 11** **1 4 40**	**0.856**	**0.726**	**Actual\Pred. 1 0** **1 11 3** **0 3 5**	**0.692**
01	02	Tree 2: 3 leaves	Actual\Pred. 0 1 0 37 7 1 12 32	0.824	0.619	Actual\Pred. 0 1 0 5 3 1 4 10	0.670
01	03	Tree 3: 2 leaves	Actual\Pred. 0 1 0 16 28 1 1 43	0.671	0.619	Actual\Pred. 0 1 0 0 8 1 0 14	0.500
02	**04**	**Tree 4: 5 leaves**	**Actual\Pred. 1 0** **1 42 2** **0 12 32**	**0.899**	**0.681**	**Actual\Pred. 1 0** **1 11 2** **0 1 8**	**0.979**
02	05	Tree 5: 3 leaves	Actual\Pred. 1 0 1 30 14 0 5 39	0.793	0.623	Actual\Pred. 1 0 1 10 3 0 0 9	0.885

The selected models are shown in bold faces.

For the MMP2 dataset, two molecular properties, namely the number of rings (*nRings*) and molecular fractional polar surface area (*MFPSA*), along with one sub-structure fingerprint, fingerprint-5 [FP-5 (FCFP_6, '136597326') /* [*]C([*])C */)], are identified as pivotal factors in distinguishing between gelatinase A inhibitors and non-inhibitors. Among the decision trees analyzed, it was determined that decision tree 1 with 4 leaves performed optimally for the MMP2 dataset (**Figure 5.22**).

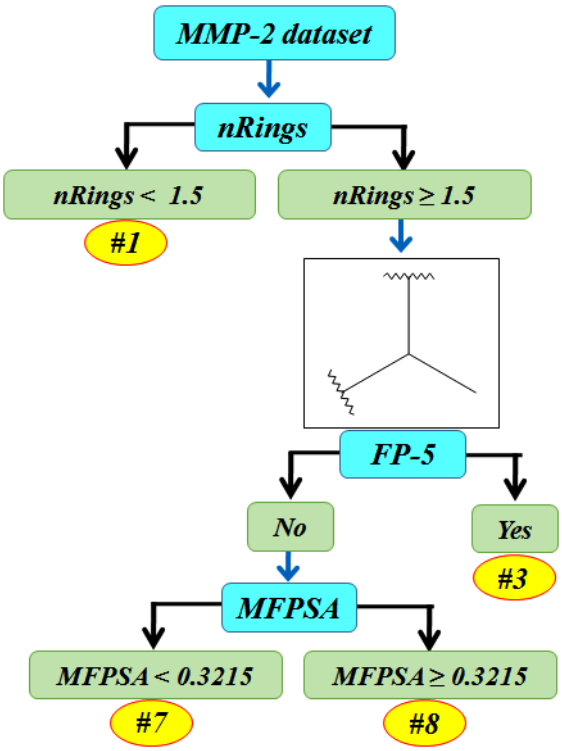

Figure 5.22. Decision tree to classify compounds into inhibitor and non-inhibitor classes of gelatinase A (MMP2) by using RP study (the Leaf ID is highlighted as '# number of leaf').

In Leaf ID #1, molecules characterized by several rings (*nRings*) less than 1.5 are predominantly associated with very poor MMP2 inhibitory activity. Consequently, a higher number of rings, exceeding 1.5, exhibits a positive correlation with gelatinase A inhibitory properties. Moving Leaf ID #3, comprises compounds with FP-5, while the remaining compounds do not possess FP-5. Notably, molecules containing FP-1 typically feature alkyl substitution in the α position relative to the hydroxamate moiety, demonstrating moderate to good MMP2 inhibition (*actives*). This α position of the hydroxamate moiety is deemed crucial for maintaining biological activity against both MMP2 and MMP9 enzymes, as well as ensuring selectivity. For instance, the

introduction of an isopropyl group enhances biological activity by inserting into the S_1 sub-site of the MMP2 catalytic domain.

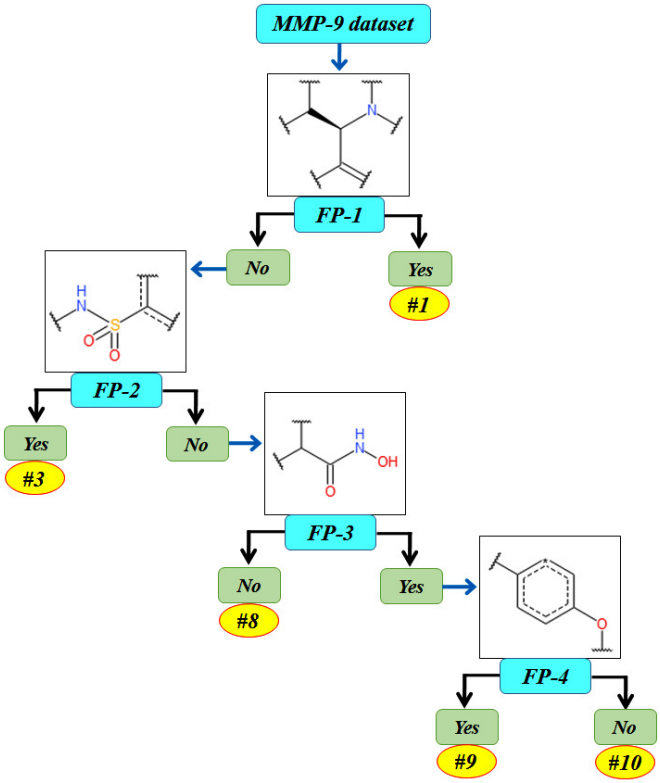

Figure 5.23. Decision tree to classify compounds into inhibitor and noninhibitor classes of MMP9 by using RP study (the Leaf ID is highlighted as '# number of leaf').

In Leaf IDs #7 and #8, molecules are categorized based on their molecular fractional polar surface area (*MFPSA*) values: compounds with *MFPSA* < 0.3215 and compounds with *MFPSA* ≥ 0.3215, respectively. *MFPSA* represents the sum of the surfaces of polar atoms (e.g., nitrogen, oxygen, and attached hydrogen atoms) in a molecule. As anticipated, compounds with *MFPSA* values ≥ 0.3215 predominantly exhibit moderate to good gelatinase A inhibition. Consequently, *MFPSA* values exceeding 0.3215 appear to be crucial for MMP2 inhibition.

For MMP9 inhibitors, the optimal RP model is represented by decision tree 4 with 5 leaves, which is composed of four fragments (**Figure 5.23**). These fragments serve as crucial features for distinguishing between *active* and *inactiv*e MMP9 inhibitors.

In Leaf ID #1, compounds possessing fingerprint-1 [FP-1 (FCFP_6, '-1946918893') /* [*]C([*])[C@@H](N([*])[*])C(=[*])[*] */)] are found. Upon analyzing compounds **B2, B27,**

B50, B53, B58, B64-B66, B68, B104, and **B110** bearing the FP-1 feature, it is suggested that FP-1 positively contributes to MMP9 inhibition. Additionally, the decision tree divides into Leaf ID #3 based on the presence or absence of fingerprint-2 [FP-2 (FCFP_6, '-1096219292') /* [*]NS(=O)(=O)[c](:[*]):[*] */)], while Leaf ID #8 consists of compounds with fingerprint-3 [FP-3 (FCFP_6, '168791128') /* [*]C([*])C(=O)NO */)]. FP-2 and FP-3 are instrumental in regulating the decision tree to distinguish between MMP9 inhibitors (*actives*) and non-inhibitors (*inactives*). The presence of sulfonamides and hydroxamates in compounds associated with these fragments suggests their importance in inhibiting the MMP9 enzyme. Furthermore, Leaf ID #9 comprises compounds with fingerprint-4 [FP-4 (FCFP_6, '1674451008') /* [*]O[c]1:c:[*]:[c]([*]):c:c:1 */)], while the remaining compounds the rest compounds not having FP-4 (Leaf ID #10). The majority of compounds in Leaf ID #9 are deemed *inactive*, implying a negative correlation between FP-4 and MMP9 inhibitory activity.

5.3.2.4. Bayesian classification study for MMP2 and MMP9 inhibitors

Model-1 and Model-2, based on molecules from MMP2 and MMP9 inhibitors in the training set, respectively, were constructed. Validation of these models utilized leave-one-out cross-validation. The Receiver Operating Characteristics (ROC) score, determined through five-fold cross-validation, is presented in **Table 5.14**.

Table 5.14. Statistics of training and test set during Bayesian model development

Model	Set	ROC Score	TP	FN	FP	TN	Sensitivity	Specificity	Concordance
1	Training[a]	0.837[b]	41	3	8	36	0.932	0.818	0.875
	Test	0.893	11	3	0	8	0.786	1.000	0.864
2	Training[c]	0.815[b]	33	11	3	41	0.750	0.932	0.841
	Test	0.932	10	3	0	9	0.769	1.000	0.864

[a]ROC score is 0.828 (leave-one-out), [b]5-Fold cross-validation; [c]ROC score is 0.810 (leave-one-out);

As anticipated, both models exhibited statistically significant results for both the training set and test set compounds. The five-fold cross-validation ROC scores for the training set compounds were 0.837 for model-1 and 0.815 for model-2, as shown in Table 5.14. Conversely, the ROC scores for the test set compounds were 0.893 for model-1 and 0.932 for model-2, indicating strong external predictability for these QSAR models. The ROC curves for the Bayesian classification models of MMP2 and MMP9 inhibitors are depicted in **Figures 5.24** and **Figures 5.25**, respectively. Furthermore, other statistical parameters for model-1 and model-2 are also

favorable. For the training set compounds, sensitivity values of 93.2% and 75.0%, along with specificity values of 81.8% and 93.2%, were observed for model-1 and model-2, respectively, as detailed in **Table 5.14**.

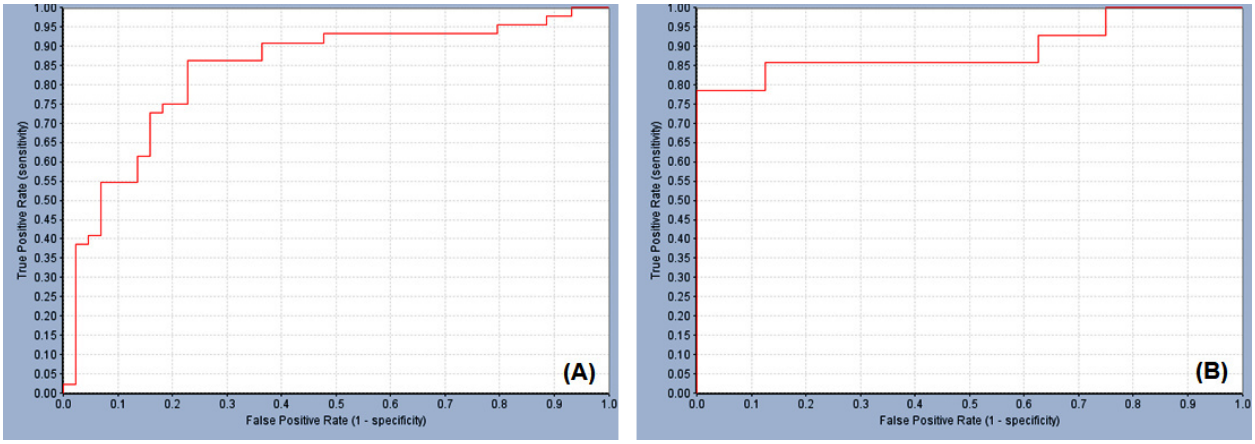

Figure 5.24. ROC curves for the Bayesian model of MMP2 inhibitors [(A) training set; (B) red test set].

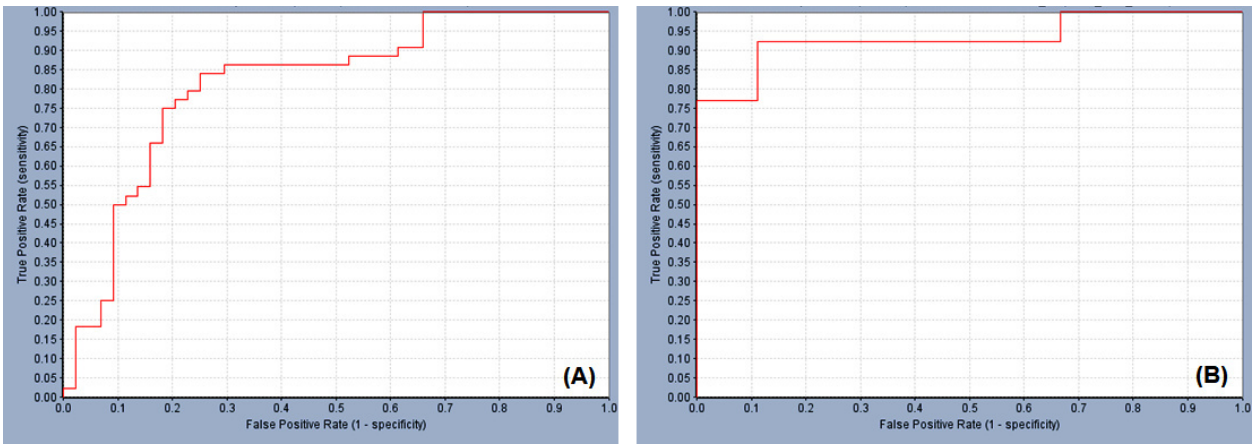

Figure 5.25. ROC curves for the Bayesian model of MMP9 inhibitors [(A) training set; (B) red test set].

The Bayesian models successfully identified the most favorable molecular sub-structures or fragments for MMP2 inhibitors as fingerprints *G1-G20* and for MMP9 inhibitors as fingerprints *G21-G40*. Conversely, fingerprints *B1-B20* for MMP2 inhibitors and *B21-B40* for MMP9 inhibitors were identified as unfavorable. These findings were derived from the descriptor known as extended connectivity of fingerprint diameter 6 (ECFP_6), as illustrated in **Figures 5.26-Figures 5.29**.

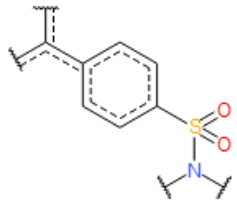 G1: 1795997462 11 out of 11 good Bayesian Score: 0.546	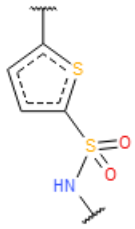 G2: -770278038 5 out of 5 good Bayesian Score: 0.482	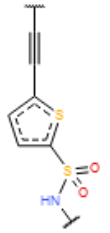 G3: -456699973 5 out of 5 good Bayesian Score: 0.482	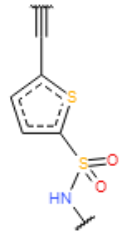 G4: -49481626 5 out of 5 good Bayesian Score: 0.482	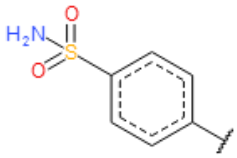 G5: -1261213389 4 out of 4 good Bayesian Score: 0.458
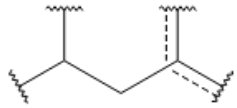 G6: 770157610 4 out of 4 good Bayesian Score: 0.458	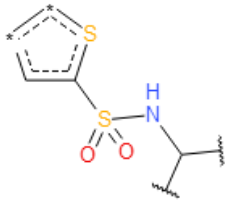 G7: 788429328 4 out of 4 good Bayesian Score: 0.458	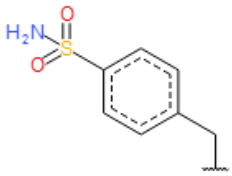 G8: -1033531113 4 out of 4 good Bayesian Score: 0.458	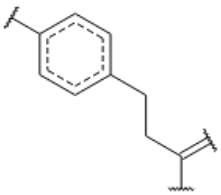 G9: 1523683691 4 out of 4 good Bayesian Score: 0.458	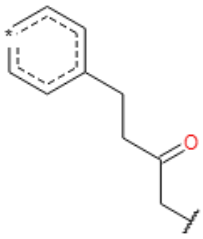 G10: 1978696119 4 out of 4 good Bayesian Score: 0.458
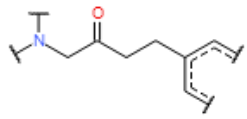 G11: 1732407293 4 out of 4 good Bayesian Score: 0.458	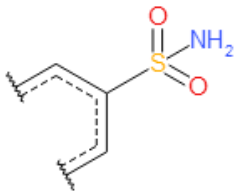 G12: -908165145 4 out of 4 good Bayesian Score: 0.458	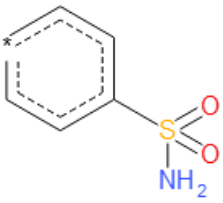 G13: 107868251 4 out of 4 good Bayesian Score: 0.458	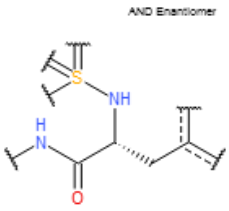 G14: 2046038860 4 out of 4 good Bayesian Score: 0.458	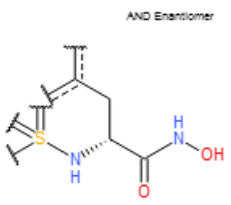 G15: 672851103 4 out of 4 good Bayesian Score: 0.458
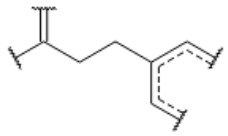 G16: -2138777629 4 out of 4 good Bayesian Score: 0.458	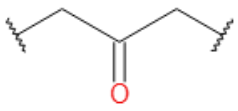 G17: -409654214 4 out of 4 good Bayesian Score: 0.458	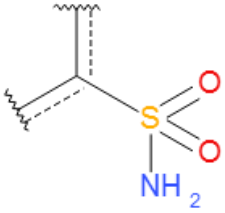 G18: -2121766239 4 out of 4 good Bayesian Score: 0.458	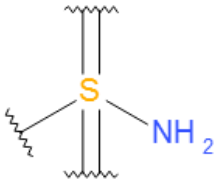 G19: -934226723 4 out of 4 good Bayesian Score: 0.458	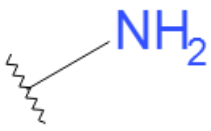 G20: 1572579716 4 out of 4 good Bayesian Score: 0.458

Figure 5.26. Good molecular fingerprints (***G1-G20***) favorable for MMP2 inhibitory activity as introduced from the *ECFP_6* fingerprint descriptor.

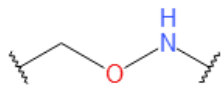 B1: -1251215744 0 out of 6 good Bayesian Score: -1.446	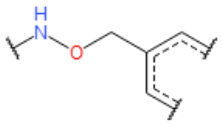 B2: 863893619 0 out of 6 good Bayesian Score: -1.446	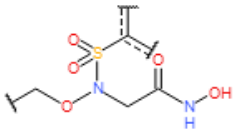 B3: -1138531770 0 out of 5 good Bayesian Score: -1.310	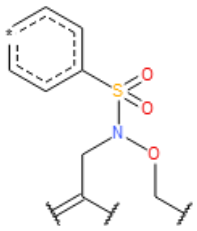 B4: -479848101 0 out of 5 good Bayesian Score: -1.310	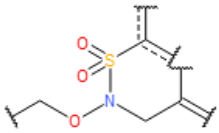 B5: 930138475 0 out of 5 good Bayesian Score: -1.310
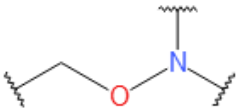 B6: -1250123285 0 out of 5 good Bayesian Score: -1.310	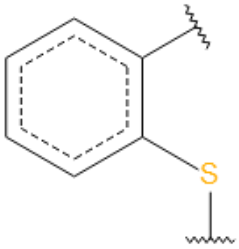 B7: 1773783205 0 out of 4 good Bayesian Score: -1.152	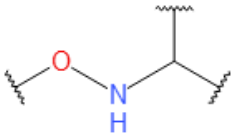 B8: 598113214 0 out of 4 good Bayesian Score: -1.152	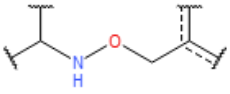 B9: -2047826459 0 out of 4 good Bayesian Score: -1.152	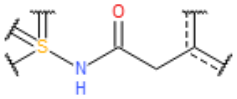 B10: 1005101173 0 out of 4 good Bayesian Score: -1.152
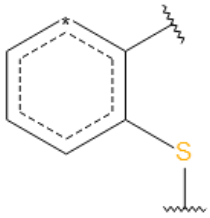 B11: 1638811552 0 out of 4 good Bayesian Score: -1.152	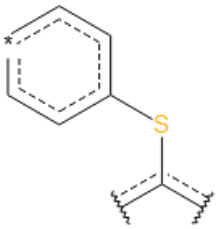 B12: -1818395972 0 out of 4 good Bayesian Score: -1.152	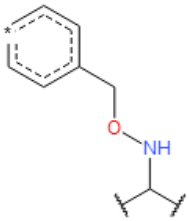 B13: 2026104518 0 out of 4 good Bayesian Score: -1.152	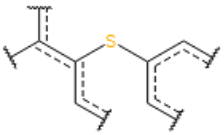 B14: 2010224992 0 out of 4 good Bayesian Score: -1.152	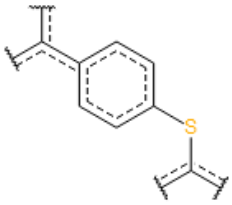 B15: -1811138302 0 out of 4 good Bayesian Score: -1.152
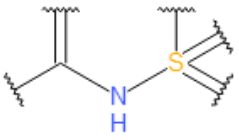 B16: 946167604 0 out of 4 good Bayesian Score: -1.152	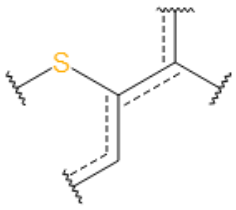 B17: 1335907850 0 out of 4 good Bayesian Score: -1.152	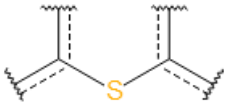 B18: -306186198 0 out of 4 good Bayesian Score: -1.152	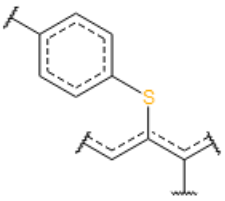 B19: 1261785985 0 out of 4 good Bayesian Score: -1.152	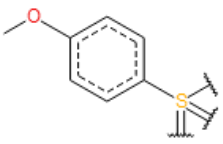 B20: -360736333 2 out of 14 good Bayesian Score: -1.050

Figure 5.27. Bad molecular fingerprints (***B1-B20***) unfavorable for MMP2 inhibitory activity as introduced from the *ECFP_6* fingerprint descriptor.

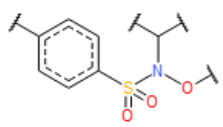 G21: -1899434736 7 out of 7 good Bayesian Score: 0.529	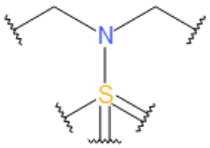 G22: -1865313055 6 out of 6 good Bayesian Score: 0.515	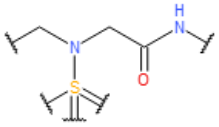 G23: 1345238030 6 out of 6 good Bayesian Score: 0.515	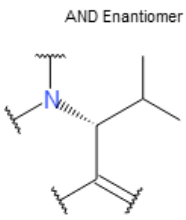 G24: 132859104 6 out of 6 good Bayesian Score: 0.515	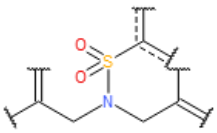 G25: 679619238 6 out of 6 good Bayesian Score: 0.515
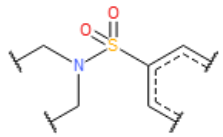 G26: -683599369 6 out of 6 good Bayesian Score: 0.515	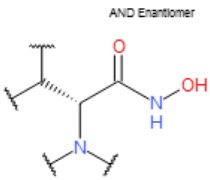 G27: -470355583 6 out of 6 good Bayesian Score: 0.515	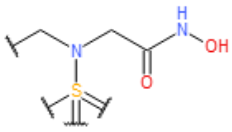 G28: -1936711257 6 out of 6 good Bayesian Score: 0.515	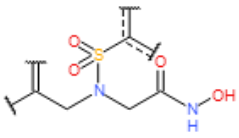 G29: 274958145 6 out of 6 good Bayesian Score: 0.515	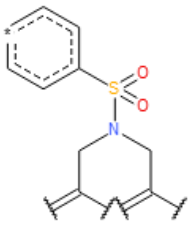 G30: 1027322164 6 out of 6 good Bayesian Score: 0.515
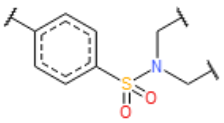 G31: 1326578773 6 out of 6 good Bayesian Score: 0.515	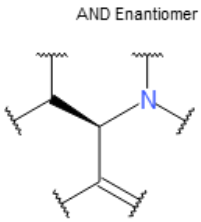 G32: -1530632622 6 out of 6 good Bayesian Score: 0.515	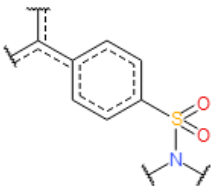 G33: 1795997462 10 out of 11 good Bayesian Score: 0.476	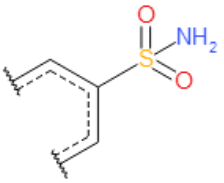 G34: -908165145 4 out of 4 good Bayesian Score: 0.471	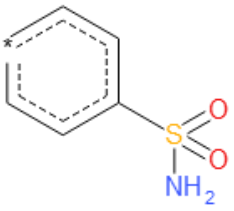 G35: 107868251 4 out of 4 good Bayesian Score: 0.471
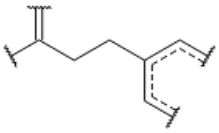 G36: -2138777629 4 out of 4 good Bayesian Score: 0.471	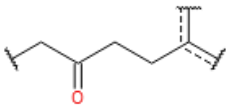 G37: -1520762831 4 out of 4 good Bayesian Score: 0.471	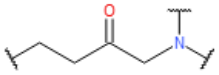 G38: 807712646 4 out of 4 good Bayesian Score: 0.471	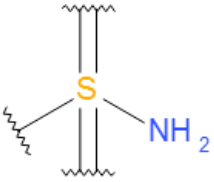 G39: -934226723 4 out of 4 good Bayesian Score: 0.471	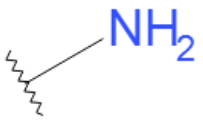 G40: 1572579716 4 out of 4 good Bayesian Score: 0.471

Figure 5.28. Good molecular fingerprints (***G21-G40***) favorable for MMP9 inhibitory activity as introduced from the *ECFP_6* fingerprint descriptor.

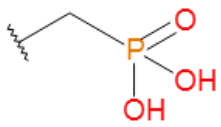 B21: -1520554837 0 out of 6 good Bayesian Score: -1.431	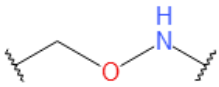 B22: -1251215744 0 out of 6 good Bayesian Score: -1.431	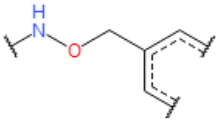 B23: 863893619 0 out of 6 good Bayesian Score: -1.431	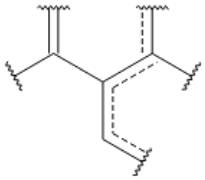 B24: 1337040050 0 out of 5 good Bayesian Score: -1.295	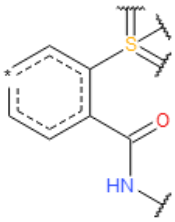 B25: -1129784398 0 out of 5 good Bayesian Score: -1.295
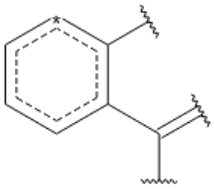 B26: 1635415905 0 out of 5 good Bayesian Score: -1.295	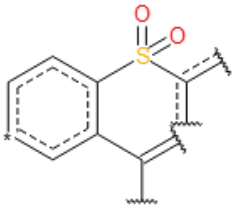 B27: -51953675 0 out of 5 good Bayesian Score: -1.295	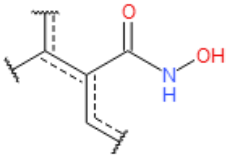 B28: -102869925 0 out of 5 good Bayesian Score: -1.295	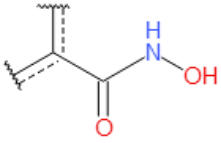 B29: 528978882 0 out of 5 good Bayesian Score: -1.295	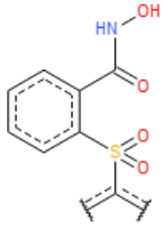 B30: -515731365 0 out of 5 good Bayesian Score: -1.295
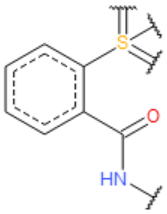 B31: 2046215440 0 out of 5 good Bayesian Score: -1.295	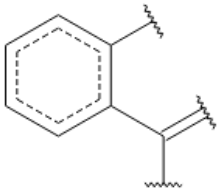 B32: 1993671714 0 out of 5 good Bayesian Score: -1.295	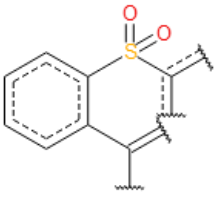 B33: -1951380942 0 out of 5 good Bayesian Score: -1.295	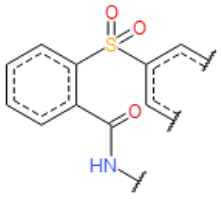 B34: -1621373059 0 out of 5 good Bayesian Score: -1.295	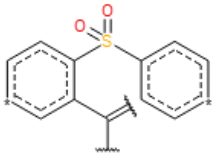 B35: -444398042 0 out of 5 good Bayesian Score: -1.295
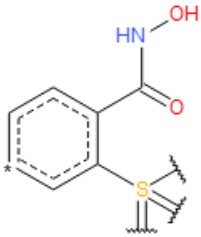 B36: 723225747 0 out of 5 good Bayesian Score: -1.295	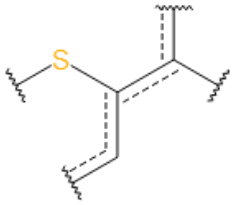 B37: 1335907850 0 out of 4 good Bayesian Score: -1.138	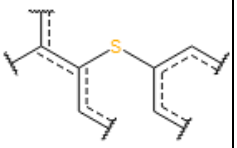 B38: 2010224992 0 out of 4 good Bayesian Score: -1.138	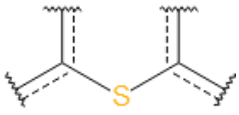 B39: -306186198 0 out of 4 good Bayesian Score: -1.138	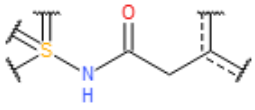 B40: 1005101173 0 out of 4 good Bayesian Score: -1.138

Figure 5.29. Bad molecular fingerprints (***B21-B40***) unfavorable for MMP9 inhibitory activity as introduced from the *ECFP_6* fingerprint descriptor.

For MMP2 inhibitors, fingerprints *G1, G5, G8, G12,* and *G13* highlight the significance of the substituted aryl sulfonamide moiety. Notably, **compound B56**, which contains this fragment within its structure, exhibited promising inhibitory activity with an IC50 value of 0.13 nM. The majority of the favorable molecular fragments depicted in **Figure 5.30** underscore the importance of the substituted aryl sulfonamide moiety for potential MMP2 inhibition.

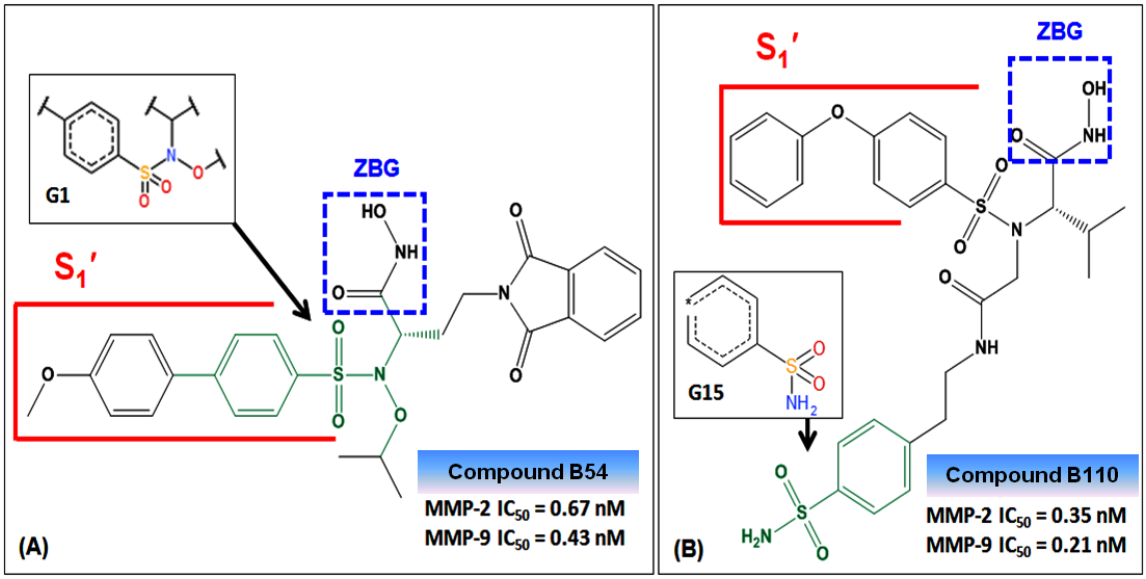

Figure 5.30. (A) Structure of **compound B54** having good *G1* fingerprint; (B) Structure of compound **110** having good *G15* fingerprint.

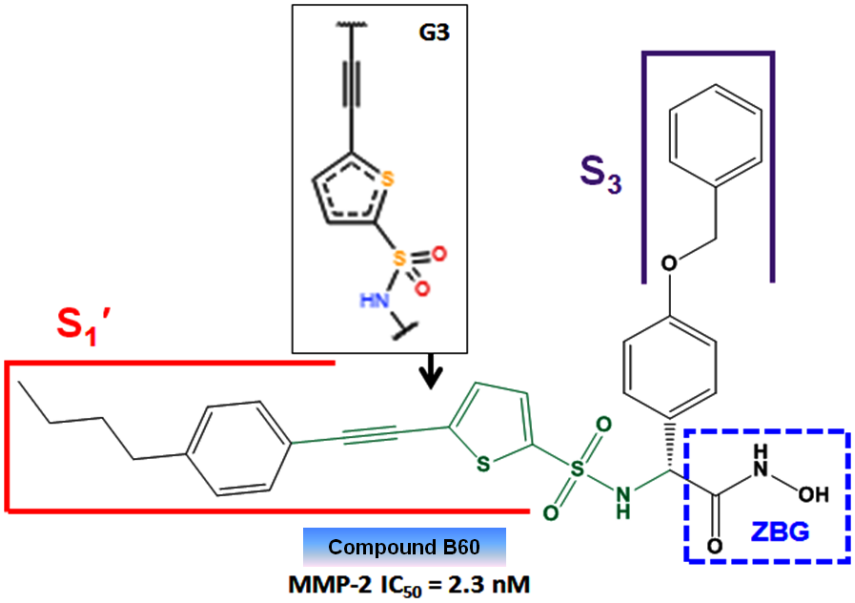

Figure 5.31. Structure of **compound B60** having good *G3* fingerprint.

Similarly, the thiophene sulfonamide moiety is identified as a positive contributor to MMP2 inhibitory activities, as evidenced by compounds **B58-B64** exhibiting favorable fingerprints *G2-G4* and *G7*, with MMP-2 IC_{50} values ranging from 1.3 to 17 nM. The sub-structural fingerprint *G2* (**Figure 5.26**) emphasizes the significance of the thiophene sulfonamide group, while sub-structural fragments fingerprints *G3* and *G4* (**Figure 5.26**) underscore the importance of the ethynyl-thiophene sulfonamide group. In compounds **B58-B64**, the ethynyl-thiophene sulfonamide-based hydroxamates demonstrate promising MMP2 inhibitory activities within the IC50 range of 1.3 to 17 nM. This observation aligns well with a molecular docking study conducted by Nuti and colleagues (Nuti et al., 2011). According to their findings, the thiophene ring system is flanked by residues L164 and V198, while the ethynyl function is positioned between residues Y233 and H201 of the MMP2 enzyme (PDB: 1QIB), enhancing its interaction with the receptor. Furthermore, the sulfonamide function of compound **B60** (**Figure 5.31**) forms hydrogen bonding interactions with the backbone NH of L164 and A165 (PDB: 1QIB), leading to improved MMP2 inhibitory activity. It's not surprising that compounds **B58-B64**, which contain the ethynyl-thiophene sulfonamide group, exhibit selectivity towards MMP2 over MMP1 and MMP14.

The unfavorable fragments, fingerprints *B1-B6* and *B8-B10*, indicate the detrimental impact of -CH2-O-N(H)- on MMP2 inhibition. Notably, compound **B79** with fingerprint *B1* exhibits very poor activity against the MMP2 enzyme (IC_{50} = 1,37,000 nM). Additionally, the contribution of N-alkyloxy substituents towards MMP2 inhibition is also negative. Analysis of compounds **B75-B80** bearing N-alkyloxy substituents suggests weak MMP2 inhibition associated with this fragment. This could be attributed to the fact that MMP2 inhibition relies on various substitutions, and compounds may not achieve sufficient inhibition unless these substitutions are optimized properly for size, shape, hydrophobicity, etc. Substructural fragments resembling fingerprints *B5-B7* and *B10-B11* (**Figure 5.27**) support the negative correlation of sulfone-based benzoic hydroxamates. From SAR studies, it can be postulated that the incorporation of an aromatic ring between the ZBG and the sulfonyl group leads to a significant change in activity. It's reported that sulfone-based benzoic hydroxamates adopt a different binding geometry for optimal interaction with the receptor and its zinc ion, thereby reducing activity. Similarly, the remaining unfavorable fingerprints indicate similar phenomena.

Interestingly, the favorable and unfavorable fragments for MMP9 inhibitors closely resemble those for MMP2 inhibitors. The correlation coefficient (r) between MMP2 and MMP9 inhibition in this dataset is found to be 0.918 (N = 110), indicating a strong correlation between the two enzymes. Most of the favorable molecular fragments in MMP9 inhibition also emphasize the significance of the substituted aryl sulfonamide moiety. Compounds **B50-B54** and compound **B56-B57**, containing the N-O-isopropyl sulfonamide fragment, exhibit good MMP9 inhibitory activities within the IC_{50} range of 0.43 to 9.0 nM. Interestingly, the sulfonamide moiety maintains its orientation at the P_1' position, allowing penetration into the hydrophobic S_1' pocket of MMP9 (PDB: 4WZV). This orientation is illustrated by the MMP9 catalytic site (PDB: 4WZV) with a co-crystallized ligand, as depicted in **Figure 5.32**.

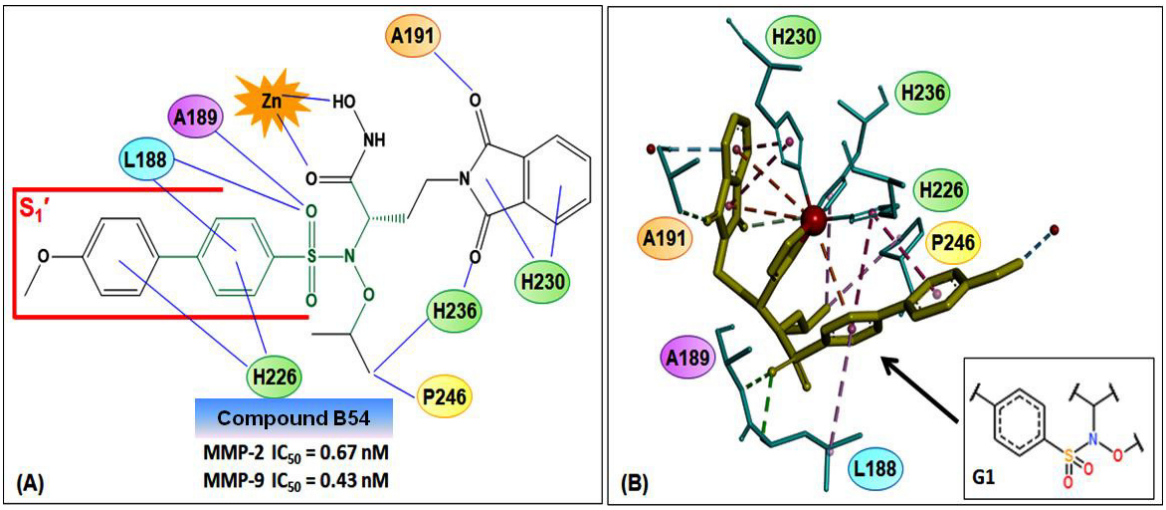

Figure 5.32. (A) 2D and (B) 3D interaction plots of compound **B54** at the catalytic site of MMP9 (PDB: 4WZV). The shared fingerprint that is critical for binding with the receptor is also shown.

In **Figure 5.32**, one of the oxygen atoms of the sulfonamide group forms a hydrogen bond with the nitrogen backbone of L188 and A189. Furthermore, the phenyl group linked to the sulfonamide structure contributes to π-π stacked and π-alkyl interactions with amino acid residues H226 and L188, respectively (**Figure 5.32**). Nuti et al. also demonstrated that the absence of the aryl sulfonyl group led to a significant decrease in gelatinases (MMP2 and MMP9) inhibition by 90 to 300-fold (compounds **B67** and **B69** compared to compounds **B78** and **B79**) (Nuti et al., 2007). Therefore, compounds containing the aryl sulfonyl group were

identified as crucial for inhibiting gelatinases. The favorable fragments, represented by fingerprints *G34-G35*, highlight the positive effects of the phenyl sulfonamide substitution, whereas fingerprints *G36-G37* demonstrate the beneficial contributions of the phenyl ethyl function. Together, the (4-sulfonamidophenyl)-ethylamine group significantly interacts with gelatinases. Interestingly, the sulfonamide phenyl ethyl moiety fits well into the S_2'-S_3' subsites. Additionally, the presence of -NH2 in compounds **B107-B110** may facilitate interaction with the receptor, with an average MMP9 IC_{50} of 30.1 nM. This finding aligns with the docking results reported by Marques et al. (Marques et al., 2008). Consequently, substructural fragments resembling fingerprints *G39-G40* support the positive influence of the amine substitution, which is suggested to be important for MMP9 inhibition (**Figure 5.28**). Conversely, the unfavorable fragments resembling fingerprints *B21* and *B22-B23* (**Figure 5.29**) indicate the negative impact of phosphonate and N-alkyloxy substituents, respectively. Compounds **B84-B86** containing the -PO_3H_2 feature exhibit poor MMP9 inhibitory activities (IC_{50} range: 1,730 to 4,100 nM) due to the phosphonate feature's poor zinc binding property (**Figure 5.33**).

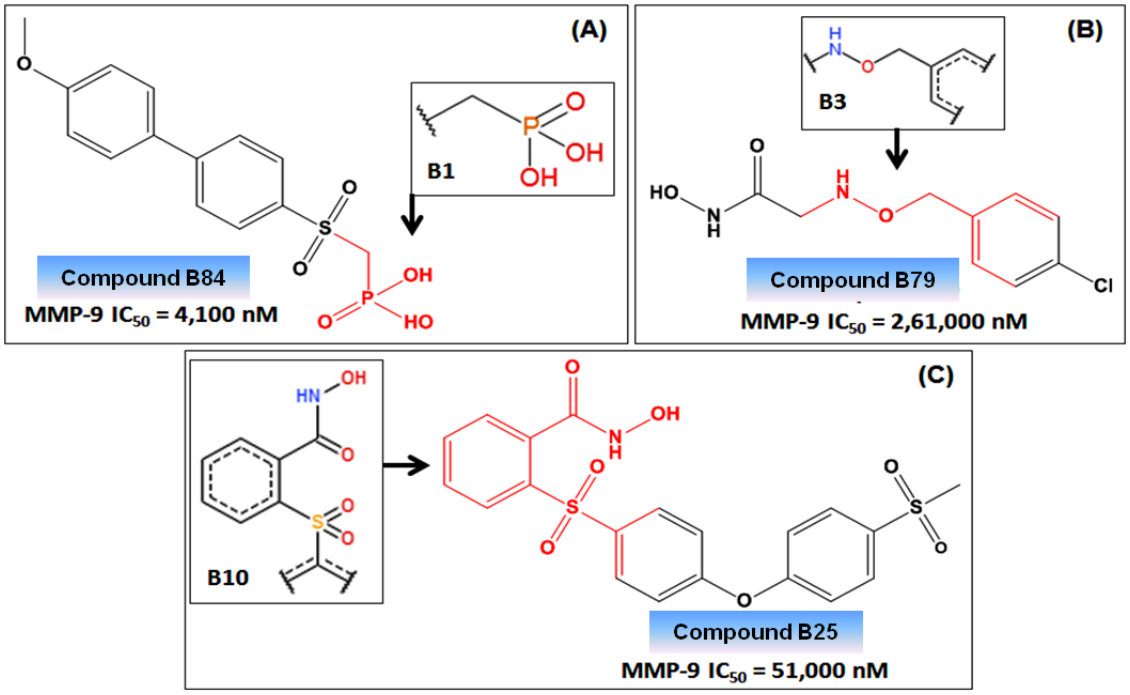

Figure 5.33. (A) Structure of compound **B84** having bad *B1* fingerprint; (B) Structure of compound **B79** having bad *B3* fingerprint; (C) Structure of compound **B25** having bad *B10* fingerprint.

Similar to MMP2 inhibitors, compounds containing the sulfone-based benzoic hydroxamate moiety (compound **B14**: MMP9 IC_{50} = 410 nM; compound **B17**: MMP9 IC_{50} = 690 nM; compound **B19**: MMP9 IC_{50} = 930 nM; compound **B22**: MMP9 IC_{50} = 7,700 nM; compound **B24**: MMP9 IC_{50} = 24,000 nM; compound **B25**: MMP9 IC_{50} = 51,000 nM) exhibit poor MMP9 inhibitory activities (average MMP9 IC_{50} = 14,121.67 nM). The contribution of the N-alkyloxy substituent is also found to be negative towards MMP9 inhibition. Analysis of compounds **B75-B80** bearing the N-alkyloxy substituent suggests that this fragment negatively impacts MMP9 inhibition (average MMP9 IC_{50} = 2,02,750 nM). Lastly, the influence of different fingerprint features on MMP2 as well as MMP9 inhibition is evident from the aforementioned discussions. Now, our focus shifts to the development of QSAR models for predicting biological activities. In this regard, regression-based linear QSAR/classical QSAR as well as non-linear QSAR studies are being utilized.

5.3.2.5. Summary of Part-IIIB

In this investigation, a range of molecular modeling methods were employed on a dataset containing 110 inhibitors targeting MMP2 and MMP9 enzymes. The primary aims were to pinpoint structural features linked with inhibiting MMP2 and MMP9 and to construct statistically validated QSAR models for the assessment and prediction of various derivatives as inhibitors of MMP2 and MMP9. The Bayesian classification analysis produced ROC values of 0.837 and 0.815 for MMP2 and MMP9, respectively, in the training dataset. The linear model additionally generated leave-one-out (LOO) cross-validated Q^2 values of 0.805 (*Eq. 1b*, MMP2) and 0.724 (*Eq. 2b*, MMP9), R^2 values of 0.845 (*Eq. 1b*, MMP2) and 0.782 (*Eq. 2b*, MMP9), and R^2_{Pred} values of 0.806 (*Eq. 1b*, MMP2) and 0.732 (*Eq. 2b*, MMP9). Likewise, non-linear learning models demonstrated statistical significance and reliability.

This study (**Part-IIIB**) underscores several critical structural prerequisites for the development of more potent inhibitors against both gelatinases (MMP2 and MMP9). These requirements include the following:

(1) The compounds within this dataset exhibit diversity, enabling exploration of the Zinc Binding Groups (ZBGs). For instance, the $-PO_3H_2$ feature demonstrates poor zinc binding capability

(**Figure 5.34**). Additionally, sub-structural fragments of sulfone-based benzoic hydroxamates further support a negative correlation with biological activity.

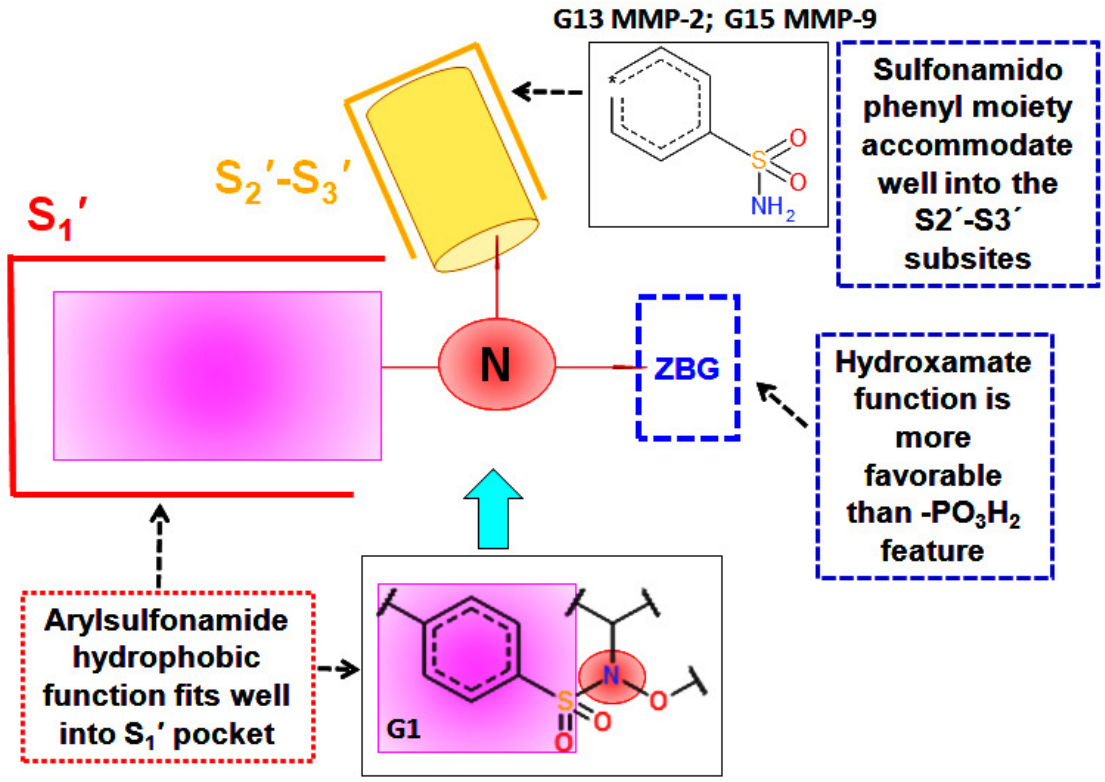

Figure 5.34. Structural requirements for better active MMP2 and MMP9 inhibitors.

(2) This QSAR analysis suggests that the insertion of an aromatic ring between the ZBG and the sulfonyl group leads to a significant decrease in activity.

(3) Notably, compounds based on N-O-isopropyl sulfonamide with a sulfonamide fragment demonstrate robust inhibition of gelatinases (**Figure 5.34**). Similarly, certain sub-structural fragments underscore the significance of the ethynyl thiophene sulfonamide group. Compounds **B58-B64**, featuring ethynyl thiophene sulfonamide-based hydroxamates, exhibit promising inhibitory activities against gelatinase A (MMP2) with IC_{50} values ranging from 1.3 to 17 nM.

(4) The introduction of N-alkyloxy substituents negatively impacts MMP2 and MMP9 inhibition. This could be attributed to the dependency of MMP2 and MMP9 inhibition on distinct substitutions, suggesting that compounds will not achieve sufficient inhibition unless substitutions are optimized for factors such as size, shape, and hydrophobicity.

5.4. Synthesis, biological studies and binding interaction studies of (*D*)-glutamine derivatives (Part-IV)

Both of the QSAR-based molecular modeling studies (**Part-IIIA** and **Part-IIIB**) highlighted the importance of aryl sulfonamide hydrophobic function to be fitted well into S_1' pocket of MMP2 and MMP9 enzymes. Likewise, the presence of a secondary nitrogen atom is also found to be important for gelatinases binding affinities in the case of studies presented in **Part-IIIA (Figure 5.17** and **Figure 5.21)** and **Part-IIIB (Figure 5.26 and Figure 5.28)**. Similarly, the positive influence of hydroxamate moiety has been observed in both of these modeling studies (**Part-IIIA** and **Part-IIIB**). Based on the QSAR analysis conducted with dataset 2 (**Figure 5.29**), it can be inferred that the introduction of a ring structure between the ZBG and the sulfonyl group led to a substantial decrease in the inhibitory activity of MMP2 and MMP9.

Therefore, learning from the literature (**Chapter 2**) and QSAR-based molecular modeling studies 31 new (*D*)-glutamine derivatives (**3a-3h, 3a′-3l′** and **5a′-5k′**) were synthesized, purified and characterized. Among these 31 synthesized compounds, 20 compounds (**3a-3h** and **3a′-3l′**) contain carboxylic acid function in their structures whereas the remaining 11 compounds (**5a′-5k′**) contain hydroxamic acid function in their structures instead of carboxylic acid group. The purified novel molecules were screened against several cancer cell lines and a few better active compounds were progressed for further biological studies to understand the mechanism of cytotoxic activity. Binding interaction studies (molecular docking and molecular dynamic simulation) with MMP2 and selected compounds (**3d**, **3h′, 5d′ and 5h′**) were also performed.

5.4.1. Synthesis of (*D*)-glutamine derivatives

Here, 31 new (*D*)-glutamine derivatives (**3a-3h, 3a′-3l′** and **5a′-5k′**) were synthesized. The general methodology and reaction parameters were discussed in **Chapter 4**. Eight structural analogs (**3a-3h**) of (*R*)-2-(*p*-nitrophenyl sulphonamide) pentanedioic acid (**1a**) were synthesized using the synthetic method as per **Scheme 4.1**. Initially, *p*-nitrobenzene sulfonyl chloride was subjected to condensation with *D*(-)-glutamic acid following Schotten-Baumann reaction in the presence of 2(N) NaOH to procure the first intermediate (*R*)-2-(*p*-nitrophenylsulfonamido) pentanedioic acid (**1a**) (**Scheme 4.1**). In the next step, compound 1a was cyclized with acetyl chloride to obtain the intermediate (*R*)-1-((4-nitrophenyl)sulfonyl)-5-oxopyrrolidine-2-

carboxylic acid (**2a**) and finally compound **2a** was converted into carboxamides (**3a-3h**) by several primary amines (R-NH_2) (**Scheme 4.1**).

Similarly, another twelve structural analogs (**3a′-3l′**) of (*R*)-5-oxo-1-tosylpyrrolidine-2-carboxylic acid **(2a′)** were prepared using the synthetic procedure outlined in **Scheme 4.1** where *p*-tosyl chloride was condensed with *D*(-)-glutamic acid to obtain the first intermediate (*R*)-2-(4-methyl phenyl sulphonamide)pentanedioic acid (**1a′**) and followed by the cyclization with acetyl chloride to obtain second intermediate, *i.e.,* (*R*)-5-oxo-1-tosylpyrrolidine-2-carboxylic acid (**2a′**). The compound was treated with different amines to obtain the desired *p*-methyl benzene sulfonyl-*D*-glutamine analogs (**3a′-3l′**).

Finally, eleven (*R*)-5-oxo-1-tosylpyrrolidine-2-carboxylic acid derivatives (**3a′-3l′**) were converted to their respective hydroxamates (**5a′-5k′**). Compounds **3a′-3j′** were synthesized by my lab junior Subha Mondal (Mondal 2020B) in my presence. Synthetic route development and optimization, purification, and chemical characterization of these compounds (**3a′-3j′**) were done by me.

5.4.2. Characterization of final compounds

All the final compounds (**3a-3h, 3a′-3l′,** and **5a′-5k′**) were characterized through FT-IR, HRMS, ^{1}H NMR, and ^{13}C NMR. The % purity of representative compounds was determined by high-performance liquid chromatography (HPLC). All the spectra of the reported compounds are provided in the **Appendix** section. The results of spectral analysis of the final compounds (**3a-3h, 3a′-3l′** and **5a′-5k′**) are given below.

5.4.2.1. (R)-5-amino-2-(4-nitrophenylsulfonamido)-5-oxopentanoic acid (3a)

The crude compound 3a was recrystallized by an isopropyl alcohol (IPA)/ water mixture (70% IPA and 30% water). The resulting compound (**3a**) was found as white solid with 82.86% yield (0.87g, 0.0026 mol) and the melting point was recorded as 172-173 °C (uncorrected). The final product was characterized by FT-IR, HRMS, ^{1}H NMR, and ^{13}C NMR analysis. These analytical data are given below:

FT-IR (cm^{-1}): 3444, 3340 (NH str of SO_2NH), 3268, 3110 (NH str of CONH), 2934 (Ar CH str), 2865 (ali CH str), 1706 (C=O str of COOH), 1526 (N=O str of Ar-NO_2), 1350, 1160 (S=O str of SO_2NH), 853, 736 (Ar C-H def). HRMS (TOF ES+), m/z, calculated [M + H^+]: 332.0552, found:

332.0554. ^{1}H NMR (300 MHz, DMSO-d_6) δ 8.38 (d, J = 8.6 Hz, 2H), 8.01 (d, J = 8.7 Hz, 2H), 7.24 (s, 1H), 6.74 (s, 1H), 3.81 (m, 1H), 2.07 (t, J = 7.5 Hz, 2H), 1.99 – 1.55 (m, 2H). ^{13}C NMR (75 MHz, DMSO-d_6) δ 173.02, 172.31, 149.40, 146.75, 128.09, 124.34, 55.45, 30.66, 27.72.

5.4.2.2. (R)-5-(methylamino)-2-(4-nitrophenylsulfonamido)-5-oxopentanoic acid (3b)

Following the synthetic procedure of 3a, starting materials 2a and 40% methyl amine resulted in 3b as a light yellow solid resulting in 84.16% yield (0.85g, 0.0025 mol) with uncorrected melting point 187-188 °C. The crude compound 3b was recrystallized by an ethanol/ water mixture (70% ethanol and 30% water). The final product was characterized by FT-IR, HRMS, ^{1}H NMR, and ^{13}C NMR analysis. These analytical data are given below:

FT-IR (cm^{-1}): 3402 (NH str of SO_2NH), 3267, 3100 (NH str of CONH), 2941 (Ar CH str), 2865 (ali CH str), 1705 (C=O str of COOH), 1515 (N=O str of Ar-NO_2), 1356, 1158 (S=O str of SO_2NH), 849, 738 (Ar C-H def). HRMS (TOF ES+), m/z, calculated [M + Na^+]: 368.0528, found: 368.0538. ^{1}H NMR (300 MHz, DMSO-d_6) δ 12.73 (s, 1H), 8.59 (d, J = 8.8 Hz, 1H), 8.39 (d, J = 8.9 Hz, 2H), 8.01 (d, J = 8.9 Hz, 2H), 7.68-7.69 (m, 1H), 3.77-3.85 (m, 1H), 2.51 (d, J = 4.5 Hz, 3H), 2.05-2.10 (m, 2H), 1.61-1.96 (m, 2H). ^{13}C NMR (75 MHz, DMSO-d_6) δ 172.34, 171.17, 149.41, 146.75, 128.10, 124.36, 55.36, 30.84, 27.81, 25.45.

5.4.2.3. (R)-5-(ethylamino)-2-(4-nitrophenylsulfonamido)-5-oxopentanoic acid (3c)

Using the procedure of synthesis of 3a, starting materials 2a and ethyl amine gave 3c as a white solid resulting in 85.08% yield (0.97g, 0.0027 mol) with an uncorrected melting point 203-204°C. The crude compound 3c was recrystallized by an ethanol/ water mixture (70% ethanol and 30% water). The final product was characterized by FT-IR, HRMS, ^{1}H NMR, and ^{13}C NMR analysis. These analytical data are given below:

FT-IR (cm^{-1}): 3394 (NH str of SO_2NH), 3258, 3116 (NH str of CONH), 2958 (Ar CH str), 2870 (ali CH str), 1713 (C=O str of COOH), 1523 (N=O str of Ar-NO_2), 1341, 1158 (S=O str of SO_2NH), 849, 738 (Ar C-H def). HRMS (TOF ES+), m/z, calculated [M + Na^+]: 382.0685, found: 382.0680. ^{1}H NMR (300 MHz, DMSO-d_6) δ 12.71 (s, 1H), 8.57 (d, J = 8.8 Hz, 2H), 8.38 (d, J = 8.8 Hz, 2H), 8.01 (d, J = 8.9 Hz, 1H), 7.74 (t, J = 5.2 Hz, 1H), 3.71-3.91 (m, 1H), 2.86-3.14 (m, 2H), 2.07 (t, J = 7.5 Hz, 2H), 1.55-1.96 (m, 2H), 0.96 (t, J = 7.2 Hz, 3H). ^{13}C NMR (75 MHz, DMSO-d_6) δ 172.32, 170.45, 149.40, 146.79, 128.10, 124.34, 55.39, 33.32, 30.98, 27.86, 14.67.

5.4.2.4. (R)-5-(isopropylamino)-2-(4-nitrophenylsulfonamido)-5-oxopentanoic acid (3d)

Following the synthetic procedure of 3a, starting materials 2a and i-propyl amine resulted in 3d as a white solid resulting in 86.55% yield (1.03g, 0.0028 mol) with uncorrected melting point 220-221 °C. The crude compound 3d was recrystallized by an ethanol/ water mixture (70% ethanol and 30% water). The final product was characterized by FT-IR, HRMS, ^{1}H NMR, and ^{13}C NMR analysis. These analytical data are given below:

FT-IR (cm^{-1}): 3393 (NH str of SO_2NH), 3258, 3110 (NH str of CONH), 2965, 2929 (Ar CH str), 2869 (ali CH str), 1715 (C=O str of COOH), 1526 (N=O str of Ar-NO_2), 1341, 1169 (S=O str of SO_2NH), 853, 738 (Ar C-H def). HRMS (TOF ES+), m/z, calculated [M + H^+]: 374.1022, found: 374.1068. ^{1}H NMR (300 MHz, DMSO-d_6) δ 12.70 (s, 1H), 8.57 (d, J = 8.9 Hz, 1H), 8.38 (d, J = 8.7 Hz, 2H), 8.00 (d, J = 8.7 Hz, 2H), 7.65 (d, J = 7.5 Hz, 1H), 3.70-3.83 (m, 2H), 2.08-2.03 (m, 2H), 1.93-1.59 (m, 2H), 0.98 (dd, J = 6.5, 2.3 Hz, 6H). ^{13}C NMR (75 MHz, DMSO-d_6) δ 172.29, 169.77, 149.39, 146.80, 128.10, 124.33, 55.41, 40.35, 31.09, 27.92, 22.36.

5.4.2.5. (R)-5-(butylamino)-2-(4-nitrophenylsulfonamido)-5-oxopentanoic acid (3e)

Using the procedure of synthesis of 3a, starting materials 2a and n-butyl amine gave 3e as a white solid resulting in 88.62% yield (1.09g, 0.0028 mol) with uncorrected melting point 205-206 °C. The crude compound 3e was recrystallized by an ethanol/ water mixture (70% ethanol and 30% water). The final product was characterized by FT-IR, HRMS, ^{1}H NMR, and ^{13}C NMR analysis. These analytical data are given below:

FT-IR (cm^{-1}): 3386 (NH str of SO_2NH), 3261, 3112 (NH str of CONH), 2955, 2924 (Ar CH str), 2869 (ali CH str), 1709 (C=O str of COOH), 1520 (N=O str of Ar-NO_2), 1341, 1169 (S=O str of SO_2NH), 853, 737 (Ar C-H def). HRMS (TOF ES+), m/z, calculated [M + H^+]: 388.1178, found: 388.1180. ^{1}H NMR (400 MHz, DMSO-d_6) δ 12.70 (s, 1H), 8.57 (d, J = 8.8 Hz, 1H), 8.38 (d, J = 8.9 Hz, 2H), 8.01 (d, J = 8.9 Hz, 2H), 7.72 (t, J = 5.5 Hz, 1H), 3.80 (dt, J = 8.7, 4.4 Hz, 1H), 2.97 (qd, J = 6.8, 2.8 Hz, 2H), 2.08 (t, J = 8.0 Hz, 2H), 1.94 - 1.84 (m, 1H), 1.71 - 1.62 (m, 1H), 1.27 (dq, J = 32.3, 7.5 Hz, 4H), 0.87 - 0.83 (m, 3H). ^{13}C NMR (101 MHz, DMSO-d_6) δ 172.03, 170.32, 149.15, 146.56, 127.83, 124.06, 55.14, 37.88, 30.92, 30.73, 27.65, 19.29, 13.38.

5.4.2.6. (R)-5-(isobutylamino)-2-(4-nitrophenylsulfonamido)-5-oxopentanoic acid (3f)

Following the synthetic procedure of **3a**, starting materials **2a** and *i*-butyl amine resulted in **3f** as a white solid resulting in 82.11% yield (1.01g, 0.0026 mol) with uncorrected melting point 217-

218 °C. The crude compound **3f** was recrystallized by an ethanol/ water mixture (70% ethanol and 30% water). The final product was characterized by FT-IR, HRMS, ^{1}H NMR, and ^{13}C NMR analysis. These analytical data are given below:

FT-IR (cm^{-1}): 3385 (NH str of SO_2NH), 3263, 3104 (NH str of CONH), 2955, 2916 (Ar CH str), 2869 (ali CH str), 1709 (C=O str of COOH), 1520 (N=O str of Ar-NO_2), 1341, 1169 (S=O str of SO_2NH), 853, 737 (Ar C-H def). HRMS (TOF ES+), m/z, calculated [M + Na^+]: 410.0998, found: 410.0998. ^{1}H NMR (300 MHz, DMSO-d_6) δ 12.73 (s, 1H), 8.59 (s, 1H), 8.39 (d, *J* = 8.9 Hz, 2H), 8.02 (d, *J* = 9.0 Hz, 2H), 7.77 (t, *J* = 5.7 Hz, 1H), 3.85-3.76 (m, 1H), 2.86-2.77 (m, 2H), 2.11 (t, *J* = 7.6 Hz, 2H), 1.97-1.83 (m, 1H), 1.73-1.56 (m, 2H), 0.80 (d, *J* = 6.7 Hz, 6H). ^{13}C NMR (75 MHz, DMSO-d_6) δ 172.30, 170.75, 149.38, 146.78, 128.11, 124.33, 55.46, 46.03, 31.02, 28.03, 20.10.

5.4.2.7. (R)-2-(4-nitrophenylsulfonamido)-5-oxo-5-(pentylamino)pentanoic acid (3g)

Using the procedure of synthesis of **3a**, starting materials **2a** and *n*-pentyl amine gave **3g** as a light yellow solid resulting in 86.61% yield (1.10g, 0.0027 mol) with an uncorrected melting point of 184-185 °C. The crude compound **3g** was recrystallized by an ethanol/ water mixture (70% ethanol and 30% water). The final product was characterized by FT-IR, HRMS, ^{1}H NMR, and ^{13}C NMR analysis. These analytical data are given below:

FT-IR (cm^{-1}): 3380 (NH str of SO_2NH), 3275, 3105 (NH str of CONH), 3055, 3024 (Ar CH str), 2902, 2775 (ali CH str), 1706 (C=O str of COOH), 1521 (N=O str of Ar-NO_2), 1341, 1169 (S=O str of SO_2NH), 853, 737 (Ar C-H def). HRMS (TOF ES+), m/z, calculated [M + H^+]: 402.1335, found: 402.2332. ^{1}H NMR (400 MHz, DMSO-d_6) δ 12.70 (s, 1H), 8.57 (d, J = 8.8 Hz, 1H), 8.38 (d, J = 8.8 Hz, 2H), 8.01 (d, J = 8.8 Hz, 2H), 7.72 (t, J = 5.5 Hz, 1H), 3.86 – 3.74 (m, 1H), 2.96 (qd, J = 7.0, 3.4 Hz, 2H), 2.08 (t, J = 7.8 Hz, 2H), 1.78 (dtd, J = 92.0, 15.1, 14.4, 7.5 Hz, 2H), 1.40 – 1.11 (m, 6H), 0.85 (t, J = 7.0 Hz, 3H). ^{13}C NMR (101 MHz, DMSO-d_6) δ 172.23, 170.52, 149.36, 146.77, 128.04, 124.27, 55.35, 38.39, 30.95, 28.68, 28.55, 27.86, 21.76, 13.84.

5.4.2.8. (R)-5-(benzylamino)-2-(4-nitrophenylsulfonamido)-5-oxopentanoic acid (3h)

Following the synthetic procedure of **3a**, starting materials **2a** and benzylamine resulted in **3h** as a light yellow solid resulting in 88.80% yield (1.19g, 0.0028 mol) with uncorrected melting point 208-209 °C. The crude compound **3h** was recrystallized by an ethanol/ water mixture (70%

ethanol and 30% water). The final product was characterized by FT-IR, HRMS, ^{1}H NMR, ^{13}C NMR, and HPLC analysis. These analytical data are given below:

FT-IR (cm^{-1}): 3407, 3371 (NH str of SO_2NH), 3268, 3110 (NH str of CONH), 3028 (Ar CH str), 2896, 2834 (ali CH str), 1703 (C=O str of COOH), 1526 (N=O str of Ar-NO_2), 1341, 1160 (S=O str of SO_2NH), 853, 745 (Ar C-H def). HRMS (TOF ES+), m/z, calculated [M + H^+]: 422.1022, found: 422.1027. ^{1}H NMR (300 MHz, DMSO-d_6) δ 12.74 (s, 1H), 8.58 (s, 1H), 8.37 (d, *J* = 8.9 Hz, 2H), 8.31 (t, *J* = 5.9 Hz, 1H), 8.01 (d, *J* = 8.6 Hz, 2H), 7.34 – 7.18 (m, 5H), 4.21 (d, *J* = 7.0 Hz, 2H), 3.83 (s, 1H), 2.18 (t, *J* = 7.5 Hz, 2H), 2.03 – 1.62 (m, 2H). ^{13}C NMR (75 MHz, DMSO-d_6) δ 172.30, 170.87, 149.41, 146.79, 139.53, 128.26, 128.11, 127.17, 126.72, 124.34, 55.43, 42.05, 30.99, 27.92. HPLC analysis: retention time = 4.72 min, peak area = 100%, theoretical plates = 10236, asymmetry = 1.12, MP> buffer: ACN = 50:50(isocratic), fr = 1 ml/min, load = 20 µl, column oven tempt = 35°c, UV detection = 265 nm, total run time = 10 min.

5.4.2.9. (R)-5-amino-2-(4-methylphenylsulfonamido)-5-oxopentanoic acid (3a')

The crude compound **3a′** was recrystallized by an isopropyl alcohol (IPA)/ water mixture (70% IPA and 30% water). The resulting compound (**3a′**) was found as white solid with 79.72% yield (0.845g, 0.0028 mol) and the melting point was recorded as 149-150 °C (uncorrected). The final product was characterized by FT-IR, HRMS, ^{1}H NMR, and ^{13}C NMR analysis. These analytical data are given below:

FT-IR (cm^{-1}): 3444, 3331 (NH str of SO_2NH), 3286, (NH str of CONH), 3241, 3213 (Ar CH str), 2951 (ali CH str), 1683 (C=O str of COOH), 1331, 1165 (S=O str of SO_2NH), 862, 815, 686 (Ar C-H def). HRMS (TOF ES+), m/z, calculated [M + Na^+]: 323.0678, found: 323.0302. ^{1}H NMR (300 MHz, DMSO-d_6) δ 8.05 (d, *J* = 8.5 Hz, 1H), 7.64 (d, *J* = 8.1 Hz, 2H), 7.34 (d, *J* = 8.1 Hz, 2H), 7.26 (s, 1H), 6.75 (s, 1H), 3.68 (q, *J* = 7.9 Hz, 2H), 2.36 (s, 3H), 2.07 (t, *J* = 7.6 Hz, 2H), 1.58-1.88 (m, 2H). ^{13}C NMR (75 MHz, DMSO-d_6) δ 173.24, 172.63, 142.51, 138.33, 129.45, 126.55, 55.30, 30.85, 28.00, 21.04.

5.4.2.10. (R)-5-(methylamino)-2-(4-methylphenylsulfonamido)-5-oxopentanoic acid (3b')

Following the procedure of synthesis of **3a′**, starting materials **2a′** and 40% methyl amine gave **3b′** as a white solid resulting 80.18% yield (0.890g, 0.0028 mol) with an uncorrected melting point of 159-160 °C. The crude compound **3b′** was recrystallized by an ethanol/ water mixture

(70% ethanol and 30% water). The final product was characterized by FT-IR, HRMS, ^{1}H NMR, ^{13}C NMR, and HPLC analysis. These analytical data are given below:

FT-IR (cm^{-1}): 3390 (NH str of SO_2NH), 3261, (NH str of CONH), 2924 (Ar CH str), 2859, 2775 (ali CH str), 1724 (C=O str of COOH), 1331, 1163 (S=O str of SO_2NH), 817, 686 (Ar C-H def). HRMS (TOF ES+), m/z, calculated [M + Na^+]: 337.0834, found: 337.2608. ^{1}H NMR (300 MHz, DMSO-d_6) δ 12.63 (s, 1H), 8.07 (d, *J* = 8.7 Hz, 1H), 7.69 (d, *J* = 4.4 Hz, 1H), 7.65 (d, *J* = 8.2 Hz, 2H), 7.35 (d, *J* = 8.1 Hz, 2H), 3.68 (q, *J* = 8.4 Hz, 1H), 2.52 (d, *J* = 4.5 Hz, 3H), 2.37 (s, 3H), 2.07 (t, *J* = 7.6 Hz, 2H), 1.60-1.91 (m, 2H). ^{13}C NMR (75 MHz, DMSO-d_6) δ 172.58, 171.29, 142.43, 138.29, 129.39, 126.51, 55.21, 31.01, 28.08, 25.47, 21.00. HPLC analysis: retention time = 2.79 min, peak area = 100%, theoretical plates = 9230, asymmetry = 1.12, MP> buffer: ACN = 50:50 (isocratic), fr = 1 ml/min, load = 20 µl, column oven tempt = 35°C, UV detection = 228 nm, total run time = 10 min.

5.4.2.11. (R)-5-(ethylamino)-2-(4-methylphenylsulfonamido)-5-oxopentanoic acid (3c')

Following the synthetic procedure of **3a′**, starting materials **2a′** and ethyl amine reacted to give **3c′** as a white solid resulting 80.17% yield (0.930g, 0.0028 mol) with an uncorrected melting point of 157-158 °C. The crude compound **3c′** was recrystallized by an ethanol/ water mixture (70% ethanol and 30% water). The final product was characterized by FT-IR, HRMS, ^{1}H NMR, and ^{13}C NMR analysis. These analytical data are given below:

FT-IR (cm^{-1}): 3380 (NH str of SO_2NH), 3260, 3068 (NH str of CONH), 2974, 2934 (Ar CH str), 2875 (ali CH str), 1710 (C=O str of COOH), 1323, 1160 (S=O str of SO_2NH), 817, 700 (Ar C-H def). HRMS (TOF ES+), m/z, calculated [M + Na^+]: 351.0991, found: 351.0001. ^{1}H NMR (300 MHz, DMSO-d_6) δ 12.63 (s, 1H), 8.06 (d, *J* = 8.7 Hz, 1H), 7.75 (t, *J* = 5.1 Hz, 1H), 7.64 (d, *J* = 8.1 Hz, 2H), 7.34 (d, *J* = 8.1 Hz, 2H), 3.67 (q, *J* = 8.2 Hz, 1H), 3.00 (p, *J* = 7.0 Hz, 2H), 2.36 (s, 3H), 2.06 (t, *J* = 7.6 Hz, 2H), 1.75 (ddt, *J* = 57.2, 13.7, 7.3 Hz, 2H), 0.97 (t, *J* = 7.2 Hz, 3H). ^{13}C NMR (75 MHz, DMSO-d_6) δ 172.57, 170.56, 142.42, 138.31, 129.39, 126.50, 55.24, 33.30, 31.15, 28.12, 20.99, 14.68.

5.4.2.12. (R)-5-(isopropylamino)-2-(4-methylphenylsulfonamido)-5-oxopentanoic acid (3d')

Following the synthetic procedure of **3a′**, starting materials **2a′** and *i*-propyl amine gave **3d′** as a white solid resulting in 81.82% yield (0.99g, 0.0029 mol) with uncorrected melting point 174-175 °C. The crude compound **3d′** was recrystallized by an ethanol/ water mixture (70% ethanol

and 30% water). The final product was characterized by FT-IR, HRMS, ^{1}H NMR, and ^{13}C NMR analysis. These analytical data are given below:

FT-IR (cm^{-1}): 3373 (NH str of SO_2NH), 3256, 3055 (NH str of CONH), 2981, 2929 (Ar CH str), 2865 (ali CH str), 1696 (C=O str of COOH), 1331, 1158 (S=O str of SO_2NH), 812, 696 (Ar C-H def). HRMS (TOF ES+), m/z, calculated [M + Na^+]: 365.1147, found: 365.0786. ^{1}H NMR (300 MHz, DMSO-d_6) δ 12.61 (s, 1H), 8.05 (d, J = 8.7 Hz, 1H), 7.64 (d, J = 8.1 Hz, 3H), 7.34 (d, J = 8.1 Hz, 2H), 3.72 - 3.84 (m, 1H), 3.63 - 3.72 (m, 1H), 2.36 (s, 3H), 2.04 (t, J = 7.6 Hz, 2H), 1.58 – 1.88 (m, 2H), 1.00 (d, J = 6.6 Hz, 6H). ^{13}C NMR (75 MHz, DMSO-d_6) δ 172.56, 169.89, 142.41, 138.32, 129.38, 126.50, 55.27, 40.35, 31.26, 28.18, 22.37, 20.98.

5.4.2.13. (R)-5-(butylamino)-2-(4-methylphenylsulfonamido)-5-oxopentanoic acid (3e')

Following the synthetic procedure of **3a′**, starting materials **2a′** and *n*-butyl amine gave **3e′** as a white solid resulting in 84.13% yield (1.06g, 0.003 mol) with uncorrected melting point 173-174 °C. The crude compound **3e′** was recrystallized by an ethanol/ water mixture (70% ethanol and 30% water). The final product was characterized by FT-IR, HRMS, ^{1}H NMR, and ^{13}C NMR analysis. These analytical data are given below:

FT-IR (cm^{-1}): 3380 (NH str of SO_2NH), 3252, 3065 (NH str of CONH), 2965, 2929 (Ar CH str), 2865 (ali CH str), 1710 (C=O str of COOH), 1336, 1160 (S=O str of SO_2NH), 813, 700 (Ar C-H def). HRMS (TOF ES+), m/z, calculated [M + Na^+]: 379.1304, found: 379.1194. ^{1}H NMR (300 MHz, DMSO-d_6) δ 12.61 (s, 1H), 8.05 (d, J = 8.7 Hz, H), 7.72 (t, J = 5.4 Hz, H), 7.64 (d, J = 8.1 Hz, 2H), 7.34 (d, J = 8.1 Hz, 2H), 3.67 (q, J = 8.4 Hz, 1H), 2.98 (q, J = 6.4 Hz, 2H), 2.36 (s, 3H), 2.06 (t, J = 7.6 Hz, 2H), 1.59 - 1.89 (m, 2H), 1.18 - 1.38 (m, 2H), 0.85 (t, J = 7.1 Hz, 3H). ^{13}C NMR (75 MHz, DMSO-d_6) δ 172.57, 170.71, 142.41, 138.32, 129.38, 126.50, 55.26, 38.14, 31.19 (d, J = 1.5 Hz), 28.20, 20.99, 19.56, 13.68.

5.4.2.14. (R)-5-(isobutylamino)-2-(4-methylphenylsulfonamido)-5-oxopentanoic acid (3f')

Following the synthetic procedure of **3a′**, starting materials **2a′** and *i*-butyl amine gave **3f′** as a white solid resulting 80.16% yield (1.01g, 0.0028 mol) with uncorrected melting point 184-185 °C. The crude compound **3f′** was recrystallized by an ethanol/ water mixture (70% ethanol and 30% water). The final product was characterized by FT-IR, HRMS, ^{1}H NMR, ^{13}C NMR, and HPLC analysis. These analytical data are given below:

FT-IR (cm^{-1}): 3376 (NH str of SO_2NH), 3266, 3057 (NH str of CONH), 2957, 2917 (Ar CH str), 2862 (ali CH str), 1710 (C=O str of COOH), 1341, 1162 (S=O str of SO_2NH), 813, 693 (Ar C-H def). HRMS (TOF ES+), m/z, calculated [M + H^+]: 357.1484, found: 357.1484. ^{1}H NMR (300 MHz, DMSO-d_6) δ 12.61 (s, 1H), 8.06 (d, *J* = 8.7 Hz, 1H), 7.76 (t, *J* = 5.6 Hz, 1H), 7.64 (d, *J* = 8.1 Hz, 2H), 7.34 (d, *J* = 8.1 Hz, 2H), 3.62 - 3.74 (m, 1H), 2.82 (t, *J* = 6.3 Hz, 2H), 2.36 (s, 3H), 2.09 (t, *J* = 7.6 Hz, 2H), 1.56 - 1.90 (m, 3H), 0.80 (d, *J* = 6.7 Hz, 6H). ^{13}C NMR (75 MHz, DMSO-d_6) δ 172.55, 170.86, 142.41, 138.32, 129.38, 126.50, 55.28, 46.02, 31.20, 28.27, 28.03, 20.98, 20.11. HPLC analysis: retention time = 2.84 min, peak area = 100%, theoretical plates = 6323, asymmetry = 1.04, MP> buffer: ACN = 50:50 (isocratic), fr = 1 ml/min, load= 20 µl, column oven temp = 35°C, UV detection=228 nm, total run time =10 min.

5.4.2.15. (R)-2-(4-methylphenylsulfonamido)-5-oxo-5-(pentylamino)pentanoic acid (3g')

Following the synthetic procedure of **3a′**, starting materials **2a′** and *n*-pintyl amine gave **3g′** as a white solid resulting in 84.16% yield (1.11g, 0.003 mol) with uncorrected melting point 163-164 °C. The crude compound **3g′** was recrystallized by an ethanol/ water mixture (70% ethanol and 30% water). The final product was characterized by FT-IR, HRMS, ^{1}H NMR, and ^{13}C NMR analysis. These analytical data are given below:

FT-IR (cm^{-1}): 3366 (NH str of SO_2NH), 3256 (NH str of CONH), 2957, 2927 (Ar CH str), 2858 (ali CH str), 1701 (C=O str of COOH), 1322, 1162 (S=O str of SO_2NH), 815, 693 (Ar C-H def). HRMS (TOF ES+), m/z, calculated [M + H^+]: 371.1641, found: 371.0670. ^{1}H NMR (400 MHz, DMSO-d_6) δ 12.60 (s, 1H), 8.01 (d, J = 7.9 Hz, 1H), 7.71 (t, J = 5.1 Hz, 1H), 7.64 (d, J = 7.7 Hz, 2H), 7.34 (d, J = 7.9 Hz, 2H), 3.66 (d, J = 5.6 Hz, 1H), 2.97 (q, J = 6.6 Hz, 2H), 2.36 (s, 3H), 2.06 (t, J = 7.6 Hz, 2H), 1.74 (ddt, J = 64.1, 13.9, 6.9 Hz, 2H), 1.35 (p, J = 7.1 Hz, 2H), 1.29 - 1.18 (m, 4H), 0.85 (t, J = 6.8 Hz, 3H). ^{13}C NMR (101 MHz, DMSO-d_6) δ 172.62, 170.84, 142.51, 138.48, 129.48, 126.61, 55.41, 38.56, 31.33, 28.85, 28.71, 28.33, 21.93, 21.08, 14.00.

5.4.2.16. (R)-5-(benzylamino)-2-(4-methylphenylsulfonamido)-5-oxopentanoic acid (3h')

Following the synthetic procedure of **3a′**, starting materials **2a′** and benzyl amine gave **3h′** as a white solid resulting 80.17% yield (1.18g, 0.003 mol) with an uncorrected melting point of 193-194 °C. The crude compound **3h′** was recrystallized by an ethanol/ water mixture (70% ethanol and 30% water). The final product was characterized by FT-IR, HRMS, ^{1}H NMR, ^{13}C NMR, and HPLC analysis. These analytical data are given below:

FT-IR (KBr, cm^{-1}): 3371 (NH str of SO_2NH), 3256 (NH str of CONH), 2948 (Ar CH str), 2908, 2854 (ali CH str), 1709 (C=O str of COOH), 1341, 1160 (S=O str of SO_2NH), 815, 721 (Ar C-H def). HRMS (TOF ES+), m/z, calculated [M + H^+]: 391.1328, found: 391.1326. ^{1}H NMR (300 MHz, DMSO-d_6) δ 12.64 (s, 1H), 8.31 (t, J = 5.9 Hz, 1H), 8.07 (d, J = 8.8 Hz, 1H), 7.64 (d, J = 8.3 Hz, 2H), 7.34 (d, J = 8.0 Hz, 2H), 7.30 (d, J = 6.8 Hz, 2H), 7.24 (d, J = 4.1 Hz, 2H), 7.21 (s, 1H), 4.22 (d, J = 5.9 Hz, 2H), 3.71 (td, J = 8.6, 5.5 Hz, 1H), 2.36 (s, 3H), 2.17 (t, J = 7.7 Hz, 2H), 1.79 (ddt, J = 50.6, 13.9, 7.1 Hz, 2H). ^{13}C NMR (75 MHz, DMSO-d_6) δ 173.03, 171.42, 142.89, 140.02, 138.78, 129.86, 128.72, 127.62, 127.16, 126.97, 55.68, 42.48, 31.56, 28.59, 21.46. HPLC analysis: retention time = 4.69 min, peak area = 100%, theoretical plates = 12839, asymmetry = 1.12, MP> buffer: ACN = 50:50 (isocratic), fr = 1 ml/min, load= 20 µl, column oven temp = 35°C, UV detection=227 nm, total run time =10 min.

5.4.2.17. (R)-2-(4-methylphenylsulfonamido)-5-oxo-5-(propylamino)pentanoic acid (3i')

Following the synthetic procedure of **3a′**, starting materials **2a′** and propyl amine gave **3i′** as a white solid resulting 61.62% yield with an uncorrected melting point of 145-146 °C. The crude compound **3i′** was recrystallized by an ethanol/ water mixture (70% ethanol and 30% water). The final product was characterized by HRMS, ^{1}H NMR, and ^{13}C NMR analysis. These analytical data are given below:

HRMS (TOF ES+), m/z, calculated [M + Na^+]: 365.1147, found: 365.0122. ^{1}H NMR (400 MHz, DMSO-d_6) δ 8.04 (d, J = 8.9 Hz, 1H), 7.75 (t, J = 5.6 Hz, 1H), 7.64 (d, J = 8.4 Hz, 2H), 7.35 (d, J = 7.9 Hz, 2H), 3.73 – 3.62 (m, 1H), 2.95 (q, J = 6.8 Hz, 2H), 2.37 (s, 3H), 2.07 (t, J = 7.1 Hz, 2H), 1.91 – 1.75 (m, 1H), 1.71 – 1.59 (m, 1H), 1.37 (h, J = 7.4 Hz, 2H), 0.82 (t, J = 7.4 Hz, 3H). ^{13}C NMR (101 MHz, DMSO-d_6) δ 173.02, 171.23, 142.88, 138.77, 129.85, 126.96, 55.72, 40.74, 31.62, 28.65, 22.79, 21.44, 11.86.

5.4.2.18. (R)-5-(hexylamino)-2-(4-methylphenylsulfonamido)-5-oxopentanoic acid (3j')

Following the synthetic procedure of **3a′**, starting materials **2a′** and *n*-hexyl amine gave **3j′** as a white solid resulting in 85.12% yield with uncorrected melting point 157-158 °C. The crude compound **3j′** was recrystallized by an ethanol/ water mixture (70% ethanol and 30% water).

The final product was characterized by HRMS, ^{1}H NMR, and ^{13}C NMR analysis. These analytical data are given below:

HRMS (TOF ES+), m/z, calculated [M + H^{+}]: 385.1797, found: 385.1533. ^{1}H NMR (400 MHz, DMSO-d_6) δ 12.61 (s, 1H), 8.05 (d, J = 8.8 Hz, 1H), 7.73 (t, J = 5.6 Hz, 1H), 7.64 (d, J = 8.4 Hz, 2H), 7.35 (d, J = 7.8 Hz, 2H), 3.75 – 3.64 (m, 1H), 2.98 (q, J = 6.9 Hz, 2H), 2.37 (s, 3H), 2.07 (t, J = 7.7 Hz, 2H), 1.87 – 1.79 (m, 1H), 1.73 – 1.60 (m, 1H), 1.38 – 1.30 (m, 2H), 1.29 – 1.19 (m, 6H), 0.86 (t, J = 6.88 Hz, 3H). ^{13}C NMR (101 MHz, DMSO-d_6) δ 173.02, 171.16, 142.87, 138.78, 129.84, 126.96, 55.71, 38.93, 31.64, 31.46, 29.49, 28.65, 26.53, 22.52, 21.44, 14.39.

5.4.2.19. (R)-5-(cyclohexylamino)-2-(4-methylphenylsulfonamido)-5-oxopentanoic acid (3k')

Following the synthetic procedure of **3a′**, starting materials **2a′** and *c*-hexyl amine gave **3k′** as a white solid resulting in 88.14% yield with uncorrected melting point 198-199 °C. The crude compound **3k′** was recrystallized by an ethanol/ water mixture (70% ethanol and 30% water). The final product was characterized by HRMS, ^{1}H NMR, and ^{13}C NMR analysis. These analytical data are given below:

HRMS (TOF ES+), m/z, calculated [M + H^{+}]: 383.1641, found: 383.0220. ^{1}H NMR (400 MHz, DMSO-d_6) δ 12.60 (s, 1H), 8.05 (d, *J* = 8.8 Hz, 1H), 7.64 (d, *J* = 8.4 Hz, 3H), 7.35 (d, *J* = 7.8 Hz, 2H), 3.73 – 3.64 (m, 1H), 3.51 – 3.42 (m, 1H), 2.37 (s, 3H), 2.06 (t, *J* = 7.7 Hz, 2H), 1.87 – 1.78 (m, 1H), 1.73 – 1.59 (m, 5H), 1.56 – 1.48 (m, 1H), 1.29 – 1.18 (m, 2H), 1.15 – 1.03 (m, 3H). ^{13}C NMR (101 MHz, DMSO-d_6) δ 173.03, 170.34, 142.88, 138.78, 129.86, 126.96, 55.72, 47.82, 32.89, 31.72, 28.67, 25.71, 25.05, 21.44.

5.4.2.20. (R)-2-(4-methylphenylsulfonamido)-5-oxo-5-(phenylamino)pentanoic acid (3l')

Following the synthetic procedure of **3a′**, starting materials **2a′** and *c*-hexyl amine gave **3l′** as a white solid resulting in 85.71% yield with uncorrected melting point 205-206 °C. The crude compound **3k′** was recrystallized by an ethanol/ water mixture (70% ethanol and 30% water). The final product was characterized by HRMS, ^{1}H NMR, and ^{13}C NMR analysis. These analytical data are given below:

HRMS (TOF ES+), m/z, calculated [M + H^+]: 399.0991, found: 399.0976. ^{1}H NMR (400 MHz, DMSO-d_6) δ 12.67 (s, 1H), 9.86 (s, 1H), 8.10 (d, J = 8.9 Hz, 1H), 7.65 (d, J = 8.4 Hz, 2H), 7.55 (d, J = 7.5 Hz, 2H), 7.29 (dd, J = 15.9, 8.6 Hz, 4H), 7.02 (t, J = 7.4 Hz, 1H), 3.78 – 3.72 (m, 1H), 2.36 (t, J = 7.5 Hz, 2H), 2.31 (s, 3H), 2.00 – 1.92 (m, 1H), 1.77 – 1.68 (m, 1H). ^{13}C NMR (101 MHz, DMSO-d_6) δ 173.11, 170.39, 142.91, 139.69, 138.69, 129.86, 129.09, 126.96, 123.41, 119.48, 55.47, 32.38, 28.11, 21.39.

5.4.2.21. (R)-N^1-hydroxy-2-(4-methylphenylsulfonamido)pentanediamide (5a')

5a′ was prepared following the procedure of synthesis mentioned in **Chapter 4** (**Scheme 4.2**), with starting materials **4a′**. The crude compound **5a′** was purified with hot ethanol and water mixture (70% ethanol and 30% water) and obtained as a white amorphous powder with 54.83% yield and the melting point was recorded as 136-137 °C (uncorrected). The final product was characterized by HRMS, ^{1}HNMR, and ^{13}CNMR analysis. These analytical data are given below:

HRMS (TOF ES+), m/z, calculated [M + K^+]: 354.0625, found: 354.0667. ^{1}H NMR (300 MHz, DMSO-d_6) δ 9.97 (s, 1H), 8.23 (s, 1H), 7.73 - 7.63 (m, 2H), 7.37 - 7.34 (m, 2H), 4.40 - 4.34 (m, 1H), 2.83 - 2.71 (m, 2H), 2.61 - 2.48 (m, 2H), 2.48 - 2.36 (m, 3H), 2.36 – 1.77 (2H), 1.22 (s, 1H). ^{13}C NMR (75 MHz, DMSO-d_6) δ 168.53, 168.26, 142.96, 139.60, 129.90, 126.92, 53.99, 30.43, 25.43, 21.43.

5.4.2.22. (R)-N^1-hydroxy-N^5-methyl-2-(4-methylphenylsulfonamido)pentanediamide (5b')

Following the procedure of synthesis of **5a′**, starting materials **4b′** (**Chapter 4; Scheme 4.2**) **5b′** was obtained. The crude compound **5b′** was purified with hot ethanol and water mixture (70% ethanol and 30% water) and obtained as white amorphous powder resulting 60.82% yield with an uncorrected melting point of 144-145 °C. The final product was characterized by HRMS, ^{1}H NMR, and ^{13}C NMR analysis. These analytical data are given below:

HRMS (TOF ES+), m/z, calculated [M + Na^+]: 352.0943, found: 352.2885. ^{1}H NMR (400 MHz, DMSO-d_6) δ 8.89 (s, 1H), 7.92 - 7.72 (m, 1H), 7.71 (d, J = 8.4 Hz, 2H), 7.68 (s, 1H), 7.40 (d, J = 8.6 Hz, 2H), 3.68 – 3.57 (m, 1H), 2.57 (d, J = 4.7 Hz, 3H), 2.43 (s, 3H), 2.06 – 1.83 (m, 2H), 1.79 – 1.59 (m, 2H). ^{13}C NMR (101 MHz, DMSO-d_6) δ 171.85, 168.64, 142.85, 138.97, 129.88, 126.85, 54.14, 31.67, 29.27, 25.82, 21.46.

5.4.2.23. (R)-N^5-ethyl-N^1-hydroxy-2-(4-methylphenylsulfonamido)pentanediamide (5c')

Following the procedure of synthesis of **5a′**, starting materials **4c′** (**Chapter 4; Scheme 4.2**) **5b′** was obtained. The crude compound **5c′** was purified with hot ethanol and water mixture (70% ethanol and 30% water) and obtained as white amorphous powder resulting 65.71% yield with an uncorrected melting point of 142-143 °C. The final product was characterized by HRMS, ^{1}H NMR, and ^{13}C NMR analysis. These analytical data are given below:

HRMS (TOF ES+), m/z, calculated [M + Na^+]: 366.1100, found: 366.1104. ^{1}H NMR (400 MHz, DMSO-d_6) δ 10.57 (s, 1H), 8.83 (s, 1H), 7.96 (s, 1H), 7.74 (t, J = 5.5 Hz, 1H), 7.66 (d, J = 8.4 Hz, 2H), 7.35 (d, J = 7.9 Hz, 2H), 3.54 (t, J = 6.8 Hz, 1H), 3.03 – 2.96 (m, 2H), 2.38 (s, 3H), 2.04 – 1.86(m, 2H), 1.73 – 1.52 (3, 2H), 0.97 (t, J = 7.3 Hz, 3H). ^{13}C NMR (101 MHz, DMSO-d_6) δ 171.13, 167.44, 142.84, 138.99, 129.88, 126.85, 54.18, 33.76, 31.82, 29.32, 21.46, 15.14.

5.4.2.24. (R)-N^1-hydroxy-N^5-isopropyl-2-(4-methylphenylsulfonamido)pentanediamide (5d')

Following the procedure of synthesis of **5a′**, starting materials **4d′** (**Chapter 4; Scheme 4.2**) **5d′** was obtained. The crude compound **5d′** was purified with hot ethanol and water mixture (70% ethanol and 30% water) and obtained as white amorphous powder resulting 55.83% yield with an uncorrected melting point of 134-135 °C. The final product was characterized by HRMS, ^{1}H NMR, and ^{13}C NMR analysis. These analytical data are given below:

HRMS (TOF ES+), m/z, calculated [M + Na^+]: 380.1256, found: 380.0315. ^{1}H NMR (400 MHz, DMSO-d_6) δ 8.83 (s, 1H), 7.66 (d, J = 8.3 Hz, 3H), 7.35 (d, J = 8.0 Hz, 2H), 3.83 – 3.71 (m, 1H), 3.54 (t, J = 7.2 Hz, 1H), 2.38 (s, 3H), 1.99 – 1.85 (m, 2H), 1.77 – 1.52 (m, 2H), 1.00 (dd, J = 6.6, 1.6 Hz, 6H). ^{13}C NMR (101 MHz, DMSO-d_6) δ 170.48, 167.43, 142.84, 139.01, 129.89, 127.11, 126.84, 54.22, 31.93, 29.38, 22.82, 21.46.

5.4.2.25. (R)-N^5-butyl-N^1-hydroxy-2-(4-methylphenylsulfonamido)pentanediamide (5e')

Following the procedure of synthesis of **5a′**, starting materials **4e′** (**Chapter 4; Scheme 4.2**) **5e′** was obtained. The crude compound **5e′** was purified with hot ethanol and water mixture (70% ethanol and 30% water) and obtained as white amorphous powder resulting 64.82% yield with an uncorrected melting point of 131-132 °C. The final product was characterized by HRMS, ^{1}H NMR, and ^{13}C NMR analysis. These analytical data are given below:

HRMS (TOF ES+), m/z, calculated [M + Na^+]: 394.1413, found: 394.1351. ^{1}H NMR (400 MHz, DMSO-d_6) δ 10.63 (s, 1H), 8.89 (s, 1H), 8.01 (s, 1H), 7.79 – 7.75 (m, 1H), 7.72 (d, *J* = 8.4 Hz, 2H), 7.41 (d, *J* = 7.9 Hz, 2H), 3.64 – 3.56 (m, 1H), 3.08 – 2.99 (m, 2H), 2.44 (s, 3H), 2.12 – 1.93 (m, 2H), 1.83 -1.57 (m, 2H), 1.43 – 1.22 (s, 4H), 0.92 (t, *J* = 7.3 Hz, 3H). ^{13}C NMR (101 MHz, DMSO-d_6) δ 171.29, 167.44, 142.84, 139.01, 129.88, 129.76, 126.84, 126.09, 54.20, 38.59, 31.86, 31.63, 29.41, 21.45, 20.00, 14.13.

5.4.2.26. (R)-N^1-hydroxy-N^5-isobutyl-2-(4-methylphenylsulfonamido)pentanediamide (5f')

Following the procedure of synthesis of **5a′**, starting materials **4f′** (**Chapter 4; Scheme 4.2**) **5f′** was obtained. The crude compound **5f′** was purified with hot ethanol and water mixture (70% ethanol and 30% water) and found as white amorphous powder resulting 60.83% yield with an uncorrected melting point of 138-139 °C. The final product was characterized by HRMS, ^{1}H NMR, and ^{13}C NMR analysis. These analytical data are given below:

HRMS (TOF ES+), m/z, calculated [M + Na^+]: 394.1413, found: 394.1270. ^{1}H NMR (400 MHz, DMSO-d_6) δ 10.50 (s, 1H), 8.76 (s, 1H), 7.88 (s, 1H), 7.68 (t, *J* = 5.8 Hz, 1H), 7.59 (d, *J* = 8.3 Hz, 2H), 7.27 (d, *J* = 8.4 Hz, 2H), 3.47 (s, 1H), 2.78 – 2.69 (m, 2H), 2.30 (s, 3H), 1.98 – 1.82 (m, 2H), 1.66 – 1.45 (m, 3H), 0.73 (d, *J* = 6.72 Hz, 6H). ^{13}C NMR (101 MHz, DMSO-d_6) δ 171.46, 167.43, 142.85, 139.01, 129.89, 126.85, 54.23, 46.47, 31.89, 29.51, 28.46, 21.46, 20.55.

5.4.2.27. (R)-N^1-hydroxy-2-(4-methylphenylsulfonamido)-N^5-pentylpentanediamide (5g')

Following the procedure of synthesis of **5a′**, starting materials **4g′** (**Chapter 4; Scheme 4.2**) **5g′** was obtained. The crude compound **5g′** was purified with hot ethanol and water mixture (70% ethanol and 30% water) and found as white amorphous powder resulting 70.82% yield with an uncorrected melting point of 141-142 °C. The final product was characterized by HRMS, ^{1}H NMR, and ^{13}C NMR analysis. These analytical data are given below:

HRMS (TOF ES+), m/z, calculated [M + Na^+]: 408.1569, found: 408.1653. ^{1}H NMR (400 MHz, DMSO-d_6) δ 10.57 (s, 1H), 8.83 (s, 1H), 7.96 (d, *J* = 8.3 Hz, 1H), 7.77 – 7.69 (m, 1H), 7.66 (d, *J* = 8.4 Hz, 2H), 7.35 (d, *J* = 8.5 Hz, 2H), 3.59 – 3.49 (m, 1H), 3.02 – 2.92 (m, 2H), 2.38 (s, 3H), 2.07 – 1.84 (m, 2H), 1.73 – 1.52 (m, 2H), 1.28 – 1.11 (m, 6H), 0.86 (t, , *J* = 6.9 Hz, 3H). ^{13}C NMR (101 MHz, DMSO-d_6) δ 171.33, 167.48, 142.36, 139.48, 129.80, 126.14, 56.62, 38.94, 31.91, 29.13, 28.95, 26.81, 22.36, 22.28, 21.47, 14.38.

5.4.2.28. (R)-N^5-benzyl-N^1-hydroxy-2-(4-methylphenylsulfonamido)pentanediamide (5h')

Following the procedure of synthesis of **5a′**, starting materials **4h′** (**Chapter 4; Scheme 4.2**) **5h′** was obtained. The crude compound **5h′** was purified with hot ethanol and water mixture (70% ethanol and 30% water) and obtained as a white solid resulting 75.74% yield with an uncorrected melting point of 159-160 °C. The final product was characterized by HRMS, ^{1}H NMR, and ^{13}C NMR analysis. These analytical data are given below:

HRMS (TOF ES+), m/z, calculated [M + Na^+]: 428.1256, found: 428.1148. ^{1}H NMR (400 MHz, DMSO-d_6) δ 10.58 (s, 1H), 8.84 (s, 1H), 8.30 (t, *J* = 6. Hz, 1H), 7.96 (s, 1H), 7.66 (d, *J* = 8.3 Hz, 2H), 7.32 (dd, *J* = 16.4, 7.9 Hz, 4H), 7.27 – 7.19 (m, 3H), 4.22 (d, *J* = 5.9 Hz, 2H), 3.58 – 3.52 (m, 1H), 2.37 (s, 3H), 2.13 – 1.96 (s, 2H), 1.80 – 1.57 (m, 2H). ^{13}C NMR (101 MHz, DMSO-d6) δ 171.52, 167.42, 142.86, 140.02, 139.01, 129.89, 128.72, 127.60, 127.17, 126.85, 54.17, 42.48, 31.81, 29.38, 21.47.

5.4.2.29. (R)-N^1-hydroxy-2-(4-methylphenylsulfonamido)-N^5-propylpentanediamide (5i')

Following the procedure of synthesis of **5a′**, starting materials **4i′** (**Chapter 4; Scheme 4.2**) **5i′** was obtained. The crude compound **5i′** was purified with hot ethanol and water mixture (70% ethanol and 30% water) and found as a white solid resulting 56.84% yield with an uncorrected melting point of 125-126 °C. The final product was characterized by HRMS, ^{1}H NMR, and ^{13}C NMR analysis. These analytical data are given below:

HRMS (TOF ES+), m/z, calculated [M + Na^+]: 380.1256, found: 380.1191. ^{1}H NMR (400 MHz, DMSO-d_6) δ 10.57 (s, 1H), 8.83 (s, 1H), 7.96 (d, *J* = 8.4 Hz, 1H), 7.78 – 7.71 (m, 1H), 7.66 (d, *J* = 8.4 Hz, 2H), 7.35 (d, *J* = 7.9 Hz, 2H), 3.54 (q, *J* = 7.3 Hz, 1H), 2.99 – 2.90 (m, 2H), 2.38 (s, 3H), 2.04 – 1.88 (m, 2H), 1.73 – 1.50 (m, 2H), 1.36 (h, *J* = 7.4 Hz, 2H), 0.81 (t, *J* = 7.4 Hz, 3H). ^{13}C NMR (101 MHz, DMSO-d_6) δ 171.33, 167.44, 142.85, 139.00, 129.88, 129.76, 126.85, 54.19, 40.73, 31.85, 29.41, 22.77, 21.46, 11.84.

5.4.2.30. (R)-N^5-hexyl-N^1-hydroxy-2-(4-methylphenylsulfonamido)pentanediamide (5j')

Following the procedure of synthesis of **5a′**, starting materials **4j′** (**Chapter 4; Scheme 4.2**) **5j′** was obtained. The crude compound **5j′** was purified with hot ethanol and water mixture (70% ethanol and 30% water) and found as a white solid resulting 84.79% yield with an uncorrected

melting point of 145-146 °C. The final product was characterized by HRMS, ^{1}H NMR, and ^{13}C NMR analysis. These analytical data are given below:

HRMS (TOF ES+), m/z, calculated [M + Na^+]: 422.1726, found: 422.1845. ^{1}H NMR (400 MHz, DMSO-d_6) δ 10.57 (s, 1H), 8.83 (s, 1H), 7.96 (d, J = 8.3 Hz, 1H), 7.77 – 7.69 (m, 1H), 7.66 (d, J = 8.4 Hz, 2H), 7.35 (d, J = 8.5 Hz, 2H), 3.59 – 3.49 (m, 1H), 3.02 – 2.92 (m, 2H), 2.38 (s, 3H), 2.07 – 1.84 (m, 2H), 1.73 – 1.52 (m, 2H), 1.37 – 1.30 (m, 2H), 1.28 – 1.11 (m, 6H), 0.86 (t, , J = 6.9 Hz, 3H). (101 MHz, DMSO-d_6) δ 171.27, 167.44, 142.83, 139.01, 129.88, 126.85, 54.20, 38.93, 31.86, 31.45, 29.47, 29.41, 26.53, 22.52, 21.46, 14.39.

5.4.2.31. (R)-N^5-cyclohexyl-N^1-hydroxy-2-(4-methylphenylsulfonamido)pentanediamide (5k')

Following the procedure of synthesis of **5a′**, starting materials **4k′** (**Chapter 4; Scheme 4.2**) **5k′** was obtained. The crude compound **5k′** was purified with hot ethanol and water mixture (70% ethanol and 30% water) and found as a white solid resulting 86.78% yield with an uncorrected melting point of 169-170 °C. The final product was characterized by HRMS, ^{1}H NMR, and ^{13}C NMR analysis. These analytical data are given below:

HRMS (TOF ES+), m/z, calculated [M + Na^+]: 420.1569, found: 420.1541. ^{1}H NMR (400 MHz, DMSO-d_6) δ 10.49 (s, 1H), 8.75 (s, 1H), 7.87 (d, J = 8.3 Hz, 1H), 7.58 (d, J = 8.3 Hz, 3H), 7.27 (d, J = 7.9 Hz, 2H), 3.46 (q, J = 7.1 Hz, 1H), 3.42 – 3.32 (m, 1H), 2.30 (s, 3H), 1.93 – 1.80 (m, 2H), 1.66 – 1.53 (m, 5H), 1.52 – 1.41 (m, 2H), 1.21 – 1.10 (m, 2H), 1.08 – 0.94 (m, 3H). ^{13}C NMR (101 MHz, DMSO-d_6) δ 170.45, 167.45, 142.84, 139.00, 129.89, 126.85, 54.21, 47.82, 32.88, 31.92, 29.42, 25.69, 25.05, 21.46.

5.4.2.32. X-ray crystallography of compound 3h'

A quality crystal of compound **3h′** was selected for data collection. The SHELXL-2018/3 program (Usón and Sheldrick, 2018) solved the molecular structure directly and refined it on F^2 by full-matrix least squares. Anisotropic thermal parameters were used to refine non-hydrogen atoms. Every hydrogen atom was positioned in an idealized geometrical configuration, riding on the parent atoms, observed in the Fourier map. The final cycle of the least-squares refinement showed a maximum shift/error of 0.001, indicating successful convergence. Data collection and structure refinement (Sheldrick, 2015) parameters and crystallographic data of the compound **3h'** are given in **Table 5.15**. **CCDC-2345358** contains the supplementary crystallographic data for

this paper. These data can be obtained free from Cambridge Crystallographic Data Centre via www.ccdc.cam.ac.uk/data_request/cif. **Figure 5.35** represents the ORTEP diagram of the asymmetric unit of compound **3h'**.

Table 5.15. Crystal data and refinement parameters of compound **3h'**

Compound	3h'
Formula	$C_{19}H_{22}N_2O_5S$
Formula weight	390.45
Crystal system	monolinic
Space group	$P2_1$
a /Å	10.9110(7)
b /Å	5.1779(4)
c /Å	16.7907(11)
α (°)	90
γ(°)	90
β(°)	93.596(2)
V /Å^3	946.74(11)
Z	2
D_c/g cm^{-3}	1.370
μ/mm^{-1}	0.204
R(int)	0.1109
Unique data	4176
Data with $I > 2\sigma(I)$	2554
R1	0.0781
*w*R2	0.1493
GOF on F^2	1.044

$$R1 = \sum||F_o| - |F_c||/\sum|F_o|,\ wR2 = \{\sum[w(F_o^2 - F_c^2)^2]/\sum w(F_o^2)^2\}^{1/2}$$

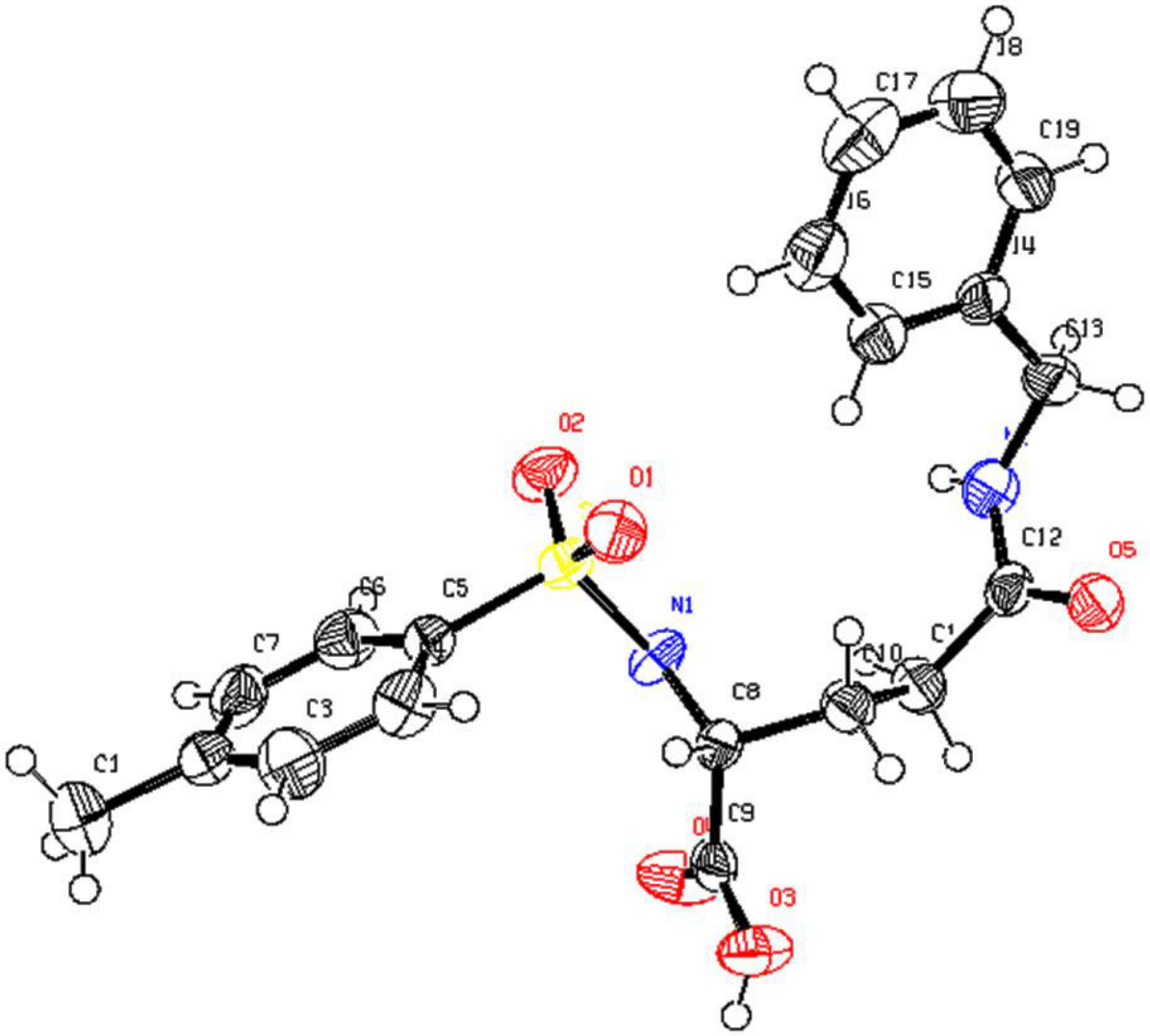

Figure 5.35. Asymmetric unit of compound **3h'** (ORTEP diagram with 30% probability).

5.4.3. Biological screening

5.4.3.1. Cell viability assay

To evaluate the anticancer activity of synthesized analogs, these compounds were tested against various cancer cell lines (K562, A549, U-87MG, and HT1080) in addition to normal human embryonic kidney cell line (HEK-293) (**Table 5.16**). The IC_{50} values of all of these compounds (**3a-3h, 3a′-3l′** and **5a′-5k′**) against normal cell line HEK-293 resulted in over ~100 µM (**Table 5.16**).

Table 5.16. Cell viability profile of synthesized compounds (**3a-3h, 3a′-3l′** and **5a′-5k′**)

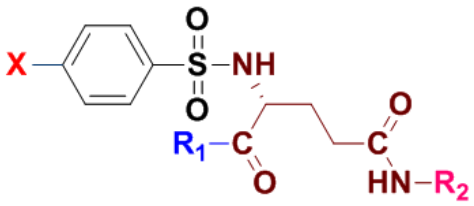

Compound	X	R_1	R_2	IC_{50} (μM)				
				K562	A549	U-87MG	HT1080	HEK-293
3a	$-NO_2$	-OH	-H	9.732	8.991	26.447	20.508	173.049
3b	$-NO_2$	-OH	$-CH_3$	5.691	20.835	20.493	24.413	416.694
3c	$-NO_2$	-OH	$-C_2H_5$	7.769	12.251	16.160	32.866	145.023
3d	$-NO_2$	-OH	$-i-C_3H_7$	11.042	10.569	37.465	43.458	271.384
3e	$-NO_2$	-OH	$-n-C_4H_9$	5.264	18.421	29.007	37.614	368.424
3f	$-NO_2$	-OH	$-i-C_4H_9$	8.068	10.848	38.470	16.224	216.965
3g	$-NO_2$	-OH	$-n-C_5H_{11}$	6.794	12.722	14.179	20.650	254.440
3h	$-NO_2$	-OH	$-CH_2-C_6H_5$	4.919	5.688	17.924	57.462	113.751
3a'	$-CH_3$	-OH	-H	2.279	8.983	19.920	18.312	278.754
3b'	$-CH_3$	-OH	$-CH_3$	2.379	5.140	28.896	25.180	202.793
3c'	$-CH_3$	-OH	$-C_2H_5$	2.549	4.824	32.308	16.515	491.161
3d'	$-CH_3$	-OH	$-i-C_3H_7$	4.245	17.336	20.307	19.495	346.714
3e'	$-CH_3$	-OH	$-n-C_4H_9$	3.751	19.544	16.793	25.891	391.087
3f'	$-CH_3$	-OH	$-i-C_4H_9$	2.354	32.233	26.273	39.202	644.676
3g'	$-CH_3$	-OH	$-n-C_5H_{11}$	8.374	14.448	33.109	27.633	408.323
3h'	$-CH_3$	-OH	$-CH_2-C_6H_5$	1.992	3.576	17.533	19.672	292.731
3i'	$-CH_3$	-OH	$-n-C_3H_7$	9.435	14.573	21.098	56.822	291.453
3j'	$-CH_3$	-OH	$-n-C_6H_{13}$	7.984	13.717	18.271	22.469	274.347
3k'	$-CH_3$	-OH	$-c-C_6H_{11}$	7.447	127.147	14.860	43.600	542.926
3l'	$-CH_3$	-OH	$-C_6H_5$	5.795	15.012	14.425	25.975	300.248
5a'	$-CH_3$	-NHOH	-H	13.691	38.544	10.382	33.623	770.888
5b'	$-CH_3$	-NHOH	$-CH_3$	10.740	29.967	18.202	16.749	599.348
5c'	$-CH_3$	-NHOH	$-C_2H_5$	8.866	20.557	13.535	13.962	411.148
5d'	$-CH_3$	-NHOH	$-i-C_3H_7$	12.470	19.733	35.102	38.729	394.668
5e'	$-CH_3$	-NHOH	$-n-C_4H_9$	5.575	33.658	9.029	20.718	673.155
5f'	$-CH_3$	-NHOH	$-i-C_4H_9$	9.709	36.840	40.460	22.956	736.792
5g'	$-CH_3$	-NHOH	$-n-C_5H_{11}$	8.009	25.803	28.397	24.289	516.059
5h'	$-CH_3$	-NHOH	$-CH_2-C_6H_5$	1.408	55.267	12.737	19.206	1105.341
5i'	$-CH_3$	-NHOH	$-n-C_3H_7$	9.514	20.767	30.271	17.565	415.332
5j'	$-CH_3$	-NHOH	$-n-C_6H_{13}$	8.086	16.018	20.987	36.081	320.352
5k'	$-CH_3$	-NHOH	$-c-C_6H_{11}$	4.064	16.517	44.205	28.397	330.358
NNGH	-	-	-	4.773	13.517	-	-	-

Regarding the cytotoxic activity in cancer cell lines (K562, A549, U-87MG, and HT1080), all of these compounds (**3a-3h, 3a′-3l′** and **5a′-5k′**) were found active. Among the cancer cell lines tested, all the synthesized compounds (**3a-3h, 3a′-3l′** and **5a′-5k′**) resulted in better cytotoxicity in K562 (except compounds **3a, 3d, 3i′, 5a′, 5d′,** and **5i′**) in comparison with other cancer cell lines (A549, U-87MG, and HT1080) (**Table 5.16**). Compound **3a** and compound **3d** showed better results against the A549 cell line than other cancer cell lines (U-87MG, and HT1080). Overall, all the synthesized compounds (**3a-3h, 3a′-3l′** and **5a′-5k′**) showed a better cytotoxicity profile against chronic myeloid leukemia cell line K562 compared to other solid tumor cell lines namely A549, U-87MG, and HT1080 (**Table 5.16**). It was also interesting to observe that all these *D*(-)glutamine derivatives exhibited several-fold selectivity towards cancer cell lines compared to their cytotoxicity in normal cell lines HEK-293. Moreover, these compounds exerted maximum selectivity toward K562 compared to HEK-293. Among compounds having carboxylic acid function (**3a-3h** and **3a′-3h′**), *p*-tosyl-*D*-glutamine derivatives (**3a′-3h′**) resulted in a better cytotoxicity profile against K562 in comparison with *p*-nitrophenyl sulfonyl-*D*-glutamine derivatives (**3a-3h**) (**Table 5.16**). Regarding the K562 inhibition, it was noticed that compounds having carboxylic acid function (**3a-3h** and **3a′-3h′**), almost all of the *p*-tosyl derivatives (**3a′-3h′**) exerted better inhibition than the respective *p*-nitro analogs (**3a** vs **3a'**; **3b** vs **3b'**; **3c** vs **3c'**; **3d** vs **3d'**; **3e** vs **3e'**; **3f** vs **3f'**; **3h** vs **3h'**) (**Table 5.16**). Only the *p*-nitro derivative with *n*-pentyl substitution (**3g**) exhibited comparatively better K562 inhibitory efficacy than the corresponding *p*-tosyl derivative with *n*-pentyl substitution (**3g'**). In the case of carboxylic acid function bearing *p*-nitrophenyl sulfonyl-*D*-glutamine derivatives (**3a-3h**), compound **3h** was found to be the best active compound against CML cell line with an IC_{50} value of 4.919 µM whereas, in the case of *p*-tosyl-*D*-glutamine derivatives having carboxylic acid function in their structure (**3a′-3h′**), compound **3h′** is the best active compound with IC_{50} value of 1.992 µM against K562 cell line (**Table 5.16**). Overall, among *p*-tosyl-*D*-glutamine derivatives (**3a′-3l′** and **5a′-5k′**), carboxylic acid function bearing *p*-nitrophenyl sulfonyl-*D*-glutamine derivatives (**3a′-3g′, 3i′** and **3j′**) showed better activity in comparison with their respective analog containing hydroxamic acid function (**5a′-5g′, 5i′** and **5j′**) except compounds contain benzyl/*c*-hexyl group (**3h′/3k′** and **5h′/5k′**) (**Table 5.16).** Compounds having a hydroxamic acid function and benzyl/*c*-hexyl group in their structure (**5h′** and **5k′**) showed better activity in comparison with their respective analogs containing a carboxylic acid group in their

structure ((**3h′** and **3k′**) (**Table 5.16**). Overall, among *p*-tosyl-*D*-glutamine derivatives (**3a′-3l′** and **5a′-5k′**), compound **3h′** is the best active compound with IC_{50} value of 1.408 µM against K562 cell line (**Table 5.16**). For further *in vitro* cell culture-based biological investigation in the case of CML, compound **3h** has been considered as the representative lead molecule among *p*-nitrophenyl sulfonyl-*D*-glutamine derivatives (**3a-3h**). In case of *p*-tosyl-*D*-glutamine derivatives (**3a′-3l′** and **5a′-5k′**), compound **3h′** has been considered as the representative lead molecule among carboxylic group containing analogs (**3a′-3l′**) whereas, compounds **5k′** and **5h′** are the representative lead of hydroxamic acid group containing analogs (**5a′-5k′**) for further *in vitro* cell culture-based biological investigation in the case of CML N-isobutyl-N-(4-methoxyphenyl sulfonyl) glycyl hydroxamic acid (**NNGH**) was used as a reference compound for cell viability assay. Interestingly, compounds **3h**, **3a', 3b', 3c', 3d', 3e', 3f', 3h', 5h',** and **5k'** exerted greater cytotoxic potential compared to the reference **NNGH** for K562 cell line.

5.4.3.2. Matrix metalloproteinase (MMP) inhibition assay

The best antileukemic compounds were further subjected to gelatinase (MMP2 and MMP9) inhibitory efficacy as well as other medium size S_1' pocket containing matrix metalloproteinases (MMP8 and MMP12) to judge both the potency and selectivity (**Table 5.17**).

Table 5.17. Gelatinase (MMP2, and MMP9), MMP8 and MMP12 inhibitory efficacy of best antileukemic compounds

Compound	IC_{50} (nM)			
	MMP2	**MMP9**	**MMP8**	**MMP12**
3e	456.05	833.21	>2000	ND
3h	273.27	560.70	>2000	1716.9
3b′	282.41	566.43	ND	ND
3f′	575.18	1173.70	>2000	ND
3h′	266.74	402.75	>2000	1237.39
5e′	172.28	461.85	>2000	ND
5h′	152.62	258.06	>2000	284.09
5k′	127.48	144.89	>2000	484.98

ND: Not determined

Interestingly, all these better cytotoxic compounds (**3e, 3h, 3b′, 3f′, 3h′, 5e′, 5h′ and 5k′**) exerted better affinity towards MMP2 than MMP9 whereas displayed a high degree of selectivity over both MMP8 and MMP12. Importantly, all these compounds were inactive in MMP8 compared to gelatinases (MMP2 and MMP9) and at least 3-fold less effective in MMP12. It was interesting to note that both the benzyl derivatives (**3h** and **3h′**) exerted maximum gelatinases (MMP2 and MMP9) inhibition among respective carboxylic acid containing molecules of *p*-nitrophenyl sulfonyl-*D*-glutamine derivatives and *p*-tosyl-*D*-glutamine derivatives. In case of hydroxamic acid containing molecules *p*-tosyl-*D*-glutamines *c*-hexyl derivative (**5k′**) showed better inhibitory activity in comparison with benzyl derivative (**5h′**). Among gelatinases (MMP2 and MMP9) all the better cytotoxic compounds (**3e, 3h, 3b′, 3f′, 3h′, 5e′, 5h′ and 5k′**) against K562 cell line showed better MMP2 enzyme inhibitory activity in comparison with MMP9.

5.4.3.2. Cell cycle analysis

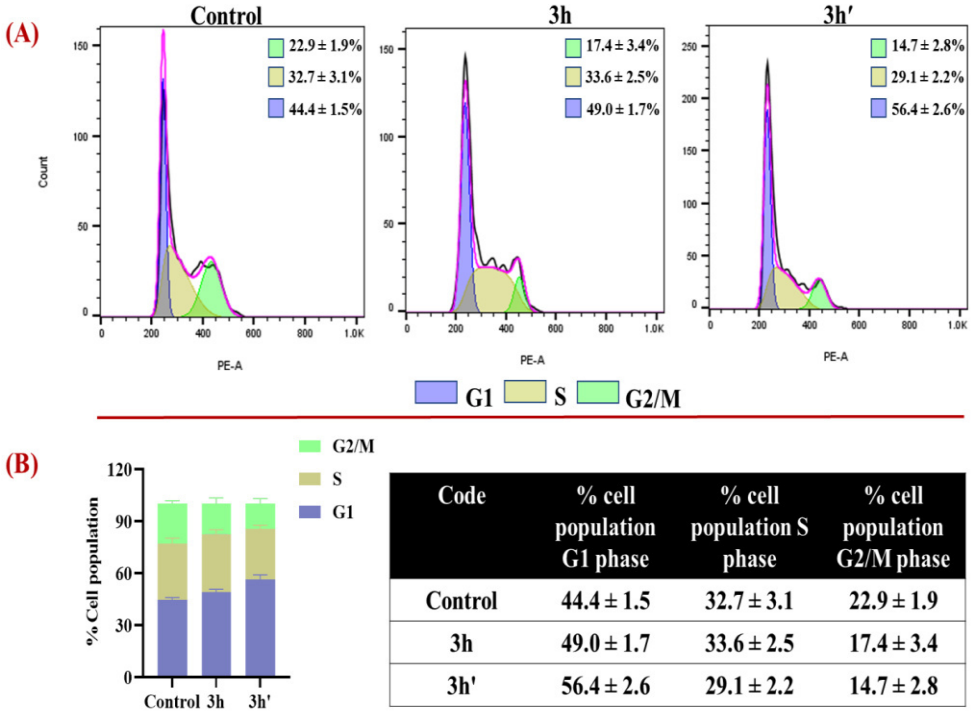

Code	% cell population G1 phase	% cell population S phase	% cell population G2/M phase
Control	44.4 ± 1.5	32.7 ± 3.1	22.9 ± 1.9
3h	49.0 ± 1.7	33.6 ± 2.5	17.4 ± 3.4
3h'	56.4 ± 2.6	29.1 ± 2.2	14.7 ± 2.8

Figure 5.36. Cell cycle analysis in K562 cells treated with vehicle (control), **3h** (4.919 µM), and **3h′** (1.992 µM) at IC_{50} concentration of the compounds for 72 h. The cell cycle analysis was carried out by Flow cytometry (BD Aria III). Data represent mean ± standard deviation, n=3. **(A)** represents a histogram plot of control and the treatments (**3h** and **3h′**); **(B)** represents a graphical representation of the % cell population of K562 cells at various phases, i.e., G1, S, and G2/M phases. Data represent mean ± standard deviation, n=3.

Cell cycle stages were determined by using flow cytometry after PI staining followed by RNAse treatment as per the earlier reported protocol (Mukherjee et al., 2017). An enhancement in the sub-G1 cell population in the cell cycle implicated the arrest of the cell cycle at the sub-G1 phase. Here, flow cytometric analysis pointed out a marked rise in the sub-diploid cell population (sub-G1) of the K562 cell line after treating with lead compounds containing carboxylic acid function (**3h** and **3h′**) (**Figure 5.36**) and also treatment with lead compounds containing hydroxamic acid function (**5h′** and **5k′**) (**Figure 5.37**).

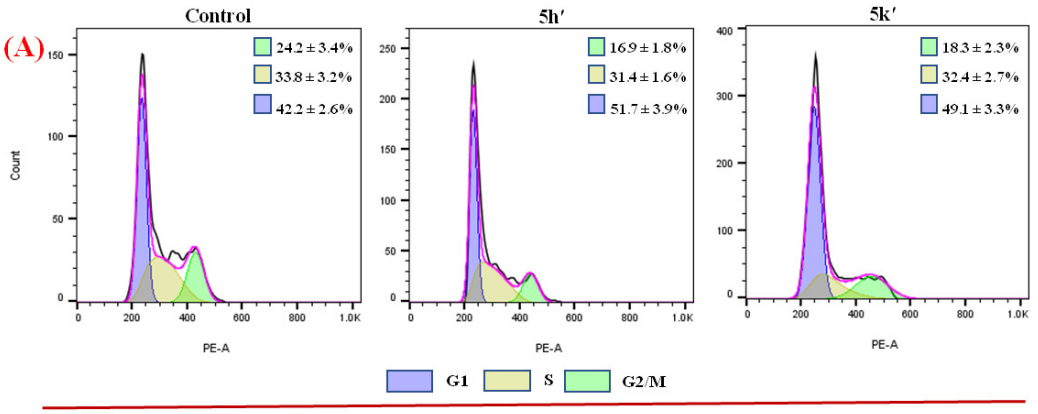

Code	% cell population G1 phase	% cell population S phase	% cell population G2 phase
Control	42.2 ± 2.6	33.8 ± 3.2	24.2 ± 3.4
5h′	51.7 ± 3.9	31.4 ± 1.6	16.9 ± 1.8
5k′	49.1 ± 3.3	32.6 ± 2.7	18.3 ± 2.3

Figure 5.37. Cell cycle analysis in K562 cells treated with vehicle (control), **5h′** (1.408 µM), and **5k′** (4.064 µM) at IC_{50} concentration of the compounds for 72 h. The cell cycle analysis was carried out by Flow cytometry (BD Aria III). Data represent mean ± standard deviation, n=3. **(A)** represents a histogram plot of control and the treatments (**5h′** and **5k′**); **(B)** represents a graphical representation of the % cell population of K562 cells at various phases, i.e., G1, S, and G2/M phases. Data represent mean ± standard deviation, n=3.

After treatment with compound **3h** and **3h′**, the increments of the sub-diploid cell population (sub-G1) were observed at 4.6% and 12%, respectively (**Figure 5.36**). Similarly, the sub-diploid cell population (sub-G1) were increased 9.5% and 6.9%, after treatment with compound **5h′** and **5k′** respectively (**Figure 5.37**). Those results suggested that lead compounds **3h, 3h′, 5h′**and **5k′**

might have the potential to restrict cell progression and survival by arresting the sub-G1 cell cycle (**Figure 5.36** and **5.37**).

5.4.3.3. Apoptotic assay by flow cytometry after annexin V/PI staining

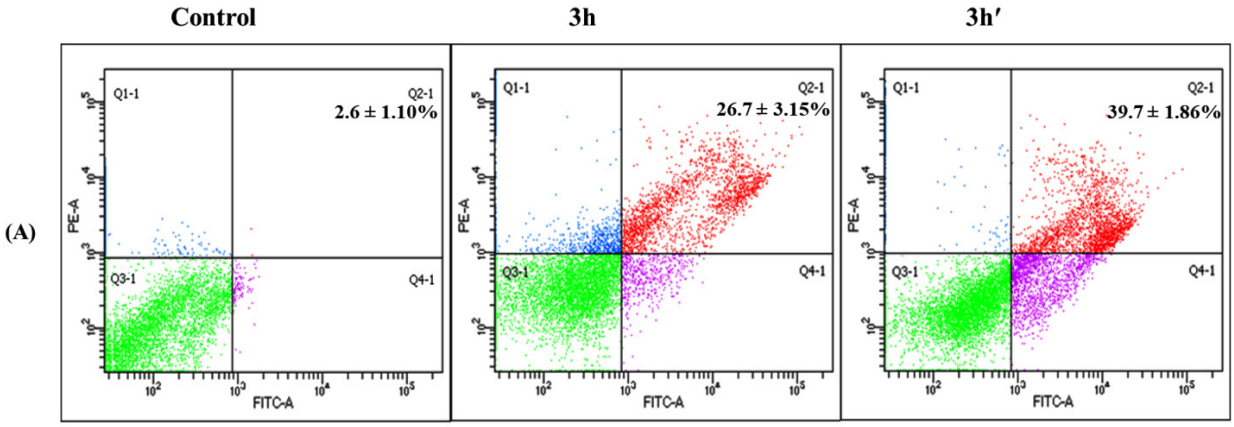

(B)

Code	% total apoptosis
Control	2.6 ± 1.1
3h	26.7 ± 3.15
3h′	39.7 ± 1.86

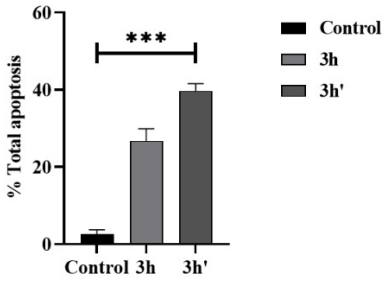

Figure 5.38. **(A)** Apoptosis analysis using Annexin-V/PI double staining assay using flow cytometry. K562 cells were treated with vehicle (control), **3h** (4.919 µM), and **3h′** (1.992 µM) at the IC_{50} concentration for 72 hours (X and Y-axis represent the intensities of annexin-V and propidium iodide respectively). Data represent mean ± standard deviation, n=3. [Each quadrant represents as follows: Q1 – necrotic cells, Q2 – late apoptosis cells, Q3 – live cells, and Q4 – early apoptotic cells. The data together in Q2 and Q4 is considered as the total apoptotic population]. **(B)** Graphical representation of total apoptotic percentage analysis in K562 cells. Data represent mean ± standard deviation, n=3.

Flow cytometry by dual staining of Annexin V and propidium iodide (PI) is a method through which apoptotic or necrotic cell death percentage is estimated (Mukherjee et al., 2017). The rise in both Annexin-V positive and PI negative cells suggested early apoptosis, as well as both Annexin-V and PI positive cells, revealed late apoptosis when flow cytometric data were

analyzed after dual staining with Annexin V-FITC and PI (Mukherjee et al., 2017). The flow cytometry unveiled a gradual enhancement in the AnnexinV-FITC positive population of cells as compared to the untreated control. K562 cells were treated with vehicle (control), **3h** (4.919 µM), and **3h′** (1.992 µM) at the IC_{50} concentration for 72 hours (X and Y-axis represent the intensities of Annexin-V and propidium iodide, respectively) (**Figure 5.38A**). After treatment with carboxlic acid function containing lead molecules lead molecules (Compounds **3h** and **3h′**), the increment of total % of apoptosis (including early and late apoptosis) was found to be 24.1% and 37.1%, respectively (**Figure 5.38B**).

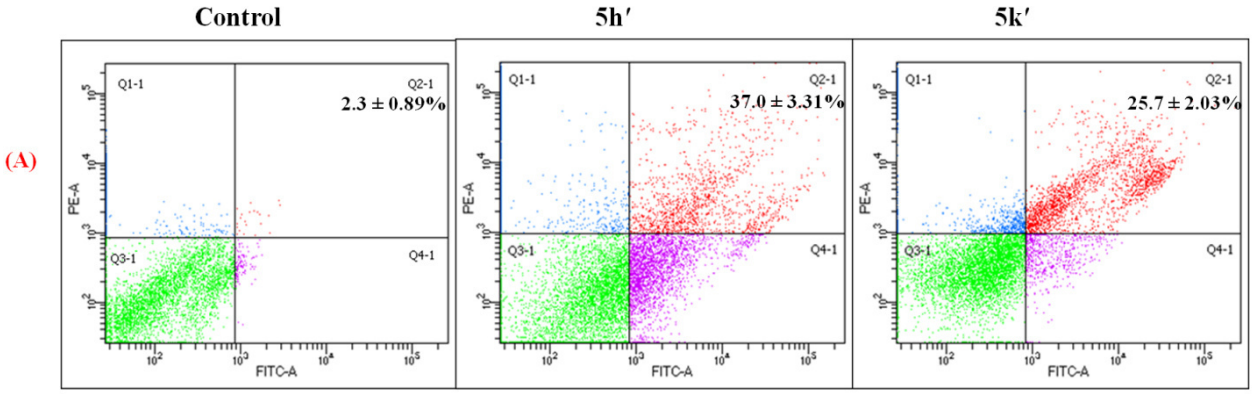

(B)

Code	% total apoptosis
Control	2.3 ± 0.89
5h′	37.0 ± 3.31
5k′	25.7 ± 2.03

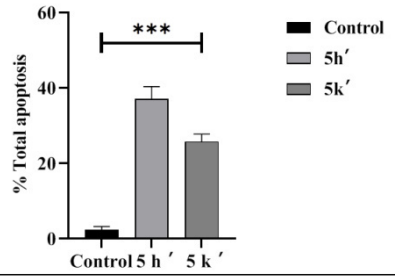

Figure 5.39. **(A)** Apoptosis analysis using Annexin-V/PI double staining assay using flow cytometry. K562 cells were treated with vehicle (control), **5h′** (1.408 µM), and **5k′** (4.064 µM) at the IC_{50} concentration for 72 hours (X and Y-axis represent the intensities of annexin-V and propidium iodide respectively). Data represent mean ± standard deviation, n=3. [Each quadrant represents as follows: Q1 – necrotic cells, Q2 – late apoptosis cells, Q3 – live cells, and Q4 – early apoptotic cells. The data together in Q2 and Q4 is considered as the total apoptotic population]. **(B)** Graphical representation of total apoptotic percentage analysis in K562 cells. Data represent mean ± standard deviation, n=3.

Similarly, K562 cells were treated with vehicle (control), **5h′** (1.408 µM), and **5k′** (4.064 µM) at the IC_{50} concentration for 72 hours (X and Y-axis represent the intensities of Annexin-V and propidium iodide, respectively) (**Figure 5.39A**). After treatment with hydroxamic acid function containing lead molecules (Compounds **5h′** and **5k′**), the increment of total % of apoptosis (including early and late apoptosis) was found to be 34.7% and 23.4%, respectively (**Figure 5.39B**).

5.4.3.4. Acridine orange/ethidium bromide (AO/EB) staining

Potential therapeutic objectives of antitumor agents include targeting cancer cells and causing their death via the apoptotic pathway. Acridine orange (AO) and ethidium bromide (EB) are examples of nucleic acid-binding dyes that can be used for dual staining to highlight the changes in cell morphological features to disclose apoptosis-mediated cell death (Arunachalam et al., 2022). Changes in cellular morphology related to apoptosis can be identified after dual AO/EB staining and examined under a fluorescent microscope. Effectively recognizing cells at various phases of apoptosis is another capability of this approach (Liu et al., 2015). Apoptosis is induced by employing typical distinctive morphological changes in cells, including cytoplasmic cell shrinkage, nuclear condensation, plasma membrane blebbing, breakage of DNA, and translocation of phosphatidylserine to the extracellular side (Arunachalam et al., 2022, and Atale et al., 2014). DNA condensation is a unique process that happens throughout the apoptotic process whereas; in the case of necrosis DNA condensation or DNA fragmentation is not observed. The necrotic cell nucleus remains intact (Kari et al., 2022). Acridine orange is used in the fluorescence staining process to color both living and dead cells. Nevertheless, ethidium bromide is used to stain cells that have damaged membranes. Via a fluorescence microscope, AO/EB-stained viable cells (**VC**) glow green, whereas non-viable cells which include apoptotic dead cells and necrotic cells (**NC**) stain red (Ou et al., 2014). The DNA becomes green as AO intercalates into it. The RNA binds to this dye as well, but it cannot intercalate, therefore the RNA stains reddish-orange. A living cell will therefore appear to be vivid green. Only nonviable cells can absorb EB. The orange color of DNA is caused by the intercalation of EB; on the other hand, RNA may seem slightly red due to EB's weak binding to it. A nonviable cell will therefore have a bright orange nucleus due to EB overpowering AO staining, and its cytoplasm will appear dark red. In living cells, the nuclei of both apoptotic and normal cells will glow brilliant green.

On the other hand, nonviable cells' normal or apoptotic nuclei will flash vivid orange. Consequently, this technique can be used to distinguish between early and late apoptotic cells. The nucleus of viable cells will be uniformly stained green and have undamaged membranes (Arunachalam et al., 2022, García-Rodríguez et al., 2013, and Niakani et al., 2020). **Figure 5.40** and **Figure 5.41** represents the time-dependent induction of apoptosis and cell viability after treatment with the best active compound **3h′** (IC_{50} = 1.992 µM) and **5h′** (IC_{50} =1.408 µM) against K562 cells respectively at the time interval of 24 hr (**Figure 5.40B** and **Figure 5.41B**), 48 hr (**Figure 5.40C** and **Figure 5.41C**) and 72 hr (**Figure 5.40D** and **Figure 5.41D**) via AO/EB staining.

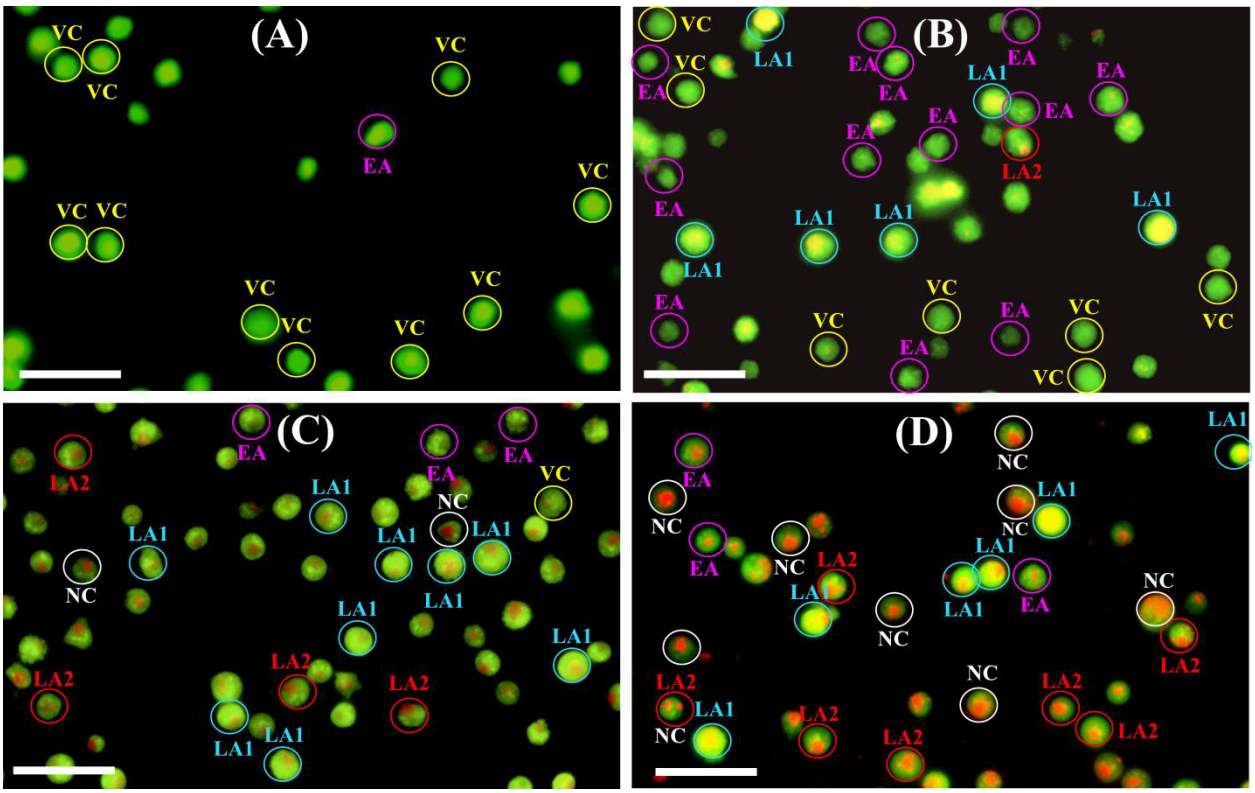

Figure 5.40. Comparison of fluorescence microscopy study by AO/EB staining of **(A)** untreated K562 cells and **(B)** best active compound 3h treated (IC_{50}; 1.992 µM) K562 cells after 24 hours, **(C)** 48 hr, and **(D)** 72 hr treatment (magnification: 40X, scale bar: 50 µm). Yellow, purple, blue, red, and white circles indicate viable cells (**VC**), early apoptotic cells (**EA**), late apoptotic viable cells (**LA1**), late apoptotic dead cells (**LA2**), and necrotic cells (**NC**) respectively.

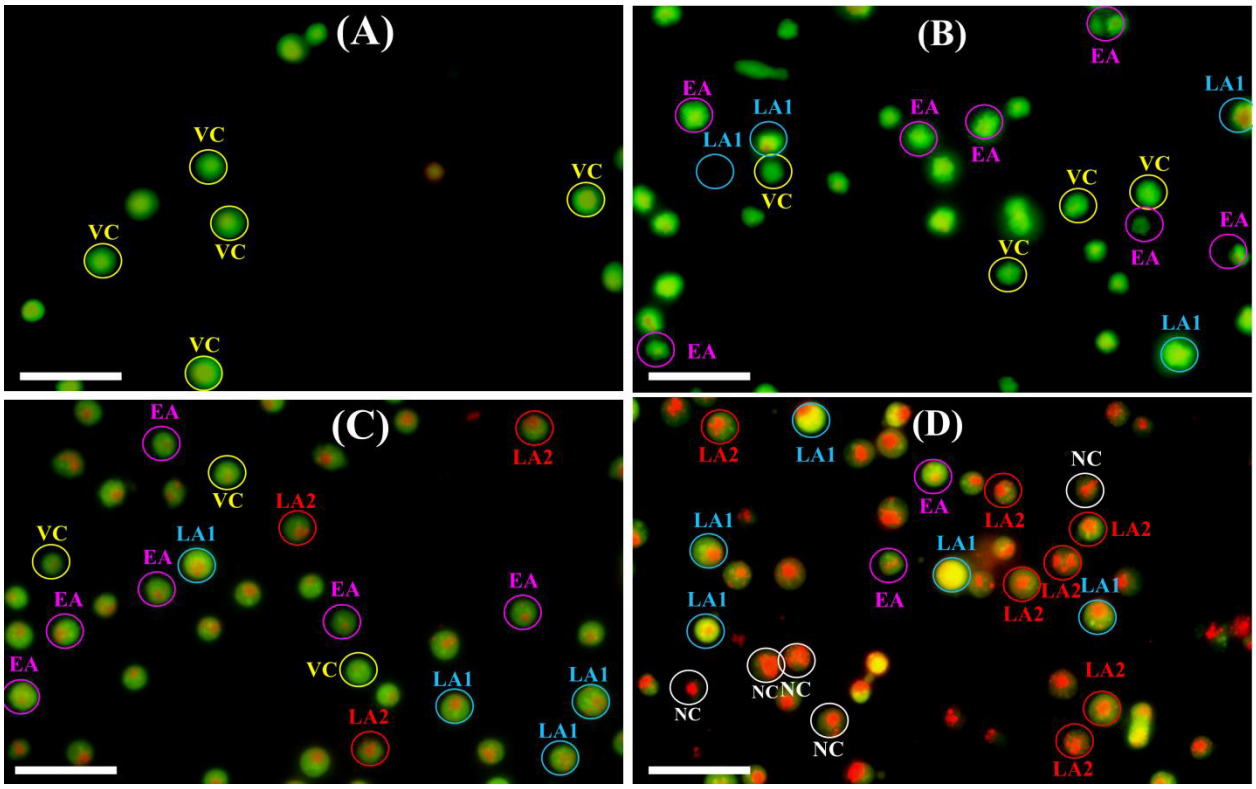

Figure 5.41. Comparison of fluorescence microscopy study by AO/EB staining of **(A)** untreated K562 cells and **(B)** best active compound **5h′** treated (IC_{50} =1.408 µM) K562 cells after 24 hours, **(C)** 48 hr, and **(D)** 72 hr treatment (magnification: 40X, scale bar: 50 µm). Yellow, purple, blue, red, and white circles indicate viable cells (**VC**), early apoptotic cells (**EA**), late apoptotic viable cells (**LA1**), late apoptotic dead cells (**LA2**), and necrotic cells (**NC**) respectively.

The well-ordered constitution of VC in the experiment results in brilliant and consistently green fluorescence in the control K562 cells (**Figure 5.40A** and **Figure 5.41A**). After treatment with compound **3h′** and **5h′** (IC_{50} dose; 1.992 µM) most of the viable cells [marked by a yellow circle in (**Figures 5.40A** and **5.41A**) became apoptotic (**Figure 5.40B-5.40D** and **Figure 5.41B-5.41D**)]. The early apoptotic cells (EA; marked by a purple circle in **Figure 5.40** and **Figure 5.41**) are live cells that only uptake AO stain resulting in green fluorescence. The late apoptotic cells may be viable late apoptotic cells (LA1; marked by the blue circle in **Figure 5.40** and **Figure 5.41**) as well as late apoptosis-mediated dead cells (LA2; marked by a red circle in **Figure 5.40** and **Figure 5.41**). In the LA1 phase plasma membrane blebbing started and the cellular membrane became more permeable concerning viable cell membranes which facilitated the uptake of both AO and EB stain resulting in greenish-orange patches. In the case of LA2, cell

membranes are fully compromised resulting in cell death which allows a greater amount of EB to enter into the interior of the cell, and fragmented DNA with red fluorescence was observed in the interior of K562 cells (**Figure 5.40B-5.40D** and **Figure 5.41B-5.41D**) (García-Rodríguez et al., 2013, and Malekshah et al., 2020). At 24 hr of treatment (**Figure 5.40B** and **Figure 5.41B**), early apoptotic cells are more in number in comparison with late apoptotic K562 cells (LA1 and LA2) where late apoptotic dead cells (LA2) are rarely found. The late apoptotic K562 cells were increased in comparison with early apoptotic K562 cells after 48 hr of treatment (**Figure 5.40C** and **Figure 5.41C**). At 72 hr of treatment (**Figure 5.40D** and **Figure 5.41D**) early apoptotic viable cells are found less in number in comparison with late apoptotic dead K562 cells (LA2) and necrotic cells (NC). The nucleus of necrotic cells of drug-treated K562 cells was not found with fragmented DNA or any other morphological changes related to apoptosis (**Figure 5.40B-5.40D** and **Figure 5.41B-5.41D**) (García-Rodríguez et al., 2013, and Niakani et al., 2020). Therefore, from the above discussion, it is clear that the lead compounds **3h′** (IC_{50} = 1.992 μM) and **5h′** (IC_{50} =1.408 μM) induce time-dependent apoptosis against K562 cells.

5.4.3.5. Angiogenesis assay

After treatment with carboxlic acid function containing lead molecules (Compounds **3h** and **3h′**), compounds **3h** and **3h′** were compared with the control in the angiogenesis assay (**Figure 5.42**). Similarly, in case of hydroxamic acid function containing lead molecules **5h′** and **5k′** were also compared with the control in the angiogenesis assay (**Figure 5.43**). Image processing was used in the study with software like ImageJ or FIJI being used to segment and evaluate the images (Carpentier et al., 2020). The images for each group were separated, making it possible to evaluate the meshes, branches, and nodes that indicate the density, complexity, and connectedness of the blood vessel network. Furthermore, quantitative measurements are taken, with an emphasis on variables like total vessel length, junctions (nodes), and branching sites, to compare the control and test groups. From this study, it was indicated clearly that the number of meshes, branches, and nodes was quite lesser with the treatment with compounds **3h** and **3h′** in comparison with the control, and similar results were also indicated in the skeleton image analysis (**Figure 5.42**). A similar result was also found in the case of treatment with a hydroxamic acid function containing lead molecules **5h′** and **5k′** in comparison with the control (**Figure 5.43**).

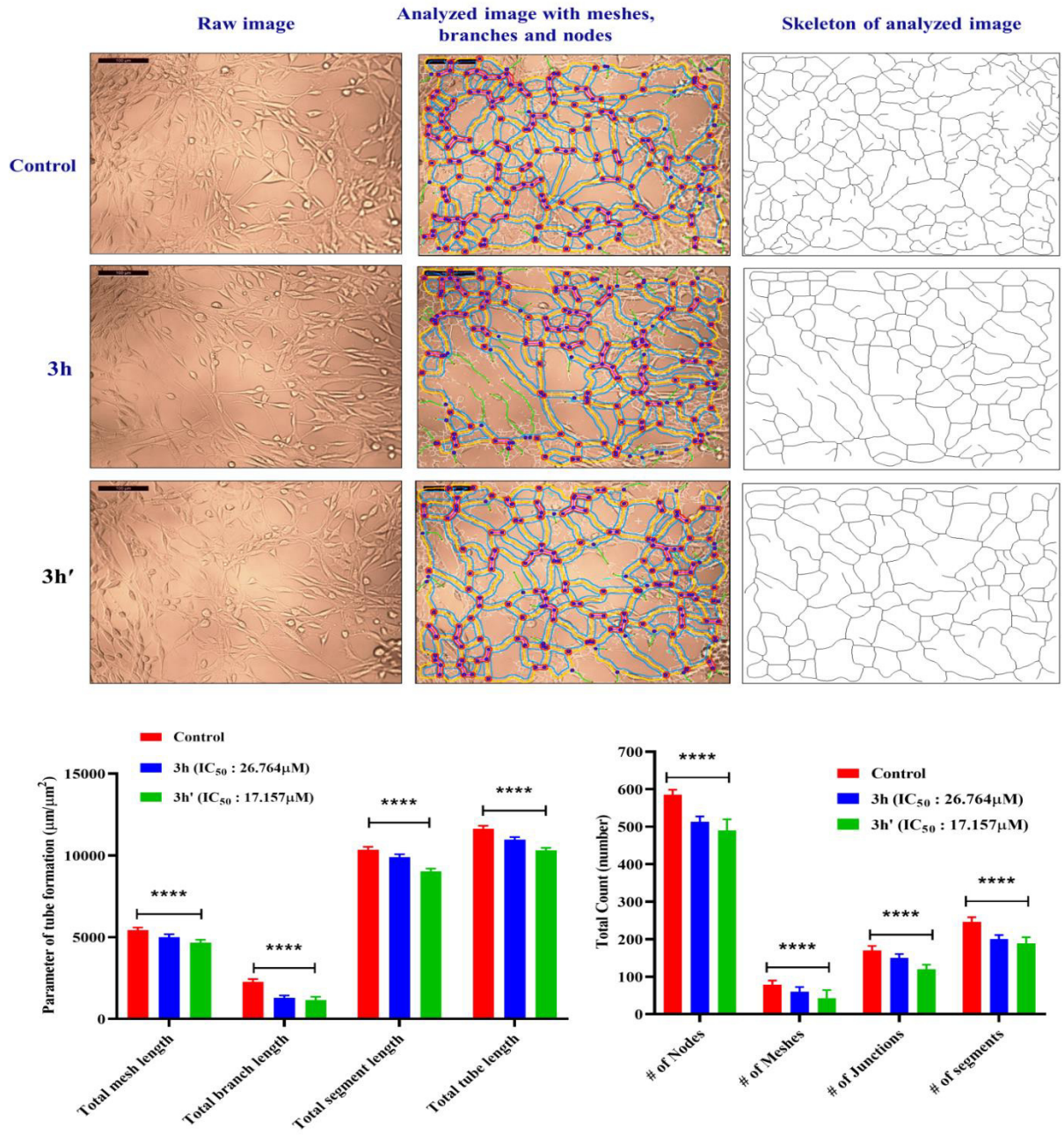

Figure 5.42. Comparative measurement of parameters obtained from image analysis in ACHN cells which were cultured for 72 hr in Cultrex with treatment (**3h;** with IC_{50} dose and **3h′;** with IC_{50} dose) and without treatment (control).

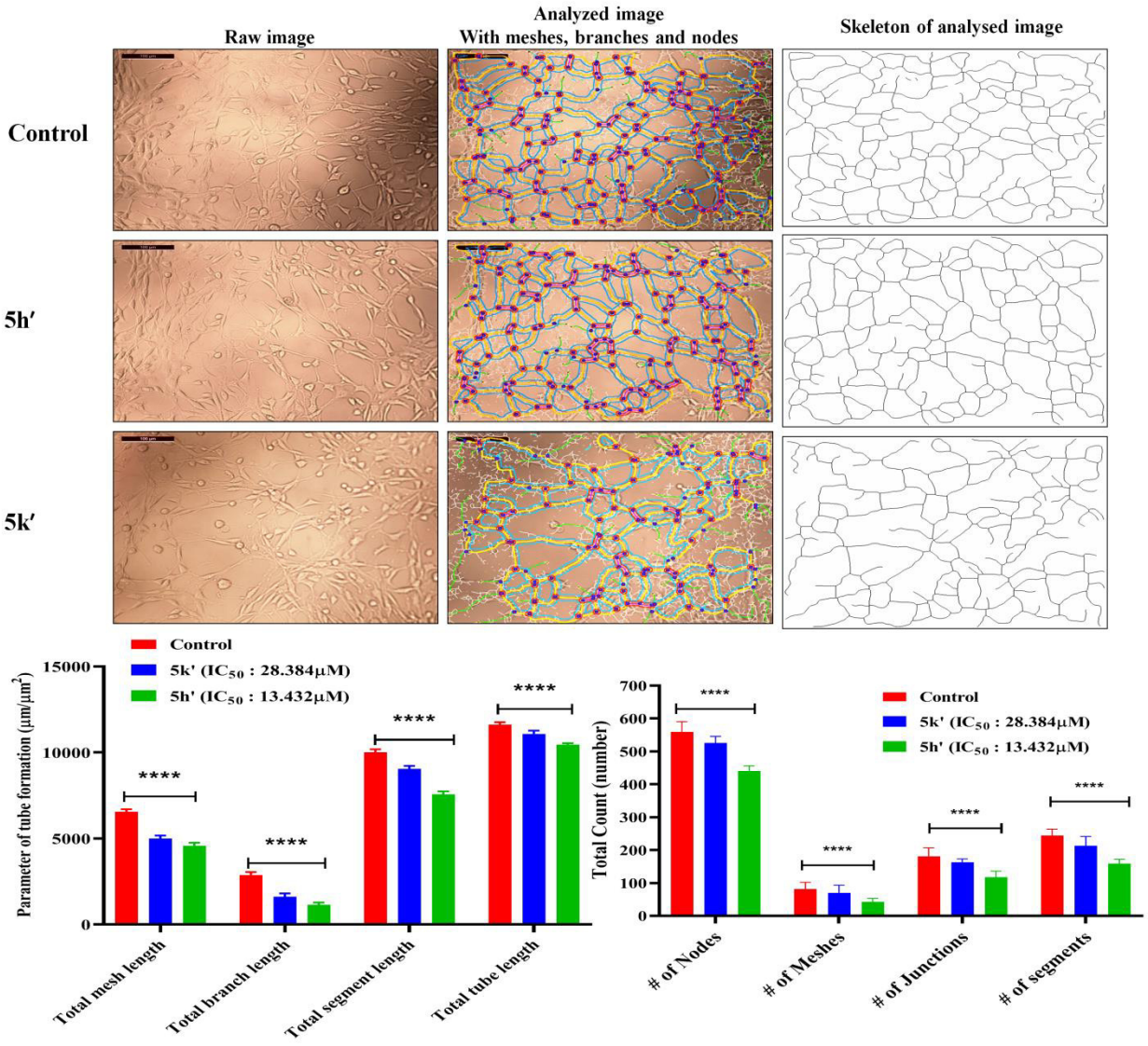

Figure 5.43. Comparative measurement of parameters obtained from image analysis in ACHN cells which were cultured for 72 hr in Cultrex with treatment (**5h′;** with IC_{50} dose and **5k′;** with IC_{50} dose) and without treatment (control).

Henceforth, the significant differences in the angiogenic potential of carboxylic acid function containing lead molecules (**3h** and **3h′**) as well as hydroxamic acid function containing lead molecules (**5h′** and **5k′**) in comparison to the respective control were ultimately revealed through the application of statistical analysis (**Figure 5.42** and **Figure 5.43**). Moreover, the comparing parameters measured from image analysis in ACHN cells, distinct groups for lead compounds of carboxylic acid function containing lead molecules (**3h** and **3h′**) as well as hydroxamic acid

function containing lead molecules (**5h′** and **5k′**) were cultured in Cultrex for 72 hours, in both intervention and non-intervention (**Figure 5.42** and **Figure 5.43**). Specific cellular properties, including cell count, morphology, and other pertinent features were quantified after image processing and interpretation. It was found that in the case of mesh length, branch length, total segment length, and total tube length were found less (% of tube formation) for both the cases of the carboxylic acid function containing lead molecules (compound **3h** and **3h′; Figure 5.42**) as well as hydroxamic acid function containing lead molecules (compound **5h′** and **5k′; Figure 5.43**) in comparison with their respective control (**Figure 5.42** and **Figure 5.43**).

5.4.3.6. MMP2 expression analysis

The lead compounds' ability to modulate MMP2 expression was also examined using flow cytometry. The changes in MMP2 expression levels in K562 cells before and after treatments with carboxylic acid function containing lead molecules **3h** and **3h′** for 48 hr at their respective IC_{50} doses were estimated by flow cytometry analysis (Mukherjee et al., 2017; Dutta et al., 2019; and Datta et al., 2022). The treated and untreated cells were fixed and subsequently stained with MMP2 primary antibody followed by treatment with the secondary antibody conjugated with FITC. The K562 cell population with MMP2 cells was found to be reduced after treatment with the carboxylic acid function containing lead molecules (**3h** and **3h′**). After 48 hours of drug treatments, flow cytometric data revealed that cellular MMP2 expression levels were reduced by 19.6% (**Figure 5.44**) in the case of **3h** (at IC_{50} of 4.919 μM) and 20.1% (**Figure 5.44**) in the case of compound **3h′** (at IC_{50} of 1.992 μM) in comparison with untreated control. Therefore, it revealed that the lead molecules (**3h** and **3h′**) also have the potential to block the cellular MMP2 expression. Similarly, The K562 cell population with MMP2 cells was found to be reduced after treatment with the hydroxamic acid function containing lead molecules **5h′** and **5k′** (**Figure 5.44**). The cellular MMP2 expression levels after 48 hours of drug treatments were reduced by 25.2% (**Figure 5.45**) in the case of **5h′** (at IC_{50} of 1.408 μM) and 28.4% (**Figure 5.45**) in the case of compound **5k′** (at IC_{50} of 4.064 μM) in comparison with untreated control.

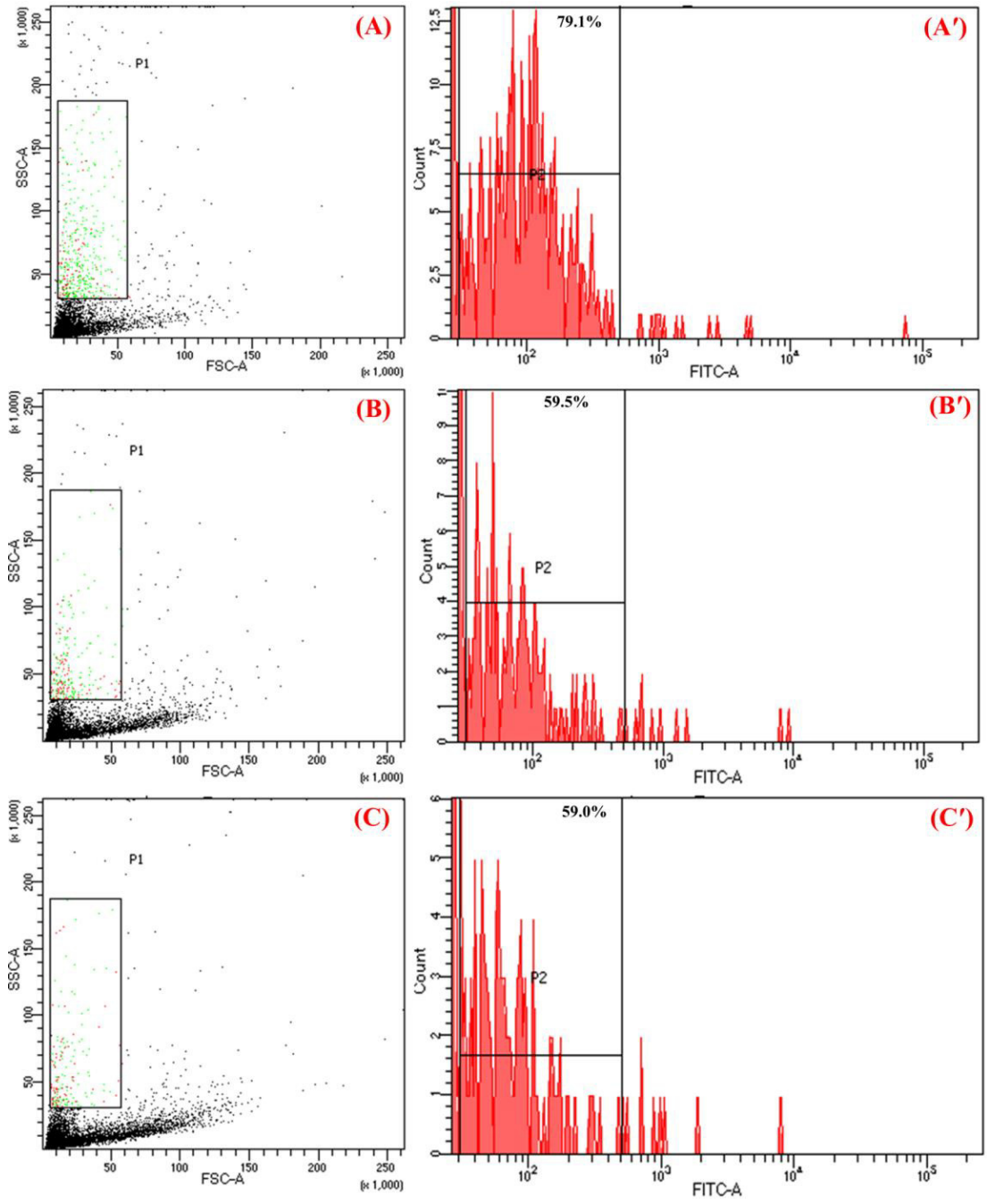

Figure 5.44. MMP2 expression analysis of K562 cells by fluorescence-activated cell sorting (FACS) after 48 hr of treatments and followed by incubation with primary (anti-MMP2) and secondary antibody (FITC conjugated anti-MMP2). **(A)** (dot plot) and **(A′)** (histogram plot) represent the Contol, **(B)** (dot plot) and **(B′)** (histogram plot) represent the treatment by **3h** with IC_{50} (4.919 µM), and **(C)** (dot plot) and **(C′)** (histogram plot) represent the treated cells by **3h′** with IC_{50} (1.992 µM).

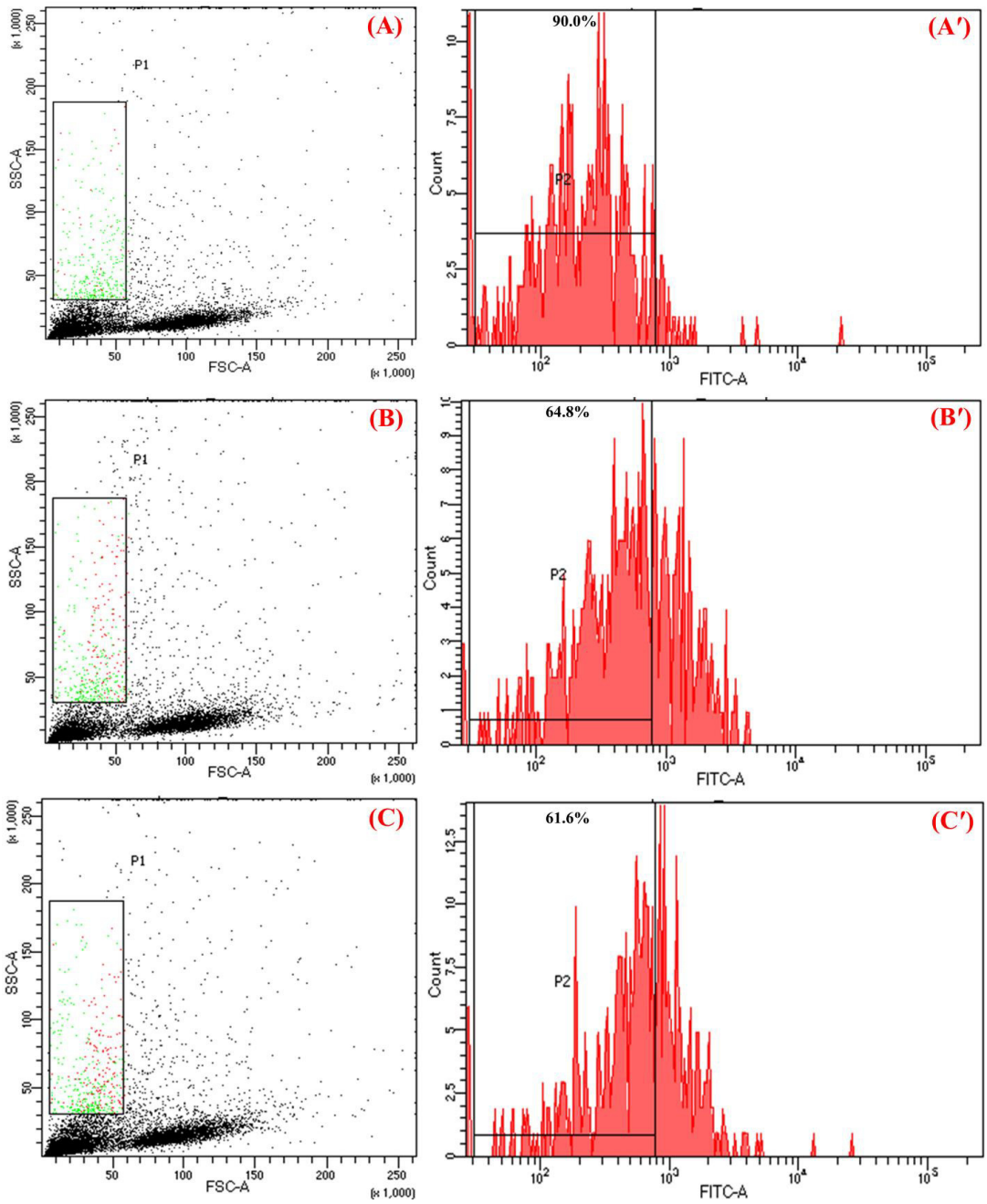

Figure 5.45. MMP2 expression analysis of K562 cells by fluorescence-activated cell sorting (FACS) after 48 hr of treatments and followed by incubation with primary (anti-MMP2) and secondary antibody (FITC conjugated anti-MMP2). **(A)** (dot plot) and **(A′)** (histogram plot) represent the Contol, **(B)** (dot plot) and **(B′)** (histogram plot) represent the treatment by **5h′** with IC_{50} (1.408 µM), and **(C)** (dot plot) and **(C′)** (histogram plot) represent the treated cells by **5k′** with IC_{50} (4.064 µM).

5.4.4. Binding interaction studies

5.4.4.1. Molecular docking study of compound 3d and 3h′

From the molecular docking study of the synthesized compounds at the active site of MMP2, MMP9, MMP8, and MMP12, the compounds showed a similar binding pattern at the active site of different isoforms.

From the binding mode of the compounds, it was observed that both the compounds **3d** and **3h′** showed similar binding to each of the MMP isoforms (**Figure 5.46**).

Despite having similar binding at the active site of each of the MMP isoforms, it was observed that the hydrophobic *p*-tosyl/*p*-nitro phenyl sulfonamide group occupied the S_1' pocket of the enzyme whereas the *i*-propyl/benzyl P_2' substituent displayed proximity toward the S_2' pocket of MMP2 (**Figure 5.46A** and **5.46B**). For the MMP9, the benzyl group of compound **3h′** was found to drift away from the S_2' pocket (**Figure 5.46A** vs **5.46B**). This may indicate the lower MMP9 inhibitory activity of compound **3h′** compared to MMP2. Furthermore, the π-π interaction between the benzyl moiety of **3h′** and Phe185 residue may be one of the prime reasons behind the low MMP12 inhibitory activity that was absent for MMP8 (**Figure 5.46H** vs **5.46F**).

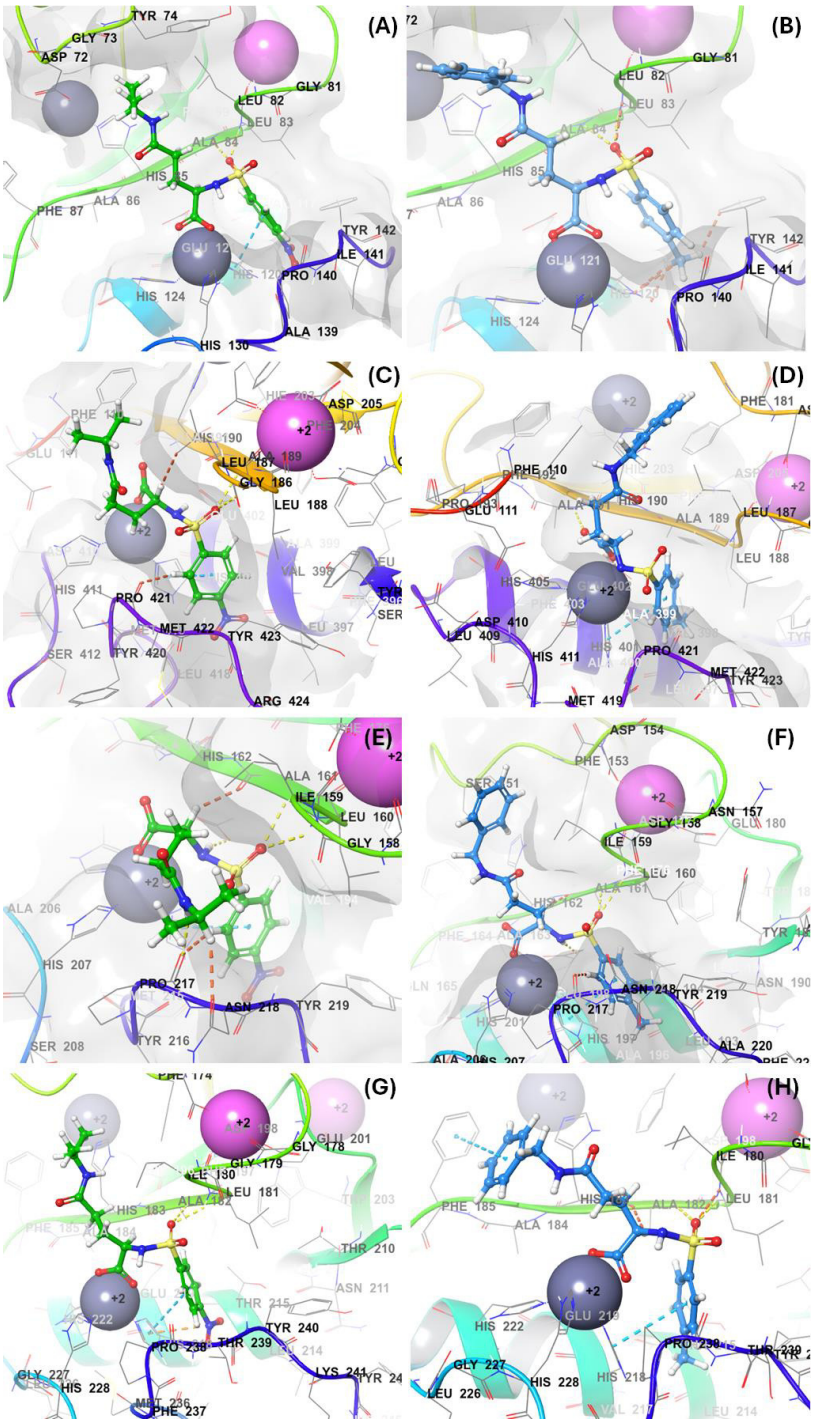

Figure 5.46. The docked poses of **(A) 3d** at MMP2 active site (PDB ID: 1HOV), **(B) 3h′** at MMP2 active site (PDB ID: 1HOV), **(C) 3d** at MMP9 active site (PDB ID: 1GKC), **(D) 3h′** at MMP9 active site (PDB ID: 1 GKC), **(E) 3d** at MMP8 active site (PDB ID: 1ZP5), **(F) 3h′** at MMP8 active site (PDB ID: 1ZP5), **(G) 3d** at MMP12 active site (PDB ID: 1RMZ), **(H) 3h′** at MMP12 active site (PDB ID: 1RMZ)

5.4.4.2. Molecular dynamics (MD) simulation study of compound 3d and 3h′

To predict the binding pattern of the synthesized compounds, the molecular dynamics (MD) simulation studies of the molecules having cytotoxic acid function zinc binding group (ZBG), *i.e.*, compound **3d** and **3h′** of the respective series were performed using the *GLIDE* and *Desmond* modules, respectively in Schrodinger Maestro v12.5 software (Schrodinger Suite 2019) using our earlier reported protocol (Baidya et al., 2023). The MMP2 solution NMR data (PDB ID: 1HOV) from the RCSB Protein Data bank (RCSB Protein Data Bank) was used for the molecular docking and MD simulation studies.

From the root means square deviation (*RMSD*) of complex trajectory obtained from the MD simulation study, it was noticed that compound **3h′** showed comparatively greater movement than compound **3d** (**Figure 5.47A** vs **5.47B**) at the binding site of MMP2 (PDB ID: 1HOV).

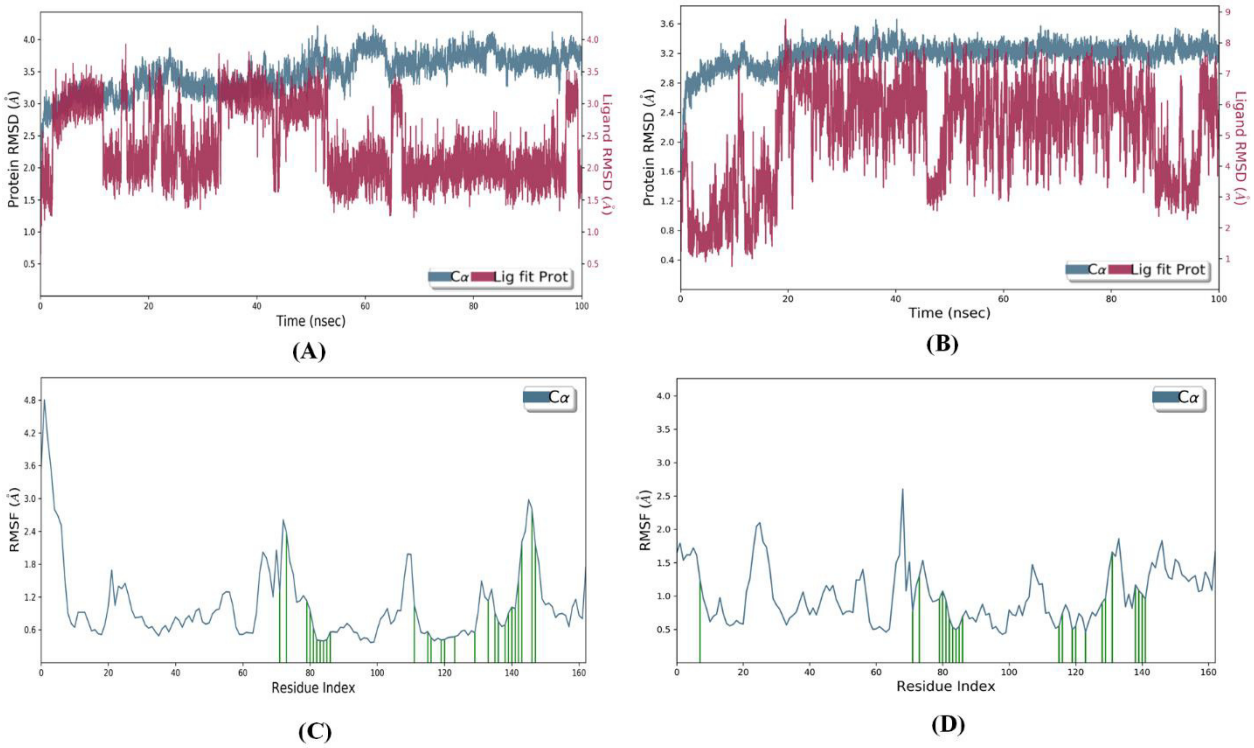

Figure 5.47. 100 ns trajectory *RMSD* plot for **(A)** compound **3d**, and **(B)** compound **3h′**, *RMSF* plot for the C-α chain residues of MMP2 (PDB ID: 1HOV) **(C)** compound **3d**, and **(D)** compound **3h′.**

However, for the root means square fluctuation (RMSF) of the amino acid residues of MMP2, it was noticed that the key catalytic site residues such as Leu82, Leu83, Ala84, His85, Glu121, and

His120, showed identical fluctuation while binding with both **3d** and **3h′ (Figure 5.47C vs 5.47D)**. Interestingly, few S1′ pocket-forming residues of MMP2 like Tyr142 and Thr143 residues showed slightly lower fluctuation while being complexed with **3h′** than **3d**. This indicates better stability of the *p*-tosyl P_1' substituent inside the S_1' pocket for **3h′** compared to the *p*-nitrophenyl group of compound **3d**. Besides, throughout the simulated timeframe, compound **3d** showed greater ionic interactions with MMP2 while greater hydrophobic contacts were noticed for compound **3h′**. Both compounds **3d** and **3h′** showed hydrogen bond interactions with Leu83, Ala84, and Pro140 residues where compound **3d** formed a greater number of hydrogen bond interactions with all active site residues unlike compound **3h′** (**Figure 5.48**).

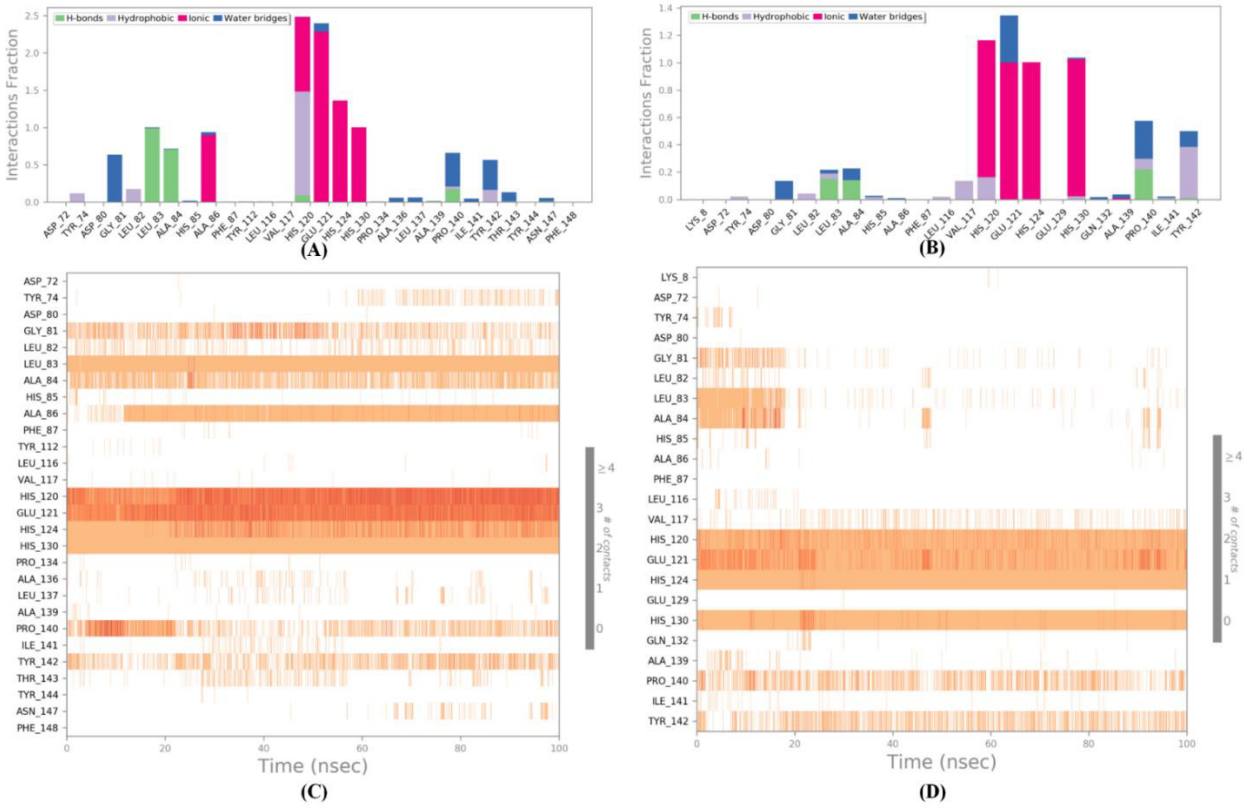

Figure 5.48. The interaction fraction recorded between **(A)** compound **3d**, and **(B)** compound **3h′** and MMP2 catalytic site (PDB ID: 1HOV), Contact frequency of **(C)** compound **3d**, and **(D)** compound **3h′** with MMP2 catalytic site residues.

Although both compounds **3d** and **3h′** showed hydrophobic interactions with the same amino acid residues, a greater hydrophobic contact was noticed between the compound **3h′** and His120,

Val117, Pro140, and Tyr142 residues (**Figure 5.48B**). Also, the hydrophobic contact between Val117 and compound **3d** was almost negligible for compound **3d** as was observed in the case of compound **3h′** (**Figure 5.48A** vs **5.48B**). Other crucial observations suggested that compound **3d** also formed a hydrogen bond interaction with His120 which was absent for compound **3h′**. Again, both **3d** and **3h′** showed almost similar fractions of water-mediated contacts with the crucial active site residues of MMP2 including the catalytic Glu121 (**Figure 5.48A** vs **5.48B**). Further analysis showed the higher contact of compound **3d** made more frequent contact with Leu83 and Ala84 residues throughout the simulated timeframe (**Figure 5.48C**) unlike compound **3h′** which showed higher contact with the mentioned residues to a greater extent up to 20 ns simulated time. Additionally, in the interactions between compounds **3d** and **3h′** with Ω-loop Pro140, compound **3h′** showed more regular contact with the residues despite compound **3d** having greater contacts with the residue up to 25 ns (**Figure 5.48C** vs **5.48D**).

An interesting observation was obtained from the interaction occupancy of **3d** and **3h′** (**Figure 5.49**). It was noticed that though both the molecules interacted with Tyr142 at the S1′ pocket of MMP2, the *p*-tosyl group of the compound **3h′** itself formed π-π stacking interactions with Tyr142 that were absent for the polar *p*-nitro phenyl group of the compound **3d**.

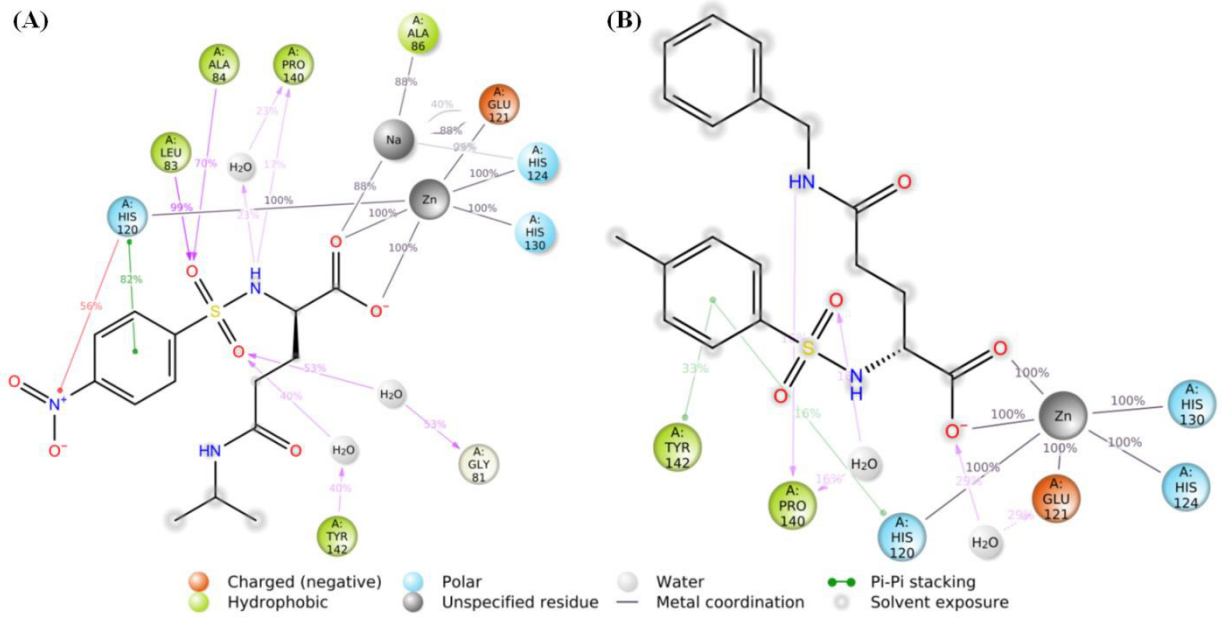

Figure 5.49. Overall contacts made by **(A)** compound **3d**, and **(B)** compound **3h′** at MMP2 active site (PDB ID: 1HOV).

Therefore, to interact with Tyr142, compound **3d** used its sulfonamido oxygen atoms to form water-mediated interactions with Tyr142 (**Figure 5.49A** and **5.49B**). These differences in the interaction of **3d** and **3h′** with Tyr142 inside the S_1' pocket led to the higher stability of the *p*-tosyl P_1' substituent at the S_1' pocket over the *p*-nitrophenyl group. Further analysis demonstrated the significance of the P_1' and P_2' substituents of these *D*(-) glutamine analogs for MMP2 binding (**Figure 5.50**).

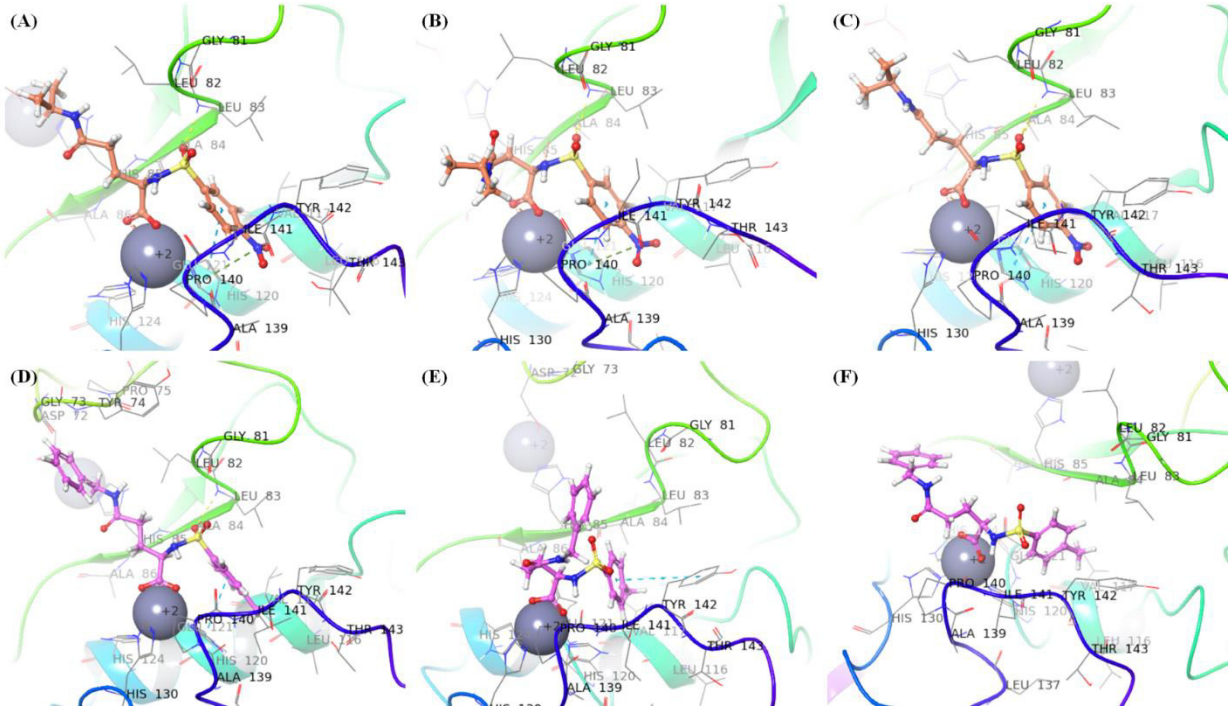

Figure 5.50. The binding mode of compound **3d** at the MMP2 active site (PDB ID: 1HOV) at **(A)** 0 ns, **(B)** 50 ns, and **(C)** 100 ns, The binding mode of compound **3h′** at the MMP2 active site (PDB ID: 1HOV) at **(D)** 0 ns, **(E)** 50 ns, and **(F)** 100 ns.

It was noticed that the π-cationic interaction between the *p*-nitro phenyl P_1' moiety of the compound **3d** and His120 residue despite showing the rigid fixating of the moiety inside the hydrophobic S_1' pocket of MMP2, also disabled the interaction between the P_1' moiety of the compound **3d** and Tyr142 (**Figure 5.50A** to **5.50C**). In contradiction, the hydrophobic *p*-tosyl group was able to interact with both His120 and Tyr142 residues inside the S_1' pocket via π-π interactions (**Figure 5.50D** to **5.50F**) due to its capability to move inside the hydrophobic pocket. Also, regarding the P_2' substituents of **3d** and **3h′**, both the *i*-propyl and benzyl moieties extended toward the S_2' pocket while showing similar movement during the simulation.

5.4.4.3. Molecular dynamics (MD) simulation study of compound 5d' and 5h′

Here compound **5d'** and compound **5h′** are taken as the representative of a lesser active and better active compound found in the cytotoxicity study against K562 cell line which has hydroxamic acid function as ZBG. To predict the binding pattern of compound **5d'** and compound **5h′** with MMP2, 100ns MD simulation studies of each MMPI at the active site of MMP2 (PDB ID: 1HOV) was performed using the *Desmond* (Schrodinger Suite 2019) module of Schrodinger Suite (Schrodinger Suite 2019) using *OPLS_2005* forcefield.

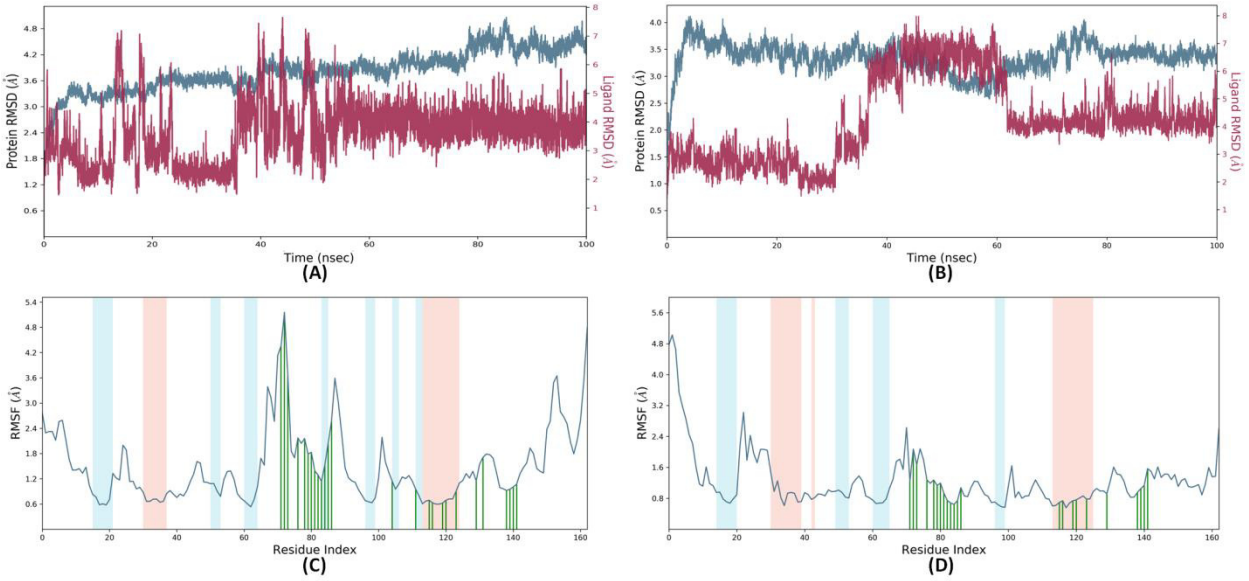

Figure 5.51. 100 ns trajectory *RMSD* plot for **(A)** compound **5h′**, and **(B)** compound **5d′**, *RMSF* plot for the C-α chain residues of MMP2 (PDB ID: 1HOV) **(C)** compound **5h′**, and **(D)** compound **5d′.**

From the trajectory RMSD analysis of the simulated complexes (**Figures 5.51A** and **5.51B**), it is noticed that the molecule showed very little deviation in their trajectory, unlike the ligand molecules that have shown comparatively higher deviation at MMP2 active site (PDB ID: 1HOV). Also, despite depicting comparatively similar fluctuation, the compound **5h′** and compound **5d'** showed comparatively stable binding with MMP2 (**Figure 5.51A** vs **5.51B**). Regarding the RMS fluctuation of the C-α chain residue, it is observed that the active site residues such as Tyr74, Lys79, Gly81, Leu82, Leu83, Ala84, and His85 residues showed a greater fluctuation while complexed with compound **5h′**. Such fluctuation of these key active site

residues displayed comparatively lower fluctuation while simulated in complex with compound **5d'**, suggesting greater interaction between the residues and compound **5d'** compared to compound **5h′** (**Figure 5.51C** vs **5.51D**).

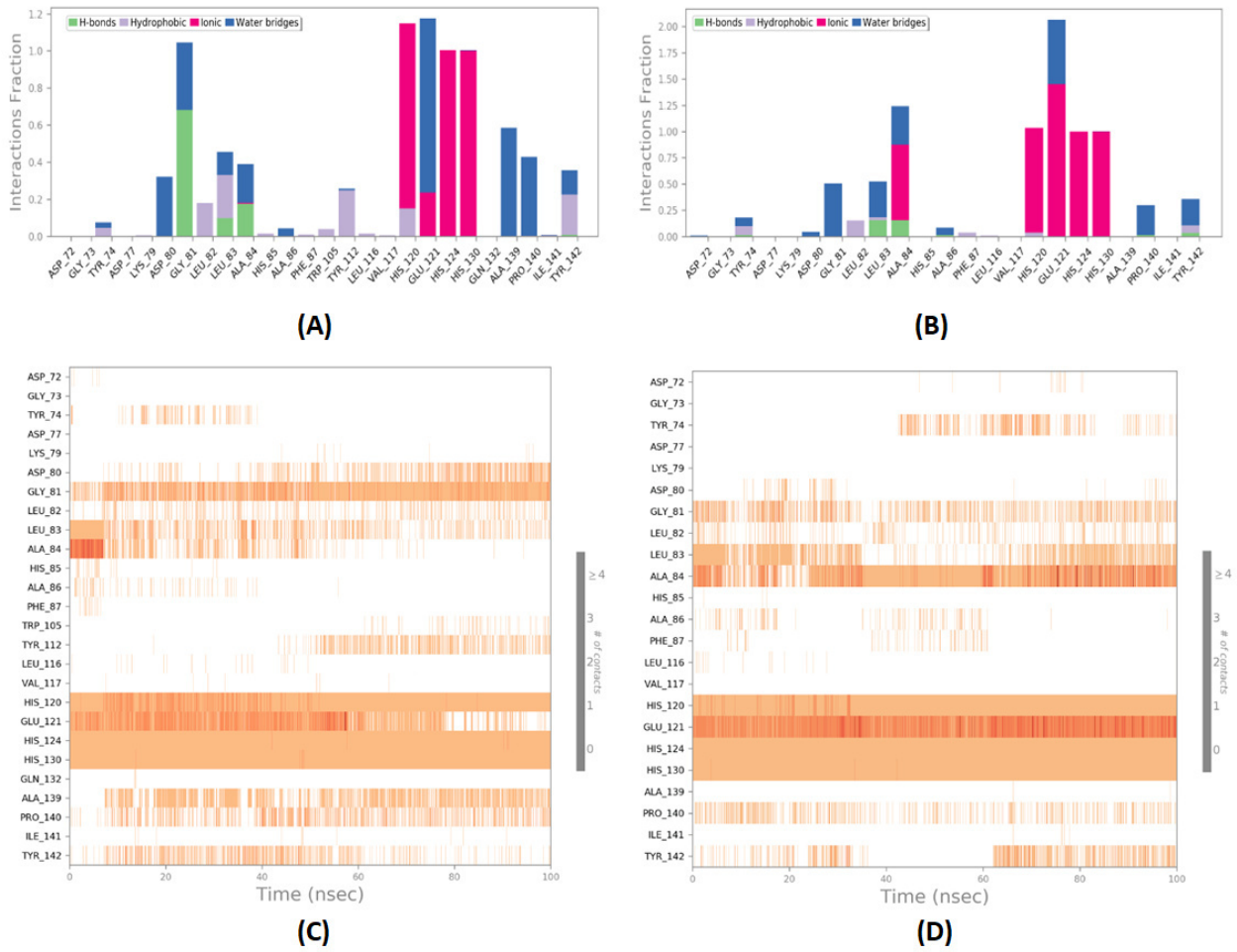

Figure 5.51. The interaction fraction recorded between **(A) compound 5h′**, and **(B) compound 5d′** and MMP2 catalytic site (PDB ID: 1HOV), Contact frequency of **(C) compound 5h′**, and **(D) compound 5d′** with MMP2 catalytic site residues.

Regarding the interactions formed by the simulated compounds at the MMP2 active site (PDB ID: 1HOV), it is visible that (**Figure 5.51A** and **5.51B**) that though the benzyl analog **compound 5h′** showed a few hydrophobic contacts with His85 residue, the isopropyl containing **compound 5d'** was unable to show any interaction due to the lack of any π-electrons in it (**Figure 5.51A** and **5.51C** vs **Figure 5.51B** and **5.51D**). Apart from that both of the compounds were found to

interact with Tyr74, Leu82, Leu83, Ala84, His120, Glu121, His124, His130, Pro140, and Tyr142 residues (**Figure 5.51A** and **5.51B**).

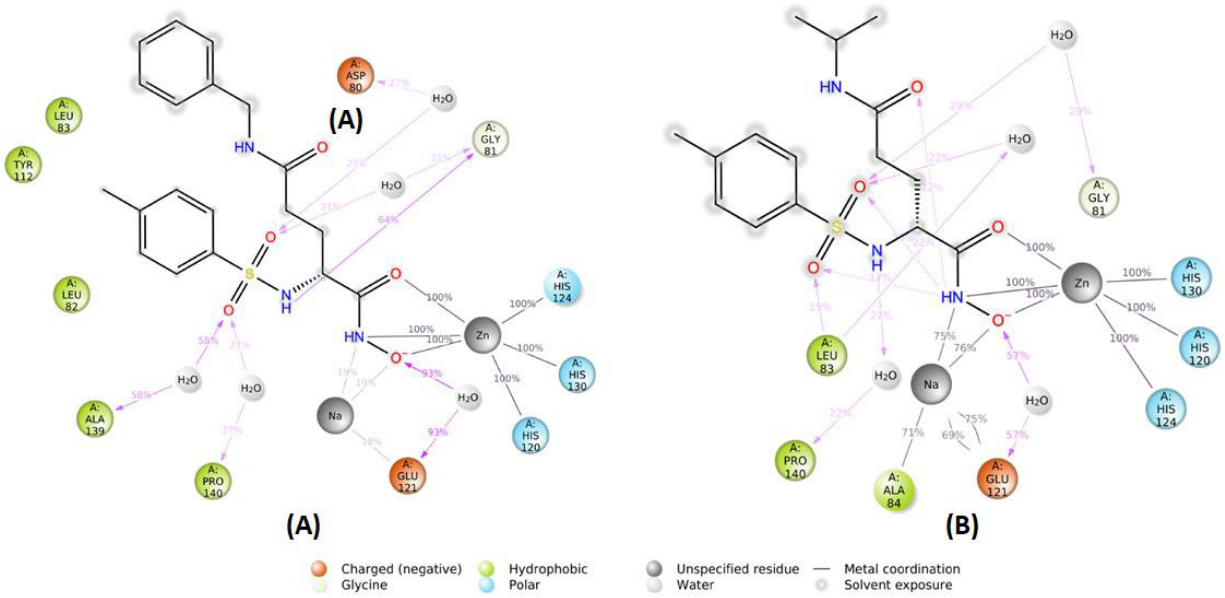

Figure 5.52. Overall contacts made by **(A) compound 5h′**, and **(B) compound 5d'** at MMP2 active site (PDB ID: 1HOV).

Regarding the bond occupancy of compound **5h′** and compound **5d'** at the MMP2 (PDB ID: 1HOV) binding site, it is observed that both of the compounds showed firm tridentate chelation of the hydroxamate moiety (interaction occupancy for 100ns simulation = 100%) (**Figure 5.52A** and **5.52B**). It is interesting to note that although the sulfonamido nitrogen atom of compound **5h′** formed a hydrogen bond interaction with Gly81 residue which was absent for compound **5d'**. Additionally, the compound compound **5h′** showed a greater occupancy (93%) of water-mediated hydrogen bond with the catalytic Glu121 residue in comparison to compound **5d'** (occupancy = 57%) (**Figure 5.52A** and **5.52B**). Therefore, despite having higher fluctuation, these additional and consistent interactions of compound **5h′** with Gly81, and catalytic Glu121 residues might have provided superior MMP2 inhibitory potency to the molecule than compound **5d'**.

5.4.5. Summary of Part-IV

Here, in **Part-IV**, New derivatives of (*D*)-glutamine, totaling 31 (designated as **3a-3h, 3a′-3l′,** and **5a′-5k′**), were synthesized, purified, and characterized based on insights gained from

existing literature (**Chapter 2**) and QSAR-based molecular modeling studies. Out of these thirty one compounds, twenty compounds (**3a-3h** and **3a′-3l′**) incorporate a carboxylic acid moiety in their structures, while the remaining 11 (**5a′-5k′**) feature a hydroxamic acid group instead of a carboxylic acid group. These compounds were further subjected to cytotoxicity evaluation as well as gelatinase inhibition against leukemia and other solid tumor cell lines as well as to adjudicate their nontoxic profile toward normal cell line. The benzyl derivatives (compounds **3h, 3h'** and **5h'**) exerted the most promising antileukemic potential (activity in lower μM) as well as the highly efficacious gelatinase inhibition (IC_{50} in lower nM). Compounds **5k'** having a hydroxamic acid function as ZBG and containing a cyclohexyl group in its structure showed highest activity in case of gelatinase inhibition (MMP2 IC_{50} = 127.48 nM and MMP9 IC_{50} = 144.89 nM). The flow cytometric analysis also explored effective sub-G1 cell cycle arrest by both of better active molecules (compounds **3h, 3h', 5h'** and **5k'**) as seen in the chronic myeloid leukemia (K562) cell line. Moreover, these molecules (compounds **3h, 3h', 5h'** and **5k'**) were found to exert a minimum of 24% apoptosis in the K562 cell line. These molecules (**3h, 3h', 5h'** and **5k'**) were found to reduce about 20% MMP2 expression in the K562 cell line. These compounds (**3h, 3h', 5h'** and **5k'**) produced effective antiangiogenic potential. Nevertheless, the best active compound (compound **3h'**) among compounds featuring a carboxylic acid group and the best active compound (compound **5h'**) among compounds featuring a hydroxamic acid group also resulted in time-dependent apoptosis in the K562 cell line at their respective IC_{50} dose as observed by AO/EB staining. Additionally, binding interaction studies, including molecular docking and molecular dynamic simulation were conducted with MMP2 and selected compounds (**3d**, **3h′, 5d′ and 5h′**). Not only that, the MD simulation study of the most effective compounds (**3h'** and **5h'**) also pointed out stable binding interaction at the MMP2 active site correlating with the highly effective MMP2 inhibition profile of compound **3h'** and compound **5h'** as well as better anti-leukemic activity.

CHAPTER 6

CONCLUSION

Chapter 6: Conclusion

By considering the relationship between cancer and glutamine or glutamic acid, three structural variants of glutamic acid (isoglutamine, pyroglutamic acid, and glutamine) are considered for the development of small-molecule anticancer agents. Histone deacetylase 8 (HDAC8), one of the crucial HDACs, affects the epigenetic gene regulating processes in solid and hematological cancer progressions, especially acute myeloid leukemia (AML), and acute lymphoblastic leukemia (ALL). On the other hand, gelatinases (MMP2 and MMP9) and other MMPs have long been linked to angiogenesis, metastasis, and solid tumor invasion; however, little information is known about the function of gelatinases in hematological cancers.

In the **Part-I** study of my PhD work, twenty nine phenyl/naphthylacetyl based (*L*)-isoglutamine derivatives HDAC inhibitors (compounds **I1-I29**) which were reported earlier, were screened against different human cancer cell lines at different concentrations. The better activities of these compounds were observed on human leukemia cell lines specifically on Jurkat E6.1 cell line. From the cytotoxicity study, the most active compound (**I27**) as well as another better active compound (**I6**) on ALL cell line (Jurkat E6.1) DNA deformation clearly and that is an indication of cell shrinkage and nuclear fragmentation in Jurkat E6.1 cell line. These better active molecules **I6** and **I27** have increased ROS production in the treated Jurkat E6.1 cell line. In the MMP2 and HDAC8 inhibitory activity of compounds **I6** and **I27** in Jurkat E6.1 cells MMP2 and HDAC8 expression assays, it was confirmed that these two compounds **I6** and **I27** have dual inhibitory properties of MMP2 and HDAC8 enzymes. These findings were further supported by results of molecular docking of these compounds **I6** and **I27** in the drug-binding pockets of MMP2 and HDAC8 enzymes. Moreover, molecular docking analysis also suggested that these two compounds (**I6** and **I27**) not only inhibit MMP2 and HDAC8 metalloenzymes but also MMP9 enzyme. Finally, this study (**Part-I**) demonstrates that compounds **I6** and **I27** have good cytotoxic activities on leukemia Jurkat E6.1 cell line and the mechanism of cytotoxicity is through inducing ROS generation and DNA deformation. Therefore, this study (**Patr-I**) suggests that the arylacetyl-(***L***)-isoglutamine-based metalloenzyme inhibitors especially MMP2, MMP9 and HDAC8 inhibitors may be a potential candidate for the management of acute lymphoblastic leukemia (ALL) (**Figure 6.1**) aiming less toxicity to normal healthy cells.

In **Part-II**, the glutamine fragment has been modified to its cyclic variant and 14 aryl sulfonyl-(*L*)-pyroglutamic acid derivatives (**P4, P6-P18**) to see whether these compounds can produce

cytotoxicities in hematological cancer cell lines like Jurkat E6.1, K562, and U937 as well as solid tumor cell line MDA-MB-231. The most potent compounds, **P10** and **P7** also showed gelatinase activity in micromolar range which may be responsible for their moderate cytotoxicities with IC_{50} values of 44.32±0.9 µM and 49.10±1.9 µM, 39.65±2.1 µM and 46.16±1.7 µM, and 52.83±3.2 µM and 60.57±2.8 µM against Jurkat E6.1, K562, and U937 cell lines, respectively. Importantly, all synthesized compounds exhibited no activity against the breast cancer MDA-MB-131 cell line and normal human PBMCs. To the pathway of cellular death was also validated by the time-dependent flow cytometric in-vitro apoptotic activities after treating with the most potent compounds, **P10** and **P7**, on Jurkat E6.1 and K562 cell lines. These compounds warrant further investigation for potential structural refinement to enhance their target specificity.

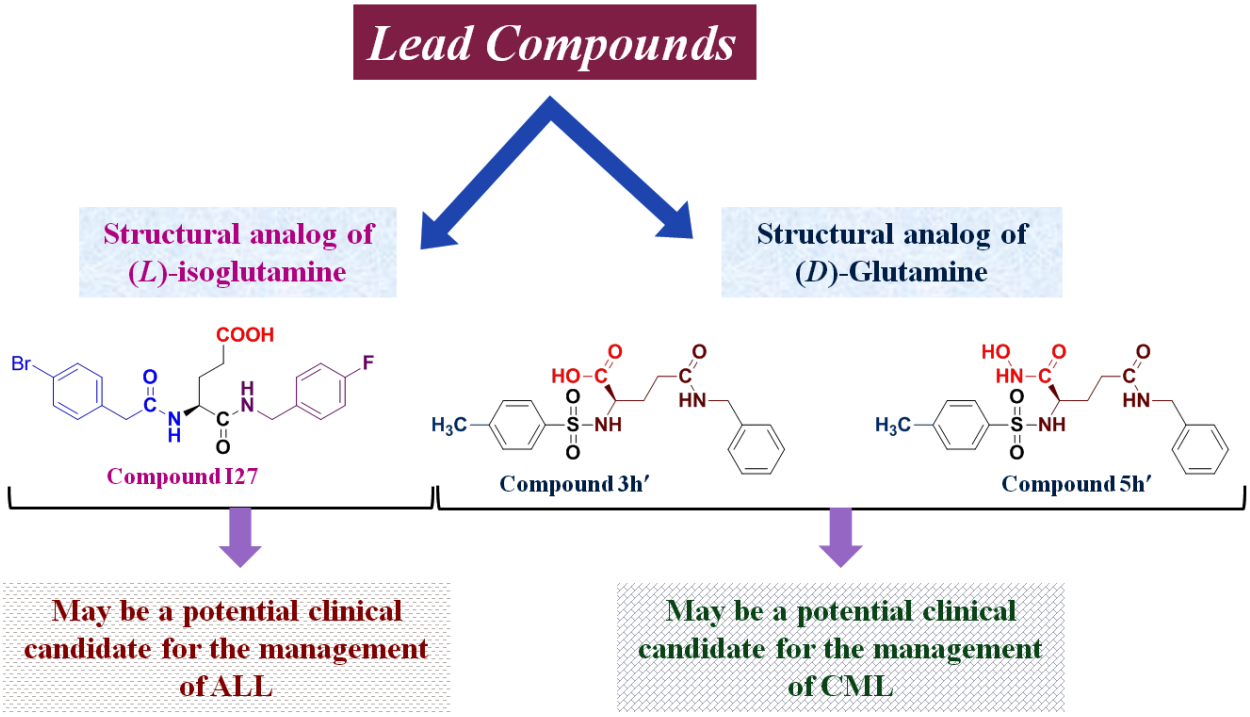

Figure 6.1. Structural analogs of (*L*)-isoglutamine (Compound **I27**) and (*D*)-glutamine (compound **3h'** and compound **5h'**) as potential leads for the management of ALL and CML respectively.

In **Part-IV**, New derivatives of arylsulfonyl-(*D*)-glutamine, totaling 31 (designated as **3a-3h**, **3a′-3l′**, and **5a′-5k′**), were synthesized, purified, and characterized based on insights gained from

existing literature (**Chapter 2**) and QSAR-based molecular modeling studies (**Part-IIIA** and **Part-IIIB**). Out of these 31 compounds, 20 (**3a-3h** and **3a′-3l′**) incorporate a carboxylic acid moiety in their structures, while the remaining 11 (**5a′-5k′**) feature a hydroxamic acid group instead of a carboxylic acid group. These compounds were further subjected to cytotoxicity evaluation as well as gelatinase inhibition against leukemia and other solid tumor cell lines as well as to adjudicate their nontoxic profile toward normal cell line. The benzyl derivatives (compounds **3h, 3h'** and **5h'**) exerted the most promising antileukemic potential (activity in lower μM) as well as the highly efficacious gelatinase inhibition (IC_{50} in lower nM). Compounds **5k'** having a hydroxamic acid function as ZBG and containing a cyclohexyl group in its structure showed highest activity in case of gelatinase inhibition (MMP2 IC_{50} = 127.48 nM and MMP9 IC_{50} = 144.89 nM). The flow cytometric analysis also explored effective sub-G1 cell cycle arrest by both of better active molecules (compounds **3h, 3h', 5h'** and **5k'**) as seen in the chronic myeloid leukemia (K562) cell line. Moreover, these molecules (compounds **3h, 3h', 5h'** and **5k'**) were found to exert a minimum of 24% apoptosis in the K562 cell line. These molecules (**3h, 3h', 5h'** and **5k'**) were found to reduce about 20% MMP2 expression in the K562 cell line. These compounds (**3h, 3h', 5h'** and **5k'**) produced effective antiangiogenic potential. Nevertheless, the best active compound (compound **3h'**) among compounds featuring a carboxylic acid group and the best active compound (compound **5h'**) among compounds featuring a hydroxamic acid group also resulted in time-dependent apoptosis in the K562 cell line at their respective IC_{50} dose as observed by AO/EB staining. Additionally, binding interaction studies, including molecular docking and molecular dynamic simulation were conducted with MMP2 and selected compounds (**3d**, **3h′, 5d′ and 5h′**). Not only that, the MD simulation study of the most effective compounds (**3h'** and **5h'**) also pointed out stable binding interaction at the MMP2 active site correlating with the highly effective MMP2 inhibition profile of compound **3h'** and compound **5h'** as well as better antileukemic activity especially against chronic myeloid leukemia (CML) aiming less toxicity to normal healthy cells (**Figure 6.1**).

CHAPTER 7

FUTURE DIRECTION

After performing all the experiments and interpreting the results this work suggested that substituted aryl acetyl-(*L*)-isoglutamines especially compound **I27** may be a potential lead for the management of acute lymphoblastic leukemia (ALL) whereas, substituted aryl sulfonyl-(*D*)-glutamine derivatives especially compound **3h'** and compound **5h'** may be potential leads with efficacious antileukemic profiles for the management of CML in the future.

The lead compounds obtained in this work should be carried forward for the lead optimization process. The future objective may be emphasized by a series of works which are discussed in the following sections in case of the lead molecule belongs to the substituted aryl acetyl-(*L*)-isoglutamines as well as the lead molecule belonging to the tosyl-(*D*)-glutamine derivatives.

7.1. Future direction with lead belong to aryl acetyl-(*L*)-isoglutamines (compound **I27)**

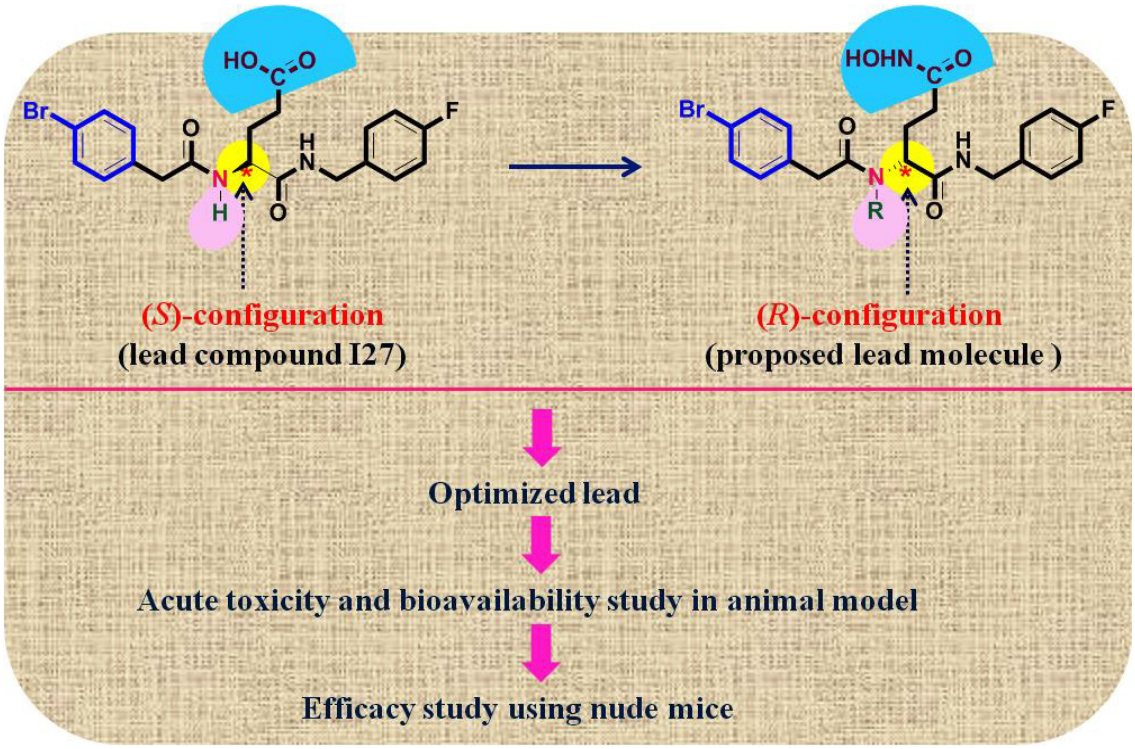

Figure 7.1. Incorporation of tertiary nitrogen (indicated by pink circle) and manipulation of zinc binding group (ZBG) (indicated by half circle) as well as inversion of configuration (indicated by yellow circle) of aryl acetyl-(*L*)-isoglutamine based lead (compound **I27**) would enhance antileukemic efficacy via the inhibition of metalloenzymes especially HDAC8, MMP2 and MMP9 for the management of CML.

a) The molecular modelling study (**Chapter 5; Part-IIIA**) also suggested that presence of the hydroxamic acid group as zinc binding group (ZBG) will enhance the activity of MMP2 and MMP9. By comparing the lead compounds (**3h′** and **5h′**) of tosyl-(*D*)-glutamine derivatives (**Chapter 5; Part-IV**), the replacement of the carboxylic acid (ZBG) function with hydroxamic acid (ZBG) increases the gelatinases (MMP2 and MMP9) inhibitory activity as well as anti-leukemic efficacy. Therefore, the conversion of carboxylic acid (ZBG) function into hydroxamic acid (ZBG) (**Figure 7.1**) may be investigated to improve the anti-leukemic efficacy.

b) From molecular modeling studies (**Chapter 5; Part-IIIA & Part-IIIB**), it was found that the presence of tertiary nitrogen in the structure of gelatinases (MMP2 and MMP9) inhibitor will enhance the inhibitory activity. Therefore, the replacement of the hydrogen atom attached to the nitrogen of the aryl acetamide group (indicated in pink color in **Figure 7.1**) with another atom or group may be investigated to improve the anti-leukemic efficacy.

c) The para nitrobenzene sulfonyl-(*D*)-glutamine derivatives (**3a-3h**) showed many fold gelatinases (MMP2 and MMP9) inhibition in comparison with the previously reported congener of para nitrobenzene sulfonyl-(*L*)-glutamine derivatives (Mukherjee et al., 2017). Therefore, in the case of aryl acetyl-(*L*)-isoglutamines, it would be a strategy of the lead optimization process to check the contribution of configuration (indicated by the yellow circle in **Figure 7.1**) towards gelatinases (MMP2 and MMP9) inhibition as well as anti-leukemic efficacy.

d) Following the completion of the lead optimization procedure, an animal model will be used to conduct acute toxicity and bioavailability studies. If the bioavailability and toxicity studies yield positive results, an efficacy investigation with optimized lead in nude mice (immunocompromised mice) is conducted as well.

7.2. Future direction with leads belong to substituted aryl sulfonyl-(*D*)-glutamine derivatives (compound 3h′ and 5h′)

(a) In case of substituted aryl sulfonyl-(*D*)-glutamine derivatives the presence of tertiary nitrogen (**Figure 7.2**; indicated by R_1 and yellow circle) in the structure of lead molecules **(**compound **3h′** and **5h′)** will also may be a future strategy of lead optimization upon enhancing the gelatinases (MMP2 and MMP9) inhibitory activity which was observed in the finding of QSAR-based molecular modelling studies (**Chapter 5; Part-IIIA & Part-IIIB**).

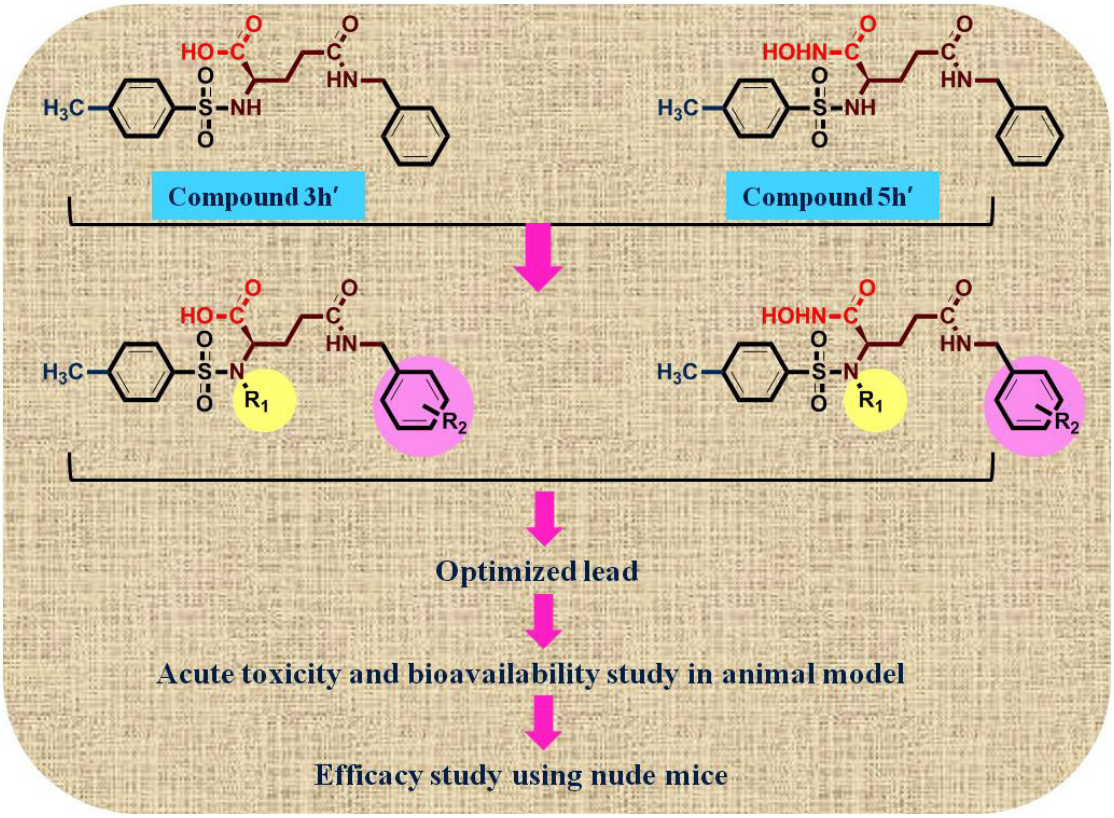

Figure 7.2. Incorporation of tertiary nitrogen (indicated by R_1 and yellow circle) and substitution of the benzene ring (indicated by R_2 pink circle) of tosyl-(*D*)-glutamine-based leads (compound **3h′** and **5h′**) would enhance antileukemic efficacy via the inhibition of metalloenzymes especially MMP2 and MMP9 for the management of CML.

(b) It was also observed that the introduction of halogen (fluorine atom) in the 4th position of benzyl ring (**Figure 7.2**; indicated by R_2 and pink circle) of aryl acetyl-(*L*)-isoglutamine (**Chapter 5**; **Table 5.1;** compound **I27**) resulted in increased anti-leukemic activity in comparison with others (Dutta et al., 2019). Therefore, in the case of tosyl-(*D*)-glutamine derivatives also substitution at the R_2 position (**Figure 7.2**; indicated by the pink circle) would be another strategy of the lead optimization process to check the contribution of efficacy against chronic myeloid leukemia cells (K562).

(c) After lead optimization process is completed, acute toxicity study as well as bioavailability study in animal model will be performed. If the result of toxicity and bioavailability study is positive, an efficacy study of optimized lead in nude mice (immunocompromised mice) also performed.

REFERENCES

References

Abagyan R, Totrov M, Kuznetsov D. ICM? A new method for protein modeling and design: Applications to docking and structure prediction from the distorted native conformation. J. Comput. Chem. 1994;15(5):488-506. doi: 10.1002/jcc.540150503.

Abagyan R, Totrov M. High-throughput docking for lead generation. Curr. Opin. Chem. Biol. 2001;5(4):375-382. doi: 10.1016/s1367-5931(00)00217-9.

Achary PGR. Applications of quantitative structure-activity relationships (QSAR) based virtual screening in drug design: A review. Mini Rev Med Chem. 2020;20(14):1375-1388. doi: 10.2174/1389557520666200429102334.

Adams M, Thomas H. A phase I study of the matrix metalloproteinase inhibitor, marimastat administered concurrently with carboplatin, to patients with relapsed ovarian cancer. InASCO Annual Meeting. 1998:838. (Abstract)

Adcock SA, McCammon JA. Molecular dynamics: survey of methods for simulating the activity of proteins. Chem Rev. 2006;106(5):1589-1615. doi: 10.1021/cr040426m.

Adhikari N, Halder AK, Mallick S, Saha A, Saha KD, Jha T. Robust design of some selective matrix metalloproteinase-2 inhibitors over matrix metalloproteinase-9 through in silico/fragment-based lead identification and de novo lead modification: Syntheses and biological assays. Bioorg. Med. Chem. 2016;24(18):4291-4309. doi: 10.1016/j.bmc.2016.07.023.

Adhikari N, Mukherjee A, Saha A, Jha T. Arylsulfonamides and selectivity of matrix metalloproteinase-2: An overview. Eur. J. Med. Chem. 2017;129:72-109. doi: 10.1016/j.ejmech.2017.02.014.

Adhikari N, Amin SA, Saha A, Jha T. Structural exploration for the refinement of anticancer matrix metalloproteinase-2 inhibitor designing approaches through robust validated multi-QSARs. J. Mol. Struct. 2018A;1156:501-515. doi: 10.1016/j.molstruc.2017.12.005.

Adhikari N, Amin SA, Saha A. Jha T. Exploring in house glutamate inhibitors of matrix metalloproteinase-2 through validated robust chemico-biological quantitative approaches. Struct. Chem. 2018B;29:285-297. doi: 10.1007/s11224-017-1028-6.

Adhikari N, Jha T, Ghosh B. Dissecting histone deacetylase 3 in multiple disease conditions: selective inhibition as a promising therapeutic strategy. J Med Chem. 2021;64(13):8827-8869. doi: 10.1021/acs.jmedchem.0c01676.

Advani AS, Gibson SE, Douglas E, Jin T, Zhao X, Kalaycio M, Copelan E, Sobecks R, Sekeres M, Sungren S, Hsi ED. Histone H4 acetylation by immunohistochemistry and prognosis in newly diagnosed adult acute lymphoblastic leukemia (ALL) patients. BMC Cancer. 2010;10:387. doi: 10.1186/1471-2407-10-387.

Agrawal A, Romero-Perez D, Jacobsen JA, Villarreal FJ, Cohen SM. Zinc-binding groups modulate selective inhibition of MMPs. ChemMedChem. 2008;3(5):812-820. doi: 10.1002/cmdc.200700290.

References

Agarwal M, Seth R, Chatterjee T. Recent advances in molecular diagnosis and prognosis of childhood B cell lineage acute lymphoblastic leukemia (B-ALL). Indian J. Hematol. Blood Transfus. 2021;37(1):10-20. doi: 10.1007/s12288-020-01295-8.

Ahmann FR, Saad F, Mercier R, Huddart RA, Roberts JT, Collier M, Bettencourt LA, Zhang M, Clendeninn NJ, Wilding G. Interim results of a phase III study of the matrix metalloprotease inhibitor prinomastat in patients having metastatic, hormone refractory prostate cancer (HRPC). InASCO. 2001:692. (Abstract)

Ajmani S, Jadhav K, Kulkarni SA. Three-dimensional QSAR using the k-nearest neighbor method and its interpretation. J. Chem. Inf. Model. 2006;46(1):24-31. doi: 10.1021/ci0501286.

Almutairi S, Kalloush HM, Manoon NA, Bardaweel SK. Matrix metalloproteinases inhibitors in cancer treatment: An updated review (2013-2023). Molecules. 2023;28(14):5567. doi: 10.3390/molecules28145567.

Ambure P, Roy K. Exploring structural requirements of leads for improving activity and selectivity against CDK5/p25 in Alzheimer's disease: An in silico approach. RSC Adv. 2014;4:6702. doi: 10.1039/c3ra46861e.

Amin SA, Gayen S. Modeling the cytotoxic activity of pyrazolo-triazole hybrids using descriptors calculated from the open source tool “PaDEL-descriptor”. J. Taibah Univ. Sci. 2016A;10:896-905. doi: 10.1016/j.jtusci.2016.04.009.

Amin SA, Adhikari N, Jha T, Gayen S. First molecular modeling report on novel arylpyrimidine kynurenine monooxygenase inhibitors through multi-QSAR analysis against Huntington's disease: A proposal to chemists! Bioorg. Med. Chem. Lett. 2016B;26(23):5712-5718. doi: 10.1016/j.bmcl.2016.10.058.

Amin SA, Adhikari N, Jha T, Gayen S. An Integrated Multi-QSAR Modeling Approach for Designing Knoevenagel- Type Indoles with Enhancing Cytotoxic Profiles. Curr. Comput. Aided. Drug Des. 2017A;13(4):336-345. doi: 10.2174/1573409913666170309150014.

Amin SA, Adhikari N, Jha T. Structure-activity relationships of hydroxamate-based histone deacetylase-8 inhibitors: reality behind anticancer drug discovery. Future Med. Chem. 2017B;9(18):2211-2237. doi: 10.4155/fmc-2017-0130.

Amin SA, Adhikari N, Jha T. Structure-activity relationships of HDAC8 inhibitors: Non-hydroxamates as anticancer agents. Pharmacol. Res. 2018;131:128-142. doi: 10.1016/j.phrs.2018.03.001.

Amin SA, Adhikari N, Gayen S, Jha T. Reliable structural information for rational design of benzoxazole type potential cholesteryl ester transfer protein (CETP) inhibitors through multiple validated modeling techniques. J. Biomol. Struct. Dyn. 2019;37:4528-4541. doi: 10.1080/07391102.2018.1552895.

Amin SA, Adhikari N, Jha T. Development of decision trees to discriminate HDAC8 inhibitors and non-inhibitors using recursive partitioning. J. Biomol. Struct. Dyn. 2021A;39(1):1-8. doi: 10.1080/07391102.2019.1661876.

References

Amin SA, Trivedi P, Adhikari N, Routholla G, Vijayasarathi D, Das S, Ghosh B, Jha T. Quantitative activity–activity relationship (QAAR) driven design to develop hydroxamate derivatives of pentanoic acids as selective HDAC8 inhibitors: Synthesis, biological evaluation and binding mode of interaction studies†. New J. Chem. 2021B;45:17149-17162.

Amin SA. (2022) *Design, synthesis, biological evaluation and molecular modelling studies of glutamate-based dual MMP-2/HDAC-8 inhibitors*. [PhD dissertation, Jadavpur University]. Index No. 256/17/Ph.

Amin SA, Khatun S, Gayen S, Das S, Jha T. Are inhibitors of histone deacetylase 8 (HDAC8) effective in hematological cancers especially acute myeloid leukemia (AML) and acute lymphoblastic leukemia (ALL)? Eur. J. Med. Chem. 2023;258:115594. doi: 10.1016/j.ejmech.2023.115594.

Anderson PM, Lalla RV. Glutamine for Amelioration of Radiation and Chemotherapy Associated Mucositis during Cancer Therapy. Nutrients. 2020;12(6):1675. doi: 10.3390/nu12061675.

Andreini C, Bertini I. A bioinformatics view of zinc enzymes. J. Inorg. Biochem. 2012;111:150-156. doi: 10.1016/j.jinorgbio.2011.11.020.

Aref S, Osman E, Mansy S, Omer N, Azmy E, Goda T, El-Sherbiny M. Prognostic relevance of circulating matrix metalloproteinase-2 in acute myeloid leukaemia patients. Hematol. Oncol. 2007;25(3):121-6. doi: 10.1002/hon.817.

Armitage JO, Weisenburger DD. New approach to classifying non-Hodgkin's lymphomas: Clinical features of the major histologic subtypes. Non-Hodgkin's Lymphoma Classification Project. J. Clin. Oncol. 1998;16(8):2780-2795. doi: 10.1200/JCO.1998.16.8.2780.

Arunachalam A, Rengan R, Umapathy D, Arockiam AJ. Impact of biphenyl benzhydrazone-incorporated arene Ru (II) complexes on cytotoxicity and the cancer cell death mechanism. Organometallics. 2022;41:2474-2486. doi: 10.1021/acs.organomet.2c00290.

Atale N, Gupta S, Yadav UC, Rani V. Cell-death assessment by fluorescent and nonfluorescent cytosolic and nuclear staining techniques. J. Microsc. 2014;255:7-19. doi: 10.1111/jmi.12133.

Baidya SK, Amin SA, Jha T. Outline of gelatinase inhibitors as anti-cancer agents: A patent mini-review for 2010-present. Eur. J. Med. Chem. 2021;213:113044. doi: 10.1016/j.ejmech.2020.113044.

Baidya, S.K.; Banerjee, S.; Ghosh, B.; Jha, T.; Adhikari, N. Exploration of structural alerts and fingerprints for novel anticancer therapeutics: a robust classification-QSAR dependent structural analysis of drug-like MMP-9 inhibitors. SAR QSAR Environ Res., 2023, 34, 299-319.

Baig MH, Ahmad K, Rabbani G, Danishuddin M, Choi I. Computer aided drug design and its application to the development of potential drugs for neurodegenerative disorders. Curr. Neuropharmacol. 2018;16(6):740-748. doi:10.2174/1570159X15666171016163510.

References

Balasubramanian S, Ramos J, Luo W, Sirisawad M, Verner E, Buggy JJ. A novel histone deacetylase 8 (HDAC8)-specific inhibitor PCI-34051 induces apoptosis in T-cell lymphomas. Leukemia. 2008;22(5):1026-1034. doi: 10.1038/leu.2008.9.

Barlaam B, Bird TG, Lambert-Van Der Brempt C, Campbell D, Foster SJ, Maciewicz R. New alpha-substituted succinate-based hydroxamic acids as TNFalpha convertase inhibitors. J. Med. Chem. 1999;42(23):4890-4908. doi: 10.1021/jm990377j.

Banerjee S, Adhikari N, Amin SA, Jha T. Histone deacetylase 8 (HDAC8) and its inhibitors with selectivity to other isoforms: An overview. Eur. J. Med. Chem. 2019;164:214-240. doi: 10.1016/j.ejmech.2018.12.039.

Banerjee S, Amin SA. Jha, T. Therapies of hematological malignancies: An overview of the potential targets and their inhibitors. Curr. Chem. Biol. 2021;15(1):19-49. doi:10.2174/2212796815666210203104446.

Barbarotta L, Hurley K. Romidepsin for the Treatment of Peripheral T-Cell Lymphoma. J. Adv. Pract. Oncol. 2015;6(1):22-36.

Bassan R, Bourquin JP, DeAngelo DJ, Chiaretti S. New approaches to the management of adult acute lymphoblastic leukemia. J. Clin. Oncol. 2018;36(35):JCO2017773648. doi: 10.1200/JCO.2017.77.3648.

Bassett SA, Barnett MP. The role of dietary histone deacetylases (HDACs) inhibitors in health and disease. Nutrients. 2014;6(10):4273-3401. doi: 10.3390/nu6104273.

Baxter CA, Murray CW, Clark DE, Westhead DR, Eldridge MD. Flexible docking using Tabu search and an empirical estimate of binding affinity. Proteins. 1998;33(3):367-382.

Beattie GJ, Smyth JF. Phase I study of intraperitoneal metalloproteinase inhibitor BB94 in patients with malignant ascites. Clin. Cancer Res. 1998;4(8):1899-1902.

Beaudry AG, Law ML. Leucine Supplementation in Cancer Cachexia: Mechanisms and a review of the pre-clinical literature. Nutrients. 2022;14(14):2824. doi: 10.3390/nu14142824.

Becker DP, Barta TE, Bedell LJ, Boehm TL, Bond BR, Carroll J, Carron CP, Decrescenzo GA, Easton AM, Freskos JN, Funckes-Shippy CL, Heron M, Hockerman S, Howard CP, Kiefer JR, Li MH, Mathis KJ, McDonald JJ, Mehta PP, Munie GE, Sunyer T, Swearingen CA, Villamil CI, Welsch D, Williams JM, Yu Y, Yao J. Orally active MMP-1 sparing α-tetrahydropyranyl and α-piperidinyl sulfone matrix metalloproteinase (MMP) inhibitors with efficacy in cancer, arthritis, and cardiovascular disease. J. Med. Chem. 2010;53(18):6653-6680. doi: 10.1021/jm100669j.

Bedard PL, Hyman DM, Davids MS, Siu LL. Small molecules, big impact: 20 years of targeted therapy in oncology. Lancet. 2020;395(10229):1078-1088. doi: 10.1016/S0140-6736(20)30164-1.

Bellamy WT, Richter L, Frutiger Y, Grogan TM. Expression of vascular endothelial growth factor and its receptors in hematopoietic malignancies. Cancer Res. 1999;59(3):728-733.

Benek O, Korabecny J, Soukup O. A Perspective on multi-target drugs for alzheimer's disease. Trends Pharmacol. Sci. 2020;41(7):434-445. doi: 10.1016/j.tips.2020.04.008.

References

Bernfeld E, Foster DA. Glutamine as an essential amino acid for KRas-driven cancer cells. Trends Endocrinol. Metab. 2019;30(6):357-368. doi: 10.1016/j.tem.2019.03.003.

Bernhard EJ, Gruber SB, Muschel RJ. Direct evidence linking expression of matrix metalloproteinase 9 (92-kDa gelatinase/collagenase) to the metastatic phenotype in transformed rat embryo cells. Proc. Natl. Acad. Sci. USA. 1994;91(10):4293-4297. doi: 10.1073/pnas.91.10.4293.

Bernhard EJ, Muschel RJ, Hughes EN. Mr 92,000 gelatinase release correlates with the metastatic phenotype in transformed rat embryo cells. Cancer Res. 1990;50(13):3872-3877.

Betz M, Huxley P, Davies SJ, Mushtaq Y, Pieper M, Tschesche H, Bode W, Gomis-Rüth FX. 1.8-A crystal structure of the catalytic domain of human neutrophil collagenase (matrix metalloproteinase-8) complexed with a peptidomimetic hydroxamate primed-side inhibitor with a distinct selectivity profile. Eur. J. Biochem. 1997;247(1):356-363. doi: 10.1111/j.1432-1033.1997.00356.x.

Bhutia YD, Ganapathy V. Glutamine transporters in mammalian cells and their functions in physiology and cancer. Biochim. Biophys. Acta. 2016;1863(10):2531-2539. doi: 10.1016/j.bbamcr.2015.12.017.

Biasone A, Tortorella P, Campestre C, Agamennone M, Preziuso S, Chiappini M, Nuti E, Carelli P, Rossello A, Mazza F, Gallina C. alpha-Biphenylsulfonylamino 2-methylpropyl phosphonates: enantioselective synthesis and selective inhibition of MMPs. Bioorg. Med. Chem. 2007;15(2):791-799. doi: 10.1016/j.bmc.2006.10.047.

Bissett D, O'Byrne KJ, von Pawel J, Gatzemeier U, Price A, Nicolson M, Mercier R, Mazabel E, Penning C, Zhang MH, Collier MA, Shepherd FA. Phase III study of matrix metalloproteinase inhibitor prinomastat in non-small-cell lung cancer. J. Clin. Oncol. 2005;23(4):842-849. doi: 10.1200/JCO.2005.03.170.

Björklund M, Koivunen E. Gelatinase-mediated migration and invasion of cancer cells. Biochim. Biophys. Acta. 2005;1755(1):37-69. doi: 10.1016/j.bbcan.2005.03.001.

Boasberg P, Harbaugh BL, Eisenberger M. Marimastat in patients with hormone refractory prostate cancer: A dose-finding study. InASCO Annual Meeting, 1997:1126. (Abstract)

Böhm HJ. The development of a simple empirical scoring function to estimate the binding constant for a protein-ligand complex of known three-dimensional structure. J Comput Aided Mol Des. 1994;8(3):243-256. doi: 10.1007/BF00126743.

Bonadonna G, Monfardini S, De Lena M, Fossati-Bellani F. Clinical evaluation of adriamycin, a new antitumour antibiotic. Br. Med. J. 1969;3(5669):503-506. doi: 10.1136/bmj.3.5669.503.

Bondarev AD, Attwood MM, Jonsson J, Chubarev VN, Tarasov VV, Schiöth HB. Recent developments of HDAC inhibitors: Emerging indications and novel molecules. Br. J. Clin. Pharmacol. 2021;87(12):4577-4597. doi: 10.1111/bcp.14889.

References

Bordone L, Guarente L. Calorie restriction, SIRT1 and metabolism: Understanding longevity. Nat Rev Mol. Cell Biol. 2005;6(4):298-305. doi: 10.1038/nrm1616.

Bramhall SR, Schulz J, Nemunaitis J, Brown PD, Baillet M, Buckels JA. A double-blind placebo-controlled, randomised study comparing gemcitabine and marimastat with gemcitabine and placebo as first line therapy in patients with advanced pancreatic cancer. Br. J. Cancer. 2002A;87(2):161-167. doi: 10.1038/sj.bjc.6600446.

Bramhall SR, Hallissey MT, Whiting J, Scholefield J, Tierney G, Stuart RC, Hawkins RE, McCulloch P, Maughan T, Brown PD, Baillet M, Fielding JW. Marimastat as maintenance therapy for patients with advanced gastric cancer: a randomised trial. Br. J. Cancer. 2002B;86(12):1864-1870. doi: 10.1038/sj.bjc.6600310.

Brinckerhoff CE, Matrisian LM. Matrix metalloproteinases: A tail of a frog that became a prince. Nat. Rev. Mol. Cell Biol. 2002;3(3):207-214. doi: 10.1038/nrm763.

Brinker BT, Krown SE, Lee JY, Cesarman E, Chadburn A, Kaplan LD, Henry DH, Von Roenn JH. Phase 1/2 trial of BMS-275291 in patients with human immunodeficiency virus-related Kaposi sarcoma: a multicenter trial of the AIDS Malignancy Consortium. Cancer. 2008;112(5):1083-1088. doi: 10.1002/cncr.23108.

Brooijmans N, Kuntz ID. Molecular recognition and docking algorithms. Annu. Rev. Biophys. Biomol. Struct. 2003;32:335-373. doi: 10.1146/annurev.biophys.32.110601.142532.

Brooks CL, Gu W. The impact of acetylation and deacetylation on the p53 pathway. Protein Cell. 2011;2(6):456-462. doi:10.1007/s13238-011-1063-9.

Brooks CL, Gu W. Ubiquitination, phosphorylation and acetylation: The molecular basis for p53 regulation. Curr. Opin. Cell Biol. 2003;15(2):164-171. doi: 10.1016/s0955-0674(03)00003-6.

Brosnan JT. Interorgan amino acid transport and its regulation. J. Nutr. 2003;133(6 Suppl 1):2068S-2072S. doi: 10.1093/jn/133.6.2068S.

Brown PD. Ongoing trials with matrix metalloproteinase inhibitors. Expert Opin. Investig. Drugs. 2000;9(9):2167-2177. doi: 10.1517/13543784.9.9.2167.

Bruker 2002. SADABS (Version 2.03), SAINT (Version 6.02a) and SMART (Version 5.618). Bruker AXS Inc., Madison, Wisconsin, USA.

Bumma N, Nagasaka M, Hemingway G, Miyashita H, Chowdhury T, Kim S, Vankayala HM, Ahmed S, Jasti P. Effect of Exposure to Agent Orange on the Risk of Monoclonal Gammopathy and Subsequent Transformation to Multiple Myeloma: A Single-Center Experience From the Veterans Affairs Hospital, Detroit. Clin. Lymphoma Myeloma Leuk. 2020;20(5):305-311. doi: 10.1016/j.clml.2019.11.014.

Burley SK, Berman HM, Christie C, Duarte JM, Feng Z, Westbrook J, Young J, Zardecki C. RCSB Protein Data Bank: Sustaining a living digital data resource that enables breakthroughs in scientific research and biomedical education. Protein Sci. 2018;27(1):316-330. doi: 10.1002/pro.3331.

References

Calderón-Montaño JM, Guillén-Mancina E, Jiménez-Alonso JJ, Jiménez-González V, Burgos-Morón E, Mate A, Pérez-Guerrero MC, López-Lázaro M. Manipulation of Amino Acid Levels with Artificial Diets Induces a Marked Anticancer Activity in Mice with Renal Cell Carcinoma. Int. J. Mol. Sci. 2022;23(24):16132. doi: 10.3390/ijms232416132.

Carpentier G, Berndt S, Ferratge S. Angiogenesis analyzer for ImageJ — a comparative morphometric analysis of "endothelial tube formation assay" and "fibrin bead assay". Sci. Rep. 2020;10:11568. doi: 10.1038/s41598-020-67289-8.

Cengiz Seval G, Beksac M. A comparative safety review of histone deacetylase inhibitors for the treatment of myeloma. Expert Opin. Drug Saf. 2019;18(7):563-571. doi: 10.1080/14740338.2019.1615051.

Chakrabarti A, Oehme I, Witt O, Oliveira G, Sippl W, Romier C, Pierce RJ, Jung M. HDAC8: a multifaceted target for therapeutic interventions. Trends Pharmacol. Sci. 2015;36(7):481-492. doi: 10.1016/j.tips.2015.04.013.

Chan WK, Horvath TD, Tan L, Link T, Harutyunyan KG, Pontikos MA, Anishkin A, Du D, Martin LA, Yin E, Rempe SB, Sukharev S, Konopleva M, Weinstein JN, Lorenzi PL. Glutaminase activity of L-asparaginase contributes to durable preclinical activity against acute lymphoblastic leukemia. Mol. Cancer Ther. 2019;18(9):1587-1592. doi: 10.1158/1535-7163.MCT-18-1329.

Chang M. Matrix metalloproteinase profiling and their roles in disease. RSC Adv. 2023;13(9):6304-6316. doi: 10.1039/d2ra07005g.

Charifson PS, Corkery JJ, Murcko MA, Walters WP. Consensus scoring: A method for obtaining improved hit rates from docking databases of three-dimensional structures into proteins. J. Med. Chem. 1999;42(25):5100-5109. doi: 10.1021/jm990352k.

Chattopadhyay S, Saha A, Azam M, Mukherjee A, Sur PK. Role of oral glutamine in alleviation and prevention of radiation-induced oral mucositis: A prospective randomized study. South Asian J. Cancer. 2014;3(1):8-12. doi: 10.4103/2278-330X.126501.

Chaudhary AK, Chaudhary S, Ghosh K, Shanmukaiah C, Nadkarni AH. Secretion and expression of matrix metalloproteinase-2 and 9 from bone marrow mononuclear cells in myelodysplastic syndrome and acute myeloid leukemia. Asian Pac. J. Cancer Prev. 2016;17(3):1519-1529. doi: 10.7314/apjcp.2016.17.3.1519.

ChemDraw Ultra 5.0, Cambridge Soft Corporation, USA, 2010.

Chen HM, Liu BF, Huang HL, Hwang SF, Ho SY. SODOCK: swarm optimization for highly flexible protein-ligand docking. J. Comput. Chem. 2007;28(2):612-623. doi: 10.1002/jcc.20542.

Chen L, Li Y, Zhao Q, Peng H, Hou T. ADME evaluation in drug discovery. 10. Predictions of P-glycoprotein inhibitors using recursive partitioning and naive Bayesian classification techniques. Mol. Pharm. 2011;8(3):889-900. doi: 10.1021/mp100465q.

References

Chen YJ, Chang LS. Gallic acid downregulates matrix metalloproteinase-2 (MMP-2) and MMP-9 in human leukemia cells with expressed Bcr/Abl. Mol. Nutr. Food Res. 2012;56(9):1398-1412. doi: 10.1002/mnfr.201200167.

Chen YJ, Chang LS. Simvastatin induces NFκB/p65 down-regulation and JNK1/c-Jun/ATF-2 activation, leading to matrix metalloproteinase-9 (MMP-9) but not MMP-2 down-regulation in human leukemia cells. Biochem. Pharmacol. 2014;92(4):530-543. doi: 10.1016/j.bcp.2014.09.026.

Chen L, Cui H. Targeting glutamine induces apoptosis: A cancer therapy approach. Int. J. Mol. Sci. 2015;16(9):22830-55. doi: 10.3390/ijms160922830.

Chen Y, Wang X, Xiang W, He L, Tang M, Wang F, Wang T, Yang Z, Yi Y, Wang H, Niu T, Zheng L, Lei L, Li X, Song H, Chen L. Development of purine-based hydroxamic acid derivatives: potent histone deacetylase inhibitors with marked in vitro and in vivo antitumor activities. J. Med. Chem. 2016;59:5488–5504. doi: 10.1021/acs.jmedchem.6b00579.

Chen AY, Adamek RN, Dick BL, Credille CV, Morrison CN, Cohen SM. Targeting metalloenzymes for therapeutic intervention. Chem. Rev. 2019;119(2):1323-1455. doi: 10.1021/acs.chemrev.8b00201.

Cheng Y, Chen H. Aberrance of zinc metalloenzymes-induced human diseases and its potential mechanisms. nutrients. 2021;13(12):4456. doi: 10.3390/nu13124456.

Cherkasov A, Muratov EN, Fourches D, Varnek A, Baskin II, Cronin M, Dearden J, Gramatica P, Martin YC, Todeschini R, Consonni V, Kuz'min VE, Cramer R, Benigni R, Yang C, Rathman J, Terfloth L, Gasteiger J, Richard A, Tropsha A. QSAR modeling: Where have you been? Where are you going to? J. Med. Chem. 2014;57(12):4977-5010. doi: 10.1021/jm4004285.

Cheshmazar N, Hamzeh-Mivehroud M, Nozad Charoudeh H, Hemmati S, Melesina J, Dastmalchi S. Current trends in development of HDAC-based chemotherapeutics. Life Sci. 2022;308:120946. doi: 10.1016/j.lfs.2022.120946.

Chhatbar DM, Chaube UJ, Vyas VK, Bhatt HG. CoMFA, CoMSIA, Topomer CoMFA, HQSAR, molecular docking and molecular dynamics simulations study of triazine morpholino derivatives as mTOR inhibitors for the treatment of breast cancer. Comput. Biol. Chem. 2019;80:351-363. doi: 10.1016/j.compbiolchem.2019.04.017.

Chirivi RG, Garofalo A, Crimmin MJ, Bawden LJ, Stoppacciaro A, Brown PD, Giavazzi R. Inhibition of the metastatic spread and growth of B16-BL6 murine melanoma by a synthetic matrix metalloproteinase inhibitor. Int. J. Cancer. 1994;58(3):460-464. doi: 10.1002/ijc.2910580326.

Chotitumnavee J, Yamashita Y, Takahashi Y, Takada Y, Iida T, Oba M, Itoh Y, Suzuki T. Selective degradation of histone deacetylase 8 mediated by a proteolysis targeting chimera (PROTAC). Chem. Commun. (Camb). 2022;58(29):4635-4638. doi: 10.1039/d2cc00272h.

References

Chu QS, Forouzesh B, Syed S, Mita M, Schwartz G, Cooper J, Curtright J, Rowinsky EK. A phase II and pharmacological study of the matrix metalloproteinase inhibitor (MMPI) COL-3 in patients with advanced soft tissue sarcomas. Invest. New Drugs. 2007;25(4):359-367. doi: 10.1007/s10637-006-9031-6. [Erratum in: Invest. New Drugs. 2007;25(4):357. Copper, Joshua (corrected to Cooper, Joshua)]

Cianfrocca M, Cooley TP, Lee JY, Rudek MA, Scadden DT, Ratner L, Pluda JM, Figg WD, Krown SE, Dezube BJ. Matrix metalloproteinase inhibitor COL-3 in the treatment of AIDS-related Kaposi's sarcoma: a phase I AIDS malignancy consortium study. J. Clin. Oncol. 2002;20(1):153-159. doi: 10.1200/JCO.2002.20.1.153.

Clinical Trials Using CB839 in Cancer. List Results. Available online: https://clinicaltrials.gov/ct2/results?cond=Cancer&term=CB839&cntry=&state=&city=&dist= (accessed on 29 December 2023).

Cohen MH, Williams G, Johnson JR, Duan J, Gobburu J, Rahman A, Benson K, Leighton J, Kim SK, Wood R, Rothmann M, Chen G, U KM, Staten AM, Pazdur R. Approval summary for imatinib mesylate capsules in the treatment of chronic myelogenous leukemia. Clin. Cancer Res. 2002;8(5):935-942.

Consonni V, Todeschini R, Pavan M. Structure/response correlations and similarity/diversity analysis by GETAWAY descriptors. 1. Theory of the novel 3D molecular descriptors. J. Chem. Inf. Comput. Sci. 2002;42(3):682-692. doi: 10.1021/ci015504a.

Corbeil CR, Williams CI, Labute P. Variability in docking success rates due to dataset preparation. J. Comput. Aided Mol. Des. 2012;26(6):775-786. doi: 10.1007/s10822-012-9570-1.

Cormerais Y, Massard PA, Vucetic M, Giuliano S, Tambutté E, Durivault J, Vial V, Endou H, Wempe MF, Parks SK, Pouyssegur J. The glutamine transporter ASCT2 (SLC1A5) promotes tumor growth independently of the amino acid transporter LAT1 (SLC7A5). J. Biol. Chem. 2018;293(8):2877-2887. doi: 10.1074/jbc.RA117.001342.

Cossarizza A, Baccarani-Contri M, Kalashnikova G, Franceschi C. A new method for the cytofluorimetric analysis of mitochondrial membrane potential using the J-aggregate forming lipophilic cation 5,5',6,6'-tetrachloro-1,1',3,3'-tetraethylbenzimidazolcarbocyanine iodide (JC-1). Biochem. Biophys. Res. Commun. 1993;197(1):40-45. doi: 10.1006/bbrc.1993.2438.

Cramer RD, Patterson DE, Bunce JD. Comparative molecular field analysis (CoMFA). 1. Effect of shape on binding of steroids to carrier proteins. J. Am. Chem. Soc. 1988;110(18):5959-5967. doi: 10.1021/ja00226a005.

Cramer RD. Topomer CoMFA: a design methodology for rapid lead optimization. J. Med. Chem. 2003;46(3):374-388. doi: 10.1021/jm020194o.

Cramer RD. Rethinking 3D-QSAR. J. Comput. Aided Mol. Des. 2011;25(3):197-201. doi: 10.1007/s10822-010-9403-z.

Cramer RD. The inevitable QSAR renaissance. J. Comput. Aided Mol. Des. 2012;26(1):35-38. doi:10.1007/s10822-011-9495-0.

References

Crilly T, Johnson D. The emergence of topological dimension theory. In: James IM, Ed., History of Topology, Elsevier, Amsterdam, 1999.

Cruzat V, Macedo Rogero M, Noel Keane K, Curi R, Newsholme P. Glutamine: Metabolism and immune function, supplementation and clinical translation. Nutrients. 2018;10(11):1564. doi: 10.3390/nu10111564.

Cuajungco MP, Ramirez MS, Tolmasky ME. Zinc: Multidimensional Effects on Living Organisms. Biomedicines. 2021;9(2):208. doi: 10.3390/biomedicines9020208.

Cui N, Hu M, Khalil RA. Biochemical and biological attributes of matrix metalloproteinases. Prog. Mol. Biol. Transl. Sci. 2017;147:1-73. doi: 10.1016/bs.pmbts.2017.02.005.

Curi R, Newsholme P, Marzuca-Nassr GN, Takahashi HK, Hirabara SM, Cruzat V, Krause M, de Bittencourt PI Jr. Regulatory principles in metabolism-then and now. Biochem. J. 2016;473(13):1845-57. doi: 10.1042/BCJ20160103.

Danishuddin, Khan AU. Descriptors and their selection methods in QSAR analysis: Paradigm for drug design. Drug Discov. Today. 2016;21(8):1291-1302. doi: 10.1016/j.drudis.2016.06.013.

Das S. (2018) *Synthesis and biological evaluation of (R)-1-([1,1'-biphenyl]-4-ylsulfonyl)-5-oxopyrrolidine-2-carboxamide derivatives as possible anticancer agents.* [M. Pharm dissertation, Jadavpur University]. Exam. Roll No.: M4PHA18003.

Das S, Amin SA, Jha T. Inhibitors of gelatinases (MMP-2 and MMP-9) for the management of hematological malignancies. Eur. J. Med. Chem. 2021A;223:113623. doi: 10.1016/j.ejmech.2021.113623.

Das S, Amin SA, Jha T. Insight into the structural requirement of aryl sulphonamide based gelatinases (MMP-2 and MMP-9) inhibitors - Part I: 2D-QSAR, 3D-QSAR topomer CoMFA and Naïve Bayes studies - First report of 3D-QSAR Topomer CoMFA analysis for MMP-9 inhibitors and jointly inhibitors of gelatinases together. SAR QSAR Environ. Res. 2021B;32(8):655-687. doi: 10.1080/1062936X.2021.1955414.

Das S, Amin SA, Gayen S, Jha T. Insight into the structural requirements of gelatinases (MMP-2 and MMP-9) inhibitors by multiple validated molecular modelling approaches: Part II. SAR QSAR Environ. Res. 2022A;33(3):167-192. doi: 10.1080/1062936X.2022.2041722.

Das P, Dutta T, Manna S, Loganathan S, Basak P. Facile green synthesis of non-genotoxic, non-hemolytic organometallic silver nanoparticles using extract of crushed, wasted, and spent Humulus lupulus (hops): Characterization, anti-bacterial, and anti-cancer studies. Environ. Res. 2022B;204(Pt A):111962. doi: 10.1016/j.envres.2021.111962.

Dastmalchi S, Hamzeh-Mivehroud M, Sokouti B. Molecular descriptors. In: Quantitative Structure–Activity Relationship: A Practical Approach. CRC Press. Boca Raton, USA. 2018A, Ch. 3, pp. 11-24.

Dastmalchi S, Hamzeh-Mivehroud M, Sokouti B. Model building. In: Quantitative Structure–Activity Relationship: A Practical Approach. CRC Press. Boca Raton, USA. 2018B, Ch. 5, pp. 35-51.

References

Datta S, Manna M, Khanra S, Ghosh M, Bhar R, Chakraborty A, Roy S.. Therapeutic immunization with radio-attenuated *Leishmania* parasites through i.m. route revealed protection against the experimental murine visceral leishmaniasis. Parasitol. Res. 2012;111:361-369. doi: 10.1007/s00436-012-2847-4.

Davies B, Brown PD, East N, Crimmin MJ, Balkwill FR. A synthetic matrix metalloproteinase inhibitor decreases tumor burden and prolongs survival of mice bearing human ovarian carcinoma xenografts. Cancer Res. 1993;53(9):2087-2091. [Erratum in: Cancer Res 1993;53(15):3652.]

Davis JR, Benjamin DJ, Jonas BA. New and emerging therapies for acute myeloid leukaemia. J. Investig. Med. 2018;66(8):1088-1095. doi: 10.1136/jim-2018-000807.

De P, Kar S, Ambure P, Roy K. Prediction reliability of QSAR models: An overview of various validation tools. Arch. Toxicol. 2022;96(5):1279-1295. doi: 10.1007/s00204-022-03252-y.

De Vitto H, Pérez-Valencia J, Radosevich JA. Glutamine at focus: versatile roles in cancer. Tumour Biol. 2016 Feb;37(2):1541-58. doi: 10.1007/s13277-015-4671-9.

Debnath B, Srikanth K, Banerjee S, Jha T. 1, 5-N, N-Disubstituted-2-(substituted benzenesulphonyl)-glutamamides as antitumor agents. Part 2. Synthesis, biological activity and QSAR Study#. Internet Electron. J. Mol. Des. 2002;1(10):488-502.

DeClerck YA, Perez N, Shimada H, Boone TC, Langley KE, Taylor SM. Inhibition of invasion and metastasis in cells transfected with an inhibitor of metalloproteinases. Cancer Res. 1992;52(3):701-708.

DeClerck YA, Yean TD, Chan D, Shimada H, Langley KE. Inhibition of tumor invasion of smooth muscle cell layers by recombinant human metalloproteinase inhibitor. Cancer Res. 1991;51(8):2151-2157.

Devinyak O, Havrylyuk D, Lesyk R. 3D-MoRSE descriptors explained. J. Mo.l Graph. Model. 2014;54:194-203. doi: 10.1016/j.jmgm.2014.10.006.

Dezube BJ, Krown SE, Lee JY, Bauer KS, Aboulafia DM. Randomized phase II trial of matrix metalloproteinase inhibitor COL-3 in AIDS-related Kaposi's sarcoma: an AIDS Malignancy Consortium Study. J. Clin. Oncol. 2006;24(9):1389-1394. doi: 10.1200/JCO.2005.04.2614.

Discovery Studio 3.0, Accelrys Inc., San Diego, USA, (2015); Software available at http://www.accelrys.com.

Dixon SL, Smondyrev AM, Knoll EH, Rao SN, Shaw DE, Friesner RA. PHASE: a new engine for pharmacophore perception, 3D-QSAR model development, and 3D database screening: 1. Methodology and preliminary results. J. Comput. Aided Mol. Des. 2006;20(10-11):647-671. doi: 10.1007/s10822-006-9087-6.

Dolomanov OV, Bourhis LJ, Gildea RJ, Howard JAK, Puschmann H. OLEX2: a complete structure solution, refinement and analysis program. J. Appl. Cryst. 2009;42:339-341. doi: 10.1107/S0021889808042726.

References

Douillard JY, Peschel C, Shepherd F, Paz-Ares L, Arnold A, Davis M, Tonato M, Smylie M, Tu D, Voi M, Humphrey J, Ottaway J, Young K, Vreckem AV, Seymour L. Randomized phase II feasibility study of combining the matrix metalloproteinase inhibitor BMS-275291 with paclitaxel plus carboplatin in advanced non-small cell lung cancer. Lung Cancer. 2004;46(3):361-368. doi: 10.1016/j.lungcan.2004.05.009.

Doweyko AM. 3D-QSAR illusions. J. Comput. Aided Mol. Des. 2004;18(7-9):587-596. doi: 10.1007/s10822-004-4068-0.

Doxorubicin Hydrochloride NDA #050467—Drugs@FDA: FDA-Approved Drugs. Available online: https://www.accessdata.fda.gov/scripts/cder/daf/index.cfm?event=overview.process&ApplNo=050467 (Accessed on 25.07.2023).

Duan W, Li J, Inks ES, Chou CJ, Jia Y, Chu X, Li X, Xu W, Zhang Y. Design, synthesis, and antitumor evaluation of novel histone deacetylase inhibitors equipped with a phenylsulfonylfuroxan module as a nitric oxide donor. J. Med. Chem. 2015;58:4325-4338. doi: 10.1021/acs.jmedchem.5b00317. [Erratum in: J. Med. Chem. 2015;58:6319.]

Dumble M, Moore L, Chambers SM, Geiger H, Van Zant G, Goodell MA, Donehower LA. The impact of altered p53 dosage on hematopoietic stem cell dynamics during aging. Blood. 2007;109(4):1736-1742. doi: 10.1182/blood-2006-03-010413.

Dushinsky R, Pleven E, Heidelberger C. The synthesis of 5-fluoropyrimidines. J. Am. Chem. Soc. 1957;79:4559-4560. doi: 10.1021/ja01573a087.

Dutta S, Halder AK, Adhikari N, Amin SA, Das S, Saha A, Jha T. Synthesis, anticancer activity, structure-activity relationship and binding mode of interaction studies of substituted pentanoic acids. Future Med. Chem. 2019;11:1679-1702. doi: 10.4155/fmc-2018-0361.

Eatock M, Cassidy J, Johnson J, Morrison R, Devlin M, Blackey R, Owen S, Choi L, Twelves C. A dose-finding and pharmacokinetic study of the matrix metalloproteinase inhibitor MMI270 (previously termed CGS27023A) with 5-FU and folinic acid. Cancer Chemother. Pharmacol. 2005;55(1):39-46. doi: 10.1007/s00280-004-0856-4.

Erlichman C, Adjei AA, Alberts SR, Sloan JA, Goldberg RM, Pitot HC, Rubin J, Atherton PJ, Klee GG, Humphrey R. Phase I study of the matrix metalloproteinase inhibitor, BAY 12-9566. Ann. Oncol. 2001;12(3):389-395. doi: 10.1023/a:1011183905848.

Eldridge MD, Murray CW, Auton TR, Paolini GV, Mee RP. Empirical scoring functions: I. The development of a fast empirical scoring function to estimate the binding affinity of ligands in receptor complexes. J. Comput. Aided Mol. Des. 1997;11(5):425-445. doi: 10.1023/a:1007996124545.

Elion GB, Burgi E, Hitchings GH. Studies on condensed pyrimidine systems. IX. The synthesis of some 6-substituted purines. J. Am. Chem. Soc. 1952;74:411-414. doi: 10.1021/ja01122a037.

Engel T. Cheminformatics in diverse dimensions. In: Clark T, Banting L, Eds., Drug Design Strategies Computational Techniques and Applications. The Royal Society of Chemistry. Cambridge, UK. 2012, pp. 164-183.

References

Eriksson M, Hardell L, Carlberg M, Akerman M. Pesticide exposure as risk factor for non-Hodgkin lymphoma including histopathological subgroup analysis. Int. J. Cancer. 2008;123(7):1657-1663. doi: 10.1002/ijc.23589.

Evgeniou T, Pontil M. Support vector machines: Theory and applications. In: Paliouras G, Karkaletsis V, Spyropoulos CD, Eds., Machine Learning and Its Applications. ACAI 1999. Lecture Notes in Computer Science. Springer, Berlin, Heidelberg. 2001, pp. 249-257.

Fabre B, Filipiak K, Zapico JM, Díaz N, Carbajo RJ, Schott AK, Martínez-Alcázar MP, Suárez D, Pineda-Lucena A, Ramos A, de Pascual-Teresa B. Progress towards water-soluble triazole-based selective MMP-2 inhibitors. Org. Biomol. Chem. 2013;11(38):6623-6641. doi: 10.1039/c3ob41046c.

Fabre B, Ramos A, de Pascual-Teresa B. Targeting matrix metalloproteinases: exploring the dynamics of the s1' pocket in the design of selective, small molecule inhibitors. J. Med. Chem. 2014;57(24):10205-10219. doi: 10.1021/jm500505f.

Fadok VA, Bratton DL, Frasch SC, Warner ML, Henson PM. The role of phosphatidylserine in recognition of apoptotic cells by phagocytes. Cell Death Differ. 1998;5(7):551-562. doi: 10.1038/sj.cdd.4400404.

Farber S, Diamond LK. Temporary remissions in acute leukemia in children produced by folic acid antagonist, 4-aminopteroyl-glutamic acid. N. Engl. J. Med. 1948;238(23):787-93. doi: 10.1056/NEJM194806032382301.

Farina AR, Mackay AR. Gelatinase B/MMP-9 in tumour pathogenesis and progression. Cancers (Basel). 2014;6(1):240-296. doi:10.3390/cancers6010240.

Fawcett, T. An introduction to ROC analysis. Pattern Recogn. Lett. 2006;27:861-874. doi: 10.1016/j.patrec.2005.10.010.

Federico S, Khan T, Fontana A, Brogi S, Benedetti R, Sarno F, Carullo G, Pezzotta A, Saraswati AP, Passaro E, Pozzetti L, Papa A, Relitti N, Gemma S, Butini S, Pistocchi A, Ramunno A, Vincenzi F, Varani K, Tatangelo V, Patrussi L, Baldari CT, Saponara S, Gorelli B, Lamponi S, Valoti M, Saccoccia F, Giannaccari M, Ruberti G, Herp D, Jung M, Altucci L, Campiani G. Azetidin-2-one-based small molecules as dual hHDAC6/HDAC8 inhibitors: Investigation of their mechanism of action and impact of dual inhibition profile on cell viability. Eur. J. Med. Chem. 2022;238:114409. doi: 10.1016/j.ejmech.2022.114409.

Feng Y, Pathria G, Heynen-Genel S, Jackson M, James B, Yin J, Scott DA, Ronai ZA. Identification and Characterization of IMD-0354 as a Glutamine Carrier Protein Inhibitor in Melanoma. Mol. Cancer Ther. 2021;20(5):816-832. doi: 10.1158/1535-7163.MCT-20-0354.

Ferreira LG, Dos Santos RN, Oliva G, Andricopulo AD. Molecular docking and structure-based drug design strategies. Molecules. 20 l5;20:13384-13421. doi: 10.3390/molecules200713384.

References

Fields GB. Mechanisms of action of novel drugs targeting angiogenesis-promoting matrix metalloproteinases. Front. Immunol. 2019A;10:1278. doi: 10.3389/fimmu.2019.01278.

Fields GB. The Rebirth of Matrix metalloproteinase inhibitors: Moving beyond the dogma. Cells. 2019B;8(9):984. doi:10.3390/cells8090984.

Fingleton B. MMPs as therapeutic targets--still a viable option? Semin. Cell Dev. Biol. 2008B;19(1):61-68. doi: 10.1016/j.semcdb.2007.06.006.

Fink K, Boratyński J.The role of metalloproteinases in modification of extracellular matrix in invasive tumor growth, metastasis and angiogenesis. Postepy Hig. Med. Dosw (Online). 2012;66:609-628. doi: 10.5604/17322693.1009705.

Fray MJ, Burslem MF, Dickinson RP. Selectivity of inhibition of matrix metalloproteases MMP-3 and MMP-2 by succinyl hydroxamates and their carboxylic acid analogues is dependent on P3' group chirality. Bioorg. Med. Chem. Lett. 2001;11(4):567-570. doi: 10.1016/s0960-894x(00)00719-8.

Freskos JN, McDonald JJ, Mischke BV, Mullins PB, Shieh HS, Stegeman RA, Stevens AM. Synthesis and identification of conformationally constrained selective MMP inhibitors. Bioorg. Med. Chem. Lett. 1999;9(13):1757-1760. doi: 10.1016/s0960-894x(99)00285-1.

Friesner RA, Banks JL, Murphy RB, Halgren TA, Klicic JJ, Mainz DT, Repasky MP, Knoll EH, Shelley M, Perry JK, Shaw DE, Francis P, Shenkin PS. Glide: a new approach for rapid, accurate docking and scoring. 1. Method and assessment of docking accuracy. J. Med. Chem. 2004;47(7):1739-1749. doi: 10.1021/jm0306430.

Galardy RE, Cassabonne ME, Giese C, Gilbert JH, Lapierre F, Lopez H, Schaefer ME, Stack R, Sullivan M, Summers B, et al. Low molecular weight inhibitors in corneal ulceration. Ann. N. Y. Acad. Sci. 1994 Sep 6;732:315-23. doi: 10.1111/j.1749-6632.1994.tb24746.x.

Gálvez-Llompart M, Recio MC, García-Domenech R. Topological virtual screening: a way to find new compounds active in ulcerative colitis by inhibiting NF-κB. Mol. Divers. 2011;15(4):917-926. doi: 10.1007/s11030-011-9323-4.

García-Rodríguez MD, Carvente-Juárez MM, Altamirano-Lozano MA. Antigenotoxic and apoptotic activity of green tea polyphenol extracts on hexavalent chromium-induced DNA damage in peripheral blood of CD-1 mice: Analysis with differential acridine orange/ethidium bromide staining. Oxid. Med. Cell Longev. 2013;2013:486419. doi: 10.1155/2013/486419.

Gatto C, Rieppi M, Borsotti P, Innocenti S, Ceruti R, Drudis T, Scanziani E, Casazza AM, Taraboletti G, Giavazzi R. BAY 12-9566, a novel inhibitor of matrix metalloproteinases with antiangiogenic activity. Clin. Cancer Res. 1999;5(11):3603-3607.

Gedeck P, Rohde B, Bartels C. QSAR--how good is it in practice? Comparison of descriptor sets on an unbiased cross section of corporate data sets. J. Chem. Inf. Model. 2006;46(5):1924-1936. doi: 10.1021/ci050413p.

Ghosh S. Cisplatin: The first metal based anticancer drug. Bioorg. Chem. 2019;88:102925. doi: 10.1016/j.bioorg.2019.102925.

References

Giannelli G, Antonaci S. Gelatinases and their inhibitors in tumor metastasis: From biological research to medical applications. Histol. Histopathol. 2002;17(1):339-345. doi: 10.14670/HH-17.339.

Gimeno A, Beltrán-Debón R, Mulero M, Pujadas G, Garcia-Vallvé S. Understanding the variability of the S1' pocket to improve matrix metalloproteinase inhibitor selectivity profiles. Drug Discov. Today. 2020;25(1):38-57. doi: 10.1016/j.drudis.2019.07.013.

Goffin JR, Anderson IC, Supko JG, Eder JP Jr, Shapiro GI, Lynch TJ, Shipp M, Johnson BE, Skarin AT. Phase I trial of the matrix metalloproteinase inhibitor marimastat combined with carboplatin and paclitaxel in patients with advanced non-small cell lung cancer. Clin. Cancer Res. 2005;11(9):3417-3424. doi: 10.1158/1078-0432.CCR-04-2144.

Gohlke H, Hendlich M, Klebe G. Knowledge-based scoring function to predict protein-ligand interactions. J. Mol. Biol. 2000;295(2):337-356. doi: 10.1006/jmbi.1999.3371.

Golbraikh A, Shen M, Xiao Z, Xiao YD, Lee KH, Tropsha A. Rational selection of training and test sets for the development of validated QSAR models. J. Comput. Aided Mol. Des. 2003;17(2-4):241-253. doi: 10.1023/a:1025386326946.

Golbraikh A, Tropsha A. Predictive QSAR modeling based on diversity sampling of experimental datasets for the training and test set selection. J. Comput. Aided Mol. Des. 2002A;16(5-6):357-369. doi: 10.1023/a:1020869118689.

Golbraikh A, Tropsha A. Beware of q2! J. Mol. Graph. Model. 2002B;20(4):269-276. doi: 10.1016/s1093-3263(01)00123-1.

Golub LM, Ramamurthy NS, McNamara TF, Greenwald RA, Rifkin BR. Tetracyclines inhibit connective tissue breakdown: new therapeutic implications for an old family of drugs. Crit. Rev. Oral Biol. Med. 1991;2(3):297-321. doi: 10.1177/10454411910020030201.

Golub LM, Lee HM, Ryan ME, Giannobile WV, Payne J, Sorsa T. Tetracyclines inhibit connective tissue breakdown by multiple non-antimicrobial mechanisms. Adv. Dent. Res. 1998;12(2):12-26. doi: 10.1177/08959374980120010501.

Gomis-Rüth FX. Catalytic domain architecture of metzincin metalloproteases. J. Biol. Chem. 2009;284(23):15353-15357. doi: 10.1074/jbc.R800069200.

Gonzalez-Avila G, Sommer B, Mendoza-Posada DA, Ramos C, Garcia-Hernandez AA, Falfan-Valencia R. Matrix metalloproteinases participation in the metastatic process and their diagnostic and therapeutic applications in cancer [published correction appears in Crit. Rev. Oncol. Hematol. 2019;138:172]. Crit. Rev. Oncol. Hematol. 2019;137:57-83. doi: 10.1016/j.critrevonc.2019.02.010.

Goodarzi M, Dejaegher B, Vander Heyden Y. Feature selection methods in QSAR studies. J. AOAC Int. 2012;95(3):636-651. doi: 10.5740/jaoacint.sge_goodarzi.

Goodman LS, Wintrobe MM, Dameshek W, Goodman MJ, Gilman A, Mclennan MT. Nitrogen mustard therapy; Use of methyl-bis (beta-chloroethyl) amine hydrochloride and tris (beta-chloroethyl) amine hydrochloride for Hodgkin's disease, lymphosarcoma, leukemia and

certain allied and miscellaneous disorders. J. Am. Med. Assoc. 1946;132:126-32. doi: 10.1001/jama.1946.02870380008004.

Gooley PR, O'Connell JF, Marcy AI, Cuca GC, Salowe SP, Bush BL, Hermes JD, Esser CK, Hagmann WK, Springer JP, et al. The NMR structure of the inhibited catalytic domain of human stromelysin-1. Nat. Struct. Biol. 1994;1(2):111-118. doi: 10.1038/nsb0294-111.

Gooyit M, Lee M, Schroeder VA, Ikejiri M, Suckow MA, Mobashery S, Chang M. Selective water-soluble gelatinase inhibitor prodrugs. J. Med. Chem. 2011;54(19):6676-6690. doi: 10.1021/jm200566e.

Gossage DL, Cieslarová B, Ap S, Zheng H, Xin Y, Lal P, Chen G, Smith V, Sundy JS. Phase 1b study of the safety, pharmacokinetics, and disease-related outcomes of the matrix metalloproteinase-9 inhibitor andecaliximab in patients with rheumatoid arthritis. Clin. Ther. 2018;40(1):156-165.e5. doi: 10.1016/j.clinthera.2017.11.011.

Gore M, A'Hern R, Stankiewicz M, Slevin M. Tumour marker levels during marimastat therapy. Lancet. 1996;348(9022):263-264. doi: 10.1016/s0140-6736(96)24030-9.

Gradishar W, Sparano J, Cobleigh M. A phase I study of marimastat in combination with doxorubicin and cyclophosphamide in patients with metastatic breast cancer. InASCO Annual Meeting. 1998:548. (Abstract)

Gramatica P. Principles of QSAR models validation: Internal and external. QSAR Comb. Sci. 2007;26(5):694-701. doi: 10.1002/qsar.200610151.

Grams F, Crimmin M, Hinnes L, Huxley P, Pieper M, Tschesche H, Bode W. Structure determination and analysis of human neutrophil collagenase complexed with a hydroxamate inhibitor. Biochemistry. 1995;34(43):14012-14020. doi: 10.1021/bi00043a007.

Grillo-López AJ, White CA, Dallaire BK, Varns CL, Shen CD, Wei A, Leonard JE, McClure A, Weaver R, Cairelli S, Rosenberg J. Rituximab: The first monoclonal antibody approved for the treatment of lymphoma. Curr. Pharm. Biotechnol. 2000;1(1):1-9. doi: 10.2174/1389201003379059. PMID: 11467356.

Gross MI, Demo SD, Dennison JB, Chen L, Chernov-Rogan T, Goyal B, Janes JR, Laidig GJ, Lewis ER, Li J, Mackinnon AL, Parlati F, Rodriguez ML, Shwonek PJ, Sjogren EB, Stanton TF, Wang T, Yang J, Zhao F, Bennett MK. Antitumor activity of the glutaminase inhibitor CB-839 in triple-negative breast cancer. Mol. Cancer Ther. 2014;13(4):890-901. doi: 10.1158/1535-7163.MCT-13-0870.

Gu W, Roeder RG. Activation of p53 sequence-specific DNA binding by acetylation of the p53 C-terminal domain. Cell. 1997;90(4):595-606. doi: 10.1016/s0092-8674(00)80521-8.

Gu Y, Lee HM, Golub LM, Sorsa T, Konttinen YT, Simon SR. Inhibition of breast cancer cell extracellular matrix degradative activity by chemically modified tetracyclines. Ann. Med. 2005;37(6):450-460. doi: 10.1080/07853890500300386.

Guillén-Mancina E, Jiménez-Alonso JJ, Calderón-Montaño JM, Jiménez-González V, Díaz-Ortega P, Burgos-Morón E, López-Lázaro M. Artificial diets with selective restriction of

amino acids and very low levels of lipids induce anticancer activity in mice with metastatic triple-negative breast cancer. Cancers (Basel). 2023;15(5):1540. doi: 10.3390/cancers15051540.

Guo T, Hu S, Xu W, Zhou J, Chen F, Gao T, Qu W, Chen F, Lv Z, Lu L. Elevated expression of histone deacetylase HDAC8 suppresses arginine-proline metabolism in necrotizing enterocolitis. iScience. 2023;26(6):106882. doi: 10.1016/j.isci.2023.106882.

Gupta RK, Patel AK, Shah N, Chaudhary AK, Jha UK, Yadav UC, Gupta PK, Pakuwal U. Oxidative stress and antioxidants in disease and cancer: a review. Asian Pac. J. Cancer Prev. 2014;15(11):4405-4409. doi: 10.7314/apjcp.2014.15.11.4405.

Gurung AB, Ali MA, Lee J, Farah MA, Al-Anazi KM. An Updated Review of Computer-Aided Drug Design and Its Application to COVID-19. Biomed. Res. Int. 2021;2021:8853056. doi: 10.1155/2021/8853056.

Halama A, Suhre K. Advancing cancer treatment by targeting glutamine metabolism-a roadmap. Cancers (Basel). 2022;14(3):553. doi: 10.3390/cancers14030553.

Halder AK, Mallick S, Shikha D, Saha A, Saha KD, Jha T. Design of dual MMP-2/HDAC-8 inhibitors by pharmacophore mapping, molecular docking, synthesis and biological activity. RSC Adv. 2015A;5:72373-72386. doi: 10.1039/C5RA12606A.

Halder AK. (2015B) Rational design of derivatives and analogs of phenylacetyl isoglutamine: Biological activity, synthesis, and molecular modeling. [PhD dissertation, Jadavpur University]. Index No. 104/10/Ph.

Halgren TA, Murphy RB, Friesner RA, Beard HS, Frye LL, Pollard WT, Banks JL. Glide: a new approach for rapid, accurate docking and scoring. 2. Enrichment factors in database screening. J. Med. Chem. 2004;47(7):1750-1759. doi: 10.1021/jm030644s.

Hall M, Frank E, Holmes G, Pfahringer B, Reutemann P. The WEKA data mining software: an update. ACM SIGKDD explor newslett. 2009;11(1):10-18. doi: 10.1145/1656274.1656278.

Hallek M. Chronic lymphocytic leukemia: 2020 update on diagnosis, risk stratification and treatment. Am. J. Hematol. 2019;94(11):1266-1287. doi: 10.1002/ajh.25595.

Halperin I, Ma B, Wolfson H, Nussinov R. Principles of docking: An overview of search algorithms and a guide to scoring functions. Proteins. 2002;47(4):409-443. doi: 10.1002/prot.10115.

Hamzeh-Mivehroud M, Sokouti B, Dastmalchi S. An introduction to the basic concepts in QSAR-aided drug design. In: Roy K, ed., Quantitative Structure-Activity Relationships in Drug Design, Predictive Toxicology, and Risk Assessment. IGI Global. Hershey, PA. 2015, pp. 1-47.

Hande K, Wilding G, Ripple G, Fry J, Arzoomanian R, Dixon M, Yuen G, Collier M. A phase I trial of AG3340, a matrix metalloproteinase inhibitor, in patients having advanced cancer. Ann. Oncol. 1998; 9 (Suppl 2): 74. (Abstract)

References

Hanemaaijer R, Visser H, Koolwijk P, Sorsa T, Salo T, Golub LM, van Hinsbergh VW. Inhibition of MMP synthesis by doxycycline and chemically modified tetracyclines (CMTs) in human endothelial cells. Adv. Dent. Res. 1998;12(2):114-118. doi: 10.1177/08959374980120010301.

Hanemaaijer R, Verheijen JH, Maguire TM, Visser H, Toet K, McDermott E, O'Higgins N, Duffy MJ. Increased gelatinase-A and gelatinase-B activities in malignant vs. benign breast tumors. Int. J. Cancer. 2000;86(2):204-207. doi: 10.1002/(sici)1097-0215(20000415)86:2<204::aid-ijc9>3.0.co;2-6.

Hao Y, Samuels Y, Li Q, Krokowski D, Guan BJ, Wang C, Jin Z, Dong B, Cao B, Feng X, Xiang M, Xu C, Fink S, Meropol NJ, Xu Y, Conlon RA, Markowitz S, Kinzler KW, Velculescu VE, Brunengraber H, Willis JE, LaFramboise T, Hatzoglou M, Zhang GF, Vogelstein B, Wang Z. Oncogenic PIK3CA mutations reprogram glutamine metabolism in colorectal cancer. Nat. Commun. 2016;7:11971. doi: 10.1038/ncomms11971.

Hassell KN. Histone deacetylases and their inhibitors in cancer epigenetics. Diseases. 2019;7(4):57. doi: 10.3390/diseases7040057.

Hayashibara T, Yamada Y, Onimaru Y, Tsutsumi C, Nakayama S, Mori N, Miyanishi T, Kamihira S, Tomonaga M, Maita T. Matrix metalloproteinase-9 and vascular endothelial growth factor: a possible link in adult T-cell leukaemia cell invasion. Br. J. Haematol. 2002;116(1):94-102. doi: 10.1046/j.1365-2141.2002.03255.x.

Heath EI, O'Reilly S, Humphrey R, Sundaresan P, Donehower RC, Sartorius S, Kennedy MJ, Armstrong DK, Carducci MA, Sorensen JM, Kumor K, Kennedy S, Grochow LB. Phase I trial of the matrix metalloproteinase inhibitor BAY12-9566 in patients with advanced solid tumors. Cancer Chemother. Pharmacol. 2001;48(4):269-274. doi: 10.1007/s002800100330.

Hemmings FJ, Farhan M, Rowland J, Banken L, Jain R. Tolerability and pharmacokinetics of the collagenase-selective inhibitor Trocade in patients with rheumatoid arthritis. Rheumatology (Oxford). 2001;40(5):537-543. doi: 10.1093/rheumatology/40.5.537.

Hildebrand PW, Rose AS, Tiemann JKS. Bringing Molecular Dynamics Simulation Data into View. Trends Biochem. Sci. 2019;44(11):902-913. doi: 10.1016/j.tibs.2019.06.004.

Hirte H, Vergote IB, Jeffrey JR, Grimshaw RN, Coppieters S, Schwartz B, Tu D, Sadura A, Brundage M, Seymour L. A phase III randomized trial of BAY 12-9566 (tanomastat) as maintenance therapy in patients with advanced ovarian cancer responsive to primary surgery and paclitaxel/platinum containing chemotherapy: a National Cancer Institute of Canada Clinical Trials Group Study. Gynecol. Oncol. 2006;102(2):300-308. doi: 10.1016/j.ygyno.2005.12.020.

Ho TCS, Chan AHY, Ganesan A. Thirty years of hdac inhibitors: 2020 insight and hindsight. J. Med. Chem. 2020;63(21):12460-12484. doi: 10.1021/acs.jmedchem.0c00830.

Hodgson J. Remodeling MMPIs. Biotechnology (N Y). 1995;13(6):554-557. doi: 10.1038/nbt0695-554.

References

Hodson N, Brown T, Joanisse S, Aguirre N, West DWD, Moore DR, Baar K, Breen L, Philp A. Characterisation of L-type amino acid transporter 1 (LAT1) expression in human skeletal muscle by immunofluorescent microscopy. Nutrients. 2017;10(1):23. doi: 10.3390/nu10010023.

Hoekstra R, Eskens FA, Verweij J. Matrix metalloproteinase inhibitors: current developments and future perspectives. Oncologist. 2001;6(5):415-427. doi: 10.1634/theoncologist.6-5-415.

Hollborn M, Stathopoulos C, Steffen A, Wiedemann P, Kohen L, Bringmann A. Positive feedback regulation between MMP-9 and VEGF in human RPE cells. Invest. Ophthalmol. Vis. Sci. 2007;48(9):4360-4367. doi: 10.1167/iovs.06-1234.

Hollingsworth SA, Dror RO. Molecular dynamics simulation for all. Neuron. 2018;99(6):1129-1143. doi: 10.1016/j.neuron.2018.08.011.

Holmbeck K, Bianco P, Caterina J, Yamada S, Kromer M, Kuznetsov SA, Mankani M, Robey PG, Poole AR, Pidoux I, Ward JM, Birkedal-Hansen H. MT1-MMP-deficient mice develop dwarfism, osteopenia, arthritis, and connective tissue disease due to inadequate collagen turnover. Cell. 1999;99(1):81-92. doi: 10.1016/s0092-8674(00)80064-1.

Hontecillas-Prieto L, Flores-Campos R, Silver A, de Álava E, Hajji N, García-Domínguez DJ. Synergistic enhancement of cancer therapy using hdac inhibitors: Opportunity for clinical trials. Front. Genet. 2020;11:578011. doi: 10.3389/fgene.2020.578011.

Horvath K, Jami M, Hill ID, Papadimitriou JC, Magder LS, Chanasongcram S. Isocaloric glutamine-free diet and the morphology and function of rat small intestine. JPEN J. Parenter. Enteral. Nutr. 1996;20(2):128-134. doi: 10.1177/0148607196020002128.

Hsiao YH, Su SC, Lin CW, Chao YH, Yang WE, Yang SF. Pathological and therapeutic aspects of matrix metalloproteinases: Implications in childhood leukemia. Cancer Metastasis Rev. 2019;38(4):829-837. doi: 10.1007/s10555-019-09828-y.

Hu ZZ, Huang H, Wu CH, Jung M, Dritschilo A, Riegel AT, Wellstein A. Omics-based molecular target and biomarker identification. Methods Mol. Biol. 2011;719:547-571. doi:10.1007/978-1-61779-027-0_26.

Hua WK, Qi J, Cai Q, Carnahan E, Ayala Ramirez M, Li L, Marcucci G, Kuo YH. HDAC8 regulates long-term hematopoietic stem-cell maintenance under stress by modulating p53 activity. Blood. 2017;130(24):2619-2630. doi: 10.1182/blood-2017-03-771386.

Huber K, Doyon G, Plaks J, Fyne E, Mellors JW, Sluis-Cremer N. Inhibitors of histone deacetylases: correlation between isoform specificity and reactivation of HIV type 1 (HIV-1) from latently infected cells. J. Biol. Chem. 2011;286:22211-22218. doi: 10.1074/jbc.M110.180224.

Huang SY, Zou X. Advances and challenges in protein-ligand docking. Int. J. Mol. Sci. 2010;11(8):3016-3034. doi: 10.3390/ijms11083016.

References

Huey R, Morris GM, Olson AJ, Goodsell DS. A semiempirical free energy force field with charge-based desolvation. J. Comput. Chem. 2007;28(6):1145-1152. doi: 10.1002/jcc.20634.

Ikejiri M, Bernardo MM, Bonfil RD, Toth M, Chang M, Fridman R, Mobashery S. Potent mechanism-based inhibitors for matrix metalloproteinases. J. Biol. Chem. 2005;280(40):33992-4002. doi: 10.1074/jbc.M504303200.

Ishak Gabra MB, Yang Y, Li H, Senapati P, Hanse EA, Lowman XH, Tran TQ, Zhang L, Doan LT, Xu X, Schones DE, Fruman DA, Kong M. Dietary glutamine supplementation suppresses epigenetically-activated oncogenic pathways to inhibit melanoma tumour growth. Nat Commun. 2020;11(1):3326. doi: 10.1038/s41467-020-17181-w.

Imperato MR, Cauchy P, Obier N, Bonifer C. The RUNX1-PU.1 axis in the control of hematopoiesis. Int. J. Hematol. 2015;101(4):319-329. doi: 10.1007/s12185-015-1762-8.

Imren S, Kohn DB, Shimada H, Blavier L, DeClerck YA. Overexpression of tissue inhibitor of metalloproteinases-2 retroviral-mediated gene transfer in vivo inhibits tumor growth and invasion. Cancer Res. 1996;56(13):2891-1895.

Ivanoff A, Ivanoff J, Hultenby K, Sundqvist KG. Infiltrative capacity of T leukemia cell lines: A distinct functional property coupled to expression of matrix metalloproteinase-9 (MMP-9) and tissue inhibitor of metalloproteinases-1 (TIMP-1). Clin. Exp. Metastasis. 1999;17(8):695-711. doi: 10.1023/a:1006749304315.

Janowska-Wieczorek A, Majka M, Marquez-Curtis L, Wertheim JA, Turner AR, Ratajczak MZ. Bcr-abl-positive cells secrete angiogenic factors including matrix metalloproteinases and stimulate angiogenesis in vivo in Matrigel implants. Leukemia. 2002;16(6):1160-1166. doi: 10.1038/sj.leu.2402486.

Janowska-Wieczorek A, Marquez LA, Matsuzaki A, Hashmi HR, Larratt LM, Boshkov LM, Turner AR, Zhang MC, Edwards DR, Kossakowska AE. Expression of matrix metalloproteinases (MMP-2 and -9) and tissue inhibitors of metalloproteinases (TIMP-1 and -2) in acute myelogenous leukaemia blasts: Comparison with normal bone marrow cells. Br. J. Haematol. 1999;105(2):402-411.

Jain S, Bhardwaj B, Amin SA, Adhikari N, Jha T, Gayen S. Exploration of good and bad structural fingerprints for inhibition of indoleamine-2,3-dioxygenase enzyme in cancer immunotherapy using Monte Carlo optimization and Bayesian classification QSAR modeling. J. Biomol. Struct. Dyn. 2020;38:1683-1696. doi: 10.1080/07391102.2019.1615000.

Jaworska J, Nikolova-Jeliazkova N, Aldenberg T. QSAR applicabilty domain estimation by projection of the training set descriptor space: a review. Altern. Lab. Anim. 2005;33(5):445-459. doi: 10.1177/026119290503300508.

Jeon HW, Lee YM. Inhibition of histone deacetylase attenuates hypoxia-induced migration and invasion of cancer cells via the restoration of RECK expression. Mol. Cancer Ther. 2010;9(5):1361-1370. doi: 10.1158/1535-7163.MCT-09-0717.

Jha T, Adhikari N, Saha A, Amin SA. Multiple molecular modelling studies on some derivatives and analogues of glutamic acid as matrix metalloproteinase-2 inhibitors. SAR QSAR Environ. Res. 2018;29(1):43-68. doi: 10.1080/1062936X.2017.1406986.

Jiménez-Alonso JJ, Guillén-Mancina E, Calderón-Montaño JM, Jiménez-González V, Díaz-Ortega P, Burgos-Morón E, López-Lázaro M. Artificial Diets Based on Selective Amino Acid Restriction versus Capecitabine in Mice with Metastatic Colon Cancer. Nutrients. 2022;14(16):3378. doi: 10.3390/nu14163378.

Jin J, Byun JK, Choi YK, Park KG. Targeting glutamine metabolism as a therapeutic strategy for cancer. Exp. Mol. Med. 2023;55(4):706-715. doi: 10.1038/s12276-023-00971-9.

John A, Tuszynski G. The role of matrix metalloproteinases in tumor angiogenesis and tumor metastasis. Pathol. Oncol. Res. 2001;7(1):14-23. doi: 10.1007/BF03032599.

Johansson N, Ahonen M, Kähäri VM. Matrix metalloproteinases in tumor invasion. Cell Mol. Life Sci. 2000;57(1):5-15. doi: 10.1007/s000180050495.

Johnson RA, Wichern DW. Principal components. In: Applied Multivariate Statistical Analysis, 6th ed. Pearson Prentice Hall, New Jersey. 2007, Ch. 8, pp.430-480.

Jolliffe IT. Principal Component Analysis, 2nd ed. Springer. 2002, pp.1-457.

Jones G, Willett P, Glen RC, Leach AR, Taylor R. Development and validation of a genetic algorithm for flexible docking. J. Mol. Biol. 1997;267(3):727-748. doi: 10.1006/jmbi.1996.0897.

Jones G, Willett P, Glen RC. Molecular recognition of receptor sites using a genetic algorithm with a description of desolvation. J. Mol. Biol. 1995;245(1):43-53. doi: 10.1016/s0022-2836(95)80037-9.

Kalyaanamoorthy S, Chen YP. Structure-based drug design to augment hit discovery. Drug Discov. Today. 2011;16(17-18):831-839. doi: 10.1016/j.drudis.2011.07.006.

Kar S, Sanderson H, Roy K, Benfenati E, Leszczynski J. Ecotoxicological assessment of pharmaceuticals and personal care products using predictive toxicology approaches. Green Chem. 2020;22:1458-1516. doi: 10.1039/C9GC03265G.

Kari S, Subramanian K, Altomonte IA, Murugesan A, Yli-Harja O, Kandhavelu M. Programmed cell death detection methods: A systematic review and a categorical comparison. Apoptosis. 2022;27:482-508. doi: 10.1007/s10495-022-01735-y.

Karplus M, McCammon JA. Molecular dynamics simulations of biomolecules. Nat. Struct. Biol. 2002;9(9):646-652. doi: 10.1038/nsb0902-646. [Erratum in: Nat. Struct. Biol. 2002;9(10):788.]

Katayama S, Morii A, Makanga JO, Suzuki T, Miyata N, Inazu T. HDAC8 regulates neural differentiation through embryoid body formation in P19 cells. Biochem. Biophys. Res. Commun. 2018;498(1):45-51. doi: 10.1016/j.bbrc.2018.02.195.

Kawamata H, Kameyama S, Kawai K, Tanaka Y, Nan L, Barch DH, Stetler-Stevenson WG, Oyasu R. Marked acceleration of the metastatic phenotype of a rat bladder carcinoma cell

line by the expression of human gelatinase A. Int. J. Cancer. 1995;63(4):568-575. doi: 10.1002/ijc.2910630418.

Keating MJ. Chronic Lymphocytic Leukemia, Editor(s): Bertino JR, Encyclopedia of Cancer (Second Edition), Academic Press, 2002, Pages 497-503.

Kalali D. The role of the matrix metalloproteinase-9 gene in tumor development and metastasis: A narrative review. Glob Med Genet. 2023;10(2):48-53. doi: 10.1055/s-0043-1768166.

Khan PM, Roy K. Current approaches for choosing feature selection and learning algorithms in quantitative structure-activity relationships (QSAR). Expert Opin. Drug Discov. 2018;13(12):1075-1089. doi: 10.1080/17460441.2018.1542428.

Khokha R. Suppression of the tumorigenic and metastatic abilities of murine B16-F10 melanoma cells in vivo by the overexpression of the tissue inhibitor of the metalloproteinases-1. J. Natl. Cancer Inst. 1994;86(4):299-304. doi: 10.1093/jnci/86.4.299.

Kikushige Y, Ishikawa F, Miyamoto T, Shima T, Urata S, Yoshimoto G, Mori Y, Iino T, Yamauchi T, Eto T, Niiro H, Iwasaki H, Takenaka K, Akashi K. Self-renewing hematopoietic stem cell is the primary target in pathogenesis of human chronic lymphocytic leukemia. Cancer Cell. 2011;20(2):246-59. doi: 10.1016/j.ccr.2011.06.029.

Kim JY, Cho H, Yoo J, Kim GW, Jeon YH, Lee SW, Kwon SH. Pathological role of HDAC8: Cancer and beyond. Cells. 2022;11(19):3161. doi: 10.3390/cells11193161.

Kim YB, Lee KH, Sugita K, Yoshida M, Horinouchi S. Oxamflatin is a novel antitumor compound that inhibits mammalian histone deacetylase. Oncogene. 1999;18:2461-2470. doi: 10.1038/sj.onc.1202564.

Kim S, Kim DH, Jung WH, Koo JS. Expression of glutamine metabolism-related proteins according to molecular subtype of breast cancer. Endocr. Relat. Cancer. 2013;20(3):339-48. doi: 10.1530/ERC-12-0398.

Kim JY, Cho H, Yoo J, Kim GW, Jeon YH, Lee SW, Kwon SH. HDAC8 deacetylates HIF-1α and enhances its protein stability to promote tumor growth and migration in melanoma. Cancers (Basel). 2023;15(4):1123. doi: 10.3390/cancers15041123.

King J, Zhao J, Clingan P, Morris D. Randomised double blind placebo control study of adjuvant treatment with the metalloproteinase inhibitor, Marimastat in patients with inoperable colorectal hepatic metastases: significant survival advantage in patients with musculoskeletal side-effects. Anticancer Res. 2003;23(1B):639-645.

Kiss S, Gede N, Soós A, Hegyi P, Nagy B, Imrei M, Czibere B, Farkas N, Hanák L, Szakács Z, Eröss B, Alizadeh H. Efficacy of first-line treatment options in transplant-ineligible multiple myeloma: A network meta-analysis. Crit. Rev. Oncol. Hematol. 2021;168:103504. doi: 10.1016/j.critrevonc.2021.103504.

Kitchen DB, Decornez H, Furr JR, Bajorath J. Docking and scoring in virtual screening for drug discovery: methods and applications. Nat. Rev. Drug Discov. 2004;3(11):935-949. doi: 10.1038/nrd1549.

References

Kivelä-Rajamäki M, Maisi P, Srinivas R, Tervahartiala T, Teronen O, Husa V, Salo T, Sorsa T. Levels and molecular forms of MMP-7 (matrilysin-1) and MMP-8 (collagenase-2) in diseased human peri-implant sulcular fluid. J. Periodontal. Res. 2003;38(6):583-590. doi: 10.1034/j.1600-0765.2003.00688.x.

Klein G, Vellenga E, Fraaije MW, Kamps WA, de Bont ES. The possible role of matrix metalloproteinase (MMP)-2 and MMP-9 in cancer, e.g. acute leukemia. Crit. Rev. Oncol. Hematol. 2004;50(2):87-100. doi: 10.1016/j.critrevonc.2003.09.001.

Klon AE, Lowrie JF, Diller DJ. Improved naïve Bayesian modeling of numerical data for absorption, distribution, metabolism and excretion (ADME) property prediction. J Chem Inf Model. 2006;46(5):1945-1956. doi: 10.1021/ci0601315.

Koivunen E, Arap W, Valtanen H, Rainisalo A, Medina OP, Heikkilä P, Kantor C, Gahmberg CG, Salo T, Konttinen YT, Sorsa T, Ruoslahti E, Pasqualini R. Tumor targeting with a selective gelatinase inhibitor. Nat. Biotechnol. 1999;17(8):768-774. doi: 10.1038/11703.

Koomagi R, Zintl F, Sauerbrey A, Volm M. Vascular endothelial growth factor in newly diagnosed and recurrent childhood acute lymphoblastic leukemia as measured by real-time quantitative polymerase chain reaction. Clin. Cancer Res. 2001;7(11):3381-3384.

Korb O, Stützle T, Exner TE. PLANTS: Application of ant colony optimization to structure-based drug design; *In* Ant colony optimization and swarm intelligence, eds M Dorigo, LM Gambardella, M Birattari, A Martinoli, R Poli, T Stützle, Berlin; Heidelberg: Springer, 2006; pp. 247-258.

Kovács D, Király P, Tóth G. Sample-size dependence of validation parameters in linear regression models and in QSAR. SAR QSAR Environ. Res. 2021;32(4):247-268. doi: 10.1080/1062936X.2021.1890208.

Krüger A, Arlt MJ, Gerg M, Kopitz C, Bernardo MM, Chang M, Mobashery S, Fridman R. Antimetastatic activity of a novel mechanism-based gelatinase inhibitor. Cancer Res. 2005;65(9):3523-3526. doi: 10.1158/0008-5472.CAN-04-3570.

Kruse JP, Gu W. Modes of p53 regulation. Cell. 2009;137(4):609-622. doi:10.1016/j.cell.2009.04.050.

Kuan JW, Su AT, Leong CF, Osato M, Sashida G. Systematic review of pre-clinical chronic myeloid leukaemia. Int. J. Hematol. 2018A;108(5):465-484. doi: 10.1007/s12185-018-2528-x.

Kuan JW, Melaine Michael S. The epidemiology of chronic myeloid leukaemia in southern Sarawak, Borneo Island. Med. J. Malays. 2018B;73(2):78–85.

Kuittinen O, Savolainen ER, Koistinen P, Möttönen M, Turpeenniemi-Hujanen T. MMP-2 and MMP-9 expression in adult and childhood acute lymphatic leukemia (ALL). Leuk. Res. 2001;25(2):125-131. doi: 10.1016/s0145-2126(00)00104-1.

Kuntz ID, Blaney JM, Oatley SJ, Langridge R, Ferrin TE. A geometric approach to macromolecule-ligand interactions. J. Mol. Biol. 1982;161(2):269-288. doi: 10.1016/0022-2836(82)90153-x.

Lacey JM, Wilmore DW. Is glutamine a conditionally essential amino acid? Nutr. Rev. 1990;48(8):297-309. doi: 10.1111/j.1753-4887.1990.tb02967.x.

Lara PN Jr, Stadler WM, Longmate J, Quinn DI, Wexler J, Van Loan M, Twardowski P, Gumerlock PH, Vogelzang NJ, Vokes EE, Lenz HJ, Doroshow JH, Gandara DR. A randomized phase II trial of the matrix metalloproteinase inhibitor BMS-275291 in hormone-refractory prostate cancer patients with bone metastases. Clin. Cancer Res. 2006;12(5):1556-1563. doi: 10.1158/1078-0432.CCR-05-2074.

Laronha H, Caldeira J. Structure and function of human matrix metalloproteinases. Cells. 2020;9(5):1076. doi: 10.3390/cells9051076.

Larson DA, Prados M, Lamborn KR, Smith V, Sneed PK, Chang S, Nicholas KM, Wara WM, Devriendt D, Kunwar S, Berger M, McDermott MW. Phase II study of high central dose Gamma Knife radiosurgery and marimastat in patients with recurrent malignant glioma. Int. J. Radiat. Oncol. Biol. Phys. 2002;54(5):1397-1404. doi: 10.1016/s0360-3016(02)03743-4.

Lee CH, Choi Y, Cho H, Bang IH, Hao L, Lee SO, Jeon R, Bae EJ, Park BH. Histone deacetylase 8 inhibition alleviates cholestatic liver injury and fibrosis. Biochem Pharmacol. 2021;183:114312. doi: 10.1016/j.bcp.2020.114312.

Lee HZ, Kwitkowski VE, Del Valle PL, Ricci MS, Saber H, Habtemariam BA, Bullock J, Bloomquist E, Li Shen Y, Chen XH, Brown J, Mehrotra N, Dorff S, Charlab R, Kane RC, Kaminskas E, Justice R, Farrell AT, Pazdur R. FDA Approval: Belinostat for the Treatment of Patients with Relapsed or Refractory Peripheral T-cell Lymphoma. Clin. Cancer Res. 2015;21(12):2666-2670. doi: 10.1158/1078-0432.CCR-14-3119.

Lee JS, Kang JH, Lee SH, Hong D, Son J, Hong KM, Song J, Kim SY. Dual targeting of glutaminase 1 and thymidylate synthase elicits death synergistically in NSCLC. Cell Death Dis. 2016;7(12):e2511. doi: 10.1038/cddis.2016.404.

Lee M, Villegas-Estrada A, Celenza G, Boggess B, Toth M, Kreitinger G, Forbes C, Fridman R, Mobashery S, Chang M. Metabolism of a highly selective gelatinase inhibitor generates active metabolite. Chem. Biol. Drug Des. 2007;70(5):371-382. doi: 10.1111/j.1747-0285.2007.00577.x.

Lee M, Celenza G, Boggess B, Blase J, Shi Q, Toth M, Bernardo MM, Wolter WR, Suckow MA, Hesek D, Noll BC, Fridman R, Mobashery S, Chang M. A potent gelatinase inhibitor with anti-tumor-invasive activity and its metabolic disposition. Chem. Biol. Drug Des. 2009;73(2):189-202. doi: 10.1111/j.1747-0285.2008.00750.x.

Lee YT, Tan YJ, Oon CE. Molecular targeted therapy: Treating cancer with specificity. Eur. J. Pharmacol. 2018;834:188-196. doi: 10.1016/j.ejphar.2018.07.034.

Leighl NB, Paz-Ares L, Douillard JY, Peschel C, Arnold A, Depierre A, Santoro A, Betticher DC, Gatzemeier U, Jassem J, Crawford J, Tu D, Bezjak A, Humphrey JS, Voi M, Galbraith S, Hann K, Seymour L, Shepherd FA. Randomized phase III study of matrix metalloproteinase inhibitor BMS-275291 in combination with paclitaxel and carboplatin in advanced non-small-cell lung cancer: National Cancer Institute of Canada-Clinical

Trials Group Study BR.18. J. Clin. Oncol. 2005;23(12):2831-2839. doi: 10.1200/JCO.2005.04.044.

Lemasters JJ, Nieminen AL, Qian T, Trost LC, Elmore SP, Nishimura Y, Crowe RA, Cascio WE, Bradham CA, Brenner DA, Herman B. The mitochondrial permeability transition in cell death: a common mechanism in necrosis, apoptosis and autophagy. Biochim. Biophys. Acta. 1998;1366(1-2):177-196. doi: 10.1016/s0005-2728(98)00112-1.

Leist M, Jäättelä M. Four deaths and a funeral: from caspases to alternative mechanisms. Nat Rev. Mol. Cell Biol. 2001;2(8):589-598. doi: 10.1038/35085008.

Leone RD, Zhao L, Englert JM, Sun IM, Oh MH, Sun IH, Arwood ML, Bettencourt IA, Patel CH, Wen J, Tam A, Blosser RL, Prchalova E, Alt J, Rais R, Slusher BS, Powell JD. Glutamine blockade induces divergent metabolic programs to overcome tumor immune evasion. Science. 2019;366(6468):1013-1021. doi: 10.1126/science.aav2588.

Levin VA, Phuphanich S, Yung WK, Forsyth PA, Maestro RD, Perry JR, Fuller GN, Baillet M. Randomized, double-blind, placebo-controlled trial of marimastat in glioblastoma multiforme patients following surgery and irradiation. J. Neurooncol. 2006;78(3):295-302. doi: 10.1007/s11060-005-9098-5.

Levitt NC, Eskens FA, O'Byrne KJ, Propper DJ, Denis LJ, Owen SJ, Choi L, Foekens JA, Wilner S, Wood JM, Nakajima M, Talbot DC, Steward WP, Harris AL, Verweij J. Phase I and pharmacological study of the oral matrix metalloproteinase inhibitor, MMI270 (CGS27023A), in patients with advanced solid cancer. Clin. Cancer Res. 2001;7(7):1912-1922.

Li K, Tay FR, Yiu CKY. The past, present and future perspectives of matrix metalloproteinase inhibitors. Pharmacol. Ther. 2020;207:107465. doi: 10.1016/j.pharmthera.2019.107465.

Li Y, Seto E. HDACs and HDAC inhibitors in cancer development and therapy. Cold Spring Harb. Perspect. Med. 2016;6(10):a026831. doi: 10.1101/cshperspect.a026831.

Liang T, Wang F, Elhassan RM, Cheng Y, Tang X, Chen W, Fang H, Hou X. Targeting histone deacetylases for cancer therapy: Trends and challenges. Acta. Pharm. Sin. B. 2023;13(6):2425-2463. doi: 10.1016/j.apsb.2023.02.007.

Lin CM, Zeng YL, Xiao M, Mei XQ, Shen LY, Guo MX, Lin ZY, Liu QF, Yang T. The relationship between MMP-2 -1306C>T and MMP-9 -1562C>T polymorphisms and the risk and prognosis of T-Cell acute lymphoblastic leukemia in a chinese population: A case-control study. Cell Physiol. Biochem. 2017;42(4):1458-1468. doi: 10.1159/000479210.

Lin LI, Lin DT, Chang CJ, Lee CY, Tang JL, Tien HF. Marrow matrix metalloproteinases (MMPs) and tissue inhibitors of MMP in acute leukaemia: Potential role of MMP-9 as a surrogate marker to monitor leukaemic status in patients with acute myelogenous leukaemia. Br. J. Haematol. 2002;117(4):835-841. doi: 10.1046/j.1365-2141.2002.03510.x.

Lin SW, Lee MT, Ke FC, Lee PP, Huang CJ, Ip MM, Chen L, Hwang JJ. TGF beta1 stimulates the secretion of matrix metalloproteinase 2 (MMP2) and the invasive behavior in human

ovarian cancer cells, which is suppressed by MMP inhibitor BB3103. Clin. Exp. Metastasis. 2000;18(6):493-499. doi: 10.1023/a:1011888126865.

Ling Y, Liu J, Qian J, Meng C, Guo J, Gao W, Xiong B, Ling C, Zhang Y. Recent advances in multi-target drugs targeting protein kinases and histone deacetylases in cancer therapy. Curr. Med. Chem. 2020;27(42):7264-7288. doi: 10.2174/0929867327666200102115720.

Liu M, Wang S. MCDOCK: a Monte Carlo simulation approach to the molecular docking problem. J. Comput. Aided Mol. Des. 1999;13(5):435-451. doi: 10.1023/a:1008005918983.

Liu LT, Chang HC, Chiang LC, Hung WC. Histone deacetylase inhibitor up-regulates RECK to inhibit MMP-2 activation and cancer cell invasion. Cancer res. 2003;63(12):3069-3072.

Liu Y, Elf SE, Asai T, Miyata Y, Liu Y, Sashida G, Huang G, Di Giandomenico S, Koff A, Nimer SD. The p53 tumor suppressor protein is a critical regulator of hematopoietic stem cell behavior. Cell Cycle. 2009A;8(19):3120-3124. doi: 10.4161/cc.8.19.9627.

Liu Y, Elf SE, Miyata Y, Sashida G, Liu Y, Huang G, Di Giandomenico S, Lee JM, Deblasio A, Menendez S, Antipin J, Reva B, Koff A, Nimer SD. p53 regulates hematopoietic stem cell quiescence. Cell Stem Cell. 2009B;4(1):37-48. doi: 10.1016/j.stem.2008.11.006.

Liu WH, Chang LS. Caffeine induces matrix metalloproteinase-2 (MMP-2) and MMP-9 down-regulation in human leukemia U937 cells via Ca2+/ROS-mediated suppression of ERK/c-fos pathway and activation of p38 MAPK/c-jun pathway. J. Cell Physiol. 2010;224(3):775-785. doi: 10.1002/jcp.22180.

Liu WH, Chen YL, Chang LS. CIL-102 induces matrix metalloproteinase-2 (MMP-2)/MMP-9 down-regulation via simultaneous suppression of genetic transcription and mRNA stability. Int. J. Biochem. Cell Biol. 2012;44(12):2212-2222. doi: 10.1016/j.biocel.2012.08.021.

Liu LL, Lu J, Lu Y, Zheng MY, Luo XM, Zhu WL, Jiang HL, Chen KX. Novel Bayesian classification models for predicting compounds blocking hERG potassium channels. Acta. Pharmacol. Sin. 2014A;35(8):1093-1102. doi: 10.1038/aps.2014.35.

Liu WH, Chen YJ, Chien JH, Chang LS. Amsacrine suppresses matrix metalloproteinase-2 (MMP-2)/MMP-9 expression in human leukemia cells. J. Cell Physiol. 2014B;229(5):588-598. doi: 10.1002/jcp.24481.

Liu K, Liu PC, Liu R, Wu X. Dual AO/EB staining to detect apoptosis in osteosarcoma cells compared with flow cytometry. Med. Sci. Monit. Basic Res. 2015;21:15-20. doi: 10.12659/MSMBR.893327.

Liu X, Shi D, Zhou S, Liu H, Liu H, Yao X. Molecular dynamics simulations and novel drug discovery. Expert Opin. Drug Discov. 2018;13(1):23-37. doi: 10.1080/17460441.2018.1403419.

Livingstone DJ, Manallack DT, Tetko IV. Data modelling with neural networks: advantages and limitations. J. Comput. Aided Mol. Des. 1997;11(2):135-142. doi: 10.1023/a:1008074223811.

References

Livingstone DJ, Manallack DT. Statistics using neural networks: chance effects. J. Med. Chem. 1993;36(9):1295-1297. doi: 10.1021/jm00061a023.

Lokeshwar BL. Chemically modified non-antimicrobial tetracyclines are multifunctional drugs against advanced cancers. Pharmacol. Res. 2011;63(2):146-150. doi: 10.1016/j.phrs.2010.11.003.

Lombard MA, Wallace TL, Kubicek MF, Petzold GL, Mitchell MA, Hendges SK, Wilks JW. Synthetic matrix metalloproteinase inhibitors and tissue inhibitor of metalloproteinase (TIMP)-2, but not TIMP-1, inhibit shedding of tumor necrosis factor-alpha receptors in a human colon adenocarcinoma (Colo 205) cell line. Cancer Res. 1998;58(17):4001-4007.

Lotem J, Sachs L. Hematopoietic cells from mice deficient in wild-type p53 are more resistant to induction of apoptosis by some agents. Blood. 1993;82(4):1092-1096.

Low JA, Johnson MD, Bone EA, Dickson RB. The matrix metalloproteinase inhibitor batimastat (BB-94) retards human breast cancer solid tumor growth but not ascites formation in nude mice. Clin. Cancer Res. 1996;2(7):1207-1214.

Lu J, Wang M, Wang Z, Fu Z, Lu A, Zhang G. Advances in the discovery of cathepsin K inhibitors on bone resorption. J. Enzyme Inhib. Med. Chem. 2018;33(1):890-904. doi: 10.1080/14756366.2018.1465417.

Lu W, Pelicano H, Huang P. Cancer metabolism: is glutamine sweeter than glucose? Cancer Cell. 2010;18(3):199-200. doi: 10.1016/j.ccr.2010.08.017.

Lu X, Ning Z, Li Z, Cao H, Wang X. Development of chidamide for peripheral T-cell lymphoma, the first orphan drug approved in China. Intractable Rare Dis. Res. 2016;5(3):185-191. doi: 10.5582/irdr.2016.01024.

Lugano R, Ramachandran M, Dimberg A. Tumor angiogenesis: Causes, consequences, challenges and opportunities. Cell Mol. Life Sci. 2020;77(9):1745-1770. doi: 10.1007/s00018-019-03351-7.

Luo J, Su F, Chen D, Shiloh A, Gu W. Deacetylation of p53 modulates its effect on cell growth and apoptosis. Nature. 2000;408(6810):377-381. doi: 10.1038/35042612.

Macaulay VM, O'Byrne KJ, Saunders MP, Braybrooke JP, Long L, Gleeson F, Mason CS, Harris AL, Brown P, Talbot DC. Phase I study of intrapleural batimastat (BB-94), a matrix metalloproteinase inhibitor, in the treatment of malignant pleural effusions. Clin. Cancer Res. 1999;5(3):513-520.

MacPherson LJ, Bayburt EK, Capparelli MP, Carroll BJ, Goldstein R, Justice MR, Zhu L, Hu S, Melton RA, Fryer L, Goldberg RL, Doughty JR, Spirito S, Blancuzzi V, Wilson D, O'Byrne EM, Ganu V, Parker DT. Discovery of CGS 27023A, a non-peptidic, potent, and orally active stromelysin inhibitor that blocks cartilage degradation in rabbits. J. Med. Chem. 1997;40(16):2525-2532. doi: 10.1021/jm960871c.

Makhoba XH, Viegas C Jr, Mosa RA, Viegas FPD, Pooe OJ. Potential impact of the multi-target drug approach in the treatment of some complex diseases. Drug. Des. Devel. Ther. 2020;14:3235-3249. doi: 10.2147/DDDT.S257494.

References

Malekshah RE, Fahimirad B, Khaleghian A. Synthesis, characterization, biomedical application, molecular dynamic simulation and molecular docking of schiff base complex of Cu (II) supported on Fe3O4/Sio2/APTS. Int. J. Nanomedicine. 2020;15:2583-25603. doi: 10.2147/IJN.S231062.

Malfetano J, Teng N, Barter J. Marimastat in patients with advanced cancer of the ovary—a dose finding study. InProc Am Soc Clin. Oncol 1997;16:373a. (Abstract)

Mann BS, Johnson JR, Cohen MH, Justice R, Pazdur R. FDA approval summary: vorinostat for treatment of advanced primary cutaneous T-cell lymphoma. Oncologist. 2007;12(10):1247-52. doi: 10.1634/theoncologist.12-10-1247.

Markouli M, Strepkos D, Piperi C. Impact of histone modifications and their therapeutic targeting in hematological malignancies. Int. J. Mol. Sci. 2022;23(21):13657. doi: 10.3390/ijms232113657.

Marques SM, Nuti E, Rossello A, Supuran CT, Tuccinardi T, Martinelli A, Santos MA. Dual inhibitors of matrix metalloproteinases and carbonic anhydrases: iminodiacetyl-based hydroxamate-benzenesulfonamide conjugates. J. Med. Chem. 2008;51(24):7968-7979. doi: 10.1021/jm800964f.

Masetti R, Serravalle S, Biagi C, Pession A. The role of HDACs inhibitors in childhood and adolescence acute leukemias. J. Biomed. Biotechnol., 2011;2011:148046. doi: 10.1155/2011/148046.

Maskos K, Fernandez-Catalan C, Huber R, Bourenkov GP, Bartunik H, Ellestad GA, Reddy P, Wolfson MF, Rauch CT, Castner BJ, Davis R, Clarke HR, Petersen M, Fitzner JN, Cerretti DP, March CJ, Paxton RJ, Black RA, Bode W. Crystal structure of the catalytic domain of human tumor necrosis factor-alpha-converting enzyme. Proc. Natl. Acad. Sci. U S A. 1998;95(7):3408-3412. doi: 10.1073/pnas.95.7.3408.

Mauri A, Consonni V, Todeschini R. Molecular descriptors. In: Leszczynski J. editor. Handbook of Computational Chemistry. Springer, Dordrecht. 2016.

Mayer M, Berger A, Leischner C, Renner O, Burkard M, Böcker A, Noor S, Weiland T, Weiss TS, Busch C, Lauer UM, Bischoff SC, Venturelli S. Preclinical efficacy and toxicity analysis of the pan-histone deacetylase inhibitor gossypol for the therapy of colorectal cancer or hepatocellular carcinoma. Pharmaceuticals (Basel). 2022;15(4):438. doi: 10.3390/ph15040438.

McMartin C, Bohacek RS. QXP: powerful, rapid computer algorithms for structure-based drug design. J. Comput. Aided Mol. Des. 1997;11(4):333-344. doi: 10.1023/a:1007907728892.

Mehrpouri M, Momeny M, Bashash D. Synergistic effects of BKM120 and panobinostat on pre-B acute lymphoblastic cells: An emerging perspective for the simultaneous inhibition of PI3K and HDACs. J. Recept. Signal Transduct. Res. 2022;42(1):100-108. doi: 10.1080/10799893.2020.1853159.

Mehrpouri M, Safaroghli-Azar A, Pourbagheri-Sigaroodi A, Momeny M, Bashash D. Anti-leukemic effects of histone deacetylase (HDAC) inhibition in acute lymphoblastic leukemia (ALL) cells: Shedding light on mitigating effects of NF-κB and autophagy on

panobinostat cytotoxicity. Eur. J. Pharmacol. 2020;875:173050. doi: 10.1016/j.ejphar.2020.173050.

Meiler J, Baker D. ROSETTALIGAND: protein-small molecule docking with full side-chain flexibility. Proteins. 2006;65(3):538-548. doi: 10.1002/prot.21086.

Meisel JE, Chang M. Selective small-molecule inhibitors as chemical tools to define the roles of matrix metalloproteinases in disease. Biochim. Biophys. Acta Mol. Cell Res. 2017;1864(11 Pt A):2001-2014. doi: 10.1016/j.bbamcr.2017.04.011.

Miller AL. Therapeutic considerations of L-glutamine: a review of the literature. Altern Med Rev. 1999;4(4):239-248.

Millar AW, Brown PD, Moore J, Galloway WA, Cornish AG, Lenehan TJ, Lynch KP. Results of single and repeat dose studies of the oral matrix metalloproteinase inhibitor marimastat in healthy male volunteers. Br. J. Clin. Pharmacol. 1998;45(1):21-26. doi: 10.1046/j.1365-2125.1998.00639.x.

Miller KD, Gradishar W, Schuchter L, Sparano JA, Cobleigh M, Robert N, Rasmussen H, Sledge GW. A randomized phase II pilot trial of adjuvant marimastat in patients with early-stage breast cancer. Ann. Oncol. 2002;13(8):1220-1224. doi: 10.1093/annonc/mdf199.

Miller KD, Saphner TJ, Waterhouse DM, Chen TT, Rush-Taylor A, Sparano JA, Wolff AC, Cobleigh MA, Galbraith S, Sledge GW. A randomized phase II feasibility trial of BMS-275291 in patients with early stage breast cancer. Clin. Cancer Res. 2004;10(6):1971-1975. doi: 10.1158/1078-0432.ccr-03-0968.

Miller MD, Kearsley SK, Underwood DJ, Sheridan RP. FLOG: a system to select 'quasi-flexible' ligands complementary to a receptor of known three-dimensional structure. J Comput. Aided Mol. Des. 1994;8(2):153-174. doi: 10.1007/BF00119865.

Mittal K, Ebos J, Rini B. Angiogenesis and the tumor microenvironment: vascular endothelial growth factor and beyond. Semin. Oncol. 2014;41(2):235-2351. doi: 10.1053/j.seminoncol.2014.02.007.

Miyagi Y, Higashiyama M, Gochi A, Akaike M, Ishikawa T, Miura T, Saruki N, Bando E, Kimura H, Imamura F, Moriyama M, Ikeda I, Chiba A, Oshita F, Imaizumi A, Yamamoto H, Miyano H, Horimoto K, Tochikubo O, Mitsushima T, Yamakado M, Okamoto N. Plasma free amino acid profiling of five types of cancer patients and its application for early detection. PLoS One. 2011;6(9):e24143. doi: 10.1371/journal.pone.0024143.

Moinul M, Amin SA, Kumar P, Patil UK, Gajbhiye A, Jha T, Gayen S. Exploring sodium glucose cotransporter (SGLT2) inhibitors with machine learning approach: A novel hope in anti- diabetes drug discovery. J. Mol. Graph. Model. 2022;111:108106. doi: 10.1016/j.jmgm.2021.108106.

Mondal S, Adhikari N, Banerjee S, Amin SA, Jha T. Matrix metalloproteinase-9 (MMP-9) and its inhibitors in cancer: A minireview. Eur. J. Med. Chem. 2020A;194:112260. doi: 10.1016/j.ejmech.2020.112260. [Erratum in: Eur. J. Med. Chem. 2020A;205:112642.]

Mondal S. (2020B) *Dual inhibitors of both MMP-2 and MMP-9 in cancer: QSAR studies on carboxylate analog of MMP-9 inhibitor*. [M. Pharm. dissertation, Jadavpur University]. Reg. No: 145373 of 2018-2019.

Monovich LG, Tommasi RA, Fujimoto RA, Blancuzzi V, Clark K, Cornell WD, Doti R, Doughty J, Fang J, Farley D, Fitt J, Ganu V, Goldberg R, Goldstein R, Lavoie S, Kulathila R, Macchia W, Parker DT, Melton R, O'Byrne E, Pastor G, Pellas T, Quadros E, Reel N, Roland DM, Sakane Y, Singh H, Skiles J, Somers J, Toscano K, Wigg A, Zhou S, Zhu L, Shieh WC, Xue S, McQuire LW. Discovery of potent, selective, and orally active carboxylic acid based inhibitors of matrix metalloproteinase-13. J. Med. Chem. 2009;52(11):3523-3538. doi: 10.1021/jm801394m.

Montero A, Beierle JM, Olsen CA, Ghadiri MR. Design, synthesis, biological evaluation, and structural characterization of potent histone deacetylase inhibitors based on cyclic α/β-tetrapeptide architectures. J. Am. Chem. Soc. 2009;131:3033-3041. doi: 10.1021/ja809508f.

Mooij WT, Verdonk ML. General and targeted statistical potentials for protein-ligand interactions. Proteins. 2005;61(2):272-287. doi: 10.1002/prot.20588.

Moore MJ, Hamm J, Dancey J, Eisenberg PD, Dagenais M, Fields A, Hagan K, Greenberg B, Colwell B, Zee B, Tu D, Ottaway J, Humphrey R, Seymour L; National Cancer Institute of Canada Clinical Trials Group. Comparison of gemcitabine versus the matrix metalloproteinase inhibitor BAY 12-9566 in patients with advanced or metastatic adenocarcinoma of the pancreas: a phase III trial of the National Cancer Institute of Canada Clinical Trials Group. J. Clin. Oncol. 2003;21(17):3296-3302. doi: 10.1200/JCO.2003.02.098.

Morii A, Katayama S, Inazu T. establishment of a simple method for inducing neuronal differentiation of p19 ec cells without embryoid body formation and analysis of the role of histone deacetylase 8 activity in this differentiation. Biol. Pharm. Bull. 2020;43(7):1096-1103. doi: 10.1248/bpb.b20-00091.

Morris GM, Goodsell DS, Halliday RS, et al. Automated docking using a Lamarckian genetic algorithm and an empirical binding free energy function. J. Comput. Chem. 1998;19(14):1639-1662. doi: 10.1002/(SICI)1096-987X(19981115)19:14<1639::AID-JCC10>3.0.CO;2-B.

Morris GM, Goodsell DS, Huey R, Olson AJ. Distributed automated docking of flexible ligands to proteins: parallel applications of AutoDock 2.4. J. Comput. Aided Mol. Des. 1996;10(4):293-304. doi: 10.1007/BF00124499.

Mukherjee A, Adhikari N, Jha T. A pentanoic acid derivative targeting matrix metalloproteinase-2 (MMP-2) induces apoptosis in a chronic myeloid leukemia cell line. Eur. J. Med. Chem. 2017;141:37-50. doi: 10.1016/j.ejmech.2017.09.052.

Mustafa S, Koran S, AlOmair L. Insights into the role of matrix metalloproteinases in cancer and its various therapeutic aspects: A review. Front. Mol. Biosci. 2022;9:896099. doi: 10.3389/fmolb.2022.896099.

Myint ZW, Sun RC, Hensley PJ, James AC, Wang P, Strup SE, McDonald RJ, Yan D, St Clair WH, Allison DB. Evaluation of Glutaminase Expression in Prostate Adenocarcinoma and Correlation with Clinicopathologic Parameters. Cancers (Basel). 2021;13(9):2157. doi: 10.3390/cancers13092157.

Nagata S, Suzuki J, Segawa K, Fujii T. Exposure of phosphatidylserine on the cell surface. Cell Death Differ. 2016;23(6):952-961. doi: 10.1038/cdd.2016.7.

Naglich JG, Jure-Kunkel M, Gupta E, Fargnoli J, Henderson AJ, Lewin AC, Talbott R, Baxter A, Bird J, Savopoulos R, Wills R, Kramer RA, Trail PA. Inhibition of angiogenesis and metastasis in two murine models by the matrix metalloproteinase inhibitor, BMS-275291. Cancer Res. 2001;61(23):8480-8485.

Namasivayam V, Günther R. pso@autodock: a fast flexible molecular docking program based on Swarm intelligence. Chem Biol Drug Des. 2007;70(6):475-484. doi: 10.1111/j.1747-0285.2007.00588.x.

Nantasenamat C, Isarankura-Na-Ayudhya C, Naenna T, Prachayasittikul V. Prediction of bond dissociation enthalpy of antioxidant phenols by support vector machine. J. Mol. Graph. Model. 2008;27(2):188-196. doi: 10.1016/j.jmgm.2008.04.005.

Nantasenamat C, Worachartcheewan A, Prachayasittikul S, Isarankura-Na-Ayudhya C, Prachayasittikul V. QSAR modeling of aromatase inhibitory activity of 1-substituted 1,2,3-triazole analogs of letrozole. Eur. J. Med. Chem. 2013;69:99-114. doi: 10.1016/j.ejmech.2013.08.015.

Nantasenamat C, Sharma V. Maximizing computational tools for successful drug discovery. Expert. Opin. Drug. Discov. 2015;10(4):321-329. doi: 10.1517/17460441.2015.1016497.

Nantasenamat C, Worachartcheewan A, Prachayasittikul S, Isarankura-Na-Ayudhya C, Prachayasittikul V. QSAR modeling of aromatase inhibitory activity of 1-substituted 1,2,3-triazole analogs of letrozole. Eur. J. Med. Chem. 2013;69:99-114. doi: 10.1016/j.ejmech.2013.08.015.

Nemunaitis J, Poole C, Primrose J, Rosemurgy A, Malfetano J, Brown P, Berrington A, Cornish A, Lynch K, Rasmussen H, Kerr D, Cox D, Millar A. Combined analysis of studies of the effects of the matrix metalloproteinase inhibitor marimastat on serum tumor markers in advanced cancer: selection of a biologically active and tolerable dose for longer-term studies. Clin. Cancer Res. 1998;4(5):1101-1109.

Neves BJ, Braga RC, Melo-Filho CC, Moreira-Filho JT, Muratov EN, Andrade CH. QSAR-Based Virtual Screening: Advances and applications in drug discovery. Front. Pharmacol. 2018;9:1275. doi: 10.3389/fphar.2018.01275.

Nguyen TL, Nokin MJ, Terés S, Tomé M, Bodineau C, Galmar O, Pasquet JM, Rousseau B, van Liempd S, Falcon-Perez JM, Richard E, Muzotte E, Rezvani HR, Priault M, Bouchecareilh M, Redonnet-Vernhet I, Calvo J, Uzan B, Pflumio F, Fuentes P, Toribio ML, Khatib AM, Soubeyran P, Murdoch PDS, Durán RV. Downregulation of Glutamine Synthetase, not glutaminolysis, is responsible for glutamine addiction in Notch1-driven

acute lymphoblastic leukemia. Mol. Oncol. 2021;15(5):1412-1431. doi: 10.1002/1878-0261.12877.

Niakani M, Majd A, Pakzad P, Malekinejad H. Prodigiosin induced the caspase-dependent apoptosis in human chronic myelogenous leukemia K562 cell. Res. Pharm. Sci. 2020;16(1):26-34. doi: 10.4103/1735-5362.305186.

Nicklin P, Bergman P, Zhang B, Triantafellow E, Wang H, Nyfeler B, Yang H, Hild M, Kung C, Wilson C, Myer VE, MacKeigan JP, Porter JA, Wang YK, Cantley LC, Finan PM, Murphy LO. Bidirectional transport of amino acids regulates mTOR and autophagy. Cell. 2009;136(3):521-534. doi: 10.1016/j.cell.2008.11.044.

Niklison-Chirou MV, Erngren I, Engskog M, Haglöf J, Picard D, Remke M, McPolin PHR, Selby M, Williamson D, Clifford SC, Michod D, Hadjiandreou M, Arvidsson T, Pettersson C, Melino G, Marino S. TAp73 is a marker of glutamine addiction in medulloblastoma. Genes Dev. 2017;31(17):1738-1753. doi: 10.1101/gad.302349.117.

Niu B, Lu Y, Wang J, Hu Y, Chen J, Chen Q, He G, Zheng L. 2D-SAR, Topomer CoMFA and molecular docking studies on avian influenza neuraminidase inhibitors. Comput. Struct. Biotechnol. J. 2018;17:39-48. doi: 10.1016/j.csbj.2018.11.007.

Niu ZS, Wang WH, Niu XJ. Recent progress in molecular mechanisms of postoperative recurrence and metastasis of hepatocellular carcinoma. World J. Gastroenterol. 2022;28(46):6433-6477. doi:10.3748/wjg.v28.i46.6433.

Nussbaumer S, Bonnabry P, Veuthey JL, Fleury-Souverain S. Analysis of anticancer drugs: A review. Talanta. 2011;85(5):2265-2289. doi: 10.1016/j.talanta.2011.08.034.

Nuti E, Orlandini E, Nencetti S, Rossello A, Innocenti A, Scozzafava A, Supuran CT. Carbonic anhydrase and matrix metalloproteinase inhibitors. Inhibition of human tumor-associated isozymes IX and cytosolic isozyme I and II with sulfonylated hydroxamates. Bioorg. Med. Chem. 2007;15(6):2298-2311. doi: 10.1016/j.bmc.2007.01.023.

Nuti E, Casalini F, Avramova SI, Santamaria S, Cercignani G, Marinelli L, La Pietra V, Novellino E, Orlandini E, Nencetti S, Tuccinardi T, Martinelli A, Lim NH, Visse R, Nagase H, Rossello A. N-O-isopropyl sulfonamido-based hydroxamates: design, synthesis and biological evaluation of selective matrix metalloproteinase-13 inhibitors as potential therapeutic agents for osteoarthritis. J. Med. Chem. 2009A;52(15):4757-4773. doi: 10.1021/jm900261f.

Nuti E, Panelli L, Casalini F, Avramova SI, Orlandini E, Santamaria S, Nencetti S, Tuccinardi T, Martinelli A, Cercignani G, D'Amelio N, Maiocchi A, Uggeri F, Rossello A. Design, synthesis, biological evaluation, and NMR studies of a new series of arylsulfones as selective and potent matrix metalloproteinase-12 inhibitors. J. Med. Chem. 2009B;52(20):6347-6361. doi: 10.1021/jm900335a.

Nuti E, Casalini F, Avramova SI, Santamaria S, Fabbi M, Ferrini S, Marinelli L, La Pietra V, Limongelli V, Novellino E, Cercignani G, Orlandini E, Nencetti S, Rossello A. Potent arylsulfonamide inhibitors of tumor necrosis factor-alpha converting enzyme able to

reduce activated leukocyte cell adhesion molecule shedding in cancer cell models. J. Med. Chem. 2010;53(6):2622-2635. doi: 10.1021/jm901868z.

Nuti E, Casalini F, Santamaria S, Gabelloni P, Bendinelli S, Da Pozzo E, Costa B, Marinelli L, La Pietra V, Novellino E, Margarida Bernardo M, Fridman R, Da Settimo F, Martini C, Rossello A. Synthesis and biological evaluation in U87MG glioma cells of (ethynylthiophene)sulfonamido-based hydroxamates as matrix metalloproteinase inhibitors. Eur. J. Med. Chem. 2011;46(7):2617-2629. doi: 10.1016/j.ejmech.2011.03.033.

Nuti E, Cantelmo AR, Gallo C, Bruno A, Bassani B, Camodeca C, Tuccinardi T, Vera L, Orlandini E, Nencetti S, Stura EA, Martinelli A, Dive V, Albini A, Rossello A. N-O-Isopropyl Sulfonamido-Based Hydroxamates as Matrix Metalloproteinase Inhibitors: Hit Selection and in Vivo Antiangiogenic Activity. J. Med. Chem. 2015;58(18):7224-7240. doi: 10.1021/acs.jmedchem.5b00367.

Nuti E, Cuffaro D, Bernardini E, Camodeca C, Panelli L, Chaves S, Ciccone L, Tepshi L, Vera L, Orlandini E, Nencetti S, Stura EA, Santos MA, Dive V, Rossello A. Development of Thioaryl-Based Matrix Metalloproteinase-12 Inhibitors with Alternative Zinc-Binding Groups: Synthesis, Potentiometric, NMR, and Crystallographic Studies. J. Med. Chem. 2018;61(10):4421-4435. doi: 10.1021/acs.jmedchem.8b00096.

O'Byrne EM, Parker DT, Roberts ED, Goldberg RL, MacPherson LJ, Blancuzzi V, Wilson D, Singh HN, Ludewig R, Ganu VS. Oral administration of a matrix metalloproteinase inhibitor, CGS 27023A, protects the cartilage proteoglycan matrix in a partial meniscectomy model of osteoarthritis in rabbits. Inflamm Res. 1995;44 Suppl 2:S117-S118. doi: 10.1007/BF01778290.

Offman MN, Krol M, Patel N, Krishnan S, Liu J, Saha V, Bates PA. Rational engineering of L-asparaginase reveals importance of dual activity for cancer cell toxicity. Blood. 2011;117(5):1614-21. doi: 10.1182/blood-2010-07-298422.

Okada Y, Nagase H, Harris JE. Matrix metalloproteinases 1, 2, and 3 from rheumatoid synovial cells are sufficient to destroy joints. J. Rheumatol. 1987:14;41-42.

Okuda T, Nishimura M, Nakao M, Fujita Y. RUNX1/AML1: A central player in hematopoiesis. Int. J. Hematol. 2001;74(3):252-257. doi: 10.1007/BF02982057.

Olson MW, Toth M, Gervasi DC, Sado Y, Ninomiya Y, Fridman R. High affinity binding of latent matrix metalloproteinase-9 to the alpha2(IV) chain of collagen IV. J. Biol. Chem. 1998;273(17):10672-10681. doi: 10.1074/jbc.273.17.10672.

Organisation for economic co-operation and development (OECD). The report from the expert group on (quantitative) structure-activity relationships [(Q)SARs] on the principles for the validation of (Q) SARs. Series on testing and assessment, 2004, pp. 206.

Ou Y, Xu S, Zhu D, Yang X. Molecular mechanisms of exopolysaccharide from aphanothece halaphytica (EPSAH) induced apoptosis in HeLa cells. Plos One. 2014;9:E87223. doi: 10.1371/journal.pone.0087223.

References

Oviedo-Orta E, Bermudez-Fajardo A, Karanam S, Benbow U, Newby AC. Comparison of MMP-2 and MMP-9 secretion from T helper 0, 1 and 2 lymphocytes alone and in coculture with macrophages. Immunology. 2008;124(1):42-50. doi: 10.1111/j.1365-2567.2007.02728.x.

Ozmeric N, Gokmenoglu C, Chemical inhibition of matrix metalloproteinases for periodontal treatment. Clin. Anti-Inflam. Anti-Allerg. Drugs. 2015;2:21-26. doi: 10.2174/2212703802011605171857 03.

Pacifico F, Leonardi A, Crescenzi E. Glutamine Metabolism in Cancer Stem Cells: A complex liaison in the tumor microenvironment. Int. J. Mol. Sci. 2023;24(3):2337. doi: 10.3390/ijms24032337.

Paemen L, Martens E, Norga K, Masure S, Roets E, Hoogmartens J, Opdenakker G. The gelatinase inhibitory activity of tetracyclines and chemically modified tetracycline analogues as measured by a novel microtiter assay for inhibitors. Biochem. Pharmacol. 1996;52(1):105-111. doi: 10.1016/0006-2952(96)00168-2.

Pallett LJ, Dimeloe S, Sinclair LV, Byrne AJ, Schurich A. A glutamine 'tug-of-war': targets to manipulate glutamine metabolism for cancer immunotherapy. Immunother. Adv. 2021;1(1):ltab010. doi: 10.1093/immadv/ltab010. [Erratum in: Immunother. Adv. 2022;2(1):ltac018.]

Pang YP, Perola E, Xu K, Prendergast FG. EUDOC: a computer program for identification of drug interaction sites in macromolecules and drug leads from chemical databases. J. Comput. Chem. 2001;22(15):1750-1771. doi: 10.1002/jcc.1129.

Park SY, Jun J, Jeong KJ, Heo HJ, Sohn JS, Lee HY, Park CG, Kang J. Histone deacetylases 1, 6 and 8 are critical for invasion in breast cancer. Oncol. rep. 2011;25(6):1677-1681. doi: 10.3892/or.2011.1236.

Park SY, Kim JS. A short guide to histone deacetylases including recent progress on class II enzymes. Exp. Mol. Med. 2020;52(2):204-212. doi: 10.1038/s12276-020-0382-4.

Parsons SL, Watson SA, Steele RJ. Phase I/II trial of batimastat, a matrix metalloproteinase inhibitor, in patients with malignant ascites. Eur. J. Surg. Oncol. 1997;23(6):526-531. doi: 10.1016/s0748-7983(97)93077-8.

Pasca S, Tomuleasa C, Teodorescu P, Ghiaur G, Dima D, Moisoiu V, Berce C, Stefan C, Ciechanover A, Einsele H. KRAS/NRAS/BRAF mutations as potential targets in multiple myeloma. Front. Oncol. 2019;9:1137. doi: 10.3389/fonc.2019.01137.

Passegué E, Wagers AJ, Giuriato S, Anderson WC, Weissman IL. Global analysis of proliferation and cell cycle gene expression in the regulation of hematopoietic stem and progenitor cell fates. J. Exp. Med. 2005;202(11):1599-1611. doi: 10.1084/jem.20050967.

Pei J, Wang Q, Liu Z, Li Q, Yang K, Lai L. PSI-DOCK: towards highly efficient and accurate flexible ligand docking. Proteins. 2006;62(4):934-946. doi: 10.1002/prot.20790.

References

Perez-Atayde AR, Sallan SE, Tedrow U, Connors S, Allred E, Folkman J. Spectrum of tumor angiogenesis in the bone marrow of children with acute lymphoblastic leukemia. Am. J. Pathol. 1997;150(3):815-821.

Pérez-Garrido A, Helguera AM, Borges F, Cordeiro MN, Rivero V, Escudero AG. Two new parameters based on distances in a receiver operating characteristic chart for the selection of classification models. J. Chem. Inf. Model. 2011;51(10):2746-2759. doi: 10.1021/ci2003076.

Peter SC, Dhanjal JK, Malik V, Radhakrishnan N, Jayakanthan M, Sundar D. Quantitative structure-activity relationship (QSAR): Modeling approaches to biological applications. In: Ranganathan S, Gribskov M, Nakai K, Schönbach C, Eds., Encyclopedia of Bioinformatics and Computational Biology. Academic Press. 2019, pp. 661-676.

Pietrzak J, Mirowski M, Świechowski R, Wodziński D, Wosiak A, Michalska K, Balcerczak E. Importance of altered gene expression of metalloproteinases 2, 9, and 16 in acute myeloid leukemia: Preliminary study. J. Oncol. 2021;2021:6697975. doi: 10.1155/2021/6697975.

Pinzi L, Rastelli G. Molecular docking: Shifting paradigms in drug discovery. Int. J. Mol. Sci. 2019;20:4331. doi: 10.3390/ijms20184331.

Piperigkou Z, Manou D, Karamanou K, Theocharis AD. Strategies to target matrix metalloproteinases as therapeutic approach in cancer. Methods Mol. Biol. 2018;1731:325-348. doi:10.1007/978-1-4939-7595-2_27.

Pirard B. Insight into the structural determinants for selective inhibition of matrix metalloproteinases. Drug Discov. Today. 2007;12(15-16):640-646. doi: 10.1016/j.drudis.2007.06.003.

Piris MA, Medeiros LJ, Chang KC. Hodgkin lymphoma: A review of pathological features and recent advances in pathogenesis. Pathology. 2020;52(1):154-165. doi: 10.1016/j.pathol.2019.09.005.

Pollard AC, Paolillo V, Radaram B, Qureshy S, Li L, Maity T, Wang L, Uddin MN, Wood CG, Karam JA, Pagel MD, Piwnica-Worms D, Millward SW, Fowlkes NW, Norton W, Engel BJ, Pisaneschi F, Zacharias NM. PET/MR Imaging of a Lung Metastasis Model of Clear Cell Renal Cell Carcinoma with (2S,4R)-4-[18F]Fluoroglutamine. Mol. Imaging Biol. 2022;24(6):959-972. doi: 10.1007/s11307-022-01747-9.

Ponomarenko EA, Poverennaya EV, Ilgisonis EV, Pyatnitskiy MA, Kopylov AT, Zgoda VG, Lisitsa AV, Archakov AI. the size of the human proteome: The width and depth. Int. J. Anal. Chem. 2016;2016:7436849. doi: 10.1155/2016/7436849.

Poole C, Adams M, Barley V, Graham J, Kerr D, Louviaux I, Perren T, Plccart M, Thomas H. Dose-fiinding study of marimastat, an oral matrix metalloproteinase inhibitor, in patients with advanced ovarian cancer. InAnn. Oncol. 1996;7:68a. (Abstract)

Poulaki V. BMS-275291. Bristol-Myers Squibb. Curr. Opin. Investig. Drugs. 2002;3(3):500-504.

References

Pourbasheer E, Riahi S, Ganjali MR, Norouzi P. QSAR study of C allosteric binding site of HCV NS5B polymerase inhibitors by support vector machine. Mol. Divers. 2011;15(3):645-653. doi: 10.1007/s11030-010-9283-0.

Pourbasheer E, Aalizadeh R, Ganjali MR, Norouzi P. QSAR study of a1b4 integrin inhibitors by GA-MLR and GA-SVM methods, Struct. Chem. 2014;25:355–370. doi: 10.1007/s11224-013-0300-7.

Pourbasheer E, Vahdani S, Malekzadeh D, Aalizadeh R, Ebadi A. QSAR study of 17β-HSD3 inhibitors by genetic algorithm-support vector machine as a target receptor for the treatment of prostate cancer. Iran J. Pharm. Res. 2017;16(3):966-980.

Pourbasheer E, Aalizadeh R, Ganjali MR. QSAR study of CK2 inhibitors by GA-MLR and GA-SVM methods. Arabian J. Chem. 2019;12:2141–2149. doi: 10.1016/j.arabjc.2014.12.021.

Poyer F, Coquerel B, Pegahi R, Cazin L, Norris V, Vannier JP, Lamacz M. Secretion of MMP-2 and MMP-9 induced by VEGF autocrine loop correlates with clinical features in childhood acute lymphoblastic leukemia. Leuk. Res. 2009;33(3):407-417. doi: 10.1016/j.leukres.2008.08.019.

Primrose J, Bleiberg H, Daniel F, Johnson P, Mansi J, Neoptolemos J, Seymour M, Van Belle S. Dose-finding study of marimastat, an oral matrix metalloproteinase inhibitor, in patients with advanced colorectal cancer. InAnn. Oncol. 1996;7:35a. (Abstract)

Pulya S, Amin SA, Adhikari N, Biswas S, Jha T, Ghosh B. HDAC6 as privileged target in drug discovery: A perspective. Pharmacol. Res. 2021;163:105274. doi: 10.1016/j.phrs.2020.105274.

Qi J, Singh S, Hua WK, Cai Q, Chao SW, Li L, Liu H, Ho Y, McDonald T, Lin A, Marcucci G, Bhatia R, Huang WJ, Chang CI, Kuo YH. HDAC8 inhibition specifically targets inv(16) acute myeloid leukemic stem cells by restoring p53 acetylation. Cell Stem Cell. 2015;17(5):597-610. doi: 10.1016/j.stem.2015.08.004.

QSAR tools, DTC laboratory, India, (2015); Software available at https://dtclab.webs.com/software-tools (accessed on 22nd January 2021).

Quintero-Fabián S, Arreola R, Becerril-Villanueva E, Torres-Romero JC, Arana-Argáez V, Lara-Riegos J, Ramírez-Camacho MA, Alvarez-Sánchez ME. Role of matrix metalloproteinases in angiogenesis and cancer. Front. Oncol. 2019;9:1370. doi: 10.3389/fonc.2019.01370.

Quirt I, Bodurth A, Lohmann R, Rusthoven J, Belanger K, Young V, Wainman N, Stewar W, Eisenhauer E; National Cancer Institute of Canada Clinical Trials Group. Phase II study of marimastat (BB-2516) in malignant melanoma: a clinical and tumor biopsy study of the National Cancer Institute of Canada Clinical Trials Group. Invest. New Drugs. 2002;20(4):431-437. doi: 10.1023/a:1020625423524.

Raeeszadeh-Sarmazdeh M, Do LD, Hritz BG. Metalloproteinases and their inhibitors: Potential for the development of new therapeutics. Cells. 2020;9(5):1313. doi:10.3390/cells9051313.

References

Ragno R. www.3d-qsar.com: a web portal that brings 3-D QSAR to all electronic devices-the Py-CoMFA web application as tool to build models from pre-aligned datasets. J. Comput. Aided Mol. Des. 2019;33(9):855-864. doi: 10.1007/s10822-019-00231-x.

Raivio KO, Andersson LC. Glutamine requirements for purine metabolism in leukemic lymphoblasts. Leuk. Res. 1982;6(1):111-115. doi: 10.1016/0145-2126(82)90049-2.

Rajaraman S, Balakrishnan R, Deshmukh D, Ganorkar A, Biswas S, Pulya S, Ghosh B. HDAC8 as an emerging target in drug discovery with special emphasis on medicinal chemistry. Future Med. Chem. 2023;15(10):885-908. doi: 10.4155/fmc-2023-0054.

Rarey M, Kramer B, Lengauer T, Klebe G. A fast flexible docking method using an incremental construction algorithm. J. Mol. Biol. 1996;261(3):470-489. doi: 10.1006/jmbi.1996.0477.

Razai AS, Eckelman BP, Salvesen GS. Selective inhibition of matrix metalloproteinase 10 (MMP10) with a single-domain antibody. J. Biol. Chem. 2020;295(8):2464-2472. doi: 10.1074/jbc.RA119.011712.

RCSB Protein Data Bank, https://www.rcsb.org/, 2023 (Accessed in 13 August 2023).

Reers M, Smiley ST, Mottola-Hartshorn C, Chen A, Lin M, Chen LB. Mitochondrial membrane potential monitored by JC-1 dye. Methods Enzymol. 1995;260:406-417. doi: 10.1016/0076-6879(95)60154-6.

Reikvam H, Hatfield KJ, Oyan AM, Kalland KH, Kittang AO, Bruserud O. Primary human acute myelogenous leukemia cells release matrix metalloproteases and their inhibitors: Release profile and pharmacological modulation. Eur. J. Haematol. 2010;84(3):239-251. doi: 10.1111/j.1600-0609.2009.01382.x.

Reinfeld BI, Madden MZ, Wolf MM, Chytil A, Bader JE, Patterson AR, Sugiura A, Cohen AS, Ali A, Do BT, Muir A, Lewis CA, Hongo RA, Young KL, Brown RE, Todd VM, Huffstater T, Abraham A, O'Neil RT, Wilson MH, Xin F, Tantawy MN, Merryman WD, Johnson RW, Williams CS, Mason EF, Mason FM, Beckermann KE, Vander Heiden MG, Manning HC, Rathmell JC, Rathmell WK. Cell-programmed nutrient partitioning in the tumour microenvironment. Nature. 2021 ;593(7858):282-288. doi: 10.1038/s41586-021-03442-1.

Reiter LA, Robinson RP, McClure KF, Jones CS, Reese MR, Mitchell PG, Otterness IG, Bliven ML, Liras J, Cortina SR, Donahue KM, Eskra JD, Griffiths RJ, Lame ME, Lopez-Anaya A, Martinelli GJ, McGahee SM, Yocum SA, Lopresti-Morrow LL, Tobiassen LM, Vaughn-Bowser ML. Pyran-containing sulfonamide hydroxamic acids: potent MMP inhibitors that spare MMP-1. Bioorg. Med. Chem. Lett. 2004;14(13):3389-3395. doi: 10.1016/j.bmcl.2004.04.083.

Ren YY, Zhou LC, Yang L, Liu PY, Zhao BW, Liu HX. Predicting the aquatic toxicity mode of action using logistic regression and linear discriminant analysis. SAR QSAR Environ. Res. 2016;27(9):721-746. doi: 10.1080/1062936X.2016.1229691.

Richter L, Wang Y, Hyde RK. Targeting binding partners of the CBFβ-SMMHC fusion protein for the treatment of inversion 16 acute myeloid leukemia. Oncotarget. 2016;7(40):66255-66266. doi: 10.18632/oncotarget.11357.

References

Ries C, Loher F, Zang C, Ismair MG, Petrides PE. Matrix metalloproteinase production by bone marrow mononuclear cells from normal individuals and patients with acute and chronic myeloid leukemia or myelodysplastic syndromes. Clin. Cancer Res. 1999;5(5):1115-1124.

Rizvi NA, Humphrey JS, Ness EA, Johnson MD, Gupta E, Williams K, Daly DJ, Sonnichsen D, Conway D, Marshall J, Hurwitz H. A phase I study of oral BMS-275291, a novel nonhydroxamate sheddase-sparing matrix metalloproteinase inhibitor, in patients with advanced or metastatic cancer. Clin. Cancer Res. 2004;10(6):1963-1970. doi: 10.1158/1078-0432.ccr-1183-02.

Robinson MM, McBryant SJ, Tsukamoto T, Rojas C, Ferraris DV, Hamilton SK, Hansen JC, Curthoys NP. Novel mechanism of inhibition of rat kidney-type glutaminase by bis-2-(5-phenylacetamido-1,2,4-thiadiazol-2-yl)ethyl sulfide (BPTES). Biochem. J. 2007;406(3):407-414. doi: 10.1042/BJ20070039.

Rodriguez MS, Desterro JM, Lain S, Lane DP, Hay RT. Multiple C-terminal lysine residues target p53 for ubiquitin-proteasome-mediated degradation. Mol Cell Biol. 2000;20(22):8458-8467. doi: 10.1128/MCB.20.22.8458-8467.2000.

Rogers D, Brown RD, Hahn M. Using extended-connectivity fingerprints with Laplacian-modified Bayesian analysis in high-throughput screening follow-up. J. Biomol. Screen. 2005;10(7):682-686. doi: 10.1177/1087057105281365.

Rogers D, Hahn M. Extended-connectivity fingerprints. J. Chem. Inf. Model. 2010;50(5):742-754. doi: 10.1021/ci100050t.

Rosemurgy A, Harris J, Langleben A, Casper E, Goode S, Rasmussen H. Marimastat in patients with advanced pancreatic cancer: a dose-finding study. Am. J. Clin. Oncol. 1999;22(3):247-252. doi: 10.1097/00000421-199906000-00007.

Rosenberg B, Vancamp L, Krigas T. Inhibition of cell division in escherichia coli by electrolysis products from a platinum electrode. Nature. 1965;205:698-699. doi: 10.1038/205698a0.

Rosenbaum E, Zahurak M, Sinibaldi V, Carducci MA, Pili R, Laufer M, DeWeese TL, Eisenberger MA. Marimastat in the treatment of patients with biochemically relapsed prostate cancer: a prospective randomized, double-blind, phase I/II trial. Clin. Cancer Res. 2005;11(12):4437-4443. doi: 10.1158/1078-0432.CCR-04-2252.

Rowinsky EK, Humphrey R, Hammond LA, Aylesworth C, Smetzer L, Hidalgo M, Morrow M, Smith L, Garner A, Sorensen JM, Von Hoff DD, Eckhardt SG. Phase I and pharmacologic study of the specific matrix metalloproteinase inhibitor BAY 12-9566 on a protracted oral daily dosing schedule in patients with solid malignancies. J. Clin. Oncol. 2000;18(1):178-186. doi: 10.1200/JCO.2000.18.1.178.

Rothenberg ML, Nelson AR, Hande KR. New drugs on the horizon: matrix metalloproteinase inhibitors. Stem Cells. 1999;17(4):237-240. doi: 10.1002/stem.170237.

Roy K, Das RN. A review on principles, theory and practices of 2D-QSAR. Curr. Drug Metab. 2014;15(4):346-379. doi: 10.2174/1389200215666140908102230.

References

Roy K, Kar S, Das RN. Selected statistical methods in QSAR. In Roy K, Kar S, Das RN, Eds., Understanding the Basics of QSAR for Applications in Pharmaceutical Sciences and Risk Assessment. Academic Press. 2015A, Ch. 6, pp. 191-229.

Roy K, Kar S, Das RN. Validation of QSAR models. In: Roy K, Kar S, Das RN, editor(s). Understanding the Basics of QSAR for Applications in Pharmaceutical Sciences and Risk Assessment. Academic Press. 2015B, Ch. 7, pp. 231-289.

Roy K, Kar S, Das RN. Statistical methods in QSAR/QSPR. In: A Primer on QSAR/QSPR modeling fundamental concepts. Springer. Cham, Switzerland. 2015C.

Roy K, Mitra I. Electrotopological state atom (E-state) index in drug design, QSAR, property prediction and toxicity assessment. Curr Comput Aided Drug Des. 2012;8(2):135-158.

Roy K, Mitra I. On various metrics used for validation of predictive QSAR models with applications in virtual screening and focused library design. Comb Chem High Throughput Screen. 2011;14(6):450-474. doi: 10.2174/138620711795767893.

Roy PP, Paul S, Mitra I, Roy K. On two novel parameters for validation of predictive QSAR models. Molecules. 2009;14(5):1660-1701. doi: 10.3390/molecules14051660.

Rubino MT, Agamennone M, Campestre C, Fracchiolla G, Laghezza A, Loiodice F, Nuti E, Rossello A, Tortorella P. Synthesis, SAR, and biological evaluation of alpha-sulfonylphosphonic acids as selective matrix metalloproteinase inhibitors. ChemMedChem. 2009;4(3):352-362. doi: 10.1002/cmdc.200800324.

Rücker C, Rücker G, Meringer M. y-Randomization and its variants in QSPR/QSAR. J. Chem. Inf. Model. 2007;47(6):2345-2357. doi: 10.1021/ci700157b.

Ruiz-Carmona S, Alvarez-Garcia D, Foloppe N, Garmendia-Doval B, Juhos S, Schmidtke P, Barril X, Hubbard RE, Morley SD. rDock: a fast, versatile and open source program for docking ligands to proteins and nucleic acids. PLoS Comput. Biol. 2014;10(4):e1003571. doi:10.1371/journal.pcbi.1003571.

Rush TS 3rd, Powers R. The application of x-ray, NMR, and molecular modeling in the design of MMP inhibitors. Curr. Top. Med. Chem. 2004;4(12):1311-1327. doi: 10.2174/1568026043387999.

Ryan ME, Usman A, Ramamurthy NS, Golub LM, Greenwald RA. Excessive matrix metalloproteinase activity in diabetes: inhibition by tetracycline analogues with zinc reactivity. Curr. Med. Chem. 2001;8(3):305-316. doi: 10.2174/0929867013373598.

Saikia S, Bordoloi M. Molecular docking: Challenges, advances and its use in drug discovery perspective. Curr. Drug Targets. 2019;20:501-521. doi: 10.2174/1389450119666181022153016.

Sakaguchi K, Herrera JE, Saito S, Miki T, Bustin M, Vassilev A, Anderson CW, Appella E. DNA damage activates p53 through a phosphorylation-acetylation cascade. Genes Dev. 1998;12(18):2831-2841. doi: 10.1101/gad.12.18.2831.

References

Salmaso V, Moro S. Bridging Molecular Docking to Molecular Dynamics in Exploring Ligand-Protein Recognition Process: An Overview. Front Pharmacol. 2018;9:923. doi: 10.3389/fphar.2018.00923.

Sánchez Alcázar JA, Oropesa Ávila M, Andrade Talavera Y, Garrido Maraver J, de Lavera I, de la Mata M, Cotán D, Villanueva Paz M, Delgado Pavón A, Alcocer Gómez E, Rodríguez Moreno A. Stabilization of apoptotic cells: Generation of zombie cells. Redox. Biol. 2015;5:416. doi: 10.1016/j.redox.2015.09.020.

Santos MA, Marques SM, Tuccinardi T, Carelli P, Panelli L, Rossello A. Design, synthesis and molecular modeling study of iminodiacetyl monohydroxamic acid derivatives as MMP inhibitors. Bioorg. Med. Chem. 2006;14(22):7539-7550. doi: 10.1016/j.bmc.2006.07.011.

Sathishkumar K, Chaturvedi M, Das P, Stephen S, Mathur P. Cancer incidence estimates for 2022 & projection for 2025: Result from National Cancer Registry Programme, India. Indian J. Med. Res. 2022;10.4103/ijmr.ijmr_1821_22. doi:10.4103/ijmr.ijmr_1821_22

Sauton N, Lagorce D, Villoutreix BO, Miteva MA. MS-DOCK: accurate multiple conformation generator and rigid docking protocol for multi-step virtual ligand screening. BMC Bioinformatics. 2008;9:184. doi: 10.1186/1471-2105-9-184.

Sawicki G, Matsuzaki A, Janowska-Wieczorek A. Expression of the active form of MMP-2 on the surface of leukemic cells accounts for their in vitro invasion. J. Cancer Res. Clin. Oncol. 1998;124(5):245-252. doi: 10.1007/s004320050161.

Sbirkov Y, Vergov B, Dzharov V, Schenk T, Petrie K, Sarafian V. Targeting glutaminolysis shows efficacy in both prednisolone-sensitive and in metabolically rewired prednisolone-resistant b-cell childhood acute lymphoblastic leukaemia cells. Int. J. Mol. Sci. 2023;24(4):3378. doi: 10.3390/ijms24043378.

Schlenk RF, Krauter J, Raffoux E, Kreuzer KA, Schaich M, Noens L, Pabst T, Vusirikala M, Bouscary D, Spencer A, Candoni A, Gil JS, Berkowitz N, Weber HJ, Ottmann O. Panobinostat monotherapy and combination therapy in patients with acute myeloid leukemia: results from two clinical trials. Haematologica. 2018;103(1):e25-e28. doi: 10.3324/haematol.2017.172411.

Schmalfeldt B, Prechtel D, Härting K, Späthe K, Rutke S, Konik E, Fridman R, Berger U, Schmitt M, Kuhn W, Lengyel E. Increased expression of matrix metalloproteinases (MMP)-2, MMP-9, and the urokinase-type plasminogen activator is associated with progression from benign to advanced ovarian cancer. Clin. Cancer Res. 2001;7(8):2396-404.

Schneider P, Costa O, Legrand E, Bigot D, Lecleire S, Grassi V, Vannier JP, Vasse M. In vitro secretion of matrix metalloprotease 9 is a prognostic marker in childhood acute lymphoblastic leukemia. Leuk. Res. 2010;34(1):24-31. doi: 10.1016/j.leukres.2009.07.039.

Schrodinger Suite. Schrodinger LLC, New York, USA, 2019.

Schölz C, Weinert BT, Wagner SA, Beli P, Miyake Y, Qi J, Jensen LJ, Streicher W, McCarthy AR, Westwood NJ, Lain S, Cox J, Matthias P, Mann M, Bradner JE, Choudhary C.

Acetylation site specificities of lysine deacetylase inhibitors in human cells. Nat. Biotechnol. 2015;33(4):415-423. doi: 10.1038/nbt.3130.

Schulte ML, Fu A, Zhao P, Li J, Geng L, Smith ST, Kondo J, Coffey RJ, Johnson MO, Rathmell JC, Sharick JT, Skala MC, Smith JA, Berlin J, Washington MK, Nickels ML, Manning HC. Pharmacological blockade of ASCT2-dependent glutamine transport leads to antitumor efficacy in preclinical models. Nat. Med. 2018;24(2):194-202. doi: 10.1038/nm.4464.

Scior T, Bender A, Tresadern G, Medina-Franco JL, Martínez-Mayorga K, Langer T, Cuanalo-Contreras K, Agrafiotis DK. Recognizing pitfalls in virtual screening: A critical review. J Chem Inf Model. 2012;52(4):867-881. doi: 10.1021/ci200528d.

Scior T, Medina-Franco JL, Do QT, Martínez-Mayorga K, Yunes Rojas JA, Bernard P. How to recognize and workaround pitfalls in QSAR studies: a critical review. Curr. Med. Chem. 2009;16(32):4297-4313. doi: 10.2174/092986709789578213.

Scozzafava A, Supuran CT. Protease inhibitors: synthesis of potent bacterial collagenase and matrix metalloproteinase inhibitors incorporating N-4-nitrobenzylsulfonylglycine hydroxamate moieties. J. Med. Chem. 2000A;43(9):1858-1865. doi: 10.1021/jm990594k.

Scozzafava A, Supuran CT. Carbonic anhydrase and matrix metalloproteinase inhibitors: sulfonylated amino acid hydroxamates with MMP inhibitory properties act as efficient inhibitors of CA isozymes I, II, and IV, and N-hydroxysulfonamides inhibit both these zinc enzymes. J. Med. Chem. 2000B;43(20):3677-3687. doi: 10.1021/jm000027t.

Scozzafava A, Supuran CT. Protease inhibitors: synthesis of matrix metalloproteinase and bacterial collagenase inhibitors incorporating 5-amino-2-mercapto-1,3,4-thiadiazole zinc binding functions. Bioorg. Med. Chem. Lett. 2002;12(19):2667-2672. doi: 10.1016/s0960-894x(02)00564-4.

Scrideli CA, Cortez MA, Yunes JA, Queiróz RG, Valera ET, da Mata JF, Toledo SR, Pavoni-Ferreira P, Lee ML, Petrilli AS, Brandalise SR, Tone LG. mRNA expression of matrix metalloproteinases (MMPs) 2 and 9 and tissue inhibitor of matrix metalloproteinases (TIMPs) 1 and 2 in childhood acute lymphoblastic leukemia: Potential role of TIMP1 as an adverse prognostic factor. Leuk. Res. 2010;34(1):32-37. doi: 10.1016/j.leukres.2009.10.007.

Sendecor GW, Johnson W G. Multiple regression in statistical methods, 6th Ed., Oxford & IBH, New Delhi, 1967.

Sepehri B, Ghavami R. Design of new CD38 inhibitors based on CoMFA modelling and molecular docking analysis of 4-amino-8-quinoline carboxamides and 2,4-diamino-8-quinazoline carboxamides. SAR QSAR Environ. Res. 2019;30(1):21-38. doi: 10.1080/1062936X.2018.1545695.

Shahlaei M. Descriptor selection methods in quantitative structure-activity relationship studies: A review study. Chem. Rev. 2013;113(10):8093-8103. doi: 10.1021/cr3004339.

Shahlaei M. Descriptor selection methods in quantitative structure-activity relationship studies: a review study. Chem. Rev. 2013;113(10):8093-8103. doi: 10.1021/cr3004339.

References

Sharma S, Bhatia V. Recent trends in QSAR in modeling of drug-protein and protein-protein interactions. Comb Chem High Throughput Screen. 2021;24(7):1031-1041. doi:10.2174/1386207323666201209093537.

Sheen-Chen SM, Chen HS, Eng HL, Sheen CC, Chen WJ. Serum levels of matrix metalloproteinase 2 in patients with breast cancer. Cancer Lett. 2001;173(1):79-82. doi: 10.1016/s0304-3835(01)00657-7.

Sheldrick GM. Crystal structure refinement with SHELXL. Acta Crystallogr. C Struct. Chem. 2015;71(Pt 1):3-8. doi: 10.1107/S2053229614024218.

Shepherd FA, Giaccone G, Seymour L, Debruyne C, Bezjak A, Hirsh V, Smylie M, Rubin S, Martins H, Lamont A, Krzakowski M, Sadura A, Zee B. Prospective, randomized, double-blind, placebo-controlled trial of marimastat after response to first-line chemotherapy in patients with small-cell lung cancer: a trial of the National Cancer Institute of Canada-Clinical Trials Group and the European Organization for Research and Treatment of Cancer. J Clin Oncol. 2002;20(22):4434-4439. doi: 10.1200/JCO.2002.02.108.

Shi W, Zhang X, Shen Q. Quantitative structure-activity relationships studies of CCR5 inhibitors and toxicity of aromatic compounds using gene expression programming. Eur J Med Chem. 2010;45(1):49-54. doi: 10.1016/j.ejmech.2009.09.022.

Shouksmith AE, Gawel JM, Nawar N, Sina D, Raouf YS, Bukhari S, He L, Johns AE, Manaswiyoungkul P, Olaoye OO, Cabral AD, Sedighi A, de Araujo ED, Gunning PT. Class I/IIb-Selective HDAC Inhibitor Exhibits Oral Bioavailability and Therapeutic Efficacy in Acute Myeloid Leukemia. ACS Med. Chem. Lett. 2019;11:56-64. doi: 10.1021/acsmedchemlett.9b00471.

Shyam SS, Sharma UC, Pokharel S. Adverse effects of tyrosine kinase inhibitors in cancer therapy: Pathophysiology, mechanisms and clinical management. Signal Transduct. Target Ther. 2023;8(1):262. doi: 10.1038/s41392-023-01469-6.

Siddhartha R, Garg M. Molecular and clinical insights of matrix metalloproteinases into cancer spread and potential therapeutic interventions. Toxicol. Appl. Pharmacol. 2021;426:115593. doi: 10.1016/j.taap.2021.115593.

Siegel RL, Miller KD, Wagle NS, Jemal A. Cancer statistics, 2023. CA Cancer. J. Clin. 2023;73(1):17-48. doi:10.3322/caac.21763.

Sledge GW Jr, Qulali M, Goulet R, Bone EA, Fife R. Effect of matrix metalloproteinase inhibitor batimastat on breast cancer regrowth and metastasis in athymic mice. J. Natl. Cancer Inst. 1995;87(20):1546-1550. doi: 10.1093/jnci/87.20.1546.

Smith TC, Frank E. Introducing machine learning concepts with WEKA. Methods Mol. Biol. 2016;1418:353-378. doi: 10.1007/978-1-4939-3578-9_17.

Sochacka-Ćwikła A, Mączyński M, Regiec A. FDA-approved drugs for hematological malignancies-the last decade review. Cancers (Basel). 2021;14(1):87. doi: 10.3390/cancers14010087.

References

Song W, Peng Z, Gooyit M, Suckow MA, Schroeder VA, Wolter WR, Lee M, Ikejiri M, Cui J, Gu Z, Chang M. Water-soluble mmp-9 inhibitor prodrug generates active metabolites that cross the blood-brain barrier. ACS Chem. Neurosci. 2013;4(8):1168-1173. doi: 10.1021/cn400077d.

Song Z, Wang J, Su Q, Luan M, Chen X, Xu X. The role of MMP-2 and MMP-9 in the metastasis and development of hypopharyngeal carcinoma. Braz. J. Otorhinolaryngol. 2021;87(5):521-528. doi: 10.1016/j.bjorl.2019.10.009.

Southey MWY, Brunavs M. Introduction to small molecule drug discovery and preclinical development. Front. Drug Discov. 2023;3:1314077. doi: 10.3389/fddsv.2023.1314077.

Sparano JA, Bernardo P, Stephenson P, Gradishar WJ, Ingle JN, Zucker S, Davidson NE. Randomized phase III trial of marimastat versus placebo in patients with metastatic breast cancer who have responding or stable disease after first-line chemotherapy: Eastern Cooperative Oncology Group trial E2196. J. Clin. Oncol. 2004;22(23):4683-4690. doi: 10.1200/JCO.2004.08.054. [Erratum in: J Clin Oncol. 2005 Jan 1;23(1):248.]

Spreafico M, Gruszka AM, Valli D, Mazzola M, Deflorian G, Quintè A, Totaro MG, Battaglia C, Alcalay M, Marozzi A, Pistocchi A. HDAC8: A promising therapeutic target for acute myeloid leukemia. Front. Cell Dev. Biol. 2020;8:844. doi: 10.3389/fcell.2020.00844.

Stack MS, Ellerbroek SM, Fishman DA. The role of proteolytic enzymes in the pathology of epithelial ovarian carcinoma. Int. J. Oncol. 1998;12(3):569-576. doi: 10.3892/ijo.12.3.569.

Stanulla M, Schrappe M. Treatment of childhood acute lymphoblastic leukemia. Semin. Hematol. 2009;46(1):52-63. doi:10.1053/j.seminhematol.2008.09.007.

Sussman JL, Silman I. Computational studies on cholinesterases: Strengthening our understanding of the integration of structure, dynamics and function. Neuropharmacology. 2020;179:108265. doi: 10.1016/j.neuropharm.2020.108265.

Suzuki T, Muto N, Bando M, Itoh Y, Masaki A, Ri M, Ota Y, Nakagawa H, Iida S, Shirahige K, Miyata N. Design, synthesis, and biological activity of NCC149 derivatives as histone deacetylase 8-selective inhibitors. ChemMedChem. 2014;9:657-664. doi: 10.1002/cmdc.201300414.

SYBYL-X 2.0. (2015). St. Louis, MO: Tripos Inc. Software available at http://www.certara.com.

Syed S, Takimoto C, Hidalgo M, Rizzo J, Kuhn JG, Hammond LA, Schwartz G, Tolcher A, Patnaik A, Eckhardt SG, Rowinsky EK. A phase I and pharmacokinetic study of Col-3 (Metastat), an oral tetracycline derivative with potent matrix metalloproteinase and antitumor properties. Clin. Cancer Res. 2004;10(19):6512-6521. doi: 10.1158/1078-0432.CCR-04-0804.

Sykes SM, Mellert HS, Holbert MA, Li K, Marmorstein R, Lane WS, McMahon SB. Acetylation of the p53 DNA-binding domain regulates apoptosis induction. Mol Cell. 2006;24(6):841-851. doi: 10.1016/j.molcel.2006.11.026.

Szeliga M, Obara-Michlewska M. Glutamine in neoplastic cells: focus on the expression and roles of glutaminases. Neurochem Int. 2009;55(1-3):71-75. doi: 10.1016/j.neuint.2009.01.008.

Takeuchi T. Antitumor antibiotics discovered and studied at the Institute of Microbial Chemistry. J. Cancer Res. Clin. Oncol. 1995;121(9-10):505-510. doi: 10.1007/BF01197761.

Tamura Y, Watanabe F, Nakatani T, Yasui K, Fuji M, Komurasaki T, Tsuzuki H, Maekawa R, Yoshioka T, Kawada K, Sugita K, Ohtani M. Highly selective and orally active inhibitors of type IV collagenase (MMP-9 and MMP-2): N-sulfonylamino acid derivatives. J. Med. Chem. 1998;41(4):640-649. doi: 10.1021/jm9707582.

Tang Y, Luo J, Zhang W, Gu W. Tip60-dependent acetylation of p53 modulates the decision between cell-cycle arrest and apoptosis. Mol Cell. 2006 Dec 28;24(6):827-839. doi: 10.1016/j.molcel.2006.11.021.

Tang Y, Zhao W, Chen Y, Zhao Y, Gu W. Acetylation is indispensable for p53 activation [published correction appears in Cell. 2008;133(7):1290]. Cell. 2008;133(4):612-626. doi:10.1016/j.cell.2008.03.025.

Taraboletti G, Garofalo A, Belotti D, Drudis T, Borsotti P, Scanziani E, Brown PD, Giavazzi R. Inhibition of angiogenesis and murine hemangioma growth by batimastat, a synthetic inhibitor of matrix metalloproteinases. J. Natl. Cancer Inst. 1995;87(4):293-298. doi: 10.1093/jnci/87.4.293.

Tautermann CS. Current and future challenges in modern drug discovery. In: Heifetz A, Ed., Quantum Mechanics in Drug Discovery. Humana, NY, 2020, pp. 1-17.

Taylor RD, Jewsbury PJ, Essex JW. A review of protein-small molecule docking methods. J. Comput. Aided Mol. Des. 2002;16(3):151-166. doi: 10.1023/a:1020155510718.

Testero SA, Lee M, Staran RT, Espahbodi M, Llarrull LI, Toth M, Mobashery S, Chang M. Sulfonate-containing thiiranes as selective gelatinase inhibitors. ACS Med. Chem. Lett. 2010;2(2):177-181. doi: 10.1021/ml100254e.

Tetko IV, Livingstone DJ, Luik AI. Neural network studies. 1. Comparison of overfitting and overtraining. J. Chem. Inf. Model. 1995;35(5):826-833. doi: 10.1021/ci00027a006.

Thorn CF, Oshiro C, Marsh S, Hernandez-Boussard T, McLeod H, Klein TE, Altman RB. Doxorubicin pathways: Pharmacodynamics and adverse effects. Pharmacogenet Genomics. 2011;21(7):440-446. doi: 10.1097/FPC.0b013e32833ffb56.

Tierney GM, Griffin NR, Stuart RC, Kasem H, Lynch KP, Lury JT, Brown PD, Millar AW, Steele RJ, Parsons SL. A pilot study of the safety and effects of the matrix metalloproteinase inhibitor marimastat in gastric cancer. Eur. J. Cancer. 1999;35(4):563-568. doi: 10.1016/s0959-8049(99)00007-6.

Tochowicz A, Maskos K, Huber R, Oltenfreiter R, Dive V, Yiotakis A, Zanda M, Pourmotabbed T, Bode W, Goettig P. Crystal structures of MMP-9 complexes with five inhibitors: contribution of the flexible Arg424 side-chain to selectivity. J. Mol. Biol.

2007;371(4):989-1006. doi: 10.1016/j.jmb.2007.05.068. [Erratum in: J. Mol. Biol. 2009;388(4):917-918. Pourmotabbed, Tayebeh (added)].

Todeschini R, Ballabio D, Grisoni F. Beware of Unreliable Q2! A Comparative Study of Regression Metrics for Predictivity Assessment of QSAR Models. J. Chem. Inf. Model. 2016;56(10):1905-1913. doi: 10.1021/acs.jcim.6b00277.

Todeschini R, Gramatica P. New 3D Molecular descriptors: The WHIM theory and QSAR applications. In: Kubinyi H, Folkers G, Martin YC. Eds., 3D QSAR in Drug Design. Springer, Dordrecht. 2002, pp. 355-380.

Todeschini R, Consonni V. Molecular descriptors for chemoinformatics. In: Mannhold R, Kubinyi H, Folkers G, Eds., Methods and Principles in Medicinal Chemistry, Wiley-VCH. Weinheim, Germany, 2009.

Tong JB, Yi F, Luo D, Wang T. QSAR studies of sulfonamide hydroxamates derivatives as mmp-2 inhibitors topomer CoMFA and molecular docking. Lett. Drug Des. Discov. 2020;17:1364–1371. doi:10.2174/1570180817999200630124920.

Tong JB, Luo D, Zhang X, Bian S. Design of novel SHP2 inhibitors using topomer CoMFA, HQSAR analysis, and molecular docking. Struct. Chem. 2021;32:1061–1076. doi:10.1007/s11224-020-01677-8.

Torres PHM, Sodero ACR, Jofily P, Silva-Jr FP. Key topics in molecular docking for drug design. Int. J. Mol. Sci. 2019;20:4574. doi: 10.3390/ijms20184574.

Tosco P, Balle T. Open3DQSAR: A new open-source software aimed at high-throughput chemometric analysis of molecular interaction fields. J. Mol. Model. 2011;17(1):201-208. doi: 10.1007/s00894-010-0684-x.

Travaglino E, Benatti C, Malcovati L, Della Porta MG, Gallì A, Bonetti E, Rosti V, Cazzola M, Invernizzi R. Biological and clinical relevance of matrix metalloproteinases 2 and 9 in acute myeloid leukaemias and myelodysplastic syndromes. Eur J Haematol. 2008;80(3):216-226. doi: 10.1111/j.1600-0609.2007.01012.x.

Trejo-Solis C, Silva-Adaya D, Serrano-García N, Magaña-Maldonado R, Jimenez-Farfan D, Ferreira-Guerrero E, Cruz-Salgado A, Castillo-Rodriguez RA. Role of glycolytic and glutamine metabolism reprogramming on the proliferation, invasion, and apoptosis resistance through modulation of signaling pathways in glioblastoma. Int. J. Mol. Sci. 2023;24(24):17633. doi: 10.3390/ijms242417633.

Tripathi A, Bankaitis VA. Molecular Docking: From Lock and Key to Combination Lock. J. Mol. Med. Clin. Appl. 2017;2(1):10.16966/2575-0305.106. doi:10.16966/2575-0305.106.

Tropsha A. Recent trends in quantitative structure-activity relationships. In: Abraham DJ, Ed., Burger's Medicinal Chemistry and Drug Discovery. John Wiley & Sons. .Hoboken, NJ. 2003A, pp. 49-76.

Tropsha A, Gramatica P, Gombar VK. The importance of being earnest: Validation is the absolute essential for successful application and interpretation of QSPR models. QSAR Comb. Sci. 2003B;22(1):69-77. doi: 10.1002/qsar.200390007.

References

Tropsha A. Best Practices for QSAR Model Development, Validation, and Exploitation. Mol. Inform. 2010;29(6-7):476-488. doi: 10.1002/minf.201000061.

Trott O, Olson AJ. AutoDock Vina: improving the speed and accuracy of docking with a new scoring function, efficient optimization, and multithreading. J. Comput. Chem. 2010;31(2):455-461. doi:10.1002/jcc.21334.

Tsai CY, Ko HJ, Chiou SJ, Lai YL, Hou CC, Javaria T, Huang ZY, Cheng TS, Hsu TI, Chuang JY, Kwan AL, Chuang TH, Huang CF, Loh JK, Hong YR. NBM-BMX, an HDAC8 Inhibitor, Overcomes Temozolomide Resistance in Glioblastoma Multiforme by Downregulating the β-Catenin/c-Myc/SOX2 Pathway and Upregulating p53-Mediated MGMT Inhibition. Int. J. Mol. Sci. 2021;22(11):5907. doi: 10.3390/ijms22115907.

Tsujimoto T, Yamamoto Y, Wasa M, Takenaka Y, Nakahara S, Takagi T, Tsugane M, Hayashi N, Maeda K, Inohara H, Uejima E, Ito T. L-glutamine decreases the severity of mucositis induced by chemoradiotherapy in patients with locally advanced head and neck cancer: a double-blind, randomized, placebo-controlled trial. Oncol. Rep. 2015;33(1):33-39. doi: 10.3892/or.2014.3564.

Tzogani K, van Hennik P, Walsh I, De Graeff P, Folin A, Sjöberg J, Salmonson T, Bergh J, Laane E, Ludwig H, Gisselbrecht C, Pignatti F. EMA Review of Panobinostat (Farydak) for the Treatment of Adult Patients with Relapsed and/or Refractory Multiple Myeloma. Oncologist. 2018;23(5):631-636. doi: 10.1634/theoncologist.2017-0301. [Erratum in: Oncologist. 2018;23(7):870.]

Updyke KM, Morales-Lappot J, Lee T. Atypical presentation of chronic myelogenous leukemia. Cureus. 2017;9(5):e1280. doi: 10.7759/cureus.1280.

Usón I, Sheldrick GM. An introduction to experimental phasing of macromolecules illustrated by SHELX; new autotracing features. Acta Crystallogr. D Struct. Biol. 2018;74(Pt 2):106-116. doi: 10.1107/S2059798317015121.

Vapnik VN. The support vector method for estimating indicator functions. In: Statistical Learning Theory. John Wiley & Sons. New York. 1998, pp. 401-440.

Vapnik VN. The nature of statistical learning theory. Second Ed. Springer, New York. 2000.

Vardiman JW, Melo JV, Baccarani M, Thiele J. Chronic myeloid leukemia, BCR-ABL1-positive. In: Swerdlow SH, Campo E, Harris NL, Jaffe ES, Pileri AS. WHO classification of tumors of hematopoietic and lymphoid tissues (Revised Fourth Edition), Lyon: IARC Press, 2017, pages 32–37.

Velec HF, Gohlke H, Klebe G. DrugScore(CSD)-knowledge-based scoring function derived from small molecule crystal data with superior recognition rate of near-native ligand poses and better affinity prediction. J. Med. Chem. 2005;48(20):6296-6303. doi: 10.1021/jm050436v.

Verdonk ML, Cole JC, Hartshorn MJ, Murray CW, Taylor RD. Improved protein-ligand docking using GOLD. Proteins. 2003;52(4):609-623. doi: 10.1002/prot.10465.

References

Verma J, Khedkar VM, Coutinho EC. 3D-QSAR in drug design--a review. Curr. Top. Med. Chem. 2010;10(1):95-115. doi: 10.2174/156802610790232260.

Verma D, Zanetti C, Godavarthy PS, Kumar R, Minciacchi VR, Pfeiffer J, Metzler M, Lefort S, Maguer-Satta V, Nicolini FE, Burroni B, Fontenay M, Krause DS. Bone marrow niche-derived extracellular matrix-degrading enzymes influence the progression of B-cell acute lymphoblastic leukemia. Leukemia. 2020;34(6):1540-1552. doi: 10.1038/s41375-019-0674-7.

Vousden KH, Lane DP. p53 in health and disease. Nat. Rev. Mol. Cell Biol. 2007;8(4):275-283. doi: 10.1038/nrm2147.

Wang C, Chen Z, Li Z, Cen J. The essential roles of matrix metalloproteinase-2, membrane type 1 metalloproteinase and tissue inhibitor of metalloproteinase-2 in the invasive capacity of acute monocytic leukemia SHI-1 cells. Leuk. Res. 2010A;34(8):1083-1090. doi: 10.1016/j.leukres.2010.01.016.

Wang JB, Erickson JW, Fuji R, Ramachandran S, Gao P, Dinavahi R, Wilson KF, Ambrosio AL, Dias SM, Dang CV, Cerione RA. Targeting mitochondrial glutaminase activity inhibits oncogenic transformation. Cancer Cell. 2010B;18(3):207-219. doi: 10.1016/j.ccr.2010.08.009. [Erratum in: Cancer Cell. 2010B;18(4):397.]

Wang YV, Leblanc M, Fox N, Mao JH, Tinkum KL, Krummel K, Engle D, Piwnica-Worms D, Piwnica-Worms H, Balmain A, Kaushansky K, Wahl GM. Fine-tuning p53 activity through C-terminal modification significantly contributes to HSC homeostasis and mouse radiosensitivity. Genes Dev. 2011;25(13):1426-1438. doi: 10.1101/gad.2024411.

Wang J, Sun F, Han L, Hou X, Pan X, Liu R, Tangb W, Fang H. Design, synthesis, and preliminary bioactivity studies of substituted purine hydroxamic acid derivatives as novel histone deacetylase (HDAC) inhibitors†. Med. Chem. Commun. 2014A;5:1887-1891. doi.org/10.1039/C4MD00203B.

Wang L, Chen L, Liu Z, Zheng M, Gu Q, Xu J. Predicting mTOR inhibitors with a classifier using recursive partitioning and Naïve Bayesian approaches. PLoS One. 2014B;9(5):e95221. doi: 10.1371/journal.pone.0095221.

Wang Z, Zhao L, Zhang B, Feng J, Wang Y, Zhang B, Jin H, Ding L, Wang N, He S. Discovery of novel polysubstituted *N*-alkyl acridone analogues as histone deacetylase isoform-selective inhibitors for cancer therapy. J. Enzyme Inhib. Med. Chem. 2023;38(1):2206581. doi: 10.1080/14756366.2023.2206581.

Watson SA, Morris TM, Robinson G, Crimmin MJ, Brown PD, Hardcastle JD. Inhibition of organ invasion by the matrix metalloproteinase inhibitor batimastat (BB-94) in two human colon carcinoma metastasis models. Cancer Res. 1995;55(16):3629-3633.

Watson RA, De La Peña H, Tsakok MT, Joseph J, Stoneham S, Shamash J, Joffe J, Mazhar D, Traill Z, Ho LP, Sue Brand S, Protheroe AS. Development of a best-practice clinical guideline for the use of bleomycin in the treatment of germ cell tumours in the UK. Br. J. Cancer. 2018;119:1044-1051. doi: 10.1038/s41416-018-0300-x.

Watters JM, Wright G, Smith MA, Shah B, Wright KL. Histone deacetylase 8 inhibition suppresses mantle cell lymphoma viability while preserving natural killer cell function. Biochem. Biophys. Res. Commun. 2021;534:773-779. doi: 10.1016/j.bbrc.2020.11.001.

Welch W, Ruppert J, Jain AN. Hammerhead: fast, fully automated docking of flexible ligands to protein binding sites. Chem. Biol. 1996;3(6):449-62. doi: 10.1016/s1074-5521(96)90093-9.

Wendt B, Mulbaier M, Wawro S, Schultes C, Alonso J, Janssen B, Lewis J. Toluidinesulfonamide hypoxia-induced factor 1 inhibitors: alleviating drug-drug interactions through use of PubChem data and comparative molecular field analysis guided synthesis. J. Med. Chem. 2011;54(11):3982-3986. doi: 10.1021/jm200272h.

Wilkes GM. Targeted therapy: Attacking cancer with molecular and immunological targeted agents. Asia. Pac. J. Oncol. Nurs. 2018;5(2):137-155. doi: 10.4103/apjon.apjon_79_17.

Wilson A, Laurenti E, Trumpp A. Balancing dormant and self-renewing hematopoietic stem cells. Curr. Opin. Genet. Dev. 2009;19(5):461-468. doi: 10.1016/j.gde.2009.08.005.

Winer A, Adams S, Mignatti P. Matrix metalloproteinase inhibitors in cancer therapy: Turning past failures into future successes. Mol. Cancer Ther. 2018;17(6):1147-1155. doi: 10.1158/1535-7163.MCT-17-0646.

Wise DR, DeBerardinis RJ, Mancuso A, Sayed N, Zhang XY, Pfeiffer HK, Nissim I, Daikhin E, Yudkoff M, McMahon SB, Thompson CB. Myc regulates a transcriptional program that stimulates mitochondrial glutaminolysis and leads to glutamine addiction. Proc. Natl. Acad. Sci. U S A. 2008;105(48):18782-18787. doi: 10.1073/pnas.0810199105.

Wojtowicz-Praga S, Low J, Marshall J, Ness E, Dickson R, Barter J, Sale M, McCann P, Moore J, Cole A, Hawkins MJ. Phase I trial of a novel matrix metalloproteinase inhibitor batimastat (BB-94) in patients with advanced cancer. Invest. New Drugs. 1996;14(2):193-202. doi: 10.1007/BF00210790.

Wojtowicz-Praga S, Torri J, Johnson M, Steen V, Marshall J, Ness E, Dickson R, Sale M, Rasmussen HS, Chiodo TA, Hawkins MJ. Phase I trial of Marimastat, a novel matrix metalloproteinase inhibitor, administered orally to patients with advanced lung cancer. J. Clin. Oncol. 1998;16(6):2150-2156. doi: 10.1200/JCO.1998.16.6.2150.

Wood ND, Aitken M, Durston S, Harris S, McClelland GR, Sharp S. Cartilage protective agent (CPA) Ro 32-3555, a new matrix metalloproteinase inhibitor for the treatment of rheumatoid arthritis. Agents Actions Suppl. 1998;49:49-55. doi: 10.1007/978-3-0348-8857-8_8.

Worachartcheewan A, Nantasenamat C, Naenna T, Isarankura-Na-Ayudhya C, Prachayasittikul V. Modeling the activity of furin inhibitors using artificial neural network. Eur. J. Med. Chem. 2009;44(4):1664-1673. doi: 10.1016/j.ejmech.2008.09.028.

Wright JC, Prigot A, Wright B, Weintraub S, Wright LT. An evaluation of folic acid antagonists in adults with neoplastic diseases: a study of 93 patients with incurable neoplasms. J. Natl. Med. Assoc. 1951;43(4):211-240.

References

www.bloodcancer.org.uk/understanding-blood-cancer/blood-cancer-types/ (Accessed on 04.12.2023)

www.cancer.gov/about-cancer/understanding/what-is-cancer (Accessed on 04.12.2023)

www.cancer.gov/publications/dictionaries/cancer-terms/def/solid-tumor (Accessed on 04.12.2023)

www.cancer.gov/types/lymphoma (Accessed on 04.12.2023)

www.cancer.org/cancer/leukemia.html (Accessed on 04.12.2023)

www.cancer.org/treatment/understanding-your-diagnosis/what-is-cancer.html (Accessed on 04.12.2023)

www.clinicaltrials.gov/search?term=Histone%20Deacetylase%20Inhibitor&cond=cancer (Accessed on 04.12.2023)

www.clinicaltrials.gov/search?term=Histone%20Deacetylase%20Inhibitor&cond=cancer (Accessed on 04.12.2023)

www.clinicaltrials.gov/search?term=Histone%20Deacetylase%20Inhibitor&cond=Hematologic%20Malignancies (Accessed on 04.12.2023)

www.clinicaltrials.gov/study/NCT04639843?term=NCT04639843&rank=1 (Accessed on 04.12.2023)

www.ebi.ac.uk/chembl/ (accessed on 01.08.2023)

www.fda.gov/drugs/resources-information-approved-drugs/fda-approves-onureg-azacitidine-tablets-acute-myeloid-leukemia (Accessed on 04.12.2023)

www.naturewise.com.tw/ (Accessed on 04.12.2023)

www.naturewise.com.tw/2023/05/22/nbm-bmx-received-usfda-approval-to-proceed-phase-ib-ii-clinical-trial-in-newly-diagnosed-glioblastoma-multiforme-gbm/ (Accessed on 04.12.2023)

www.ncbi.nlm.nih.gov/books/NBK499969/ (Accessed on 04.12.2023)

www.ncbi.nlm.nih.gov/books/NBK534764/ (Accessed on 04.12.2023)

www.ncbi.nlm.nih.gov/books/NBK559328/ (Accessed on 04.12.2023)

www.who.int/news-room/fact-sheets/detail/cancer (Accessed on 04.12.2023)

Xiang L, Mou J, Shao B, Wei Y, Liang H, Takano N, Semenza GL, Xie G. Glutaminase 1 expression in colorectal cancer cells is induced by hypoxia and required for tumor growth, invasion, and metastatic colonization. Cell Death Dis. 2019;10(2):40. doi: 10.1038/s41419-018-1291-5.

Xiao L, Huang Y, Zhen R, Chiao JW, Liu D, Ma X. Deficient histone acetylation in acute leukemia and the correction by an isothiocyanate. Acta Haematol. 2010;123(2):71-76. doi: 10.1159/000264628.

References

Yang JS, Lin CW, Su SC, Yang SF. Pharmacodynamic considerations in the use of matrix metalloproteinase inhibitors in cancer treatment. Expert. Opin. Drug Metab. Toxicol. 2016A;12(2):191-200. doi:10.1517/17425255.2016.1131820.

Yang Y, Karakhanova S, Hartwig W, D'Haese JG, Philippov PP, Werner J, Bazhin AV. Mitochondria and Mitochondrial ROS in Cancer: Novel Targets for Anticancer Therapy. J. Cell Physiol. 2016B;231(12):2570-2581. doi: 10.1002/jcp.25349.

Yang Y, Li S, Wang Y, Zhao Y, Li Q. Protein tyrosine kinase inhibitor resistance in malignant tumors: Molecular mechanisms and future perspective. Signal Transduct. Target Ther. 2022;7(1):329. doi: 10.1038/s41392-022-01168-8.

Yao XJ, Panaye A, Doucet JP, Zhang RS, Chen HF, Liu MC, Hu ZD, Fan BT. Comparative study of QSAR/QSPR correlations using support vector machines, radial basis function neural networks, and multiple linear regression. J. Chem. Inf. Comput. Sci. 2004;44(4):1257-1266. doi: 10.1021/ci049965i.

Yap CW. PaDEL-descriptor: an open source software to calculate molecular descriptors and fingerprints. J. Comput. Chem. 2011;32(7):1466-1474. doi: 10.1002/jcc.21707.

Yoo C, Shahlaei M. The applications of PCA in QSAR studies: A case study on CCR5 antagonists. Chem. Biol. Drug Des. 2018;91(1):137-152. doi: 10.1111/cbdd.13064.

Yoo HC, Yu YC, Sung Y, Han JM. Glutamine reliance in cell metabolism. Exp. Mol. Med. 2020;52(9):1496-1516. doi: 10.1038/s12276-020-00504-8.

Yu CF, Chen FH, Lu MH, Hong JH, Chiang CS. Dual roles of tumour cells-derived matrix metalloproteinase 2 on brain tumour growth and invasion. Br. J. Cancer. 2017;117(12):1828-1836. doi: 10.1038/bjc.2017.362.

Yuriev E, Holien J, Ramsland PA. Improvements, trends, and new ideas in molecular docking: 2012-2013 in review. J. Mol. Recognit. 2015;28(10):581-604. doi: 10.1002/jmr.2471.

Zaknoen S, Wolff R, Cox C. Marimastat in advanced progressive colorectal cancer-a dose-finding study. In ASCO Annual Meeting. 1997:968. (Abstract)

Zaragozá R. Transport of amino acids across the blood-brain barrier. Front. Physiol. 2020;11:973. doi: 10.3389/fphys.2020.00973.

Zhang Y, Sanjose SD, Bracci PM, Morton LM, Wang R, Brennan P, Hartge P, Boffetta P, Becker N, Maynadie M, Foretova L, Cocco P, Staines A, Holford T, Holly EA, Nieters A, Benavente Y, Bernstein L, Zahm SH, Zheng T. Personal use of hair dye and the risk of certain subtypes of non-Hodgkin lymphoma. Am. J. Epidemiol. 2008;167(11):1321-1331. doi: 10.1093/aje/kwn058.

Zhang C, Zhong JF, Stucky A, Chen XL, Press MF, Zhang X. Histone acetylation: Novel target for the treatment of acute lymphoblastic leukemia. Clin. Epigenetics., 2015;7:117. doi: 10.1186/s13l48-015-015l-8.

Zhang H, Ding L, Zou Y, Hu SQ, Huang HG, Kong WB, Zhang J. Predicting drug-induced liver injury in human with Naïve Bayes classifier approach. J. Comput. Aided Mol. Des. 2016;30(10):889-898. doi: 10.1007/s10822-016-9972-6.

References

Zhang K, Lai F, Lin S, Ji M, Zhang J, Zhang Y, Jin J, Fu R, Wu D, Tian H, Xue N, Sheng L, Zou X, Li Y, Chen X, Xu H. Design, Synthesis, and Biological Evaluation of 4-Methyl Quinazoline Derivatives as Anticancer Agents Simultaneously Targeting Phosphoinositide 3-Kinases and Histone Deacetylases. J. Med. Chem. 2019;62:6992-7014. doi: 10.1021/acs.jmedchem.9b00390.

Zhang L, Nguyen LXT, Chen YC, Wu D, Cook GJ, Hoang DH, Brewer CJ, He X, Dong H, Li S, Li M, Zhao D, Qi J, Hua WK, Cai Q, Carnahan E, Chen W, Wu X, Swiderski P, Rockne RC, Kortylewski M, Li L, Zhang B, Marcucci G, Kuo YH. Targeting miR-126 in inv(16) acute myeloid leukemia inhibits leukemia development and leukemia stem cell maintenance. Nat. Commun. 2021;12(1):6154. doi: 10.1038/s41467-021-26420-7.

Zhao C, Chen D, Suo F, Setroikromo R, Quax WJ, Dekker FJ. Discovery of highly potent HDAC8 PROTACs with anti-tumor activity. Bioorg. Chem. 2023;136:106546. doi: 10.1016/j.bioorg.2023.106546.

Zhao L, Lv C, Sun L, Li Q, Wang Y, Wu M, Wang Y, Guo Z, Bian S, Kong D, Lin L, Wang Y, Zhou J, Li Y. Histone deacetylase inhibitor chidamide regulates the Wnt/β-catenin pathway by MYCN/DKK3 in B-ALL. Invest. New Drugs. 2021;39(4):961-970. doi: 10.1007/s10637-021-01079-5.

Zhong L, Li Y, Xiong L, Wang W, Wu M, Yuan T, Yang W, Tian C, Miao Z, Wang T, Yang S. Small molecules in targeted cancer therapy: advances, challenges, and future perspectives. Signal Transduct. Target Ther. 2021;6(1):201. doi: 10.1038/s41392-021-00572-w.

Zhou X, Chen H, Shi Y, Li J, Ma X, Du L, Hu Y, Tao M, Zhong Q, Yan D, Zhuang S, Liu N. Histone deacetylase 8 inhibition prevents the progression of peritoneal fibrosis by counteracting the epithelial-mesenchymal transition and blockade of M2 macrophage polarization. Front. Immunol. 2023;14:1137332. doi: 10.3389/fimmu.2023.1137332.

Zhou Z, Apte SS, Soininen R, Cao R, Baaklini GY, Rauser RW, Wang J, Cao Y, Tryggvason K. Impaired endochondral ossification and angiogenesis in mice deficient in membrane-type matrix metalloproteinase I. Proc. Natl. Acad. Sci. U S A. 2000;97(8):4052-4057. doi: 10.1073/pnas.060037197.

Zhu B, Zhang J, Chen J, Li C, Wang X. Molecular biological characteristics of the recruitment of hematopoietic stem cells from bone marrow niche in chronic myeloid leukemia. Int. J. Clin. Exp. Pathol. 2015;8(10):12595-12607.

Zhu GH, Dai HP, Shen Q, Ji O, Zhang Q, Zhai YL. Curcumin induces apoptosis and suppresses invasion through MAPK and MMP signaling in human monocytic leukemia SHI-1 cells. Pharm. Biol. 2016;54(8):1303-1311. doi: 10.3109/13880209.2015.1060508.

Zhu G, Shen Q, Jiang H, Ji O, Zhu L, Zhang L. Curcumin inhibited the growth and invasion of human monocytic leukaemia SHI-1 cells in vivo by altering MAPK and MMP signalling. Pharm. Biol. 2020;58(1):25-34. doi: 10.1080/13880209.2019.1701042.

APPENDIX

Table A1. Structure of aryl sulfonamides with MMP2 and MMP9 binding affinity values (K_i) of the compounds of **dataset 1**.

Compound number	R	MMP2 K_i (nM)	MMP9 K_i (nM)	MMP2 pK_i	MMP9 pK_i
	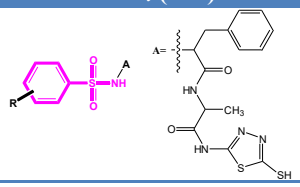				
A1	H-	18,000	15,000	4.745	4.824
A2	4-F-	17,000	14,000	4.770	4.854
A3	4-Cl-	16,000	15,000	4.796	4.824
A4	4-Br-	15,000	21,000	4.824	4.678
A5	4-I-	17,000	18,000	4.770	4.745
A6	4-CH3-	20,000	20,000	4.699	4.699
A7	4-O_2N-	12,000	18,000	4.921	4.745
A8	3-O_2N-	12,000	18,000	4.921	4.745
A9	2-O_2N-	15,000	14,000	4.824	4.854
A10	4-$NHCOCH_3$-	8,000	10,000	5.097	5.000
A11	2,3,4,5,6-(F)5-	6,000	2,000	5.222	5.699
A12	3-CF_3-	11,000	5,000	4.959	5.301
A13	2,5-Cl_2-	10,000	17,000	5.000	4.770
A14	4- CH_3O-	18,000	21,000	4.745	4.678
A15	2,4,6-$(CH_3)_3$-	24,000	29,000	4.620	4.538
	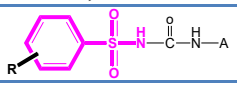				
A16	H-	5,000	4,000	5.301	5.398
A17	4-F-	2,000	300	5.699	6.523
A18	4-Cl-	4,000	400	5.398	6.398
A19	4-CH_3-	7,000	5,000	5.155	5.301
A20	2-CH_3-	8,000	7,000	5.097	5.155
	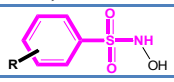				
A21	H-	70,000	78,000	4.155	4.108
A22	4-F-	72,000	73000	4.143	4.137
A23	4-Cl-	70,000	76,000	4.155	4.119
A24	4-Br-	65,000	66,000	4.187	4.180
A25	4-I-	72,000	69,000	4.143	4.161
A26	4-Me-	77,000	60,000	4.114	4.222
A27	4-NO_2-	21,000	14,000	4.678	4.854
A28	3- NO_2-	23,000	13,000	4.638	4.886
A29	2- NO_2-	38,000	23,000	4.420	4.638
A30	3-Cl-4-NO_2-	14,000	13,000	4.854	4.886
A31	4-$NHCOCH_3$-	9,000	10,000	5.046	5.000
A32	4-NH_2-	15,000	24,000	4.824	4.620
A33	4- CH_3O-3-NH_2-	11,000	9,000	4.959	5.046
A34	4-CH_3O-	14,000	12,000	4.854	4.921
A35	2,4,6- $(CH_3)_3$-	21,000	34,000	4.678	4.469
A36	2,3,4,5,6-$(F)_5$-	900	1,300	6.046	5.886

A37	3-CF_3-	120	1,700	6.921	5.770
A38	2-HOOC-	90	100	7.046	7.000
	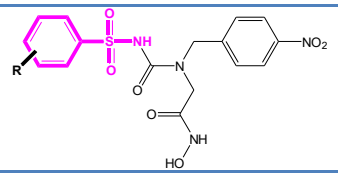				
A39	**H-**	5	3	8.301	8.523
A40	**4-F-**	3	7	8.523	8.155
A41	**4-Cl-**	3	5	8.523	8.301
A42	**4-CH_3-**	6	8	8.222	8.097
A43	**2-CH_3-**	8	7	8.097	8.155
	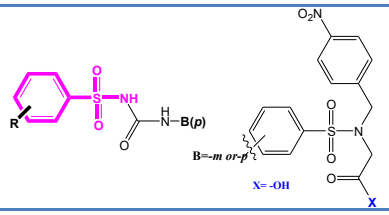				
A44	**H-**	18	21	7.745	7.678
A45	**4-F-**	16	23	7.796	7.638
A46	**4-Cl-**	21	36	7.678	7.444
A47	**4-CH_3-**	24	25	7.620	7.602
A48	**2-CH_3-**	25	29	7.602	7.538
	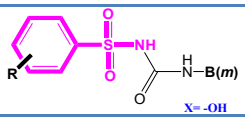				
A49	H-	19	22	7.721	7.658
A50	4-F-	15	18	7.824	7.745
A51	4-Cl-	18	23	7.745	7.638
A52	4-CH_3-	21	21	7.678	7.678
A53	2-CH_3-	24	28	7.620	7.553
	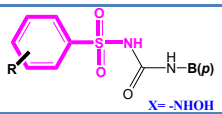				
A54	H-	0.6	0.9	9.222	9.046
A55	4-Cl-	0.8	1	9.097	9.000
A56	4-CH_3-	0.7	0.5	9.155	9.301
A57	2-CH_3-	1.6	0.7	8.796	9.155
A63	4-F-	0.6	1.2	9.222	8.921
	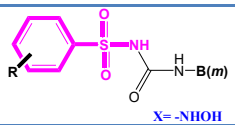				
A58	H-	1.2	1.3	8.921	8.886
A59	4-F-	1.8	2.5	8.745	8.602
A60	4-Cl-	1.5	1.6	8.824	8.796
A61	4-CH_3-	2.5	3.1	8.602	8.509
A62	2-CH_3-	2.8	3	8.553	8.523

Table A2. Correlation matrix among biological activity and selected parameters of **(A)** ***Eq. 1a*** **- (B)** ***Eq. 2a***

(A) Eq. 6

Eq. 6	*nsssN*	*SHBint6*	*SHBint7*	*PubchemFP629*	*MMP2 pKi*
nsssN	1.00	0.19	-0.18	0.35	0.94
SHBint6		1.00	0.01	-0.24	0.43
SHBint7			1.00	-0.26	-0.04
PubchemFP629				1.00	0.30
MMP2 pKi					1.00

(B) Eq. 7

Eq. 7	*nsssN*	*SHBint10*	*AATS2i*	*nHBint10*	*MMP9 pKi*
nsssN	1.00	0.36	-0.08	0.11	0.94
SHBint10	0.36	1.00	0.01	0.89	0.58
AATS2i	-0.08	0.01	1.00	-0.08	0.08
MMP9 pKi	0.94	0.58	0.08	0.35	1.00

Table A3. R^2 and Q^2 values after several Y-randomization tests for MMP2 inhibitors

MODEL TYPE	*R*	R^2	$Q^2_{(LOO)}$
Original	**0.989**	**0.978**	**0.972**
Random 1	0.290	0.084	-0.149
Random 2	0.308	0.095	-0.110
Random 3	0.134	0.018	-0.242
Random 4	0.172	0.029	-0.198
Random 5	0.351	0.123	-0.087
Random 6	0.409	0.168	-0.041
Random 7	0.307	0.094	-0.119
Random 8	0.215	0.046	-0.180
Random 9	0.333	0.111	-0.103
Random 10	0.165	0.027	-0.200
Random 11	0.230	0.053	-0.177
Random 12	0.157	0.025	-0.228
Random 13	0.362	0.131	-0.067
Random 14	0.323	0.105	-0.119
Random 15	0.326	0.106	-0.125
Random 16	0.306	0.094	-0.131
Random 17	0.431	0.185	-0.021
Random 18	0.179	0.032	-0.195
Random 19	0.401	0.161	-0.060
Random 20	0.237	0.056	-0.191
Random 21	0.347	0.120	-0.100

Random 22	0.164	0.027	-0.253
Random 23	0.351	0.123	-0.088
Random 24	0.339	0.115	-0.090
Random 25	0.224	0.050	-0.192
Random 26	0.382	0.146	-0.047
Random 27	0.395	0.156	-0.009
Random 28	0.265	0.070	-0.148
Random 29	0.377	0.142	-0.061
Random 30	0.370	0.137	-0.048
Random 31	0.193	0.037	-0.250
Random 32	0.146	0.021	-0.227
Random 33	0.357	0.127	-0.132
Random 34	0.374	0.140	-0.061
Random 35	0.256	0.066	-0.159
Random 36	0.383	0.147	-0.075
Random 37	0.418	0.175	-0.036
Random 38	0.079	0.006	-0.238
Random 39	0.232	0.054	-0.176
Random 40	0.420	0.176	-0.027
Random 41	0.231	0.053	-0.186
Random 42	0.146	0.021	-0.190
Random 43	0.365	0.133	-0.091
Random 44	0.191	0.037	-0.186
Random 45	0.301	0.090	-0.145
Random 46	0.169	0.028	-0.196
Random 47	0.305	0.093	-0.118
Random 48	0.211	0.044	-0.197
Random 49	0.236	0.056	-0.167
Random 50	0.271	0.074	-0.145

Table A4. R^2 and Q^2 values after several Y-randomization tests for MMP9 inhibitors

MODEL TYPE	R	R^2	$Q^2_{(LOO)}$
Original	**0.987**	**0.974**	**0.969**
Random 1	0.262	0.069	-0.127
Random 2	0.133	0.018	-0.168
Random 3	0.292	0.085	-0.074
Random 4	0.312	0.098	-0.112
Random 5	0.291	0.085	-0.112
Random 6	0.103	0.011	-0.197
Random 7	0.289	0.084	-0.092
Random 8	0.230	0.053	-0.112

Random 9	0.394	0.155	0.025
Random 10	0.155	0.024	-0.124
Random 11	0.119	0.014	-0.215
Random 12	0.271	0.074	-0.083
Random 13	0.107	0.011	-0.193
Random 14	0.274	0.075	-0.121
Random 15	0.237	0.056	-0.161
Random 16	0.202	0.041	-0.175
Random 17	0.334	0.111	-0.041
Random 18	0.113	0.013	-0.285
Random 19	0.347	0.121	-0.027
Random 20	0.253	0.064	-0.098
Random 21	0.241	0.058	-0.217
Random 22	0.245	0.060	-0.122
Random 23	0.119	0.014	-0.193
Random 24	0.124	0.015	-0.243
Random 25	0.245	0.060	-0.084
Random 26	0.176	0.031	-0.171
Random 27	0.438	0.192	0.059
Random 28	0.185	0.034	-0.159
Random 29	0.435	0.189	0.061
Random 30	0.143	0.020	-0.231
Random 31	0.203	0.041	-0.114
Random 32	0.094	0.009	-0.162
Random 33	0.392	0.153	0.009
Random 34	0.321	0.103	-0.044
Random 35	0.290	0.084	-0.109
Random 36	0.150	0.023	-0.179
Random 37	0.196	0.038	-0.138
Random 38	0.210	0.044	-0.121
Random 39	0.230	0.053	-0.096
Random 40	0.137	0.019	-0.198
Random 41	0.091	0.008	-0.206
Random 42	0.198	0.039	-0.216
Random 43	0.243	0.059	-0.155
Random 44	0.065	0.004	-0.244
Random 45	0.280	0.078	-0.126
Random 46	0.163	0.027	-0.174
Random 47	0.303	0.092	-0.060
Random 48	0.421	0.177	0.050
Random 49	0.222	0.049	-0.163
Random 50	0.421	0.177	-0.032

Table A5. The *t*-Value, *p*-level and Variation inflation factor (VIF) for each descriptor of **(A)** ***Eq. 1a*** **- (B)** ***Eq. 2a***

(A) *Eq. 1a*	t(43)	p-level	VIF
Intercept	45.539	0.000	--
nsssN	34.896	0.000	1.267
SHBint6	11.683	0.000	1.172
SHBint7	6.003	0.000	1.085
PubchemFP629	3.740	0.001	1.350

(B) *Eq. 2a*	t(44)	p-level	VIF
Intercept	-3.625	0.001	--
nsssN	32.563	0.000	1.160
SHBint10	10.020	0.000	1.153
AATS2i	5.873	0.000	1.009

Table A6. Y_{obs} (observed activity of training set compounds), Y_{pred} (calculated/predicted activity of training set compounds), Absolute Residual and Residual^2 values from both MLR-model (***Eq. 1a***) and LOO predicted

Compno	Y_{obs} (Train)	Y_{pred} (MLR model)	Absolute Residual (MLR)	Residual^2 [MLR]	Y_{pred} (LOO)	AbsoluteResidual(LOO)	Residual^2 [LOO]
A2	4.770	4.936	0.167	0.028	4.945	0.176	0.031
A3	4.796	4.701	0.095	0.009	4.696	0.100	0.010
A4	4.824	4.691	0.133	0.018	4.684	0.140	0.020
A5	4.770	4.691	0.078	0.006	4.687	0.083	0.007
A6	4.699	4.691	0.008	0.000	4.690	0.009	0.000
A9	4.824	4.734	0.090	0.008	4.730	0.094	0.009
A11	5.222	5.589	0.367	0.135	5.622	0.400	0.160
A12	4.959	5.453	0.495	0.245	5.506	0.547	0.299
A13	5.000	4.681	0.319	0.102	4.664	0.336	0.113
A14	4.745	4.785	0.040	0.002	4.787	0.042	0.002
A16	5.301	5.186	0.115	0.013	5.180	0.121	0.015
A17	5.699	5.203	0.496	0.246	5.174	0.525	0.275
A19	5.155	5.183	0.028	0.001	5.185	0.030	0.001
A20	5.097	5.182	0.085	0.007	5.187	0.090	0.008
A22	4.143	4.829	0.687	0.471	4.865	0.723	0.522
A23	4.155	4.077	0.078	0.006	4.069	0.086	0.007
A24	4.187	4.032	0.155	0.024	4.015	0.173	0.030
A26	4.114	4.032	0.081	0.007	4.023	0.091	0.008
A27	4.678	4.292	0.386	0.149	4.257	0.421	0.177
A28	4.638	5.130	0.492	0.242	5.237	0.599	0.359
A29	4.420	4.452	0.032	0.001	4.454	0.034	0.001

A32	4.824	5.201	0.377	0.142	5.219	0.395	0.156
A33	4.959	5.227	0.269	0.072	5.285	0.327	0.107
A34	4.854	4.338	0.516	0.266	4.302	0.552	0.305
A36	6.046	6.035	0.011	0.000	6.033	0.013	0.000
A37	6.921	6.445	0.476	0.227	6.210	0.711	0.506
A39	8.301	8.341	0.040	0.002	8.349	0.048	0.002
A40	8.523	8.348	0.175	0.031	8.310	0.213	0.045
A42	8.222	8.343	0.121	0.015	8.369	0.147	0.022
A43	8.097	8.347	0.250	0.063	8.402	0.305	0.093
A44	7.745	7.960	0.216	0.046	7.979	0.235	0.055
A45	7.796	7.977	0.181	0.033	7.992	0.196	0.039
A46	7.678	7.953	0.275	0.076	7.977	0.299	0.090
A47	7.620	7.953	0.333	0.111	7.983	0.363	0.132
A48	7.602	7.948	0.346	0.120	7.979	0.377	0.142
A50	7.824	7.619	0.205	0.042	7.587	0.237	0.056
A51	7.745	7.619	0.126	0.016	7.599	0.145	0.021
A52	7.678	7.619	0.059	0.003	7.610	0.068	0.005
A53	7.620	7.619	0.001	0.000	7.619	0.001	0.000
A54	9.222	8.936	0.286	0.082	8.894	0.328	0.107
A55	9.097	8.927	0.170	0.029	8.902	0.195	0.038
A56	9.155	8.927	0.228	0.052	8.894	0.261	0.068
A57	8.796	8.921	0.125	0.016	8.939	0.143	0.020
A59	8.745	8.592	0.153	0.023	8.571	0.174	0.030
A60	8.824	8.588	0.236	0.056	8.556	0.268	0.072
A61	8.602	8.588	0.014	0.000	8.586	0.016	0.000
A62	8.553	8.587	0.034	0.001	8.592	0.039	0.002
A63	9.222	8.954	0.268	0.072	8.914	0.308	0.095

Note: Absolute Residual = $(Y_{obs} - Y_{pred})$, Residual^2 = $(Y_{obs} - Y_{pred})^2$.

Table A7. Y_{obs} (observed activity of test set compounds), Y_{pred} (predicted activity of test set compounds), Absolute Residual and Residual^2 values from ***Eq. 1a***

CompNo	Y_{obs}(Test)	Y_{pred}(Test)	Absolute Residual (Test)	(Residual)^2[Test]
A1	4.745	4.697	0.048	0.002
A7	4.921	4.402	0.519	0.270
A8	4.921	5.347	0.426	0.181
A10	5.097	5.670	0.573	0.328
A15	4.620	4.665	0.045	0.002
A18	5.398	5.183	0.215	0.046
A21	4.155	4.032	0.123	0.015
A25	4.143	4.032	0.111	0.012
A30	4.854	4.300	0.554	0.307

A31	5.046	5.253	0.207	0.043
A35	4.678	4.032	0.646	0.417
A38	7.046	4.452	2.594	6.728
A41	8.523	8.343	0.179	0.032
A49	7.721	7.619	0.103	0.011
58	8.921	8.590	0.331	0.109

Note: Absolute Residual = $(Y_{obs} - Y_{pred})$, Residual^2 = $(Y_{obs} - Y_{pred})^2$.

Table A8. Y_{obs} (observed activity of training set compounds), Y_{pred} (calculated/predicted activity of training set compounds), Absolute Residual and Residual^2 values from both MLR-model (***Eq. 2a***) and LOO predicted

Com pNo	Y_{obs} (Train)	Y_{pred} (MLR model)	Absolute Residual (MLR)	Residual^2 [MLR]	Y_{pred} (LOO)	AbsoluteResidual(LOO)	Residual^2 [LOO]
A2	4.854	4.788	0.066	0.004	4.784	0.070	0.005
A3	4.824	4.683	0.141	0.020	4.673	0.151	0.023
A4	4.678	4.655	0.022	0.001	4.654	0.024	0.001
A5	4.745	4.623	0.122	0.015	4.614	0.131	0.017
A6	4.699	4.748	0.049	0.002	4.751	0.052	0.003
A9	4.854	4.756	0.098	0.010	4.750	0.104	0.011
A11	5.699	5.966	0.267	0.072	6.005	0.306	0.094
A12	5.301	5.227	0.074	0.005	5.220	0.081	0.007
A13	4.770	5.027	0.258	0.066	5.093	0.324	0.105
A14	4.678	4.869	0.191	0.037	4.880	0.202	0.041
A16	5.398	5.638	0.240	0.058	5.666	0.268	0.072
A17	6.523	5.726	0.797	0.636	5.634	0.889	0.790
A19	5.301	5.678	0.377	0.142	5.722	0.421	0.177
A20	5.155	5.679	0.524	0.275	5.740	0.585	0.342
A22	4.137	4.598	0.462	0.213	4.629	0.492	0.243
A23	4.119	4.255	0.135	0.018	4.270	0.151	0.023
A24	4.180	4.166	0.015	0.000	4.163	0.017	0.000
A26	4.222	4.451	0.230	0.053	4.469	0.248	0.061
A27	4.854	4.485	0.369	0.136	4.458	0.396	0.157
A28	4.886	4.485	0.401	0.161	4.455	0.431	0.186
A29	4.638	4.485	0.153	0.023	4.474	0.165	0.027
A32	4.620	4.482	0.138	0.019	4.472	0.148	0.022
A33	5.046	4.896	0.149	0.022	4.884	0.162	0.026
A34	4.921	4.789	0.132	0.017	4.780	0.141	0.020
A36	5.886	5.779	0.107	0.011	5.713	0.173	0.030
A37	5.770	5.820	0.051	0.003	5.855	0.085	0.007
A39	8.523	8.317	0.206	0.042	8.305	0.218	0.047
A40	8.155	8.434	0.279	0.078	8.454	0.299	0.089
A42	8.097	8.352	0.255	0.065	8.368	0.271	0.073

A43	8.155	8.352	0.197	0.039	8.364	0.209	0.044
A44	7.678	7.617	0.061	0.004	7.611	0.066	0.004
A45	7.638	7.705	0.067	0.004	7.711	0.072	0.005
A46	7.444	7.602	0.159	0.025	7.617	0.173	0.030
A47	7.602	7.661	0.059	0.003	7.666	0.064	0.004
A48	7.538	7.661	0.123	0.015	7.672	0.134	0.018
A50	7.745	7.705	0.040	0.002	7.701	0.043	0.002
A51	7.638	7.602	0.036	0.001	7.599	0.039	0.002
A52	7.678	7.661	0.017	0.000	7.660	0.018	0.000
A53	7.553	7.661	0.108	0.012	7.671	0.118	0.014
A54	9.046	8.893	0.153	0.023	8.874	0.172	0.030
A55	9.000	8.878	0.122	0.015	8.863	0.137	0.019
A56	9.301	8.929	0.372	0.138	8.882	0.419	0.176
A57	9.155	8.929	0.226	0.051	8.900	0.255	0.065
A59	8.602	8.638	0.036	0.001	8.645	0.043	0.002
A60	8.796	8.539	0.257	0.066	8.487	0.309	0.095
A61	8.509	8.590	0.081	0.007	8.606	0.097	0.009
A62	8.523	8.590	0.067	0.004	8.603	0.080	0.006
A63	8.921	8.978	0.057	0.003	8.985	0.064	0.004

Note: Absolute Residual = $(Y_{obs} - Y_{pred})$, Residual^2 = $(Y_{obs} - Y_{pred})^2$.

Table A9. Y_{obs} (observed activity of test set compounds), Y_{pred} (predicted activity of test set compounds), Absolute Residual and Residual^2 values from ***Eq. 2a***

CompNo	Y_{obs}(Test)	Y_{pred}(Test)	Absolute Residual (Test)	(Residual)^2[Test]
A1	4.824	4.698	0.126	0.016
A7	4.745	4.790	0.046	0.002
A8	4.745	4.756	0.012	0.000
A10	5.000	5.324	0.324	0.105
A15	4.538	4.832	0.295	0.087
A18	6.398	5.624	0.774	0.599
A21	4.108	4.303	0.195	0.038
A25	4.161	4.060	0.101	0.010
A30	4.886	4.441	0.445	0.198
A31	5.000	4.990	0.010	0.000
A35	4.469	4.632	0.163	0.027
A38	7.000	4.257	2.743	7.525
A41	8.301	8.298	0.003	0.000
A49	7.658	7.617	0.041	0.002
A58	8.886	8.553	0.333	0.111

Note: Absolute Residual = $(Y_{obs} - Y_{pred})$, Residual^2 = $(Y_{obs} - Y_{pred})^2$.

Table A10. Y_{obs} (observed activity), Y_{pred} (predicted activity) values of training set compounds from the topomer CoMFA models 1 and 2 for MMP2 and MMP9 inhibitors respectively

CompNo	MMP2 inhibitors		MMP9 inhibitors	
	YObs	YPred	YObs	YPred
A2	4.770	4.855	4.854	4.841
A3	4.796	4.707	4.824	4.652
A4	4.824	4.680	4.678	4.578
A5	4.770	4.666	4.745	4.603
A6	4.699	4.660	4.699	4.574
A9	4.824	4.725	4.854	4.825
A11	5.222	5.209	5.699	5.881
A12	4.959	5.495	5.301	5.470
A13	5.000	4.991	4.770	4.945
A14	4.745	4.644	4.678	4.853
A16	5.301	5.238	5.398	5.483
A17	5.699	5.250	6.523	5.679
A19	5.155	5.120	5.301	5.548
A20	5.097	5.197	5.155	5.478
A22	4.143	4.782	4.137	4.604
A23	4.155	4.634	4.119	4.415
A24	4.187	4.607	4.181	4.341
A26	4.114	4.586	4.222	4.337
A27	4.678	4.611	4.854	4.682
A28	4.638	5.303	4.886	5.019
A29	4.420	4.651	4.638	4.587
A32	4.824	4.697	4.620	4.602
A33	4.959	5.090	5.046	5.135
A34	4.854	4.570	4.921	4.616
A36	6.046	5.135	5.886	5.644
A37	6.921	5.422	5.770	5.233
A39	8.301	8.237	8.523	8.162
A40	8.523	8.249	8.155	8.358
A42	8.222	8.120	8.097	8.227
A43	8.097	8.196	8.155	8.157
A44	7.745	7.823	7.678	7.506
A45	7.796	7.833	7.638	7.701
A46	7.678	7.805	7.444	7.648
A47	7.620	7.706	7.602	7.572
A48	7.602	7.782	7.538	7.501
A50	7.824	7.738	7.745	7.806
A51	7.745	7.709	7.638	7.753
A52	7.678	7.609	7.678	7.676

A53	7.620	7.685	7.553	7.605
A54	9.222	9.061	9.046	9.011
A55	9.097	9.044	9.000	9.154
A56	9.155	8.943	9.301	9.077
A57	8.796	9.020	9.155	9.007
A59	8.745	8.879	8.602	8.671
A60	8.824	8.851	8.796	8.617
A61	8.602	8.750	8.509	8.540
A62	8.553	8.826	8.523	8.470
A63	9.222	9.072	8.921	9.208

Table A11. List of Y_{obs} (observed activity), Y_{pred} (predicted activity) values of the test set compounds from the topomer CoMFA models 1 and 2 for MMP2 and MMP9 inhibitors respectively

CompNo	MMP2 inhibitors		MMP9 inhibitors	
	Y_{obs}	Y_{pred}	Y_{obs}	Y_{pred}
A1	4.745	4.879	4.824	4.731
A7	4.921	6.474	4.745	6.332
A8	4.921	5.377	4.745	5.256
A10	5.097	4.600	5.000	4.666
A15	4.620	4.876	4.538	5.340
A18	5.398	5.221	6.398	5.625
A21	4.155	4.805	4.108	4.494
A25	4.143	4.593	4.161	4.366
A30	4.854	5.037	4.886	5.137
A31	5.046	4.527	5.000	4.429
A35	4.678	4.802	4.469	5.103
A38	7.046	5.629	7.000	5.306
A41	8.523	8.220	8.301	8.304
A49	7.721	7.726	7.658	7.610
A58	8.921	8.867	8.886	8.474

Table B1. Experimental Inhibitory Activity (IC_{50}, nM) and Smile notation of the compounds of **dataset 2.**

Comp	SMILE	MMP2*	MMP9*	MMP9 Binary	MMP2 Binary
B1	c1cc(ccc1S(=O)(=O)NC(C(=O)NO)CCNC(=O)C)c1ccccc1	0.7	8.6	1	1
B2	c1cccc2c1C(=O)N(C2=O)CC[C@@H](N(S(=O)(=O)c1ccc(cc1)OCC#CC)CC(C)C)C(=O)NO	21	13	1	1
B3	c1cc(ccc1S(=O)(=O)N[C@@H](C(=O)NO)CCNC(=O)OCc1ccccc1)OCC#CC	17	46	1	1
B4	c1cc(ccc1S(=O)(=O)N[C@@H](C(=O)NO)CCNC(=O)C)Br	190	190	1	0
B5	c1cc(ccc1S(=O)(=O)NCC(=O)NO)Br	40	290	1	1
B6	c1cccc2c1C(=O)N(C2=O)CC[C@@H](NS(=O)(=O)c1ccc(cc1)c1ccccc1C(F)(F)F)C(=O)NO	390	430	0	0
B7	c1cccc2c1C(=O)N(C2=O)CC[C@@H](NS(=O)(=O)c1ccc(cc1)Br)C(=O)NO	1.5	1.1	1	1
B8	c1cccc2c1C(=O)N(C2=O)CC[C@@H](NS(=O)(=O)c1ccc(cc1)OCC#CC)C(=O)NO	4.2	3.5	1	1
B9	c1(ccccc1S(=O)(=O)c1ccc(cc1)c1ccc(cc1)OC)C(C(=O)NO)C	7	69	1	1
B10	c1(ccccc1S(=O)(=O)c1ccc(cc1)c1ccc(cc1)OC)CC(=O)NO	9.7	94	1	1
B11	c1(ccccc1S(=O)(=O)c1ccc(cc1)OC)CC(=O)NO	230	98	1	0
B12	c1(ccccc1S(=O)(=O)c1ccc(cc1)c1ccccc1)CC(=O)NO	38	310	1	1
B13	c1(ccccc1S(=O)(=O)c1ccc(cc1)c1ccccc1)C(C(=O)NO)C	73	340	1	1
B14	c1(ccccc1S(=O)(=O)c1ccc(cc1)Oc1ccc(cc1)OC)C(=O)NO	1,300	410	0	0
B15	c1(ccccc1S(=O)(=O)c1ccc(cc1)Oc1ccc(cc1)OC)CC(=O)O	710	420	0	0
B16	c1(ccccc1S(=O)(=O)c1ccc(cc1)Oc1ccc(cc1)OC)CC(=O)NO	3.5	0.8	1	1
B17	c1(ccccc1S(=O)(=O)c1ccc(cc1)Oc1ccccc1)C(=O)NO	1,200	690	0	0
B18	c1(ccccc1S(=O)(=O)c1ccc(cc1)c1ccc(cc1)OC)CC(=O)O	47	730	0	1
B19	c1(ccccc1S(=O)(=O)c1ccc(cc1)c1ccc(cc1)OC)C(=O)NO	100	930	0	1
B20	c1(ccccc1S(=O)(=O)c1ccc(cc1)c1ccc(cc1)OC)C(C(=O)O)C	190	3,000	0	0
B21	c1(ccccc1S(=O)(=O)c1ccc(cc1)c1ccccc1)CC(=O)O	510	7,300	0	0
B22	c1(ccccc1S(=O)(=O)c1ccc(cc1)c1ccccc1)C(=O)NO	1,300	7,700	0	0
B23	c1(ccccc1S(=O)(=O)c1ccc(cc1)c1ccccc1)C(C(=O)O)C	2,400	20,000	0	0
B24	c1(ccccc1S(=O)(=O)c1ccc(cc1)OC)C(=O)NO	35,000	24,000	0	0
B25	c1(ccccc1S(=O)(=O)c1ccc(cc1)Oc1ccc(cc1)[S@@](=O)C)C(=O)NO	9,900	51,000	0	0
B26	c1cc(ccc1S(=O)(=O)N(CC(=O)NO)OC(C)C)c1ccc(cc1)OCCCC	5.5	44	1	1
B27	c1cc(ccc1S(=O)(=O)N([C@H](C(C)C)C(=O)NO)O	9.6	69	1	1

	C(C)C)c1ccc(cc1)OCc1ccc(cc1)Cl				
B28	c1cc(ccc1S(=O)(=O)N(CC(=O)NO)OC(C)C)c1ccc(cc1)SC	1.5	77	1	1
B29	c1cc(ccc1S(=O)(=O)N(CC(=O)NO)OC(C)C)Oc1cccc1	26	110	1	1
B30	c1cc(ccc1S(=O)(=O)N(CC(=O)NO)OC(C)C)c1ccc(cc1)OC	4.2	160	1	1
B31	c1(S(=O)(=O)N(CC(=O)NO)OC(C)C)ccc(s1)c1ccc(cc1)OC	17	250	1	1
B32	c1(S(=O)(=O)N(CC(=O)NO)OC(C)C)ccc(s1)c1ccc(cc1)CC	56	680	0	1
B33	c1cc(ccc1S(=O)(=O)N(CC(=O)NO)OC(C)C)c1ccc(cc1)OCc1ccc(cc1)Cl	40	1,100	0	1
B34	c1cc(ccc1S(=O)(=O)N(CC(=O)NO)OC(C)C)/C=C/c1ccc(cc1)c1ccccc1	74	2,300	0	1
B35	c1(S(=O)(=O)N(CC(=O)NO)OC(C)C)ccc(s1)c1ccc(cc1)F	310	3,200	0	0
B36	c1(S(=O)(=O)N(CC(=O)NO)OC(C)C)ccc(s1)C#Cc1ccc(cc1)CCCC	360	4,400	0	0
B37	c1c(ccc(c1)c1ccc(cc1)Sc1ccccc1CC(=O)NO)OC	6.8	120	1	1
B38	c1c(ccc(c1)c1ccc(cc1)Sc1ccccc1CC(=O)O)OC	114	830	0	0
B39	S(c1ccc(c2ccc(cc2)OC)cc1)c1ccccc1CP(=O)(O)O	250	1,120	0	0
B40	O=S(=O)(c1ccc(c2ccc(cc2)OC)cc1)c1ccccc1C1C(=O)N(C(=O)CC1)O	414	1,430	0	0
B41	O=S(=O)(c1ccc(c2ccc(cc2)OC)cc1)c1ccccc1CP(=O)(O)O	380	2,500	0	0
B42	c1c(ccc(c1)c1ccc(cc1)Sc1ccccc1C(C(=O)O)CCC(=O)O)OC	660	2,960	0	0
B43	O=S(=O)(NC(=O)Cc1c(S(=O)(=O)c2ccc(c3ccc(cc3)OC)cc2)cccc1)C	3,600	3,700	0	0
B44	c1c(ccc(c1)c1ccc(cc1)Sc1ccccc1C1C(=O)N(C(=O)CC1)O)OC	670	5,800	0	0
B45	O=S(=O)(c1ccc(c2ccc(cc2)OC)cc1)c1ccccc1C(C(=O)O)CCC(=O)O	1,350	14,300	0	0
B46	O=S(=O)(NC(=O)Cc1c(Sc2ccc(c3ccc(cc3)OC)cc2)cccc1)C	5,300	18,000	0	0
B47	O=S(=O)(NC(=O)Cc1c(S(=O)(=O)c2ccc(c3ccc(cc3)OC)cc2)cccc1)C(F)(F)F	2,500	24,500	0	0
B48	O=S(=O)(NC(=O)Cc1c(Sc2ccc(c3ccc(cc3)OC)cc2)cccc1)C(F)(F)F	46,000	50,000	0	0
B49	O=S(=O)(CC(=O)c1c(Sc2ccc(c3ccc(cc3)OC)cc2)cccc1)C	230,000	332,000	0	0
B50	N(CC[C@H](C(=O)NO)N(S(=O)(=O)c1ccc(cc1)c1ccccc1)OC(C)C)C(=O)Cc1ccccc1	1.4	6.4	1	1
B51	N(CC[C@H](C(=O)NO)N(S(=O)(=O)c1ccc(cc1)c1ccccc1)OC(C)C)C(=O)C	0.33	6.5	1	1
B52	N(CC[C@H](C(=O)NO)N(S(=O)(=O)c1ccc(cc1)c1ccccc1)OC(C)C)S(=O)(=O)C	1	8.6	1	1
B53	C(=O)(c1ccccc1)NCC[C@H](C(=O)NO)N(S(=O)(=O)c1ccc(cc1)c1ccccc1)OC(C)C	1.5	9	1	1
B54	N1(CC[C@H](C(=O)NO)N(S(=O)(=O)c2ccc(cc2)c2ccc(cc2)OC)OC(C)C)C(=O)c2c(C1=O)cccc2	0.67	0.43	1	1
B55	N(CC[C@H](C(=O)NO)N(S(=O)(=O)c1ccccc1)OC(C)C)C(=O)C	590	3,900	0	0

B56	N(CC[C@H](C(=O)NO)N(S(=O)(=O)c1ccc(cc1)c1ccc(cc1)OC)OC(C)C)C(=O)C	0.13	2	1	1
B57	N(CC[C@H](C(=O)NO)N(S(=O)(=O)c1ccc(cc1)c1ccc(cc1)OC)OC(C)C)C(=O)Cc1ccccc1	0.37	2.9	1	1
B58	S1CN([C@@H](C1)C(=O)NO)S(=O)(=O)c1ccc(s1)C#Cc1ccc(cc1)CCCC	2.5	21	1	1
B59	O=S(=O)(c1ccc(s1)C#Cc1ccc(cc1)CCCC)N[C@@H](C(=O)NO)Cc1ccc(cc1)C(=O)c1ccccc1	4	50	1	1
B60	O=S(=O)(c1ccc(s1)C#Cc1ccc(cc1)CCCC)N[C@@H](C(=O)NO)Cc1ccc(cc1)OCc1ccccc1	2.3	63	1	1
B61	O=S(=O)(N[C@@H](C(=O)NO)Cc1c[nH]c2c1cccc2)c1ccc(s1)C#Cc1ccc(cc1)CCCC	6	77	1	1
B62	O=S(=O)(c1ccc(s1)C#Cc1ccc(cc1)CCCC)NCC(=O)NO	1.5	79	1	1
B63	C(=O)([C@@H](Cc1csc2c1cccc2)NS(=O)(=O)c1ccc(s1)C#Cc1ccc(cc1)CCCC)NO	17	650	0	1
B64	C1N([C@H](Cc2ccccc12)C(=O)NO)S(=O)(=O)c1ccc(s1)C#Cc1ccc(cc1)CCCC	1.3	4.3	1	1
B65	C(=O)(NO)C(N(S(=O)(=O)c1ccc(cc1)OC)Cc1cccnc1)C(C)C	25	4.8	1	1
B66	c1c(ccc(c1)OC)S(=O)(=O)N(OC(CC)C)C(C(=O)NO)C(C)C	730	286	1	0
B67	c1c(ccc(c1)OC)S(=O)(=O)N(OCc1ccc(cc1)Cl)CC(=O)NO	1,500	330	1	0
B68	c1c(ccc(c1)OC)S(=O)(=O)N(OC(C)C)C(C(=O)NO)C(C)C	660	370	1	0
B69	c1c(ccc(c1)OC)S(=O)(=O)N(OCc1ccccc1)CC(=O)NO	1,060	870	0	0
B70	c1c(ccc(c1)OC)S(=O)(=O)N(OCc1ccc(cc1)OCc1ccccc1)CC(=O)NO	2,100	1,830	0	0
B71	C1C2CC3CC1CC(C2ON(S(=O)(=O)c1ccc(cc1)OC)CC(=O)NO)C3	1,980	2,000	0	0
B72	c1c(ccc(c1)OC)S(=O)(=O)N(OCC)CC(=O)NO	9,600	2,200	0	0
B73	c1c(ccc(c1)OC)S(=O)(=O)N(OC(C)C)CC(=O)NO	4,900	3,400	0	0
B74	c1c(ccc(c1)OC)S(=O)(=O)N(OCCCCCCCCCCCCCC)CC(=O)NO	30,000	33,000	0	0
B75	ONC(=O)C(NOCc1ccccc1)CCCC	81,500	33,700	0	0
B76	ONC(=O)C(NOCc1ccc(cc1)Cl)CCCC	125,000	81,800	0	0
B77	ONC(=O)C(NOCc1ccc(cc1)Cl)C	141,000	68,000	0	0
B78	ONC(=O)CNOCc1ccccc1	256,000	94,000	0	0
B79	ONC(=O)CNOCc1ccc(cc1)Cl	261,000	137,000	0	0
B80	ONC(=O)C(NOCc1ccccc1)C(CC)C	352,000	151,000	0	0
B81	c1cc(ccc1S(=O)(=O)CP(=O)(O)O)c1ccccc1	13,200	520	0	0
B82	c1cc(ccc1S(=O)(=O)CC(=O)O)c1ccccc1	212,000	12,500	0	0
B83	c1cc(ccc1S(=O)(=O)CC(=O)NO)c1ccccc1	140	0.6	1	1
B84	c1cc(ccc1S(=O)(=O)CP(=O)(O)O)c1ccc(cc1)OC	141	4,100	0	0
B85	c1cc(ccc1S(=O)(=O)CP(=O)(O)O)c1ccc(cc1)Cl	69	1,730	0	1
B86	c1cc(ccc1S(=O)(=O)CP(=O)(O)O)c1cccs1	2,300	96	0	1
B87	c1cc(ccc1S(=O)(=O)N[C@@H](C(C)C)P(=O)(O)O)c1ccc(cc1)OC	1.5	8	1	1
B88	c1cc(ccc1S(=O)(=O)N[C@@H](C(C)C)P(=O)(O)O)	0.39	0.56	1	1

	c1ccc(cc1)OCC				
B89	c1cc(ccc1S(=O)(=O)N[C@@H](C(C)C)P(=O)(O)O)c1ccc(cc1)OC(C)C	1.8	24	1	1
B90	c1cc(ccc1S(=O)(=O)N[C@@H](C(C)C)P(=O)(O)O)c1ccc(cc1)F	20	59	1	1
B91	c1cc(ccc1S(=O)(=O)N[C@@H](C(C)C)P(=O)(O)O)c1ccc(cc1)Cl	8.7	21	1	1
B92	c1cc(ccc1S(=O)(=O)N[C@@H](C(C)C)P(=O)(O)O)c1ccc(cc1)C	2.3	4.1	1	1
B93	c1cc(ccc1S(=O)(=O)N[C@@H](C(C)C)P(=O)(O)O)c1cc(ccc1)F	53	170	1	1
B94	c1cc(ccc1S(=O)(=O)N[C@@H](C(C)C)P(=O)(O)O)c1cc(ccc1)Cl	30	160	1	1
B95	c1cc(ccc1S(=O)(=O)N[C@@H](C(C)C)P(=O)(O)O)c1cc(ccc1)C	24	64	1	1
B96	c1cc(ccc1S(=O)(=O)N[C@@H](C(C)C)P(=O)(O)O)CCc1ccccc1	980	7,100	0	0
B97	c1cc(ccc1S(=O)(=O)N[C@@H](C(C)C)P(=O)(O)O)CCc1ccc(cc1)OC	790	680	0	0
B98	ONC(=O)CN(CC(=O)O)Cc1ccc(cc1)c1ccccc1	79,400	70,800	0	0
B99	ONC(=O)CN(CC(=O)O)Cc1ccc(cc1)Oc1ccccc1	238,000	74,600	0	0
B100	ONC(=O)CN(CC(=O)O)CCN1CCCCC1	300,000	217,400	0	0
B101	ONC(=O)CN(CC(=O)O)S(=O)(=O)c1ccc(cc1)OC	193	322	1	0
B102	ONC(=O)CN(CC(=O)O)S(=O)(=O)c1ccc(cc1)c1ccccc1	46.1	155	1	1
B103	ONC(=O)CN(CC(=O)O)S(=O)(=O)c1ccc(cc1)Oc1ccccc1	1.2	3.2	1	1
B104	N(C(=O)[C@H](N(CC(=O)O)S(=O)(=O)c1ccc(cc1)OC)C(C)C)O	145	62	1	0
B105	N(C(=O)[C@H](N(CC(=O)O)S(=O)(=O)c1ccc(cc1)c1ccccc1)C(C)C)O	24.7	27.7	1	1
B106	N(C(=O)[C@H](N(CC(=O)O)S(=O)(=O)c1ccc(cc1)Oc1ccccc1)C(C)C)O	0.5	0.77	1	1
B107	N(C(=O)CN(CC(=O)CCc1ccc(cc1)S(=O)(=O)N)S(=O)(=O)c1ccc(cc1)OC)O	25.3	53.7	1	1
B108	N(C(=O)CN(CC(=O)CCc1ccc(cc1)S(=O)(=O)N)S(=O)(=O)c1ccc(cc1)c1ccccc1)O	16.2	66	1	1
B109	N(C(=O)CN(CC(=O)CCc1ccc(cc1)S(=O)(=O)N)S(=O)(=O)c1ccc(cc1)Oc1ccccc1)O	1.57	0.51	1	1
B110	N(C(=O)[C@H](N(CC(=O)CCc1ccc(cc1)S(=O)(=O)N)S(=O)(=O)c1ccc(cc1)Oc1ccccc1)C(C)C)O	0.35	0.21	1	1

* IC_{50} (nM)

Table B2. Correlation matrix among biological activity and selected parameters of ***Eq. 1b***

	minsOH	***PubchemFP643***	***R_TpiPCTPC***	***PubchemFP33***	***PubchemFP338***	***nHBAcc_Lipinski***	***GATS8i***	***GATS3m***	***MMP2 pIC_{50}***
minsOH	1.00	-0.12	-0.13	0.01	0.18	0.16	-0.33	0.11	0.30
PubchemFP643		1.00	-0.38	-0.16	0.30	0.38	-0.25	0.04	0.21
R_TpiPCTPC			1.00	0.43	-0.37	-0.36	0.34	-0.15	0.39
PubchemFP33				1.00	-0.12	0.31	-0.29	0.24	0.61
PubchemFP338					1.00	0.28	-0.12	-0.35	0.21
nHBAcc_Lipinski						1.00	-0.55	0.42	0.40
GATS8i							1.00	-0.46	-0.12
GATS3m								1.00	0.14
MMP2 pIC_{50}									1.00

Table B3. Correlation matrix among biological activity and selected parameters of ***Eq. 2b***

	ATS5s	***VE2_Dze***	***PubchemFP33***	***minsOH***	***PubchemFP643***	***ATSC7m***	***SpMax1_Bhs***	***PubchemFP21***	***MMP2 pIC_{50}***
ATS5s	1.00	-0.07	0.54	0.14	0.31	-0.24	0.49	0.33	0.67
VE2_Dze		1.00	-0.07	0.17	0.10	0.08	0.15	0.03	-0.07
PubchemFP33			1.00	0.01	-0.16	-0.25	0.38	0.07	0.58
minsOH				1.00	-0.12	-0.24	-0.23	0.07	0.31
PubchemFP643					1.00	-0.29	0.27	0.10	0.28
ATSC7m						1.00	-0.09	0.00	-0.14
SpMax1_Bhs							1.00	0.12	0.19
PubchemFP21								1.00	0.39
MMP2 pIC_{50}									1.00

Table B4. VIF, *t*-Value and *p*-Value for ***Eq. 1b*** and ***Eq. 2b***

Eq. 1b	***t*-Value**	***p*-level**	**VIF**
Intercept	-7.021	0.000	
minsOH	8.326	0.000	1.284
PubchemFP643	8.096	0.000	1.484
R_TpiPCTPC	7.654	0.000	2.264
PubchemFP33	7.397	0.000	2.109
PubchemFP338	5.067	0.000	1.854
nHBAcc_Lipinski	3.155	0.002	2.287
GATS8i	5.369	0.000	2.045
GATS3m	3.424	0.001	2.011
Eq. 2b	**t-Value**	***p*-level**	**VIF**
Intercept	2.740	0.008	
ATS5s	2.170	0.033	2.570
VE2_Dze	-2.040	0.045	1.211
PubchemFP33	9.034	0.000	2.064
minsOH	5.729	0.000	1.479
PubchemFP643	7.186	0.000	1.781
ATSC7m	4.697	0.000	1.409
SpMax1_Bhs	-2.942	0.004	1.721
PubchemFP21	4.034	0.000	1.149

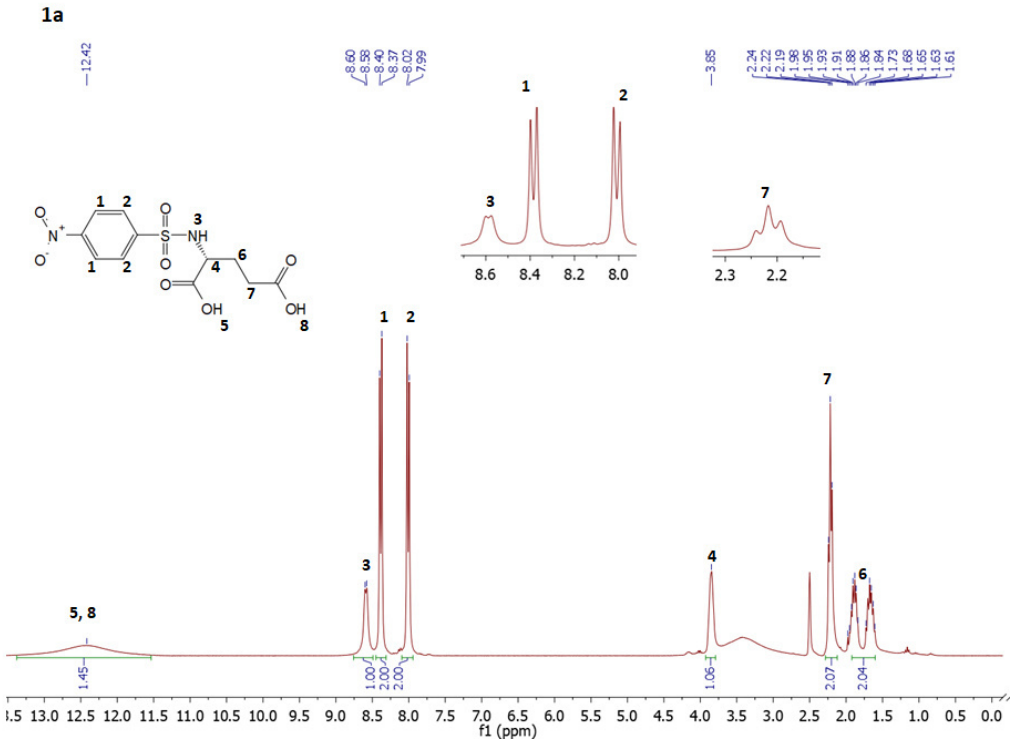

Figure A1: ^{1}H NMR Spectra for the compound **1a**.

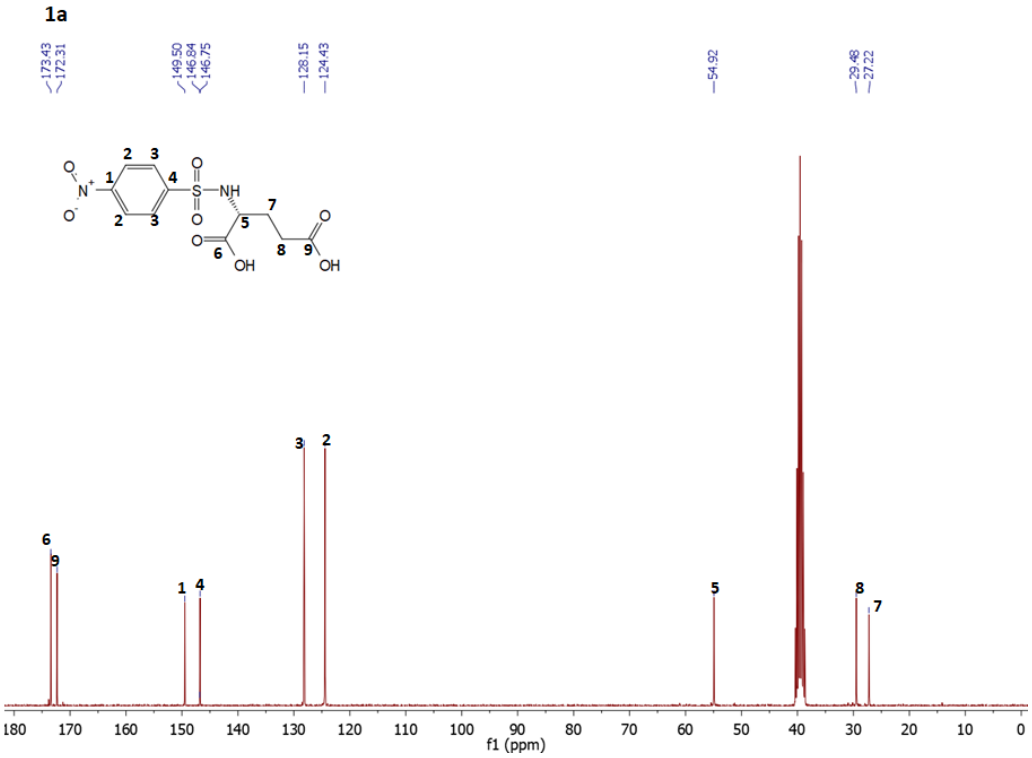

Figure A2: ^{13}C NMR Spectra for the compound **1a**.

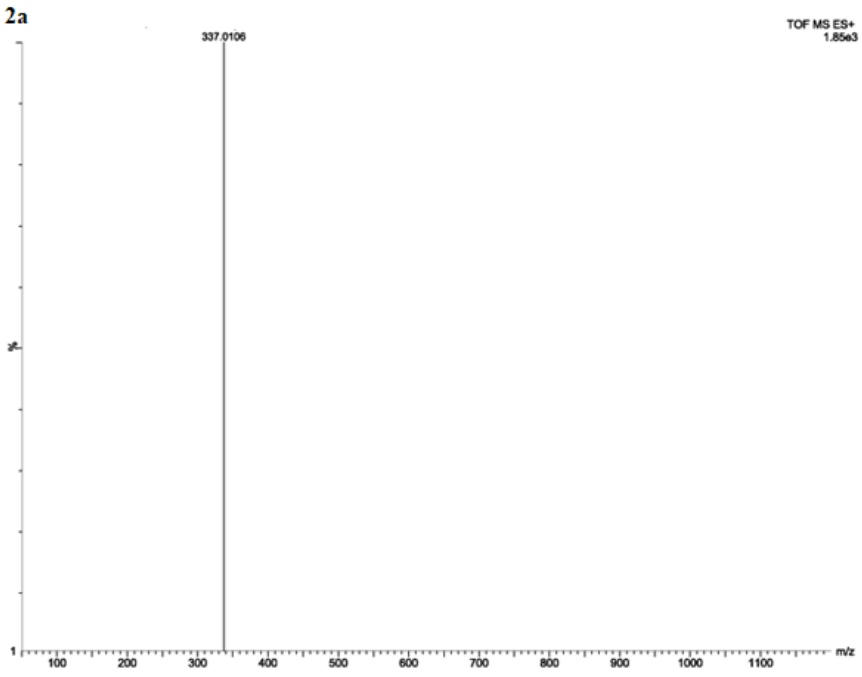

Figure A3: HRMS Spectra for the compound **2a**.

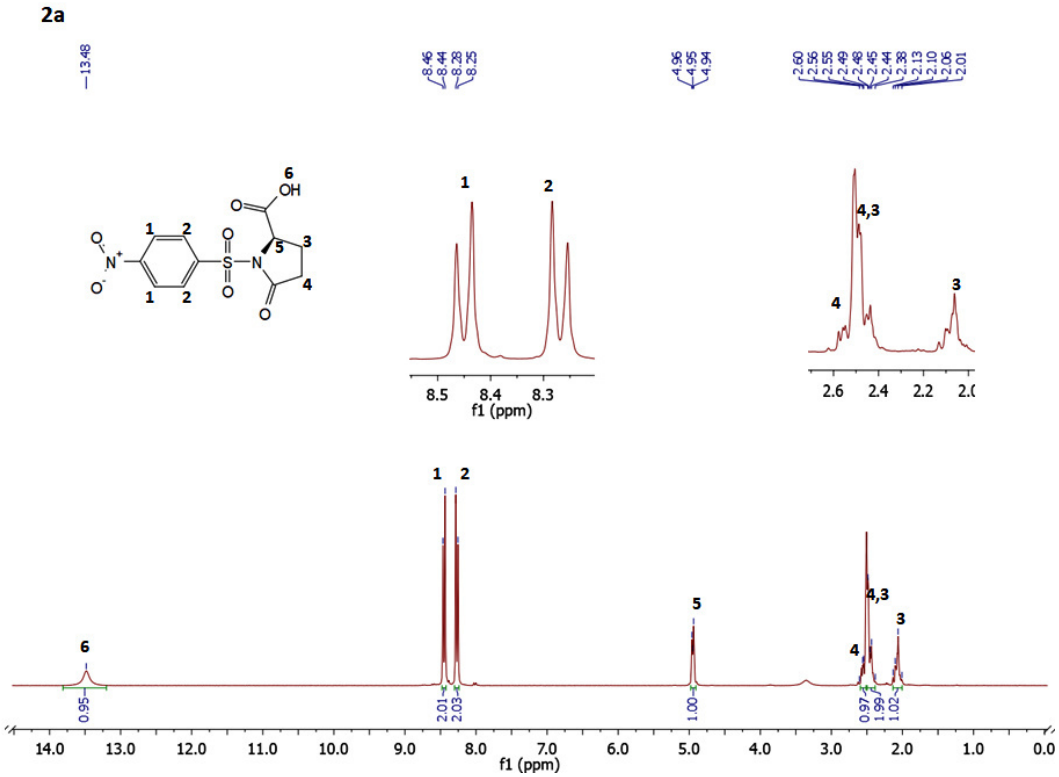

Figure A4: ^{1}H NMR Spectra for the compound **2a**.

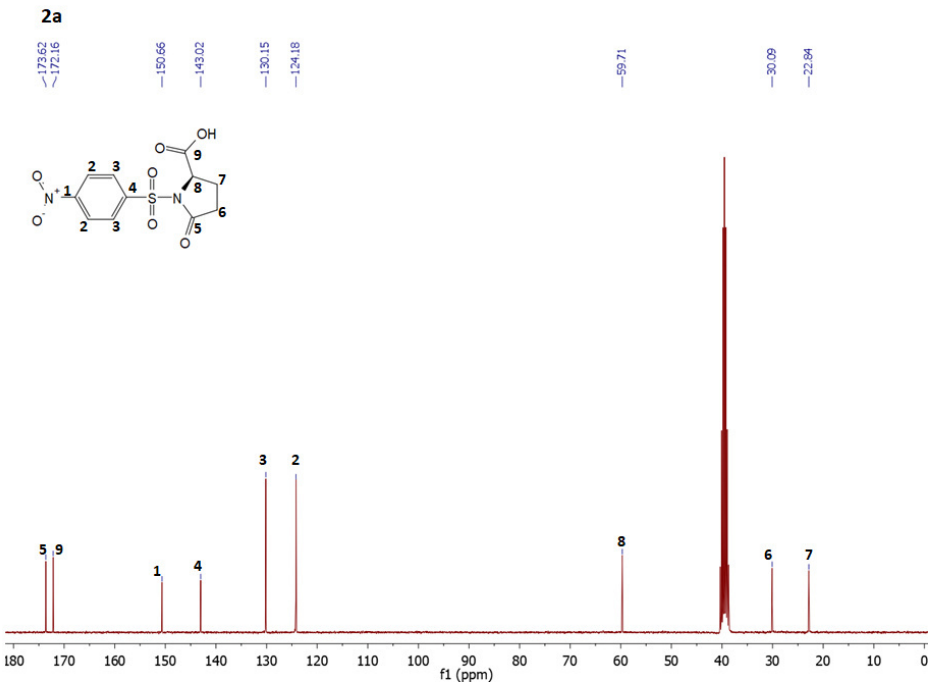

Figure A5: ^{13}C NMR Spectra for the compound **2a**.

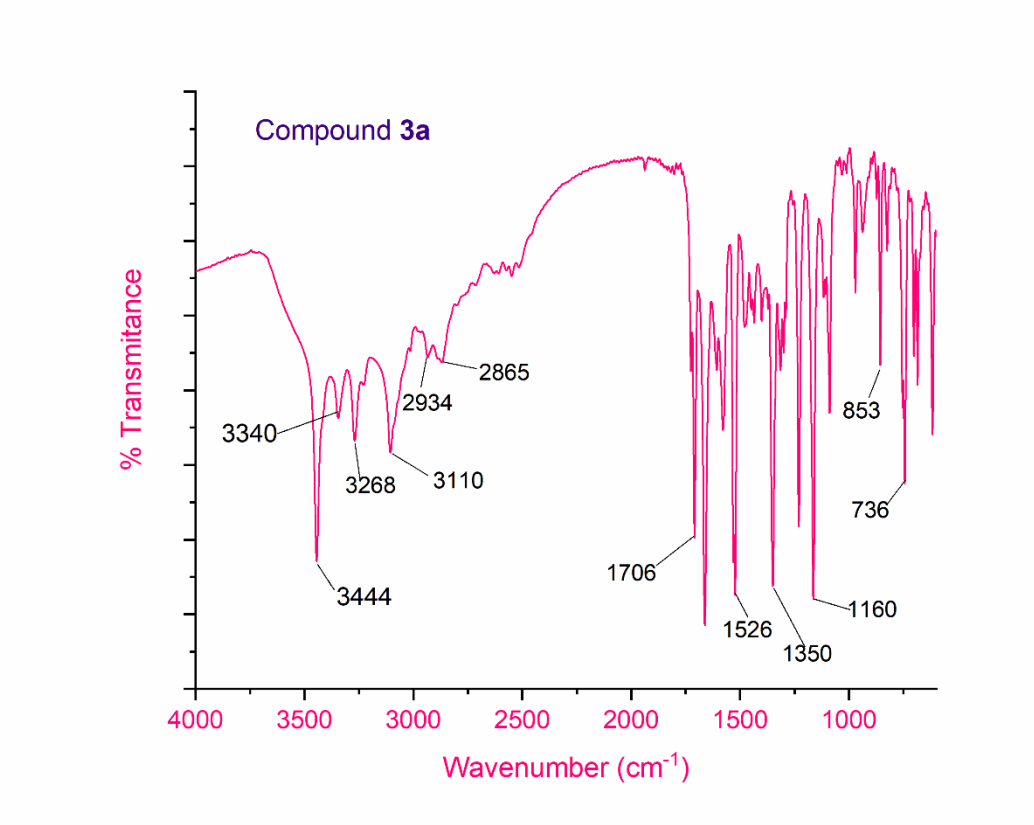

Figure A6: FT-IR Spectra for the compound **3a**.

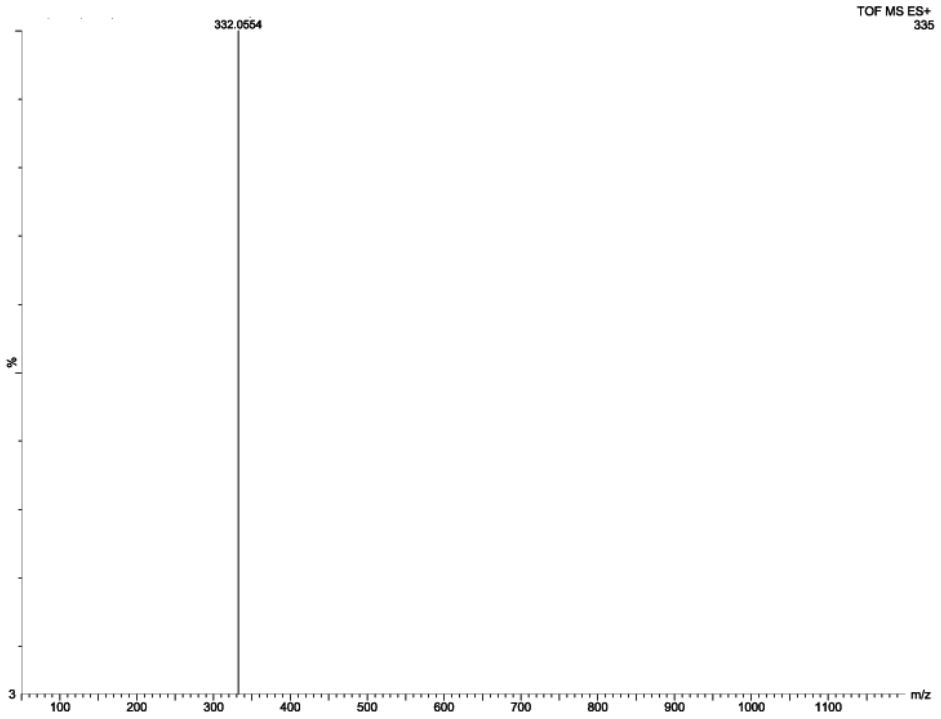

Figure A7: HRMS Spectra for the compound **3a**.

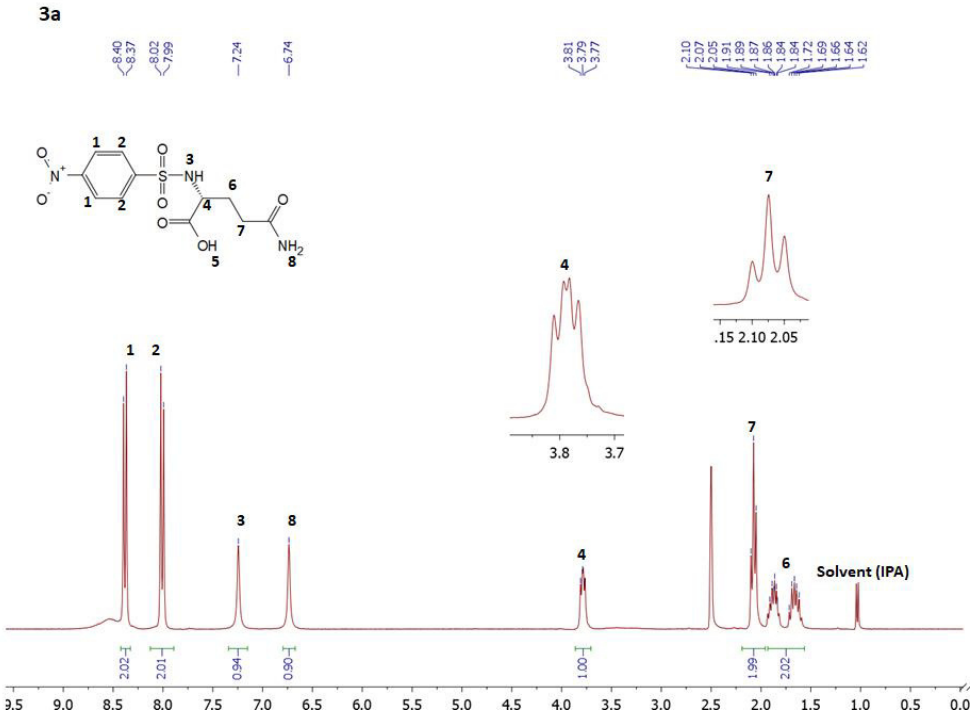

Figure A8: ^{1}H NMR Spectra for the compound **3a**.

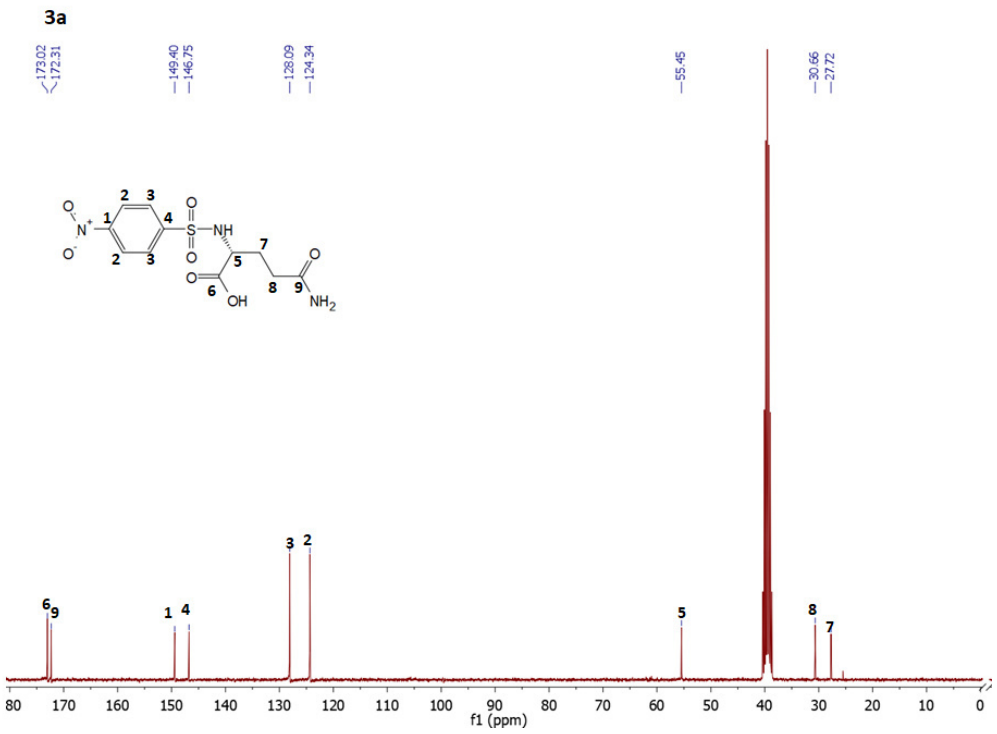

Figure A9: ^{13}C NMR Spectra for the compound **3a**.

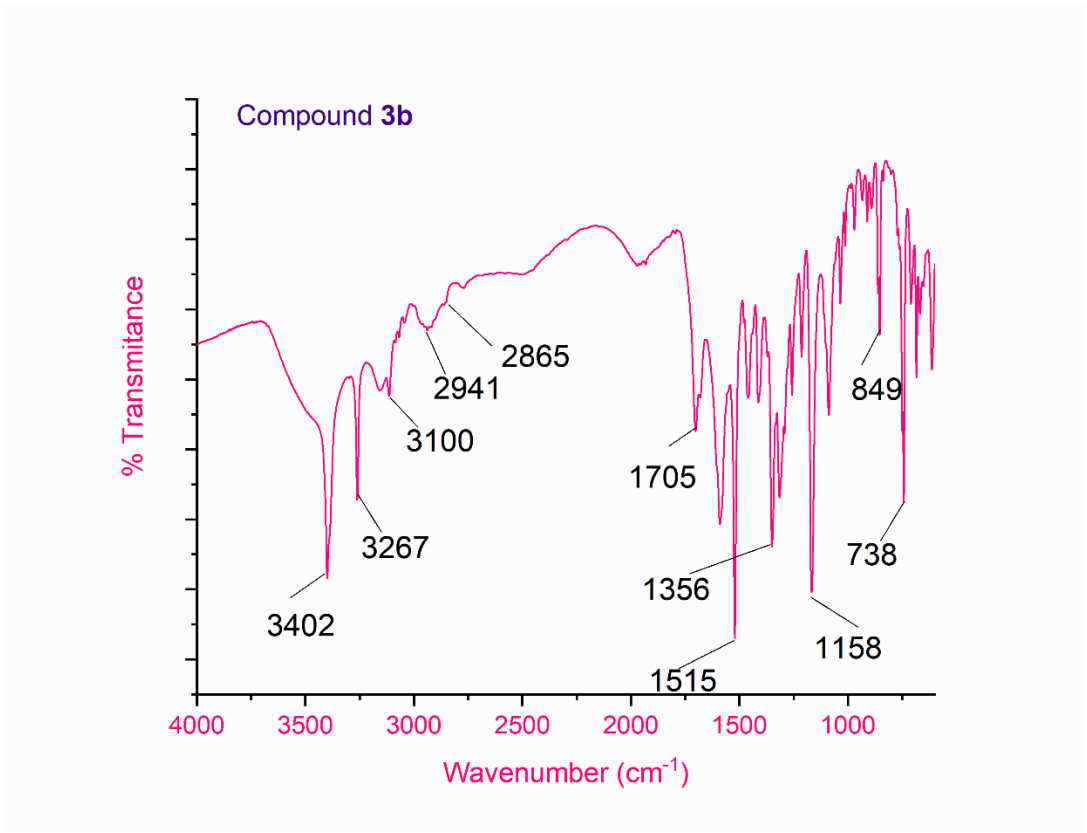

A10: FT-IR Spectra for the compound **3b**.

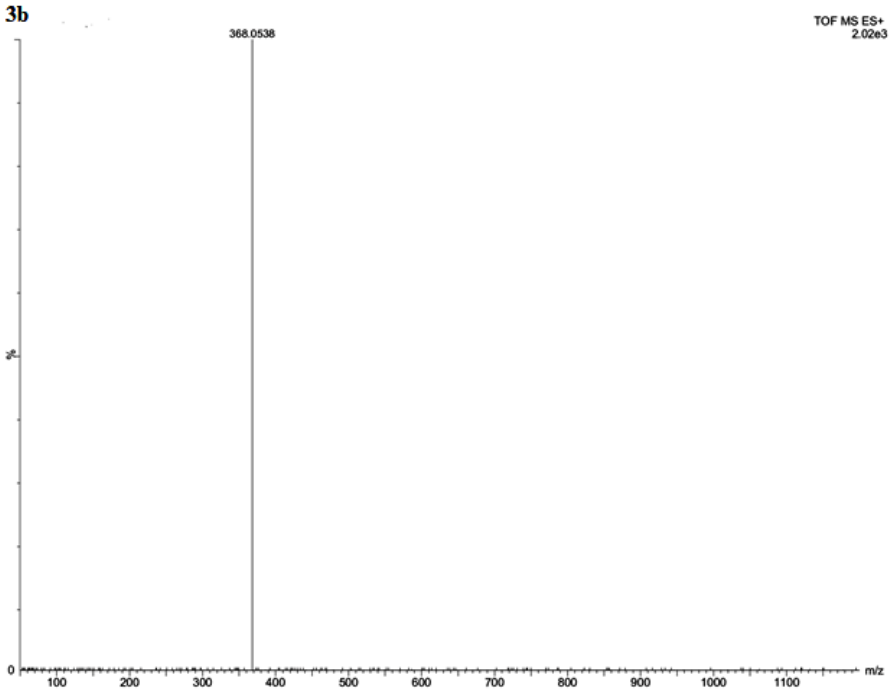

Figure A11: HRMS Spectra for the compound **3b**.

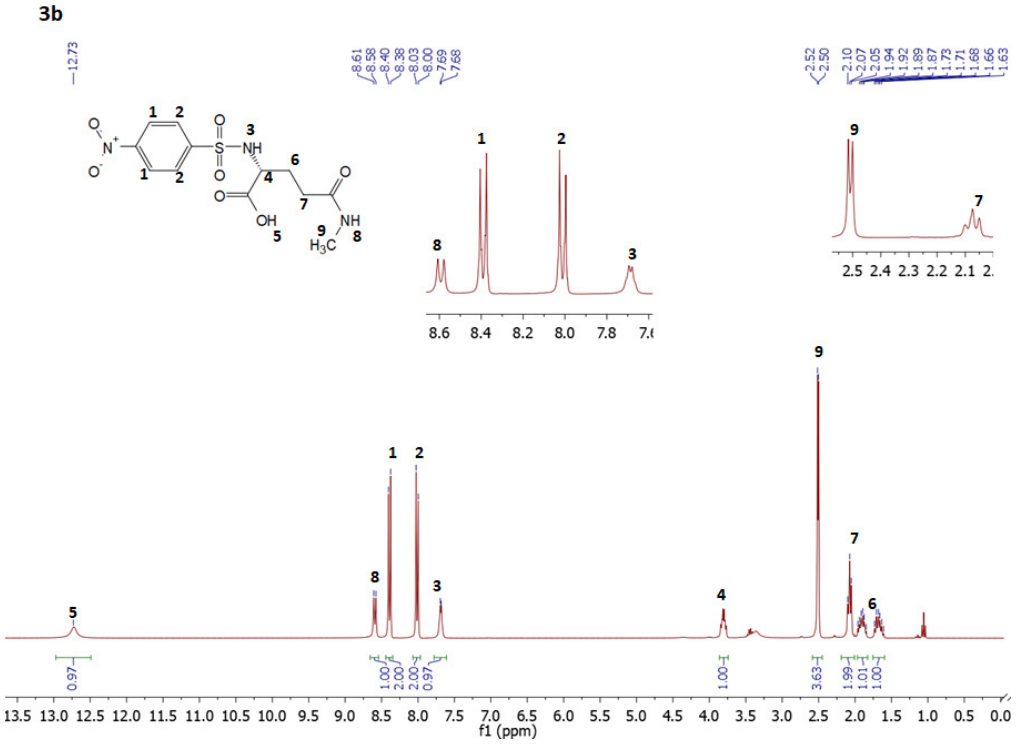

Figure A12: ^{1}H NMR Spectra for the compound **3b**.

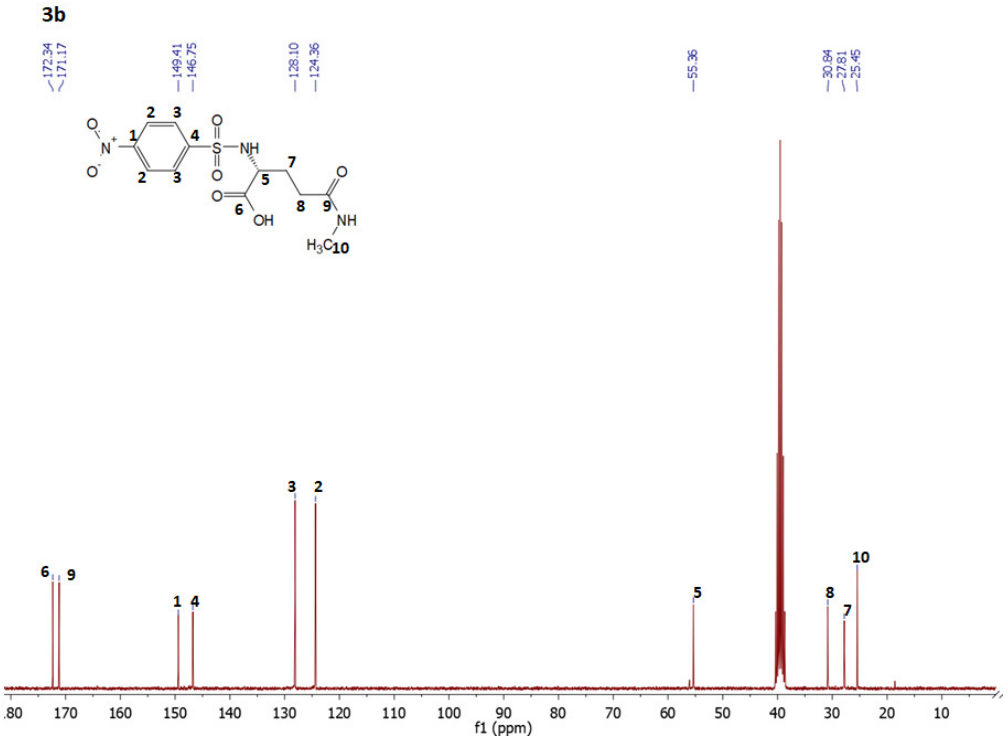

Figure A13: ^{13}C NMR Spectra for the compound **3b**.

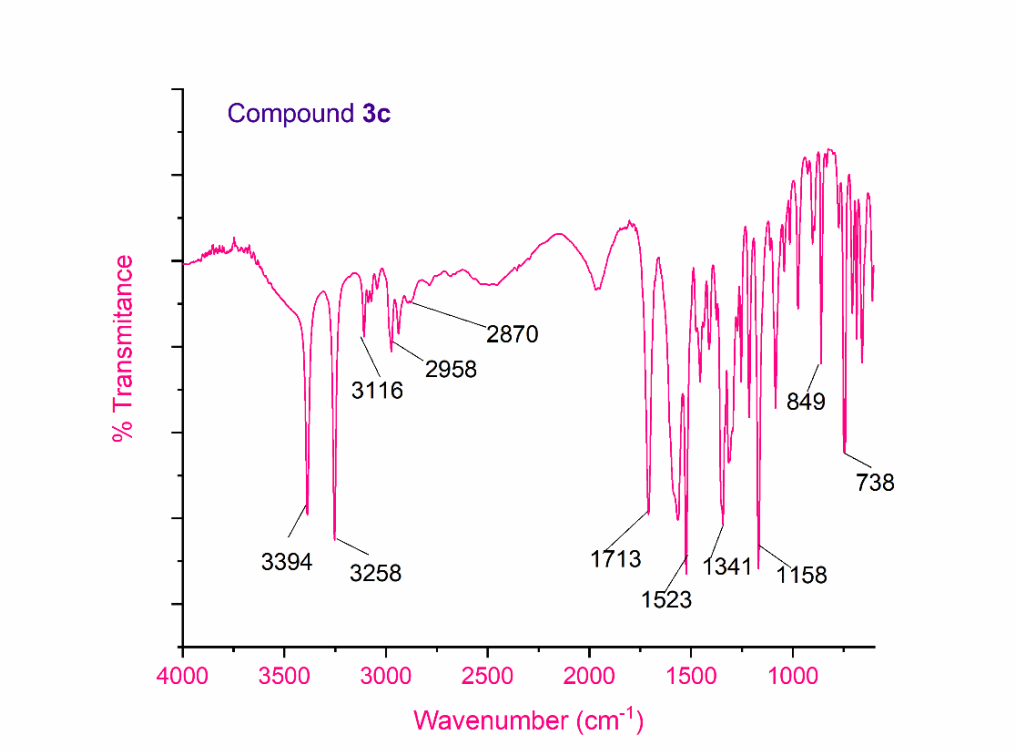

Figure A14: FT-IR Spectra for the compound **3c**.

Figure A15: HRMS Spectra for the compound **3c**.

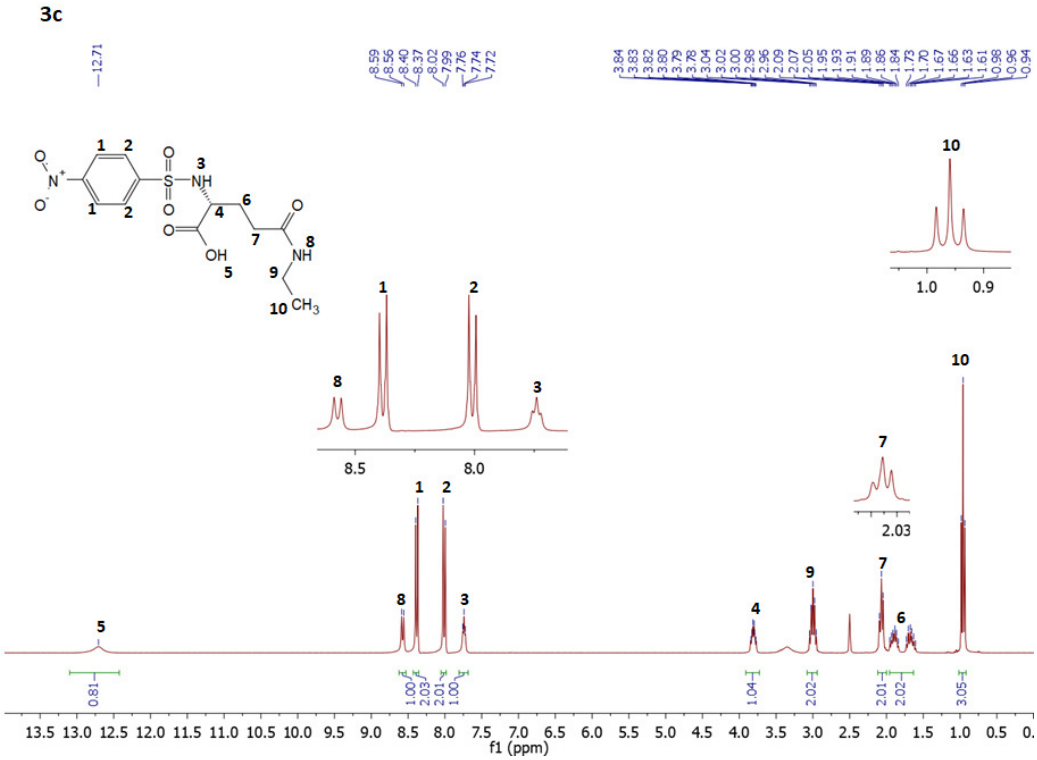

Figure A16: ^{1}H NMR Spectra for the compound **3c**.

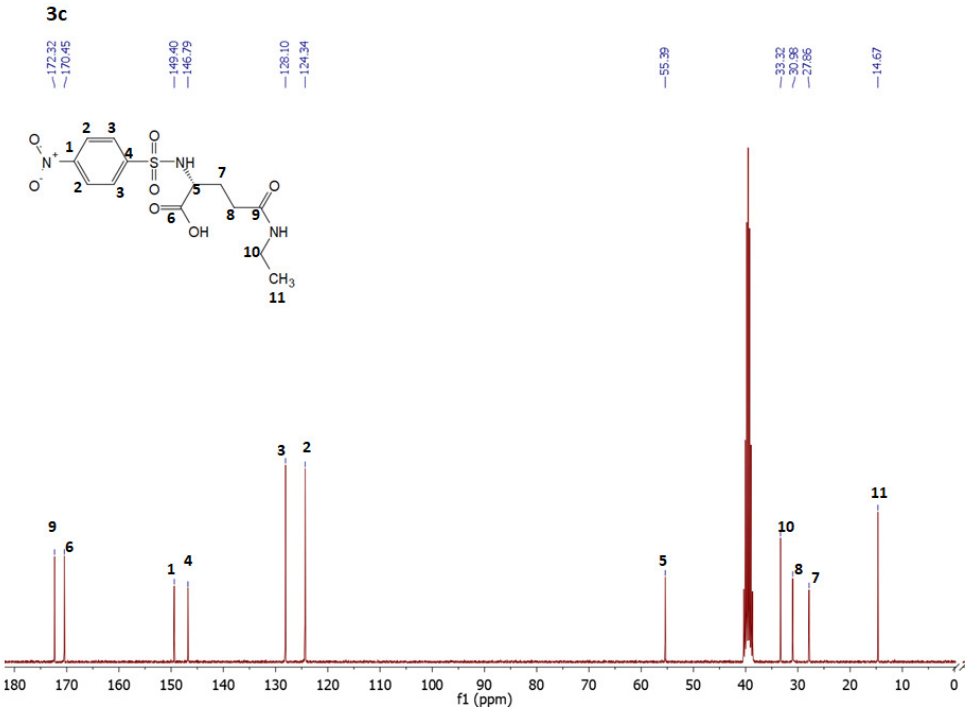

Figure A17: ^{13}C NMR Spectra for the compound **3c**.

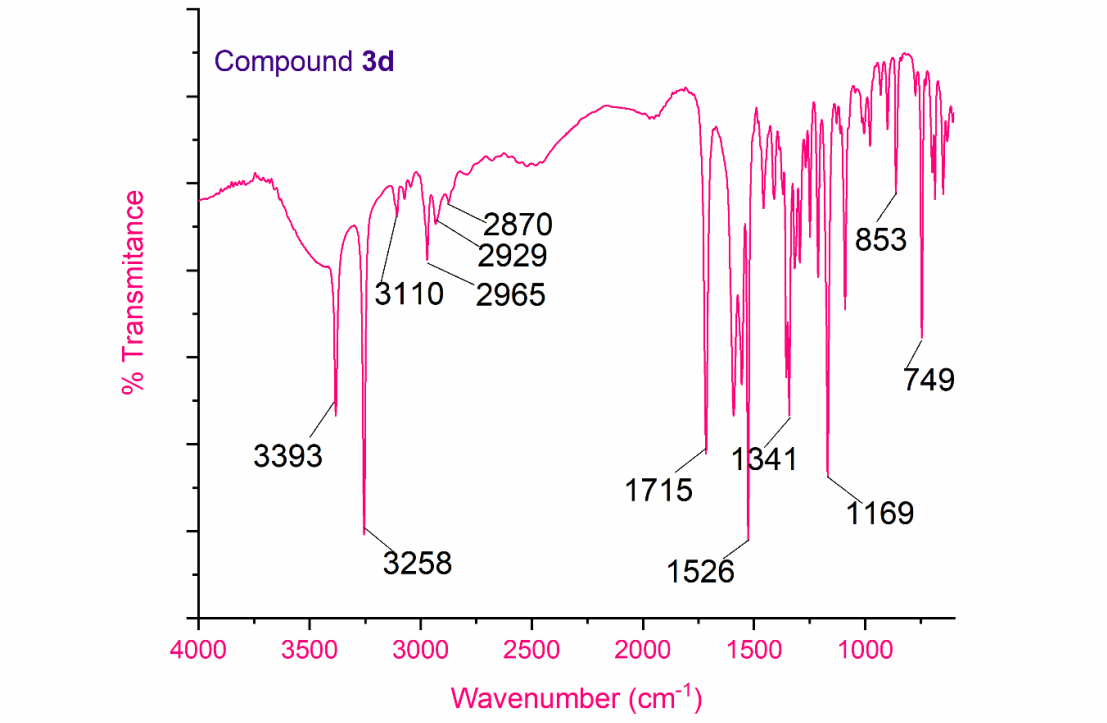

Figure A18: FT-IR Spectra for the compound **3d**.

Figure A19: HRMS Spectra for the compound **3d**.

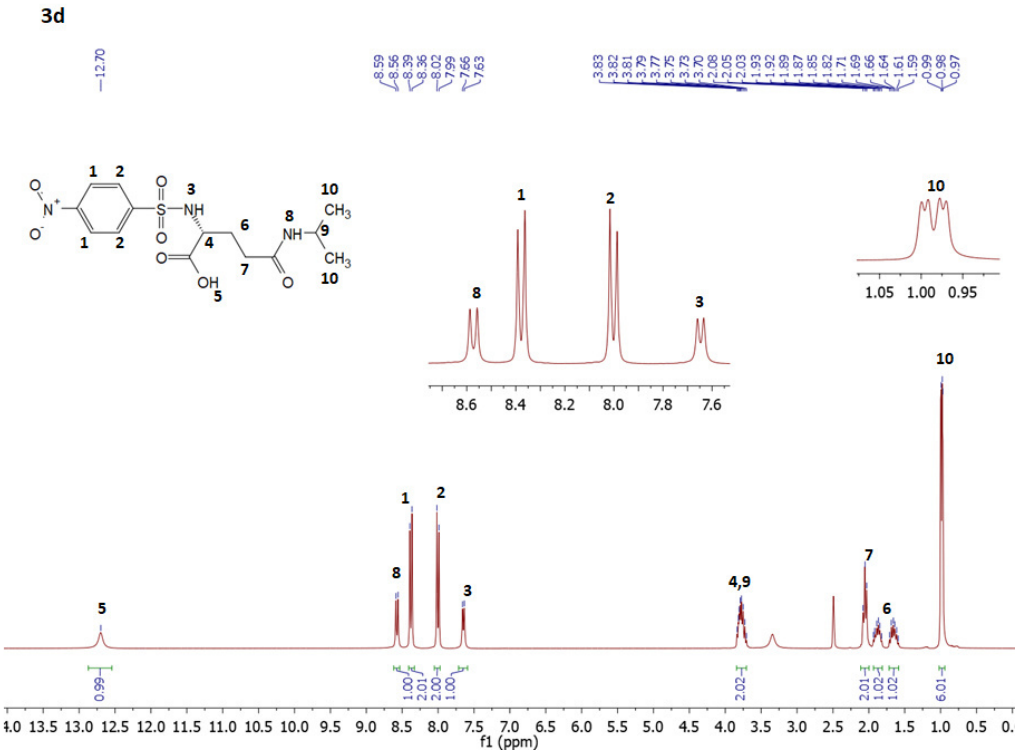

Figure A20: ^{1}H NMR Spectra for the compound **3d**.

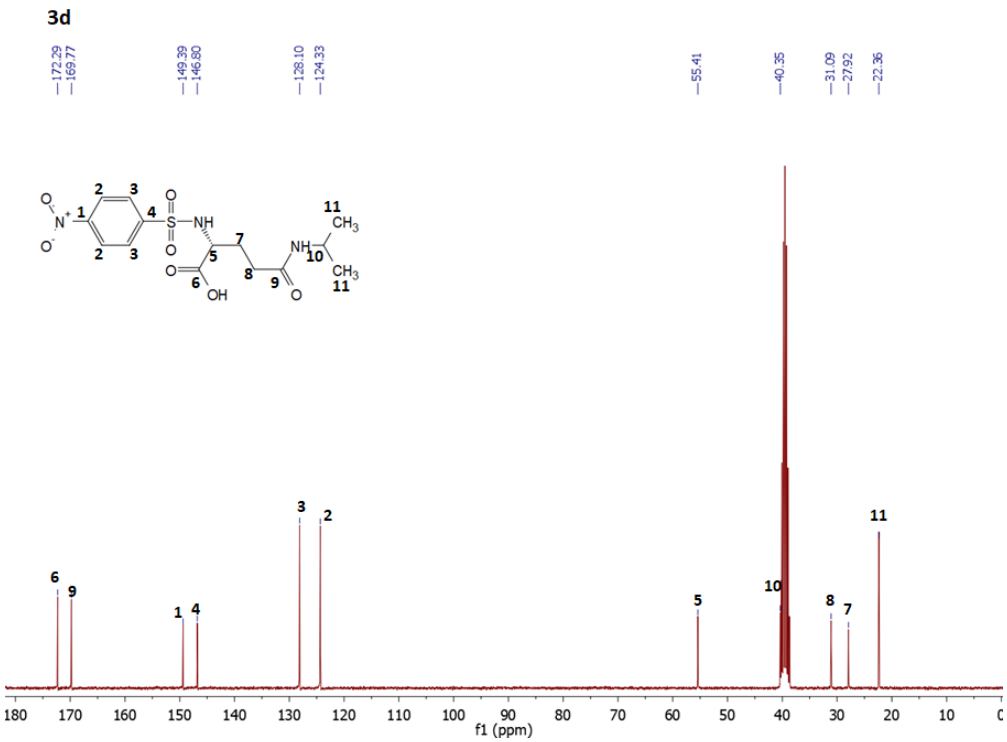

Figure A21: ^{13}C NMR Spectra for the compound **3d**.

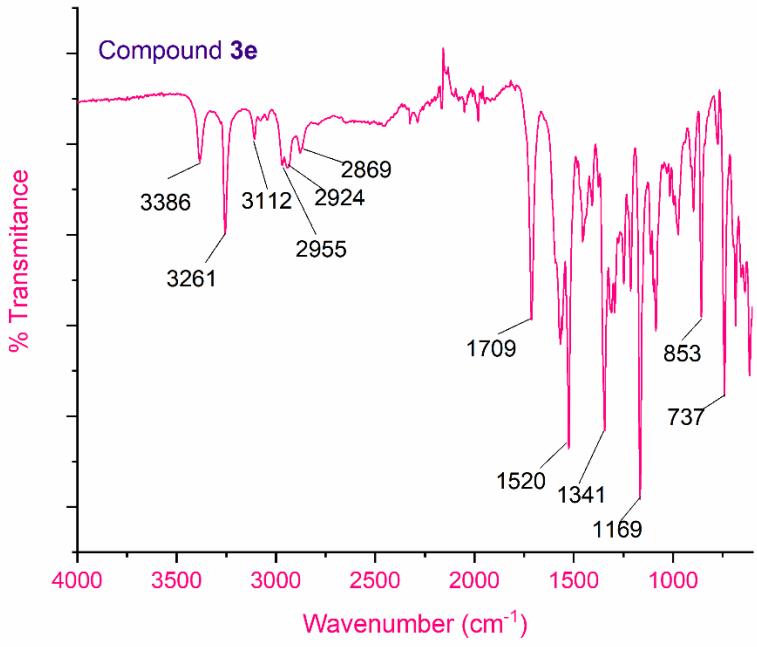

Figure A22: FT-IR Spectra for the compound **3e**.

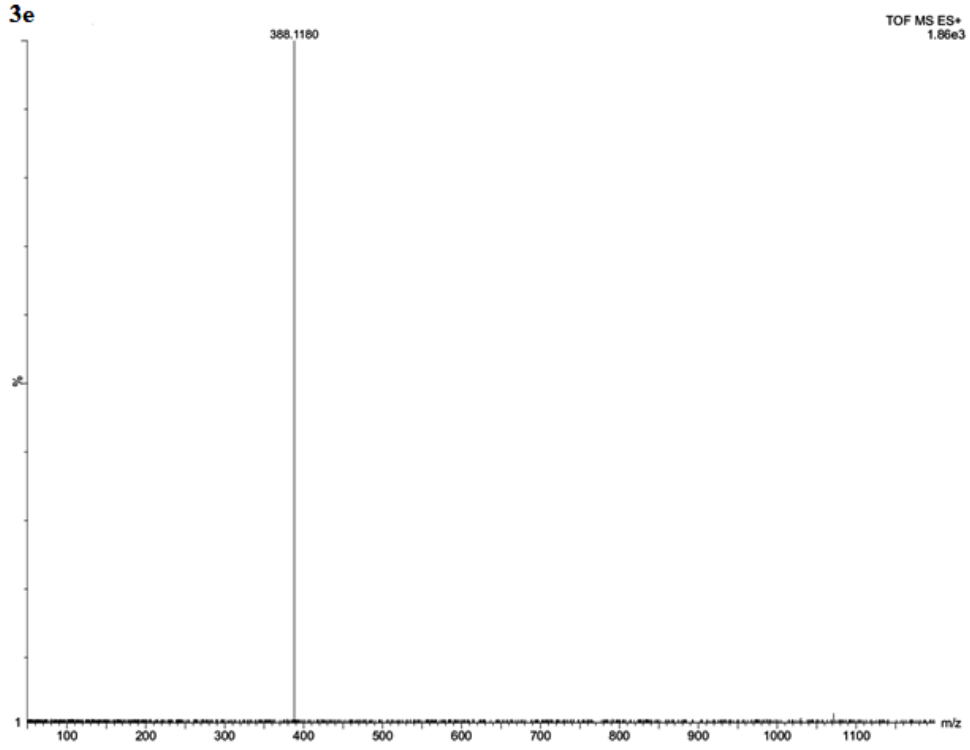

Figure A23: HRMS Spectra for the compound **3e**.

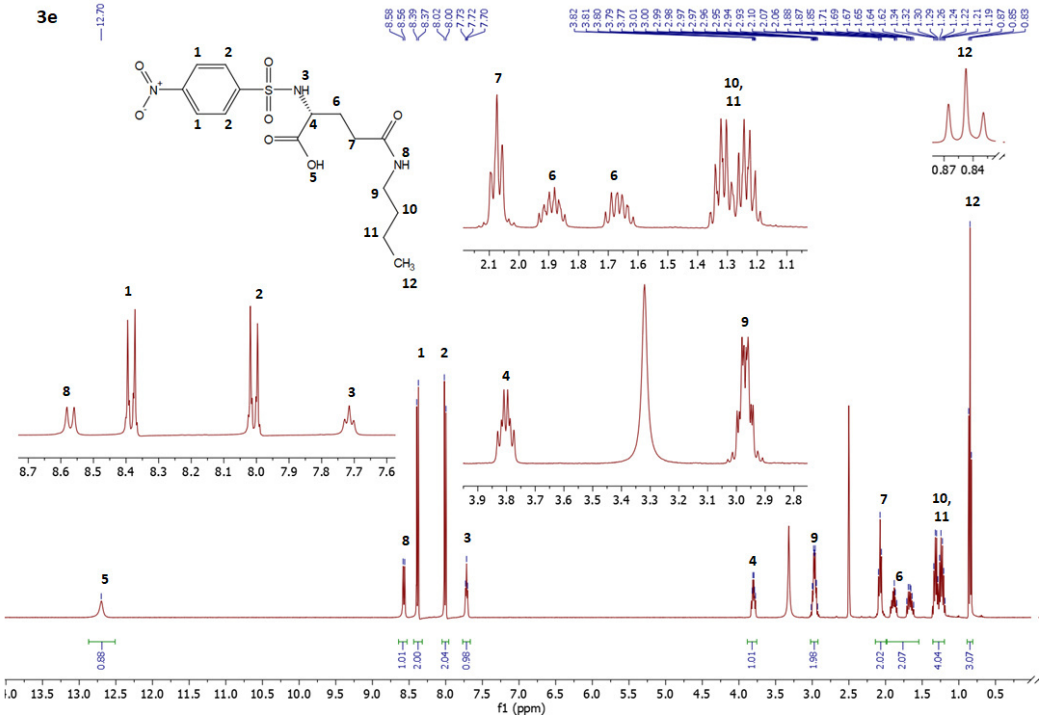

Figure A24: ^{1}H NMR Spectra for the compound **3e**.

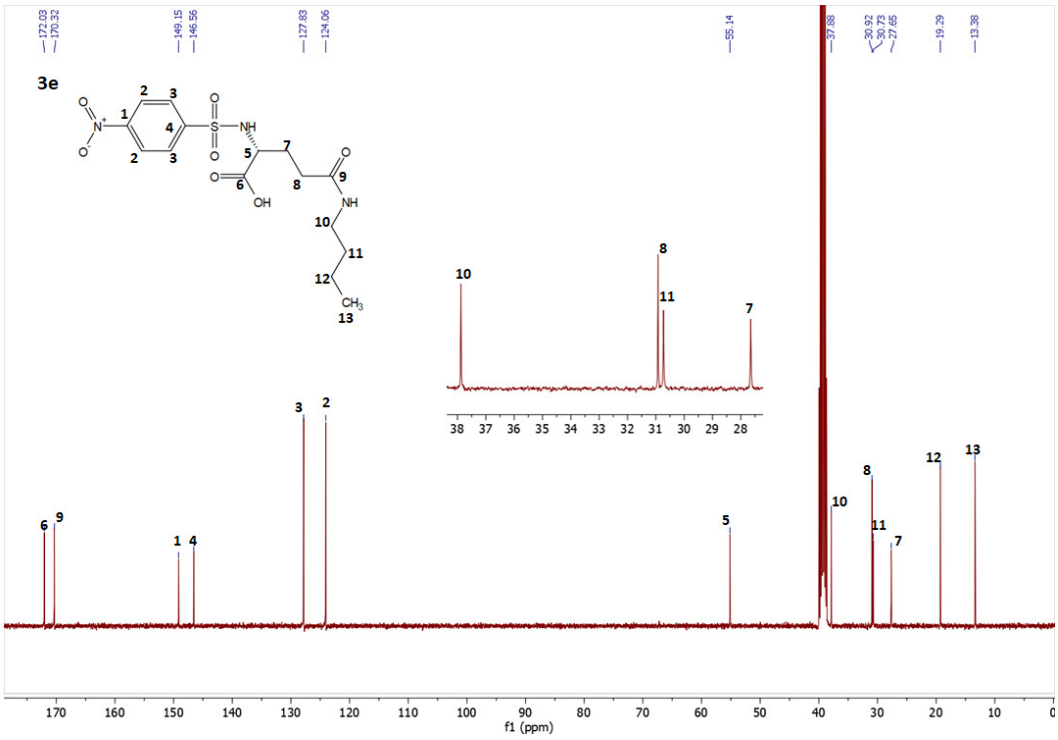

Figure A25: ^{13}C NMR Spectra for the compound **3e**.

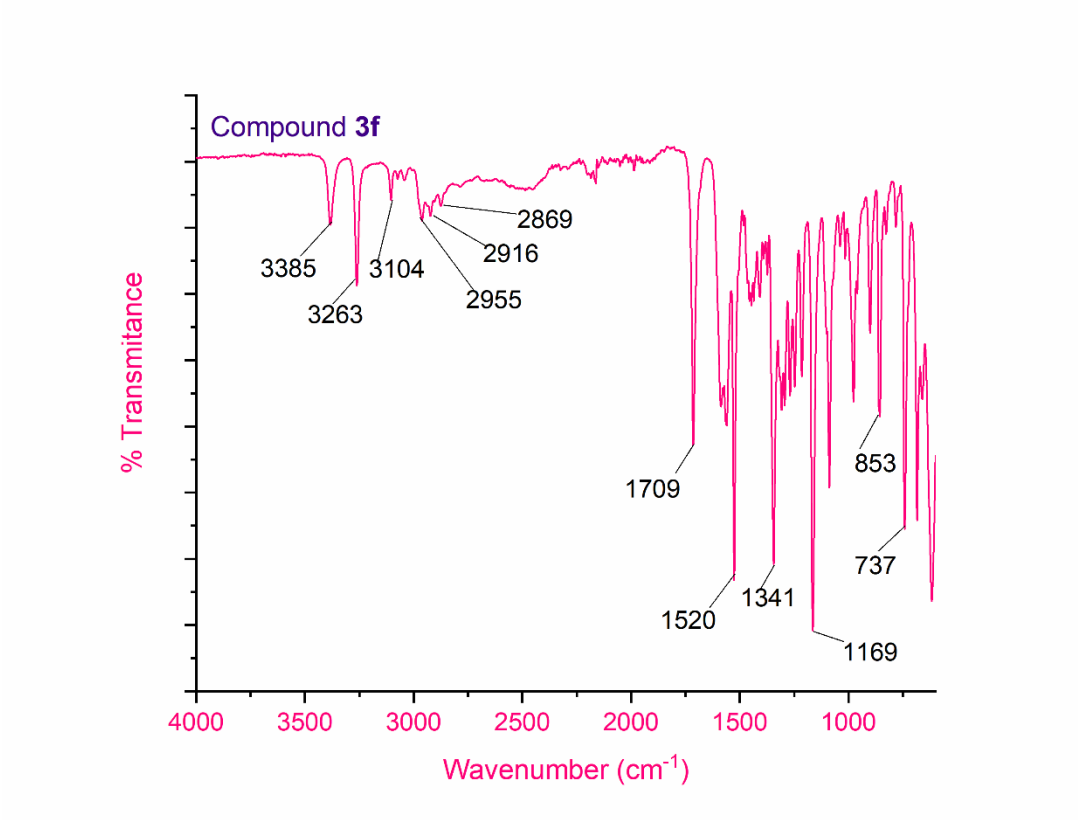

Figure A26: FT-IR Spectra for the compound **3f**.

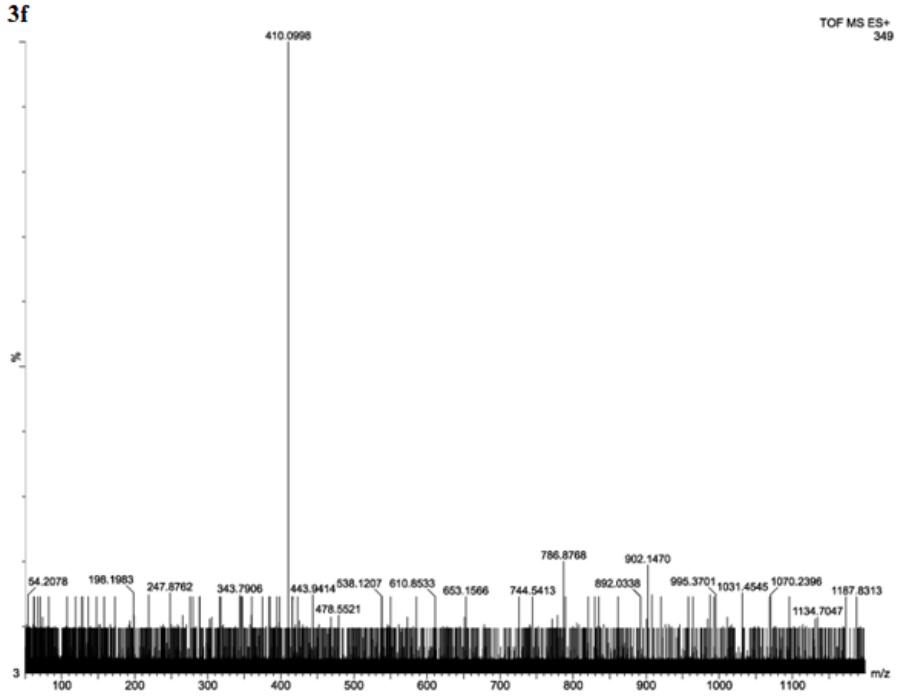

Figure A27: HRMS Spectra for the compound **3f**.

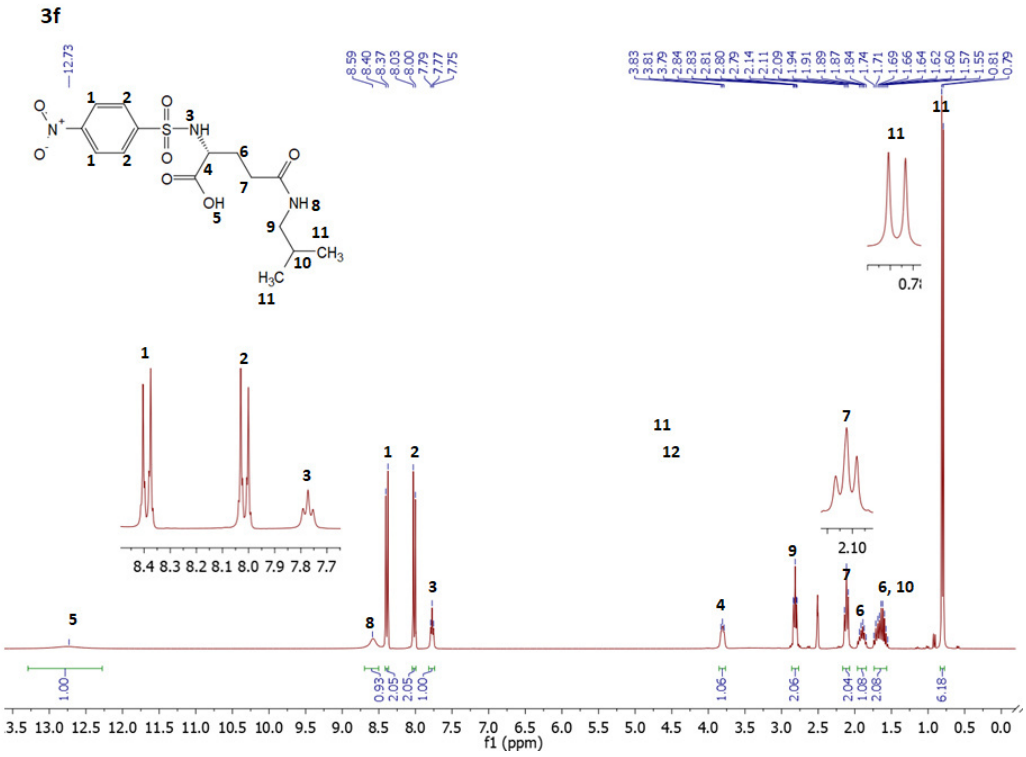

Figure A28: ^{1}H NMR Spectra for the compound **3f**.

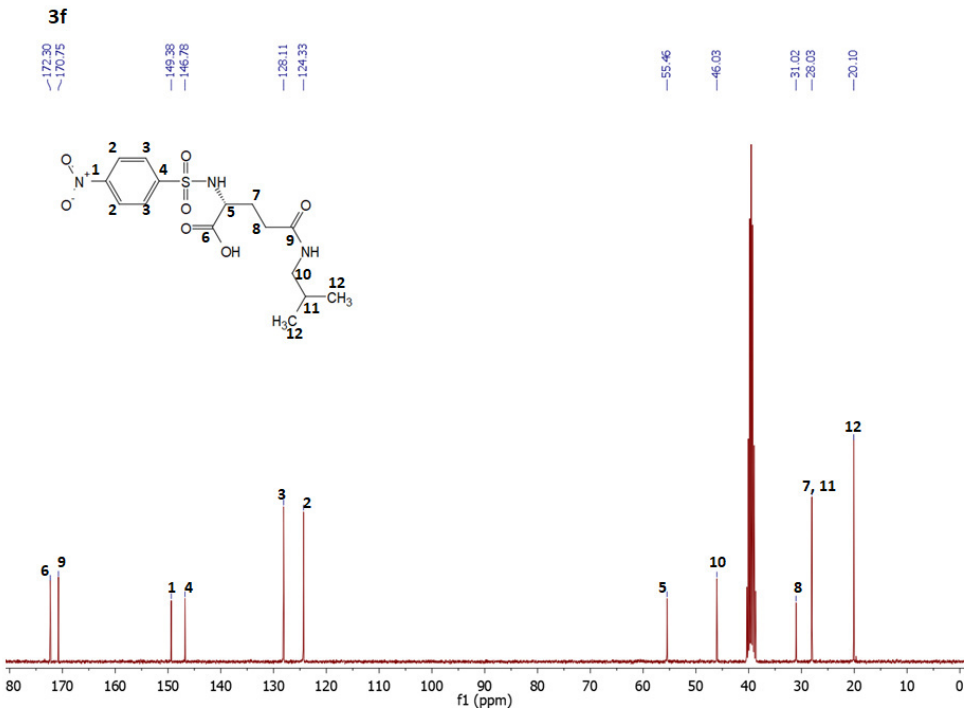

Figure A29: ^{13}C NMR Spectra for the compound **3f**.

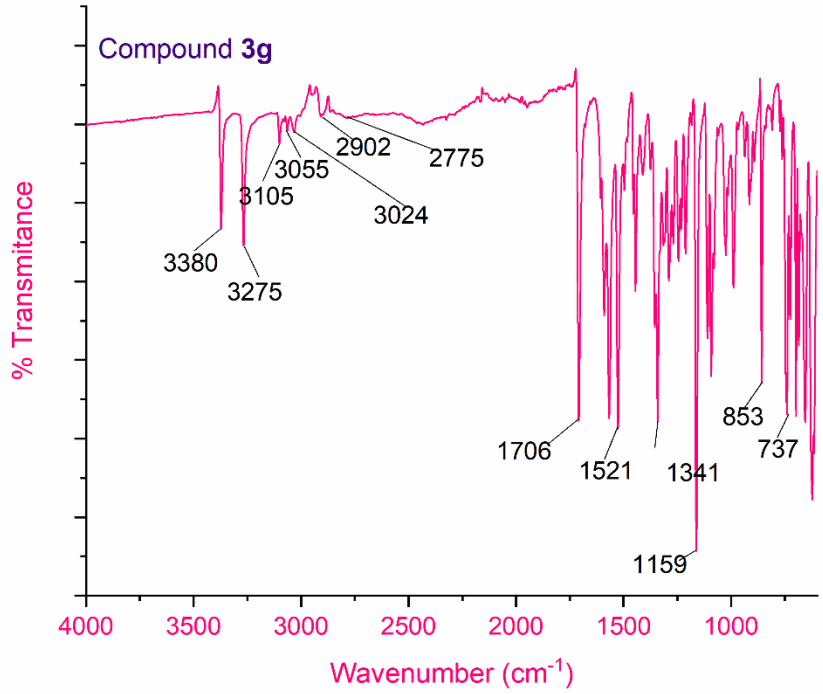

Figure A30: FT-IR Spectra for the compound **3g**.

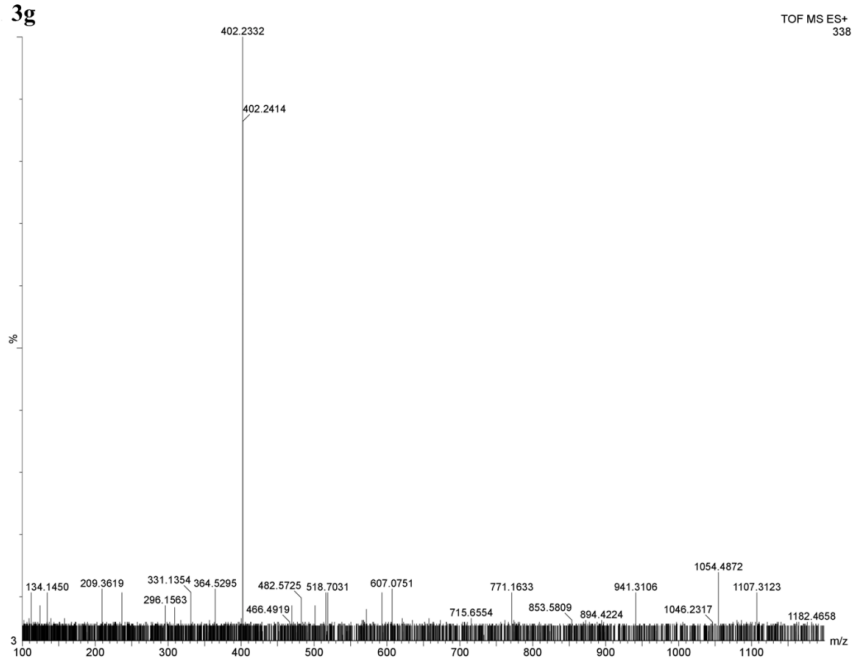

Figure A31: HRMS Spectra for the compound **3g**.

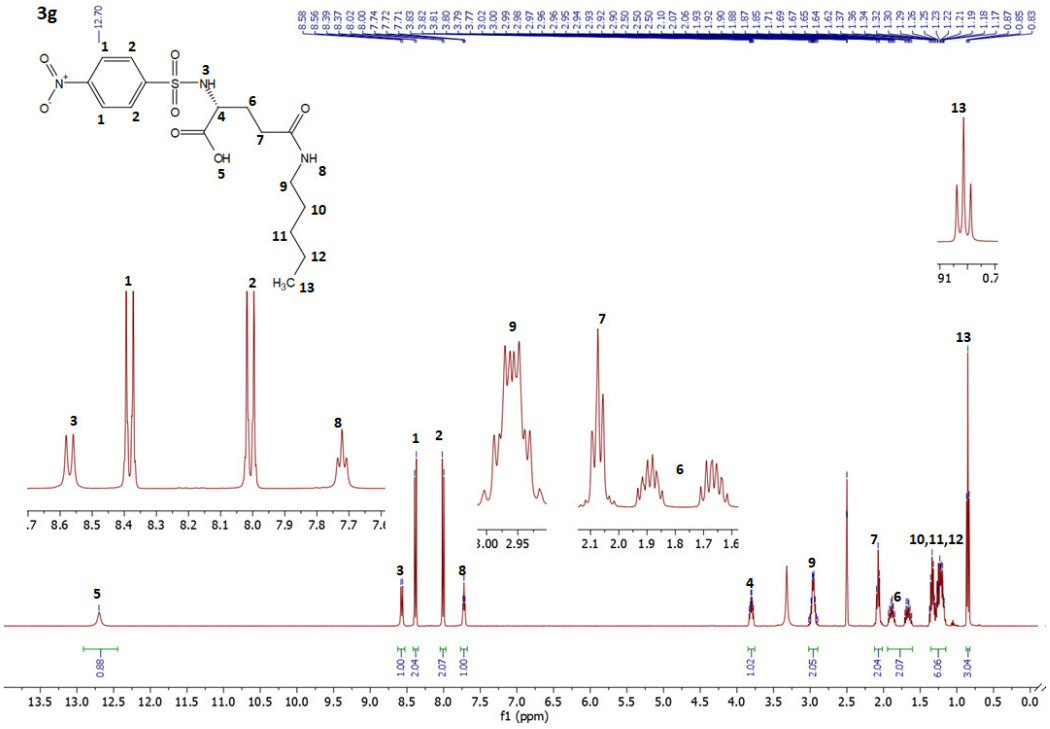

Figure A32: ^{1}H NMR Spectra for the compound **3g**.

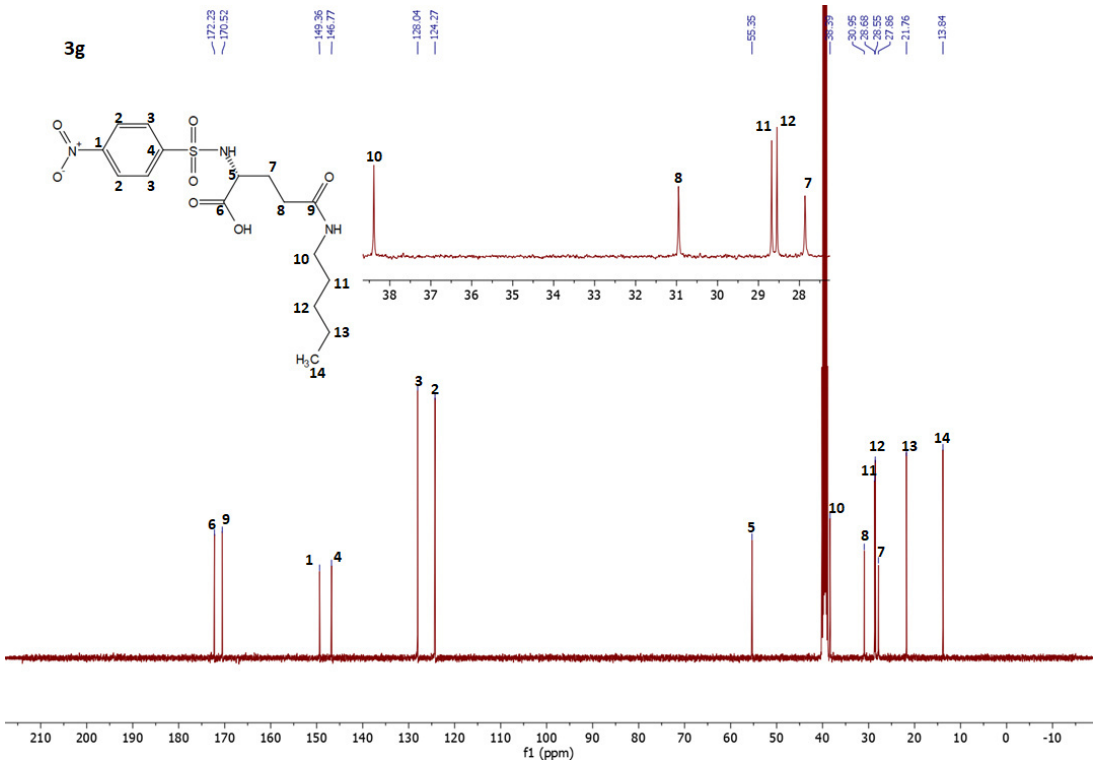

Figure A33: ^{13}C NMR Spectra for the compound **3g**.

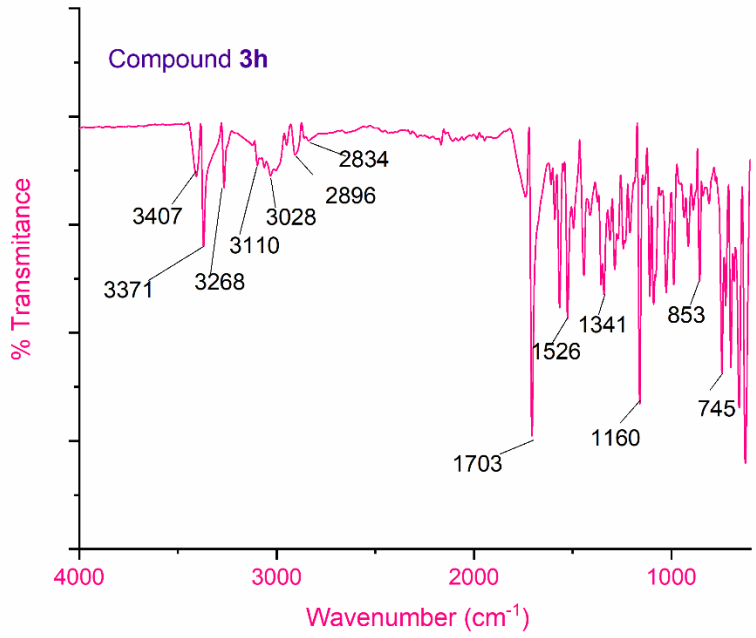

Figure A34: FT-IR Spectra for the compound **3h**.

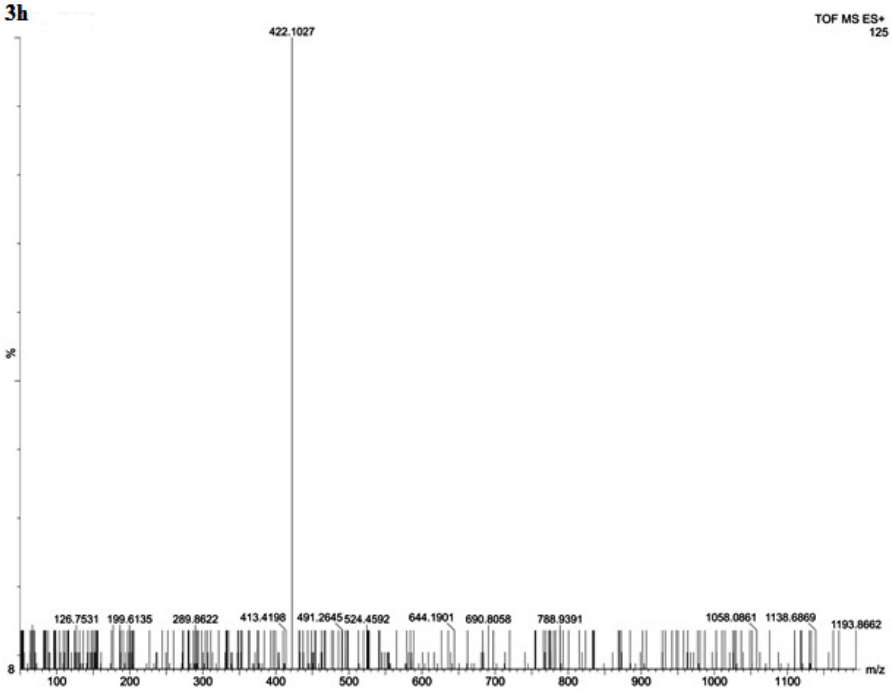

Figure A35: HRMS Spectra for the compound **3h**.

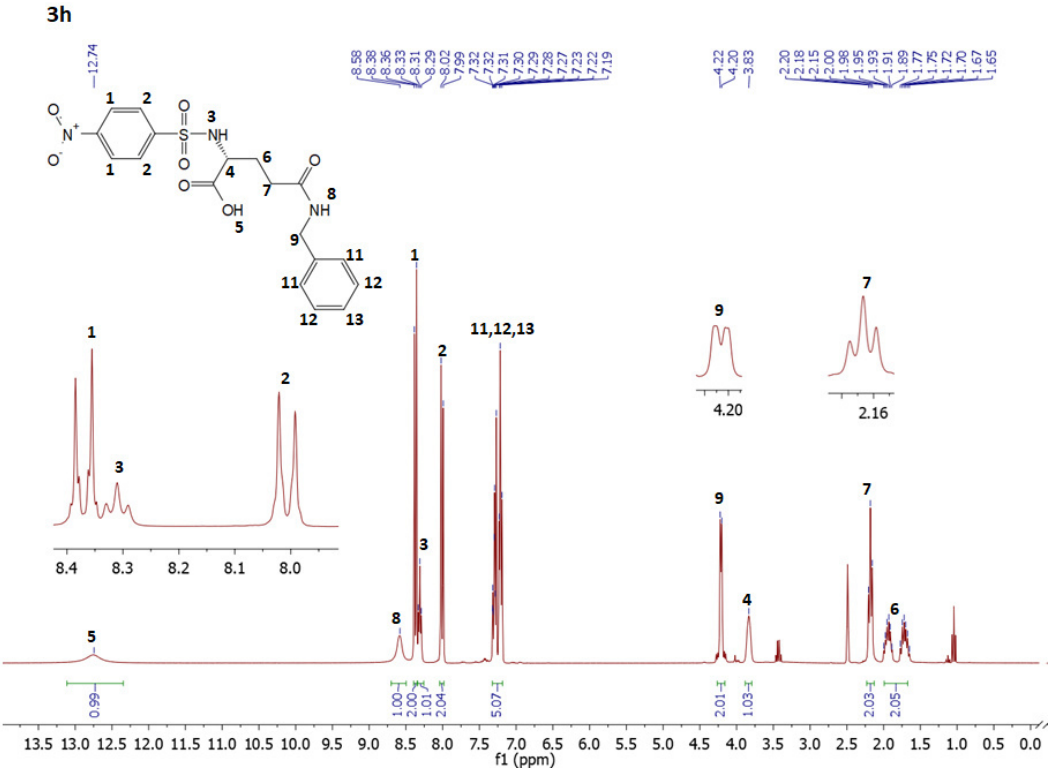

Figure A36: ^{1}H NMR Spectra for the compound **3h**.

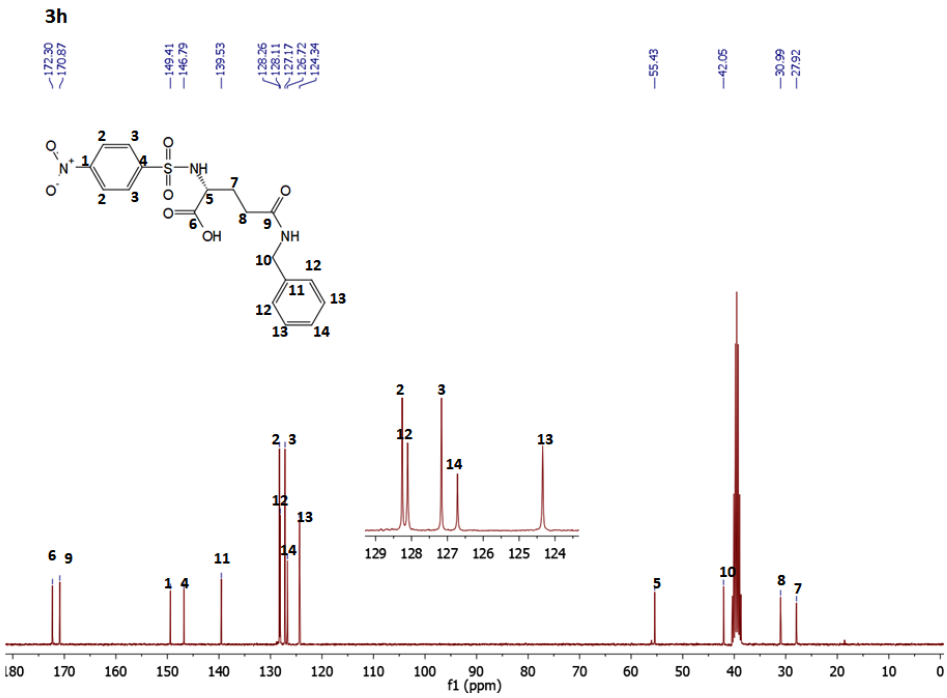

Figure A37: ^{13}C NMR Spectra for the compound **3h**.

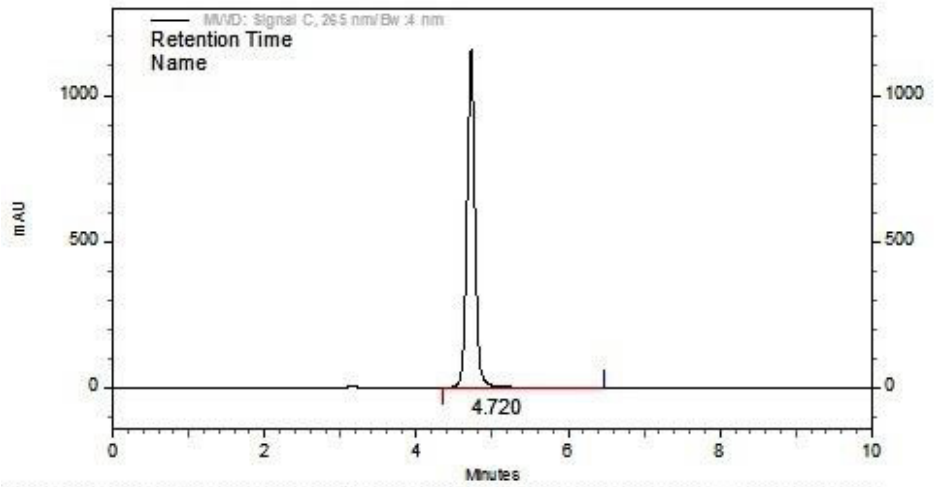

MWD: Signal C, 265 nm/Bw:4 nm Results				
Retention Time	Area	Area %	Theoretical plates (USP)	Asymmetry (10%)
4.72	17865746	100.00	10236	1.12
Totals				
	17865746	100.00		

Figure A38: HPLC Spectra for the compound **3h**.

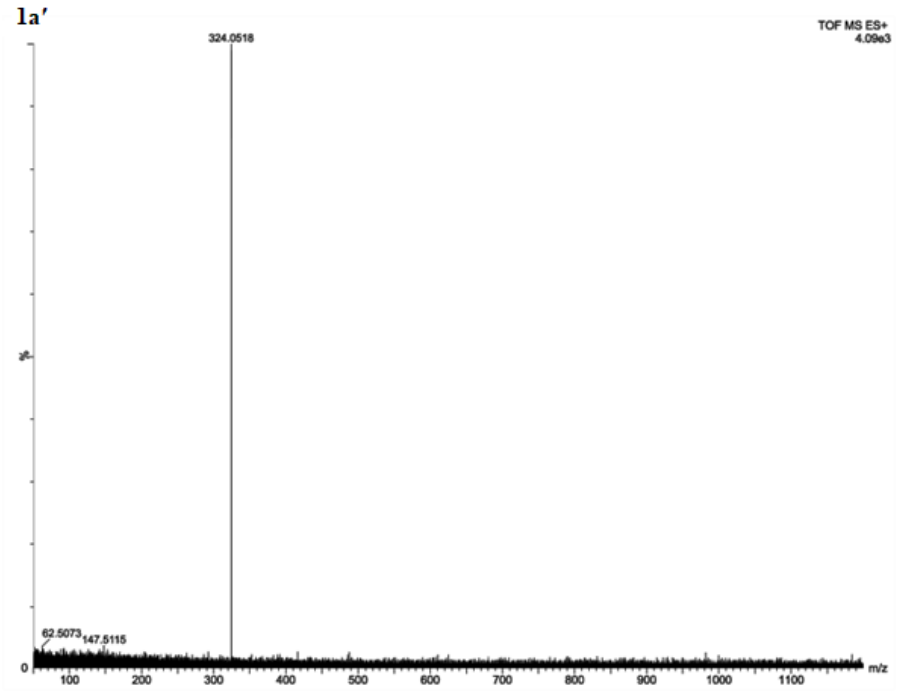

Figure A39: HRMS Spectra for the compound **1a′**.

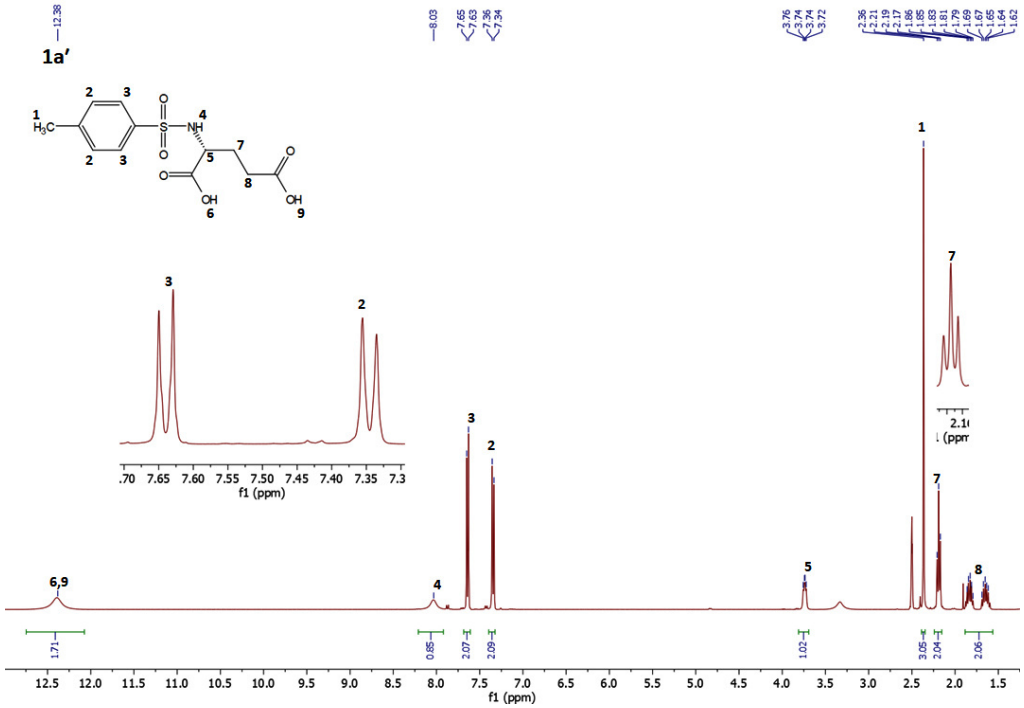

Figure A40: ^{1}H NMR Spectra for the compound **1a′**.

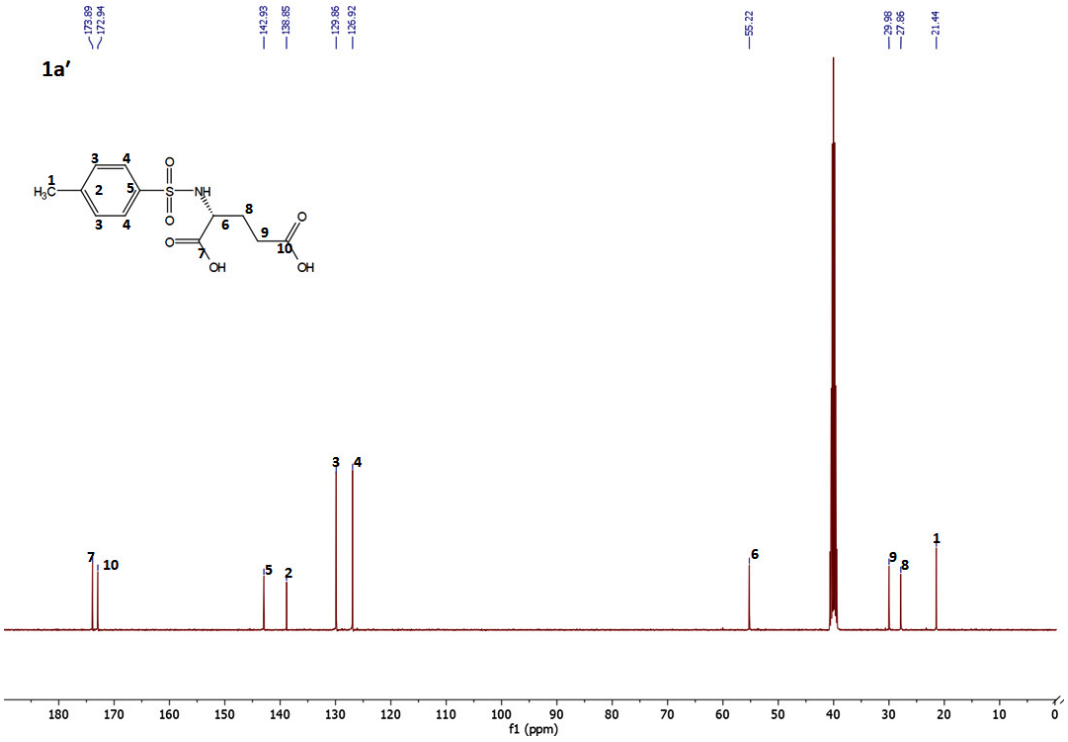

Figure A41: ^{13}C NMR Spectra for the compound **1a′**.

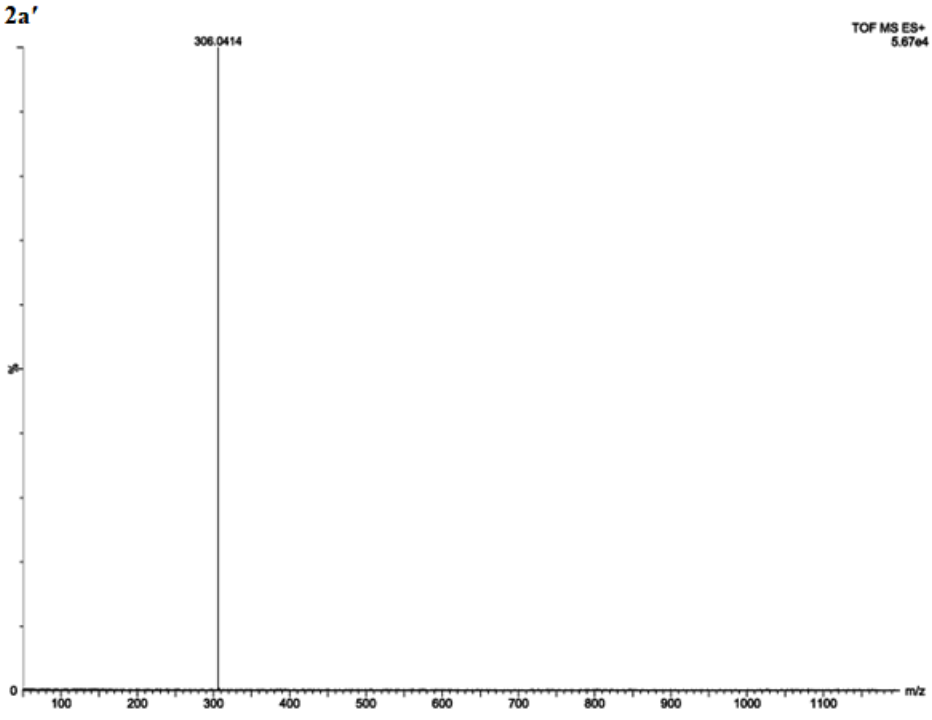

Figure A42: HRMS Spectra for the compound **2a′**.

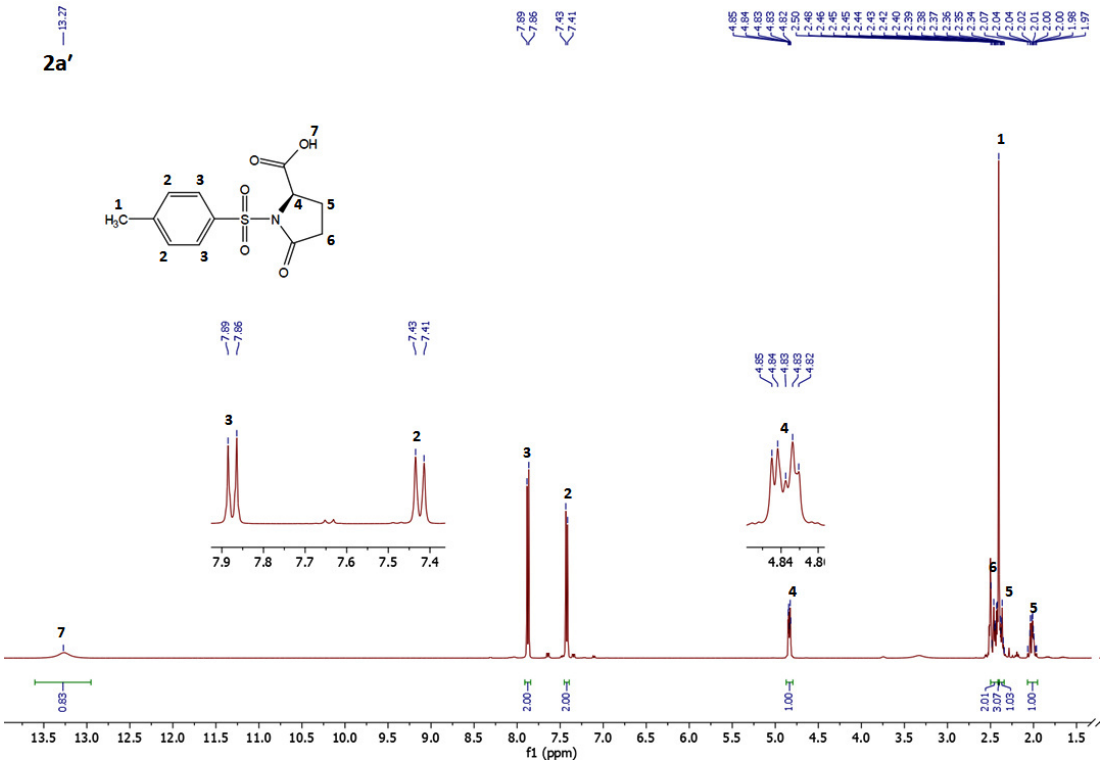

Figure A43: ^{1}H NMR Spectra for the compound **2a′**.

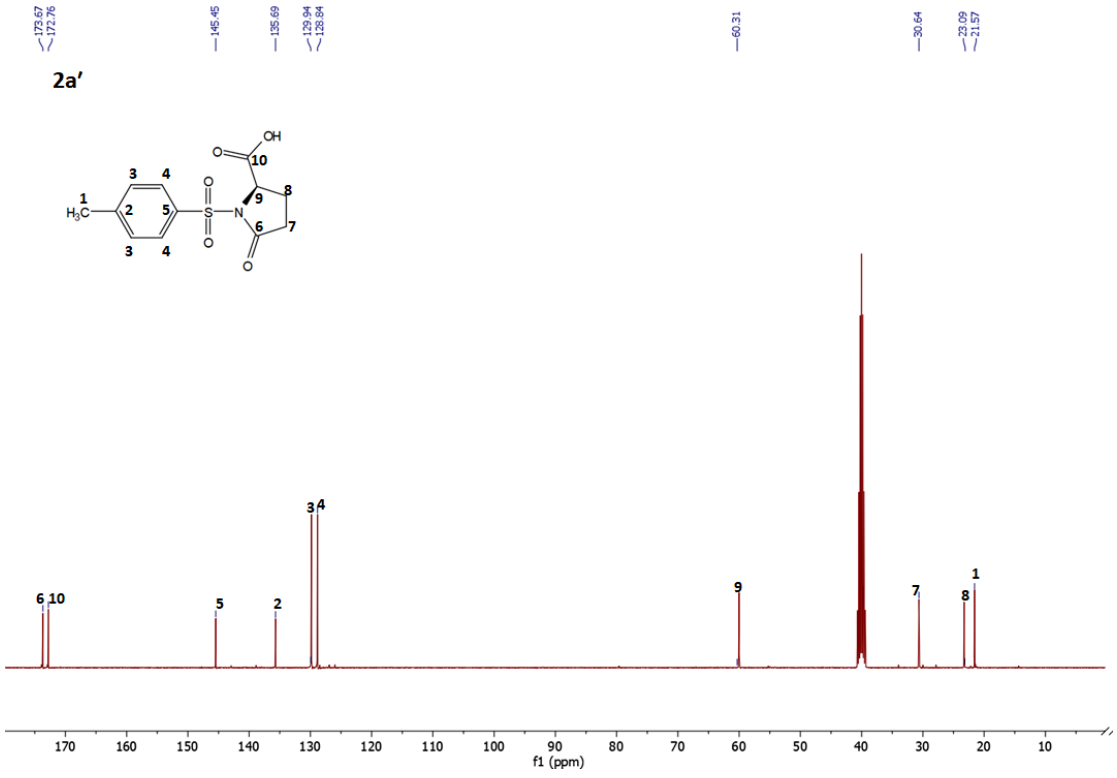

Figure A44: ^{13}C NMR Spectra for the compound **2a′**.

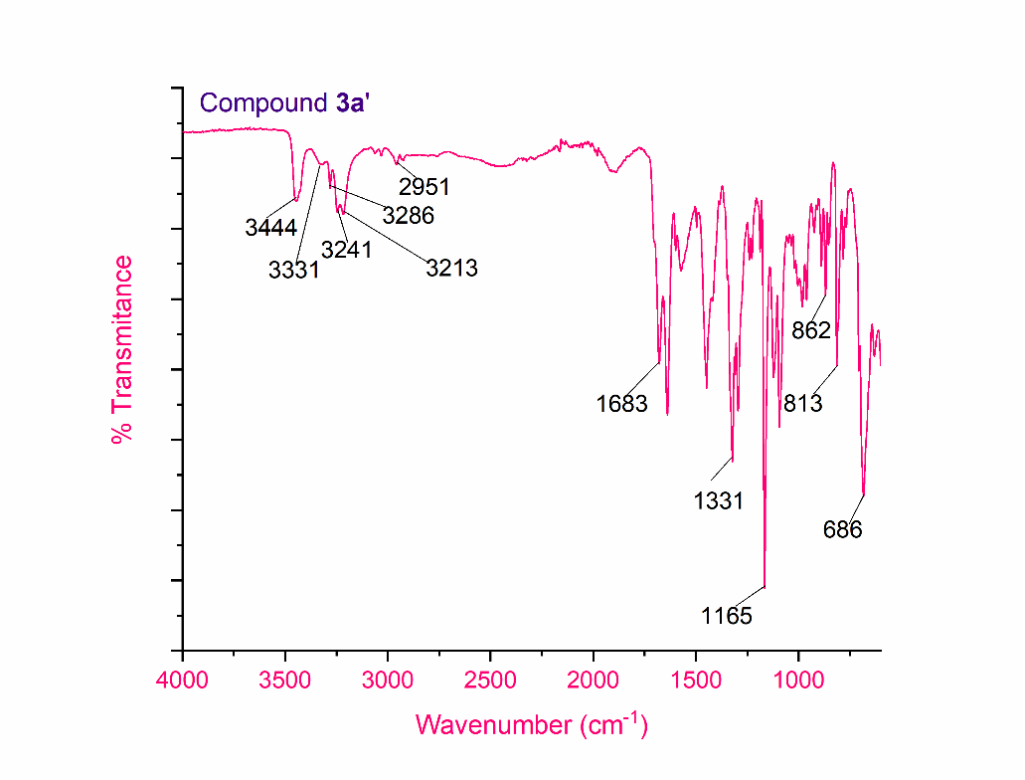

Figure A45: FT-IR Spectra for the compound **3a′**.

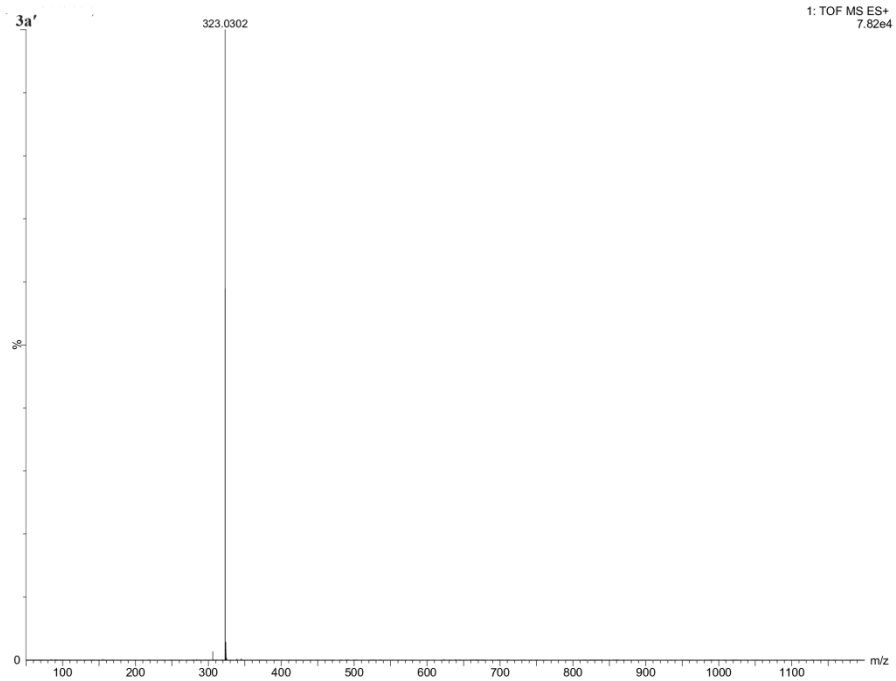

Figure A46: HRMS Spectra for the compound **3a′**.

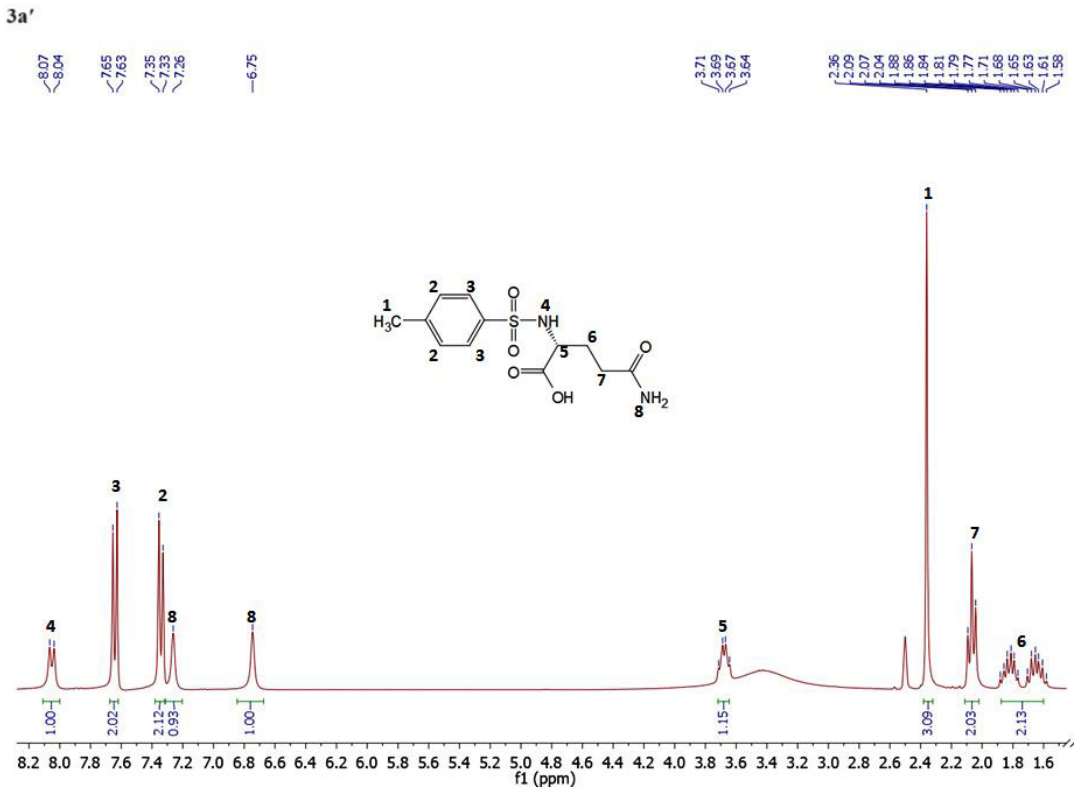

Figure A47: ^{1}H NMR Spectra for the compound **3a′**.

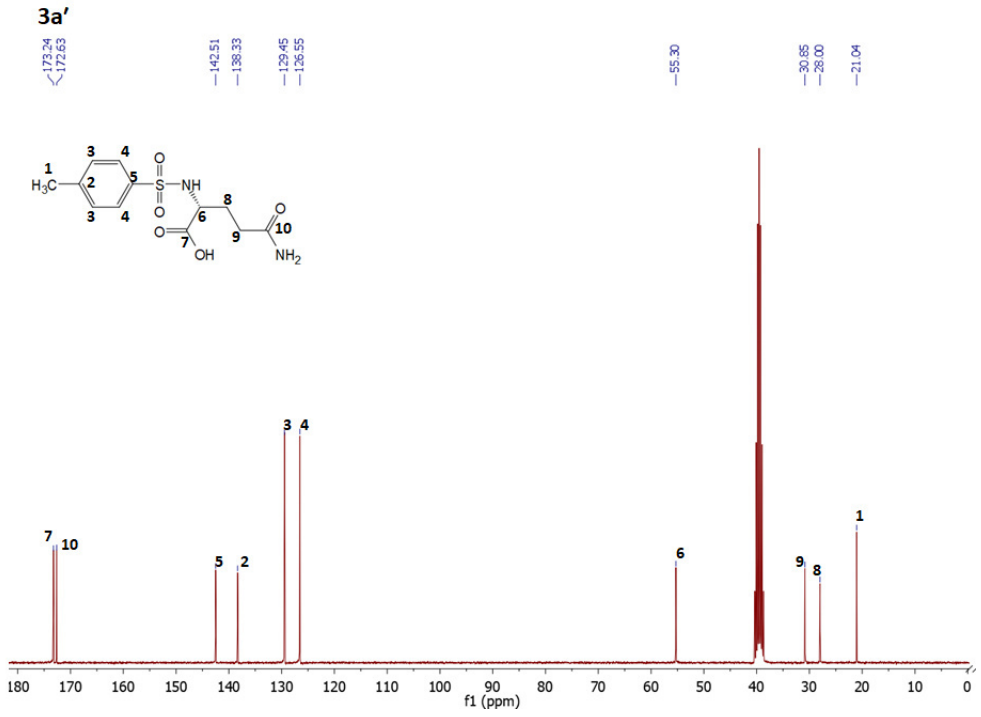

Figure A48: ^{13}C NMR Spectra for the compound **3a′**.

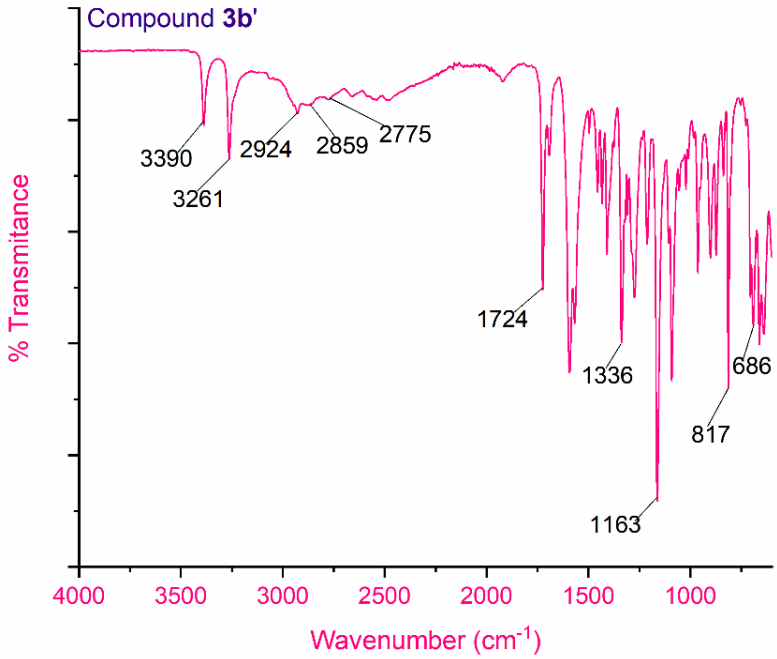

Figure A49: FT-IR Spectra for the compound **3b′**.

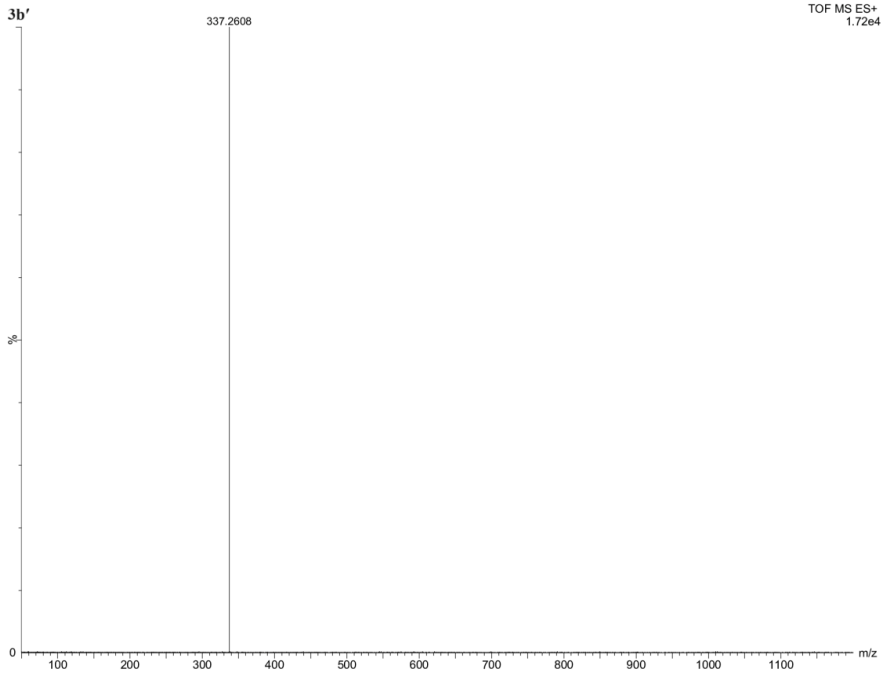

Figure A50: HRMS Spectra for the compound **3b′**.

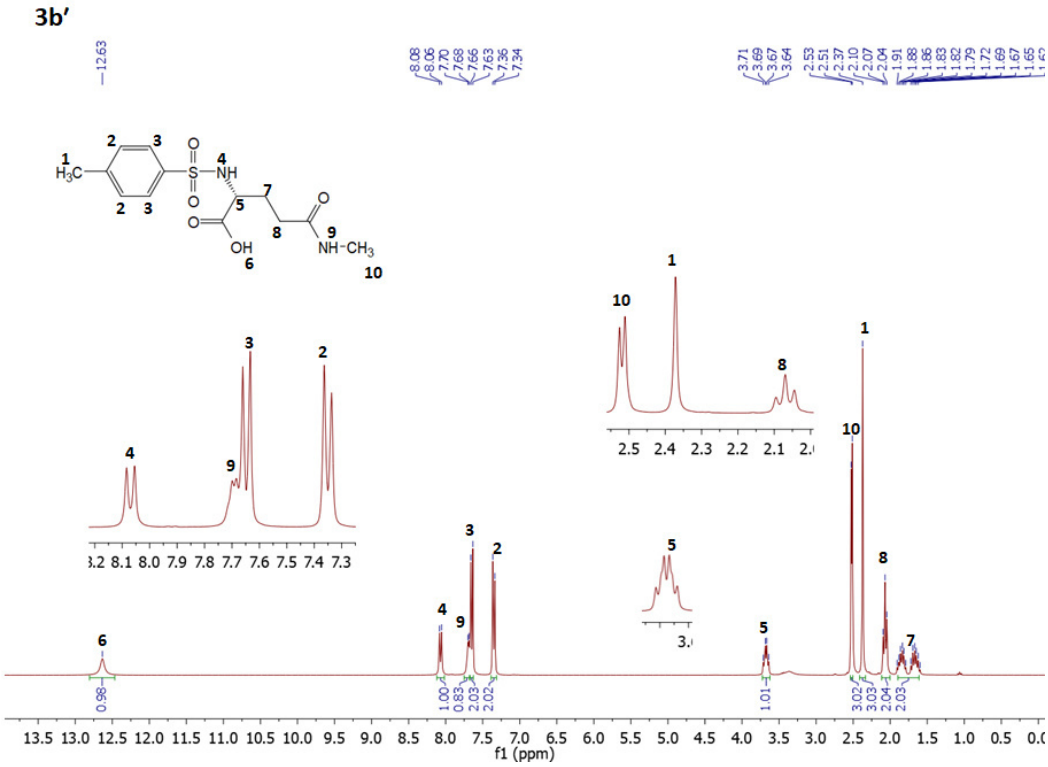

Figure A51: ^{1}H NMR Spectra for the compound **3b′**.

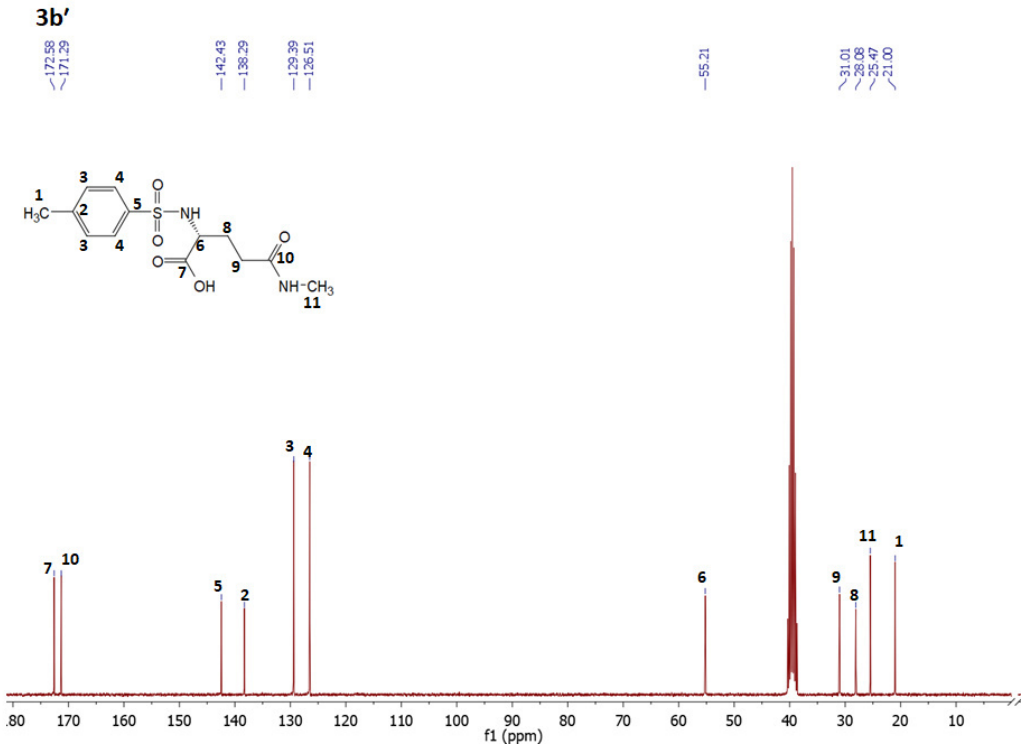

Figure A52: ^{13}C NMR Spectra for the compound **3b′**.

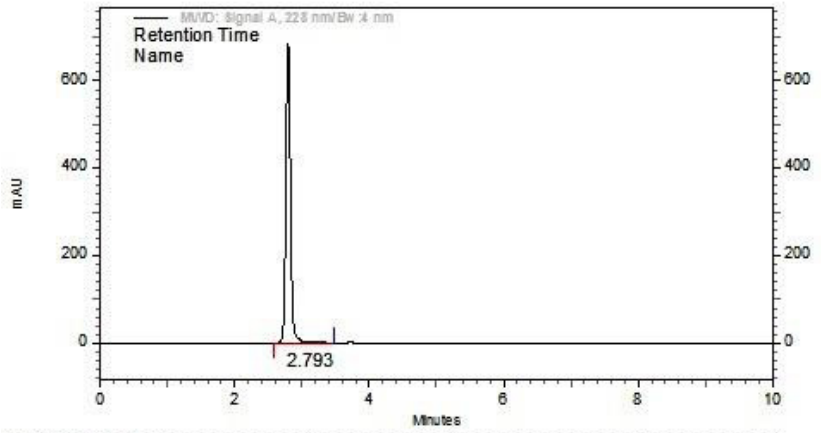

MWD: Signal A, 228 nm/Bw:4 nm Results				
Retention Time	Area	Area %	Theoretical plates (USP)	Asymmetry (10%)
2.79	6622504	100.00	9230	1.12
Totals				
	6622504	100.00		

Figure A53: HPLC Spectra for the compound **3b′**.

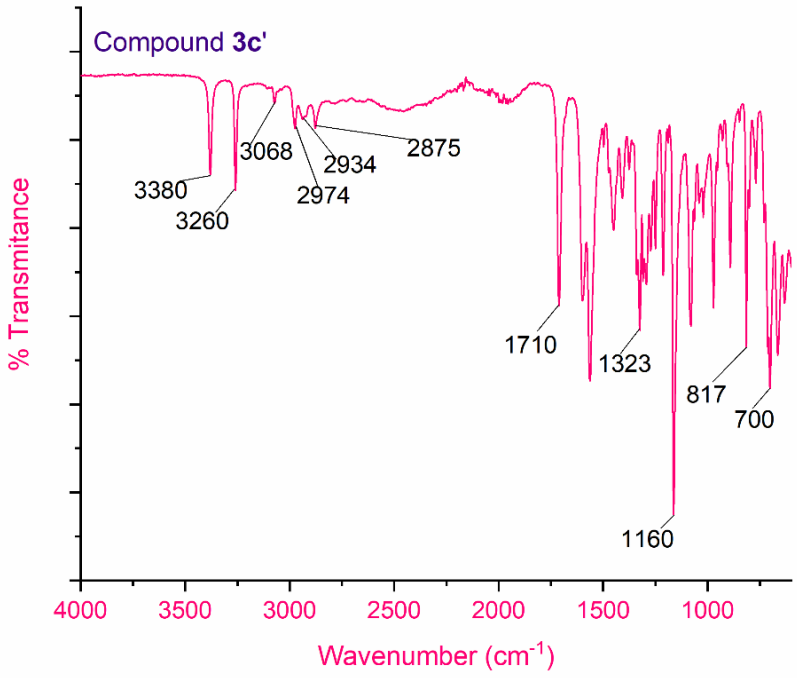

Figure A54: FT-IR Spectra for the compound **3c′**.

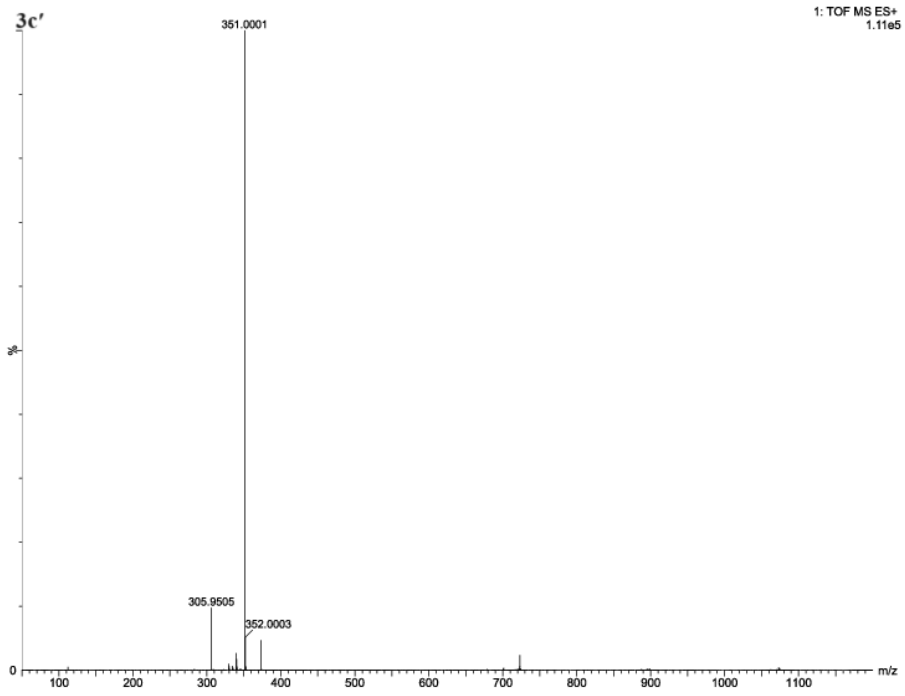

Figure A55: HRMS Spectra for the compound **3c′**.

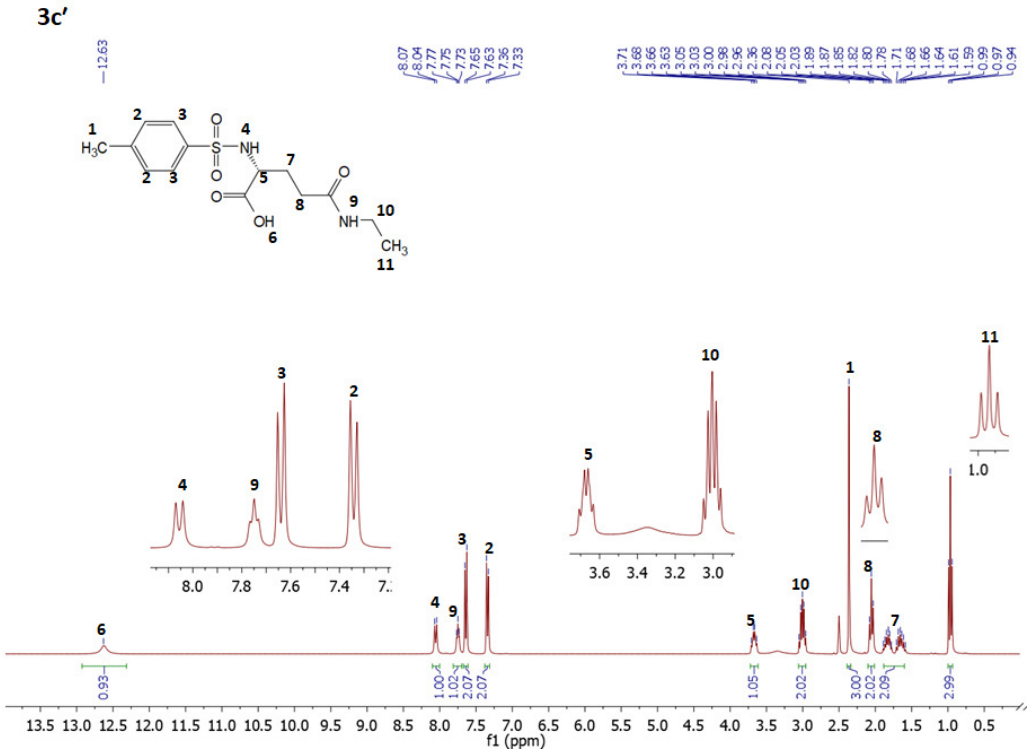

Figure A56: ^{1}H NMR Spectra for the compound **3c′**.

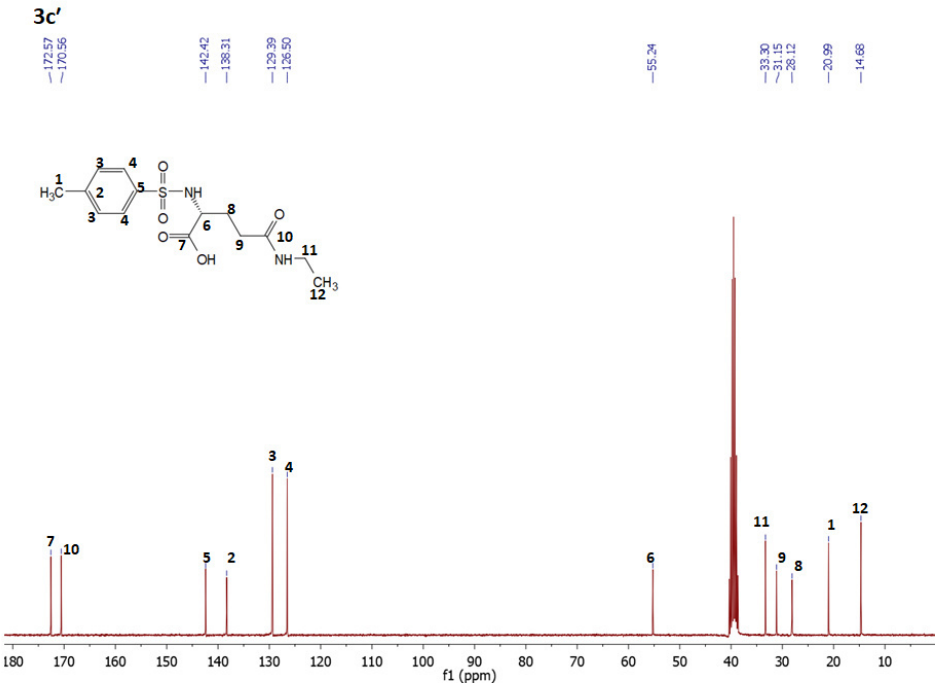

Figure A57: ^{13}C NMR Spectra for the compound **3c′**.

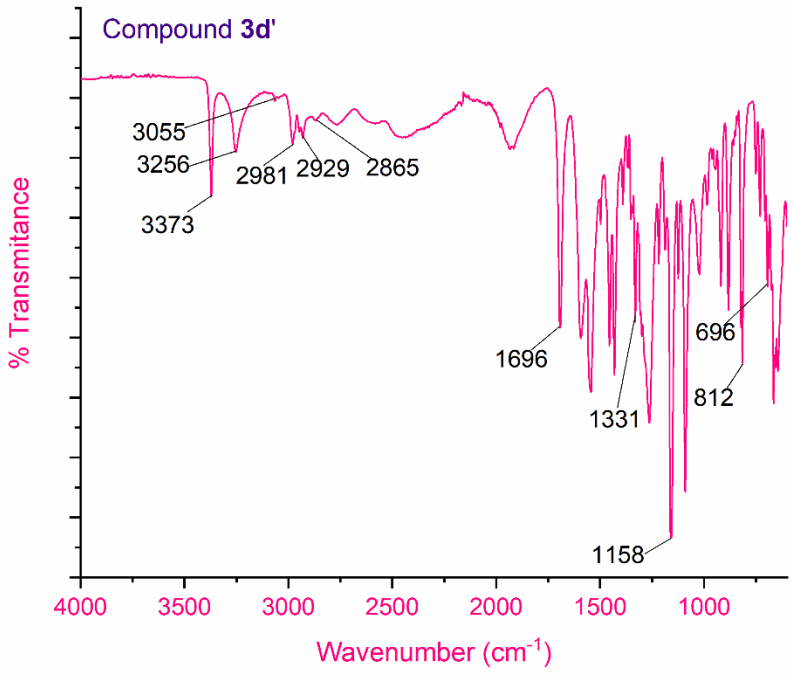

Figure A58: FT-IR Spectra for the compound **3d′**.

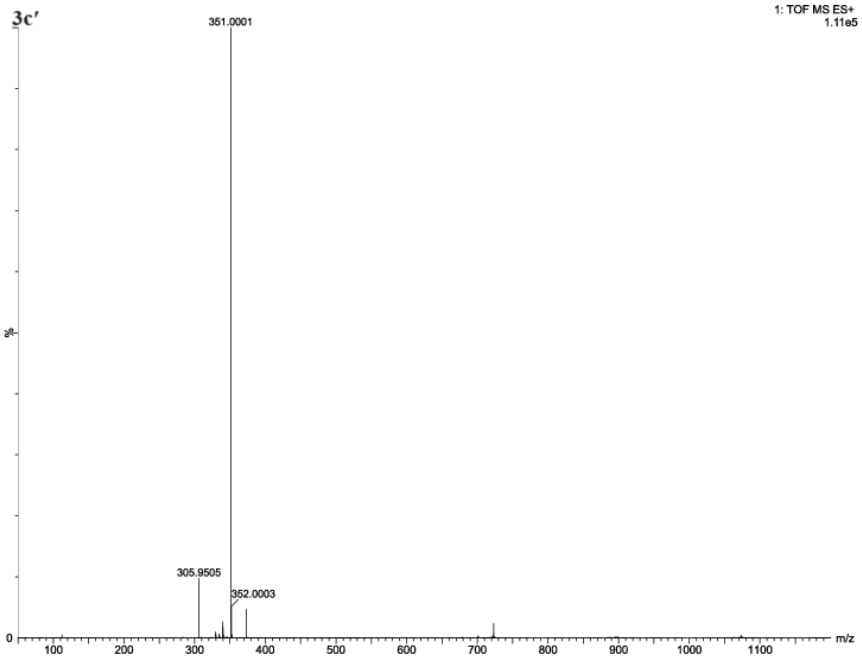

Figure A59: HRMS Spectra for the compound **3d′**.

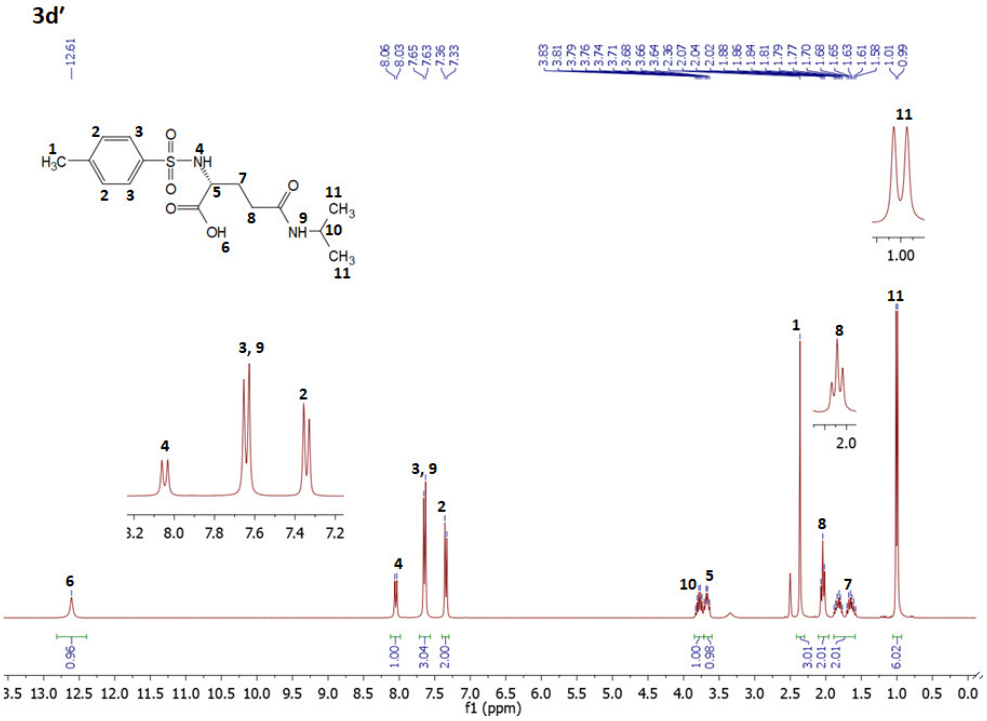

Figure A60: ^{1}H NMR Spectra for the compound **3d′**.

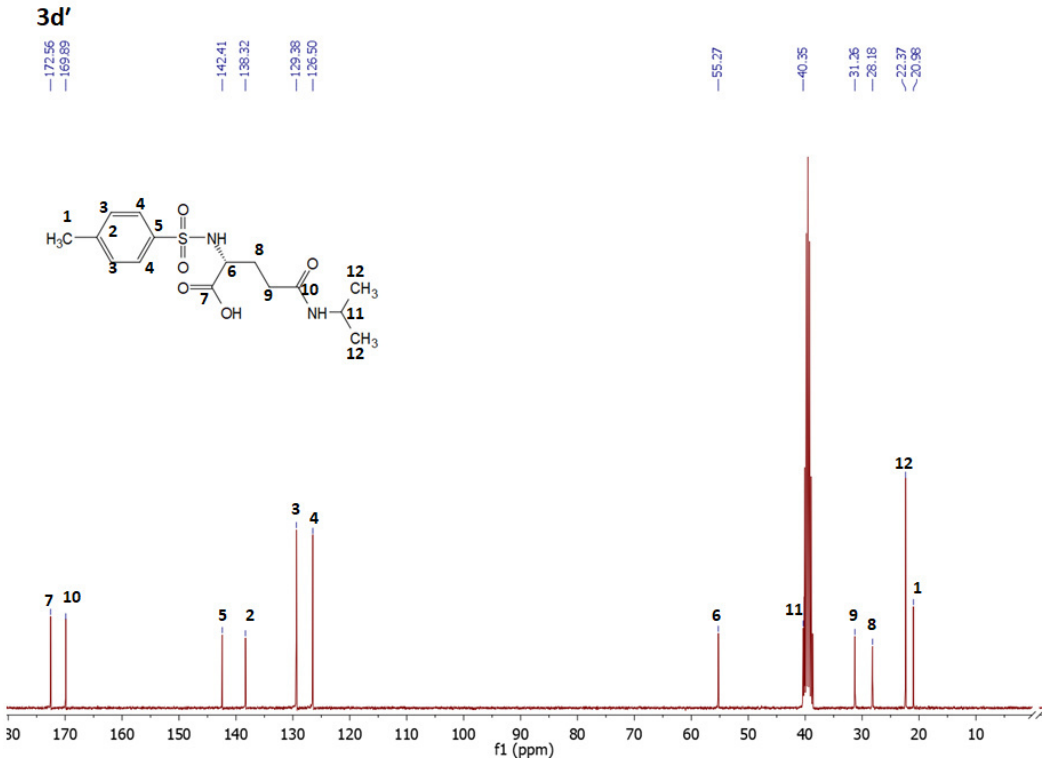

Figure A61: ^{13}C NMR Spectra for the compound **3d′**.

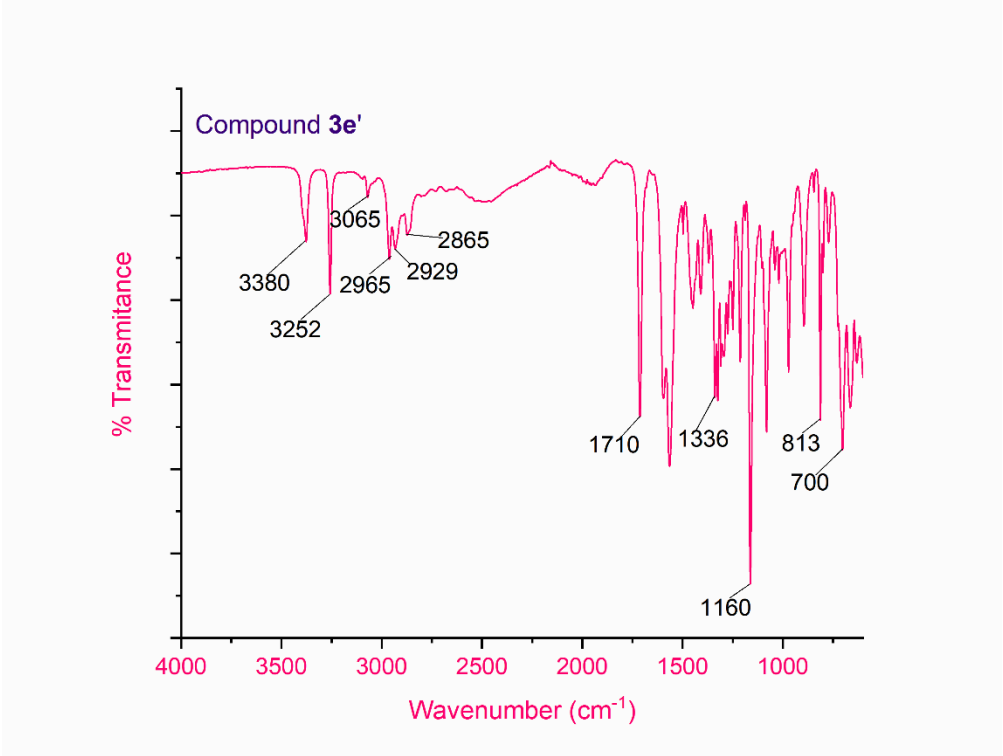

Figure A62: FT-IR Spectra for the compound **3e′**.

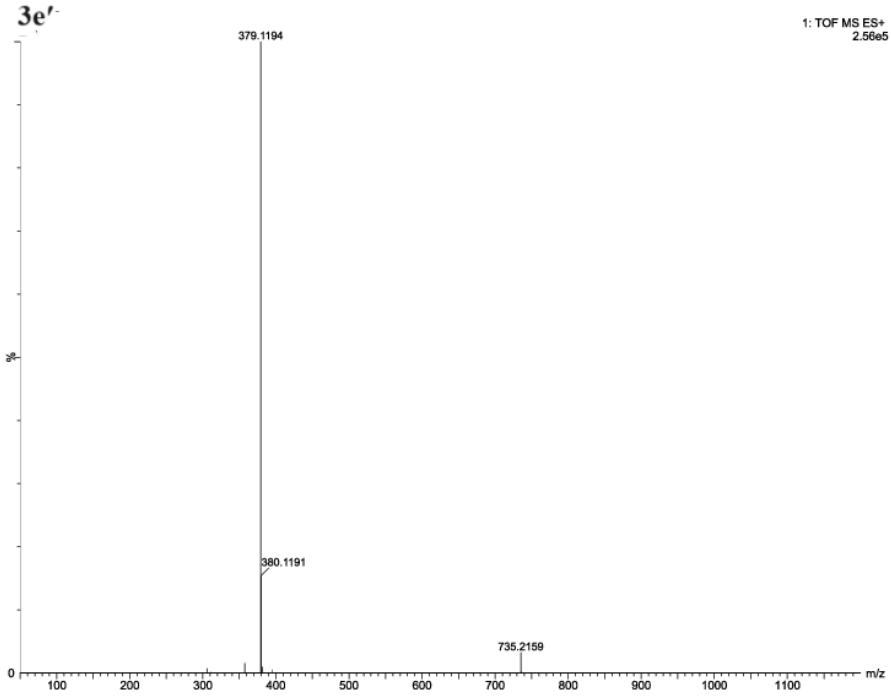

Figure A63: HRMS Spectra for the compound **3e′**.

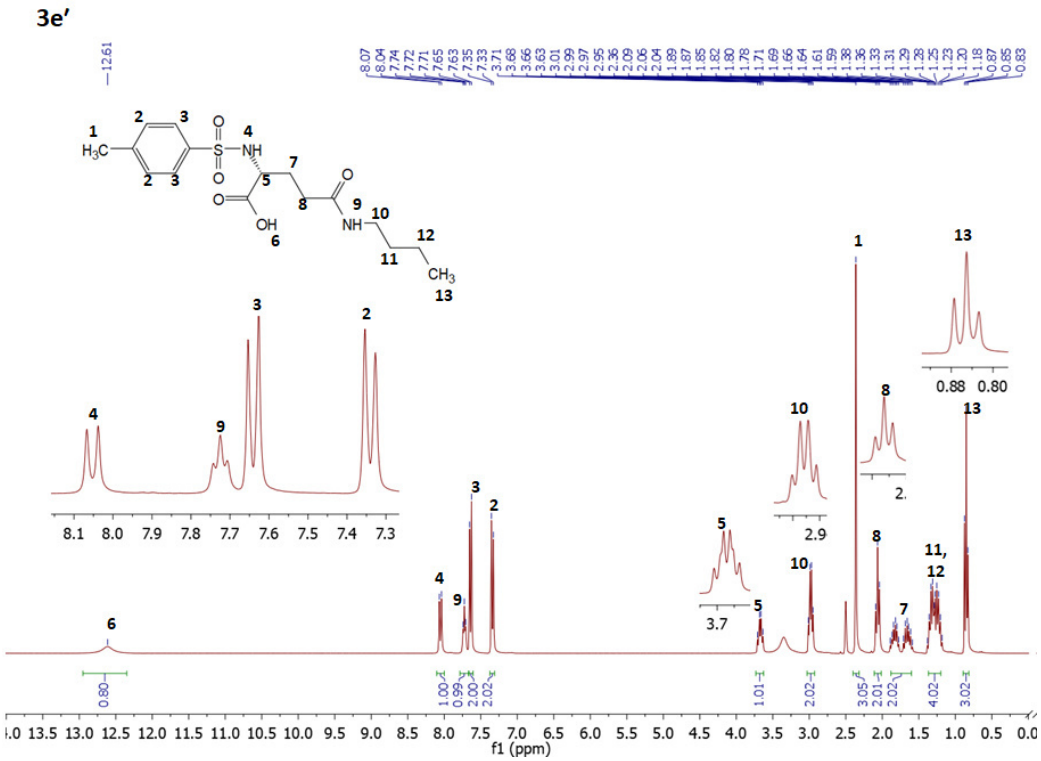

Figure A64: ^{1}H NMR Spectra for the compound **3e′**.

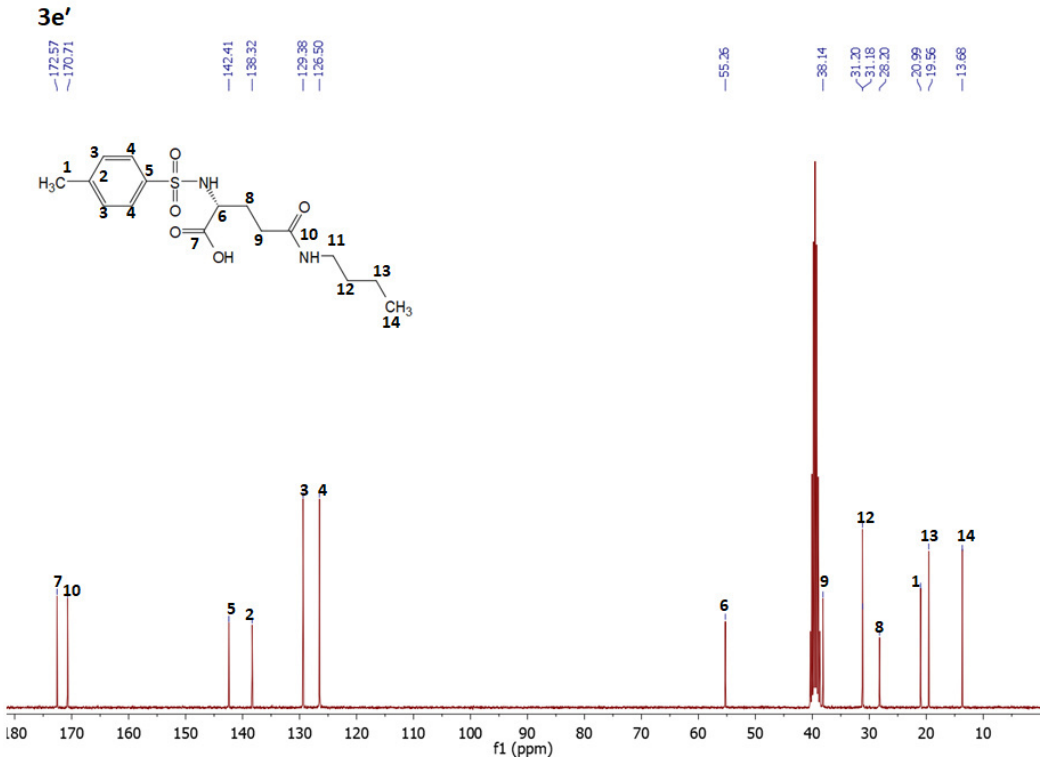

Figure A65: ^{13}C NMR Spectra for the compound **3e′**.

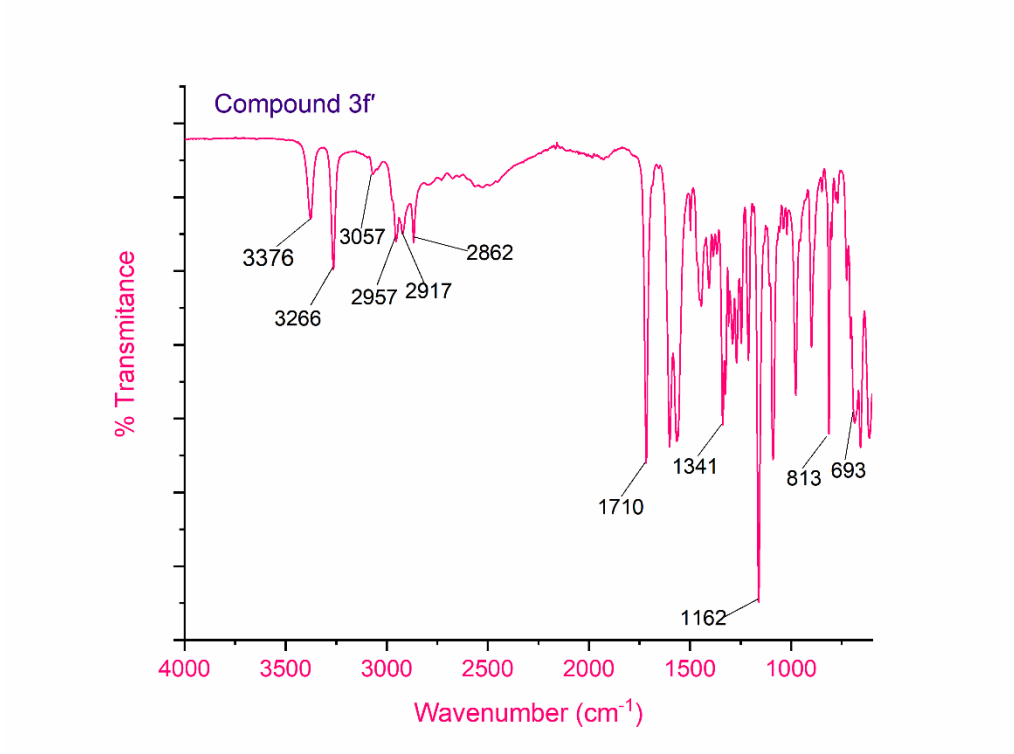

Figure A66: FT-IR Spectra for the compound **3f′**.

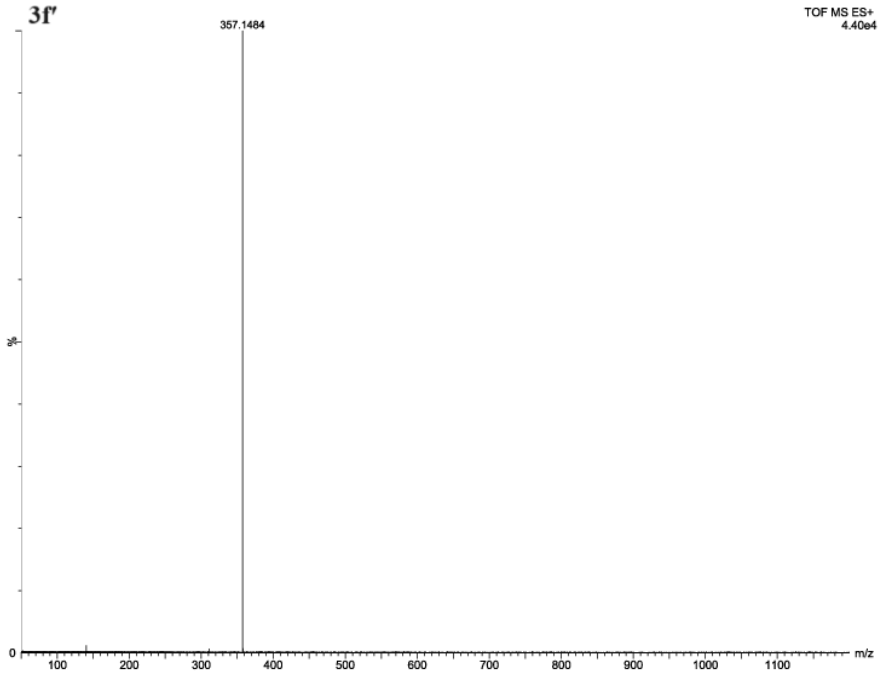

Figure A67: HRMS Spectra for the compound **3f′**.

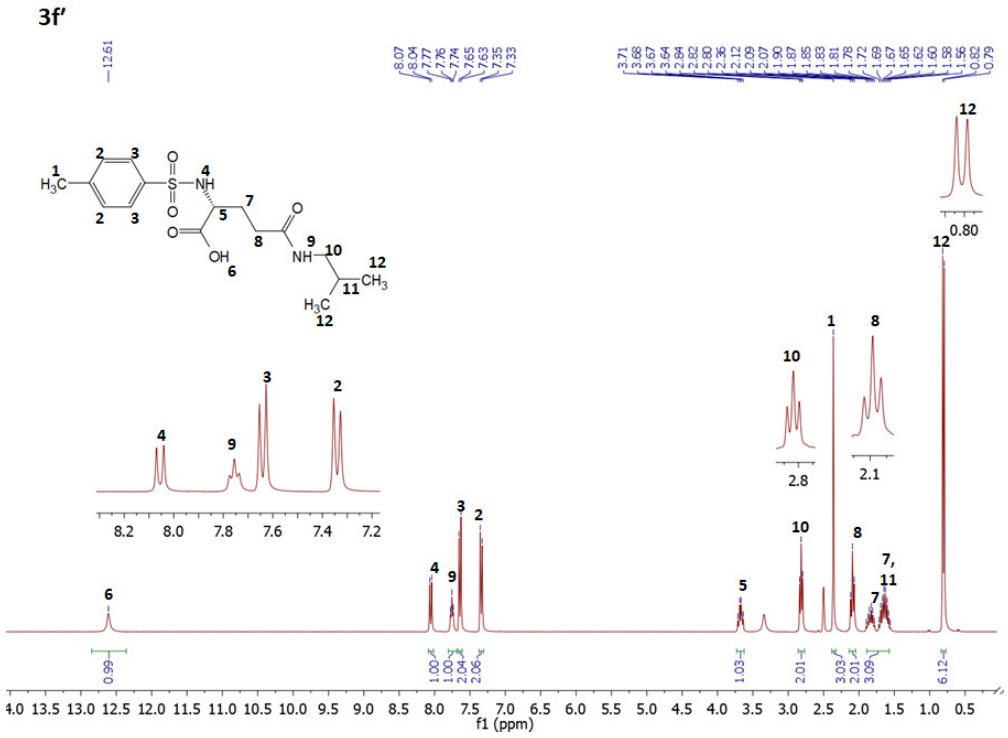

Figure A68: ^{1}H NMR Spectra for the compound **3f′**.

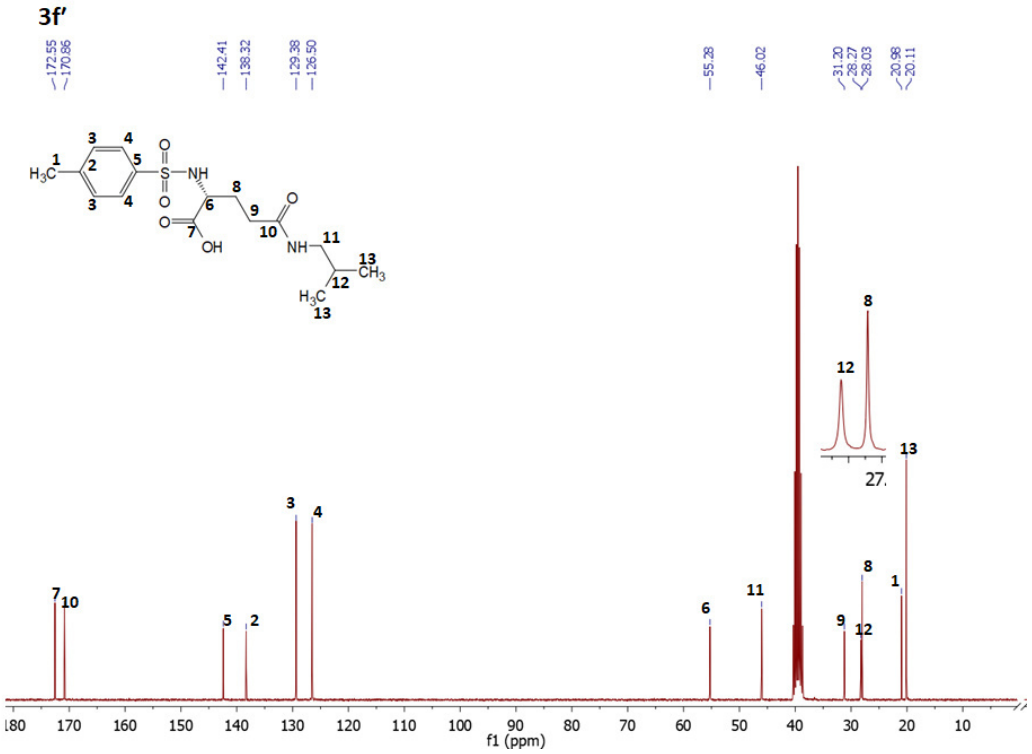

Figure A69: ^{13}C NMR Spectra for the compound **3f′**.

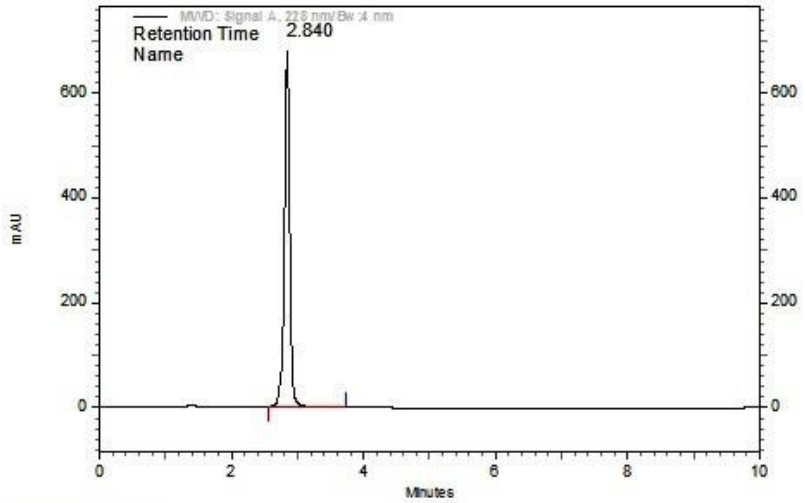

MWD: Signal A, 228 nm/Bw:4 nm Results				
Retention Time	Area	Area %	Theoretical plates (USP)	Asymmetry (10%)
2.84	8181285	100.00	6323	1.04
Totals				
	8181285	100.00		

Figure A70: HPLC Spectra for the compound **3f′**.

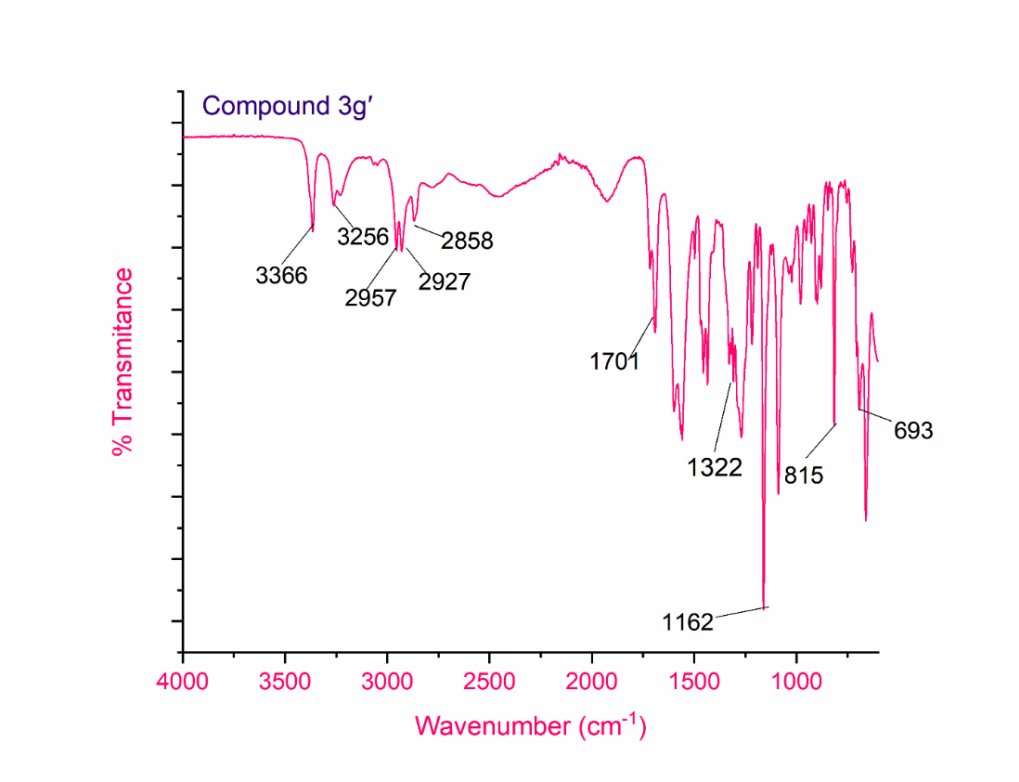

Figure A71: FT-IR Spectra for the compound **3g′**.

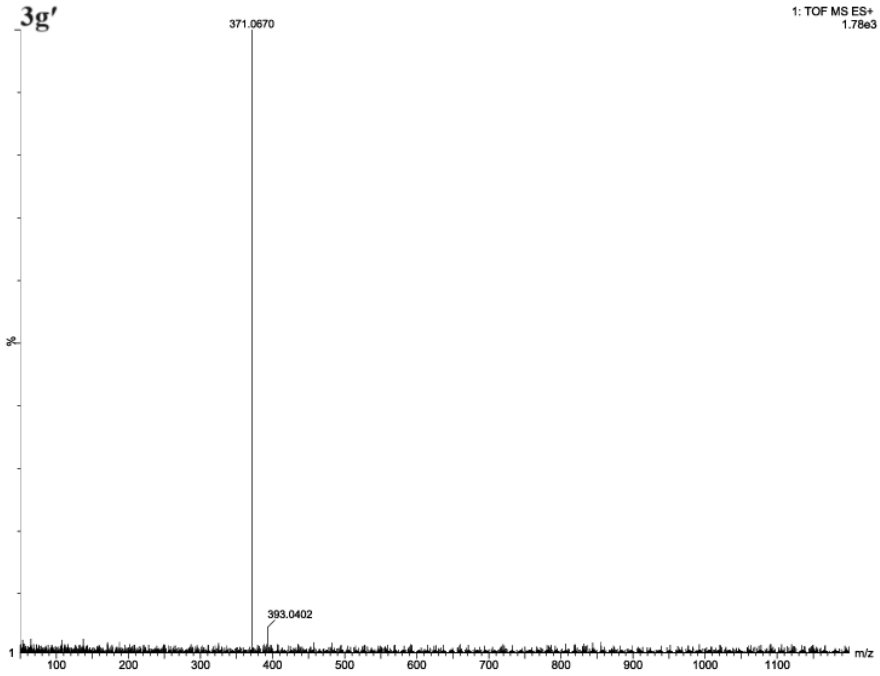

Figure A72: HRMS Spectra for the compound **3g′**.

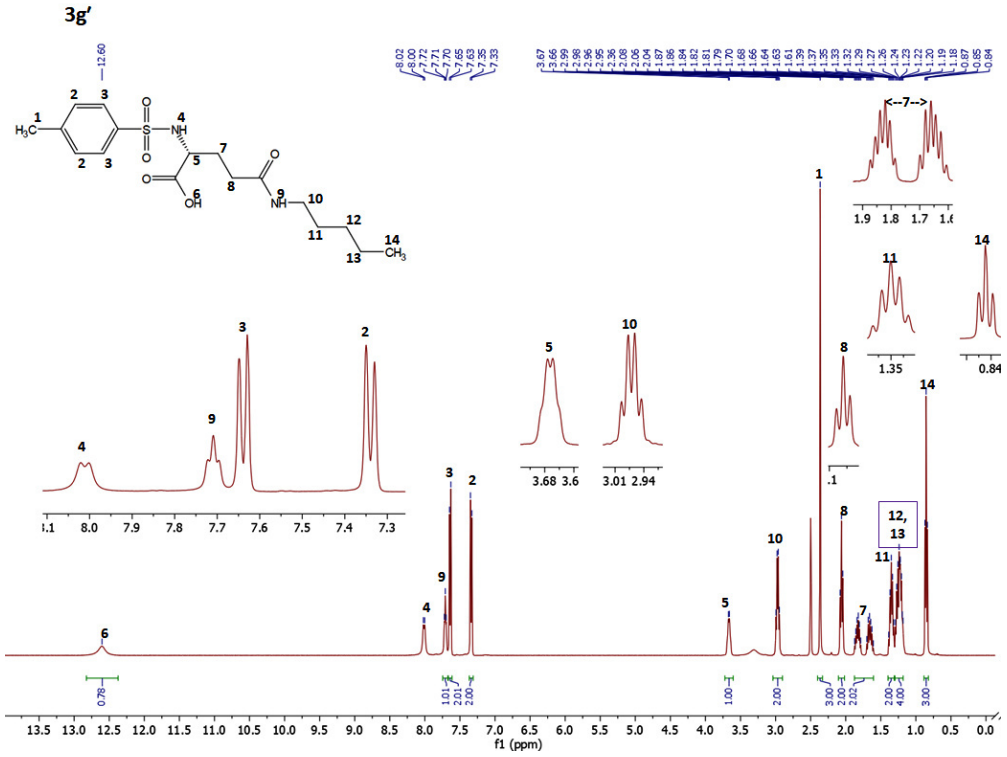

Figure A73: ^{1}H NMR Spectra for the compound **3g′**.

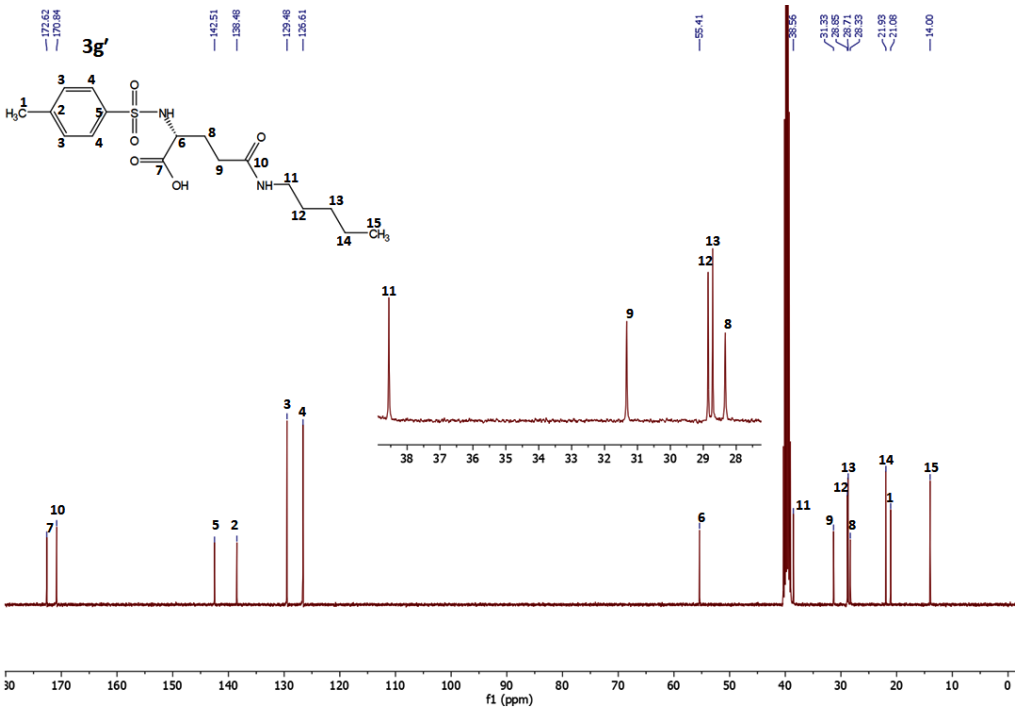

Figure A74: ^{13}C NMR Spectra for the compound **3g′**.

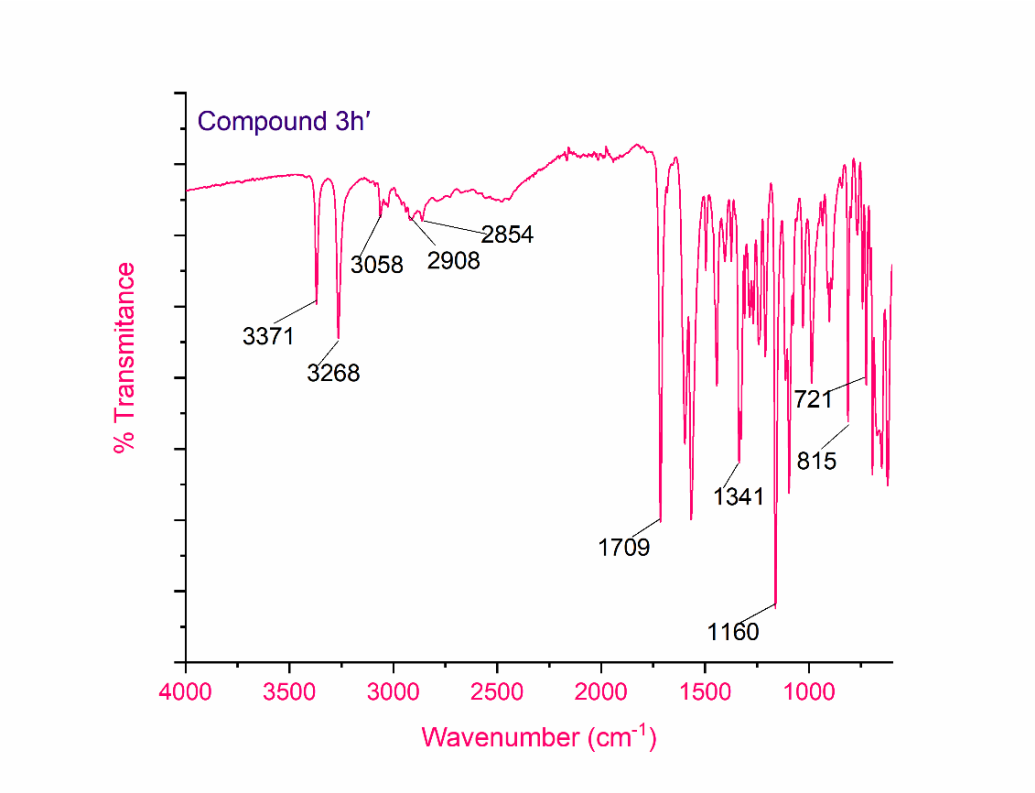

Figure A75: FT-IR Spectra for the compound **3h′**.

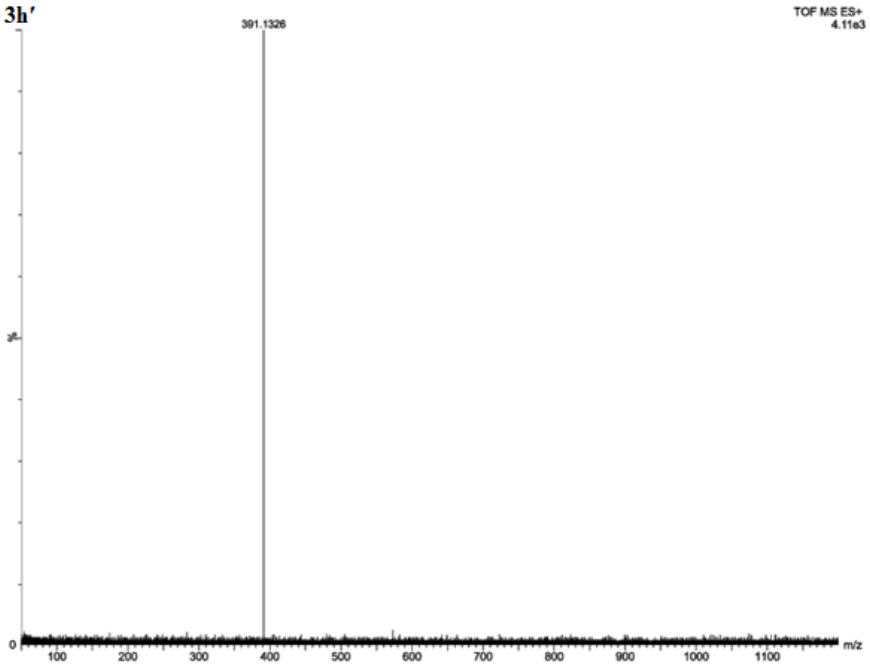

Figure A76: HRMS Spectra for the compound **3h′**.

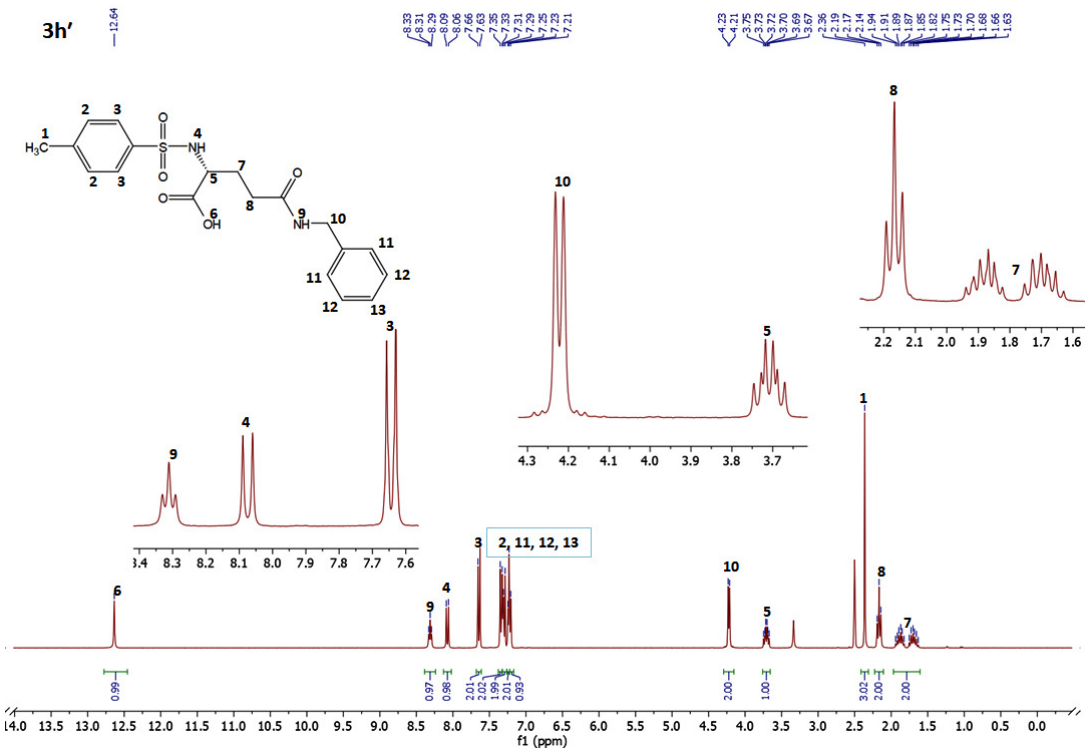

Figure A77: ^{1}H NMR Spectra for the compound **3h′**.

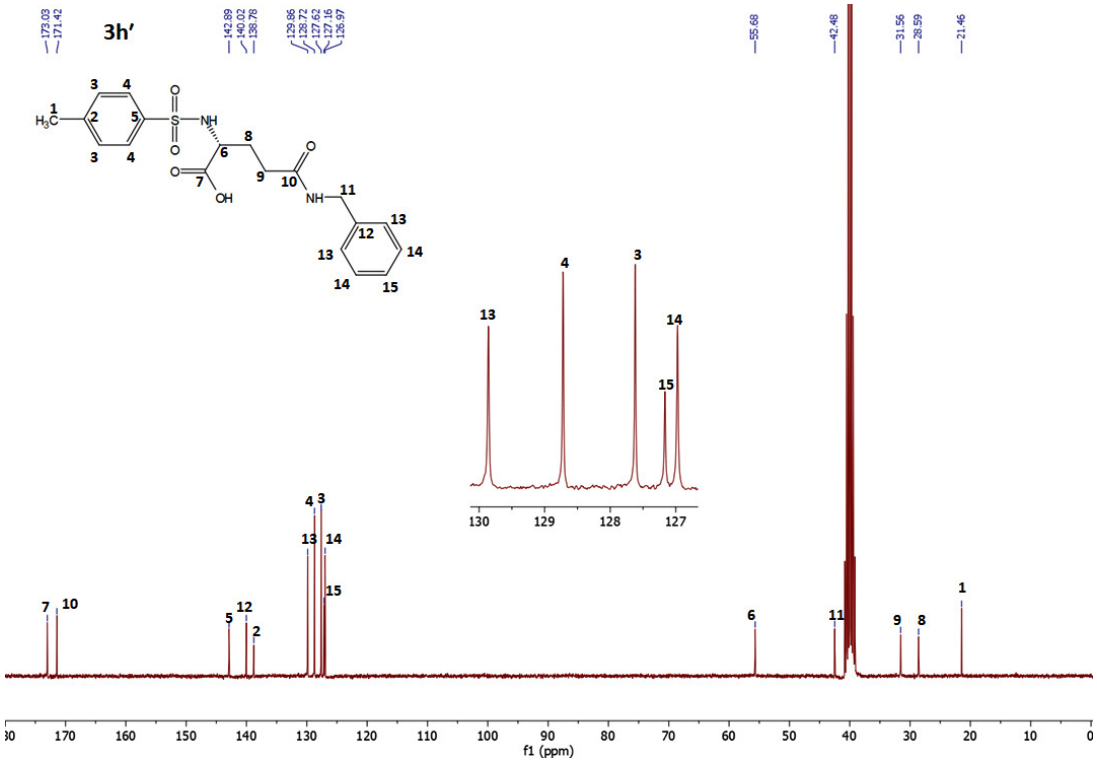

Figure A78: ^{13}C NMR Spectra for the compound **3h′**.

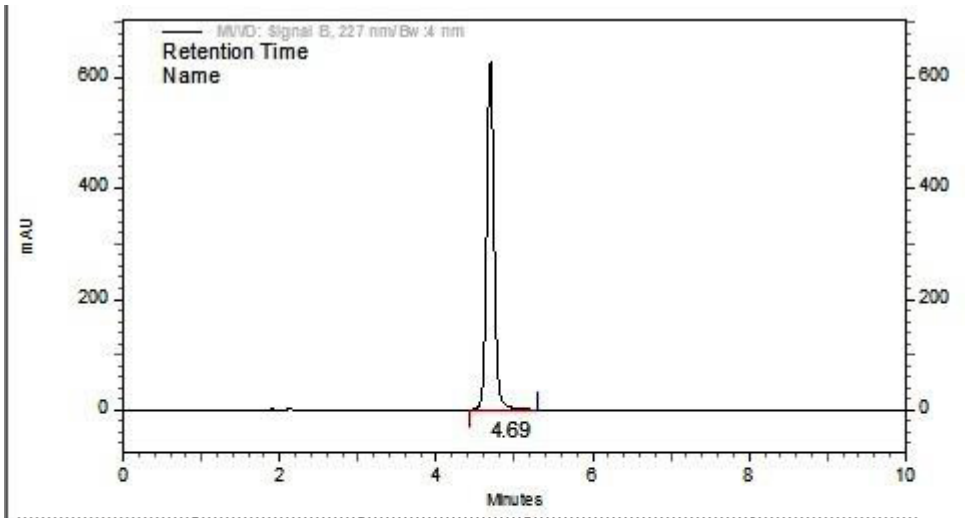

MWD: Signal B, 227 nm/Bw:4 nm Results

Retention Time	Area	Area %	Theoretical plates (USP)	Asymmetry (10%)
4.69	8663051	100.00	12829	1.12
Totals				
	8663051	100.00		

Figure A79: HPLC Spectra for the compound **3h′**.

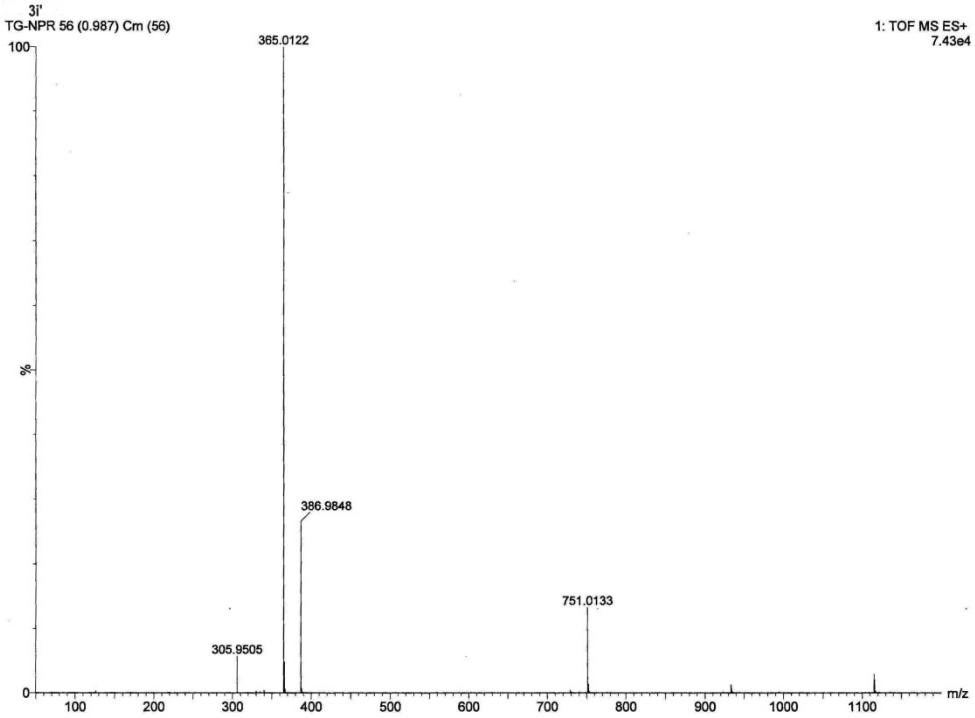

Figure A80: HRMS Spectra for the compound **3i′**.

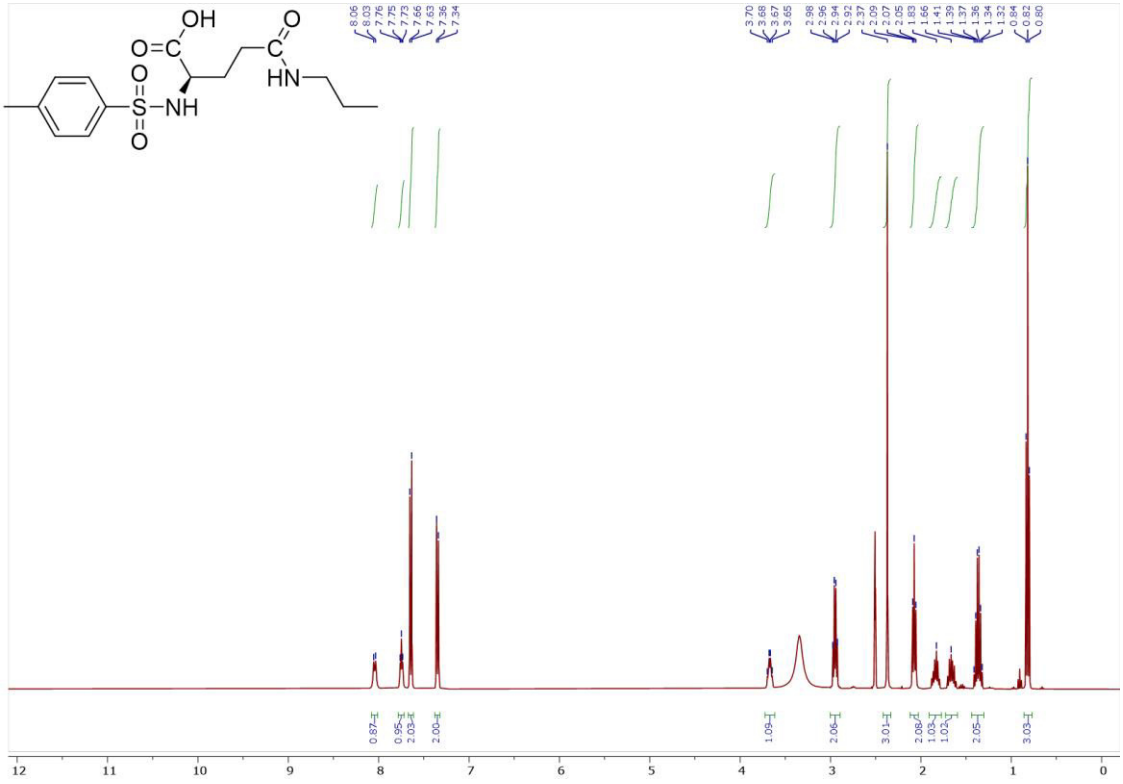

Figure A81: ^{1}H NMR Spectra for the compound **3i′**.

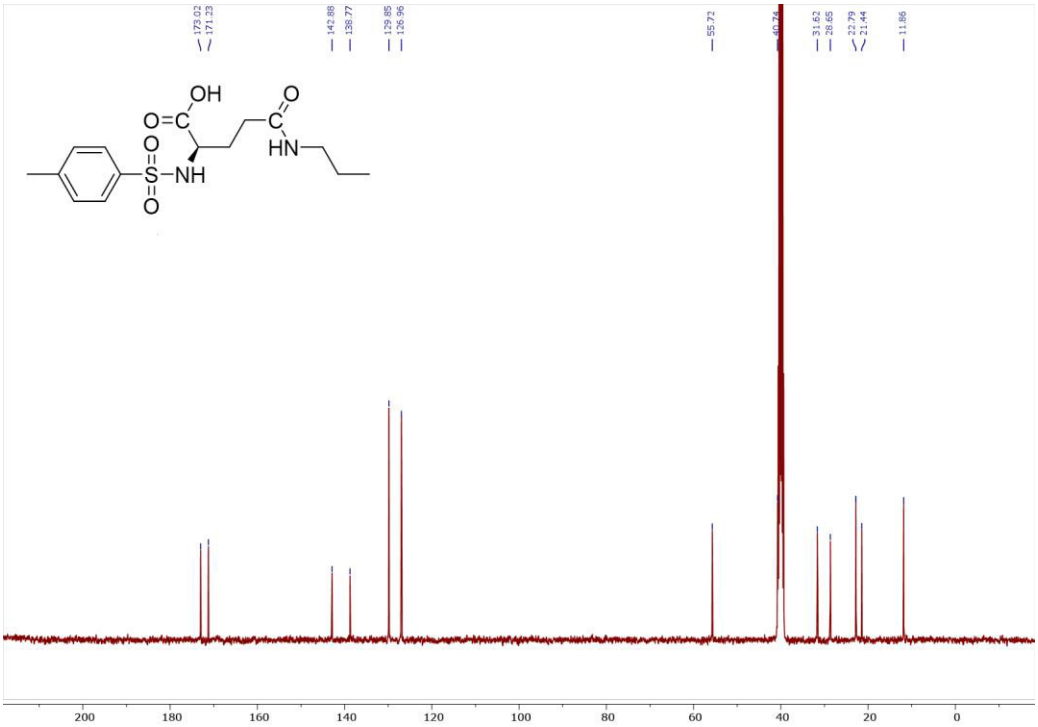

Figure A82: ^{13}C NMR Spectra for the compound **3i′**.

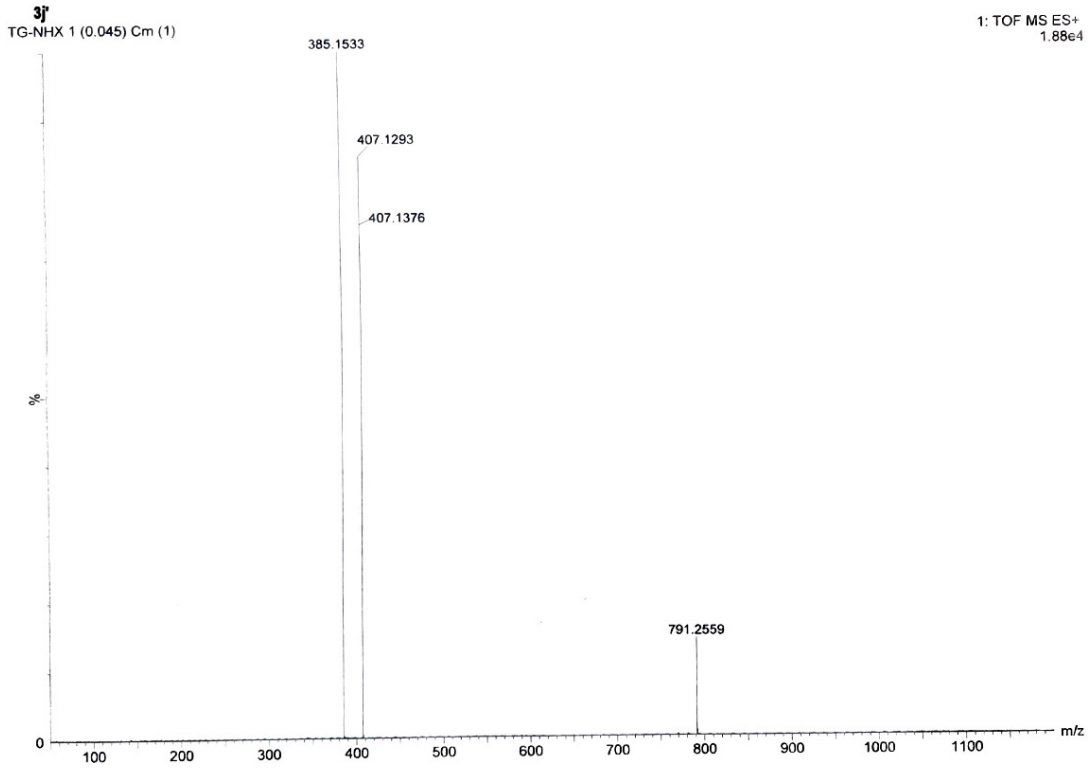

Figure A83: HRMS Spectra for the compound **3j′**.

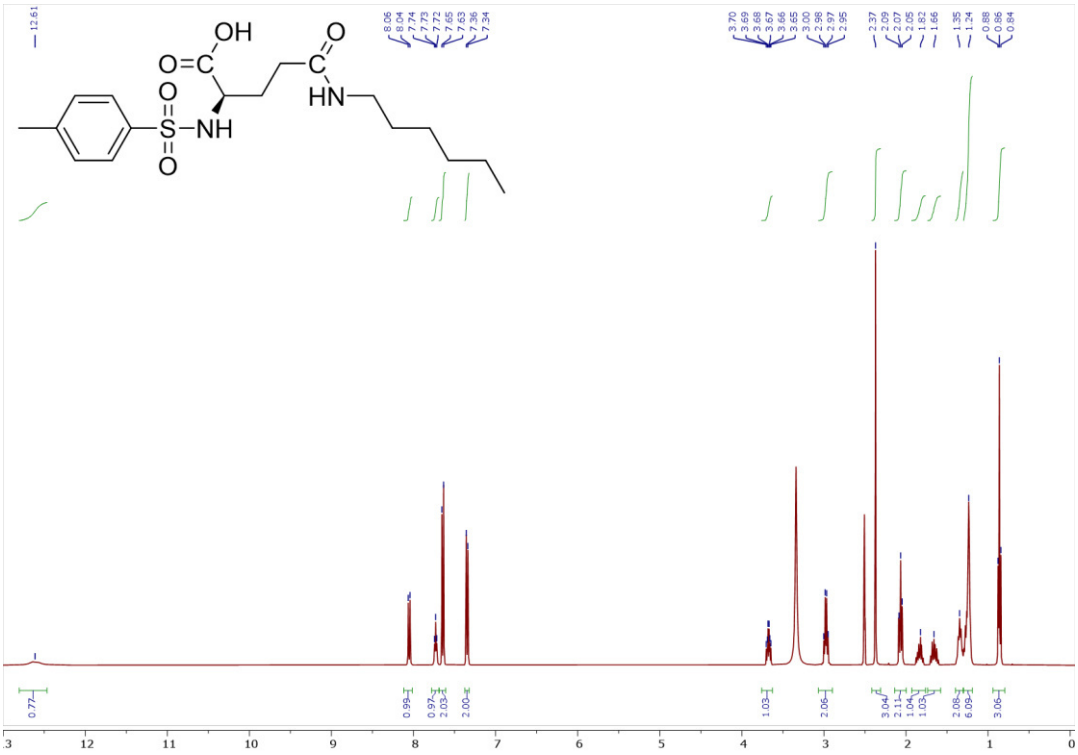

Figure A84: ^{1}H NMR Spectra for the compound **3j′**.

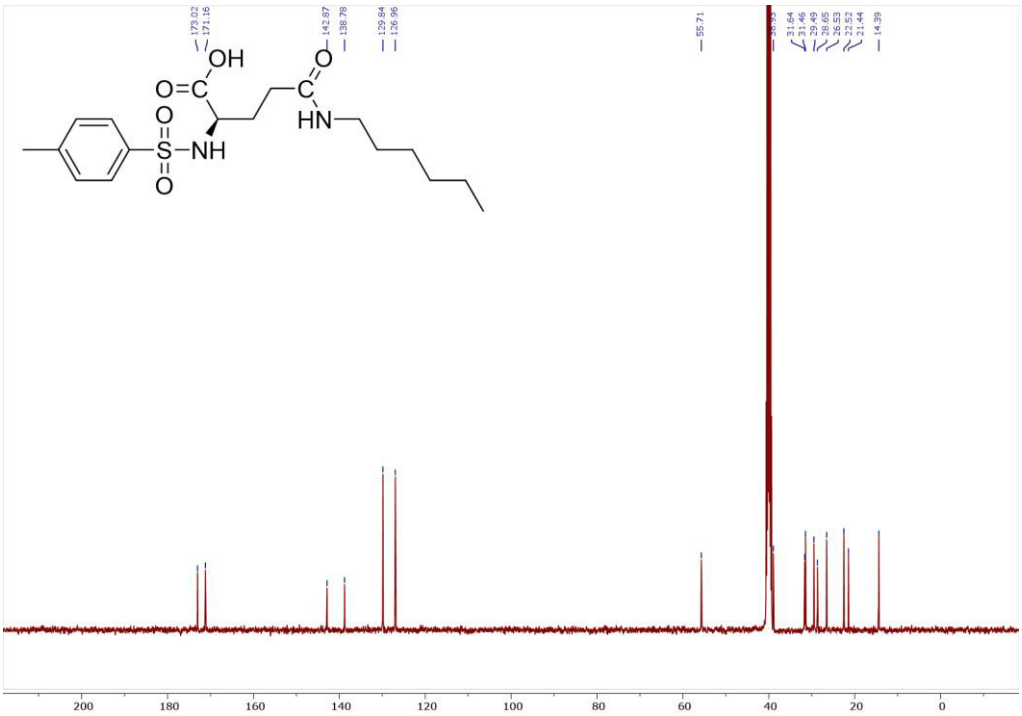

Figure A85: ^{13}C NMR Spectra for the compound **3j′**.

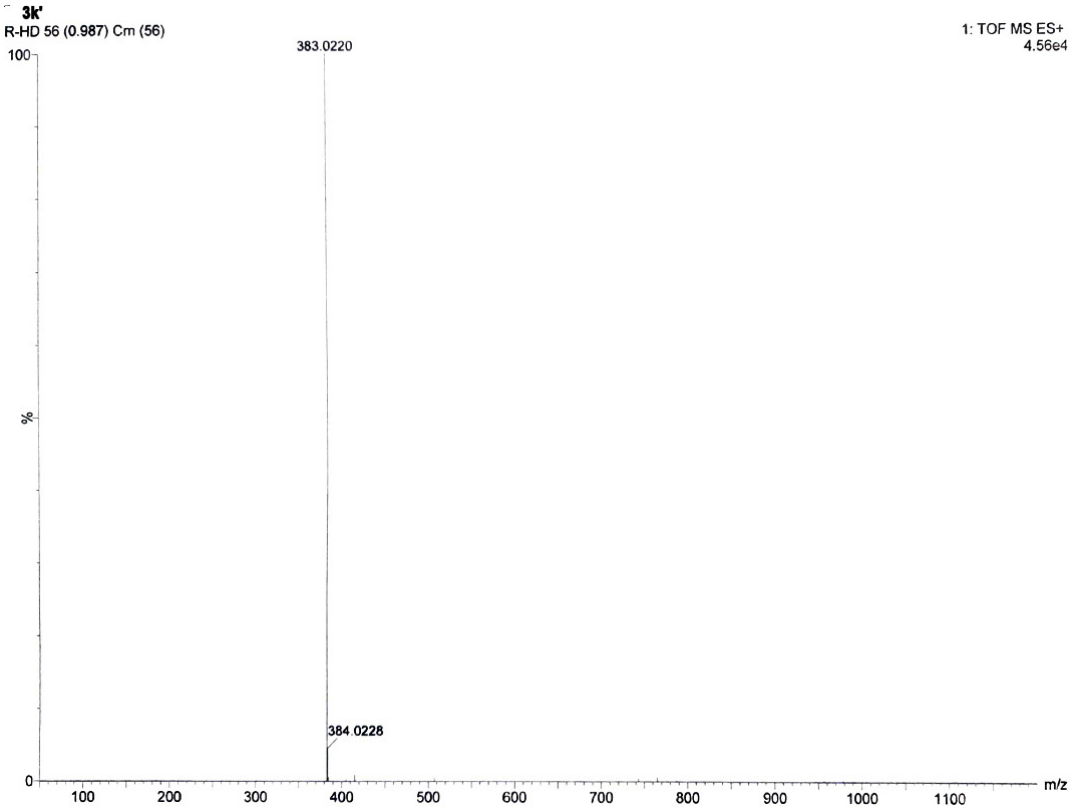

Figure A86: HRMS Spectra for the compound **3k′**.

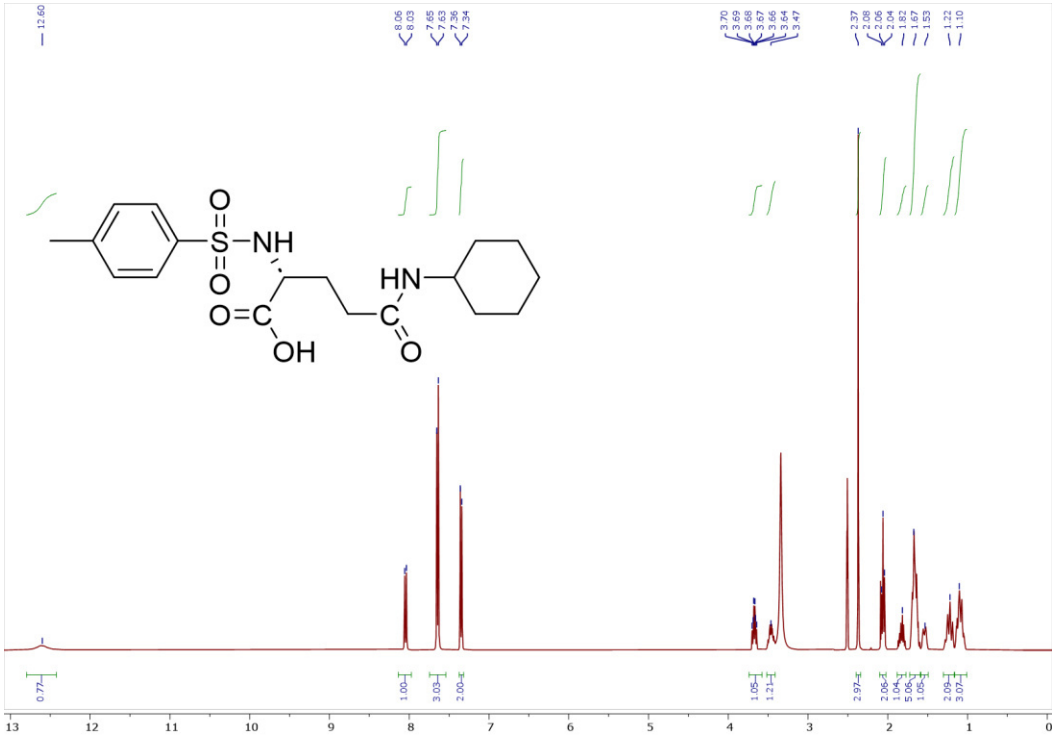

Figure A87: ^{1}H NMR Spectra for the compound **3k′**.

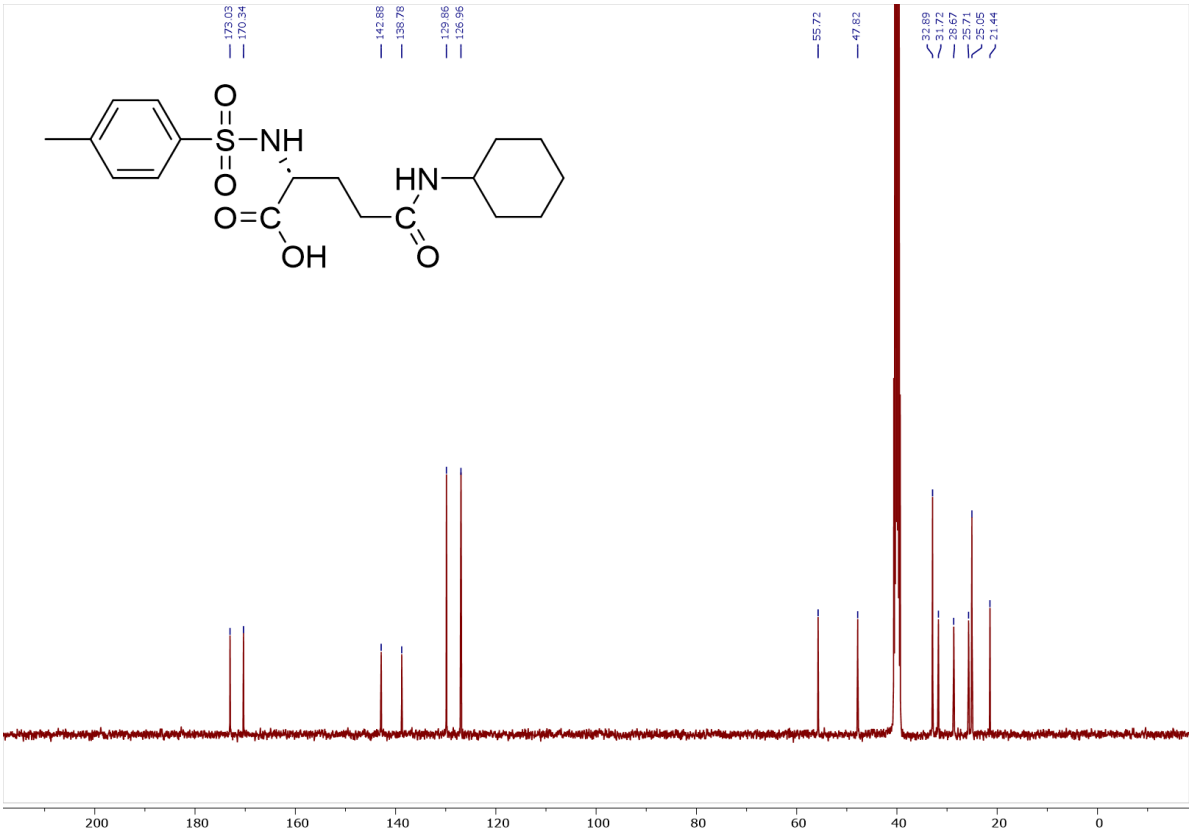

Figure A88: ^{13}C NMR Spectra for the compound **3k′**.

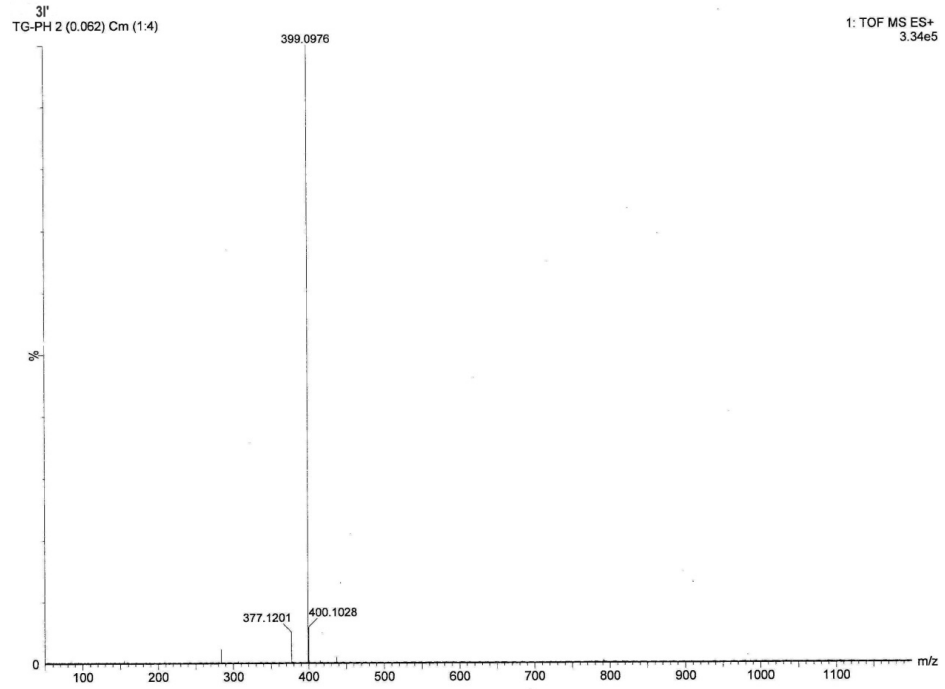

Figure A89: HRMS Spectra for the compound **3l′**.

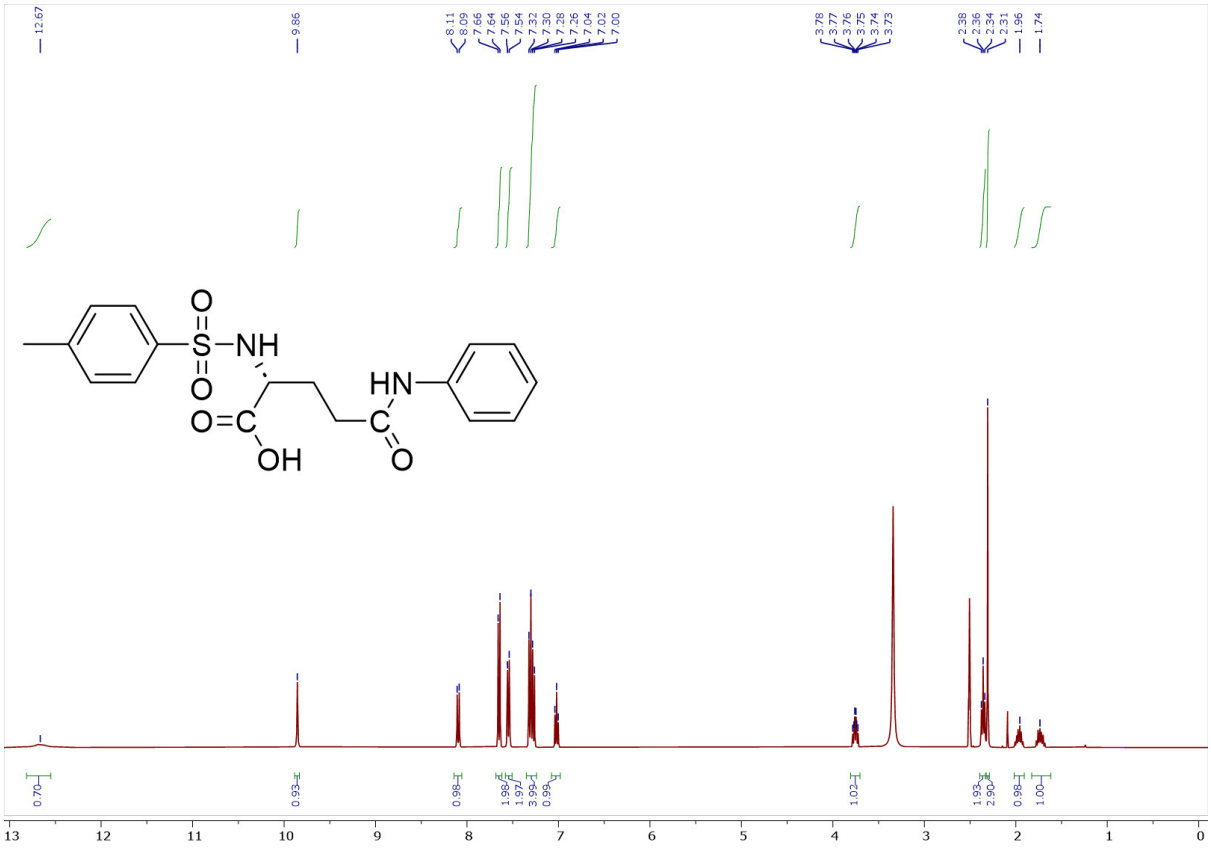

Figure A90: ^{1}H NMR Spectra for the compound **3l′**.

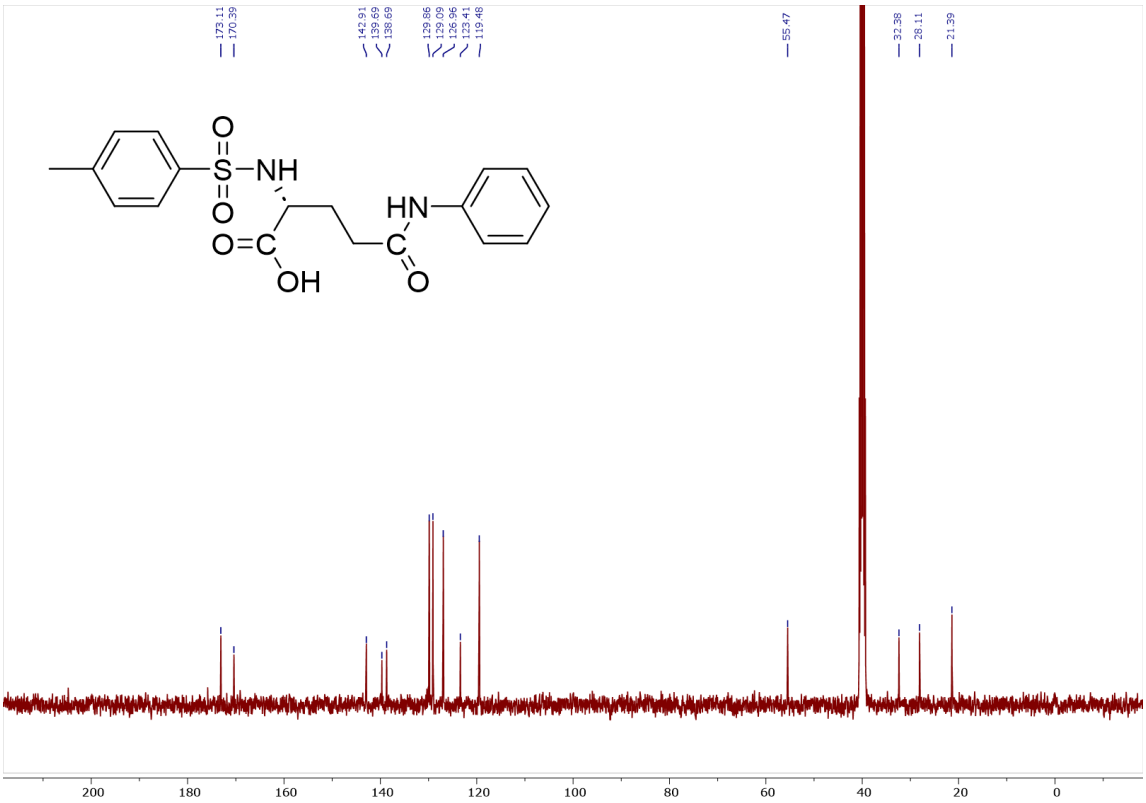

Figure A91: ^{13}C NMR Spectra for the compound **3l′**.

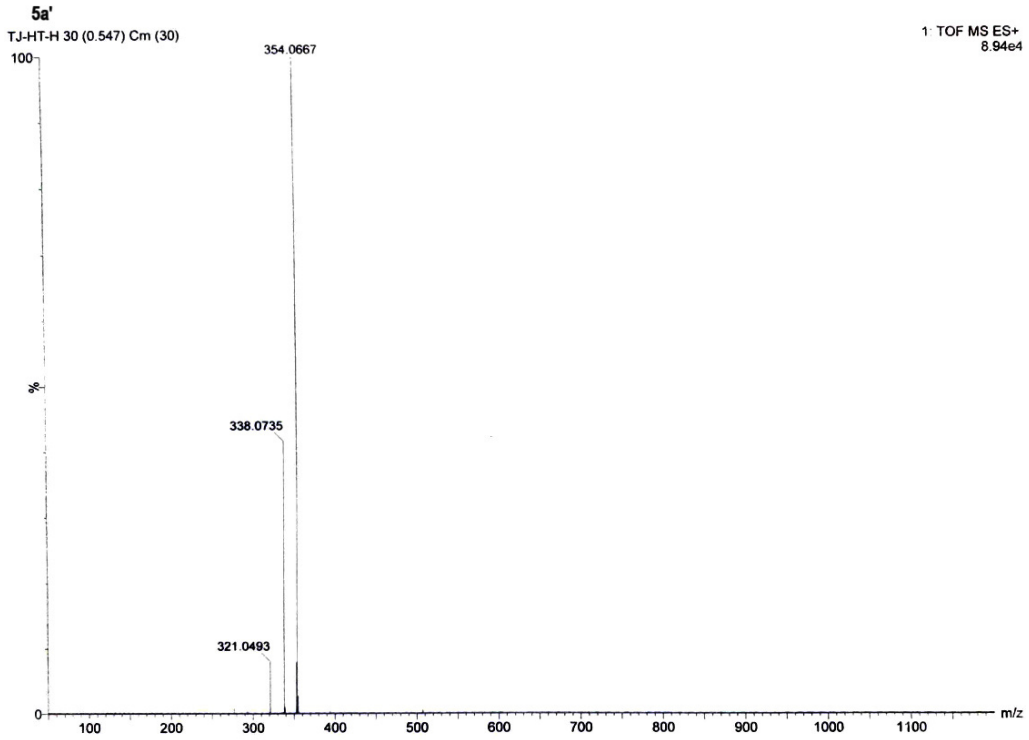

Figure A92: HRMS Spectra for the compound **5a′**.

Figure A93: ^{1}H NMR Spectra for the compound **5a′**.

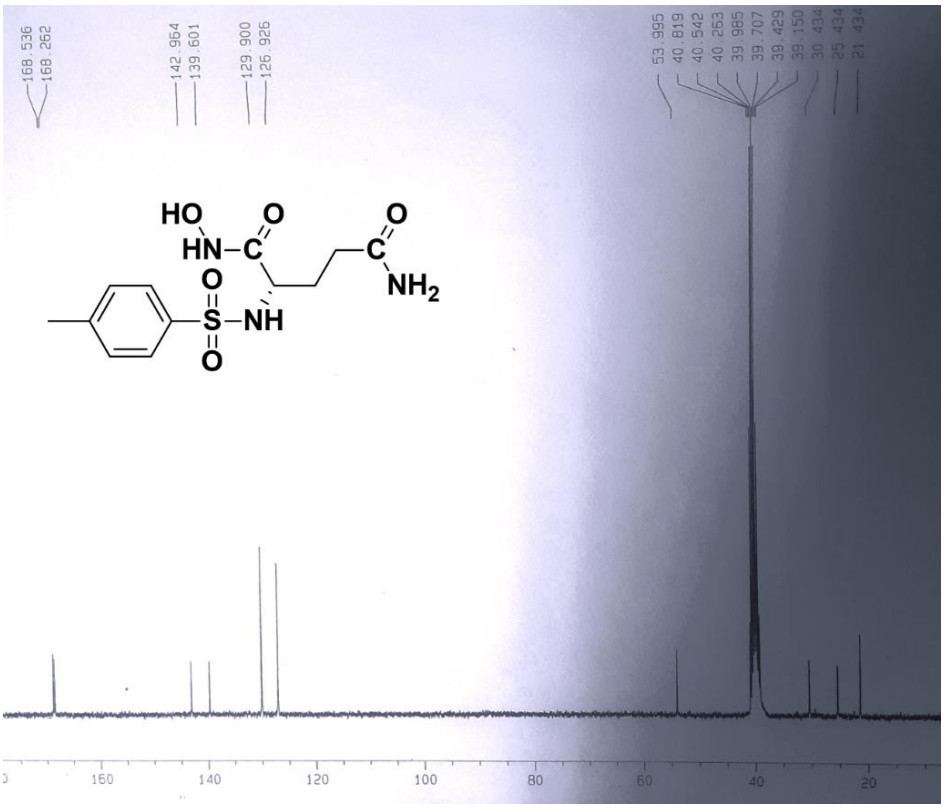

Figure A94: ^{13}C NMR Spectra for the compound **5a′**.

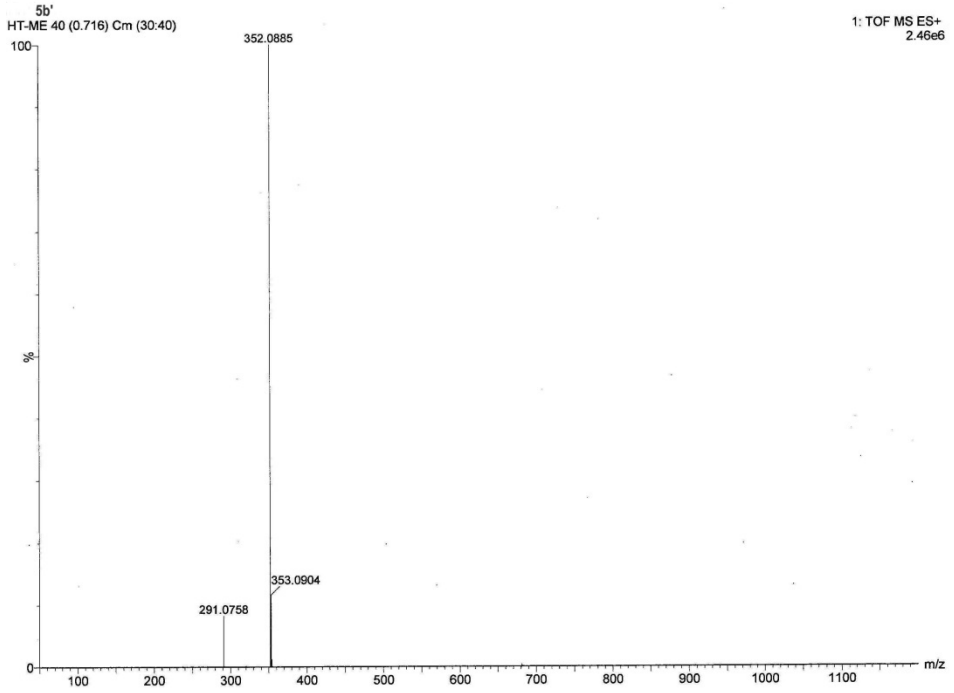

Figure A95: HRMS Spectra for the compound **5b′**.

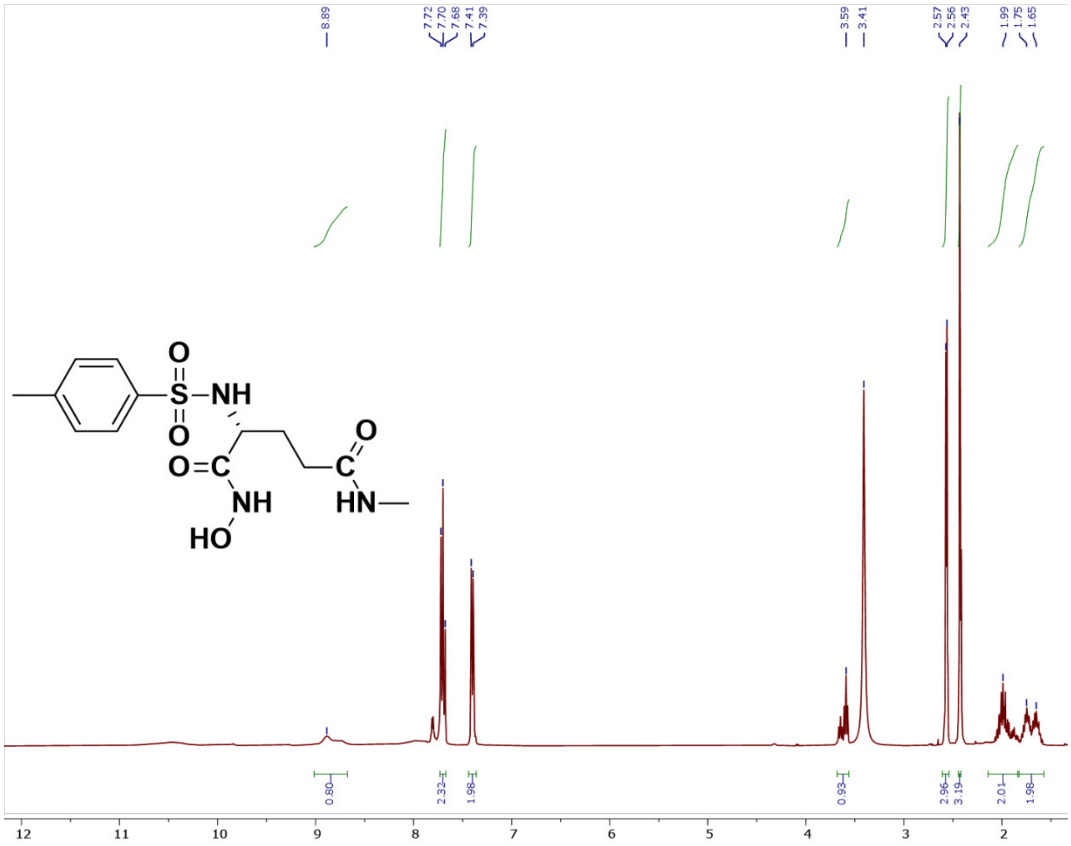

Figure A96: ^{1}H NMR Spectra for the compound **5b′**.

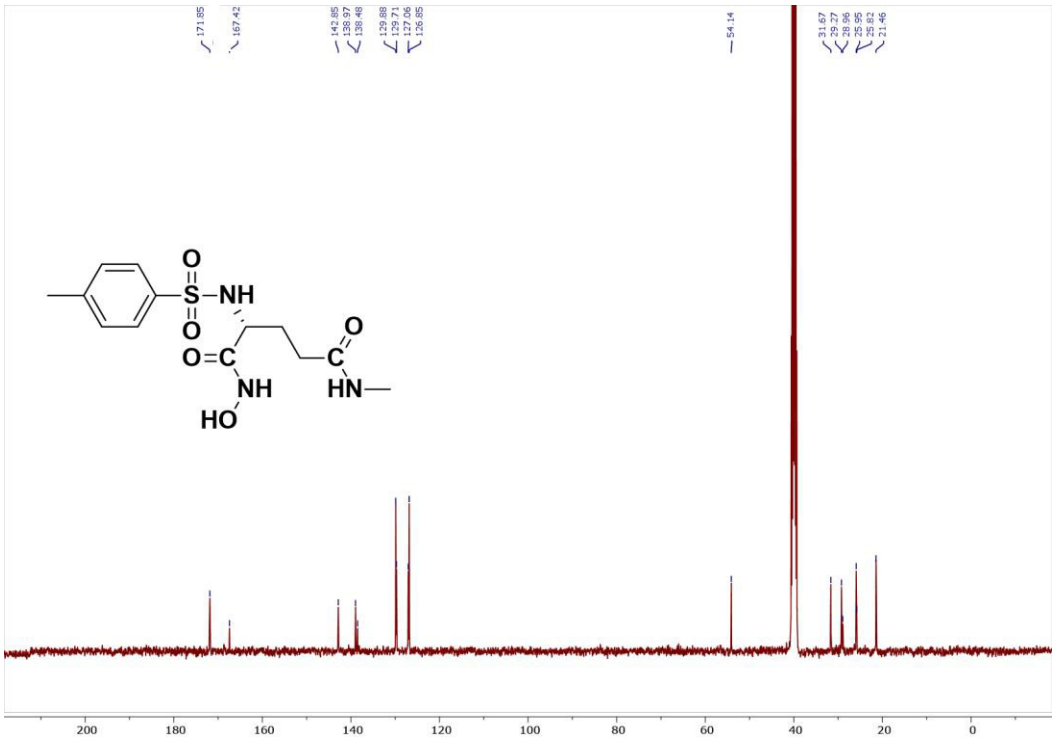

Figure A97: ^{13}C NMR Spectra for the compound **5b′**.

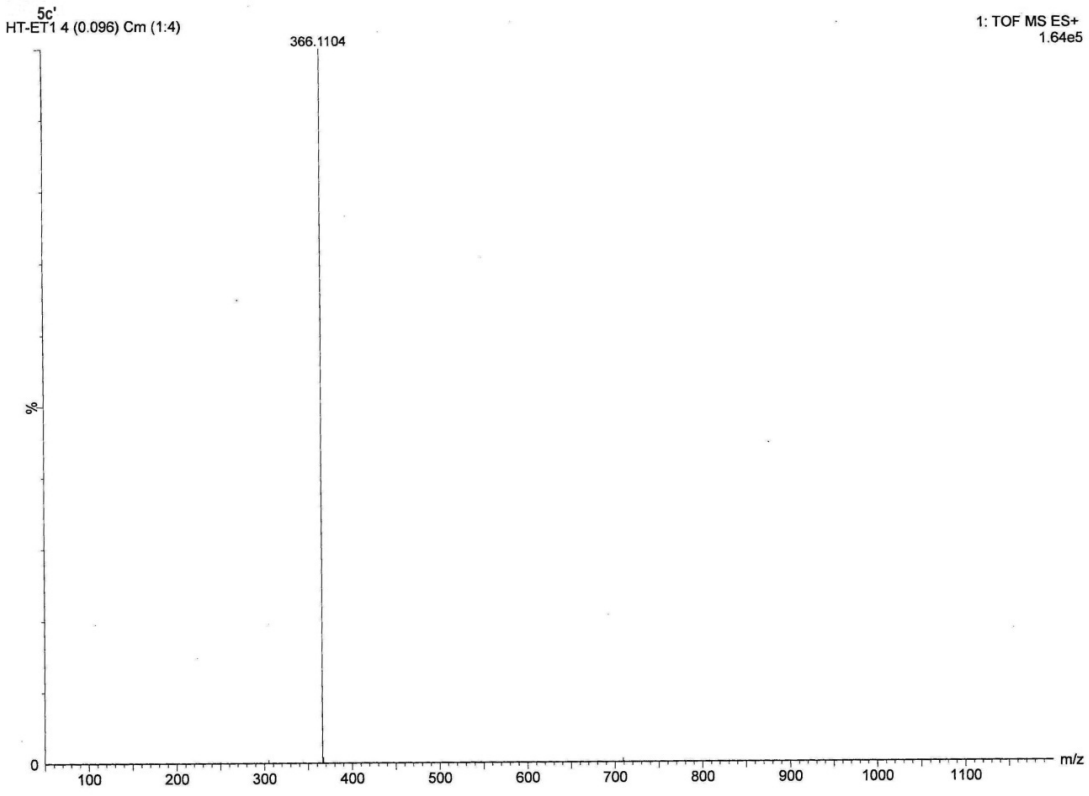

Figure A98: HRMS Spectra for the compound **5c′**.

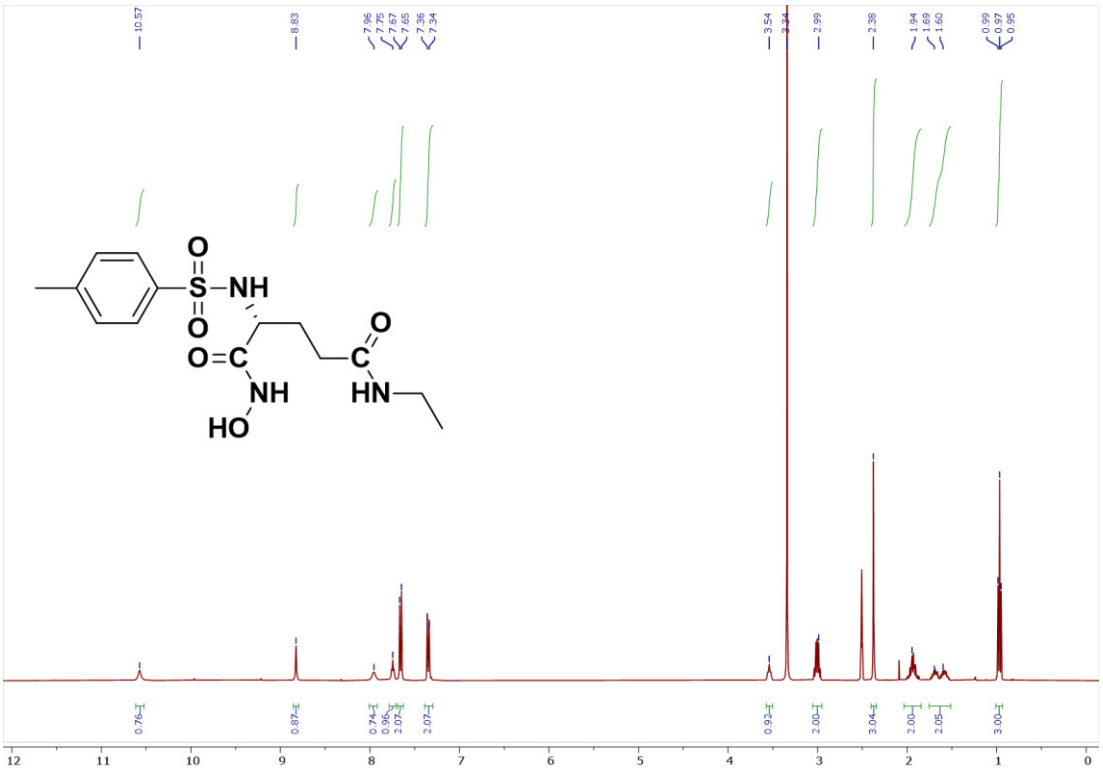

Figure A99: ^{1}H NMR Spectra for the compound **5c′**.

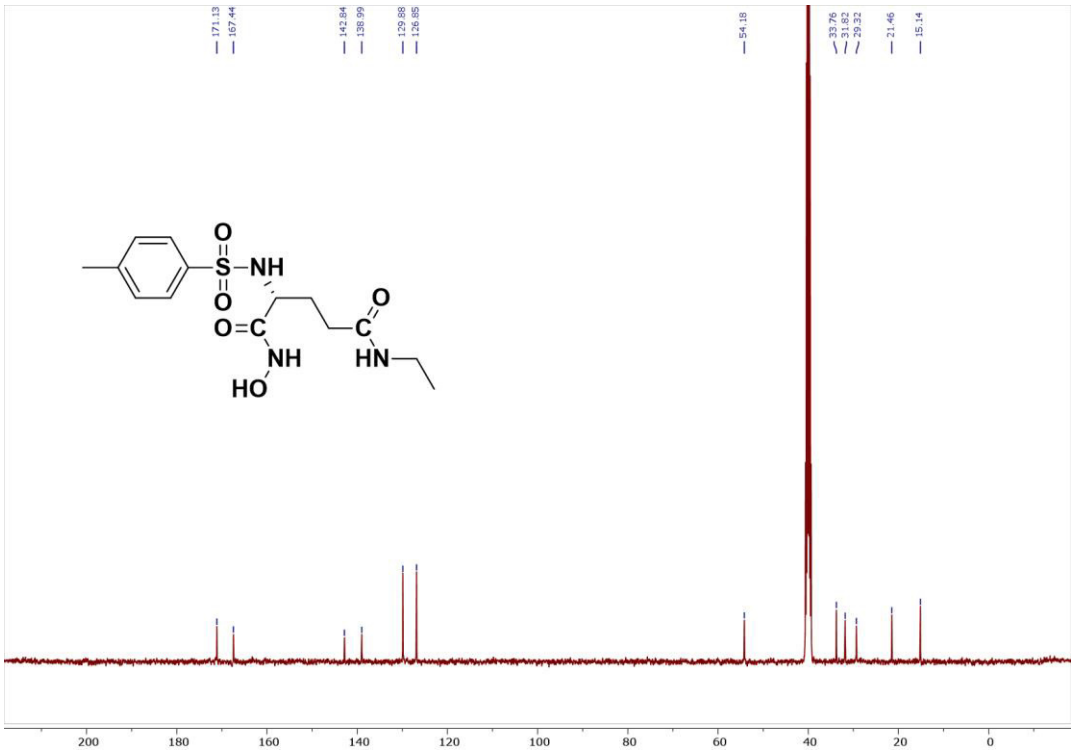

Figure A100: ^{13}C NMR Spectra for the compound **5c′**.

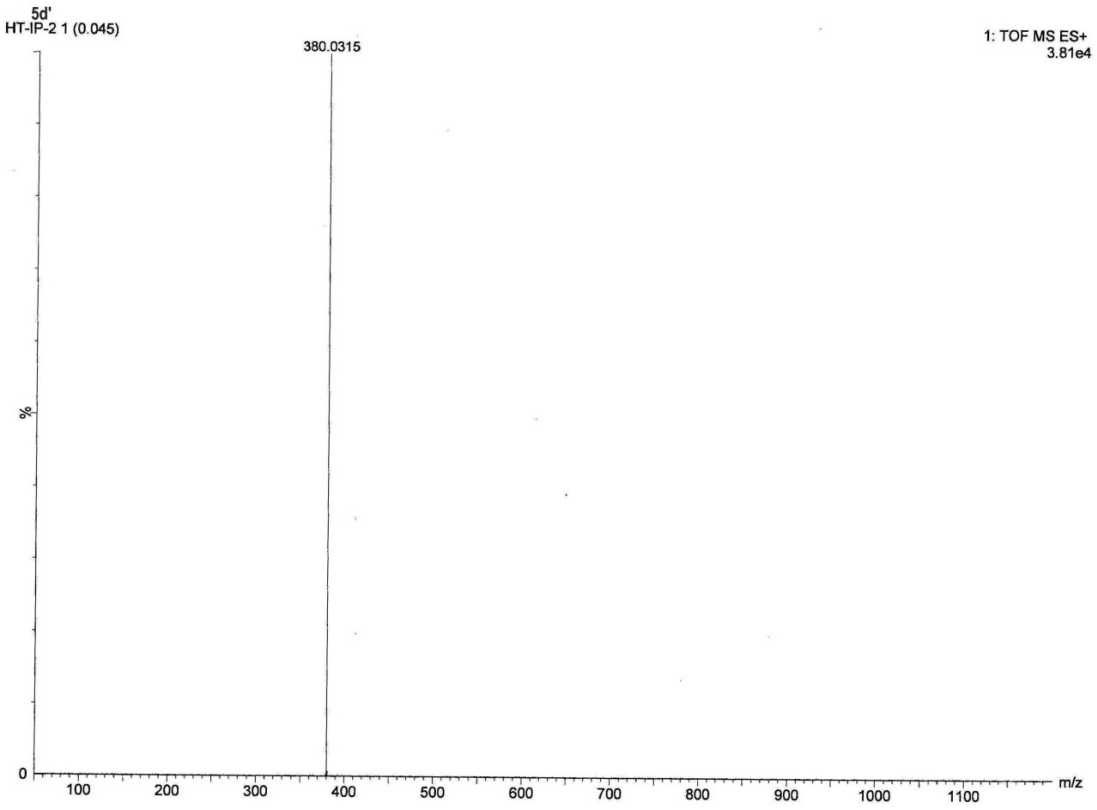

Figure A101: HRMS Spectra for the compound **5d′**.

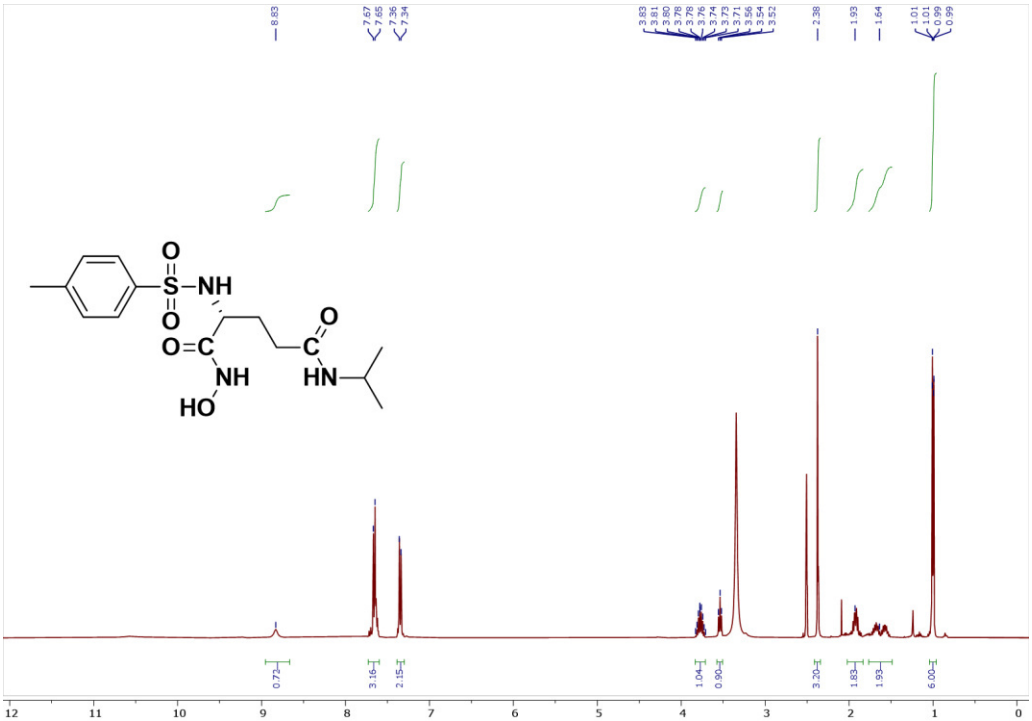

Figure A102: ^{1}H NMR Spectra for the compound **5d′**.

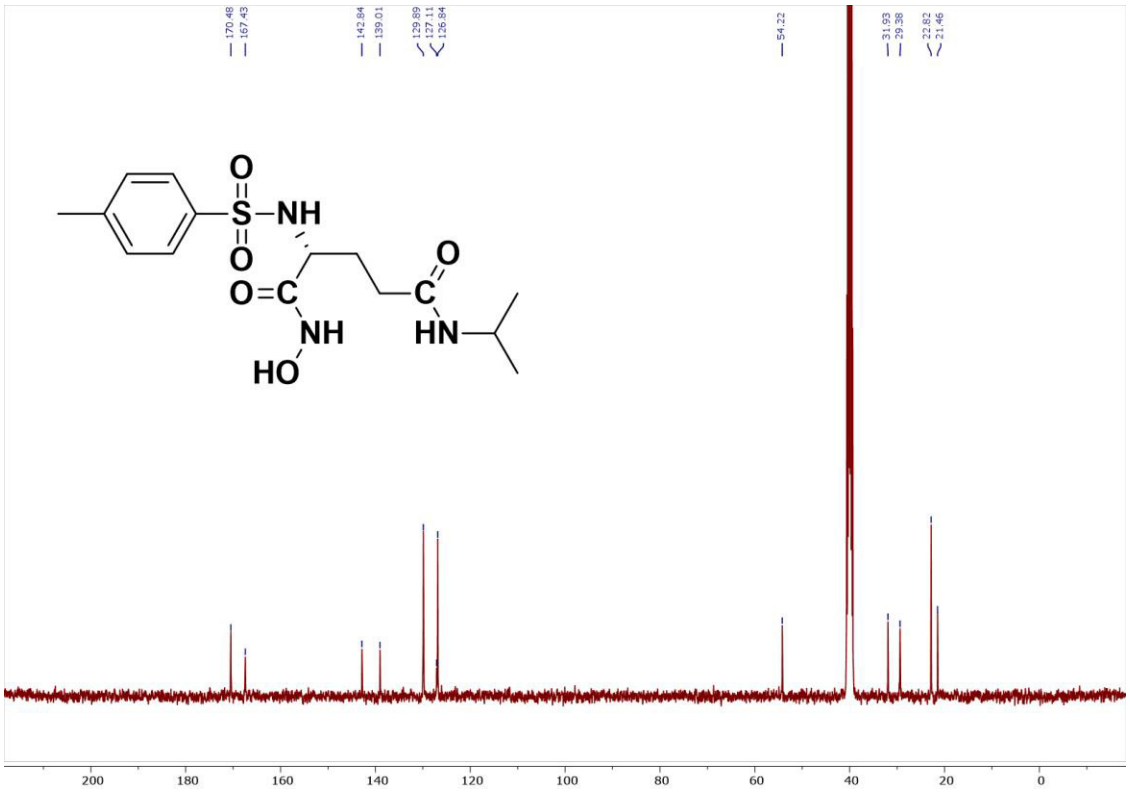

Figure A103: ^{13}C NMR Spectra for the compound **5d′**.

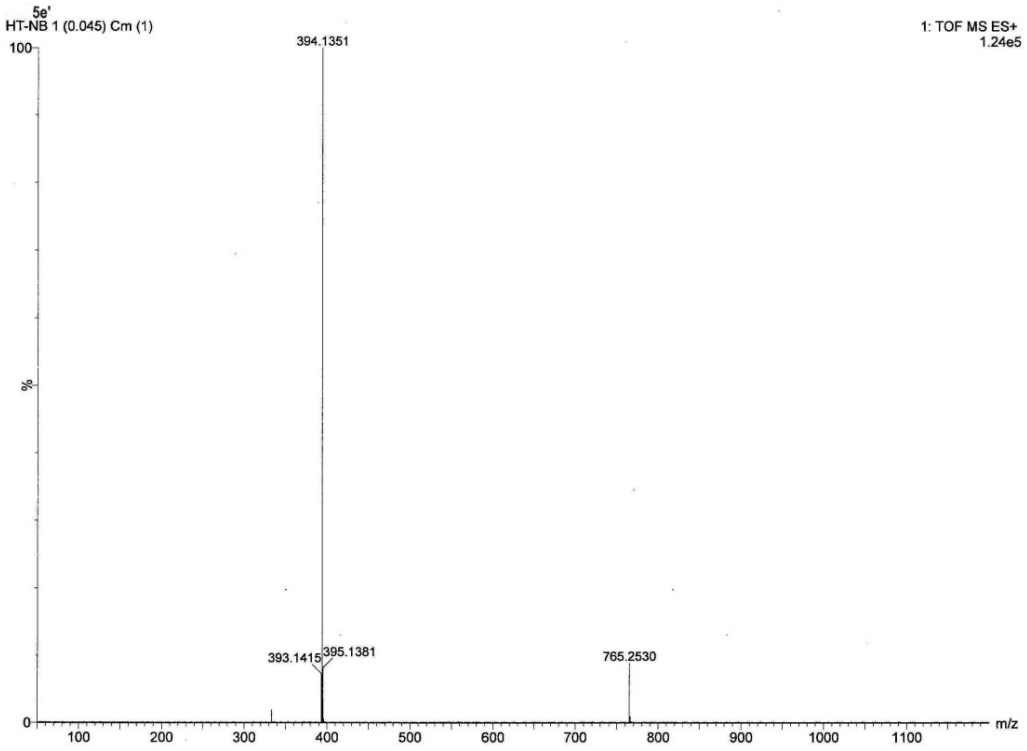

Figure A104: HRMS Spectra for the compound **5e′**.

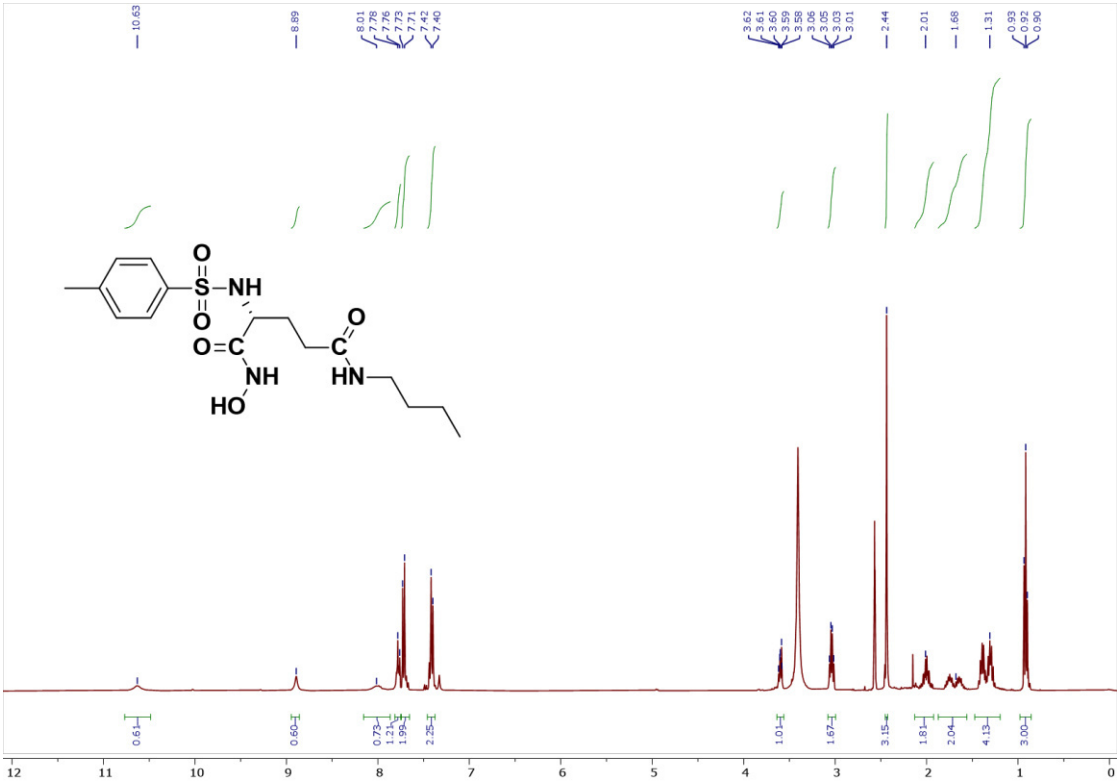

Figure A105: ^{1}H NMR Spectra for the compound **5e′**.

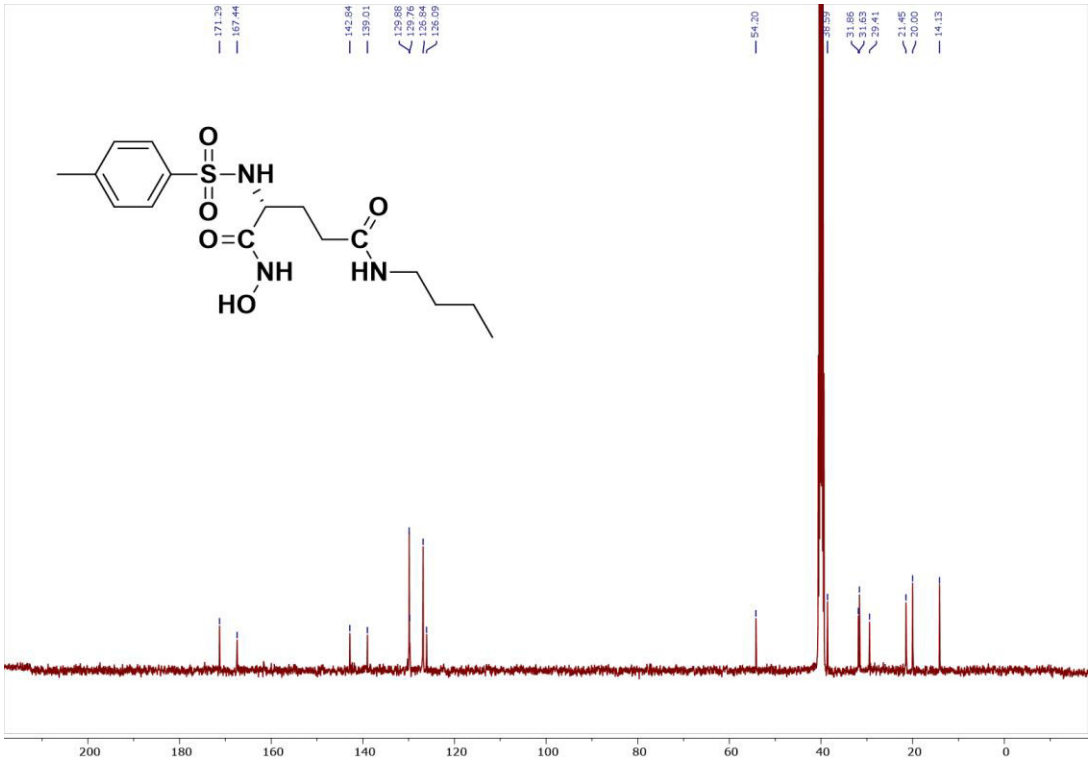

Figure A106: ^{13}C NMR Spectra for the compound **5e′**.

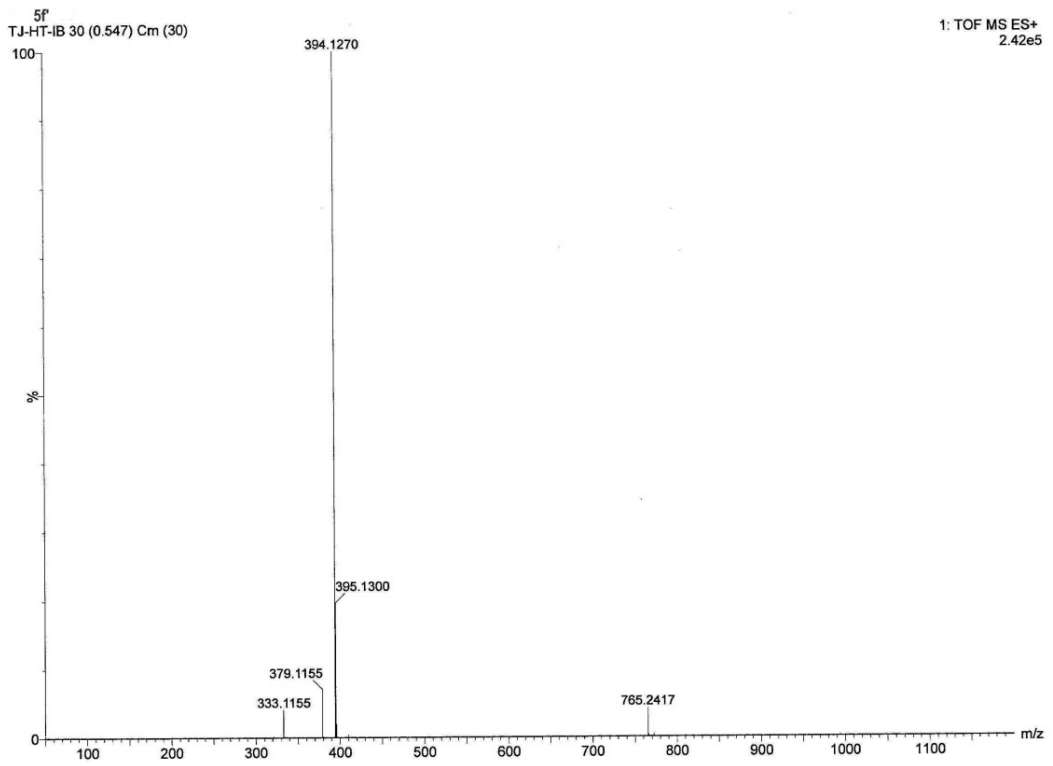

Figure A107: HRMS Spectra for the compound **5f′**.

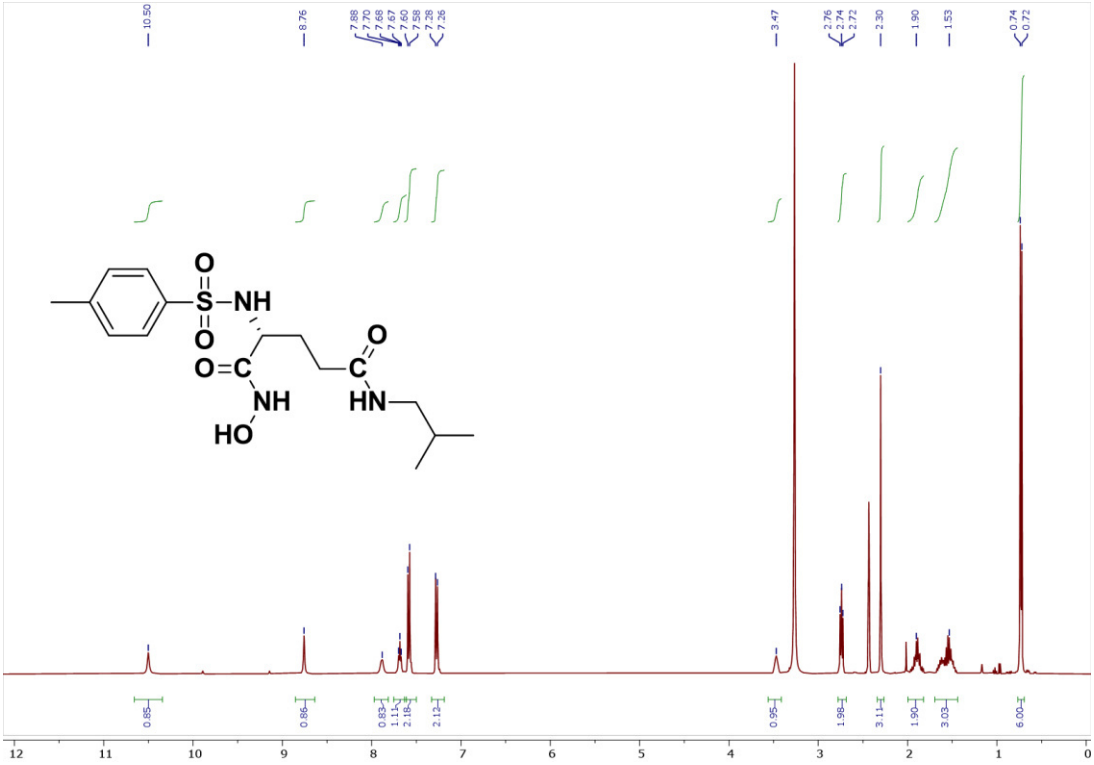

Figure A108: ^{1}H NMR Spectra for the compound **5f′**.

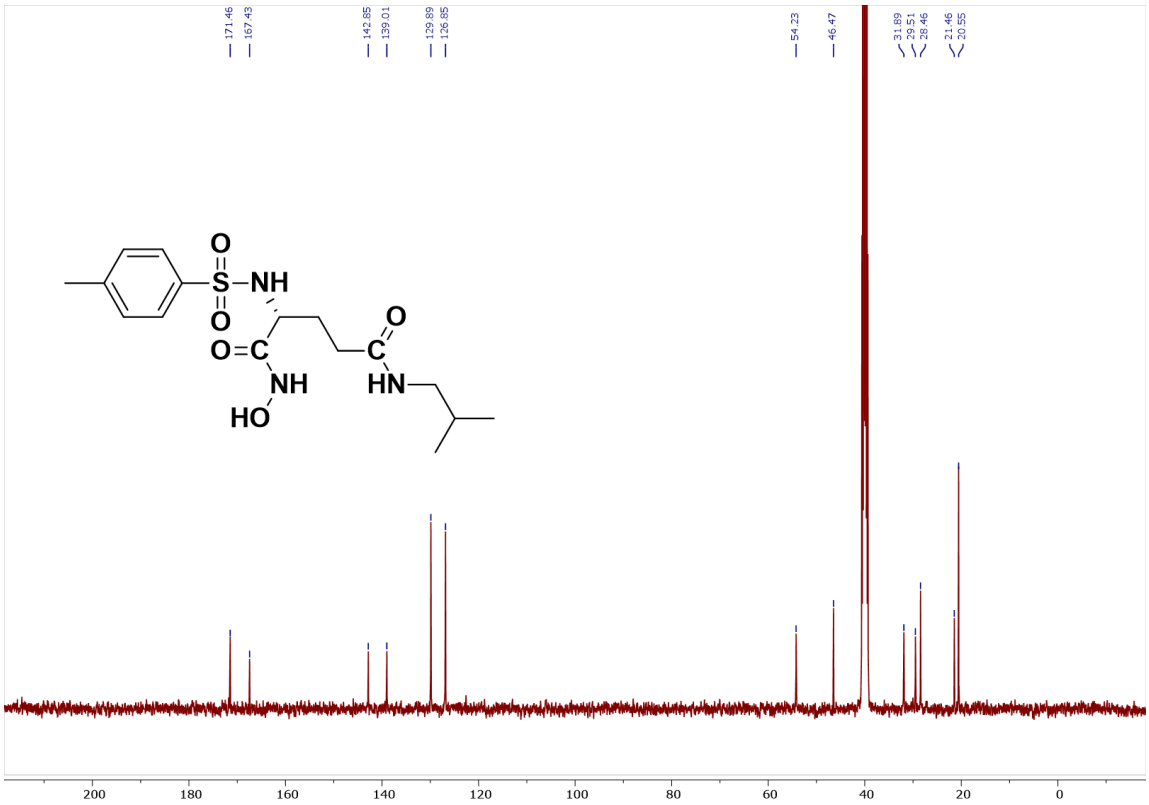

Figure A109: ^{13}C NMR Spectra for the compound **5f′**.

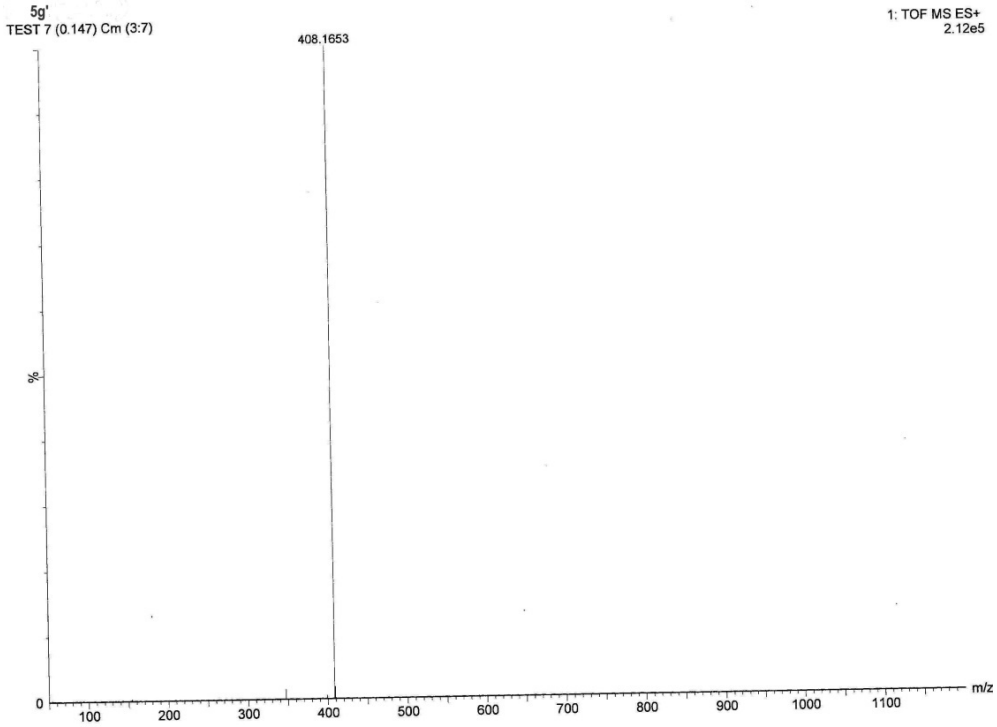

Figure A110: HRMS Spectra for the compound **5g′**.

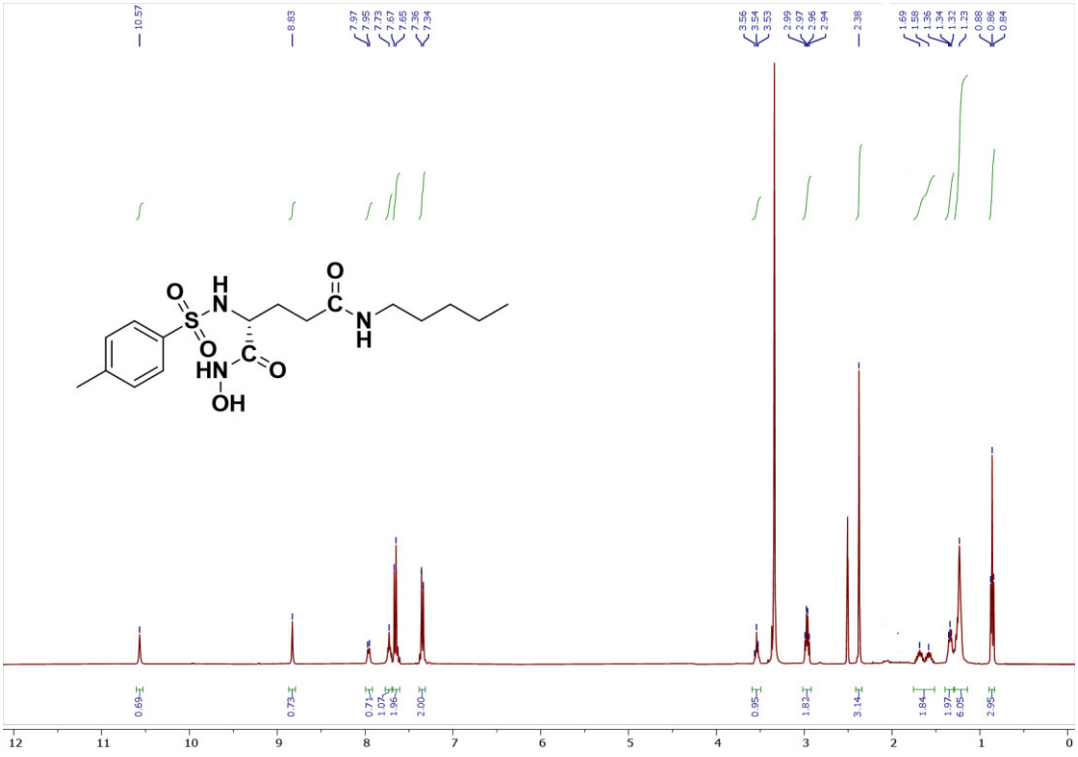

Figure A111: ^{1}H NMR Spectra for the compound **5g′**.

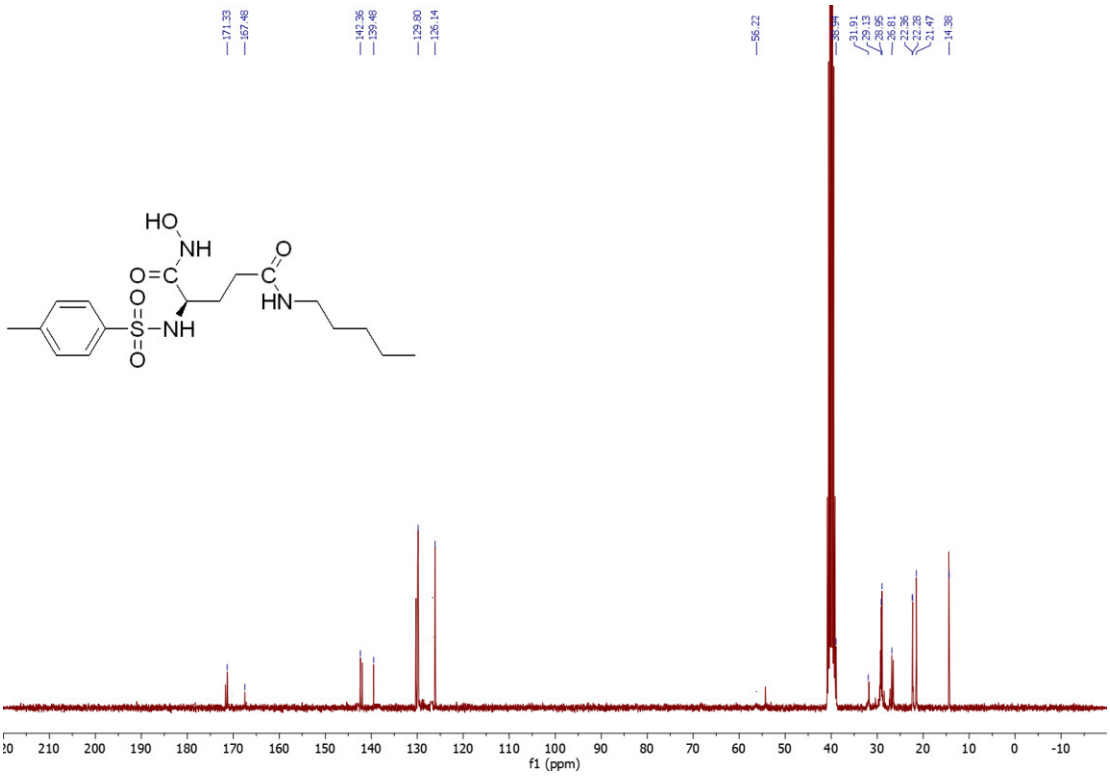

Figure A112: ^{13}C NMR Spectra for the compound **5g′**.

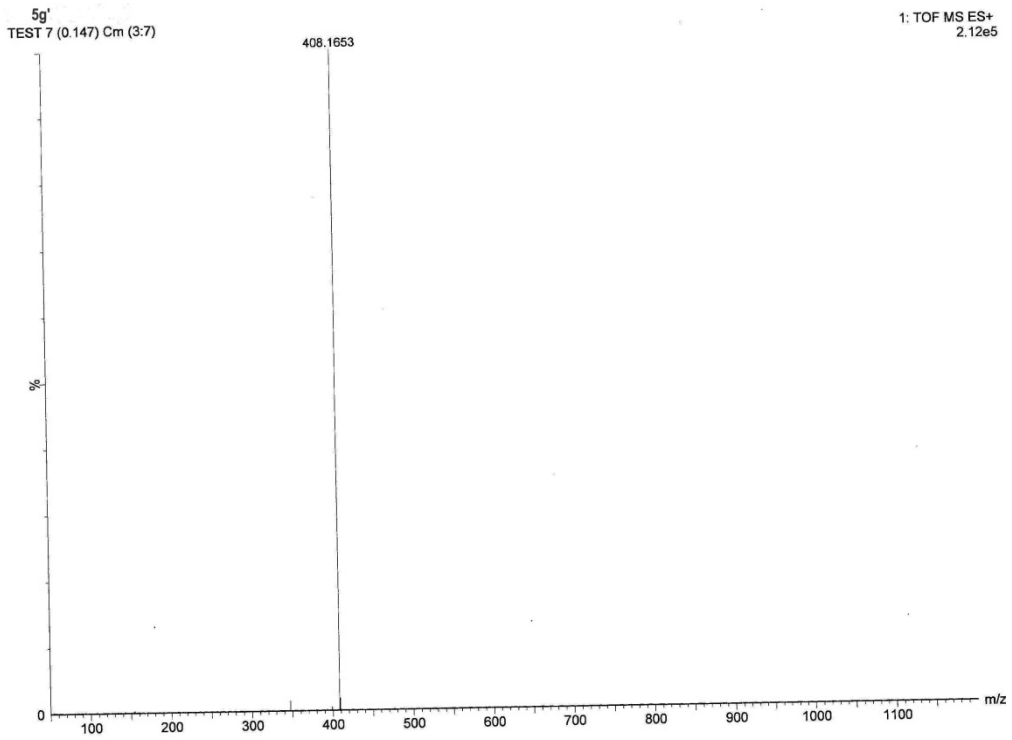

Figure A113: HRMS Spectra for the compound **5h′**.

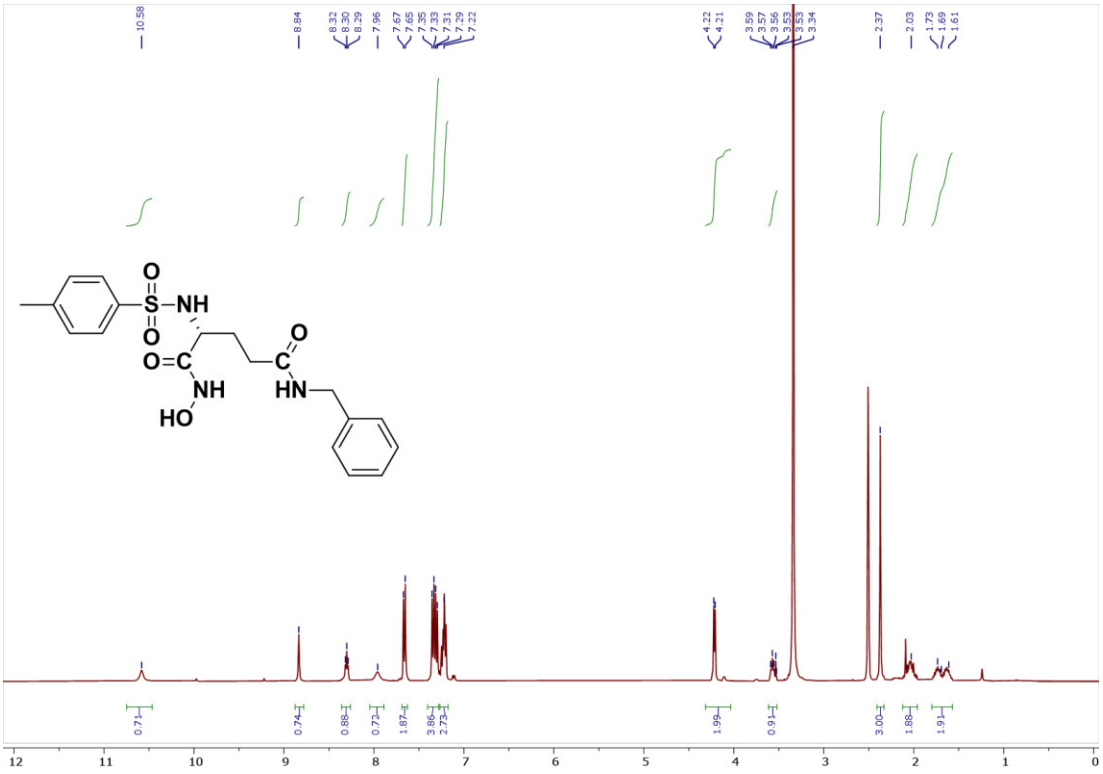

Figure A114: ^{1}H NMR Spectra for the compound **5h′**.

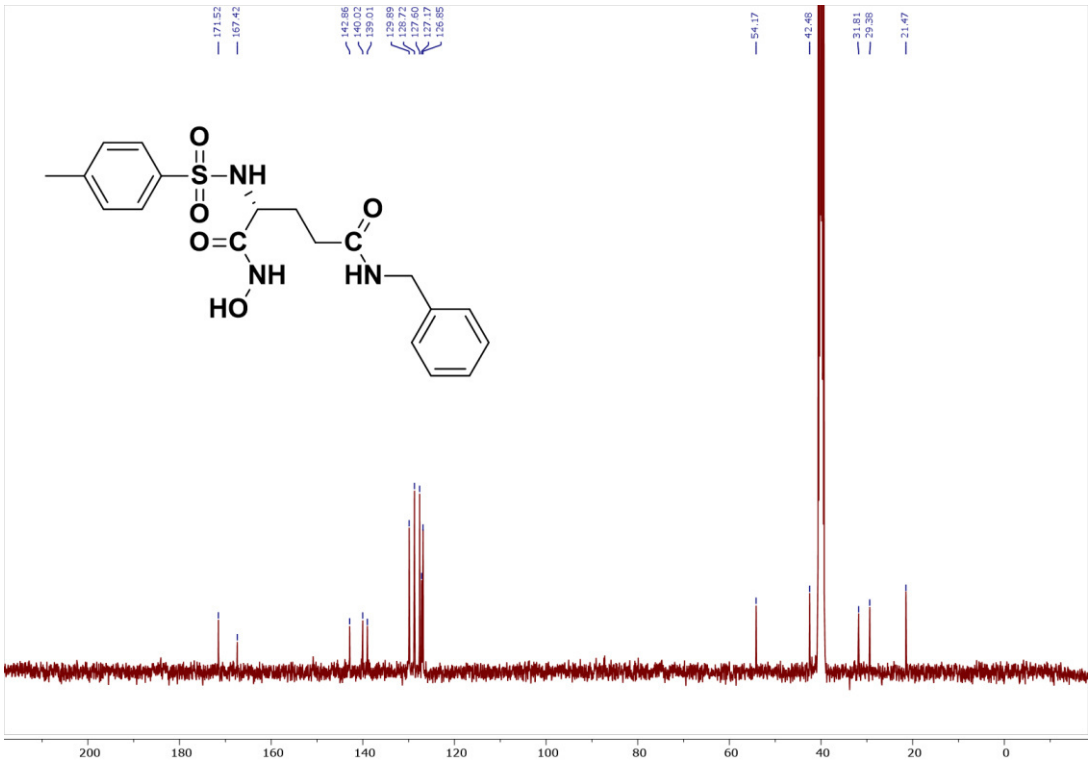

Figure A115: ^{13}C NMR Spectra for the compound **5h′**.

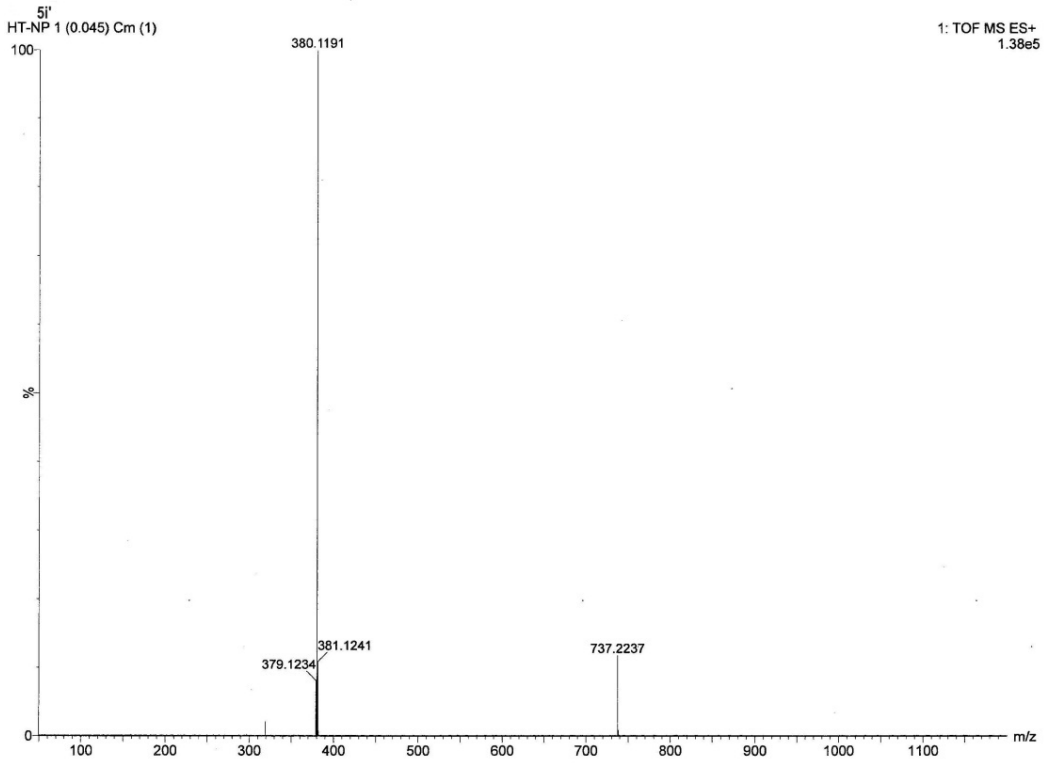

Figure A116: HRMS Spectra for the compound **5i′**.

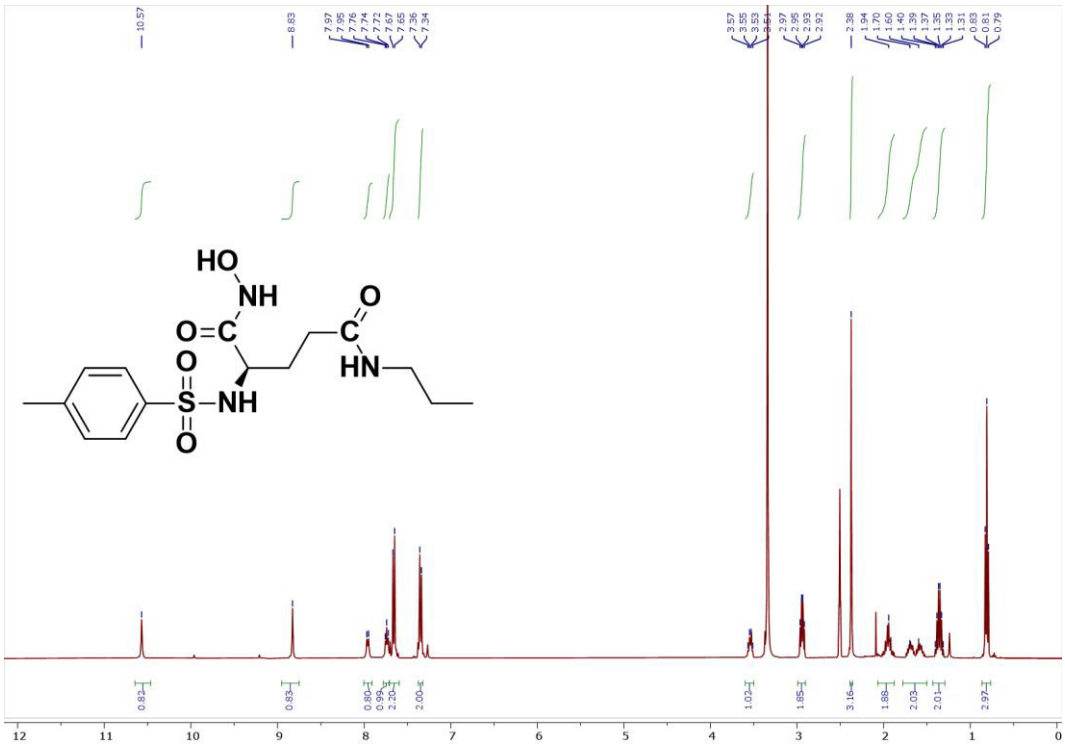

Figure A117: ^{1}H NMR Spectra for the compound **5i′**.

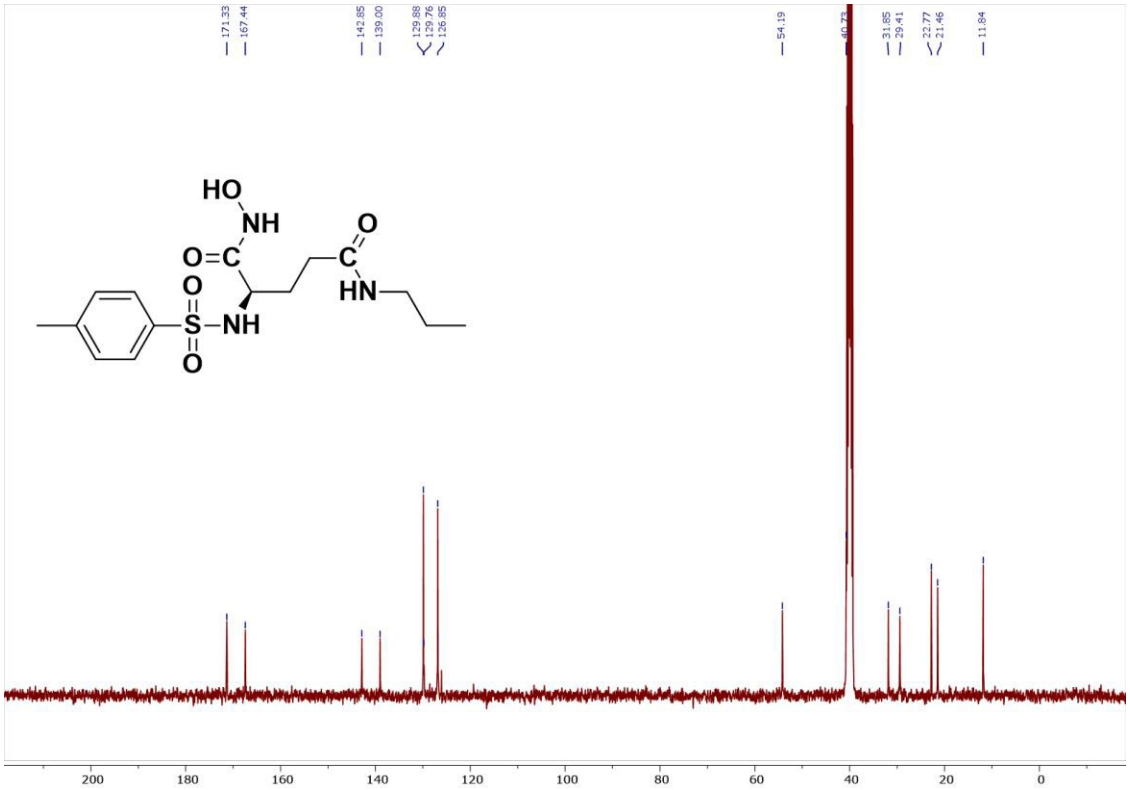

Figure A118: ^{13}C NMR Spectra for the compound **5i′**.

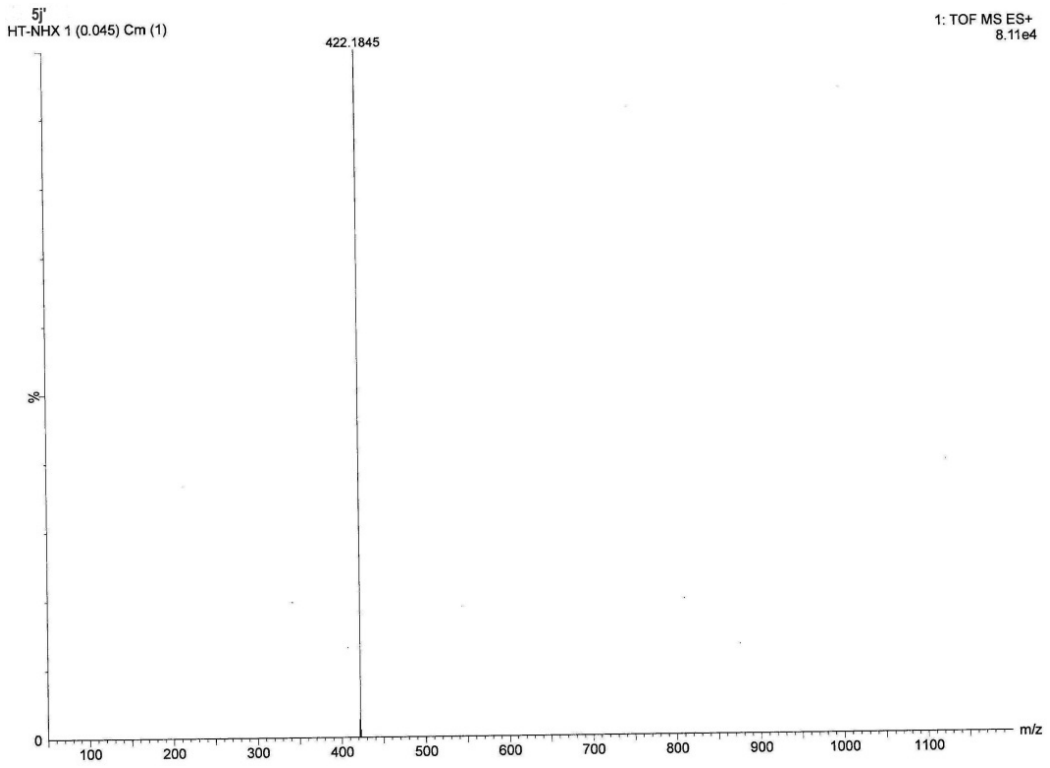

Figure A119: HRMS Spectra for the compound **5j′**.

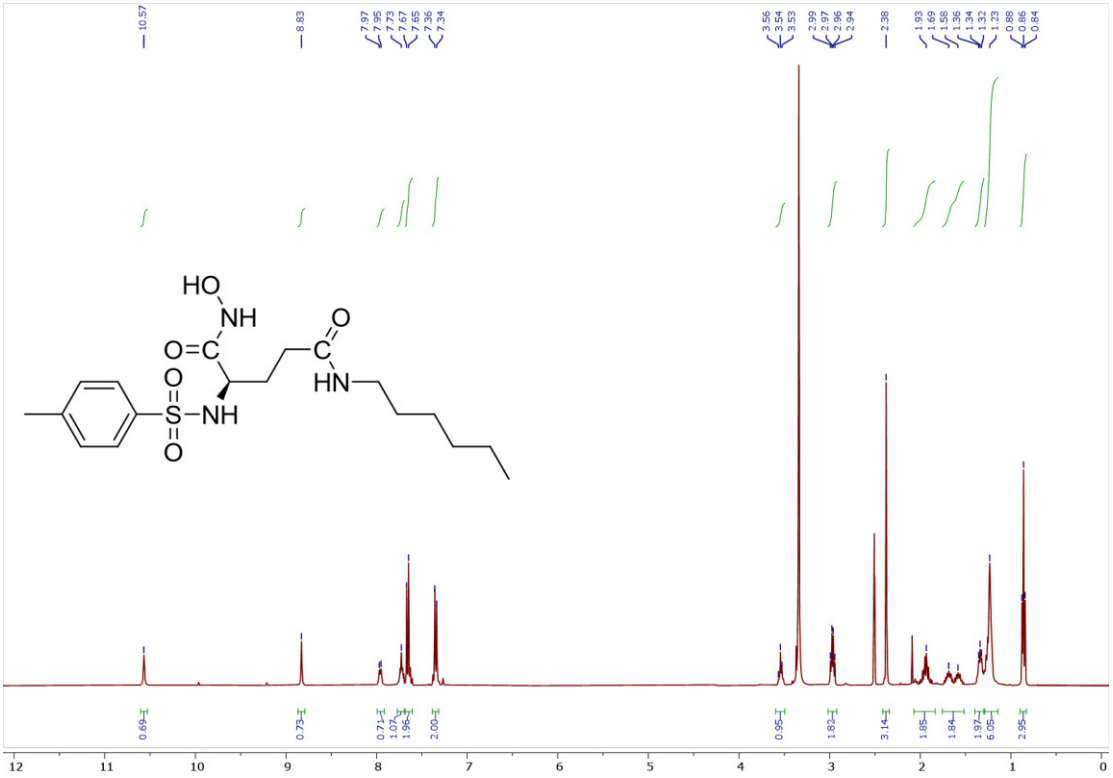

Figure A120: ^{1}H NMR Spectra for the compound **5j′**.

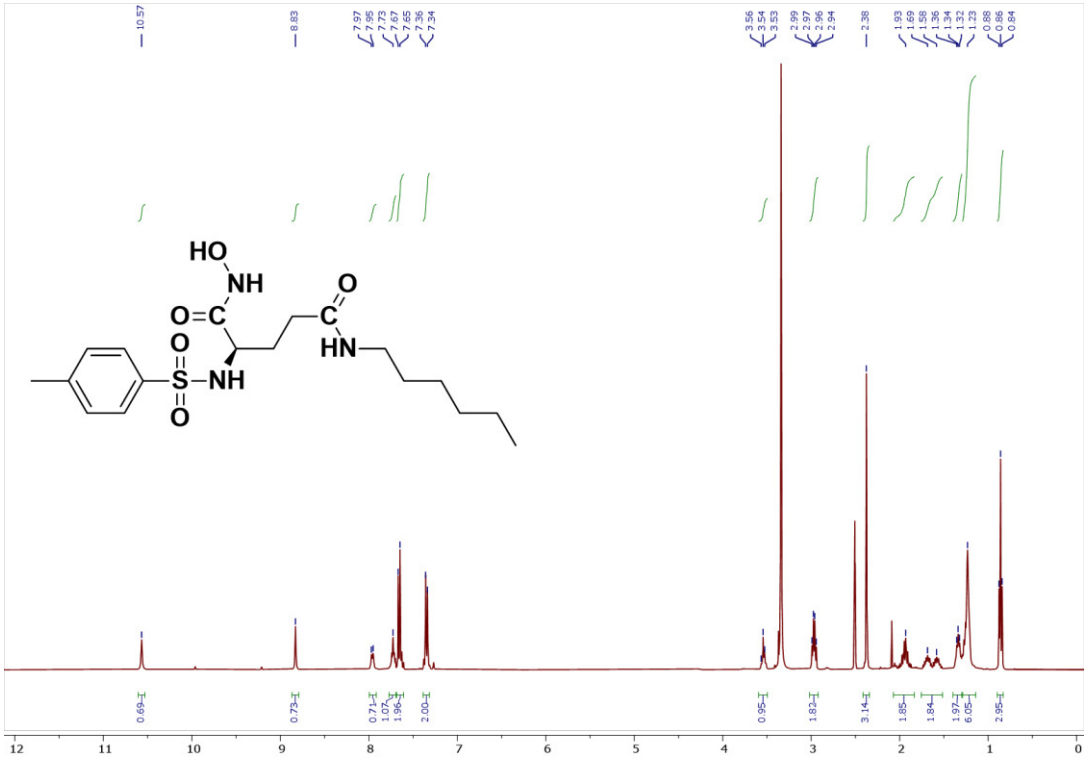

Figure A121: ^{13}C NMR Spectra for the compound **5j′**.

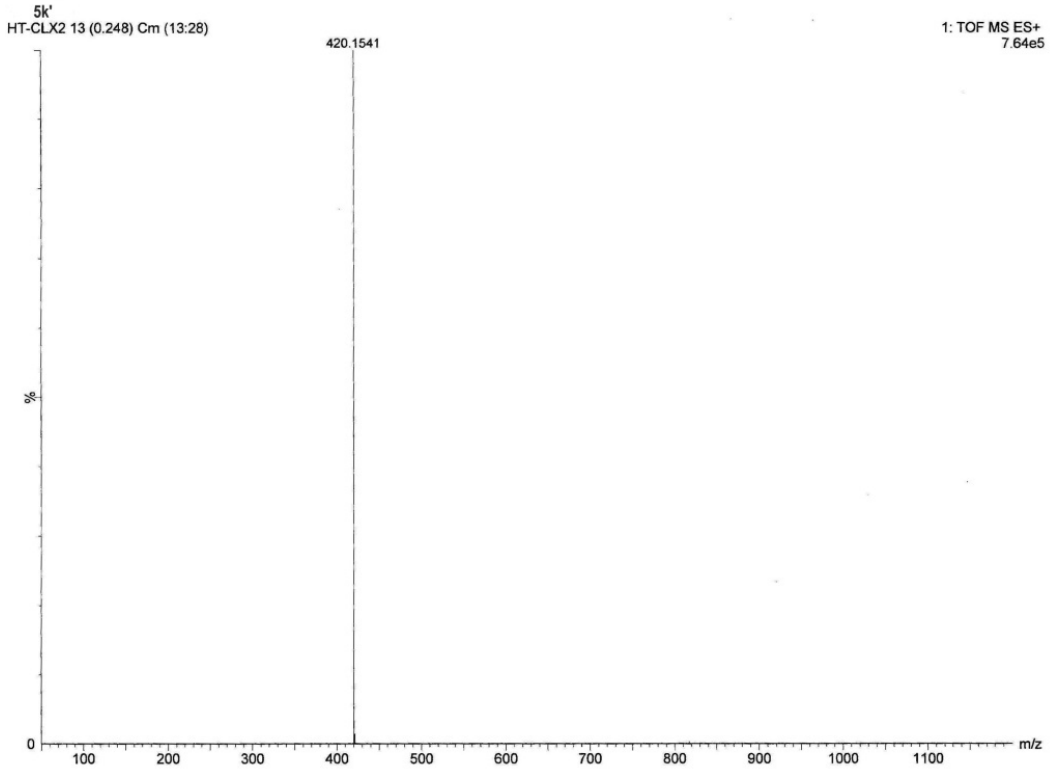

Figure A122: HRMS Spectra for the compound **5k′**.

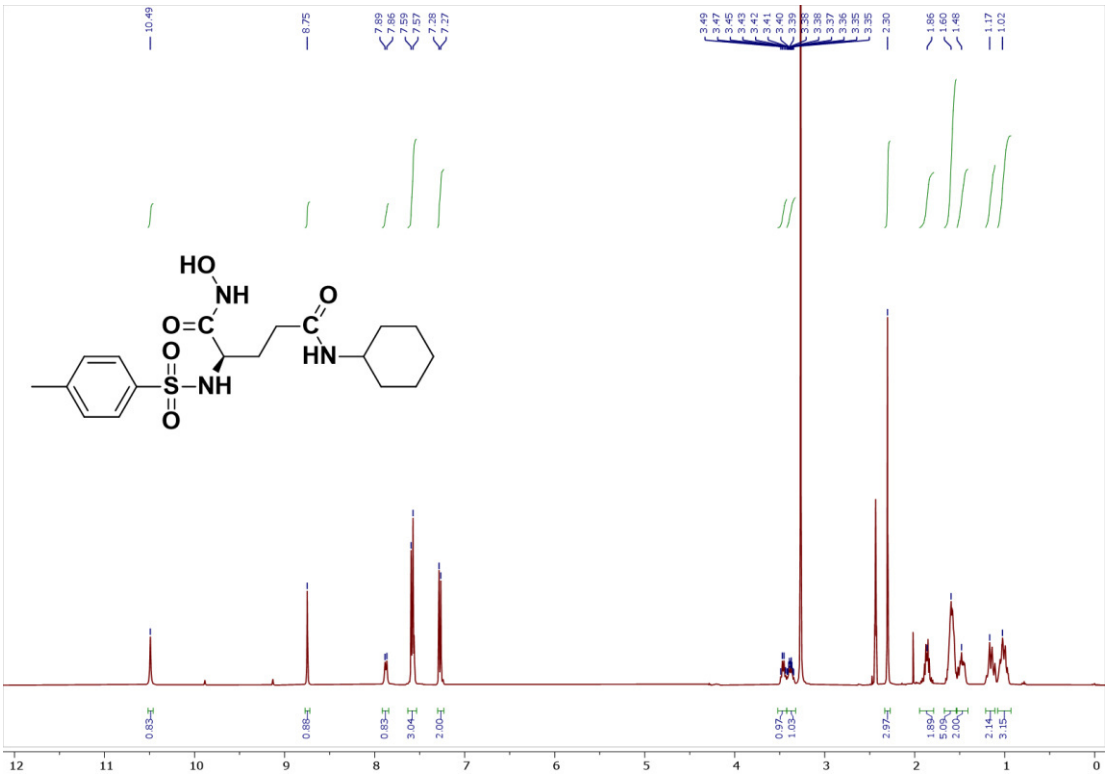

Figure A123: ^{1}H NMR Spectra for the compound **5k′**.

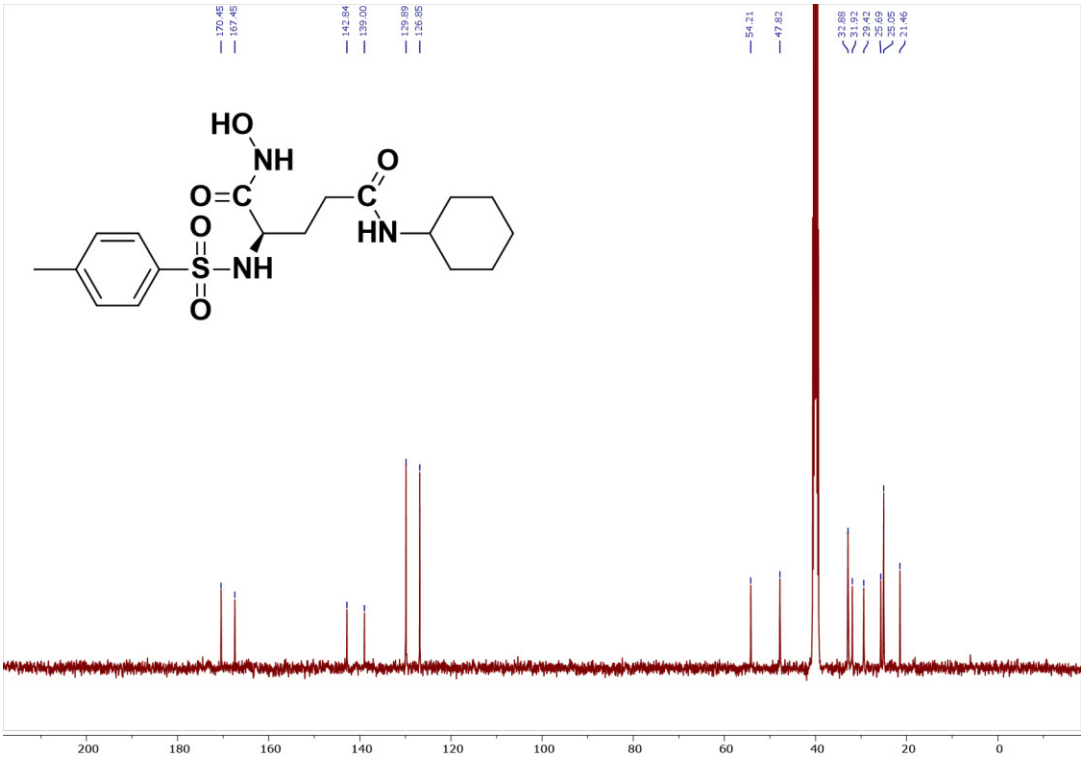

Figure A124: ^{13}C NMR Spectra for the compound **5k′**.

ANNEXURES

Annexures

Annexure 1

European Journal of Medicinal Chemistry 258 (2023) 115594

Contents lists available at ScienceDirect

European Journal of Medicinal Chemistry

journal homepage: www.elsevier.com/locate/ejmech

Review article

Are inhibitors of histone deacetylase 8 (HDAC8) effective in hematological cancers especially acute myeloid leukemia (AML) and acute lymphoblastic leukemia (ALL)?

Sk Abdul Amin [a,b], Samima Khatun [c], Shovanlal Gayen [c,**], Sanjib Das [a], Tarun Jha [a,*]

[a] Natural Science Laboratory, Division of Medicinal and Pharmaceutical Chemistry, Department of Pharmaceutical Technology, Jadavpur University, Kolkata, 700032, India
[b] Department of Pharmaceutical Technology, JIS University, 81, Nilgunj Road, Agarpara, Kolkata, West Bengal, India
[c] Laboratory of Drug Design and Discovery, Department of Pharmaceutical Technology, Jadavpur University, Kolkata, 700032, India

ARTICLE INFO

Keywords:
Cancer
Hematological malignancy
HDAC
HDAC8 inhibitor
Enzyme selectivity

ABSTRACT

Histone deacetylase 8 (HDAC8) aberrantly deacetylates histone and non-histone proteins. These include structural maintenance of chromosome 3 (SMC3) cohesin protein, retinoic acid induced 1 (RAI1), p53, etc and thus, regulating diverse processes such as leukemic stem cell (LSC) transformation and maintenance. HDAC8, one of the crucial HDACs, affects the gene silencing process in solid and hematological cancer progressions especially on acute myeloid leukemia (AML) and acute lymphoblastic leukemia (ALL). A specific HDAC8 inhibitor PCI-34051 showed promising results against both T-cell lymphoma and AML. Here, we summarize the role of HDAC8 in hematological malignancies, especially in AML and ALL. This article also introduces the structure/function of HDAC8 and a special attention has been paid to address the HDAC8 enzyme selectivity issue in hematological cancer especially against AML and ALL.

1. Introduction

Hematological cancers are a cluster of blood and bone marrow related disorders. These are defined as the clonal proliferation of blood-forming cells [1,2]. Abnormal hematopoietic and related processes are often associated with dysfunction of bone marrow. The cancer statistics by GLOBACAN 2020 depicted 11,95,275 diagnosed hematological malignancy-related cases. This also shows 6,88,464 death cases related to such malignancies including leukemia, non-Hodgkin lymphoma and multiple myeloma only in the year 2020 [3]. Hematological malignancies can be broadly categorized into two major groups such as lymphoid and myeloid disorders. Depending on the phenotype, manifestation and clinical characteristics, hematological malignancies are further classified into specific disorders including leukemias, lymphomas, myelomas and melanoma [2]. Myeloid tumors such as acute myeloid leukemia (AML), chronic myeloid leukemia (CML), polycythemia, myelodysplastic syndrome, idiopathic thrombocytosis, and primary myelofibrosis are developed primarily in the bone marrow. Lymphatic tumors are characterized by the accumulation of lymphocytes in the blood, lymph nodes, bone marrow, or organs. These include acute lymphoblastic leukemia (ALL), chronic lymphocytic leukemia (CLL) and lymphoma [1].

Recent insights have shown that genetic alterations manifest the development as well as maintenance of childhood and adolescence cancers including acute lymphoblastic leukemia (ALL) [4–9]. Epigenetics is concerned with genetic control by factors without alterations in the DNA sequence [10–12]. The word "epigenetic" means "in addition to changes in genetic sequence" [13]. Growing evidence advocates that abnormal epigenetic regulation is correlated to cancer genesis. Post-translational modifications (PTMs) of histones are the most comprehensively studied pathways of epigenetic control of gene expression [14–18]. Histones undergo several PTMs that include methylation, phosphorylation, acylation, acetylation and ubiquitination [19–22]. Acetylation of lysine residues of histones is a dynamic process. This involves two families of enzymes with opposing activities namely histone/lysine acetyltransferases (HATs) and histone deacetylases (HDACs) [23,24]. Histone deacetylation condenses chromatin structure and subsequently suppresses gene expression [25,26]. Deacetylation of

* Corresponding author.
** Corresponding author.
E-mail addresses: pharmacist.amin@gmail.com (S.A. Amin), shovanlal.gayen@gmail.com (S. Gayen), tjupharm@yahoo.com (T. Jha).

https://doi.org/10.1016/j.ejmech.2023.115594
Received 3 April 2023; Received in revised form 17 June 2023; Accepted 23 June 2023
Available online 25 June 2023

Annexure 2

European Journal of Medicinal Chemistry 223 (2021) 113623

Contents lists available at ScienceDirect

European Journal of Medicinal Chemistry

journal homepage: http://www.elsevier.com/locate/ejmech

Review article

Inhibitors of gelatinases (MMP-2 and MMP-9) for the management of hematological malignancies

Sanjib Das, Sk Abdul Amin, Tarun Jha*

Natural Science Laboratory, Division of Medicinal and Pharmaceutical Chemistry, Department of Pharmaceutical Technology, Jadavpur University, Kolkata, 700032, India

ARTICLE INFO

Article history:
Received 22 February 2021
Received in revised form
18 May 2021
Accepted 3 June 2021
Available online 12 June 2021

Keywords:
Matrix metalloproteinase (MMP)
Extracellular matrix (ECM)
Cancer
Clinical trial
Matrix metalloproteinase inhibitor (MMPI)
Hematological malignancy

ABSTRACT

Matrix metalloproteinase-2 (MMP-2) and matrix metalloproteinase-9 (MMP-9) are collectively known as gelatinases whereas MMP-2 is gelatinase-A and MMP-9 is termed as gelatinase-B. Gelatinases and other matrix metalloproteinases (MMPs) have long been associated with solid tumor invasion, metastasis and angiogenesis. However, there is paucity of data available regarding the role of gelatinases in hematological malignancies. Recent studies have shown that gelatinases activities or functions are correlated with hematological malignancies. Strategies for designing more specific gelatinase inhibitors like catalytic (CAT) domain inhibitors and hemopexin (PEX) domain inhibitors as well as signaling pathway based or gelatinase expression inhibitors had been reported against hematologic malignant cells. Several substrate based non-selective to non-substrate based relatively selective synthetic matrix metalloproteinase inhibitors (MMPIs) had been developed. Few MMPIs had reached in clinical trials during the period of 1990s–2000s. Unfortunately the anti-tumor and anti-metastatic efficacies of these MMPIs were not justified with patients having several advanced stage solid tumor cancers in any substantial number of clinical trials. Till date not a single MMPI passed phase III clinical trials designed for advanced metastatic cancers due to adverse events as well as lack of ability to show uniformity in disease prolongation. With the best of our knowledge no clinical trial study has been reported with small molecule synthetic inhibitors against hematological malignancies. This review looks at the outcome of clinical trials of MMPIs for advanced stage solid tumors. This can therefore, act as a learning experience for future development of successful gelatinase inhibitors for the management of hematological malignancies.

Contents

Abbreviations: MMPs, matrix metalloproteinases; CAT, catalytic; PEX, hemopexin; MMPI, matrix metalloproteinase inhibitor; ECM, extracellular matrix; FGFR1, fibroblast growth factor receptor 1; IGF-BP, insulin-like growth factor-binding protein; IL-1β, interleukin-1β; TNF-α, tumor necrosis factor-α; TGF-β, transforming growth factor-β; MSS, musculoskeletal syndrome; TIMPs, tissue inhibitors of metalloproteinases; MT-MMPs, membrane-type MMPs; GPI, glycosyl phosphatidylinositol; HFC, human fibroblast collagenase; HNC, human neutrophil collagenase; IP, intraperitoneal; PSA, prostate specific antigen; CEA, carcinoembryonic antigen; CA 125, cancer antigen 125; CA 19-9, cancer antigen 19-9; NSCLC, non-small cell lung cancer; SCLC, small cell lung cancer; EMT, epithelial–mesenchymal transition; mTOR, mammalian target of rapamycin; EGFR, epidermal growth factor receptor; TKI, tyrosine kinase inhibitor; ADAM, a disintegrin and metalloproteinase; PEX9, hemopexin domain of MMP-9; ALL, acute lymphoblastic leukemia; VEGF, vascular endothelial growth factor; PDGF-BB, platelet derived growth factor-BB; EGF, epidermal growth factor; CLL, chronic lymphocytic leukemia; HSC, hematopoietic stem cell; B-CLL, B-cell chronic lymphocytic leukemia; HUVECs, human umbilical vein endothellial cells; ERK, extracellular signal-regulated kinase; PI3-K, phosphoinositide 3-kinase; NF-kB, nuclear factor kappa-light-chain-enhancer of activated B cells; STAT3, signal transducer and activator of transcription 3; AML, acute myeloid leulemia; CML, chronic myeloid leukemia; BM-MNCs, bone marrow mononuclear cells; MDS, myelodysplastic syndromes; HDAC, histone deacetylases; FAK, focal adhesion kinase; MAPK, mitogen-activated protein kinases; JNK, c-Jun N-terminal kinase; SAR, structure-activity relationship.

* Corresponding author.
E-mail addresses: sanjibip@gmail.com (S. Das), pharmacist.amin@gmail.com, skabdulamin.rs@jadavpuruniversity.in (S.A. Amin), tjupharm@yahoo.com (T. Jha).

https://doi.org/10.1016/j.ejmech.2021.113623
0223-5234/

Annexure 3

FUTURE MEDICINAL CHEMISTRY, VOL. 14, NO. 1 | RESEARCH ARTICLE

Synthesis, anticancer activity, SAR and binding mode of interaction studies of substituted pentanoic acids: part II

Sanchita Datta, Amit Kumar Halder, Nilanjan Adhikari, Sk Abdul Amin, Sanjib Das & Tarun Jha

Published Online: 25 Nov 2021 | https://doi.org/10.4155/fmc-2021-0049

Abstract

Aim: Our previous results suggest that phenyl/naphthylacetyl pentanoic acid derivatives may exhibit dual MMP-2 and HDAC8 inhibitory activities and show effective cytotoxic properties. **Methodology:** Here, 13 new compounds (**C1–C13**) were synthesized and characterized. Along with these new compounds, 16 previously reported phenyl/napthylacetyl pentanoic acid derivatives (**C14–C29**) were biologically evaluated. **Results:** Compounds **C6** and **C27** showed good cytotoxicity against leukemia cell line Jurkat E6.1. The mechanisms of cytotoxicity of these compounds were confirmed by DNA deformation assay and reactive oxygen species assay. MMP-2 and HDAC8 expression assays suggested the dual inhibiting property of these two compounds. These findings were supported by results of molecular docking studies. *In silico* pharmacokinetic properties showed compounds **C6** and **C27** have high gastrointestinal absorption. **Conclusion:** This study highlights the action of phenyl/naphthylacetyl pentanoic acid derivatives as anticancer agents.

Keywords: DNA deformation • HDAC8 • Jurkat E6.1 • MMP-2 • pentanoic acid • ROS

Annexure 4

Journal of Molecular Structure 1248 (2022) 131512

Contents lists available at ScienceDirect

Journal of Molecular Structure

journal homepage: www.elsevier.com/locate/molstr

Synthesis, biological activity, structure activity relationship study and liposomal formulation development of some arylsulfonyl pyroglutamic acid derivatives

Sanjib Das, Sk Abdul Amin, Sanchita Datta, Nilanjan Adhikari, Tarun Jha*

Natural Science Laboratory, Division of Medicinal and Pharma ceutical Chemistry, Department of Pharmaceutical Technology, PO Box 17020, Jadavpur University, Kolkata 700032, India

ARTICLE INFO

Article history:
Received 30 May 2021
Revised 6 September 2021
Accepted 15 September 2021
Available online 18 September 2021

Keywords:
Pyroglutamic acid
Leukemia
Cytotoxicity
Jutkat e6.1 cell line
K562 cell line
Apoptosis

ABSTRACT

In this study, we have synthesized some 4-biphenylsulphonyl-L(+)-pyroglutamic acid and pyroglutamines as we have already reported the corresponding glutamic acids and glutamines. The synthesized compounds were characterized and screened against human cancer cell lines (K562, Jurkat E6.1, U937 and MDA-MB-231) as well as normal human peripheral blood mononuclear cells (PBMCs) for their possible cytotoxic activity by MTT assay. All these synthesized compounds are cytotoxic towards leukemia cell lines (K562, Jurkat E6.1 and U937) and inactive against breast cancer cell line (MDA-MB-231) as well as normal human PBMCs. Two most active compounds in cytotoxicity study (compound **7** and compound **10**) were further investigated by flow cytometric *in-vitro* apoptosis assay against Jurkat E6.1 and K562 cell lines. Compound **7** and compound **10** induced apoptosis significantly in both Jurkat E6.1 and K562 cell lines ($p < 0.05$) in a time dependent fashion. Mitochondrial membrane potential detection study as well as DNA deformation assay also confirmed apoptosis mediated cellular cytotoxicity. Compound **7** and compound **10** were encapsulated into liposomes (**7a** and **10a**). Drug loaded liposomes, **7a** and **10a** are more than 8 fold cytotoxic in comparison with compound **7** and compound **10** against Jurkat E6.1 and K562 cell lines. In conclusion, compound **7** and compound **10** may be considered as potential lead molecules for the development of target specific anti-leukemic agents with minimal untoward events to normal human cells.

1. Introduction

Cancer is positioned as a principal barricade to expand life expectancy and recently left behind stroke and coronary heart disease in mortality rate all over the world [1]. Within the age limit of 70 years, cancer ranked as the first or second leading cause of death among 112 of 183 countries in 2019. Within 2040, the global cancer burden is expected to increase 47% in comparison to 2020 [1]. In 1949, mechlorethamine, the first anticancer drug, was available in the market and the worldwide life expectancy was 46.8 years [2]. In 2015, approximately 160 anticancer drugs were available and the life expectancy reached 71.4 years [2]. Significant number of anticancer agents currently hit the market are either antibody-drug conjugates (ADCs) or monoclonal antibodies (mAbs) [2]. The aim of this work is to get preliminary information with regard to the development of small molecule synthetic anti-cancer potential lead compounds.

In medicinal chemistry, amide bond formation is one of the most important chemical transformations as carboxamide functionality is a common feature in most of the small or complex synthetic or natural bioactive molecules [3]. The drug like features of amides such as stability, neutrality, hydrogen bond donating and hydrogen bond accepting capabilities are reasons behind utmost importance of carboxamides to medicinal chemists. Amide function appears in more than 25% of the marketed drugs [4]. Glutamine is an important biomolecule and most copiously found amino acid in human body [5]. Glutamine acts as the nitrogen atom donor to the biosynthesis of amino acids and nucleotides as well as aids to uptake essential amino acids in the body [6]. For rapid proliferation of neoplastic cells, glutamine is extensively used for energy production and also used as a precursor for the required biomass [7]. Several glutamine or glutamic acid analogs have been reported for their antineoplastic activity. The glutamine antagonist 6-diazo-5-oxo-L-norleucine (DON) has been studied for more than 6 decades as a potential anticancer agent which have structural similarity with glutamic acid [8]. JHU-083, a pro-drug of 6-diazo-5-oxo-L-norleucine, induced apoptosis and

* Corresponding author.
E-mail address: tjupharm@yahoo.com (T. Jha).

https://doi.org/10.1016/j.molstruc.2021.131512
0022-2860/

Annexure 5

SAR AND QSAR IN ENVIRONMENTAL RESEARCH
2021, VOL. 32, NO. 8, 655–687
https://doi.org/10.1080 1062936X.2021.1955414

Insight into the structural requirement of aryl sulphonamide based gelatinases (MMP-2 and MMP-9) inhibitors – Part I: 2D-QSAR, 3D-QSAR topomer CoMFA and Naïve Bayes studies – First report of 3D-QSAR Topomer CoMFA analysis for MMP-9 inhibitors and jointly inhibitors of gelatinases together

S. Das*, S.A. Amin and T. Jha

Natural Science Laboratory, Division of Medicinal and Pharmaceutical Chemistry, Department of Pharmaceutical Technology, Jadavpur University, Kolkata, India

ABSTRACT

Gelatinases [gelatinase A – matrix metalloproteinase-2 (MMP-2), gelatinase B – matrix metalloproteinase-9 (MMP-9)] play key roles in many disease conditions including cancer. Despite some research work on gelatinases inhibitors both jointly and individually had been reported, challenges still exist in achieving potency as well as selectivity. Here in part I of a series of work, we have reported the structural requirement of some arylsulfonamides. In particular, regression-based 2D-QSARs, topomer CoMFA (comparative molecular field analysis) and Bayesian classification models were constructed to refine structural features for attaining better gelatinase inhibitory activity. The 2D-QSAR models exhibited good statistical significance. The descriptors nsssN, SHBint6, SHBint7, PubchemFP629 were directly correlated with the MMP-2 binding affinities whereas nsssN, SHBint10 and AATS2i were directly proportional to MMP-9 binding affinities. The topomer CoMFA results indicated that the steric and electrostatic fields play key roles in gelatinase inhibition. The established Naïve Bayes prediction models were evaluated by fivefold cross validation and an external test set. Furthermore, important molecular descriptors related to MMP-2 and MMP-9 binding affinities and some active/inactive fragments were identified. Thus, these observations may be helpful for further work of aryl sulphonamide based gelatinase inhibitors in future.

ARTICLE HISTORY
Received 1 June 2021
Accepted 11 July 2021

KEYWORDS
Gelatinase; cancer; QSAR; S-MLR; ANN; SVM; topomer CoMFA; Naïve Bayes; fingerprint

Introduction

In human gelatinase A, i.e. matrix metalloproteinase-2 (MMP-2) and gelatinase B, i.e. matrix metalloproteinase-9 (MMP-9) belong to MMP family along with other 22 members. MMPs are zinc-dependent peptidases which are responsible for the digestion of non-terminal peptide bond during the course of several physiological and pathological processes [1–3]. Unlike other endopeptidases in the MMP family, in the *N*-terminous of

CONTACT T. Jha tjupharm@yahoo.com
*These authors contributed equally to this work
Supplemental data for this article can be accessed at: https://doi.org/10.1080/1062936X.2021.1955414.

Annexure 6

SAR AND QSAR IN ENVIRONMENTAL RESEARCH
2022, VOL. 33, NO. 3, 167–192
https://doi.org/10.1080 1062936X.2022.2041722

Insight into the structural requirements of gelatinases (MMP-2 and MMP-9) inhibitors by multiple validated molecular modelling approaches: Part II

S. Das[a#], S.A. Amin[a#], S. Gayen[b] and T. Jha[a]

[a]Natural Science Laboratory, Division of Medicinal and Pharmaceutical Chemistry, Department of Pharmaceutical Technology, Jadavpur University, Kolkata, India; [b]Laboratory of Drug Design and Discovery, Department of Pharmaceutical Technology, Jadavpur University, Kolkata, India

ABSTRACT

Inhibition of the matrix metalloproteinases (MMPs) is effective against metastasis of secondary tumours. Previous MMP inhibitors have failed in clinical trials due to their off-target toxicity in solid tumours. Thus, newer MMP inhibitors now have paramount importance. Here, different molecular modelling techniques were applied on a dataset of 110 gelatinase (MMP-2 and MMP-9) inhibitors. The objectives of the present study were to identify structural fingerprints for gelatinase inhibition and also to develop statistically validated QSAR models for the screening and prediction of different derivatives as MMP-2 (gelatinase A) and MMP-9 (gelatinase B) inhibitors. The Bayesian classification study provided the ROC values for the training set of 0.837 and 0.815 for MMP-2 and MMP-9, respectively. The linear model also produced the leave-one-out cross-validated Q^2 of 0.805 (eq. 1, MMP-2) and 0.724 (eq. 2, MMP-9), an r^2 of 0.845 (eq. 1, MMP-2) and 0.782 (eq. 2, MMP-9), an r^2_{Pred} of 0.806 (eq. 1, MMP-2) and 0.732 (eq. 2, MMP-9). Similarly, non-linear learning models were also statistically significant and reliable. Overall, this study may help in the rational design of newer compounds with higher gelatinase inhibition to fight against both primary and secondary cancers in future.

ARTICLE HISTORY
Received 13 December 2021
Accepted 3 February 2022

KEYWORDS
Cancer; gelatinases; recursive partitioning; Bayesian classification; classical 2D-QSAR; non-linear 2D-QSAR

Introduction

Matrix metalloproteinases (MMPs) are zinc-dependent multidomain endopeptidases having primary function in the extracellular region and responsible for the digestion of the nonterminal peptide bond during the course normal homoeostasis as well as pathogenesis [1]. There are 28 MMP family members found in the vertebrate, and at least 23 MMPs are expressed in human tissues [2]. In general, MMPs contain a propeptide domain, a zinc-containing catalytic domain, a linker peptide and a hemopexin domain [2]. Commonly, MMPs are classified as collagenases (MMP-1, MMP-8, MMP-13 and MMP-18), gelatinases (MMP-2 and MMP-9), stromelysins (MMP-3, MMP-10 and MMP-11), matrilysins (MMP-7 and MMP-26), membrane-type MMPs (MMP-

CONTACT T. Jha tjupharm@yahoo.com; S. Gayen shovanlal.gayen@gmail.com
^Part I: S. Das, S.A. Amin, and T. Jha, SAR QSAR Environ. Res. 32 (2021), pp. 655-687.
#Authors have equal contribution
Supplemental data for this article can be accessed at: https://doi.org/10.1080/1062936X.2022.2041722.

Annexure 7

ARTICLE IN PRESS

Materials Today: Proceedings xxx (xxxx) xxx

Contents lists available at ScienceDirect

Materials Today: Proceedings

journal homepage: www.elsevier.com/locate/matpr

In-house glutamine based compound loaded poly-(*D-L*-lactide-coglycolide) nanoparticles as a possible candidate for the management of chronic myeloid leukemia

Sanjib Das [a,*], Shovanlal Gayen [b], Tarun Jha [a]

[a] *Natural Science Laboratory, Division of Medicinal and Pharmaceutical Chemistry, Department of Pharmaceutical Technology, Jadavpur University, Kolkata 700032, India*

[b] *Laboratory of Drug Design and Discovery, Department of Pharmaceutical Technology, Jadavpur University, Kolkata 700032, India*

ARTICLE INFO

Keywords:
Synthesis
Drug Encapsulation
PLGA nanoparticles
Chronic Myeloid Leukemia

ABSTRACT

The development of targeted medicines such tyrosine kinase inhibitors (TKIs) have turned chronic myeloid leukemia (CML) from a potentially fatal illness into a manageable chronic condition for many individuals. But in case of TKIs, some serious drug induced adverse events as well as drug resistance were reported. In continuation of our earlier work, we have synthesized two *p*-nitrobenzenesulfonyl-*D*-glutamine derivatives which were screened against human CML cell line (K562). In comparison with earlier reported *p*-nitrobenzenesulfonyl-*L*-glutamine derivatives (**Compound 1** and **Compound 2**), newly synthesized compounds showed more than 3 times better activity against K562 cell line. The best active compound (**Compound 3**) was encapsulated into Poly-(*D-L*-lactide-coglycolide) nanoparticles (NPs). The NPs were characterized and screened against K562 and human PBMC cell line. The IC_{50} value of **NP** of **Compound 3** was found in the nanomolar range (**522 nM**) against K562 cell line which is more than 10 times better active than **Compound 3**. DNA deformation assay also indicates cell shrinkage and nuclear fragmentation which are associated with apoptosis-mediated cell death. The prepared NPs of **Compound 3** (**NP3**) are very much less toxic against normal human PBMC (IC_{50} value > 500 μM). The current study implies that **NP3** holds promise for managing chronic myeloid leukemia.

1. Introduction

Billions of cells will typically grow and divide in our body as needed throughout our lifetime. Most cells die when they become aberrant or aged. When something goes wrong during this process, our cells continue to divide, preventing the old or abnormal cells from dying as they should. This is how cancer develops [1]. Cancer is the second-leading cause of death in the United States and is a serious global public health concern. According to projections, there will be 609,820 cancer fatalities and 1,958,310 new cases of the disease in the United States (US) in 2023. Accordingly, in 2023, there will be 4 new instances of cancer and 1 cancer-related death per minute in the US [2]. Cancers have been classified into solid tumors and blood cancers by oncologists. Blood cancers, commonly referred to as hematologic cancers; affect the blood cells, whereas solid tumor malignancies affect any other organ or tissue in the body. Leukemia, lymphoma, and multiple myeloma are examples of hematologic malignancies, which affect blood cells [1]. Leukemia is defined as a primary or secondary process by the generation of aberrant leukocytes. Despite an increase in the prognosis for leukemia patients due to cutting-edge advancements in treatment approaches, leukemia is still a cancer that poses a serious threat to life [3]. Leukemia is the 11th leading cause of cancer-related death globally in 2020 and the 15th most frequently discovered new case of cancer [4]. Depending on how quickly they proliferate and the cell from which they originated, they can be categorized as acute or chronic myeloid or lymphoid diseases. Acute lymphoblastic leukemia (ALL), chronic lymphocytic leukemia (CLL), and acute myeloid leukemia (AML) are the three most common subtypes, all of which affect the myeloid lineage [5]. One of the most prevalent types of leukemia in adults is CML. According to the report of the American Cancer Society, there were estimated about 8,930 new CML cases diagnosed and 1,310 deaths reported in 2023 in the U.S. [6]. Similar to other leukemias, CML is a disease of the hematopoietic stem cells (HSCs) [7]. CML frequently exhibits the Philadelphia chromosome, a reciprocal translocation involving chromosomes

* Corresponding author.
E-mail address: sanjibip@gmail.com (S. Das).

https://doi.org/10.1016/j.matpr.2023.10.158
Received 14 August 2023; Received in revised form 5 October 2023; Accepted 30 October 2023

Please cite this article as: Sanjib Das et al., *Materials Today: Proceedings*, https://doi.org/10.1016/j.matpr.2023.10.158

Annexure 8

Research Article

For reprint orders, please contact: reprints@future-science.com

Future Medicinal Chemistry

Synthesis, anticancer activity, structure–activity relationship and binding mode of interaction studies of substituted pentanoic acids

Sanchita Dutta[1,2], Amit Kumar Halder[1], Nilanjan Adhikari[1], Sk. Abdul Amin[1], Sanjib Das[1], Achintya Saha[2] & Tarun Jha*,[1]

[1]Natural Science Laboratory, Division of Medicinal & Pharmaceutical Chemistry, Department of Pharmaceutical Technology, Jadavpur University, PO Box 17020, Kolkata 700032, West Bengal, India

[2]Department of Chemical Technology, University of Calcutta, 92 APC Ray Road, Kolkata 700009, India

*Author for correspondence: tjupharm@yahoo.com

Aim: Simultaneous inhibition of MMP-2 and HDAC8 may be an effective strategy to target cancer. **Methodology:** In continuation of our earlier efforts, a series of substituted pentanoic acids (**1–18**) were synthesized and checked for their biological activity along with some earlier reported compounds (**19–35**). **Results:** Compounds **18** and **31** were found to induce apoptosis effectively in a dose-dependent fashion in Jurkat-E6.1 cell line. They reduced the expression of both MMP-2 and HDAC8 effectively. **31** also produced prominent intensity of fluorescence to bring nick in Jurkat-E6.1 cells. **31** also showed cellular arrest in sub-G0 phase. **Conclusion:** Such compounds may be useful to battle against cancer.

First draft submitted: 30 July 2018; Accepted for publication: 26 April 2019; Published online: 2 August 2019

Keywords: apoptosis • cell cycle • cytotoxicity • flow cytometry • leukemia • metalloenzyme • mitochondrial membrane potential • molecular docking • pentanoic acid • SAR

Zinc-dependent metalloenzymes such as MMPs, HDACs and APN have been implicated in cancer cell progression, differentiation, migration, invasion, metastatis and angiogenesis [1–18]. Ranogajec et al. [6] exhibited that the combined expression of APN, MMP-2 and MMP-9 along with other related factors may serve as the poor prognosis for breast cancer patients. Moreover, APN has also been found to exert a positive correlation with the MMP-2 expression as well as cellular migration as evidenced in ovarian cancer (OVCA) cell lines [19]. Again, small interfering ribonucleic acid (siRNA)-mediated silencing of APN markedly decrease the VEGF expression along with a down regulation of MMP-2 as seen in OVCA cells [19]. Liu *et al.* explored that 14-3-3σ protein-induced expression of MMPs are related to APN in hepatocellular cancer [20]. Nevertheless, silencing of APN produces an abrogating r14-3-3σ-protein that stimulated the expression of MMPs including MMP-2 and -9 in HS68 fibroblasts [20]. Western blot analysis revealed that APN signalling has been involved in the activation of nuclear factor (NF)-κB and NF-κB further regulates MMP-2 and MMP-9 through mediating PI3K and MAPK pathways as seen in the osteosarcoma cell line [21]. Therefore, treatment with APN inhibitor bestatin decreases all these APN, MMP-2 and MMP-9 enzymatic activities along with their mRNA expression [21]. Recently, Amin *et al.* [7] proposed the utility of simultaneous dual inhibition of MMP-2 and HDAC8 for combating haematological malignancies. Nevertheless, HDAC inhibitors has also been found to decrease the activity of MMP-2 activation along with cellular invasion of lung cancer through upregulation of the reversion-inducing-cysteine-rich protein with kazal motifs (RECK) [3,22]. RECK has been established to exert inhibitory mechanisms on the activity of MMP-2 and MMP-9 enzymes [22–25], crucial regulators of tumor growth, cell proliferation, angiogenesis and apoptosis [26]. Oh *et al.* [25] also suggested that RECK is directly involved in the reduction of active MMP-2 in HT1080 fibrosarcoma cell line. RECK is also found to suppress the release of pro-MMP-9 and subsequently hinders metastasis and invasion of tumor cells [24]. Nevertheless, an inverse correlation between RECK expression and activation of MMP-2 has also been established [23]. Not only that, tumors having higher RECK expression reveal a lower expression of

newlands press

Annexure 9

NJC

ROYAL SOCIETY OF CHEMISTRY

PAPER

View Article Online
View Journal | View Issue

Cite this: *New J. Chem.*, 2021, 45, 17149

Quantitative activity–activity relationship (QAAR) driven design to develop hydroxamate derivatives of pentanoic acids as selective HDAC8 inhibitors: synthesis, biological evaluation and binding mode of interaction studies†

Sk. Abdul Amin,[a] Prakruti Trivedi,[b] Nilanjan Adhikari,[a] Ganesh Routholla,[b] Dhanya Vijayasarathi,[b] Sanjib Das,[a] Balaram Ghosh*[b] and Tarun Jha*[a]

Received 29th May 2021,
Accepted 12th August 2021

DOI: 10.1039/d1nj02636d

rsc.li/njc

Histone deacetylase 8 (HDAC8) has been implicated as a potential drug target of many diseases including cancer. HDAC8 isoform selectivity over other class-I HDACs is a major concern nowadays. In this work, a series of pentanoic acid based hydroxamates with different substituted cap groups have been designed, synthesized, characterized, and screened against class-I HDACs. A quantitative activity–activity relationship (QAAR) model was developed to design HDAC8 selective inhibitors. The designed compounds obtained through the molecular modeling study were synthesized, characterized, and their enzymatic as well as cytotoxic activities were measured. Two compounds **7i** and **7f** are found to be selective HDAC8 inhibitors over other class-I HDACs. These compounds possess better antiproliferative activities against some cancer cell lines. These observations are in agreement with the molecular docking studies for the binding mode of interactions. Further studies show that compounds **7i** and **7f** induce significant cell growth arrest in the G2/M phase, indicating their anticancer potentials. In summary, our study confirms pentanoic acid based hydroxamate as selective HDAC8 inhibitors and two compounds **7i** and **7f** may serve as lead molecules for further investigation.

Introduction

Epigenetic regulation of genes *via* post-translational modulation in proteins results in a heritable change in gene function that culminates in a phenotypic change without altering DNA sequences. Epigenetics plays important roles in cellular and molecular regulatory processes.[1–3] It is associated with DNA methylation, histone modification, chromatin structural remodeling, and noncoding RNA regulation. Among these, histone acetylation and deacetylation are widely occurring post-translational modification processes. Histone deacetylases (HDACs) constitute about 23% of the total domain of epigenetic targets after methyltransferases.[2] These are mainly responsible for balancing the acetylation/deacetylation of lysine amino acids on histone/nonhistone proteins along with histone acetyltransferase (HAT).[3]

The aberrant expression of various HDACs has been observed in many human diseases, especially in cancer, which makes them important therapeutic targets for many human cancers.[4,5] Overexpression of classical HDACs has been represented in the pathological situation. Hence, histone deacetylase inhibitors (HDACIs) have emerged as promising cancer therapeutic agents.[6]

Zinc dependent HDACs are divided into three main classes: class-I HDACs (HDAC1, 2, 3, 8), class-II consists of class-IIa HDACs (HDAC4, 5, 7, 9) and class-IIb HDACs (HDAC6, 10), class-IV HDAC (HDAC11).[7] The class-III HDACs are called sirtuins and depend on nicotinamide adenine dinucleotide (NAD). These have different mechanism from classical zinc dependent HDACs.[7] HDAC8, a class I HDAC enzyme, is expressed in various tissues and involved in the genesis of malignancy. HDAC8 is localized in the nucleus and expressed ubiquitously (cytogenetic location: Xq 13.1). It also alters epigenetic modification.[6] HDAC8 pivotally controls cellular processes, such as muscle contraction, energy homeostasis, and separation of sister chromatid.[3,5] It is one of the essentials

[a] *Natural Science Laboratory, Division of Medicinal and Pharmaceutical Chemistry, Department of Pharmaceutical Technology, Jadavpur University, Kolkata 700032, India. E-mail: tjupharm@yahoo.com*

[b] *Epigenetic Research Laboratory, Department of Pharmacy, BITS-Pilani, Hyderabad Campus, Shamirpet, Hyderabad 500078, India. E-mail: balaram@hyderabad.bits-pilani.ac.in*

† Electronic supplementary information (ESI) available. See DOI: 10.1039/d1nj02636d

Annexure 10

Journal of Molecular Structure 1260 (2022) 132833

Contents lists available at ScienceDirect

Journal of Molecular Structure

journal homepage: www.elsevier.com/locate/molstr

Binary quantitative activity-activity relationship (QAAR) studies to explore selective HDAC8 inhibitors: In light of mathematical models, DFT-based calculation and molecular dynamic simulation studies

Sk. Abdul Amin[a], Janish Kumar[b], Samima Khatun[c], Sanjib Das[a], Insaf Ahmed Qureshi[b], Tarun Jha[a,*], Shovanlal Gayen[c,*]

[a] Natural Science Laboratory, Division of Medicinal and Pharmaceutical Chemistry, Department of Pharmaceutical Technology, Jadavpur University, Kolkata 700 032, India
[b] Department of Biotechnology and Bioinformatics, School of Life Sciences, University of Hyderabad, Hyderabad, Telangana 500 046, India
[c] Laboratory of Drug Design and Discovery, Department of Pharmaceutical Technology, Jadavpur University, Kolkata 700 032, India

ARTICLE INFO

Article history:
Received 20 January 2022
Revised 8 March 2022
Accepted 13 March 2022
Available online 16 March 2022

Keywords:
HDAC8
Selective inhibitor
QAAR
DFT
HOMO
LUMO
Molecular dynamic simulation

ABSTRACT

Histone deacetylase 8 (HDAC8) selectivity over other HDACs is a major concern of interest, since HDAC8 has been implicated as a potential drug target of many diseases including haematological malignancy. Quantitative activity-activity relationship (QAAR) study is a good strategy to explore the possible features to design HDAC8 selective inhibitors. Here, a mathematical framework has been constructed to understand the important molecular fragments responsible for HDAC8 selectivity over HDAC1, 2 and 3. This study also deals with binary QAAR-based HDAC8 selectivity screening of some *in-house* molecules and understanding the toxicity of the *in-house* molecules using DFT-based descriptors. Further, this study explores the possible binding mechanism of *in-house* compounds with HDAC8 by molecular dynamic simulation. Hence, the comparative learning amongst the mathematical models, DFT-based calculation and molecular dynamic simulation methods will surely enrich the scientific community to design selective HDAC8 inhibitors in future.

1. Introduction

Histone deacetylases (HDACs) are found to express aberrantly in many human diseases. Evidences suggest the importance of HDACs as therapeutic targets for many human cancers [1–3]. Zinc and nicotinamide adenine dinucleotide (NAD) dependant HDACs are identified so far. Class-I HDACs (HDAC1, 2, 3, 8), class-II consists of class-IIa HDACs (HDAC4, 5, 7, 9) and class-IIb HDACs (HDAC6, 10), class-IV HDAC (HDAC11) belong to the zinc dependant HDACs, whereas, class-III HDACs (sirtuins) are NAD dependant [4,5]. HDAC8 belongs to class I HDAC enzyme which is expressed in various tissues and involved in cancer progression. HDAC8 is localized in the nucleus and expressed ubiquitously [6–10]. It is also found to alter the epigenetic modification [7]. Nowadays, HDAC8 has been implicated as a potential drug target of acute myeloid leukaemia, neuroblastoma, T cell leukaemia, etc [10]. Hence, HDAC8 selectivity over other HDACs is a major concern of interest. Currently available HDAC inhibitors in the clinics are pan-HDAC inhibitors which inhibit many of the Class I, II and IV isoforms [2,5,11,12].

HDAC8 is emerged as an anticancer target to design molecules against acute myeloid leukaemia (AML) also [10]. HDAC8 is also reported as one of binding partners of fusion protein CBFβ-SMMHC (core binding factor β-smooth muscle myosin heavy chain) (Fig. 1).

HDAC8-mediated deacetylation of p53 in inv(16)+ AML CD34+ cells promote inactivation of p53 and consequently promotes leukaemic stem cells (LSC) transformation and maintenance [10]. From Fig. 1, it can be shown that HDAC8 inhibition by selective HDAC8 inhibitor resulted in restoring p53 acetylation in inv(16)+ AML CD34+ cells.

Quantitative structure-activity relationship (QSAR) approach has shown its acceptability in many fields. QSAR mostly deals with the correlation of chemical descriptors with targeted biological end points in combination with robust statistical and machine learning studies. It reduces the development time and cost in the drug

* Corresponding authors.
E-mail addresses: pharmacist.amin@gmail.com, skabdulamin.rs@jadavpuruniversity.in (Sk.A. Amin), tjupharm@yahoo.com (T. Jha), shovanlal.gayen@gmail.com (S. Gayen).

https://doi.org/10.1016/j.molstruc.2022.132833
0022-2860/

Annexure 11

Journal of Molecular Structure 1271 (2023) 133967

Contents lists available at ScienceDirect

Journal of Molecular Structure

journal homepage: www.elsevier.com/locate/molstr

A detail survey and analysis of selectivity criteria for indole-based histone deacetylase 8 (HDAC8) inhibitors

Md. Moinul[a,b,#], Sk. Abdul Amin[c,d,#], Samima Khatun[a], Sanjib Das[c], Tarun Jha[c,*], Shovanlal Gayen[a,*]

[a] Laboratory of Drug Design and Discovery, Department of Pharmaceutical Technology, Jadavpur University, Kolkata, 700032, India
[b] Calcutta Institute of Pharmaceutical Technology & Allied Health Sciences, Uluberia, Howrah, 711316, India
[c] Natural Science Laboratory, Division of Medicinal and Pharmaceutical Chemistry, Department of Pharmaceutical Technology, Jadavpur University, Kolkata, 700032, India
[d] Department of Pharmaceutical Technology, JIS University, 81, Nilgunj Road, Agarpara, Kolkata, 700109, India

ARTICLE INFO

Article history:
Received 23 May 2022
Revised 3 August 2022
Accepted 16 August 2022
Available online 18 August 2022

Keywords:
HDAC8
selectivity
isoform
indole
structure-activity relationships
QAAR

ABSTRACT

Histone deacetylases (HDACs) are attractive therapeutic targets due to their involvement in a variety of human diseases including cancer. All FDA-approved HDAC-targeting drugs are pan-HDAC inhibitors and these drugs possess unwanted effects at therapeutic doses. In this scenario selective HDAC8 inhibition can offer beneficial therapeutic effects. Here, HDAC8 inhibition and selectivity over other HDACs are discussed for indole-based HDAC inhibitors (iHDAC) on the basis of extensive literature review and molecular modeling studies. Indole scaffold is one of the main contributors in FDA approved anticancer drugs, and discovery of a potent and selective indole-based iHDAC8 (PCI-34051) created huge attention in the development of indole-based iHDAC. Our critical analysis has given important insights into the specific structural features of iHDAC8 and selectivity over other HDACs (HDAC1, 2, 3 and 6). The present work also aims at predicting/screening selective inhibitors against HDAC8 with the QAAR models. The developed QAAR models may be used in future design as well as the prediction of HDAC8 inhibitory activities of indole derivatives and others.

1. Introduction

HDACs are a group of reversible enzymes, responsible for the removal of acetyl group from lysine residue in the NH_2 terminal tail of core histone and non-histone protein (tubulin and p53) [1,2]. This process tightens the interaction between the positively charged histone and the negatively charged DNA that helps in chromatin folding and repression of mRNA synthesis and finally prevents the gene expression [1]. HDACs work collectively with HAT (histone acetyltransferases) in the deacetylation and acetylation of histone protein and play critical role because of their involvement in gene expression, cellular differentiation, proliferation, protein DNA interaction, post translational modification (PTM), senescence and finally in apoptosis [3–5]. It was seen that hypoacetylation is the reason of transcriptional repression and further hyperacetylation is correlated with transcriptional activation. Deregulation of HDACs and HAT causes pathological problem of different types of disease like cancer, neurodegeneration, cardiovascular disease and inflammatory diseases. Due to this reason, inhibitor of HDACs (iHDAC) illustrate a new novel class of drugs for treatment of cancer in chemotherapy [3,6,7]. HDACs are divided into mainly four classes. These divisions are done on their amino acid residue, catalytic activity and location in cell. Class I contains HDAC1, 2, 3 and 8, while class II is subdivided into class IIa and IIb, where HDAC4, 5, 7 and 9 are allocated into class IIa and class IIb comprising of HDAC6 and 10. Further, class III contains sirtuins and class IV includes HDAC11 [2,8-14]. The iHDAC successfully inhibit the deacetylation of histone proteins and leading to chromatin condensation and repression of gene expression (Fig. 1).

A number of iHDACs have been identified and approved by the United States Food and Drug Administration (US-FDA). The first iHDAC that received approval of US-FDA was Vorinostat (SAHA) in 2006 for the treatment of cutaneous T cell lymphoma. Other US-FDA approved iHDACs are Belinostat (PXD101), Panabinostat (LBH589), Romidepsin, while Chidamide (HBI8000) has been approved by Chinese FDA [7]. However, nowadays numerous academic groups a as well as pharmaceutical companies have begun to focus on the designing of isoform selective iHDACs.

* Corresponding authors.
E-mail addresses: pharmacist.amin@gmail.com (Sk.A. Amin), tjupharm@yahoo.com (T. Jha), shovanlal.gayen@gmail.com (S. Gayen).
# Authors have equal contribution

https://doi.org/10.1016/j.molstruc.2022.133967
0022-2860/

Annexure 12

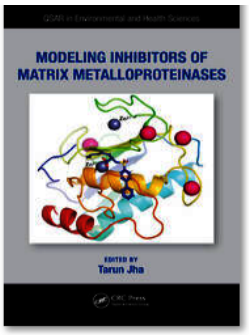

Chapter

2D-QSAR Studies

Regression and Classification-Based QSAR Studies

By Sanjib Das, Sk. Abdul Amin, Shovanlal Gayen, Tarun Jha

Book Modeling Inhibitors of Matrix Metalloproteinases

Edition	1st Edition
First Published	2023
Imprint	CRC Press
Pages	29
eBook ISBN	9781003303282

ABSTRACT

In this chapter, the implication of 2D-QSAR in drug design and discovery is explained in detail. Various types of QSAR methodologies, such as linear regression-dependent QSARs (namely 2D-QSAR, linear discriminant analysis), as well as non-linear QSARs (namely artificial neural network, support vector machine, Bayesian classification, and recursive partitioning), are described. The implication of descriptors and statistical validation metrics is explained in detail. In addition, various types of software useful in performing such QSAR analysis are also mentioned. This chapter clearly illustrates the 2D-QSAR methodologies aiding in drug discovery processes.

Annexure 13

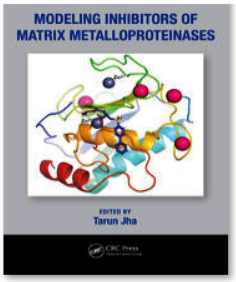

Other Modeling Approaches

Pharmacophore Mapping, Molecular Docking, and Molecular Dynamic Simulation Studies

By Sk. Abdul Amin, Shovanlal Gayen, Sanjib Das, Tarun Jha

Book Modeling Inhibitors of Matrix Metalloproteinases

Edition	1st Edition
First Published	2023
Imprint	CRC Press
Pages	33
eBook ISBN	9781003303282

Share

ABSTRACT

In this chapter, the application of other molecular modeling techniques (namely ligand- and structure-based pharmacophore mapping followed by virtual screening as well as molecular docking and molecular dynamics simulation) in drug design and discovery are discussed in detail. Currently, such types of molecular modeling studies not only strengthen conventional QSAR and related drug designing strategies but also offer a new avenue in the binding mode of interaction analysis followed by the screening of appropriate drug molecules from databases and proper pharmacophoric features of ligands/molecules to get relevant ideas regarding structures and functions for designing potential and effective bioactive compounds.

Annexure 14

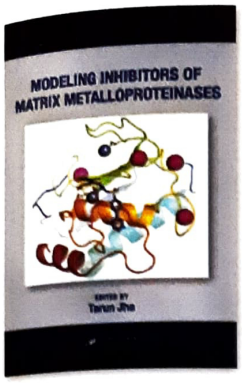

Chapter

Gelatinases and Their Inhibitors

By Sk. Abdul Amin, Sanjib Das, Shovanlal Gayen, Tarun Jha

Book Modeling Inhibitors of Matrix Metalloproteinases

Edition	1st Edition
First Published	2023
Imprint	CRC Press
Pages	35
eBook ISBN	9781003303282

ABSTRACT

Gelatinases, also called matrix metalloproteinase-2 (MMP-2) and matrix metalloproteinase-9 (MMP-9), have been targets of choice for drug development for many years. Therefore, their inhibitors may serve as an important weapon against cancer, neurological conditions, and lung diseases, as well as cardiovascular disease prevention and treatment. In this chapter, the structure, as well as the function of gelatinases, are discussed. Various gelatinase inhibitors with different zinc-binding groups (ZBGs) and non-zinc binding characters are illustrated. This chapter summarizes potent gelatinase-selective inhibitors. The prime objective is to give an overview and detailed insight into these gelatinase inhibitors to the scientific community to allow further development. This is a part of the continuous efforts toward the identification of potent gelatinase-selective inhibitors. This chapter provides crucial insights to explore inhibitors for future endeavors to speed up drug discovery efforts.

Sanjib Das
08/05/2024

Sanjib Das
06/05/24

Tarun Jha
6.5.2024

TARUN JHA, Ph.D
Ex-Professor
Dept. of Pharm. Tech.
Jadavpur University
Kolkata-700 032

Shovanlal Gayen
6.5.24

DR. SHOVANLAL GAYEN
Assistant Professor
Dept. of Pharmaceutical Technology
Jadavpur University
Kolkata - 700 032, INDIA